

ANNUAL REPORTS ON NMR SPECTROSCOPY

Volume 29



ACADEMIC PRESS

ANNUAL REPORTS ON

NMR SPECTROSCOPY

This Page Intentionally Left Blank

ANNUAL REPORTS ON
NMR SPECTROSCOPY

Edited by

G. A. WEBB

Department of Chemistry, University of Surrey, Guildford, Surrey, England

VOLUME 29



ACADEMIC PRESS

Harcourt Brace & Company, Publishers

London • San Diego • New York
Boston • Sydney • Tokyo • Toronto

ACADEMIC PRESS LIMITED
24-28 Oval Road,
LONDON NW1 7DX

U.S. Edition Published by

ACADEMIC PRESS INC.
San Diego, CA 92101

This book is printed on acid free paper

Copyright © 1994 ACADEMIC PRESS LIMITED

All Rights Reserved

No part of this book may be reproduced or transmitted in any form or by any means, electronic or mechanical including photocopying, recording, or any information storage and retrieval system without permission in writing from the publisher

**A catalogue record for this book is available from the
British Library**

ISBN 0-12-505329-0
ISSN 0066-4103

Phototypesetting by Keyset Composition, Colchester, Essex
Printed by TJ Press Ltd, Padstow, Cornwall

List of Contributors

Tetsuo Asakura, *Department of Biotechnology, Tokyo University of Agriculture and Technology, Koganei, Tokyo 184, Japan.*

D. B. Chesnut, P. M. Gross *Chemical Laboratory, Duke University, Durham, North Carolina 27708, USA.*

I-Ssuer Chuang, *Department of Chemistry, Colorado State University, Fort Collins, Colorado 80523, USA.*

T. A. Cross, *National High Magnetic Field Laboratory, Institute of Molecular Biophysics and Department of Chemistry, Florida State University, Tallahassee, Florida 32306, USA.*

Makoto Demura, *Department of Biotechnology Tokyo University of Agriculture and Technology, Koganei, Tokyo 184, Japan.*

Angel C. de Dios, *Department of Chemistry, University of Illinois at Urbana-Champaign, 505 South Mathews Avenue, Urbana, Illinois 61801, USA.*

Tetsuo Hayashi, *Plastics Research Laboratory, Tokuyama Corp. Ltd, 1-1 Harumi-chou, Tokuyama, Yamaguchi 745, Japan.*

Cynthia J. Jameson *Department of Chemistry M/C 111, University of Illinois at Chicago, 845 W. Taylor, Chicago, Illinois 60607, USA.*

Gary E. Maciel, *Department of Chemistry, Colorado State University, Fort Collins, Colorado 80523, USA.*

Graeme Moad, *CSIRO, Division of Chemicals and Polymers, Private Bag 10, Clayton, Victoria 3168, Australia.*

This Page Intentionally Left Blank

Preface

The NMR chemical shift and the information it can provide on structure and environment is admirably reviewed by Professor C. J. Jameson and Dr A. C. DeDios in the first chapter of the present volume of *Annual Reports on NMR*. This is a welcome complement and extension of the review by Professor Jameson and Dr H. J. Osten in Volume 17 of this series. Following this is a very interesting account of *ab initio* calculations of NMR chemical shieldings, by Professor D. B. Chesnut which builds on his previous review in Volume 21 of *Annual Reports on NMR*.

The remaining four chapters cover various aspects of applications of NMR to polymers. Professor T. A. Cross reviews applications of solid state NMR to the structures of peptides and proteins in synthetic membrane environments. This is followed by an account of the NMR characterization of complex organic resins by Dr I-Ssuer Chuang and Professor G. E. Maciel. Dr G. Moad covers applications of labelling and multidimensional NMR in the characterization of synthetic polymers and the final chapter is by Professor T. Asakura, Dr M. Demura and Dr T. Hayashi who deal with ^{13}C NMR assignments of polyolefines and olefine copolymers based on ^{13}C NMR chemical shift calculations and 2D INADEQUATE data.

It is a very great pleasure for me to have the opportunity to thank all of these contributors for the preparation and timely submission of their reviews and the staff at Academic Press (London) for their help and co-operation in the production of this volume.

University of Surrey
Guildford, Surrey
England

G. A. WEBB

This Page Intentionally Left Blank

Contents

List of Contributors	v
Preface	vii

The NMR Chemical Shift: Insight into Structure and Environment **1** ANGEL C. de DIOS and CYNTHIA J. JAMESON

1. Introduction	2
2. Shielding surfaces	4
3. Dynamic averages on shielding surfaces, comparisons with experiments	29
4. Applications to more complex systems	51
5. Conclusions	63
Acknowledgement	64
References	64

***Ab Initio* Calculations of NMR Chemical Shielding** **71** D. B. CHESNUT

1. Introduction	71
2. The general problem	72
3. Basic theory	75
4. Self-consistent field approaches.	82
5. Effects of correlation	106
6. Concluding remarks	118
References	119

Structural Biology of Peptides and Proteins in Synthetic Membrane Environments by Solid-state NMR Spectroscopy **123** T. A. CROSS

1. The new frontiers in structural biology	124
2. Molecular examples	129
3. Other experimental techniques in structural biology	132
4. Solid-state NMR	135
5. Applications	144
6. Conclusions	161
Acknowledgements.	161
References	161

169

NMR Characterization of Complex Organic Resins
I-SSUER CHUANG and GARY E. MACIEL

1. Introduction	170
2. Solid-state NMR	171
3. Solid-state NMR characterization of complex organic resins	179
4. Resins in polymer blends and composite materials	271
References	274

287

**Applications of Labelling and Multidimensional NMR in the Characterization
of Synthetic Polymers**
GRAEME MOAD

1. Introduction	287
2. Chemical microstructure structure of polymer chains	288
3. Synthesis of labelled monomers	296
4. Detection and quantitation of polymer end-groups	297
5. Synthesis of labelled initiators	318
Acknowledgements	318
Abbreviations	318
References	319

325

**¹³C NMR Assignments of Polyolefines and Olefine Copolymers Based
on the ¹³C NMR Chemical Shift Calculations and
2D INADEQUATE NMR**
TETSUO ASAKURA, MAKOTO DEMURA and TETSUO HAYASHI

1. Introduction	326
2. Calculation	328
3. NMR observation	338
4. Polyolefines	339
5. Ethylene-olefine copolymers	370
6. Conclusion	401
Acknowledgements.	401
References	401

Index	405
-----------------	-----

The NMR Chemical Shift: Insight into Structure and Environment

ANGEL C. de DIOS

Department of Chemistry, University of Illinois at Urbana-Champaign, 505 South Mathews Avenue, Urbana, Illinois 61801, USA

CYNTHIA J. JAMESON

Department of Chemistry M/C 111, University of Illinois at Chicago, 845 W. Taylor, Chicago, Illinois 60607, USA

1. Introduction	2
2. Shielding surfaces	4
2.1. Intramolecular shielding surfaces	5
2.1.1. Dependence on bond length in diatomic molecules	5
2.1.2. Bond extension and angle deformation in small molecules	7
2.1.3. Dihedral angle	12
2.1.4. Remote bond extension	17
2.2. Intermolecular shielding surfaces	19
2.2.1. Distance dependence	19
2.2.2. Scaling of intermolecular shielding	21
2.2.3. Additivity and non-additivity	22
2.2.4. Hydrogen bonding	22
2.3. Electric field effects and dispersion contributions	25
2.4. Is there a global shape for the traces on shielding surfaces?	27
3. Dynamic averages on shielding surfaces, comparisons with experiments	29
3.1. The temperature dependence of the shielding in a molecule	30
3.2. Isotope effects	34
3.3. Intermolecular shifts	39
3.3.1. The chemical shift in the gas phase	40
3.3.2. The average chemical shifts of Xe in zeolites	42
3.3.2. Gas-to-liquid and gas-to-solution shifts	47
4. Applications to more complex systems	51
4.1. Separation of short-range and long-range effects on shielding	51
4.2. Use of scaling and additivity	54
4.3. Use of electric field effects and dynamic averaging	58
4.4. Predicting shifts in complex systems from shielding surfaces of model systems	60
5. Conclusions	63
Acknowledgement	64
References	64

1. INTRODUCTION

The NMR chemical shift is well known to be extremely sensitive to the environment of the nucleus. The chemical shift of a methyl proton is in a region of the proton shift that is well separated from the chemical shift of a proton in a CH_2 group, for example. Furthermore, the two protons in a CH_2 group could have distinct chemical shifts depending on the immediate neighbouring atoms of each proton. The ease of discrimination between *cis* and *trans*, *syn* and *anti* even under the lower resolution of the early spectrometers, was well known. With present-day instrumentation even subtle differences are easily observed. The NMR chemical shift discriminates between S and R enantiomers in a chiral solvent and between the various alanine residues in the same protein molecule, for example. There is no other property that has this degree of sensitivity to the electronic environment. In condensed phases there are gas-to-liquid shifts or solvent shifts, matrix-induced chemical shifts, site-dependent shielding tensors in crystalline solids, and adsorption shifts for molecules on surfaces. The Xe chemical shift of xenon gas trapped in the channels and cages of zeolites exhibits large changes with type of zeolite, and for the same zeolite it is found to be extremely dependent on the amount of adsorbed xenon, changing with loading in a way that is unique for each zeolite type so that such behaviour serves as a fingerprint of zeolites. There are no changes in molecular geometry or bonding involved here, merely the effects of neighbouring atoms on the Xe chemical shift, that is, the oxygen atoms of the framework, the counter-ions, and the other Xe atoms that it encounters in the intrazeolitic pores. Even where the average distance between neighbouring atoms is extremely large, as in the dilute gas phase, the NMR chemical shift is found to change with this average distance, exhibiting a dependence on the density and the temperature. This second virial coefficient of shielding can be measured more accurately than the second virial coefficient of any other molecular electronic property. When the chemical shift in a molecule in the gas phase is extrapolated to zero density, one would expect to obtain the chemical shift of an effectively isolated molecule, with no neighbour effects. This too is found to be changing with temperature. Furthermore, when a molecule is observed in the same solution with its deuterated counterpart, a nucleus in the heavier isotopomer is usually more shielded than the same nucleus in the lighter isotopomer. This isotope shift is sometimes observed even when the NMR nucleus and the site of isotopic substitution are separated by several bonds, as many as nine or more bonds, the signs and magnitudes of the isotope shifts changing across the periodic table.

How do we explain these observations? We shall see that these phenomena are due to the dependence of the nuclear shielding on the configuration of the nuclei, the distances between them, the bond angles and

torsion angles between them; in other words, we shall consider the multidimensional shielding surface which describes the variation of the shielding with nuclear positions, analogous to the potential energy multidimensional surface. Not only is the value on this shielding surface at the minimum energy (equilibrium) geometry closely associated with the value that is observed, but the averaging over this surface during the rotation, vibration, and translational motions of the nuclei determines the shielding value that is observed. The observed chemical shift is averaged not only over all the populated rovibrational states, torsions and librations, but also over all the ensembles of the molecule with its neighbours in the gas or solution or adsorbed fluid on a heterogeneous surface. No other molecular electronic property has been characterized so well in terms of the virial coefficients, the mass dependence, and the temperature dependence. The ultra-high resolution afforded by the NMR measurement combined with the exquisite sensitivity of the shielding together make it possible to characterize this molecular property in detail experimentally. The change of the electric dipole polarizability with internuclear separation in a rare gas pair, for example, is one of the "pair interaction properties" that serve very well as tests of theories and physical models but are very difficult to measure. Contrast this with the ^{129}Xe shielding as a function of density and temperature in the dilute gas. Few property surfaces have been explored in their dependence on intramolecular nuclear coordinates. The only electronic property that has a well-known dependence on bond length is the dipole moment, and then only for a diatomic molecule. The experimental observations of the temperature dependence in the rotating-vibrating isolated molecule and the changes upon substitution of a remote atom by a heavier isotope are well characterized in the chemical shift, unlike any other molecular electronic property. The theories associated with the rovibrational averaging of any electronic property can be tested for this property, where both experiments and theoretical calculations are feasible. In other words, the NMR shielding serves as a paradigm for the exploration of the dependence of a molecular electronic property on intramolecular coordinates and masses, as well as intermolecular separations, dependence on the temperature, electric fields and field gradients, and grand ensemble configurations.

In this review we will consider nuclear shielding surfaces in simple systems: diatomic molecules to focus on the variation with bond length, H_2O , NH_3 , PH_3 and CH_4 to consider bond angles and bond lengths, CH_3CH_3 through isobutane to see the dihedral angle dependence and bond angle effects. The variations with ϕ , ψ and χ angles are explored in various model peptides, and finally the remote bond stretches. Following the intramolecular shielding surfaces we move on to intermolecular shielding in atom-atom pairs, atom-ion, and atom-molecule pairs, and clusters of three or more, including up to five or 16 polar solvent molecules. The effects of

electric fields and electric field gradients on shielding are considered separately. Finally we tie these all together in an examination of possible global shapes of the traces on shielding surfaces. Dynamic averages over these surfaces are necessary for comparisons with experiment. Here we show the origin of the temperature dependence, the isotope shifts, the shifts with density and solvent, and hydrogen-bonding shifts. Ensemble averages are sometimes necessary to account properly for the observed cluster shifts and the average chemical shifts under fast exchange in porous media. Finally, we consider the prognosis for more complex systems. What can we say, in general, from the studies on these systems that may shed some light on shielding in more complex systems? How may the methods applicable to small systems be brought to bear on the prediction of chemical shifts in complex materials such as proteins where some electrostatics, some hydrogen bonding, some local bond angle and torsional constraints, and some long-range contributions apply?

2. SHIELDING SURFACES

A shielding surface is a mathematical surface providing the nuclear shielding value (usually the isotropic average over all magnetic field directions, but may also be an individual tensor component) as a function of the nuclear coordinates of the system. In the case of an isolated molecule, the intramolecular shielding surface is usually expressed in terms of nuclear displacement coordinates, such as curvilinear internal coordinates or the symmetry adapted linear combinations of these, the symmetry coordinates. In the case of intermolecular shielding surfaces, the internal coordinates of the supermolecule are used and the shielding is expressed relative to the completely separated interacting molecules including counterpoise corrections. The theoretical shielding surfaces that will be discussed in this review have been calculated using a variety of methods. The conventional Coupled Hartree Fock (CHF) method involves using a common gauge origin in the calculation and generally requires a larger set of basis functions to achieve the gauge independence. This method has been developed by Stevens, Pitzer and Lipscomb,¹ and by Lazzeretti and Zanasi.² At the next level the common origin method is employed in Second Order Polarization Propagation Approach (SOPPA) primarily by Oddershede and coworkers³ and in Coupled MP2 by Bishop and Cybulski,⁴ traditionally using large basis sets to achieve gauge independence. There are several distributed gauge origin approaches: the localized orbital local origin method (LORG) devised by Hansen and Bouman,⁵ and its correlated level called SOLO (Second Order LORG),⁶ the Individual Gauge for Localized Orbitals (IGLO) which has been developed by Schindler and Kutzelnigg,⁷ and its correlated version MC-IGLO by van Wüllen and Kutzelnigg,⁸ and a third method, Gauge-

including Atomic Orbitals (GIAO) originally introduced by Ditchfield,⁹ used extensively by Chesnut, made more efficient by Wolinski, Hinton and Pulay,¹⁰ and rederived especially for correlated calculations by Gauss in MP2-GIAO.¹¹ The review by Chesnut in this volume¹² discusses the recent developments in these *ab initio* methods, and is not a subject of the present review. Our main concern is the resulting shielding surfaces, calculated by one of these methods at some appropriate basis set size. Theoretical calculations of nuclear shielding surfaces for small molecules have been reviewed recently.¹³

2.1. Intramolecular shielding surfaces

2.1.1. Dependence on bond length in diatomic molecules

The first complete shielding surface was calculated for the H_2^+ molecule by Hegstrom.¹⁴ This surface showed the nuclear shielding for the separated atoms, all the way from 22 a.u. to the united atom, which in this case was an He^+ ion. From the large positive united atom value, the shielding is found to decrease until it reaches a minimum which occurs at an internuclear separation much longer than the equilibrium bond length and proceeds to the limiting value at infinite separation. Prior to this complete surface, however, the behaviour of the shielding in diatomic molecules in the immediate vicinity of the equilibrium geometry had already been discovered in the calculations by Stevens and coworkers for LiH ,¹⁵ HF ,¹⁶ CO ,¹⁷ and N_2 .¹⁸ The derivative of the shielding with bond distance was found to be negative in all cases except for the Li nucleus in LiH . Ditchfield's calculations of shieldings in the vicinity of the equilibrium bond length verified these results for LiH and for HF , and in addition provided similar results for the H_2 molecule.¹⁹ Chesnut evaluated first derivatives of the shielding for the first- and second-row hydrides and found similar results for H_2 , HF and HCl : NaH behaved similarly to LiH ²⁰ and the second derivatives in HCl and HF ,²¹ as well as CO , N_2 , CN^- , and F_2 ,²² were also negative for all nuclei. That is, both nuclei in the diatomic molecule become deshielded as the bond lengthens, with the exception of the Li and the Na nuclei in LiH and NaH . The unusual behaviour of the alkali nuclei remained a puzzle until the complete shielding surface of the NaH molecule was calculated by Jameson and de Dios.²³ The complete surface for ^{23}Na in the NaH molecule looks very similar to the shielding surface for the H_2^+ molecule, as shown in Fig. 1. The equilibrium internuclear separation occurs at a bond length shorter than that separation at which the shielding is a minimum in H_2^+ , as it does for the nuclei in diatomic molecules mentioned above and also for ClF .²³ On the other hand, the equilibrium internuclear separation occurs at a distance longer than that for the minimum in the shielding surface of the Na nucleus in the NaH molecule.

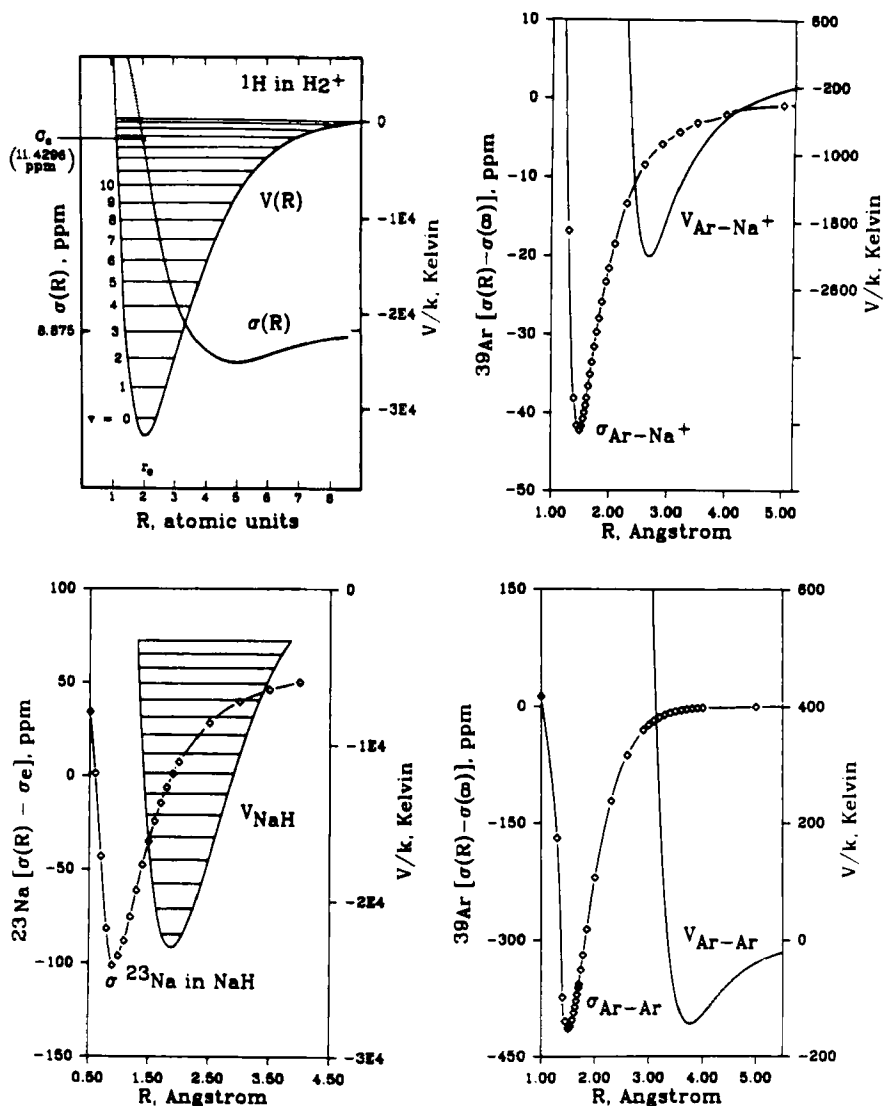


Fig. 1. Nuclear shielding surfaces from *ab initio* calculations. Reproduced from Ref. 23, with permission. The H_2^+ surface is from Hegstrom,¹⁴ the ^{23}Na in NaH surface is from Ref. 23, and the ^{39}Ar in $\text{Ar}-\text{Na}^+$ and $\text{Ar}-\text{Ar}$ intermolecular shielding surfaces are from Ref. 24. The last three were calculated using the LORG method.²⁵ The corresponding potential energy surfaces are from Wind,²⁶ Giroud and Nedelec,²⁷ Viehland,²⁸ and Aziz and Chen,²⁹ respectively.

2.1.2. Bond extension and angle deformation in small molecules

For triatomic and larger polyatomic molecules, the shielding surface is of higher dimension. The surface is best expressed in the nuclear displacement coordinates of the molecule, such as symmetry coordinates. Derivatives evaluated at the equilibrium geometry are, of course, easily converted from one set of coordinates to another. Examination of the details of the shielding surface is best carried out by displaying traces on the surface corresponding to keeping some of the coordinates constant. This was done for the first time by Raynes and coworkers for the nuclei in the H_2O molecule,³⁰ followed by the nuclei in the CH_4 molecule.³¹ Jameson, de Dios and Jameson calculated the shielding surfaces for the N nucleus in NH_3 ³² and P in PH_3 .³³ In these calculations the inversion coordinates of both NH_3 and PH_3 were explored over a wide range of values.^{32,33} When examined together (Fig. 2), these four surfaces have some features in common. The shielding of the non-H nuclei uniformly decreases with an increase in the symmetric stretch coordinate. The asymmetric stretch coordinates and the asymmetric angle deformation coordinates have zero first derivatives by symmetry, and therefore these traces are symmetric functions with respect to positive or negative displacements away from the equilibrium coordinates. They are concave in opposite directions. One (the asymmetric stretch) is concave downward (deshielding with increasing displacement from equilibrium), whereas the other (the asymmetric angle bend) is concave upward (increasing shielding with increasing displacement from equilibrium). A very interesting result is found when the variation of the shielding with respect to the opening of the bond angle is examined in the H_2O , NH_3 , and PH_3 molecules, the bond lengths being kept constant. This trace on the shielding surface is concave upward and has its minimum shielding at the tetrahedral angle.³³ Chesnut had reported some calculations in which the bond lengths are continuously optimized while the bond angle is varied. This is of course a more complicated representation in that both bond length and bond angle are changing at once. Nevertheless, he finds that the shielding surfaces are concave upwards and in H_2S the surface is very flat from 90° to 140° in this representation and for PH_3 his minimum also occurs at the tetrahedral angle.²⁰ The equilibrium angle for H_2O and NH_3 is very close to tetrahedral, whereas for H_2S , H_2Se , and PH_3 it is less than tetrahedral. H_2Se and PH_3 shielding surfaces have a sizeable slope at the equilibrium bond angle.^{33,34}

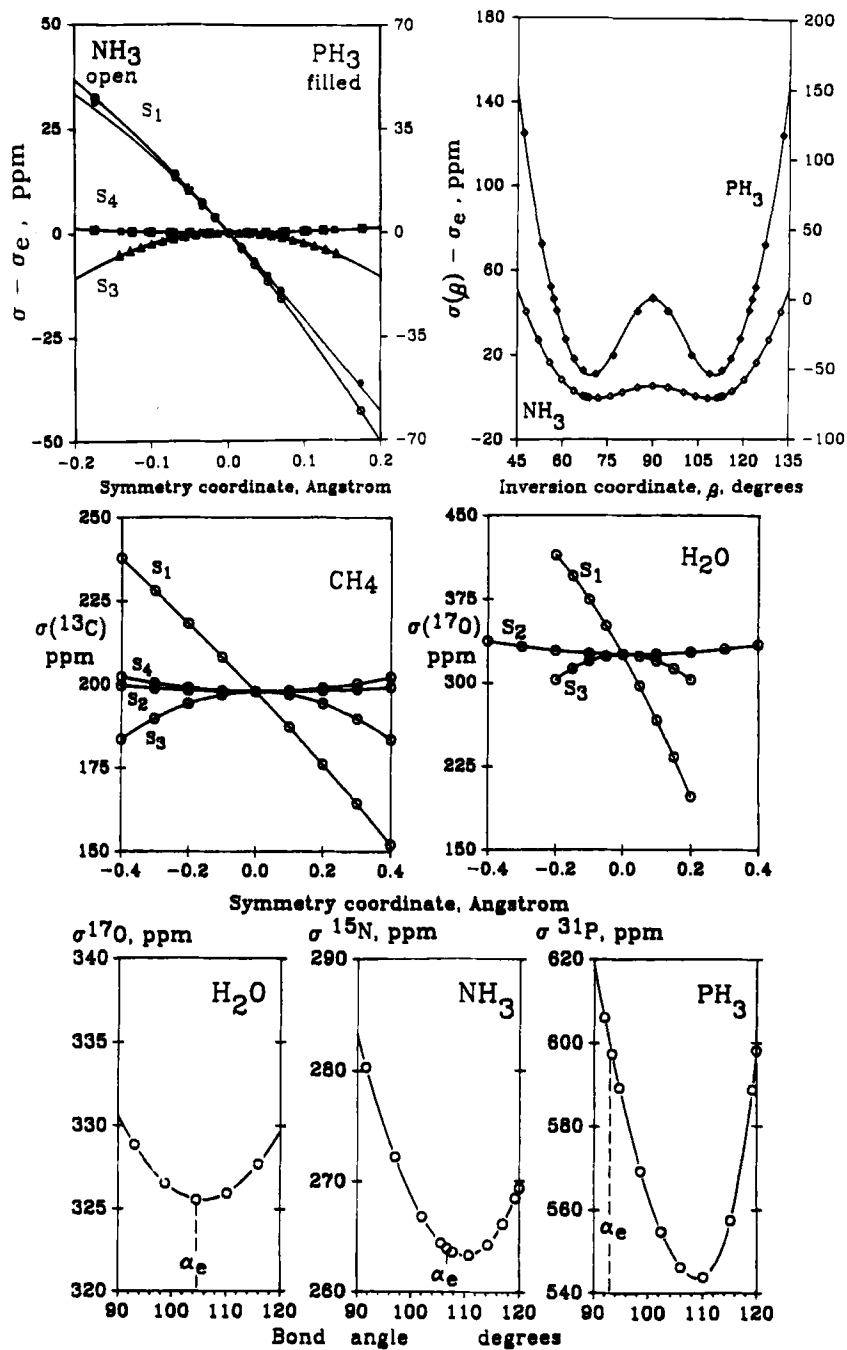
Other molecules have only been studied in terms of the derivatives of the shielding with respect to bond extension at the equilibrium geometry. The first derivatives of the shielding with respect to bond lengthening in the first- and second-row hydrides were calculated by Chesnut.²⁰ Be in BeH_2 , Mg in MgH_2 , B in BH_3 and Al in AlH_3 , all were found to have positive derivatives. The first derivatives of the non-H nuclear shielding in these

hydrides changed smoothly in going from left to right in the Periodic Table, rising to a maximum at group 2 and dropping to large negative values toward group 7. This smooth change has been explained²³ as we shall find in a later section of this review. A comprehensive survey of first and second derivatives of the shielding for molecules containing first-row atoms by Chesnut and Wright³⁵ confirmed earlier predictions. In discussing these we make a distinction of primary (with respect to the stretch of the bond to the nucleus in question) and secondary (with respect to the stretch of a remote bond) derivatives:

- (1) Most of the primary first derivatives are negative, that is, a nucleus tends to become deshielded upon extension of a bond in which it is involved. In this study, only 13 out of about 270 primary first derivatives were found to be positive. Negative derivatives ranged from -4 to $-2784 \text{ ppm } \text{\AA}^{-1}$. The few positive derivatives ranged from $+0.3$ to $+39.0 \text{ ppm } \text{\AA}^{-1}$.
- (2) The derivatives with respect to extension of a multiple bond are generally larger than those involving the extension of a single bond.
- (3) The shielding derivatives with respect to extension of a bond to hydrogen are generally smaller than those involving extension of bonds to heavy atoms.
- (4) The paramagnetic terms dominate the shielding derivatives.
- (5) The shielding derivatives of non-hydrogen nuclei tend to parallel the equilibrium isotropic shielding itself, independent of the nuclear species involved, that is, the shielding derivative decreases algebraically as the isotropic shielding of the nucleus decreases, but especially so for multiple bonds. An example is shown in Fig. 3.

It should be noted that all these general trends had already been proposed much earlier by Jameson³⁶⁻³⁸ and by Jameson and Osten^{39,40} (see Ref. 40 for references) in their interpretation of the very large body of experimental isotope shift data and the temperature dependence of the chemical shifts in the zero-pressure limit of ^{19}F in several molecules and ^{13}C in CO and CO_2 , ^{15}N in N_2 and NNO . Indeed it was the general trends in the experimental data that formed the basis for the interpretation. While the rovibrational averaging theory was complete, the experimental data could not be inverted

Fig. 2. Traces on the shielding surfaces of ^{17}O in the H_2O molecule,³⁰ ^{13}C in CH_4 ,³¹ ^{15}N in NH_3 ,³² and ^{31}P in PH_3 .³³ The symmetry coordinate S_1 is the totally symmetric stretch, S_2 is the symmetric angle deformation or the inversion coordinate (in the case of NH_3 and PH_3). S_3 and S_4 are the asymmetric stretches and angle deformations, respectively.



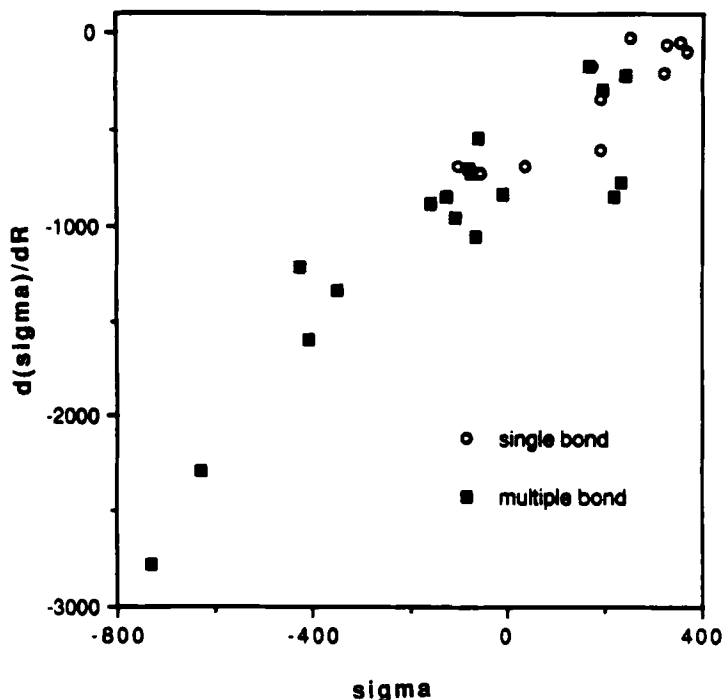


Fig. 3. The first derivatives of the ^{17}O shielding with respect to extension of the bond correlates with the absolute shielding. Reproduced from Ref. 35 with permission of John Wiley & Sons, Inc. Copyright © 1991 John Wiley & Sons, Inc. These are *ab initio* values calculated using the GIAO method.

to provide more than the empirical derivatives $(\partial\sigma^X/\partial r_{AX})_{\text{eq}}$. The ability of local origin methods to describe adequately the shielding even with modest basis sets has now made possible the theoretical investigations of these earlier conclusions and to find their limitations and conditions of applicability.³⁵ Furthermore, Chesnut's survey of shielding derivatives offers new information about second derivatives $(\partial^2\sigma^X/\partial r_{AX}^2)_{\text{eq}}$. Most of the second derivatives are negative, that is, a nucleus tends to become deshielded upon bond extension in a more pronounced way than linearly. Of the 210 second derivatives, 42 were found to be positive (these involved proton shieldings in most cases). Second derivatives are not small, that is, the trace along the shielding surface corresponding to a symmetric stretch of the bonds is not linear at the point corresponding to the equilibrium geometry of the molecule.

The shielding dependence on bond length has also been examined in model fragments (*N*-formyl-L-amino acid amide) for glycine, alanine and valine residues in proteins.⁴¹ Likewise, in these model compounds, the first

and second derivatives of the C^α chemical shielding with respect to its bond lengths, $C^\alpha-N$, $C^\alpha-C^O$, $C^\alpha-H^\alpha$ and $C^\alpha-C^\beta$ (for alanine and valine) are found to be negative. The magnitudes of these derivatives were sufficiently large (40–90 ppm \AA^{-1}) to permit an evaluation of the spread of bond length values for a particular residue reported in X-ray structures of proteins.⁴² After considering the range of chemical shift inequivalencies observed in proteins, it has been deduced that the differences in bond lengths currently reported in X-ray structures are too large to be consistent with NMR data.

An interesting observation that can be made from these studies is the apparent transferability of these shielding derivatives from one amino acid to another. Both alanine and valine have very similar first derivatives for the shielding of C^α with respect to the $C^\alpha-N$ stretch (Ala; $-88 \text{ ppm } \text{\AA}^{-1}$, Val; $-84 \text{ ppm } \text{\AA}^{-1}$), $C^\alpha-C^O$ (Ala; $-57 \text{ ppm } \text{\AA}^{-1}$, Val; $-60 \text{ ppm } \text{\AA}^{-1}$), and $C^\alpha-C^\beta$ (Ala; $-16 \text{ ppm } \text{\AA}^{-1}$, Val; $-17 \text{ ppm } \text{\AA}^{-1}$). On the other hand, even though glycine lacks C^β , its derivatives are not too far from alanine and valine: $C^\alpha-N$ ($-69 \text{ ppm } \text{\AA}^{-1}$) and $C^\alpha-C^O$ ($-48 \text{ ppm } \text{\AA}^{-1}$). The glycine derivatives being numerically 80% of the alanine and valine derivatives may reflect in the ground-state vibrational corrections as pointed out by Laws *et al.*⁴²

The corresponding C^β shielding derivatives also show some interesting characteristics. First of all, the first derivatives of C^β shielding with respect to the bond lengths $C^\alpha-N$ and $C^\alpha-C^O$ were found to be positive in sign.⁴¹ On the other hand, its derivative with respect to $C^\alpha-H^\alpha$ is still negative but an order of magnitude smaller ($-7 \text{ ppm } \text{\AA}^{-1}$ for C^β compared to $-57 \text{ ppm } \text{\AA}^{-1}$ for C^α). The dependence of the C^β shielding on the bond length $C^\alpha-C^\beta$ appears to be normal. It is noteworthy, however, that the two model fragments, alanine and valine, differ greatly in magnitude in terms of this shielding derivative. Alanine has $-36 \text{ ppm } \text{\AA}^{-1}$ for $\partial\sigma^{C^\beta}/\partial r(C^\alpha-C^\beta)$ while valine has $-69 \text{ ppm } \text{\AA}^{-1}$, nearly twice the value for alanine. This difference indicates that the presence of methyl groups on C^β in valine leads to a greater sensitivity of the C^β shielding to the $C^\alpha-C^\beta$ bond length. This is consistent with the well-known incremental effects of methyl substitution in deuterium-induced isotope shifts.

The dependence of shielding on bond angle as seen in small molecules is much more complicated than its dependence on bond length. In fact, using the first derivative of the shielding with respect to bond length normally would suffice. On the other hand, the shielding as a function of bond angle in Fig. 2 shows definite curvature. And as observed in the small hydrides (Fig. 2), an extremum (minimum shielding) is found near the tetrahedral value. Hence, in order to take into account bond angle influences on shielding, one needs to take into account higher-order derivatives. The same trends are seen in model fragments for amino acid residues in proteins. Glycine, for example, shows a minimum for the C^α shielding when the $N-C^\alpha-C^O$ angle is close to the tetrahedral value,⁴¹ the surprising feature

seen in small hydrides.³³ Alanine and valine also show a minimum, although at a smaller value of this angle.

Since the shielding derivatives with respect to bond angle changes are smaller in absolute terms compared to bond length derivatives, the experimental verification of the bond angle dependence of shielding is more difficult. It is unlikely for observed shielding changes to be dominated by bond angle contributions. The temperature dependence of the ^{15}N shielding in ammonia is indeed a rare case. In this molecule, it is the large-amplitude inversion motion that makes bond angle contributions to the observed temperature dependence significant.

2.1.3. Dihedral angle

In addition to the previously discussed bond length and bond angle dependencies, the chemical shielding also exhibits sensitivity to torsion angles. For example, the phenomenon called the γ -gauche effect, first discovered by Paul and Grant⁴³ in hydrocarbons, indicates that ^{13}C nuclei at γ -positions are ~ 5 ppm more shielded in a *gauche* than in a *trans* conformation. Moreover, Anet and Cheng⁴⁴ have also demonstrated that the α - and β -positions are likewise deshielded in the *trans* conformation. Recently, Webb and coworkers⁴⁵ have attempted to explain the observed γ -gauche effect using *n*-octane as a model compound. Their results indicated that the γ -position is indeed more shielded in the *gauche*-conformation, about 3 ppm compared to the *trans*-conformer. It is important to note that in these calculations, the bond lengths and bond angles were relaxed at each torsion angle. Hence, the changes in shielding may not be direct consequences of variations in the torsion angle. Prior to Webb's work, there have been a number of previous studies on how dihedral angles influence shielding. The simplest case of ^{13}C shielding dependence on dihedral angles is found in ethane where Chesnut *et al.*⁴⁶ have shown using the GIAO method that the ^{13}C nuclei in the eclipsed conformation are 4.66 ppm more shielded than in the staggered conformation. Geometry optimizations were also performed at each dihedral angle. Using calculated shielding derivatives with respect to bond length and bond angle changes and knowing how much these geometrical parameters had changed upon minimization, they were able to extract the change in shielding that can be directly attributed to the torsion angle variation. They arrived at the conclusion that nearly 90% of the change in shielding is due to torsion angle effect alone. IGLO calculations on ethane as reported by Kutzelnigg *et al.*⁴⁷ agree favourably with Chesnut's results. As in the earlier work, the contributions from relaxing the other geometrical parameters are also found to be very small. Barfield and coworkers have studied the influence of the torsion angle in a variety of hydrocarbons.^{48,49} In these investigations, geometry optimizations were also employed making it difficult to assign how much of the change in

shielding was directly caused by altering the dihedral angle. Geometry optimizations, in addition to being time-consuming, preclude a more specific analysis of torsion angle influences on shielding. Oldfield *et al.*^{41,50,51} have generated shielding traces and surfaces that map only the changes in shielding that are a direct consequence of a change in a given torsion angle in a series of compounds ranging from small hydrocarbons to peptide models like *N*-formyl-L-valine amide. These shielding surfaces, besides being free from geometry relaxation effects, surprisingly have been found to be sufficient in explaining ¹³C chemical shifts in proteins.⁵¹ The torsion angle dependence of shielding in small molecules is difficult to extract: it normally manifests itself in the temperature dependence of the chemical shift along with equally significant contributions from centrifugal distortion. In addition, a change in a dihedral angle manifests itself strongly in the overall shape of a small molecule thereby inducing additional effects from the environment. On the other hand, proteins serve as excellent systems for studying the torsion angle effects on chemical shifts for several reasons. Variable temperature studies are not necessary because a protein already provides sites that differ from each other primarily in torsion angles. Second, a protein being a large molecule assumes an overall shape which is not contingent on one particular torsion angle.

Focusing on the shielding of the nuclei at the α - and β -positions with respect to the dihedral angle of interest, interesting trends are apparent.⁵⁰ For small compounds that can be regarded as substituted ethane molecules, substitution at C^α causes a much larger change in the dihedral angle effects on C^β than on C^α shielding. χ^1 denotes the dihedral angle defined by $H^\alpha-C^\alpha-C^\beta-H^\beta$. For example, in the series of hydrocarbons: ethane, propane and 2-methylpropane, as shown in Fig. 4A, the C^α shieldings as functions of χ^1 are very similar. On the other hand, it is obvious from Fig. 4B that the sensitivity of the C^β shielding to χ^1 diminishes with methyl substitution at C^α . A similar situation exists when one introduces functional groups like $-C=O$ and $-NH_2$ on the C^α site.⁵⁰ The amino group is found to reduce significantly the sensitivity of the C^β shielding on the torsion angle while the C^α shielding function remains similar to that of the hydrocarbons. In proteins, if one can regard the amino acid residues as substituted ethanes, the presence of amide groups introduces two additional torsion angles that can influence the shieldings of C^α and C^β . These torsion angles are $\phi_{(i-1)C^O-iN-iC^\alpha-iC^O}$ and $\psi_{(iN-iC^\alpha-iC^O-i+1N)}$. In Fig. 5, the χ^1 dependence of the shielding in C^α and C^β sites of *N*-formyl-L-alanine amide at various ϕ and ψ angles is shown. The C^α shielding as a function of χ^1 does not seem to change shape with variations in ϕ and ψ as shown in Fig. 5A. On the other hand, C^β (Fig. 5B) behaves differently. First of all, its shielding is less sensitive to changes in χ^1 . It no longer resembles the shape of the potential function, the eclipsed conformation (0°) does not exhibit a maximum value for C^β shielding. In fact, when the torsion angle ϕ is

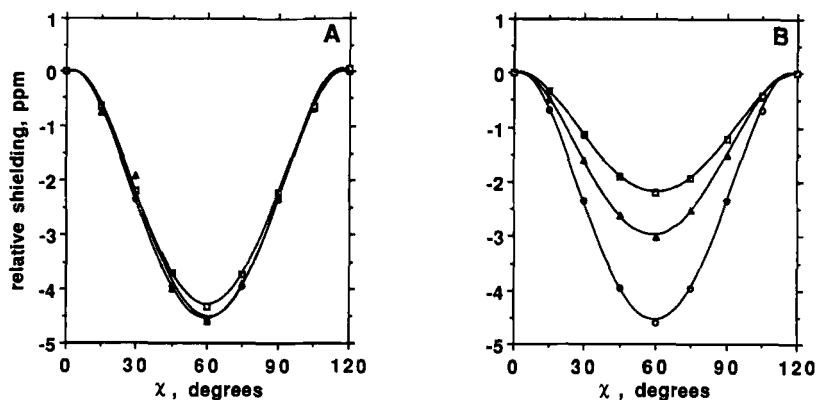


Fig. 4. Calculated ^{13}C shieldings as a function of the torsion angle, $\chi(\text{H}_1-\text{C}_1-\text{C}_2-\text{H}_2)$, with increasing methylation. (A) C_2 (C^α) shielding of ethane (\circ), propane (Δ), and isobutane (\square). (B) as in (A) but for (methyl) C_1 (C^β). Reproduced from Ref. 50, with permission. Copyright 1993, American Chemical Society.

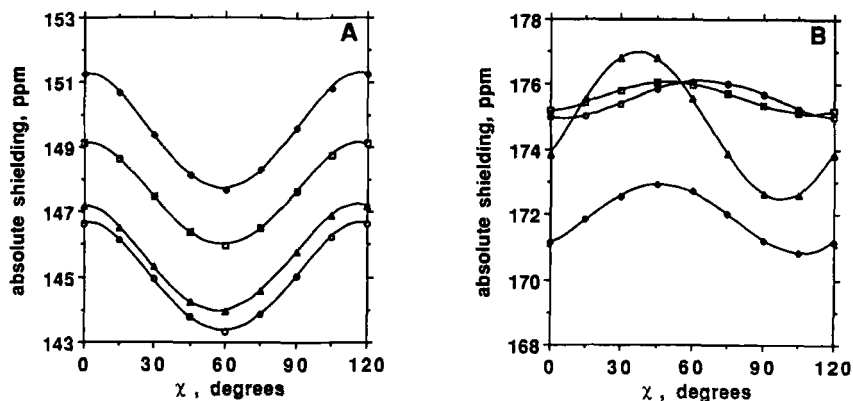


Fig. 5. Calculated ^{13}C shieldings as a function of the torsion angle, χ , for an alanine model fragment, at various ϕ and ψ angles. (A) C^α shielding for helix ($\phi = -58^\circ, \psi = -51^\circ$) (\circ), turn ($\phi = 55^\circ, \psi = 50^\circ$) (Δ), sheet 1 ($\phi = -140^\circ, \psi = 140^\circ$) (\diamond), and sheet 2 ($\phi = -71^\circ, \psi = 140^\circ$) (\square). (B) as in (A) but for (methyl) C^β . Reproduced from Ref. 50, with permission. Copyright 1993, American Chemical Society.

positive, the shielding function also loses a relative extremum at the staggered conformation (60°). Interestingly, positive ϕ angles correspond to conformations in which C^β is close to C^α . Secondly, the χ^1 dependence of the C^β shielding varies with ϕ and ψ . What is clear in both C^α and C^β pictures, however, is that the shielding inequivalencies observed between sheet and helical residues are dominated by ϕ and ψ effects. Since the range

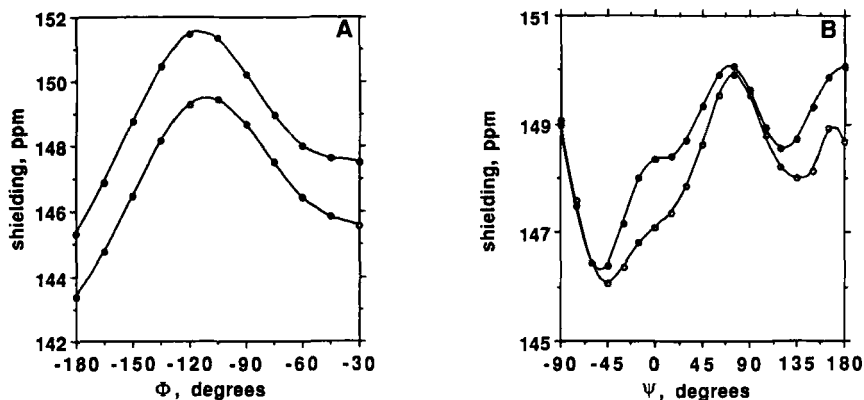


Fig. 6. (A) Calculated C α shielding for an alanine model fragment as a function of the torsion angle ϕ , at different ψ angles: $\psi = 60^\circ$ (\circ) and 135° (\bullet). (B) as in (A) but as a function of ψ , at different ϕ angles: $\phi = -60^\circ$ (\circ) and -150° (\bullet).

of ϕ and ψ values normally observed in proteins is large, traces with respect to one torsion angle on the shielding surface are not sufficient. To demonstrate this, Fig. 6 shows how the shielding function with respect to one torsion angle changes when one varies the other torsion angle. Although ϕ and ψ describe rotation about a bond that consists not only of sp 3 -hybridized C as in χ^1 but also N (in ϕ) and C O (in ψ), resemblances to the χ^1 dependence seen in hydrocarbons are present. For example, conformations in which bulky groups are close to each other result in greater shielding while staggered conformations are deshielded. Figure 6A shows the dependence of C α shielding on the torsion angle ϕ at fixed values of ψ (-60° (\circ) and 135° (\bullet)). The curves are almost parallel to each other indicating that separating the ϕ effects from ψ contributions is possible. However, in Fig. 6B, it can be seen that this observation is caused by a fortuitous choice of ψ angles in Fig. 6A. Although the curves still exhibit similar shapes, their separation is clearly not constant within the range of ψ angles shown. The ψ dependence clearly changes with variations in ϕ . Thus, it can be deduced from this figure that the C α shielding equivalencies arise from a combination of ϕ and ψ effects and, apparently, do not lend themselves to separability. Surfaces are therefore needed to describe how ϕ and ψ influence chemical shielding in proteins. Figure 7 shows a ϕ - ψ shielding surface for the model alanine compound.^{41,51}

For the valine model compound, *N*-formyl-L-valine amide, the presence of substituents at the C $^\beta$ site not only reduces the symmetry but also induces a larger χ^1 dependence for the shielding of both C α and C $^\beta$ nuclei. These expected characteristics are certainly observed, as shown in Fig. 8. In valine the staggered conformations at $\chi^1 = 60^\circ$, -60° and 180° are unique

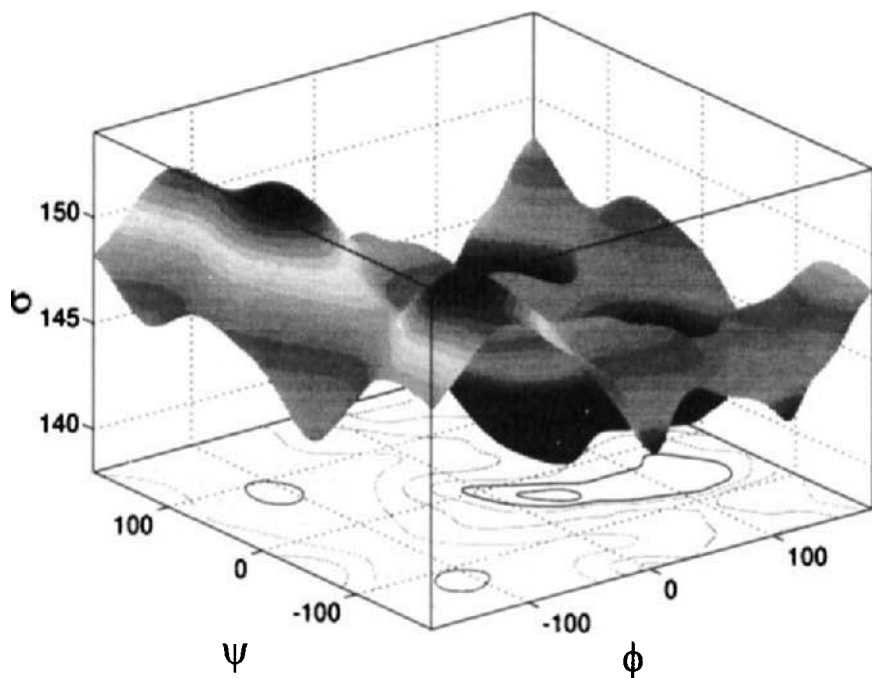


Fig. 7. The C^α shielding for an alanine model fragment as a function of the torsion angles ϕ and ψ . Reproduced from Ref. 51.

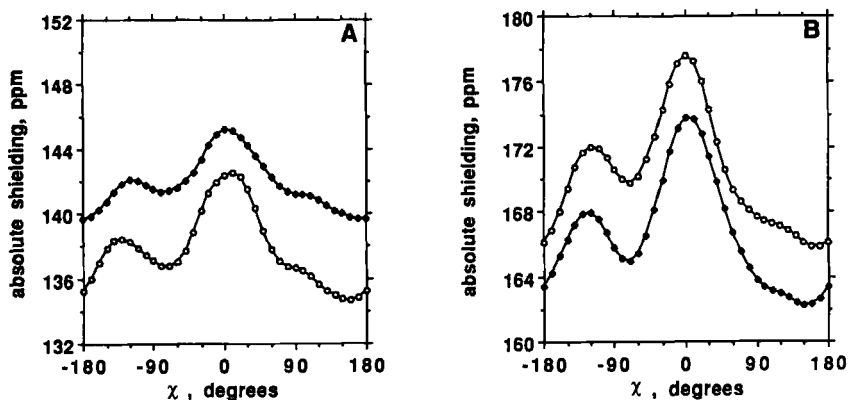


Fig. 8. Calculated ^{13}C shieldings as a function of the torsion angle, χ^1 , for a valine model fragment, at different ϕ and ψ angles. (A) C^α shielding for helix ($\phi = -55^\circ, \psi = -55^\circ$) (○) and sheet ($\phi = -136^\circ, \psi = 143^\circ$) (◇). (B) as in (A) but for C^β . Reproduced from Ref. 50, with permission. Copyright 1993, American Chemical Society.

conformations. The *trans*-conformer is clearly deshielded compared to the *gauche*-conformers for both C^α and C^β whether the compound has sheet-like (\diamond) or helical (\circ) ϕ and ψ angles. Consequently, in order to describe the chemical shift equivalencies observed for C^α and C^β in valine sites in proteins, one needs to take into account not only ϕ and ψ effects but χ^1 as well. Thus, in the most recent work of de Dios and Oldfield,⁵⁰ ϕ - ψ shielding surfaces for both C^α and C^β in *N*-formyl-L-valine amide were reported at each of the staggered conformations, and these are shown in Fig. 9. As a dramatic demonstration of the usefulness of these surfaces, the side-chain conformations of valine sites in the protein Calmodulin have been determined successfully.⁵⁰ Effects of the torsion angles ϕ , ψ and χ^1 are not exclusive to C^α and C^β chemical shifts. It has been shown that ^{15}N likewise shows dependence on these dihedral angles.^{52,53} For ^{15}N sites in valine residues, the sensitivity of ^{15}N shielding to the torsion angle χ^1 has been demonstrated using a model valine fragment;⁵² a range of at least 10 ppm is predicted for the ^{15}N chemical shift for the three staggered conformations. Empirical studies⁵³ also show that ^{15}N chemical shifts in proteins are strongly influenced by ϕ and ψ_{i-1} (the ψ angle of the preceding residue).

The differences in side-chains of the various amino acids result in a need for individual shielding surfaces. A generalized ϕ - ψ chemical shift surface obtained empirically is already available⁵⁴ but the applicability of such a surface is now in question after seeing that χ^1 effects in valine can contribute as much as 4 ppm. Theoretical shielding surfaces offer several advantages over empirical ones. First, one is not limited to the range of ϕ and ψ angles that has been observed in proteins. Second, the shielding changes due solely to torsion angle changes can be obtained from theory directly. Lastly, each amino acid is treated separately. Although the building of theoretical shielding surfaces is an enormous task, this is certainly feasible with the computer resources presently available.

2.1.4. Remote bond extension

It had been suggested that chemical shifts due to isotopic substitution at positions two or more bonds away from the resonant nucleus could be attributed predominantly to the change in dynamic averaging at the substitution site coupled with the shielding derivative with respect to the remote bond extension.^{55,56} Chesnut and Wright found that these so-called secondary derivatives for molecules containing atoms in the first row of the Periodic Table are not always smaller than the primary first derivatives.³⁵ That is, it can happen that the shielding of a nucleus is changed more substantially by the stretch of a remote bond (especially a multiple bond) than by the stretch of a bond in which it is a participant. The general observation is that the secondary first derivatives in nearly half the cases are comparable to or greater in magnitude than their associated primary

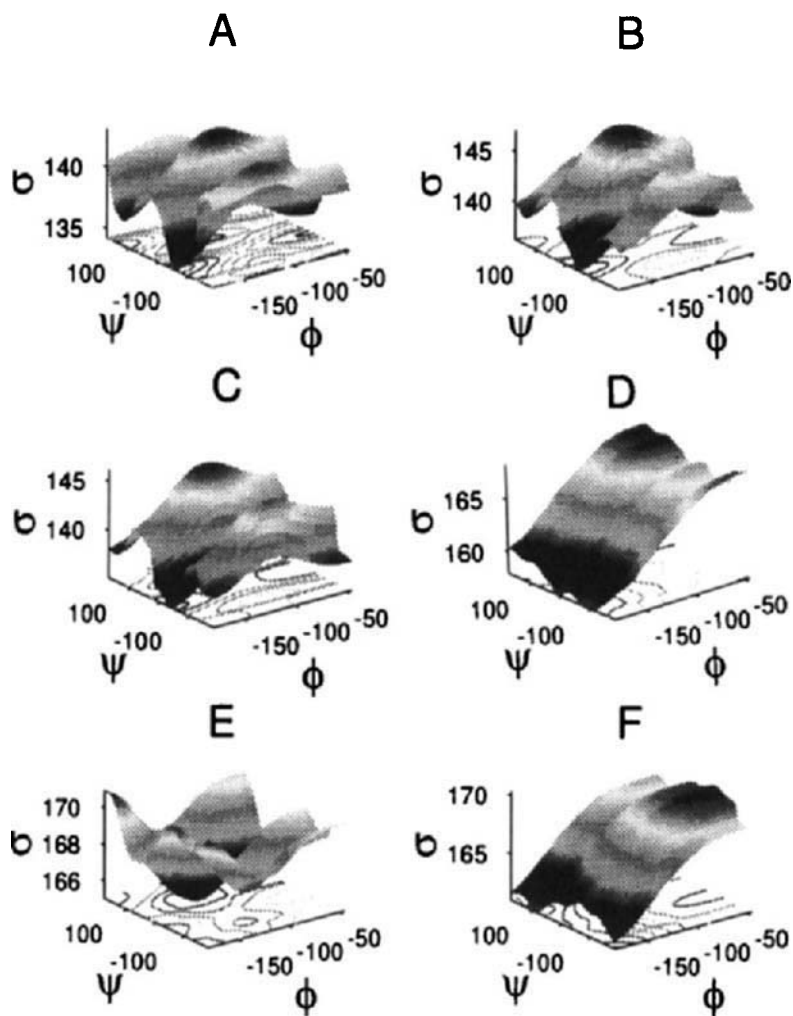


Fig. 9. The C^α and C^β shielding for a valine model fragment as a function of the torsion angles ϕ and ψ (at various χ^1 values). (A), C^α , $\chi^1 = 180^\circ$, (B) C^α , $\chi^1 = 60^\circ$, (C) C^α , $\chi^1 = -60^\circ$, (D) C^β , $\chi^1 = 180^\circ$, (E) C^β , $\chi^1 = 60^\circ$, and (F) C^β , $\chi^1 = -60^\circ$. Reproduced from Ref. 50, with permission. Copyright 1993, American Chemical Society.

derivatives. A corollary to this is the finding that modification of a remote single bond is not propagated as efficiently in the molecular framework as is modifying a multiple bond.

2.2. Intermolecular shielding surfaces

The intermolecular shielding function is obtained by a supermolecule calculation involving the cluster of two or more interacting molecules as a function of the distances and orientations of the monomers. The intermolecular part of the shielding is then obtained by subtracting out the monomer contributions which have been calculated separately at each configuration by including counterpoise corrections. The latter are necessary in order to take into account the much larger basis set in which the cluster calculations are carried out, and a usual type of approach is to use the full set of orbitals, including the ghost orbitals (without the atoms) centered at the positions of the interaction partners.⁵⁷ Intermolecular shielding surfaces prior to 1993 have been reviewed.¹³

2.2.1. Distance dependence

It had been suggested, in an attempted inversion of the experimental second virial coefficient of the Xe shielding in pure xenon gas that the shape of the intramolecular shielding function for two interacting rare gas atoms is similar to the shape of the H_2^+ intramolecular shielding surface, having a minimum in the shielding at some internuclear separation close to the minimum of the potential energy surface.⁵⁸ However, previous theoretical calculations exhibited a positive shielding in this vicinity, which would have given rise to a density dependence of opposite sign to that universally observed. The first theoretical indication of a minimum in the intermolecular shielding was obtained by Grayce and Harris who calculated the prototypical intermolecular shielding function, that is, the intermolecular shielding surface of the triplet state of the H_2 molecule, by a truly gauge-invariant density functional method using an electron gas approximation.⁵⁹ The very early calculation by Marshall and Pople for the same system using a minimal basis set did not exhibit such a minimum.⁶⁰ Owing to the approximate nature of these calculations, the definitive shape of the intermolecular shielding function was not established until the LORG and SOLO calculations of the ^{39}Ar shielding in the interacting Ar–Ar system by Jameson and de Dios.²⁴ Figure 1 shows this surface. Subsequently, the ^{39}Ar shielding in Ar–Ne, the Ne shielding in Ne–Ne and Ne–He²³ (shown in Fig. 10) and the He shielding in the He–He system⁴⁷ were reported. The latter exhibited a minimum only at the correlated level of calculation (MC-IGLO) whereas the correlation contributions to the ^{39}Ar shielding in the Ar–Ar system had

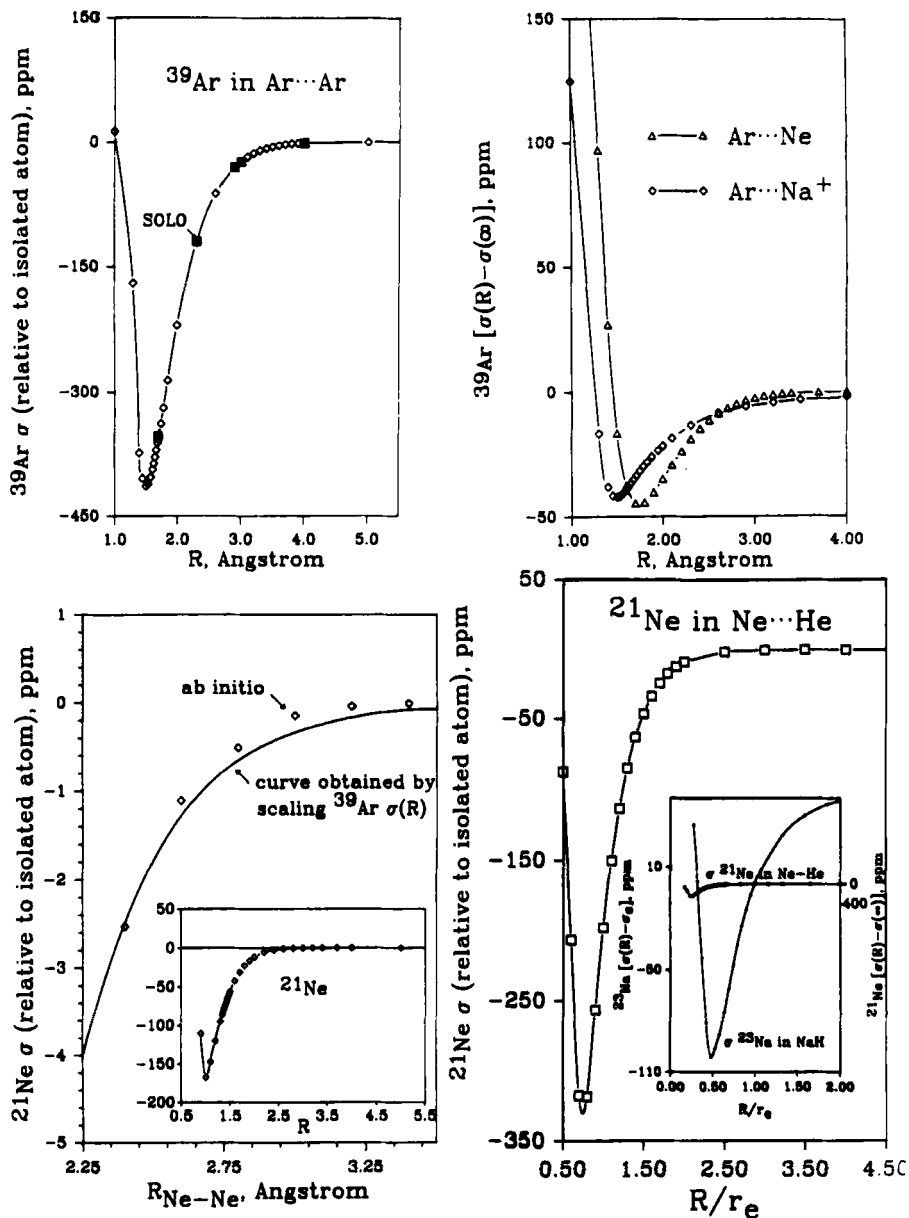


Fig. 10. Intermolecular shielding surfaces for ^{39}Ar in $\text{Ar}\cdots\text{Ne}$, ^{21}Ne in $\text{Ne}\cdots\text{Ne}$, and ^{21}Ne in $\text{Ne}\cdots\text{He}$. Reproduced from Ref. 23, with permission. The ^{39}Ar in $\text{Ar}\cdots\text{Ar}$ surface scaled down to ^{21}Ne in $\text{Ne}\cdots\text{Ne}$ agrees reasonably well with the *ab initio* $\text{Ne}\cdots\text{Ne}$ surface. The magnitude of the intermolecular shielding in the $\text{Ne}\cdots\text{He}$ system is compared with that of the intramolecular ^{23}Na surface in the isoelectronic NaH molecule by scaling the vertical axes according to $\langle a_0^3/r^3 \rangle$ of ^{21}Ne and ^{23}Na .

been shown by SOLO calculations to be negligibly small. In all rare gas pairs the minimum in the shielding surface occurs at a distance that is well inside r_0 , the separation at which the potential energy of interaction goes to zero. An interesting result which was found in comparing common-origin CHF calculations with local origin LORG calculations for the shielding in Ar_2 is that the common origin CHF results show an artefactual positive hump in the region of interest whereas the local origin calculations give only negative intermolecular shielding in this region. The earlier CHF calculations for proton and He shielding in the H_2 -He system⁶¹ do show the same positive hump, leading us to believe that this behaviour is an artefact of the gauge problems associated with common-origin calculations using modestly large basis sets. The dependence on the internuclear separation in those regions where sampling at ordinary temperatures would occur for ^{39}Ar shielding is $R^{-6.67}$ for Ar-Ar, $R^{-6.79}$ for Ar-Ne, and for ^{21}Ne shielding it is $R^{-6.74}$ for Ne-Ne, $R^{-7.41}$ for Ne-He.²³

2.2.2. *Scaling of intermolecular shielding*

It is well known that the sensitivity of the chemical shifts to changes in chemical environment scale according to the characteristic $\langle a_0^3/r^3 \rangle$ of the free atom in its ground state, clearly demonstrated by the correlation of the ranges of the chemical shifts of the nuclei with this quantity.^{62,63} We therefore expect the intermolecular shielding function to scale approximately according to this atomic property. Furthermore, to the extent that the intermolecular shielding is effected by the distortion of the electron charge distribution of the atom in response to the presence of the other atom, the magnitude of the effect could be related to the usual quantities that appear in the London model for dispersion energy. It is found that the shapes of the intermolecular shielding surfaces for rare gas pairs are very similar, and the nearly identical R dependence at separations around or larger than r_0 suggests that they may be conformal in the same sense that the law of corresponding states suggests that potential energy surfaces are conformal.²⁴ It has been found that the rare gas intermolecular shielding functions do scale according to factors that have to do with the sensitivity of the nuclear shielding to the presence of a neighbour. The suggested factors for the shielding of 1 due to the presence of 2 are:

$$\alpha_1 \langle a_0^3/r^3 \rangle_1 \alpha_2 U_1 U_2 / (U_1 + U_2),$$

where α_1 is the electric dipole polarizability of the rare gas atom in question and $\langle a_0^3/r^3 \rangle_1$ is characteristic of the atom in its ground state, which is a well-known measure of the sensitivity of nuclear shielding,^{62,63} and U_1 is the first ionization potential of the atom. These scaling factors have been tested in several ways. First, the shielding function from the scaled ^{39}Ar in Ar-Ar

was compared to the *ab initio* shielding function of ^{21}Ne in Ne–Ne in the region of interest.²⁴ This produced curves that were nearly superposable in the range of distances of interest, as shown in Fig. 10. Second, the ^{39}Ar shielding in Ar–Ar, scaled to the ^{129}Xe shielding in Xe–Ar, Xe–Kr, and Xe–Xe, produced intermolecular shielding curves for ^{129}Xe which provided excellent agreement with experiment when used to calculate the magnitudes and temperature dependence of the second virial coefficient of the ^{129}Xe nuclear shielding in the rare gas mixtures.²⁴

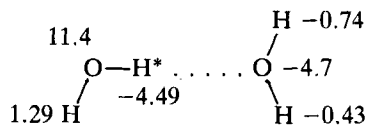
2.2.3 Additivity and non-additivity

The additivity of intermolecular shielding has been tested in polar and non-polar systems. In the simplest case, the ^{39}Ar shielding in the presence of two neighbour Ar atoms in the Ar_3 cluster in the form of an equilateral triangle and also in the ^{39}Ar in linear symmetrical Ar_3 , can be compared with the ^{39}Ar shielding with only one neighbour in Ar_2 . It is found that in the region where the internuclear distances are close to or larger than r_0 of the Ar_2 potential, the intermolecular shielding function for the central ^{39}Ar in the linear trimer and the Ar in the triangular trimer are nearly exactly superposable with 2.0 times the intermolecular shielding function of Ar in the dimer.²⁴ Therefore, except at close distances that are sampled only at very high temperatures or pressures, the intermolecular shielding of rare gas atoms are additive. It is this additivity that can be called upon to provide interpretation of the ^{129}Xe chemical shifts in the clusters Xe_1 , Xe_2 , Xe_3 , . . . , Xe_8 trapped in the alpha cages of zeolite NaA.⁶⁴

In another example involving larger systems, the solvation shifts due to one HF up to five HF molecules at specific sites around the ^{19}F of the fluorobenzene molecule have been calculated. It is found that the solvation shifts due to two up to five HF molecules are reproduced by a sum of the individual solvation shifts.⁶⁵

2.2.4. Hydrogen bonding

The changes of shielding upon formation of hydrogen bonds have been used empirically as a diagnostic tool. The water dimer serves as an example of the shielding changes in the donor and the acceptor molecules.^{66–68} In a calculation using the GIAO approach and ice geometry, and using counterpoise corrections, the shielding changes (ppm) are as shown below:⁶⁷



The nuclei of the molecule that donates the proton become more shielded. The nuclei of the molecule that accepts the proton become deshielded, as

does the donated proton H^* . The shielding changes in the donor molecule are larger than the corresponding changes in the acceptor molecule, the most profound change occurring in the donated proton. Even more drastic is the change in the anisotropy of the proton. In ice, where every proton is involved in a hydrogen bond, it is not sufficient to do a dimer calculation to reproduce the large anisotropy of the proton shielding. For this system, it is found that both the first and the second solvation shells contribute. A calculation on the $(H_2O)_{17}$ cluster in the ice geometry leads to the proton shielding tensor components 11.97, 12.19, 46.91 ppm, with an anisotropy of 34.8 ppm.⁶⁹ This is in excellent agreement with the experimental data of Pines *et al.* at 183 K,⁷⁰ which when converted to absolute shielding are 12.4, 12.4, 46.4 ppm, with an anisotropy of 34 ± 2 ppm. The calculated anisotropy of the proton shielding in an isolated water molecule is only 15.7 ppm. The profound effect of hydrogen bonding on the anisotropy of the proton was well known experimentally, but was calculated successfully only recently.

The shielding surface was not calculated in the above examples. In the hydrogen bonding situation in the aqueous NH_4^+ ion, modeled by the clusters $NH_4^+(H_2O)$ and $NH_4^+(H_2O)_4$, the shielding surfaces for the N nucleus, for the donated proton (H^*), and for the spectator protons attached to the N have been calculated by Munch *et al.*⁷¹ The shieldings change monotonically with $N \cdots O$ distance. On the other hand, for a fixed $N \cdots O$ distance, shown in Fig. 11, both the H^* shielding and the N shielding change with $N-H^*$ distance in a non-monotonic way, exhibiting a minimum. At the typical hydrogen-bonded geometry, the N shielding surface has a negative slope with increasing $N-H^*$ distance, as it does in the isolated NH_4^+ ion. The H^* shielding surface has a negative slope at this same distance, just like the H shielding in the isolated NH_4^+ ion, but the spectator H shielding surface has a positive slope. It is the latter that is thought to be responsible for the unusual sign of the isotope shift on the protons in $NH_nD_{4-n}^+$ ion. The shapes of these surfaces may be more general. The opposite signs of the slopes of the 1H shielding surfaces of the spectator proton compared to the hydrogen-bonded H^* for changes in the $N \cdots H^*$ distance may also be the basis for the D -induced proton isotope shifts in the hydrogen-bonded sugars, where the H^* has a usual sign isotope shift upon deuteration at the acceptor oxygen, whereas the spectator proton on the acceptor has an unusual sign isotope shift upon deuteration of the H^* .⁷²

The increased shielding of the atom which donates its attached proton to a hydrogen bond is typical. Even in internal hydrogen bonding, such as in phenols, it has been found that the ^{17}O shielding increases upon formation of an internal hydrogen bond.⁷³ In contrast, using model fragments for a dipeptide, Chesnut and Phung⁷⁴ and de Dios *et al.*⁵² found that the shielding of an amide N, although much less sensitive to hydrogen bonding compared to O, decreased.

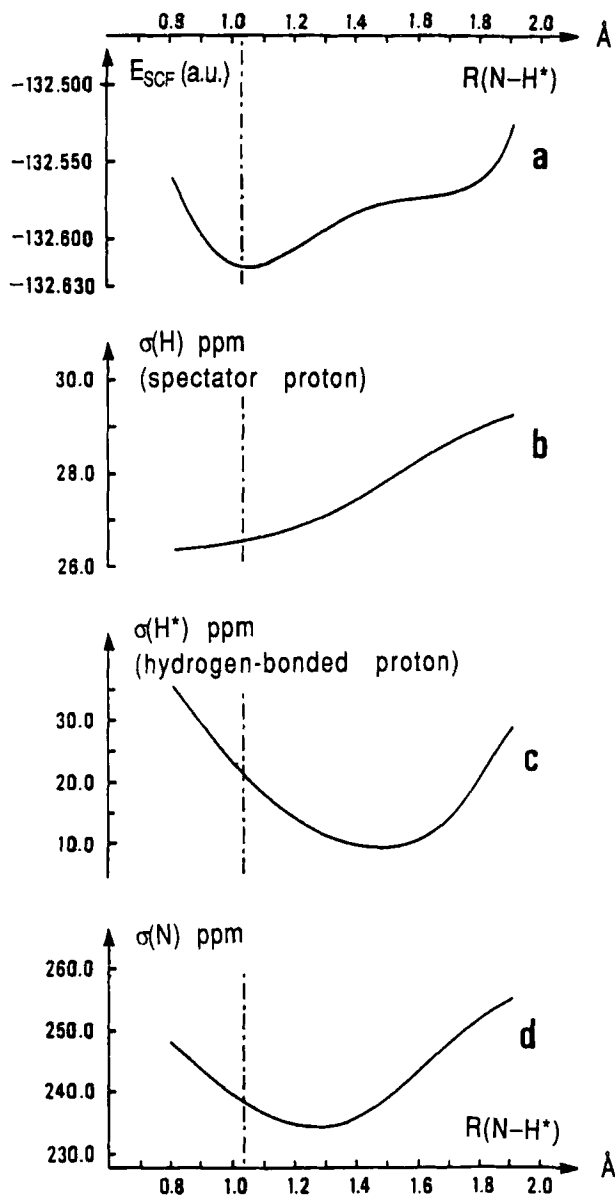


Fig. 11. Shielding surfaces in a hydrogen-bonded system $\text{NH}_4^+ - \text{OH}_2$. Reproduced from Ref. 71, with permission from *Acta Chemica Scandinavica* (a) The potential energy surface for a fixed N-O distance, varying the position of the H^* along the N-O internuclear line (the x axis gives the N-H* separation). (b) The shielding surface of the spectator proton attached to the N. (c) The shielding surface of the hydrogen bonded proton H^* . (d) The N shielding surface. The experimental optimum N-H* separation is marked.

2.3. Electric field effects and dispersion contributions

The idea that observed changes in nuclear shielding could be explained in part by the effects of electric fields generated intermolecularly or intramolecularly was proposed by Stephen⁷⁵ and Buckingham.⁷⁶ The shielding of a nucleus in a molecule in the presence of a uniform electric field \mathbf{F} was expressed by Buckingham as follows:

$$\sigma_{\alpha\beta} = \sigma_{\alpha\beta}^{(0)} + \sigma_{\alpha\beta\gamma}^{(1)}F_{\gamma} + \sigma_{\alpha\beta\gamma\delta}^{(2)}F_{\gamma}F_{\delta} \quad (1)$$

where the field-independent tensor components $\sigma_{\alpha\beta\gamma}^{(1)}$ and $\sigma_{\alpha\beta\gamma\delta}^{(2)}$ have a number of non-zero independent values depending on the nuclear site symmetry.^{77,78} For example, for a $C_{\infty v}$ site, the electric field dependence of the shielding is

$$\sigma_{xx} = \sigma_{xx}^{(0)} + \sigma_{xxz}^{(1)}F_z + (1/2)\sigma_{xxxx}^{(2)}F_x^2 + (1/2)\sigma_{xxzz}^{(2)}F_z^2 + \dots \quad (2)$$

$$\sigma_{yy} = \sigma_{xx}^{(0)} + \sigma_{xxz}^{(1)}F_z + (1/2)\sigma_{yyxx}^{(2)}F_x^2 + (1/2)\sigma_{yyzz}^{(2)}F_z^2 + \dots \quad (3)$$

$$\sigma_{zz} = \sigma_{zz}^{(0)} + \sigma_{zzz}^{(1)}F_z + (1/2)\sigma_{zzxx}^{(2)}F_x^2 + (1/2)\sigma_{zzzz}^{(2)}F_z^2 + \dots \quad (4)$$

It is useful to average all directions of the magnetic field but to leave the molecule fixed relative to the electric field. For a $C_{\infty v}$ site, one then obtains

$$\sigma - \sigma^{(0)} = -AF_{||} - B_{||}F^2 - B_{\perp}F^2 \quad (5)$$

where

$$A = -(1/3) [2\sigma_{xxz}^{(1)} + \sigma_{zzz}^{(1)}] \quad (6)$$

$$B_{||} = -(1/6) [2\sigma_{xxzz}^{(2)} + \sigma_{zzzz}^{(2)}] \quad (7)$$

$$B_{\perp} = -(1/6) [\sigma_{xxxx}^{(2)} + \sigma_{yyxx}^{(2)} + \sigma_{zzxx}^{(2)}] \quad (8)$$

The first-order and second-order electric field coefficients of the shielding have been given the name shielding polarizabilities and hyperpolarizabilities.⁷⁹ There are analogous coefficients of the electric field gradients and hypergradients as well.^{80,81} The physical picture is as follows: when an electric field is applied along the molecular axis of CO for example, the field induces an electric dipole, which means that charge is shifted along the molecular axis; the charge density will increase at one end of the molecule and decrease at the other end. In a CO molecule oriented such that the electric field is in the O-C direction the field draws charge from C towards O. ¹³C deshields whereas ¹⁷O becomes more shielded. By

symmetry, the signs change when the field direction is reversed. It is very important to have the same definition of the axis system (the positive direction of the z axis) used in the computations when comparing calculations in different molecules and especially when comparing calculations by different authors. As might be expected in a linear molecule, the larger effect is in the shielding tensor component perpendicular to the molecular axis, whereas the purely diamagnetic parallel component exhibits a much smaller change.⁸² All the calculations so far reported have involved using a common gauge origin.^{79, 81–86} The most important conclusions so far are (a) the shielding polarizabilities are larger for ^{19}F than ^{13}C , and smallest for ^1H ,^{82,87} and (b) that the electric field coefficients are very dependent on the chemical bonding of the nucleus in question. For example, they are roughly an order of magnitude larger for ^{17}O in H_2CO than in CO .⁸⁷ For the highly symmetric nuclear sites of ^{13}C in CH_4 and ^{29}Si in SiH_4 only the B term is non-zero and these are found to be of opposite signs, with the ^{29}Si being unusual.⁸⁷ These quantities are interesting in their own right as molecular electronic properties. It has been found that the contributions to the shielding due to the second-order terms (hyperpolarizabilities) are rather small,^{81,88} contrary to the original contention that the B terms were responsible for most of the large medium effects on Xe chemical shifts and on ^{31}P in P_4 . The full *ab initio* calculations on the rare gas pairs have of course already shown that the short range (which might be termed overlap compression and exchange) contributions are large whereas the dispersion contributions are small.²⁴

Although the original idea of Raynes, Buckingham and Bernstein⁸⁹ to replace the dispersion contributions to the shielding by the effects of fluctuating electric fields^{90,91} for which the B term in the uniform electric field calculations can then be applied is no longer sustainable, the distance dependence predicted by a consideration of the electric fields due to a point charge or a permanent electric dipole continues to be useful.²³ By a consideration of the shielding response to a point charge, electric dipole, quadrupole, etc., the proper responses in the long-range limiting situation, it has been possible to understand the distance dependence that has been found in the *ab initio* calculations of ^{39}Ar in the presence of Na^+ ion and NaH molecule.²³ The former has a nearly R^{-4} dependence at large separations whereas the latter has more nearly an R^{-6} dependence.

In the context of this review, however, the importance of these electric field and field gradient terms in the shielding is underscored in the consideration of electrostatic effects of counterions and polar groups. The effects of the very large numbers of water molecules solvating a protein, for example, cannot be taken into account computationally by doing calculations in the presence of realistic water molecules. One approach to the shielding contributions due to distant parts of the protein has been suggested by Oldfield and coworkers:⁵² to replace the shielding contributions from

distant residues by considering only the classical electric fields and field gradients generated by electrostatic models (AMBER point charges for example) at the nucleus in question coupled with the response of the nuclear shielding to such electric fields and field gradients.

These ideas present two challenges. One is, how well does representing the solvent molecule by a point charge model evoke the appropriate shielding response? Second, how well does the use of the product of the shielding polarizability with the electric field at the nucleus replace this response? The answer to the first question is obtained by comparing two *ab initio* shielding calculations: one is a supermolecule calculation for the solute molecule in the presence of the solvent molecules and the other is for the solute molecule in the presence of the point charge models for the solvent molecules. This comparison has been done for the ^{19}F nucleus in fluorobenzene with various numbers of HF as solvent.⁶⁵ In the answer to the second question, comparing results obtained from full *ab initio* computations with those derived from the shielding polarizability approach, it has been evident that in order to reach agreement, terms up to the hypergradient of the field need to be considered.⁸¹ On the other hand, terms arising from the shielding hyperpolarizability can be neglected. However, caution should be exercised in applying such conclusions reached in calculations on rigid static systems to real systems where there is motional averaging. In the presence of motion, it is only expected that the various electric field terms would average differently.

2.4. Is there a global shape for the traces on shielding surfaces?

The similarities found in those shielding surfaces that have been calculated over a fairly wide region of configuration space^{13,23,33} offer some hope of being able to transfer some of the insight gained in the few calculations to a more general application to more complex systems. First, it has been noted that the intramolecular shielding surfaces of the small molecules H_2O , CH_4 , NH_3 , and PH_3 have shapes in common with respect to the shielding dependence on the nuclear displacement coordinates such as the symmetry coordinates of the molecule.³³ Then, it was suggested that the intramolecular shielding surfaces in terms of the changes in shielding upon bond extension of diatomic molecules related in the Periodic Table can be scaled to one another, at least in the vicinity of the equilibrium geometry, by use of the factors $R_e \langle a_0^3/r^3 \rangle$.²³ The suggested global characteristics of shielding functions are analogous to the global shape of diatomic molecule potential functions in the vicinity of the equilibrium geometry and the relationships between the Morse parameters associated with bond stretching.⁹² Third, it has been noted that the intermolecular shielding functions for rare gases have fairly similar R-dependence in the interesting region of internuclear

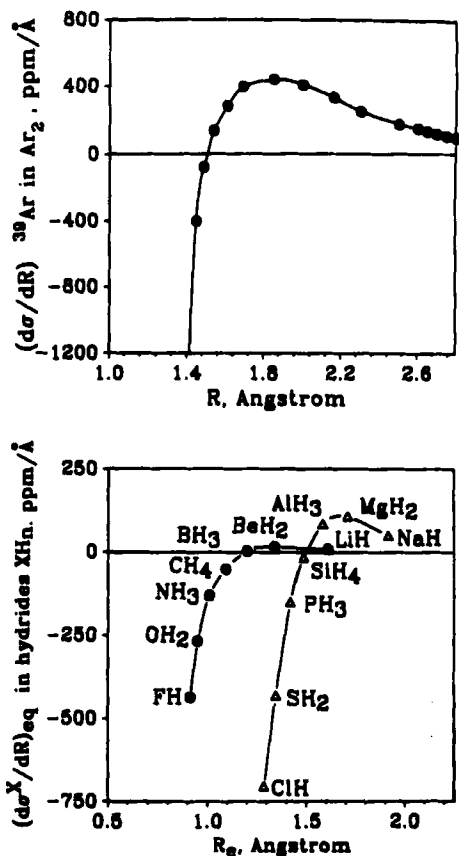


Fig. 12. The upper figure is the derivative of the ^{39}Ar shielding surface in $\text{Ar}-\text{Ar}$ as a function of the internuclear separation. Below are the derivatives of the X shielding surface at the equilibrium geometries of the hydrides XH_n , plotted against their experimental equilibrium X-H bond lengths. Reproduced from Ref. 23, with permission.

separations, having R^{-n} shapes at large R , when n ranges from -6.6 to -7.4 , and the shielding functions at these separations were found to scale by factors that are related to the susceptibility of the rare gas atom to a distortion away from spherical symmetry in the presence of a neighbour atom and the sensitivity of the shielding to such distortions,²³ already mentioned in Section 2.2.2. Fourth, the similarity in the overall shape of the intermolecular shielding surface to the intramolecular shielding surface of one of the nuclei in a diatomic molecule has been discussed,²³ and exhibited in Fig. 1. Fifth, the variation in the derivatives of the X shielding surfaces of the hydrides XH_n of the first and second rows of the Periodic Table has been found to be easily understood in terms of a natural progression in the

equilibrium X-H bond length in going from left to right in the Periodic Table, thereby providing a systematic progression in the derivative of the shielding in that part of the shielding surface that is at the equilibrium bond length, as can be seen in Fig. 12. Thus, the systematic algebraic change from the positive (unusual sign) shielding derivatives with respect to the bond stretch for the alkali and alkaline earth hydrides to the large negative derivatives for the hydrogen halides can be viewed as a natural consequence of a systematic progression from one part of the same-shape shielding surface to another. The preponderance of the negative first derivatives of shielding with respect to bond stretching is then merely a consequence of the scarcity of experimental data in the nuclei of groups 1-3 of the Periodic Table. The results of the survey of such derivatives by Chesnut and Wright³⁵ are entirely consistent with this notion.

The similarities of the shielding surfaces in somewhat larger molecules can be discovered by examining traces on the surfaces along particular displacement coordinates. It has been found⁴¹ that the traces which display the shielding dependence on bond angle are very similar to the previous findings in the H₂O, NH₃, and PH₃ molecules shown in Fig. 2.

Of particular interest in the dependence of the shielding of the dihedral angle, which is less global in nature. It has been found that in nearly all of the systems studied, eclipsed conformations lead to greater shielding of the nuclei in the α - and β -positions, while in the staggered conformers they are most deshielded. In the small model compounds that have been studied,⁵⁰ it is also found that substitutions at the α -position influence the dihedral angle dependence of the shielding of the nucleus in the β -position, while the α -position shows insensitivity. However, this observation is true only if substitutions were restricted to the α -position. In the case of the valine model fragment, both C $^{\alpha}$ and C $^{\beta}$ show dihedral angle dependencies that are significantly different from the smaller compounds.

3. DYNAMIC AVERAGES ON SHIELDING SURFACES, COMPARISONS WITH EXPERIMENTS

Many calculations of nuclear shielding are done at the energy-optimized molecular geometry, and the values of tensor components are compared directly with experimental chemical shift components. This has proven to be an excellent application of the *ab initio* calculations; calculations are sometimes indispensable for establishing the assignment of the tensor components.⁹³⁻⁹⁷ In many cases there simply is no other information available to provide the orientations of the principal axes of the shielding tensor, which in turn provide a reliable index of the chemical bond. The chemical shift tensor is singular among the molecular electronic properties in the precision and detail with which the tensor information has been

obtained.⁹⁸ However, there are many applications in which the value of the shielding at a single point on the shielding surface does not properly account for the observations. Indeed, in every case an accurate comparison with experiment can only be done when dynamic averaging is carried out over those portions of the shielding surface which correspond to the portions of configuration space of the molecule(s) that are sampled by the motions that occur within the NMR time frame. For the intramolecular shielding surfaces this means rovibrational averaging, which requires the simultaneous knowledge of the shielding surface and the intramolecular potential energy surface. As we shall see, it is generally not sufficient to assume harmonic vibrations for this purpose. In a sense, the nuclear shielding probes the intramolecular potential surface in those regions close to the deep pockets that correspond to the immediate vicinity of the equilibrium nuclear configuration. A general treatment of the rovibrational averaging of molecular electronic properties, including the nuclear shielding provides the theoretical formalism and the perspective.^{99,100} For intermolecular shielding surfaces the dynamic averaging is even more important, since the portions of configuration space that are sampled experimentally are much more extensive. In these cases it is simply not possible to consider the observed chemical shifts in terms of only one or more energetically favoured configurations.^{101,102}

3.1. The temperature dependence of the shielding in a molecule

We discuss here those experimental observations that are due entirely to the dynamic averaging over the shielding surfaces. The intermolecular effects in the gas phase are easily understood to be temperature dependent since the number and nature of the collisions between molecules are clearly temperature dependent; these will be discussed in a later section. What we consider here is the observed temperature dependence of the chemical shift in the limit of zero density, where the number of collisions is sufficiently low that intermolecular interactions cannot account for the temperature dependence of the chemical shifts.¹⁰³ It was found that the shielding of ^{19}F nuclei in molecules such as CF_4 , SiF_4 , BF_3 , SF_6 ,¹⁰³ and F_2 ¹⁰⁴ decreased with increasing temperature, as shown in Fig. 13. Many other examples were reported thereafter, involving not only ^{19}F but also ^{11}B , ^{15}N , ^{13}C , ^{31}P , ^{77}Se and ^{125}Te .^{32-33, 106-111} These observations were postulated to arise from the existence of a shielding surface which was characterized by an expansion of the shielding in terms of nuclear displacement coordinates such as the internal coordinates or normal coordinates of the molecule.^{36,112} The experimental value of the chemical shift was postulated to be the resulting thermal average of the shielding resulting from employing the thermal averages of the nuclear displacement coordinates. An equivalent approach,

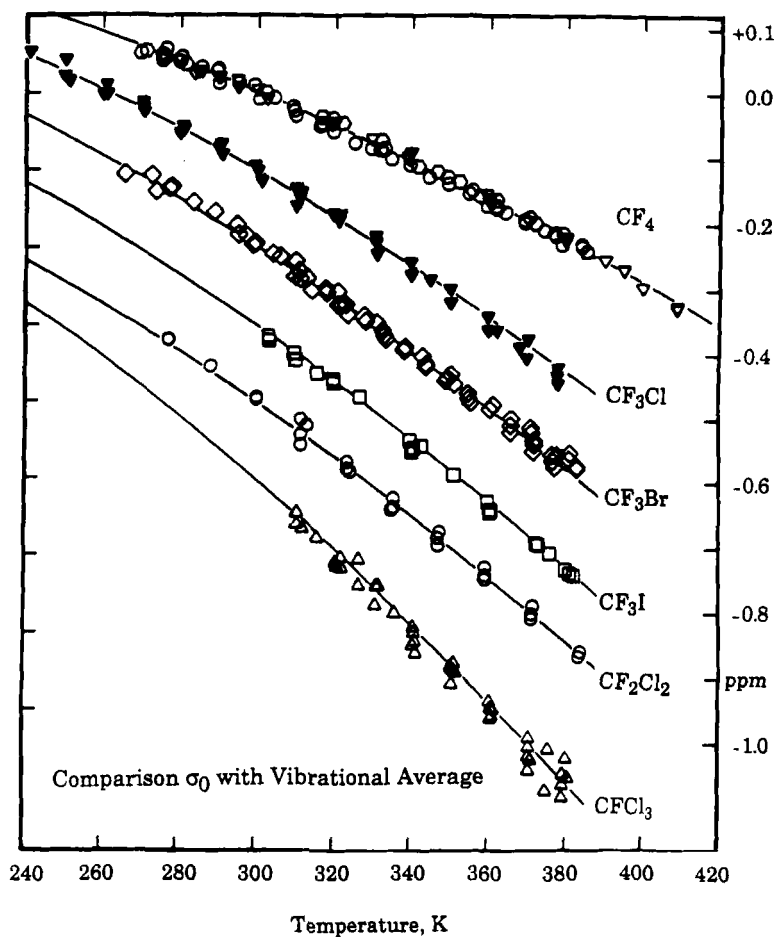


Fig. 13. The temperature dependence of the ^{19}F shielding in several fluoromethanes in the isolated-molecule limit. Reproduced from Ref. 105, with permission. The shielding scale on the y axis is set to zero for the CF_4 molecule at 300 K; the zeroes for the other molecules have been arbitrarily displaced for clarity. The curves are the one-parameter fit interpretation of the thermal average shielding obtained using a modified Urey-Bradley force field in the vibrational averaging.¹⁰⁵ The curvature in each case is a natural consequence of the non-linear dependence on temperature of the dynamically averaged displacements of the C-F distance from its equilibrium value in an anharmonic system.

especially for larger excursions such as inversion, is to carry out explicitly the averaging over the vibrational wavefunctions and then to average over these according to the populations:

$$\langle \sigma \rangle^T = \frac{\sum_{vJK} (2J+1) g_{N_s} \langle \sigma \rangle_{vJK} \exp(-E_{vJK}/kT)}{\sum_{vJK} (2J+1) g_{N_s} \exp(-E_{vJK}/kT)} \quad (9)$$

The rovibrational averages $\langle \sigma \rangle_{vJK}$ can be evaluated directly by integrating over the vibrational wavefunctions or in terms of the derivatives of the shielding surface with respect to nuclear displacements, as with any other molecular electronic property surface. The general formulas have been derived in terms of these derivatives and the derivatives of the potential energy surface (quadratic and higher force constants).^{99,113} It was recognized fairly early that the anharmonic contributions to the mean bond displacement Δr (the so-called "mechanical anharmonicity" together with the centrifugal stretching associated with the rotational averaging for a non-rigid rotor) constitute the most important contributions.^{36,112,114} There are, of course, contributions from the mean square displacement $(\Delta r)^2$ in the diatomic molecule, but these result from the counterpart of "electrical anharmonicity" in the dipole moment, that is, the second and higher derivatives of the shielding surface with respect to the bond stretch. We now know from the survey of such derivatives by Chesnut and Wright that these terms are not necessarily small.³⁵ The observed temperature dependencies of the chemical shifts in "isolated molecules" were reasonably large; the temperature coefficients were of the order of -0.001 to -0.034 ppm deg^{-1} for ^{19}F , for example. Here too, a nucleus such as ^{19}F with a large chemical shift range provides a large, easily measurable temperature coefficient which parallels the paramagnetic shielding of ^{19}F in the molecule, as shown in Fig. 14.^{38,115} Other nuclei such as ^{13}C have considerably smaller shifts with temperature.¹¹⁶ For the small molecules H_2O , CH_4 , NH_3 , and PH_3 whose shielding surfaces have been extensively characterized, a more complete dynamic averaging has been possible.^{30,32,33,117} For the NH_3 molecule the trace on the shielding surface corresponding to variations in the inversion coordinate has been used to carry out the full dynamic averaging using the numerical vibrational wavefunctions obtained by solving the nuclear motion problem using the empirical potential energy surface.³² For these four molecules, the full dynamic averaging has been possible since both the anharmonic potential surface and the shielding surface are known. The complete set of symmetry coordinates of the molecule has been used to calculate all the contributions to the shielding, including higher-order terms. When the dynamic averaging is carried out for more than one isotopomer of the molecule, then the mass dependence of the dynamically averaged

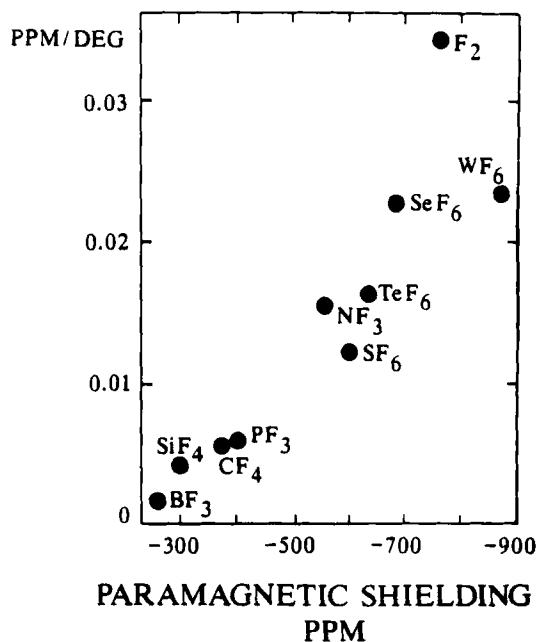


Fig. 14. The temperature coefficient of the shielding of ^{19}F in the binary fluorides in the isolated-molecule limit correlate with the paramagnetic shielding in these molecules (obtained from the absolute shielding and the calculated diamagnetic shielding using Flygare's method). Reproduced from Ref. 115, with permission.

shielding can also be obtained. The temperature dependence of the shielding of the ^{13}C in CH_4 , the ^{15}N in NH_3 , and the ^{31}P in PH_3 relatively small and that of the ^{17}O in H_2O has not been measured yet. Nevertheless, these comprehensive studies provide the basis for the interpretation of the observed large temperature dependences in other molecules and the first accurate calculations of the isotope effects on the chemical shifts in polyatomic molecules. The magnitudes of the rovibrational corrections in some small molecules shown in Table 1 illustrate that these are not small corrections and should always be taken into consideration in making a comparison between the calculated shielding at the equilibrium molecular geometry and the experimental absolute shielding.

Averaging over the torsional motions could be important, especially in the case of saturated carbon nuclear sites which have intrinsically small derivatives with respect to bond extension. It has been suggested that the averaging over torsional motions provides increased shielding with increasing temperature.^{46,120} Bennett and Raynes have found that the temperature coefficients of ^{13}C in molecules having CH_3 groups that can undergo torsional motion about a carbon-carbon single bond are positive.^{116,121} The temperature coefficients of the shielding in conformationally inhomogeneous

Table 1. Typical vibrational corrections [$\sigma(300\text{ K}) - \sigma_e$], ppm.

Term ^a	CH ₄ ¹¹⁷	NH ₃ ³²	PH ₃ ³³	H ₂ O ¹¹⁸	H ₂ Se ^c
P _r	-4.368	-7.69	-9.16	-10.835	-43.3
P _{rr}	-1.696	-3.59	-5.97	-4.824	-19.3
P _{α} + P _{$\alpha\alpha$}	+2.573	+2.49	+2.25	+1.524	+3.7
Other	-0.10	-0.02	+0.10	+0.565	Neglected
Total	-3.591	-8.81	-12.78	-13.57	-58.9

^aP_r denotes terms involving the first derivative of nuclear shielding with respect to the bond stretch P_{rr} denotes terms involving the second derivative P _{α} + P _{$\alpha\alpha$} include terms in the first and second derivatives of shielding with respect to bond angle deformation.

^bMixed terms and higher order terms.

^cCalculated by Ref. 119 based on the points on the *ab initio* shielding surface of Ref. 34.

n-butane and iso-pentane are of the same order of magnitude as for the conformationally homogeneous ethane, propane, isobutane, and neopentane molecules. Thus, Raynes and Bennett make the important point that any attempt to obtain shielding values for individual conformers from the measurement of the temperature dependences of carbon shielding based on the notion of temperature-dependent equilibria between a small number of conformers is naive, since this notion ignores the contributions of geometries of the torsionally distorted conformers.¹²¹

3.2. Isotope effects

The mass dependence of the chemical shift was discovered even earlier than the temperature dependence;¹²² however, it was not until the recognition of the shielding surface that a single theoretical formalism could be established to explain both phenomena.^{36,37} It is in the context of the Born-Oppenheimer separation that the possibility of considering a molecular electronic property surface, such as the shielding surface, is achieved. In this context the shielding surface, being entirely an electronic property calculated for the various configurations of the nuclei, is the same for all isotopomers of the molecule. The observed mass-dependence of the shielding is then entirely a result of the differential dynamic averaging in a heavy isotopomer compared to the light one. When the observed nucleus itself is isotopically replaced, the shielding average is changed. This is the primary isotope effect and is most conveniently observed indirectly as the chemical shift between two different molecular species. The secondary isotope shift is observed when the mass of an atom one or more bonds away is different. Although the shielding difference is best written out in terms of the two isotopomers, such as [$\sigma(^{15}\text{N}, ^{15}\text{NH}_3) - \sigma(^{15}\text{N}, ^{15}\text{ND}_3)$], the commonly observed additivity in the isotope effects on shielding¹²²⁻¹²⁴ allows the

isotope shifts to be reported in terms of single substitutions, as follows: ${}^n\Delta^{13}\text{C}(2/1\text{H})$ is the shielding difference between the normal and the deuterated isotopomer for a single substitution n bonds away from the observed ${}^{13}\text{C}$ nucleus.¹²⁵ The isotope shift is ubiquitous and literally thousands of examples are found in the literature.^{122,126} The isotope shifts come about because the dynamic averaging by the heavy isotopomer involves smaller amplitudes of nuclear motion than the dynamic averaging by the light isotopomer over the identical shielding surface.³⁷ On the average, the lighter isotopomer samples a larger region of the shielding surface than does the heavier isotopomer in its excursions away from the equilibrium molecular geometry. We have seen the global shape of the shielding surface in Fig. 1. When the point of minimum energy (equilibrium geometry) happens to fall in that part of the shielding surface in which the shielding is sharply decreasing with bond extension, then the larger amplitudes of motion in the averaging of the lighter molecule over the regions of the shielding surface that correspond to the immediate vicinity of the equilibrium arrangement produces greater deshielding than does the smaller amplitudes of motion of the heavier molecule. This leads to the usually observed negative sign of the isotope shift. On the other hand, in those cases where the minimum on the potential energy surface happens to fall on the other side of the shielding surface where bond stretching leads to increased shielding, as for the Li nucleus, the sign of the isotope shift is opposite to the usual; the larger excursions of the light molecule leads to a more shielded average than for the heavy molecule. Indeed, for isotopic substitution one to three bonds away, Li isotope shifts in organolithium compounds are found to be opposite to the usual sign.^{127,128} Now consider the trace of the shielding surface along the bond angle deformation. This portion of the shielding function having a minimum at the tetrahedral angle, the averaging over the bond angle deformations generally leads to increased shielding when the equilibrium bond angle is not too far from tetrahedral.^{30,32} However, it has been found that the isotope shift is dominated by the bond stretching,³³ even in the case of NH_3 where averaging over the inversion coordinate is complete; see for example the relative contributions in Table 2. It is not too surprising, then, to find that one-bond isotope shifts are fairly predictable in sign.⁴⁰ The trends in isotope shifts have been explained theoretically,^{40,56} including the additivity,¹³⁴ the dependence on the fractional change in mass,¹³⁵ and the observed linear dependence on $[1 - (\mu/\mu')^{1/2}]$ or the $(m' - m)/m'$ factor for a series of isotopes of the same element.^{115,135} The isotope shifts in isolated molecules can now be said to be completely understood and can be calculated, in principle. For example, for the CO molecule, the observed temperature dependence of the ${}^{13}\text{C}$ shielding, the ${}^{13}\text{C}$ isotope shifts due to ${}^{17}\text{O}/{}^{16}\text{O}$ and ${}^{18}\text{O}/{}^{16}\text{O}$ substitution, and the ${}^{17}\text{O}$ shift due to ${}^{13}\text{C}/{}^{12}\text{C}$ substitution, all have been calculated¹³⁶ and found to agree fairly well with experimental

Table 2. Isotope shifts [$\sigma^X(\text{XH}_n) - \sigma^X(\text{XD}_n)$], ppm, calculated for ^{13}C , ^{15}N , ^{31}P , ^{17}O and ^{77}Se nuclei.

Term ^a	CH_4^{129}	NH_3^{32}	PH_3^{33}	H_2O^{118}	H_2Se^b
P_r	-1.169	-2.05	-2.44	-2.847	-11.66
P_{rr}	-0.453	-0.97	-1.68	-1.316	-5.59
$P_\alpha + P_{\alpha\alpha}$	+0.686	+0.66	+0.67	+0.404	+1.25
Other ^c	-0.042	-0.004	0.002	+0.08	Neglect
Total	-0.978	-2.36	-3.45	-3.68	-16.0
Expt	-0.774 ¹³⁰	-1.87 ¹²⁴	-2.53 ¹³¹	-3.09 ^{124d}	-14.04 ¹³²

^aSame definitions as in Table 1.^bCalculated by Ref. 119 based on the points on the *ab initio* shielding surface of Ref. 34.^cMixed terms and higher-order terms.^dIn the gas phase a value of -4.04 ppm has been reported.¹³³

values.^{106,137} The isotope shifts of ^{17}O in H_2O and D_2O , ^{13}C in $^{13}\text{CH}_n\text{D}_{4-n}$, ^{15}N in $^{15}\text{NH}_3$ and $^{15}\text{ND}_3$ and ^{31}P in PH_3 and PD_3 have all been calculated using the full shielding surfaces for these nuclei.^{30,32,33,117} A complete calculation for larger molecules may be limited by the lack of accurate potential energy surfaces or simply by the large number of nuclear displacement coordinates. Therefore, the knowledge gained from complete calculations using all the symmetry coordinates in these small molecules helps to gauge the limits of applicability of using a less complete picture, such as, for example, using a dynamic average of a local displacement coordinate at the substitution site coupled with the shielding derivative with respect to that remote displacement, as we shall see below.

The magnitude of the isotope shift depends on several factors which have been discussed in detail in previous reviews.^{40,56} (a) The magnitude of the isotope shift is a function of the observed nucleus and reflects its chemical shift range. The sensitivity of the nuclear shielding (the derivatives of the shielding surface at the equilibrium geometry are large) of ^{129}Xe leads to isotope shifts as large as -0.58, -0.52, and -0.69 ppm for $^{18}\text{O}/^{16}\text{O}$ substitution in XeOF_4 , XeO_2F_2 , and XeOF_3^+ .¹³⁸ The shielding sensitivity depends on $\langle a_0^3/r^3 \rangle$ for the atom, and the shielding derivatives appear to scale accordingly. The shielding surfaces of related diatomic molecules in the vicinity of the equilibrium geometry (e.g. the surfaces of ^{35}Cl in ClF and ^{19}F in F_2 , ^{35}Cl in HCl and ^{19}F in HF , ^{23}Na in NaH and ^6Li in LiH) have been found to be superimposable with each other upon using a scaling factor $R_e \langle a_0^3/r^3 \rangle$.²³ (b) Upon substitution with a heavier isotope the NMR signal of the nearby nucleus usually shifts towards lower frequencies (higher shielding). The survey of *ab initio* derivatives of shielding surfaces by Chesnut and Wright³⁵ confirms the preponderance of negative first (and second) derivatives. (c) The magnitude of the shift is related to the fractional change in mass upon isotopic substitution. This is directly a result of the dynamic averaging and has been verified by calculations of vibrational

averages.¹¹⁵ The mass factor comes from the mean bond displacement and mean square amplitudes, that is, the amplitudes of motions on the surface depend in an explicit way on the masses of the atoms undergoing the excursions, and are best treated in terms of curvilinear internal coordinates, taking into account the symmetry of the whole molecule. Nevertheless, some simplifying assumptions lead to the proportionality of the isotope shifts of multiple isotopes on the mass factors $[1 - (\mu/\mu')^{1/2}]$ or $(m' - m)/m'$ that had been derived for diatomic molecules^{37,135} and found empirically valid for polyatomics.¹¹⁵ (d) The additivity exhibited by isotope shifts is also a consequence of the dynamic averaging and has been theoretically derived¹³⁴ and experimentally verified exhaustively. Where sizeable deviations from additivity occur, intermolecular effects have been found to play an important role.

There are some qualitative trends which have been observed, correlating isotope shifts with molecular structure, which are less universal in nature but nevertheless useful on occasion. These trends were attributed entirely to the dependence of the derivatives of the shielding surfaces on various indices of the chemical bond.³⁹ *Ab initio* calculations of such derivatives reaffirm these notions which had been based entirely on experimental data and the dynamic averaging model:

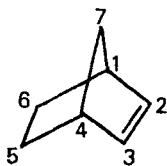
- (1) One-bond isotope shifts tend to increase with increasing bond order (and the accompanying decreasing bond length) between the observed nucleus and the substituted atom. The nature of the chemical bond determines the shape of the shielding surface at the equilibrium geometry; thus, Chesnut's survey of shielding derivatives shows trends with respect to bond orders³⁵ (as in Fig. 3).
- (2) When an end atom is observed, the isotope shift correlates with the chemical shift of the observed nucleus; that is, the less shielded nuclei have larger isotope shifts. This is a parallel behaviour to that of the temperature coefficient shown in Fig. 14. Both correlations had been interpreted to mean that the first derivatives of shielding surfaces with respect to bond extension correlate with the shielding value at the equilibrium geometry.³⁸ ¹⁹F and ¹⁷O shielding surfaces have subsequently been found to possess derivatives that do correlate with the shielding values at equilibrium. Thus, ¹³C in C=O functional groups and ¹⁹F in fluorocarbons give a nice experimental correlation in isotope shifts (or temperature coefficients) vs. shielding and also a nice correlation between *ab initio* shielding derivatives and shielding. When observing other than terminal atoms, the situation becomes clouded by the multiple terms that contribute to the shielding in various bonding situations, thus, derivatives with respect to stretching of one of the bonds do not correlate well with shielding in these situations.

- (3) The isotope shifts tend to be larger in the presence of a lone pair or a net negative charge, or when electronegative substituents are introduced at the nuclear site, as in H_2O , H_3O^+ , NH_3 , NH_4^+ , PH_2^- , PH_3 , PH_4^+ , SnH_3^- , SnH_4 , SnH_3^+ .^{124,131,139,140} Where they had been calculated, the shielding derivatives are indeed found to be larger negative in H_2O than in H_3O^+ , NH_3 than in NH_4^+ , PH_3 than in PH_4^+ , for example. Table 2 shows that in those cases where the multidimensional shielding surface has been calculated in the immediate vicinity of the equilibrium geometry and the complete dynamic averaging has been done properly, the largest contributions to the isotope shifts are due to the terms in Δr and $(\Delta r)^2$. With estimates for the thermal averages of Δr and $(\Delta r)^2$ being readily available,¹³⁵ isotope shifts can be used to estimate shielding derivatives directly from the experimental data.^{40,56}

The isotope shift depends in principle on all the shielding derivatives and the dynamic averages of all the internal coordinates of a molecule.³⁷ Isotope shifts due to substitution at a remote bond would at first glance involve only higher-order terms since the local mass effect on the dynamic averaging occurs primarily at the substitution site which is remote from the nucleus whose shielding is observed. On the other hand the mass effects at the bonds directly attached to this nucleus are expected to come entirely from the coupling between vibrations involving displacements of the atoms where isotopic substitution takes place and those involving displacements of the bonds directed to the observed nucleus. Of these two types of higher-order terms, it was predicted that the secondary shielding derivative with respect to remote bond extension together with the primary mass effect at the substitution site dominates the isotope shifts over two or more bonds.⁵⁵ This means that these long-range isotope shifts contain electronic information and can serve as a gauge of the electronic transmission through bonds between the observed nucleus and the substitution site, certainly more useful than a gauge of long-range coupling of local vibrational modes. The 2-bond and 3-bond isotope shifts had been attributed to the secondary derivative, that is the non-negligible derivative of the shielding with respect to the stretching of the remote bond at which the isotopic substitution has taken place.^{55,141,142} Chesnut's survey of shielding derivatives indeed shows the importance of secondary derivatives.³⁵ The usual fall-off of the magnitude of the isotope shift with the remoteness of the substitution had been explained in terms of the secondary derivatives being generally smaller than the primary derivatives.⁴⁰ Chesnut and Wright find that this is not always true; there are some secondary derivatives that are comparable to and occasionally even larger than the primary derivatives.³⁵ Also, these derivatives can be of either sign, although large values are usually negative. The observed correlations of 2-bond and 3-bond isotope shifts with the

corresponding coupling constants^{122,143} indicate involvement of the electronic transmission path between the nuclear site and isotope substitution site, which further supports the importance of the secondary derivatives. The fall-off with distance from the resonant ^{13}C nucleus in an aromatic system is not nearly as fast as in saturated ones. For example, in adamantane and derivatives, the isotope shifts for $n = 1$ –5 bonds away are 400–800 ppb, 85–200 ppb, 8–46 ppb, 0–20 ppb, and 0–10 ppb,¹⁴⁴ whereas for $n = 1$ –3 bonds in aromatic systems they are 190–380 ppb, 50–213 ppb, 28–100 ppb.¹⁴⁵

The remote secondary shielding derivatives associated with long-range isotope shifts can be of either sign, and even in the same molecule both signs can be obtained. To illustrate this, we consider norbornene, in which the deuterium-induced ^{13}C shifts have all been measured and found to be of both signs, negative (usual) for carbons 1–4 and positive (unusual) for carbons 5, 6, and 7 upon deuteration at the ethylenic carbon.¹⁴⁶ We have



carried out *ab initio* GIAO calculations of the traces corresponding to the variation of the symmetry coordinate, the symmetric stretch, $S_1 = [\Delta r(\text{C}_2\text{--H}_2) + \Delta r(\text{C}_3\text{--H}_3)]$ in the ^{13}C shielding surfaces of all carbons in this molecule.¹⁴⁷ These calculations reveal that in the vicinity of the equilibrium geometry, the traces for $^{13}\text{C}_1$ and $^{13}\text{C}_4$, $^{13}\text{C}_2$ and $^{13}\text{C}_3$ shielding decrease monotonically with increasing S_1 , whereas the $^{13}\text{C}_5$, $^{13}\text{C}_6$ and $^{13}\text{C}_7$ shielding definitely increase (albeit only slightly) with increasing S_1 . Thus, in the same molecule the ^{13}C shielding derivatives with respect to remote C–H stretching are of opposite signs, consistent with the corresponding signs of the observed isotope shifts.

3.3. Intermolecular shifts

Solvent shifts can sometimes involve the formation of hydrogen bonds or the formation of an association complex. For example, the very useful shifts that distinguish between the left- and right-handed forms of a molecule by the different chemical shifts they exhibit in association with a chiral solvent are entirely due to differential intermolecular shieldings, the averages over the configurations of the diastereomer R–C being slightly different from the averages over the configurations of the diastereomer S–C when solvent C is chiral. Observed chiral shifts are of the order of 0.025 ppm for ^1H ,¹⁴⁸ 0.036 ppm for ^{19}F ,¹⁴⁹ and 0.164–0.685 for ^{15}N .¹⁵⁰ In these applications, the

observed nucleus generally has to be fairly close to the chiral centre, but not necessarily. A dramatic example is a chiral auxiliary reagent with a ^{77}Se nucleus in a selenocarbonyl group which exhibits sufficient sensitivity to report on more distant chiral centres. The diastereomers which result from the coupling of the reagent to (R,S) lipoic acid have the chiral centre of the lipoyl group eight bonds away from the ^{77}Se , yet the ^{77}Se NMR spectrum features two clearly resolved resonances separated by 0.119 ppm.¹⁵¹ Because stereospecific interactions between such solute and solvent molecules at short range lead to a correlated intermolecular geometry, corresponding nuclei in S and R enantiomers in the diastereomeric pairs will experience different shieldings via the usual mechanisms operating in intermolecular effects on shielding, leading in many instances to an experimentally significant shielding non-equivalence. The differential averages over the orientations of the benzene solvent molecules for a rod-shaped solute and a spherical solute molecule account for the observed chemical shifts in aromatic solvents, which was explained by Buckingham *et al.* in terms of the anisotropy of the magnetic susceptibility of the aromatic solvent molecules.¹⁵² What we discuss in this section, however, are those theoretically calculable intermolecular shifts, which serve as quantitative paradigms for the dynamic averaging over the intermolecular shielding surfaces where no specific interactions or associations need be invoked, and can therefore serve as the examples of ever-present intermolecular shieldings.

3.3.1. The chemical shift in the gas phase

The shielding, just as any other molecular electronic property measured in the bulk, can be expressed in terms of an expansion in the density:¹⁵³

$$\sigma(\text{T},\rho) = \sigma_0(\text{T}) + \sigma_1(\text{T})\rho + \sigma_2(\text{T})\rho^2 + \sigma_3(\text{T})\rho^3 + \quad (10)$$

where $\sigma_1(\text{T})$ is the second virial coefficient of nuclear shielding. The early measurements of the virial coefficients of shielding involved protons in molecules such as HCl. The interpretation of these shifts by Raynes, Buckingham and Bernstein was largely tied up with the notion that the intermolecular shifts could be viewed in terms of electric field effects.⁸⁹ With the use of the Drude model this was extended to fluctuating electric fields to represent the dispersion contributions,⁸⁹ not so important in protons.¹⁵⁴ However, the large magnitudes of the intermolecular shifts of ^{129}Xe in mixtures of Xe with rare gases and other molecules severely tested the model, requiring a rather large dispersion contribution to account for the large second virial coefficients of shielding for this nucleus.¹⁵⁵ Furthermore, the rather large temperature dependence also presented a problem.¹⁵⁶ The lack of reliable intermolecular potentials at that time left the problem unresolved. Reliable calculations of the B coefficient, supposedly the same

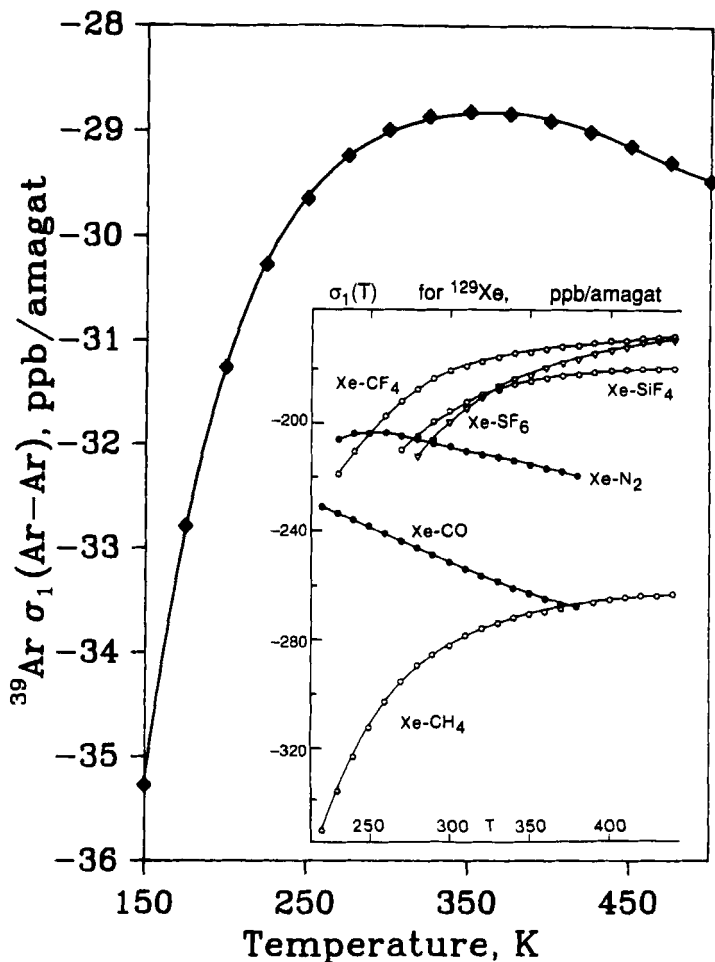


Fig. 15. The second virial coefficient of shielding $\sigma_1(T)$ for ^{39}Ar in argon gas,²⁴ calculated from the *ab initio* shielding surface and the potential surface from Aziz-Chen.²⁹ Most experimental $\sigma_1(T)$ curves exhibit the behaviour similar to that calculated for argon below 350 K, that is, the magnitude of the density coefficient of the chemical shift in the gas phase decreases with increasing temperature. There are, however, at least two examples (Xe-CO and Xe-N₂) of behaviour like the calculated curve above 350 K.

one for the fluctuating electric fields as for a uniform static field, were not available until a much later date. Given the theoretical shielding surfaces for rare gas pairs,^{23,24} and the reliable potential surfaces now available, it is possible to carry out the proper averaging to obtain the second virial coefficients as a function of temperature. An example is shown for the ^{39}Ar in Ar_2 virial coefficient of shielding in Fig. 15. The behaviour of this $\sigma_1(T)$

over a wide temperature range is typical of most of the experimental ^{129}Xe $\sigma_1(T)$ values that are known. The sign is negative at all temperatures, that is, intermolecular effects are generally deshielding.^{101,114} The temperature dependence that has been observed for most of the ^{129}Xe $\sigma_1(T)$ is such as to make the deshielding effect more exaggerated at lower temperatures. However, there have been at least two examples, Xe in CO and Xe in N_2 mixtures, in which the behaviour is opposite.¹⁵⁷ We see in Fig. 15 that both behaviours are present; it is only the range of temperatures relative to the well depth that limits the observations to one or the other side of the maximum in the $\sigma_1(T)$ function in most cases. The calculated $\sigma_1(T)$ for the ^{129}Xe nucleus in Xe–Ar, Xe–Kr, and Xe–Xe interactions in the gas phase are shown in Fig. 16. The agreement with the experimental data is reasonably good: the signs are correct, the relative magnitudes are correct, and the temperature dependences are about right. With this, the density dependence of the chemical shift in the gas phase may be said to be understood. The intermolecular shifts of molecules with structure are rather more difficult to calculate because not only the distance but the orientations have to be considered in constructing the shielding surface and in the dynamic averaging. There are some ^{13}C σ_1 data which have recently been measured; these are also found to be uniformly negative.¹¹⁶ Other nuclei for which fairly large $\sigma_1(T)$ values have been measured in the gas phase are ^{19}F nuclei in various fluorocarbons, with values ranging from -0.0048 to -0.045 ppm amagat⁻¹.¹⁰¹

The striking examples of intermolecular shifts that have positive σ_1 are the shifts of N nuclei in the types of nitrogen environments that involve low-lying $n\text{-}\pi^*$ excited states in the shielding, for example, HCN, MeCN, pyridine.¹⁵⁹ To interpret these observations it is necessary to calculate the whole shielding surface for at least the dimer and then do a proper averaging over the surface. This has not yet been done; however, there is at least one configuration for the dimer in which increased N shielding compared to the monomer MeCN has been calculated.¹⁶⁰ HCN is known to form linear hydrogen-bonded complexes $(\text{HCN})_n$ which leave the C–H bond intact upon exchange. A proper average would allow the size of the n -mers to vary. This, alas, is not yet possible. In the following section, however, we consider a system in which a proper average over all the configurations of the n -mer is carried out at each temperature and the average chemical shifts agree with experiment.

3.3.2. *The average chemical shifts of Xe in zeolites*

Physisorption is a result of intermolecular interactions between an adsorbate and the atoms of the host matrix. The sorbate–sorbate interactions affect the observed adsorption isotherms and other properties including diffusion of the sorbate molecules through the host lattice. One particularly interesting

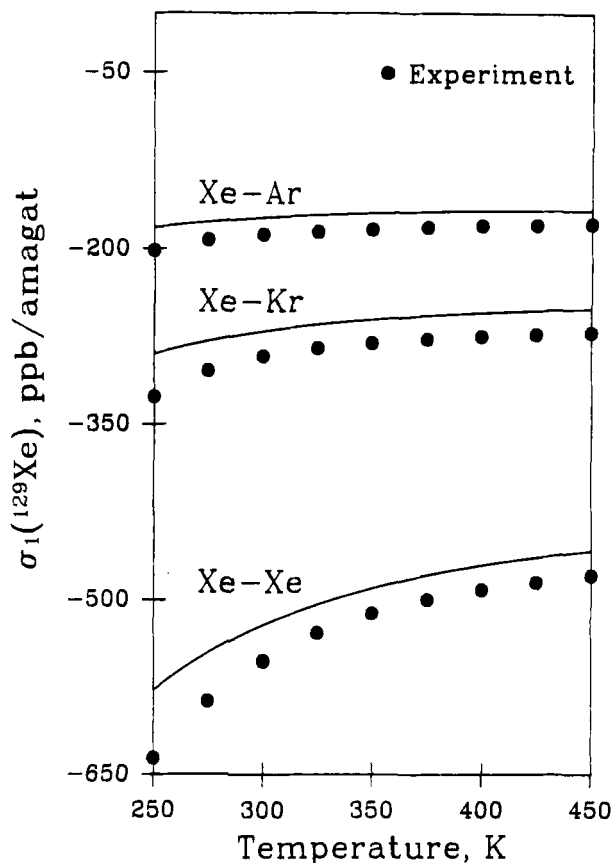


Fig. 16. The second virial coefficients of shielding $\sigma_1(T)$ for ^{129}Xe for Xe in Ar, Xe in Kr, and Xe in pure Xe gas have been calculated from the *ab initio* Ar-Ar shielding surface scaled to ^{129}Xe in Xe-Ar, Xe-Kr and Xe-Xe respectively. The results agree with experiment in sign, in relative magnitudes, and in the temperature dependences. Experimental values are from Refs 156 and 158.

example of this phenomenon is the intermolecular shifts of the Xe nucleus due to the interactions with the atoms of a zeolite. The ^{129}Xe chemical shift in the limit of extremely low loading of xenon in the zeolite (relative to the isolated Xe atom) has been found to vary greatly depending on the internal structure of the zeolite and the types of counterions that are present in it. Furthermore, the effects of the sorbate-sorbate interactions on the chemical shifts are very large, with the ^{129}Xe chemical shift increasing with increasing average number of Xe atoms per unit cell. These shifts are of the order of tens and hundreds of ppm. Since the Xe-Xe shielding surface has been derived, it should be possible to calculate the grand canonical average of the ^{129}Xe chemical shift under those conditions in which the major contributions

to the shielding are indeed due to the sampling of all possible Xe–Xe distances. In order to do this, we need to consider a shielding surface that can be calculated on the fly, changing with the numbers of neighbours as the numbers of sorbate atoms fluctuate in the grand canonical ensemble. We have seen already in the example of the triangular and linear Ar_3 clusters that as long as the Ar atoms do not get much closer than about $0.9r_0$, the isotropic shielding contributions can be obtained by additivity. We therefore construct the ^{129}Xe shielding surface as we go, summing up over all the atoms that are sufficiently close (less than 12 Å). An approximate shielding surface has been constructed to include interactions with the oxygen atoms in the zeolite framework and the Na^+ ions which provide the counterbalancing charges in this particular aluminosilicate (zeolite NaA). The observations in this particular zeolite are even more detailed than in all other cases. Here, what is observed is not an average chemical shift under fast exchange of the Xe with a very large number of cavities containing a varying number of Xe atoms, but rather the individual chemical shifts of trapped clusters of Xe atoms, Xe_1 , Xe_2 , Xe_3 , . . . up to Xe_8 . The chemical shifts have been measured as a function of temperature and these pose dynamical averaging challenge for the theory.⁶⁴ Typical spectra of samples of xenon in zeolite NaA are shown in Fig. 17. The shielding of the ^{129}Xe in the Xe_n clusters changes according to n ; the most deshielded nuclei are in the Xe_8 cluster. It is of interest that the cluster shift is in the direction given by $\sigma_1(\text{T})$ observed in the gas phase. However, the incremental change is not a fixed amount but increases slightly in going from 1 to 6. Furthermore, there is a big change in shielding in going from Xe_6 to Xe_7 and then again in going from Xe_7 to Xe_8 . These are all consequences of the dynamic averaging over these various shielding surfaces. Given the potential function for the interaction of a single Xe atom with the lattice and the Na^+ ions, given that the total potential energy is assumed to be a sum over all the pairwise interactions at distances less than some cutoff distance, and given the interaction potential function for the Xe–Xe interactions, likewise taken to be pairwise additive, then the properly weighted large number of configurations (a million or so) can be summed in a Grand Canonical Monte Carlo (GCMC) scheme. At each of these configurations the shielding of every Xe nucleus is calculated. Thus, the average chemical shift of a ^{129}Xe nucleus can be calculated. The isotropic shielding averaged over all the Xe atoms in the cluster is separately stored for each of the eight cluster types so that the average chemical shift for each Xe_n can be obtained. This is done at each temperature. The temperature and the chemical potential of the adsorbed xenon are set, while the numbers of xenon atoms are allowed to fluctuate. The averages at various temperatures can then be compared with the experimental chemical shifts at these temperatures. We show the results in Table 3 and in Fig. 18. The agreement of the GCMC average with experiment is excellent, especially considering that there are no adjustable parameters here; none of

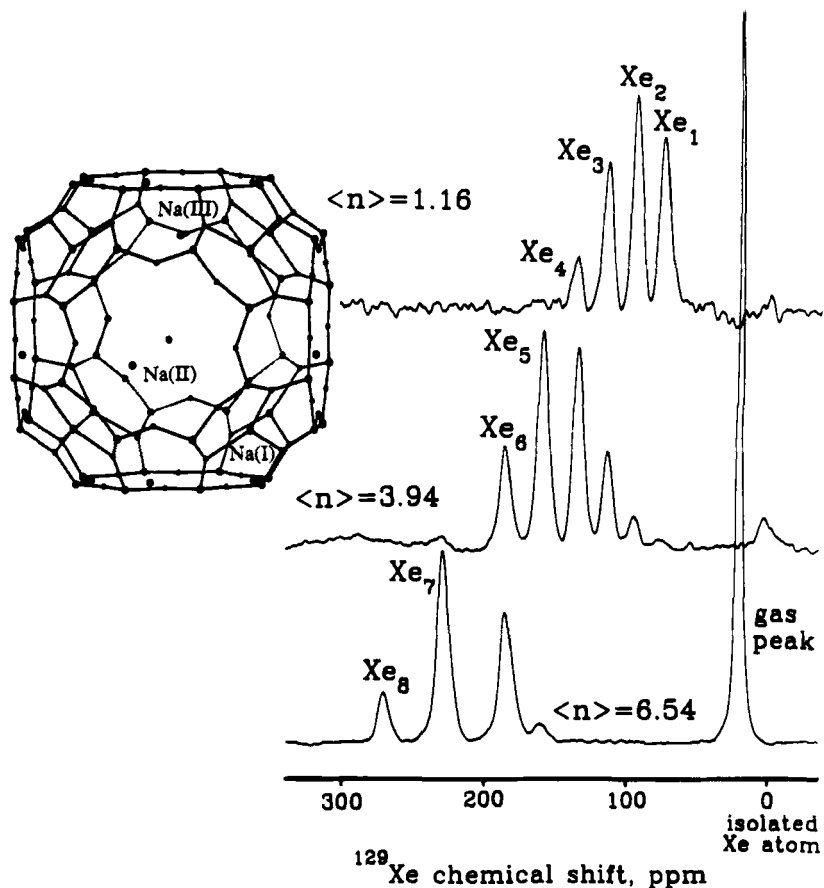


Fig. 17. The ^{129}Xe NMR spectra of xenon atoms trapped in the alpha cages of zeolite NaA, showing the large intermolecular chemical shifts which are absolutely referenced to an isolated Xe atom. The observed $^{129}\text{Xe}_n$ chemical shift is a thermal average over all sampled configurations of the Xe_n in an alpha cage. The intensities of the signals from the cages containing 1, 2, 3, . . . , 8 Xe atoms provide the distributions of occupancies in each of the three samples at low, medium, and high xenon loading.^{64,102}

the experimental values has been used to adjust any of the chemical shifts. The calculated and experimental quantities being compared are in absolute terms, that is, the shieldings are relative to the free Xe atom in both calculation and experiment. A very important point to be made here is that the proper averaging had to be carried out. There is a large number of local minima in the configuration space of each of the clusters. The shielding of Xe in these minimum energy configurations for the clusters have also been calculated. It is important to note that the shieldings from these minimum

Table 3. Shielding of Xe_n clusters trapped in the alpha cages of zeolite NaA, ppm.

n	$\langle\sigma(\text{Xe}_n) - \sigma(\text{free atom})\rangle$		Increments $\langle\sigma(\text{Xe}_n)\rangle - \langle\sigma(\text{Xe}_{n+1})\rangle$	
	EXPT ⁶⁴	GCMC ¹⁰²	EXPT ⁶⁴	GCMC ¹⁰²
1	-74.8	-77.2		
2	-92.3	-92.6	17.5	15.5
3	-111.7	-109.6	19.4	17.0
4	-133.2	-129.9	21.5	20.3
5	-158.4	-155.4	25.2	25.5
6	-183.5	-184.2	25.1	28.9
7	-228.3	-226.0	45.1	41.7
8	-272.3	-269.7	43.7	43.7

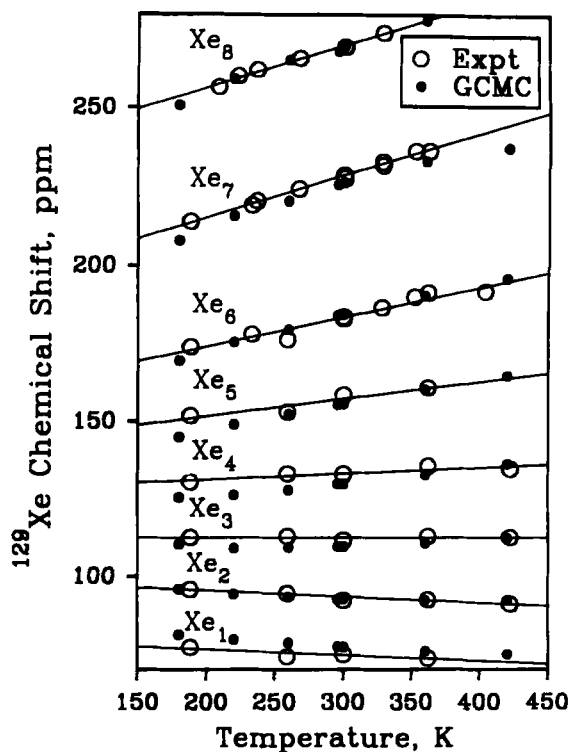


Fig. 18. The temperature dependence of the average ^{129}Xe chemical shift in each of the Xe_n clusters trapped in the alpha cages of zeolite NaA is reproduced by taking a Grand Canonical Monte Carlo average, using a ^{129}Xe shielding surface that is a sum of pairwise intermolecular shielding functions derived from *ab initio* calculations.^{64,102}

energy configurations provide chemical shielding increments from one cluster to the next that are not at all like the ones obtained from the GCMC averaging. The observed incremental shifts from one cluster to another cannot be reproduced if only the minimum energy cluster structures are considered. The proper average over the configurations dictated by the multidimensional potential energy surface had to be carried out. This dynamic averaging becomes even more important when the molecule is freely migrating from one cage to another, sampling a variety of occupancies within the NMR time scale in zeolites with open cages. The single peak observed there provides a chemical shift that is averaged not only over the possible configurations of the xenon atoms within one cage, but also averaged over the distribution of occupancies throughout the zeolite.

The gas-to-adsorbate shift, that is, the chemical shift of a single Xe atom in a zeolite cavity, was also well reproduced in this case. However, this is more fortuitous than real, given that the Xe-zeolite shielding function was only approximate.

3.3.3. Gas-to-liquid and gas-to-solution shifts

In the above example, the number of atoms involved in the averaging was finite. Although the zeolite contributions to the shielding changed somewhat from cluster to cluster, the major shielding differences came from the varying magnitudes of Xe-Xe contributions to the shielding. We now consider a situation more comparable to the single average shielding observed under fast exchange conditions. An obvious intermolecular shift is the gas-to-liquid shift or the gas-to-solution shift. In Fig. 19, the ^{19}F chemical shifts in the liquid and in the vapour observed in equilibrium with it are temperature dependent due to intermolecular interactions and intramolecular vibrational averaging. On the other hand, the gas-to-liquid shift $[\sigma_{\text{liq}} - \sigma_{\text{vap}}]$ is entirely an intermolecular shift and is a function of the change in $[\rho_{\text{liq}} - \rho_{\text{vap}}]$ with temperature. Note that the gas-to-liquid shifts are expected to approach zero at the critical temperature. For each of four monosubstituted fluoroethenes, each distinct nucleus in the same molecule has an intermolecular shift that is related to its distance from the molecular centre of mass, a nuclear site effect that comes from slightly different dynamic averaging in each case. Note that for a fluoroethene with a substituent lighter than F, the order of intermolecular shifts is different than for a fluoroethene with a substituent heavier than F. It is found that the σ_1 are in the same rank order as the $[\sigma_{\text{liq}} - \sigma_{\text{vap}}]$ in Fig. 19. When the substituent is H, the σ_1 values at 300 K are -11.8 , -19.0 , -18.9 ppb amagat $^{-1}$ for F_A , F_B , F_C , respectively. For fluoroethene itself, it is -17.8 ppb amagat $^{-1}$. When the substituent is Cl, the σ_1 values at 300 K are -26.7 , -25.1 , -24.8 ppb amagat $^{-1}$ for F_A , F_B , F_C , respectively; when it is Br, the σ_1 values at 300 K are -31.4 , -26.8 , -26.7 ppb amagat $^{-1}$.

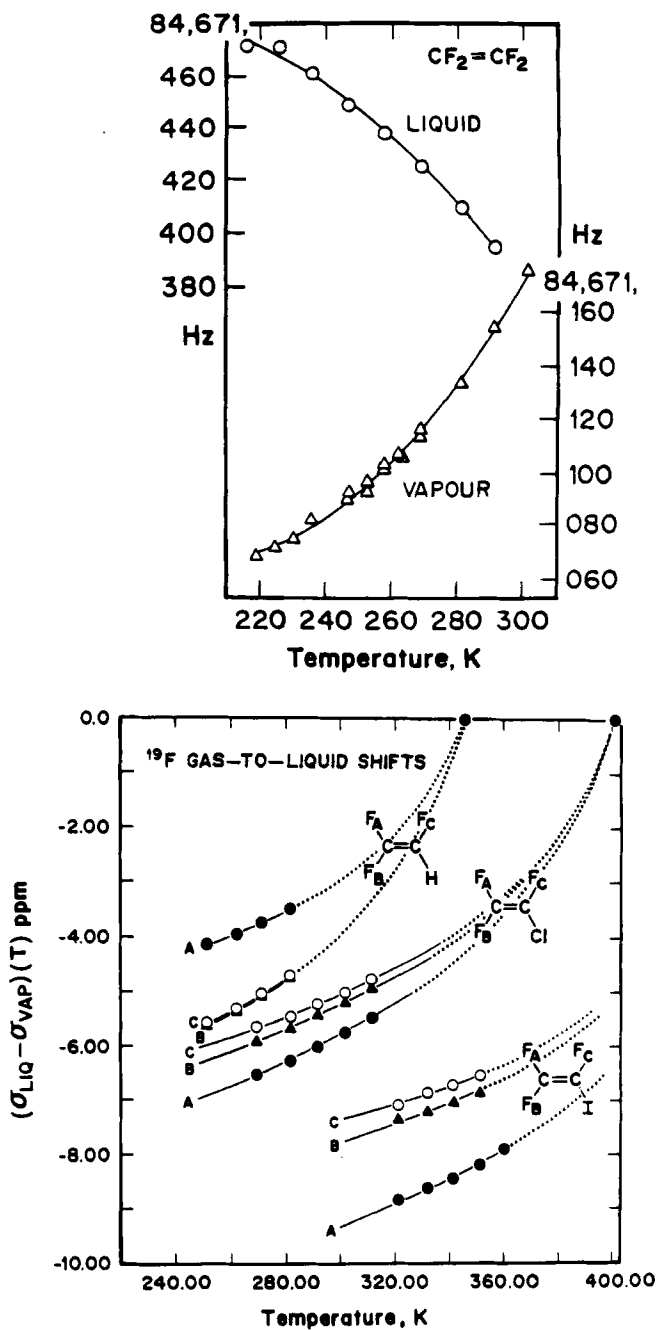


Fig. 19. The temperature dependence of the gas-to-liquid shifts in fluororoethenes. Reproduced from Ref. 161, with permission.

Table 4. Experimental gas-to-liquid shifts.

Nucleus	Molecule	ppm	T, K	Ref.
^1H	NH_3	-1.75	300	162
	H_2O	-4.368	298.2	163
^{17}O	H_2O	-36	300	133
^{13}C	C_6H_6	-1.5	300	164
	TMS	-4	300	164
^{15}N	HCN	-7.68	346.6	159
	NH_3	-19.5	300	162
	HCN	+10.4	346.6	159
	MeCN	+11.3	227.5	165
^{19}F	CF_3Cl	-3.65	280	166
	CF_3I	-5.305	280	166
	CFCl_3	-5.994	340	167
	SeF_6	-4.8	300	115
	WF_6	-7.4	300	115
	CH_3F	-7.7	260	168
	ClF	-25.6	220	169
^{31}P	P_4	-77	526	170
^{77}Se	SeF_6	-1.38	300	115
	H_2Se	-120	300	115
^{129}Xe	Xe	-200	244	171-172

respectively; and when the substituent is I, the σ_1 values at 300 K are -61.8, -51.2, -49.7 ppb amagat $^{-1}$ respectively for F_A , F_B , F_C .¹⁶¹ To calculate these intermolecular shifts due to interactions between freely rotating molecules, the ensemble average has to be carried out over all orientations and distances; a nucleus that is further from the centre of mass will sample somewhat shorter interaction distances than one that is closer to the centre of mass in the same molecule. Intermolecular shielding functions of the form similar to those in Fig. 10 have larger negative values at shorter distances. Thus, the ensemble average $\sigma_1(\text{T})$ is largest negative for the nucleus which is furthest from the centre of mass. This is indeed what is found consistently in each of the substituted fluoroethenes. Evidence such as this underscores the importance of dynamic averaging to the understanding of observed chemical shifts.

Many gas-to-liquid shifts have been measured for ^{19}F nuclei, and a selected few for other nuclei. It is interesting to compare the relative sensitivity of different nuclei to deshielding effects of the surrounding medium. Table 4 shows a few examples. The ^{17}O in H_2O and ^{77}Se in H_2Se gas-to-liquid shifts are proportionately large, as may be expected, according to either $\langle a_0^3/r^3 \rangle$ for the atoms or the ranges in the O and Se chemical shifts. The magnitudes of these shifts of course depend on temperature and the density of the liquid. Where exactly the same set of solvents is used and

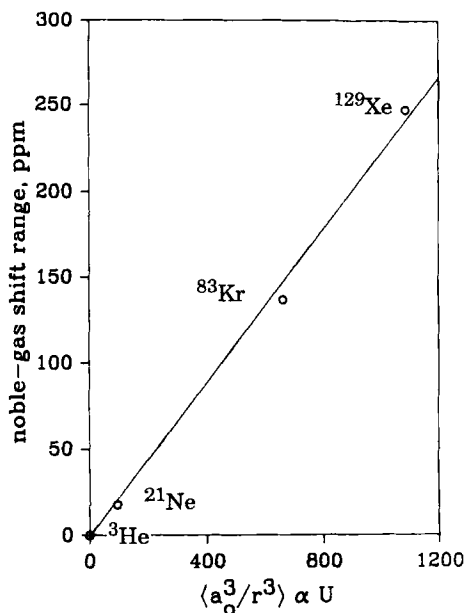


Fig. 20. The ranges of the chemical shifts of the rare gas atoms dissolved in the same set of organic solvents¹⁷³⁻¹⁷⁶ are proportional to the scaling factors $\langle a_0^3/r^3 \rangle \propto U$ for the atom.

the chemical shifts of the solutes (in the limit of infinite dilution) can be compared, some interesting trends emerge. For example He, Ne, Kr, and Xe solution shifts have been measured in exactly the same set of organic solvents.¹⁷³⁻¹⁷⁶ It is found that the chemical shift range in these solvents correlates with some properties of the rare gas. In Fig. 20 we show the correlation with the fundamental quantities which are properties of the rare gas atom in question, the same factors that have been used for scaling the shielding surfaces: $\langle a_0^3/r^3 \rangle \propto U$. The sensitivity of a nucleus to the deshielding effects of intermolecular interactions depends on the rare gas atom's ability to polarize and be polarized by the solvent. At the same time, the intrinsic sensitivity of its shielding to such changes in electronic environment is dependent on the factor $\langle a_0^3/r^3 \rangle$. Of course, this is not a unique correlation, and in fact the authors¹⁷⁴ had previously proposed a proportionality to the diamagnetic shielding σ^d of the rare gas atom, although it is not obvious why such a correlation should exist since it is the paramagnetic term that is largely responsible for the deshielding effects of intermolecular interactions for the rare gas atoms.²³ The chemical shift ranges of Xe:Kr:Ne:He in the set of solvents are 250:140:15:0.78.¹⁷⁶ With the same solvents ^{13}C in CH_4 has a relative sensitivity of 9.

4. APPLICATIONS TO MORE COMPLEX SYSTEMS

4.1. Separation of short-range and long-range effects on shielding

Disk space, memory size and computation time often limit the size of the molecule that one can study using *ab initio* methods. During the past few years, nuclear magnetic shielding calculations gained considerable momentum from the developments in both hardware and software. For example, shielding calculations for a molecule with 50 atoms or more are now possible on workstations through direct algorithms.¹⁷⁷⁻¹⁷⁹ With faster processors, the time needed for evaluating two-electron integrals has significantly decreased, rendering the storage of these integrals no longer necessary. Current work in parallelization of code¹⁷⁹ which allows for sharing of computer resources would further ameliorate the present limitations. Simultaneous with these algorithmic advances is the evolution of techniques designed to lessen the computational requirements. The introduction of local origins in the GIAO, IGLO and LORG methods has considerably decreased the saturated basis set size to a manageable level. In addition, the local nature of chemical shielding permitted the use of attenuated basis sets¹⁸⁰ in which only the nucleus of interest and its immediate neighbours are assigned a large number of basis functions. On the other hand, in common origin calculations, it has been observed¹⁸¹ that a monotonic basis set dependence of the shielding could be established in a small model molecular fragment as in the molecule benzene. Calculations for molecules that are much larger but still similar to benzene (e.g. fullerenes) can then be performed with small basis sets and later extrapolated to the infinite basis size value using the basis set dependence found in benzene. Clearly, the use of physical insight drawn from *ab initio* calculations on small molecules can indeed help in devising strategies to overcome the present practical limitations.

An understanding of the nature and origins of the chemical shift permits categorization and, in turn, can make the computation more manageable. For example, the shielding at a particular nucleus can be subdivided into the following contributions:⁶⁵

$$\sigma_{\text{total}} = \sigma_s + \sigma_l + \sigma_o. \quad (11)$$

The first term, σ_s , represents the short-range contributions to the shielding. In this first term, local structural factors such as bond lengths, bond angles and torsion angles are taken into account. Their evaluation requires full *ab initio* calculations; that is, all atoms contributing to the chemical shift are assigned basis functions and this aspect distinguishes σ_s from the rest of the terms in Eq. (11). Since the categorization is an operational one, interactions other than those arising from changes in the local geometry around the nucleus of interest that likewise needs a full *ab initio* treatment are also

included in σ_s . Examples are intermolecular interactions that occur at shorter distances ($< 2.5 \text{ \AA}$) and these can either be attractive as in hydrogen bonding^{52,71,182} or repulsive as in molecules colliding in the gas phase.²⁴

The second term, σ_1 , representing the long-range electrostatic contribution, arises from polarization of the electron clouds around the nucleus concerned. Having a relevant range of distances that is much longer than in σ_s , σ_1 can be evaluated through a variety of methods. A reaction field could be used. This represents all the atoms not included in σ_s by a uniform dielectric medium. The disadvantage of this approach is that the environment is treated with a strictly non-atomistic model so that differences in configurations of atoms providing the environment outside of σ_s cannot be taken into account at all. A better approach is to replace all other atoms not included in σ_s by point charges or by point electric multipoles, and then calculate the long-range contributions to the shielding due to these point charges and/or multipoles. One method to do this is the charge-field perturbation (CFP) method which is a full *ab initio* treatment of the fragment that includes all atoms participating in σ_s in the presence of the point charges. This method has been shown⁶⁵ to give results that compare favourably with supermolecule calculations. Figure 21 exemplifies this favourable agreement in the system where fluorobenzene interacts with hydrogen fluoride. It can be seen that the results obtained using point charges to represent the perturbing HF molecule are very close to the values obtained when basis sets are also assigned to the HF molecule. This approach, the CFP method, can actually be regarded as an extreme case of the locally dense basis technique introduced by Chesnut and Moore.¹⁸⁰ Another method is to do *ab initio* calculations of the fragment (that includes all atoms participating in σ_s) in the presence of a uniform field at various strengths⁸² to obtain the shielding polarizabilities defined in Eq. (1) and in an electric field gradient to obtain the shielding derivatives with respect to a field gradient. Alternatively, all these derivatives can be obtained at the same time by Derivative Hartree-Fock (DHF) theory.¹⁸³ The Taylor series expansion Eq. (1) plus the gradient terms proposed by Buckingham and Lawley⁸⁰ then provide the shielding under any conditions of perturbing electric fields. Only the coefficients in Eq. (1) require *ab initio* methods. Hence, this method offers a fast evaluation of the electrostatic contribution to the shielding provided that the derivatives are already known and only the perturbing electric field needs to be computed classically from point charges or permanent electric multipoles. Shielding polarizabilities and hyperpolarizabilities are now available for a considerable number of small molecules.⁸¹⁻⁸⁸ Interestingly, the derivatives calculated for small molecules are also found to be suitable for larger but related systems. As an example, using the ^{19}F shielding polarizabilities in fluorobenzene, the observed ^{19}F shielding inequivalencies in the 5-F-tryptophan-labelled galactose-binding protein (GBP) can be satisfactorily reproduced.^{52,184} A recent study shows

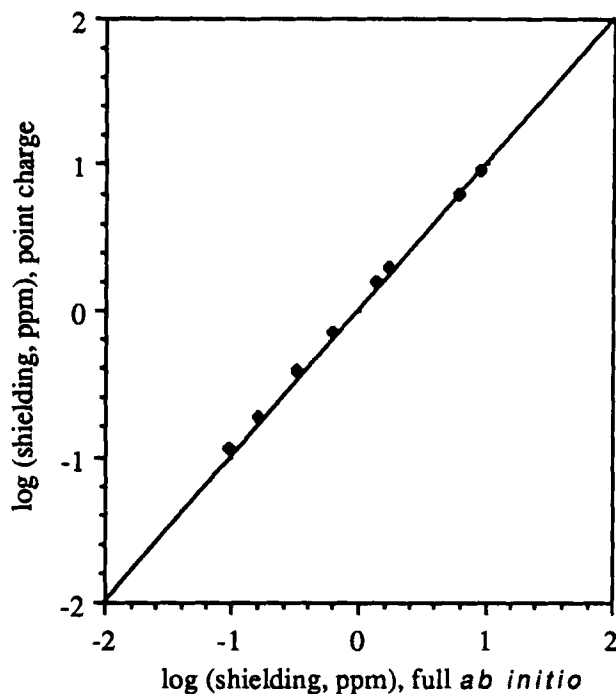


Fig. 21. Chemical shieldings of F in fluorobenzene in a series of C_6H_5F -HF dimers calculated using a full *ab initio* method versus shieldings computed using point charges to represent the HF molecule, as a function of separation distance ($r = 2.5 \rightarrow 20$ Å). Reproduced from Ref. 65, with permission.

that it is in fact necessary to include hypergradient terms in evaluating long-range electrostatic contributions to shielding.⁸¹ Unlike the shielding polarizability approach, the charge-field perturbation method does not rely on the convergence behaviour of the Taylor series expansion in Eq. (1). Representation of all atoms outside of σ_s with point charges resembles closely the non-uniformity of the electric field found in real systems.

The last term in Eq. (11), σ_o , consists of magnetic effects arising from bulk susceptibility, ring-current effects and anisotropy of functional groups such as C=O. Since this contribution to the shielding is due to a variation of the local magnetic field at the site of the nucleus, σ_o is independent of the identity of the nucleus. Consequently, for nuclei other than hydrogen, this term becomes significantly smaller than σ_s and σ_l combined and, at the present level of accuracy of *ab initio* methods, σ_o is still well within the error margin (~ 1 ppm) and, thus, can be neglected.

4.2. Use of scaling and additivity

In addition to having methods that are specialized for a particular shielding contribution, the categorization also allows for the determination of which terms are dominant. And for each of these elements, strategies can be drawn to overcome computational limitations. For example, although the determination of the shielding dependence on internuclear separation has recently become routine, systems involving heavier elements (beyond the third row of the Periods Table) still pose significant computational difficulties. Furthermore, the presence of more than two interacting bodies as observed in real systems can considerably increase the size of the computation. The previous work on Xe systems²⁴ addresses both these problems by employing scaling and additivity. Using Ar as a model, the shielding behaviour of ¹²⁹Xe in the gas phase, in solution or as adsorbed species, has been well explained. The scheme involves a scaling procedure similar to what is employed at long range in potential functions²⁹ except for an additional factor, $\langle a_0^3/r^3 \rangle$ of the ground electronic state of the atom, which takes into account the sensitivity of its shielding to electronic perturbations.^{62,63} Thus, from the internuclear dependence of the Ar shielding in the system Ar–Ar, the corresponding shielding functions for Xe–Ar, Xe–Kr and Xe–Xe, for example, can be obtained. Also, the applicability of the functions derived by this scaling procedure to real systems has been verified²⁴ in reproducing the temperature-dependent second virial coefficients of chemical shielding measured in the gas phase.^{156,158} Thus, the presence of scaling factors can be utilized in studying the shielding behaviour of heavier elements. Since *ab initio* calculations are performed on lighter atoms, large basis sets can be used and even inclusion of second-order correlation effects is possible. This is certainly the case for ³⁹Ar in Ar₂ where the second-order LORG (SOLO) method of Bouman and Hansen⁶ with a McLean–Chandler 6-311G basis augmented with three sets of *d*-type polarization functions¹⁸⁵ can be accomplished without any difficulty. And from this model study, the conclusion that second-order correlation contributions to shielding are negligible was reached,²⁴ an observation that is certainly much more difficult to gather for ¹²⁹Xe.

Real systems, especially in condensed phase, consist of more than a pair of interacting atoms or molecules. The question of how applicable the shielding functions of two-atom systems are to larger clusters comes into the picture. Calculations of ³⁹Ar shielding in argon clusters²⁴ indicate that there is additivity; that is, the intermolecular shielding of the central Ar atom in a linear Ar₃ cluster with interatomic distances of *R* is equivalent to twice that of an Ar₂ dimer separated by the same distance *R*. And using this additivity, a successful quantitative prediction of the ¹²⁹Xe chemical shifts of Xe, Xe₂ up to Xe₈ trapped in cages of zeolite NaA has been achieved.¹⁰² Likewise, it should be of no surprise to see that the long-range electrostatic effects are

also additive.⁶⁵ However, caution should be exercised, for the additivity breaks down at some distances depending on the type of interaction present. For interacting pairs of rare gas atoms, the importance of three-body terms starts to appear only at separations well inside the repulsive regions. And in the case of long-range electrostatic effects, mutual polarizations seem to be unimportant as long as the distances of interactions are longer than 2.5 Å.

The presence of scaling factors is not exclusive to an interacting pair of rare gas atoms. At much shorter distances and stronger interactions, as in the vicinity of the equilibrium bond length in diatomic hydrides, a similar relationship exists.²³ The Cl and F shieldings over the range of bond lengths within the classical turning-points of the ground vibrational states of HCl and HF are made superposable upon scaling by the factors $\langle a_0^3/r^3 \rangle R_e$, where R_e is the equilibrium bond length. This appears to be true as well for ClF and F₂. Even with the alkali hydrides, as in ²³Na in NaH and ⁷Li in LiH, although less ideal, the scaling still seems to work. Furthermore, it is unlikely that this relationship is restricted to diatomics especially when the first hints of the $\langle a_0^3/r^3 \rangle$ dependence of the internuclear shielding traces originated from studies of ¹⁵N in NH₃ and ³¹P in PH₃.^{32,33} However, the scaling holds only in a narrow range. In diatomic molecules, beyond the turning-points of the ground vibrational state, the breakdown is already imminent.

The additivity of contributions to the shielding originates from their separability from each other. It may even be possible to consider separate contributions to the short-range part: local geometry factors, hydrogen bonding and repulsive orbital overlap contributions. The local geometry factors can be evaluated separately into bond length, bond angle and dihedral angle effects. This separability manifests itself in the relatively lower magnitudes of the mixed shielding derivatives. And as deduced from *ab initio* calculations of shielding traces for ¹⁵N in NH₃³² and ³¹P in PH₃,³³ the mixed derivative of the shielding with respect to simultaneous changes in bond length and bond angle is negligibly small at the equilibrium geometry. Furthermore, the mixed terms contribute only very little to the rovibrational corrections at 300 K for these molecules. The universal additivity of isotope shifts is a consequence of the very small mixed derivatives of shielding with respect to different stretches, stretch and angle deformation, stretch and torsion, etc. Separability enables the recognition of which factors contribute the most. For example, analysis of the various contributions to ground-state vibrational corrections for the shielding of the heavy atom in the following hydrides: H₂O,³⁰ CH₄,¹¹⁷ NH₃³² and PH₃,³³ reveals that bond length effects are dominant. Likewise, the dominance of the bond length contribution is also evident in the secondary deuterium isotope shifts.

The above observations are not exclusive to the shielding surfaces of simple hydrides. Molecules as complex as amino acid derivatives also exhibit the separability of the short-range contributions to the shielding into bond

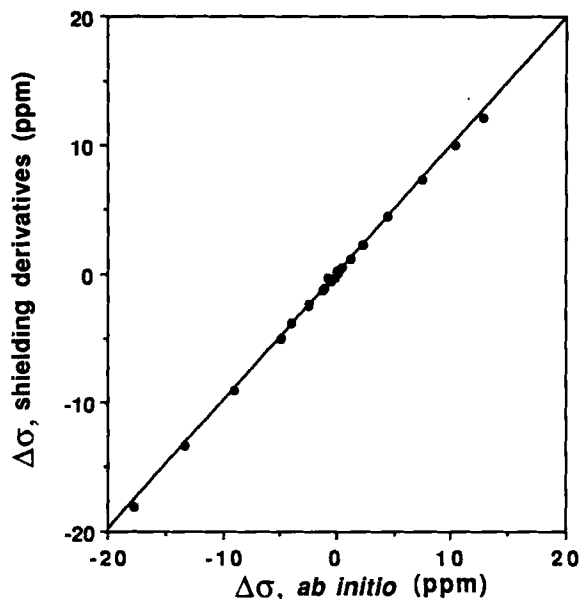


Fig. 22. Effects of simultaneously varying $C^\alpha-N$ and $C^\alpha-C^O$ bond lengths on the C^α shielding, calculated using a full *ab initio* treatment (horizontal axis) or using the bond length shielding derivatives (vertical axis). Reproduced from Ref. 41, with permission. Copyright 1993, American Chemical Society.

length, bond angle and torsion angle effects.⁴¹ Figure 22 shows the separability of the $C^\alpha-N$ and $C^\alpha-C^O$ bond length effects on the C^α shielding in formyl-L-alanine amide. It is clear that in this case, based on the excellent agreement between full *ab initio* treatment and individual shielding derivative treatment, the bond effects are additive and can be evaluated separately. This is a very significant finding: that there is no need to calculate complete shielding hypersurfaces since individual traces apparently suffice. Figure 23 shows the separability of bond length effects from the torsion angle contributions. Bond lengths normally do not vary too much, thus, traces that cover a range of 0.2 \AA are more than adequate. On the other hand, the range of torsion angles observed for amino acid residues in proteins covers a significant region of the whole space. In Figure 23, it can be seen that even with large changes in torsion angles, the shielding dependence on the bond length is unchanged. Thus, in this particular case, there is enough confidence that a shielding trace with respect to bond length changes evaluated at specific torsion angles is equally valid for other torsion angles. Determining beforehand the contributions that can be treated individually can greatly reduce the computational effort required. Unfortunately, separability does not hold for all internal coordinates. For example,

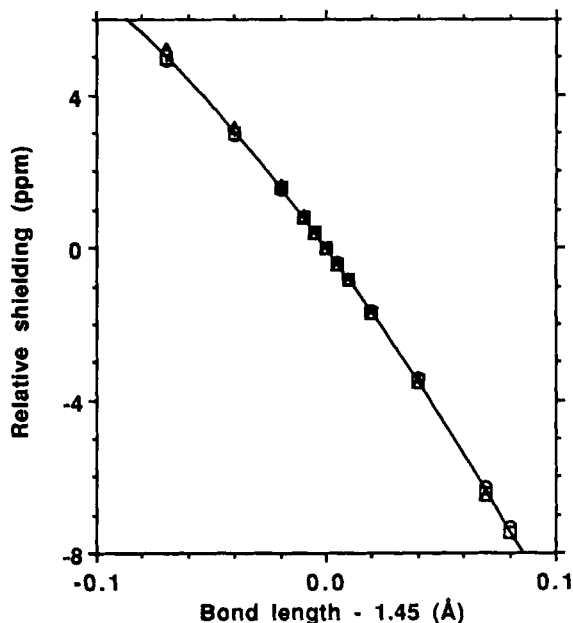


Fig. 23. Alanine C^α shielding as a function of the C^α -N bond length at different ϕ and ψ angles: helix ($\phi = -58$, $\psi = -51$) (\circ), turn ($\phi = 55$, $\psi = 50$) (\triangle), and sheet ($\phi = -71$, $\psi = 140$) (\square). Reproduced from Ref. 41, with permission. Copyright 1993, American Chemical Society.

the huge range of values of backbone torsion angles ϕ and ψ observed in proteins precludes the use of individual torsion angle shielding traces. Moreover, in other amino acids where the side-chain is more complicated than that of alanine, an additional torsion angle, χ^1 , needs consideration. This demands computation of shielding hypersurfaces that takes into account ϕ , ψ and χ^1 effects.⁵⁰

The assumption of separability of contributions to shielding combined with *ab initio* calculations of model fragments has permitted leaps in the progress in our understanding of the chemical shift in complex systems. Although chemical shift inequivalencies in protein NMR have been observed for some time,¹⁸⁶⁻¹⁸⁸ the long-awaited explanation for the origins of such inequivalencies became evident only recently via partitioning of the shielding contributions.^{41,42,50-52,65} In these studies, the dominant factors that cause the range of chemical shifts of ^{13}C , ^{15}N and ^{19}F in proteins have been identified. The differences observed in C^α shielding of alanine sites in proteins have been mainly attributed to the backbone torsion angles ϕ and ψ .^{41, 50-52} The C^β shielding, on the other hand, in addition to its sensitivity to the torsion angles, is also influenced by long-range electrostatic factors.⁵⁰ In both cases, C^α and C^β , it would have been impossible to reproduce the

experimentally observed trends using *ab initio* methods by simply using coordinates directly obtained from an X-ray structure. The large spread of values in bond lengths for the same type of residue in a single protein leads to calculated chemical shielding values that correlate with neither the range nor the pattern of observed shifts. Knowing how sensitive the chemical shielding is to bond length variations and comparing the experimentally observed shift range with the values one would obtain from the bond lengths directly extracted from an X-ray structure, it has become apparent that the variations in bond lengths presently found in X-ray structures cannot be reconciled with chemical shift range and trends. On the other hand, by simply taking into account the contributions arising from torsion angles, one can, in fact, reproduce quite well the observed C^α chemical shifts in proteins.⁵¹ The nucleus ^{19}F , although not naturally occurring in proteins, serves as an excellent probe for studying electrostatic effects on the chemical shift. Being an atom that sits on the periphery and having a substantial shielding polarizability,¹⁸⁴ the fluorine shielding inequivalencies observed in ^{19}F -tryptophan-labelled proteins can be expected to be dominated by long-range electrostatic factors. And it has been shown that the experimentally observed trend for ^{19}F NMR in proteins can be reproduced by using either a charge-field perturbation⁵² or the shielding polarizability approach.¹⁸⁴ Lastly, ^{15}N chemical shifts prove to be the most complicated. The short-range factors now include not only the torsion angles, ϕ , ψ and χ^1 of the residue which carries that ^{15}N nucleus of interest but also the torsion angles of the preceding residue.⁵²⁻⁵³ To further complicate the situation, hydrogen bonding and long-range electrostatic effects are also important.⁵² However, as long as one can take into account all of these factors, a quantitative prediction of the ^{15}N chemical shifts in proteins is still possible. In addition, it is noteworthy to point out that some of the contributions to ^{15}N chemical shifts are separable, indicating that some of these can be evaluated individually⁵² if computer resources prevent a full *ab initio* treatment.

Indeed, by separating the contributions to chemical shielding and taking advantage of their additivities, complicated systems ranging from species adsorbed in zeolite cages to large molecules such as proteins become tractable even with limited computer resources.

4.3. Use of electric field effects and dynamic averaging

As mentioned earlier, the time period of an NMR measurement allows for sampling over various conformations. Motions that are faster than the NMR time scale result in an averaging of the shielding in all three contributions: short-range, long-range and magnetic effects. The extent and significance of the dynamic averaging in each of these contributions depend on their

sensitivity to such motions. As seen in small molecules,^{30,32,33,117} ground-state vibrational corrections to the shielding are largely due to bond stretching. Of course, upon seeing how dramatic the shielding changes with variations in bond lengths, this observation should come as no surprise at all. The relative importance of motional averaging in each of the contributions also depends on which trend in experimental chemical shifts is of interest. Although the contributions of bond angle changes to the ground-state vibrational corrections are less than substantial, when it comes to the temperature dependence of the chemical shift in isolated molecules, bending motions and internal rotations begin acquiring active roles. The magnitude of the motional sampling evidently depends on the amplitude of such motion, and the shape of the potential surface dictates this amplitude. Thus, dynamic averaging of the shielding involves two surfaces: the shielding surface, this describes how shielding changes with motion; and the potential surface, this governs which configurations are possible and which ones are sampled most often. Invoking a categorization of the dynamic averaging of the shielding into various short-range effects and long-range electrostatic contributions therefore faces additional complications. The question arises, for example, of how motions involving changes in the local geometry around the nucleus affect its shielding polarizability. Separability does not apply if the motions cannot be treated individually. Fortunately, there are some cases wherein the system allows for such separation.

Thus, before one steps into more complicated systems, it is necessary to begin with systems that can serve as tests specific for a particular contribution. This has been one of the primary aims of the Jameson group and other laboratories such as Raynes', evident in their long list of chemical shift measurements in the gas phase [see Ref. 101 and references therein]. Through chemical shift measurements at various densities and temperatures in the gas phase, data that involve only the dynamic averaging of collision effects (σ_1 and its temperature dependence) or data that pertain only to the isolated molecule (rovibrational effects) can be obtained. And with these numbers available, the gauging of computational strategies designed to evaluate a particular contribution to shielding has been made possible. The shielding of rare gas atoms provides an excellent case for studying the averaging of collision effects on shielding. The excellent agreement between calculated and experimental σ_1 values for ^{129}Xe provides a strong indication that the scaling of interatomic shielding traces for rare gas atoms is a working procedure.²⁴ The successful quantitative prediction of the ^{129}Xe chemical shifts in Xe adsorbed in the alpha cages of zeolite NaA as a function of cluster size and temperature strongly supports the additivity of environmental effects to shielding.¹⁰² And for contributions arising from bond length and bond angle changes, the works on ^{13}C in CH_4 ,¹¹⁷ ^{15}N in NH_3 ,³² and ^{31}P in PH_3 ³³ offer convincing support for current rovibrational averaging methods.

Incorporation of dynamics has not been limited to small systems. The first successful attempt in reproducing chemical shifts in proteins that includes effects of motional averaging has already been reported.¹⁸⁴ This case illustrates an example wherein one factor, long-range electrostatics, dominates. By combining shielding polarizabilities, how the shielding tensor elements respond to the uniform field components and their gradient terms, with the values of the fields and field gradients obtained from molecular dynamics, a series of "shielding trajectories" can be generated. In this work, the results greatly depend on how adequate current force fields for proteins are, and, in particular, on how precise methods of computing protein electrostatics are. The Local Reaction Field model and the protein atomic charge set employed in the current ENZYME program of Lee *et al.*¹⁸⁹ appear to be useful in generating long-range electrostatic "shielding trajectories" that can explain experimental trends. One special feature of this charge set is that the sum of the atomic charges of all side-chains is zero. The absence of ionized groups apparently accounts for the insensitivity of the chemical shift to charged surface side-chains, as observed in experiment.¹⁹⁰ However, since this study involves only ¹⁹F chemical shifts in proteins in which long-range electrostatic contributions dominate, general conclusions regarding the construction of "shielding trajectories" should be drawn with caution. In this special case, the most crucial part of the computation is the evaluation of electrostatic terms. In order to verify the rest of protein force fields that describe stretches, bendings and internal rotations, nuclear shielding that exhibits sensitivity to short-range effects needs to be considered. In this respect the C^α and C^β nuclei are excellent candidates. Since the range of the torsion angles ϕ , ψ and χ^1 observed in proteins prohibits the use of shielding traces, the fastest way to evaluate the shielding at any given set of torsion angles requires shielding surfaces or even hypersurfaces. Thus, shielding surfaces serving as look-up tables for torsion angle effects, combined with shielding traces expressed as Taylor expansions that enable fast evaluation of bond length and bond angle changes, plus the use of shielding polarizabilities, provide an excellent route for incorporating molecular dynamics into protein chemical shift calculations. The strategy is certainly conceivable; however, the accuracy of the shielding surfaces still requires validation.

4.4. Predicting shifts in complex systems from shielding surfaces of model systems

As mentioned earlier in this review, it has been demonstrated that using coordinates from relaxed X-ray structures of proteins (where the large variations in bond lengths have been removed),⁵² the observed chemical shift inequivalencies in protein NMR spectroscopy can be quantitatively

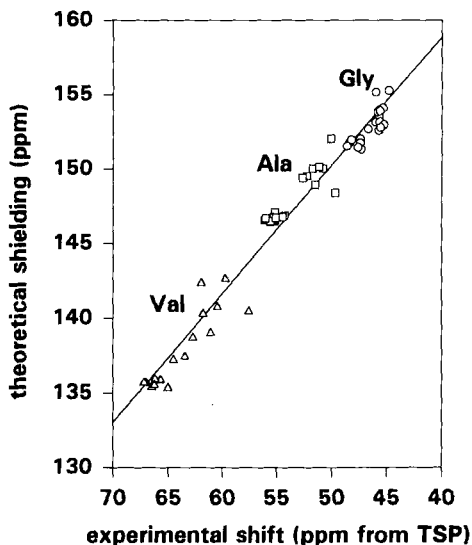


Fig. 24. Theoretical C^α shieldings extracted from ϕ - ψ surfaces versus experimental C^α shifts in glycine, alanine and valine residues of calmodulin and SNase. Reproduced from Ref. 51.

predicted using *ab initio* methods. In addition, it is already known that the chemical shift dispersion seen in C^α resonances for a given residue is mainly due to differences in the torsion angles ϕ , ψ and χ^1 .⁴¹⁻⁴² The C^α chemical shifts in proteins can therefore serve as a gauge for evaluating the accuracy of torsion angle shielding surfaces.

Influences of the torsion angle on the chemical shift are considered short range. Hence, a molecular model fragment that resembles a particular amino acid residue in its ϕ , ψ and χ^1 angles should be adequate in constructing the shielding surfaces. Model compounds in the form of *N*-formyl-L-amino acid amide have been used, for example, to describe the torsion angle effects on the C^α shielding in glycine, alanine and valine residues.^{41,50,51} One example of these surfaces (alanine) was shown in Fig. 7. Using the shielding surfaces derived from the small model compounds and the torsion angles extracted from X-ray structures of the proteins *Vertebrae calmodulin*¹⁹¹ and *staphylococcal nuclease (SNase)*,¹⁹² the pattern observed for the C^α chemical shifts in glycine, alanine and valine residues of this protein is well reproduced⁵¹ as shown in Fig. 24. The r.m.s.d. of the points from the fitted curve is only 1.0 ppm and the slope of the line is 0.9. The good correlation between theory and experiment seen from a total of 57 points derived from two proteins convincingly manifests the usefulness of the torsion angle shielding surfaces determined from small model fragments and the dominance of the short-range contributions. A similar situation

exists in C^β shifts, although less ideal than in C^α . The difficulty in quantitatively reproducing C^β shifts is not due to inaccuracy of the shielding surfaces but to the long-range electrostatic effects becoming significant for the shielding of these nuclei.⁵⁰

Thus, there is sufficient indication that generating "shielding trajectories" which take into account not only the dynamic averaging of long-range electrostatic effects but also bond length, bond angle and torsion angle effects is feasible. The success in interpreting experimental results using shielding trajectories, however, relies on factors other than the applicability of shielding traces, surfaces and polarizabilities. The shielding surface is only half the picture of dynamic averaging. The other half is the potential surface. How adequate are the potential surfaces in use now? Based on preliminary results, there is indication that model force fields currently available may not be generally applicable for this purpose. For example, relaxation by steepest descent in 2000 steps of the protein X-ray structure using the AMBER¹⁹³ force field worsens the correlation between calculated shieldings and experimental shifts for the C^α site in glycine residues in the two proteins, calmodulin and SNase.^{42,51} On the other hand, both C^α and C^β shieldings in the alanine residues benefit from the minimization of the X-ray structure. This means that the force field leads to a minimum energy configuration that is not good enough to provide internally consistent chemical shifts to within NMR experimental accuracy. The NMR chemical shift provides an additional observable to help in studying protein mechanics and dynamics.

Lastly, the goal of theoretical studies of the chemical shielding is not simply to reproduce experimentally observed chemical shifts. By separating the various contributions to the chemical shift, a powerful tool in analysing structure and dynamics can be realized. The contributions, whether short range as in bond lengths, bond angles or torsion angles, hydrogen-bonding or non-bonded overlap, or long-range electrostatic, are of great interest for their own sake, and knowing how to relate the observed chemical shift to these factors is indeed a powerful tool in studying complex systems. For example, the ability to predict ^{129}Xe chemical shifts of the xenon clusters trapped inside cages of zeolite NaA has significantly contributed to our understanding of the nature of these clusters.¹⁰² The chemical shifts and their temperature dependence have shown how valid Grand Canonical Monte-Carlo methods are in describing the dynamics of xenon atoms inside zeolite cages. With the analysis of the origins of chemical shift inequivalencies in proteins, it is now known that bond lengths in proteins are more uniform than what present X-ray structures provide. More importantly, the dominance of torsion angle effects in backbone ^{13}C shifts has opened a new route in predicting and refining protein structure. A well-defined relationship between the torsion angles and chemical shielding allows for extracting secondary structure information from measured NMR chemical

shifts. Oldfield and coworkers have already taken advantage of this relationship by employing what they call a Z-surface,⁵¹ a probability function that gives the most likely values of the angles ϕ and ψ given a measured chemical shift:

$$Z_i(\phi, \psi) = \exp - \left\{ \frac{P_i - f_i(\phi, \psi)}{W_i} \right\}^2 \quad (13)$$

This equation, not exclusive to chemical shifts but applicable to other observables, compares the experimental value of property P_i with that obtained from either an empirical or *ab initio* surface f_i . A good match, for example, between the calculated shielding surface and the observed chemical shift leads to a large value of Z . The whole torsion angle space can then be explored and, at the end, regions represented by Gaussians having width W_i (standard deviation derived from a comparison between experimental values and those obtained from the surface in a system with known structure) reflecting the most probable ϕ and ψ pairs of values are obtained. Individual Z-surfaces obtained from independent observables that are functions of the same ϕ and ψ angles, such as chemical shifts of other nuclei in the same residue or spin-spin coupling constants, can be combined until one has narrowed down the non-zero areas of the Z-surface into a unique solution of ϕ and ψ angles. Preliminary studies have shown that, with this approach, values for ϕ and ψ are obtained within 10° from their X-ray values.⁵¹

5. CONCLUSIONS

The NMR chemical shift serves as a paradigm for the effects of intramolecular dynamics and intermolecular interactions on molecular electronic properties. Details of the property surface, its dependence on internuclear distances, bond angles, and torsion angles, its response to electric fields and electric field gradients, have been explored to a greater extent than any other molecular electronic property. The rovibrational averaging on this surface leads to the observed temperature dependence in the gas at the zero-pressure limit and the mass dependence in the vast number of observed isotope shifts. Averaging over the intermolecular collisions in a dilute gas leads to the observed temperature-dependent virial coefficients of this property, again serving as an example for other properties. It has become clear that only a proper dynamic averaging over the intermolecular shielding surface can account for the virial coefficients, their dependence on temperature and on the nuclear site. Averaging the shielding function in a grand canonical ensemble for an inhomogeneous fluid inside the pores of a zeolite

leads to the observed temperature-dependent average chemical shifts of the trapped clusters in zeolite pores containing one, or two, up to eight atoms. The combination of the ultra-high-resolution measurements with the nuclear site specificity of the NMR chemical shift and the feasibility of *ab initio* quantum mechanical calculations has permitted the exploration of this electronic property surface and dynamic averaging on it. The remaining challenges, in addition to relativistic and electron-correlated *ab initio* computations of shielding surfaces to include heavy nuclei such as those of transition metal elements and post-transition nuclei, appear to be in the proper treatment of extended networks. At the present time, only small fragments of such networks have been treated quantum-mechanically, such as the $[\text{SiO}_4]^{-4}$ unit to represent silicates. Approaches to complex systems such as proteins that have been developed provide new insight into the interdependence of shielding and structure. However, other systems such as ionic and covalent solids have so far been treated only at the empirical level. Although the NMR chemical shift tensors in these solids have been used as tools for characterization, a level of theory such as has been described in this review has not yet proved feasible.

ACKNOWLEDGEMENT

CJJ is grateful for the continuing support of the National Science Foundation (Grant CHE92-10790).

REFERENCES

1. R. M. Stevens, R. M. Pitzer and W. N. Lipscomb, *J. Chem. Phys.*, 1963, **38**, 550.
2. P. Lazzeretti and R. Zanasi, *J. Chem. Phys.*, 1978, **68**, 1523.
3. J. Oddershede, P. Jorgensen and D. L. Yeager, *Comput. Phys. Rep.*, 1984, **2**, 33.
4. D. M. Bishop and S. M. Cybulski, *J. Chem. Phys.*, 1993, **98**, 8057.
5. A. E. Hansen and T. D. Bouman, *J. Chem. Phys.*, 1985, **82**, 5035.
6. T. D. Bouman and A. E. Hansen, *Chem. Phys. Lett.*, 1990, **175**, 292.
7. M. Schindler and W. Kutzelnigg, *J. Chem. Phys.*, 1982, **76**, 1919.
8. C. van Wüllen and W. Kutzelnigg, *Chem. Phys. Lett.*, 1993, **205**, 563.
9. R. Ditchfield, *Mol. Phys.*, 1974, **27**, 789.
10. K. Wolinski, J. Hinton and P. Pulay, *J. Am. Chem. Soc.*, 1990, **112**, 8251.
11. J. Gauss, *Chem. Phys. Lett.*, 1992, **191**, 614.
12. D. B. Chesnut, *Annual Reports on NMR Spectroscopy*, ed. G. A. Webb, Academic Press, London, 1994, pp. 71–122, this volume.
13. C. J. Jameson and A. C. de Dios, in *Nuclear Magnetic Shieldings and Molecular Structure*, ed. J. A. Tossell, NATO ASI Series C Vol. 386, Kluwer, Dordrecht, 1993, pp. 95–116.
14. R. A. Hegstrom, *Phys. Rev. A*, 1979, **19**, 17.
15. R. M. Stevens and W. N. Lipscomb, *J. Chem. Phys.*, 1964, **40**, 2238.
16. R. M. Stevens and W. N. Lipscomb, *J. Chem. Phys.*, 1964, **41**, 184.

17. R. M. Stevens and M. Karplus, *J. Chem. Phys.*, 1968, **49**, 1094.
18. E. A. Laws, R. M. Stevens and W. N. Lipscomb, *J. Chem. Phys.*, 1971, **54**, 4269.
19. R. Ditchfield, *Chem. Phys.*, 1981, **63**, 185.
20. D. B. Chesnut, *Chem. Phys.*, 1986, **110**, 415.
21. D. B. Chesnut and C. K. Foley, *J. Chem. Phys.*, 1986, **85**, 2814.
22. D. B. Chesnut and C. K. Foley, *J. Chem. Phys.*, 1986, **84**, 852.
23. C. J. Jameson and A. C. de Dios, *J. Chem. Phys.*, 1993, **98**, 2208.
24. C. J. Jameson and A. C. de Dios, *J. Chem. Phys.*, 1992, **97**, 417.
25. RPAC, T. D. Bouman, Southern Illinois University, Edwardsville, and A. E. Hansen, H. C. Oersted Institute, Copenhagen, Denmark.
26. H. Wind, *J. Chem. Phys.*, 1965, **42**, 2371; 1965, **43**, 2956.
27. M. Giroud and O. Nedelec, *J. Chem. Phys.*, 1980, **73**, 4151.
28. L. A. Viehland, *Chem. Phys.*, 1984, **85**, 291.
29. G. C. Maitland, M. Rigby, E. B. Smith and W. A. Wakeham, *Intermolecular Forces, Their Origin and Determination*, Clarendon, Oxford, 1981.
30. P. W. Fowler, G. Riley and W. T. Raynes, *Mol. Phys.*, 1981, **42**, 1463.
31. P. Lazzeretti, R. Zanasi, A. J. Sadlej and W. T. Raynes, *Mol. Phys.*, 1987, **62**, 605.
32. C. J. Jameson, A. C. de Dios and A. K. Jameson, *J. Chem. Phys.*, 1991, **95**, 1069.
33. C. J. Jameson, A. C. de Dios and A. K. Jameson, *J. Chem. Phys.*, 1991, **95**, 9042.
34. J. A. Tossell and P. Lazzeretti, *J. Magn. Reson.*, 1988, **80**, 39.
35. D. B. Chesnut and D. W. Wright, *J. Comput. Chem.*, 1991, **12**, 546.
36. C. J. Jameson, *J. Chem. Phys.*, 1977, **66**, 4977.
37. C. J. Jameson, *J. Chem. Phys.*, 1977, **66**, 4983.
38. C. J. Jameson, *Mol. Phys.*, 1985, **54**, 73.
39. C. J. Jameson and H. J. Osten, *J. Am. Chem. Soc.*, 1985, **107**, 4158.
40. C. J. Jameson and H.-J. Osten, *Ann. Rept NMR Spectrosc.*, 1986, **17**, 1.
41. A. C. de Dios, J. G. Pearson and E. Oldfield, *J. Am. Chem. Soc.*, 1993, **115**, 9768.
42. D. D. Laws, A. C. de Dios and E. Oldfield, *J. Biomol. NMR*, 1993, **3**, 607.
43. E. G. Paul and D. M. Grant, *J. Am. Chem. Soc.*, 1963, **85**, 1701.
44. F. A. L. Anet and A. K. Cheng, *J. Am. Chem. Soc.*, 1975, **97**, 2420.
45. H. Kurosu, I. Ando and G. A. Webb, *Magn. Reson. Chem.*, 1993, **31**, 399.
46. D. B. Chesnut, D. W. Wright and R. A. MacPhail, *Chem. Phys. Lett.*, 1988, **151**, 415.
47. W. Kutzelnigg, C. van Wüllen, U. Fleischer, R. Franke, and T. van Mourik, in *Nuclear Magnetic Shieldings and Molecular Structure*, ed. J. A. Tossell, NATO ASI Series C Vol. 386, Kluwer, Dordrecht, 1993, pp. 141–161.
48. M. Barfield and S. H. Yamamura, *J. Am. Chem. Soc.*, 1990, **112**, 4747.
49. M. Barfield, in *Nuclear Magnetic Shieldings and Molecular Structure*, ed. J. A. Tossell, NATO ASI Series C Vol. 386, Kluwer, Dordrecht, 1993, pp. 523–537.
50. A. C. de Dios and E. Oldfield, *J. Am. Chem. Soc.*, 1994, **116**, 5307.
51. J. G. Pearson, H. Le, A. C. de Dios and E. Oldfield, *J. Am. Chem. Soc.*, in press.
52. A. C. de Dios, J. G. Pearson and E. Oldfield, *Science*, 1993, **260**, 1491.
53. H. Le and E. Oldfield, *J. Biomol. NMR*, 1994, **4**, 341.
54. S. Spera and A. Bax, *J. Am. Chem. Soc.*, 1991, **113**, 5490.
55. C. J. Jameson and H. J. Osten, *J. Chem. Phys.*, 1984, **81**, 4293.
56. C. J. Jameson, in *Isotopes in the Physical and Biomedical Sciences*, ed. E. Buncel and J. R. Jones, Vol. 2 Isotopic Applications in NMR Studies, Elsevier, Amsterdam, 1991, pp. 1–54.
57. S. F. Boys and F. Bernardi, *Mol. Phys.*, 1970, **19**, 553.
58. C. J. Jameson, *J. Chem. Phys.*, 1975, **63**, 5296.
59. C. J. Grayce and R. A. Harris, *Mol. Phys.*, 1991, **72**, 523.
60. T. W. Marshall and J. A. Pople, *Mol. Phys.*, 1960, **3**, 339.
61. J. P. Riley, I. H. Hillier and W. T. Raynes, *Mol. Phys.*, 1979, **38**, 353.
62. C. J. Jameson and H. S. Gutowsky, *J. Chem. Phys.*, 1964, **40**, 1714.

63. C. J. Jameson and J. Mason in *Multinuclear Nuclear Magnetic Resonance*, ed. J. Mason, Plenum Press, London, 1987, pp. 51–88.
64. C. J. Jameson, A. K. Jameson, R. E. Gerald II and A. C. de Dios *J. Chem. Phys.*, 1992, **96**, 1676.
65. A. C. de Dios and E. Oldfield, *Chem. Phys. Lett.*, 1993, **205**, 108.
66. R. Ditchfield, *Chem. Phys.*, 1981, **63**, 185.
67. D. B. Chesnut and C. G. Phung, *Chem. Phys.*, 1990, **147**, 91.
68. J. F. Hinton and D. L. Bennet, *Chem. Phys. Lett.*, 1985, **116**, 292.
69. J. F. Hinton, P. Guthrie, P. Pulay and K. Wolinski, *J. Am. Chem. Soc.*, 1992, **114**, 1604.
70. A. Pines, D. J. Ruben, S. Vega and M. Mehring, *Phys. Rev. Lett.*, 1976, **36**, 110.
71. M. Munch, A. E. Hansen, P. E. Hansen and T. D. Bouman, *Acta Chem. Scand.*, 1992, **46**, 1065.
72. J. C. Christofides and D. B. Davies, *Magn. Reson. Chem.*, 1985, **23**, 582.
73. J. C. Facelli, R. H. Contreras and M. F. Tufro, *J. Mol. Structure (Theochem)*, 1993, **281**, 61.
74. D. B. Chesnut and C. G. Phung, in *Nuclear Magnetic Shieldings and Molecular Structure*, ed. J. A. Tossell, NATO ASI Series C Vol. 386, Kluwer, Dordrecht, 1993, pp. 221–243.
75. M. J. Stephen, *Mol. Phys.*, 1958, **1**, 223.
76. A. D. Buckingham, *Can. J. Chem.*, 1960, **38**, 300.
77. A. D. Buckingham and S. M. Malm, *Mol. Phys.*, 1971, **22**, 1127.
78. W. T. Raynes and R. Ratcliffe, *Mol. Phys.*, 1979, **37**, 571.
79. J. D. Augspurger, C. E. Dykstra and E. Oldfield, *J. Am. Chem. Soc.*, 1991, **113**, 2447.
80. A. D. Buckingham and K. P. Lawley, *Mol. Phys.*, 1960, **3**, 219.
81. J. D. Augspurger, A. C. de Dios, E. Oldfield and C. E. Dykstra, *Chem. Phys. Lett.*, 1993, **213**, 211.
82. M. J. Packer and W. T. Raynes, *Mol. Phys.*, 1990, **69**, 391.
83. W. T. Raynes, in *Nuclear Magnetic Shieldings and Molecular Structure*, ed. J. A. Tossell, NATO ASI Series C Vol. 386, Kluwer, Dordrecht, 1993, pp. 401–420.
84. M. Grayson and W. T. Raynes, *Mol. Phys.*, 1994, **81**, 533.
85. J. D. Augspurger and C. E. Dykstra, *Mol. Phys.*, 1992, **76**, 229.
86. D. M. Bishop and S. M. Cybulski, *Mol. Phys.*, 1993, in press.
87. J. D. Augspurger and C. E. Dykstra, *J. Phys. Chem.*, 1991, **95**, 9230.
88. D. M. Bishop and S. M. Cybulski, *J. Magn. Reson., A*, 1994, **107**, 99.
89. W. T. Raynes, A. D. Buckingham and H. J. Bernstein, *J. Chem. Phys.*, 1961, **36**, 3481.
90. F. London, *Z. Phys. Chem. (Leipzig) B*, 1930, **11**, 222.
91. F. London, *Trans. Faraday Soc.*, 1937, **33**, 8.
92. D. R. Herschbach and V. W. Laurie, *J. Chem. Phys.*, 1961, **35**, 458.
93. J. C. Facelli, A. M. Orendt, M. S. Solum, G. Depke, D. M. Grant and J. Michl, *J. Am. Chem. Soc.*, 1986 **108**, 4268.
94. M. S. Solum, J. C. Facelli, J. Michl and D. M. Grant, *J. Am. Chem. Soc.*, 1986, **108**, 6464.
95. J. C. Facelli, A. M. Orendt, A. J. Beeler, M. S. Solum, G. Depke, K. D. Malsch, J. W. Downing, P. S. Murthy, D. M. Grant and J. Michl, *J. Am. Chem. Soc.*, 1985, **107**, 6749.
96. J. C. Facelli, D. M. Grant and J. Michl, *Acc. Chem. Research*, 1987, **20**, 152.
97. A. M. Orendt, J. C. Facelli, A. J. Beeler, K. Reuter, W. J. Horton, P. Cutts, D. M. Grant and J. Michl, *J. Am. Chem. Soc.*, 1988, **110**, 3386.
98. T. M. Duncan, *A Compilation of Chemical Shift Anisotropies*, Farragut Press, Chicago, 1990.
99. C. J. Jameson, in *Theoretical Models of Chemical Bonding*, ed. Z. B. Maksic, Part 3. Molecular Spectroscopy, Electronic Structure and Intramolecular Interactions, Springer-Verlag, Berlin, 1991, pp. 457–519.
100. G. Riley, W. T. Raynes and P. W. Fowler, *Mol. Phys.*, 1979, **38**, 877.
101. C. J. Jameson, *Chem. Rev.*, 1991, **91**, 1375.

102. C. J. Jameson, A. K. Jameson, B. I. Baello and H. M. Lim, *J. Chem. Phys.*, 1994, **100**, 5965.
103. C. J. Jameson, A. K. Jameson and S. M. Cohen, *J. Chem. Phys.*, 1977, **67**, 2771.
104. A. K. Jameson, K. Schuett, C. J. Jameson and S. M. Cohen, *J. Chem. Phys.*, 1977, **67**, 2821.
105. C. J. Jameson and H. J. Osten, *Mol. Phys.*, 1985, **55**, 383.
106. C. J. Jameson, A. K. Jameson, S. Wille and P. M. Burrell, *J. Chem. Phys.*, 1981, **74**, 853.
107. C. J. Jameson, A. K. Jameson, H. Parker, S. M. Cohen, and C. L. Lee, *J. Chem. Phys.*, 1978, **68**, 2861.
108. C. J. Jameson, A. K. Jameson and H. Parker, *J. Chem. Phys.*, 1978, **69**, 1318.
109. C. J. Jameson, A. K. Jameson and S. Wille, *J. Phys. Chem.*, 1979, **83**, 3372.
110. C. J. Jameson and A. K. Jameson, *J. Magn. Reson.*, 1985, **62**, 209.
111. C. J. Jameson, A. K. Jameson and D. Oppusunggu, *J. Chem. Phys.*, 1985, **83**, 5420.
112. C. J. Jameson, *J. Chem. Phys.*, 1977, **67**, 2814.
113. P. W. Fowler, *Mol. Phys.*, 1981, **46**, 591.
114. C. J. Jameson, *Bull. Magn. Reson.*, 1980, **3**, 3.
115. C. J. Jameson, A. K. Jameson and D. Oppusunggu, *J. Chem. Phys.*, 1986, **85**, 5480.
116. B. Bennett and W. T. Raynes, *Magn. Reson. Chem.*, 1991, **29**, 946.
117. W. T. Raynes, P. W. Fowler, P. Lazzeretti, R. Zanasi and M. Grayson, *Mol. Phys.*, 1988, **64**, 143.
118. P. W. Fowler and W. T. Raynes, *Mol. Phys.*, 1981, **43**, 65.
119. C. J. Jameson, in *Nuclear Magnetic Resonance*, ed. G. A. Webb, Royal Society of Chemistry, London, 1989, Vol. 19, pp. 1–33.
120. J. C. Facelli and D. M. Grant, *Topics Stereochem.*, 1989, **19**, 1.
121. W. T. Raynes and B. Bennett, *Magn. Reson. Chem.*, 1991, **29**, 955.
122. H. Batiz-Hernandez and R. A. Bernheim, *Prog. NMR Spectrosc.*, 1967, **3**, 63.
123. R. E. Wasylishen and J. O. Friedrich, *J. Chem. Phys.*, 1984, **80**, 585.
124. R. E. Wasylishen and J. O. Friedrich, *Can. J. Chem.*, 1987, **65**, 2238.
125. W. Gombler, *J. Am. Chem. Soc.*, 1982, **104**, 6616.
126. P. E. Hansen, *Prog. NMR Spectrosc.*, 1988, **20**, 207.
127. O. Eppers and H. Gunther, *Helv. Chim. Acta*, 1990, **73**, 2071.
128. O. Eppers and H. Gunther, *Helv. Chim. Acta*, 1992, **72**, 2553.
129. W. T. Raynes, *Mol. Phys.*, 1988, **63**, 719.
130. M. Alei and W. E. Wageman, *J. Chem. Phys.*, 1978, **68**, 783.
131. A. K. Jameson and C. J. Jameson, *J. Magn. Reson.*, 1978, **32**, 455.
132. H. J. Jakobsen, A. J. Zozulin, P. D. Ellis and J. D. Odom, *J. Magn. Reson.*, 1980, **38**, 219.
133. W. T. Raynes, *Mol. Phys.*, 1983, **49**, 443.
134. C. J. Jameson and H. J. Osten, *J. Chem. Phys.*, 1984, **81**, 4293.
135. C. J. Jameson and H. J. Osten, *J. Chem. Phys.*, 1984, **81**, 4300.
136. I. Paidarova, J. Komasa and J. Oddershede, *Mol. Phys.*, 1991, **72**, 559.
137. R. E. Wasylishen, J. O. Friedrich, S. Mooibroek and J. B. Macdonald, *J. Chem. Phys.*, 1985, **83**, 548.
138. H. P. A. Mercier, J. C. P. Saunders, G. J. Schrobilgen and S. S. Tsai, *Inorg. Chem.*, 1993, **32**, 386.
139. R. E. Wasylishen and N. Burford, *Can. J. Chem.*, 1987, **65**, 2707.
140. K. L. Leighton and R. E. Wasylishen, *Can. J. Chem.*, 1987, **65**, 1469.
141. H. J. Osten, C. J. Jameson and N. Craig, *J. Chem. Phys.*, 1985, **83**, 5434.
142. C. J. Jameson, D. Rehder and M. Hoch, *J. Am. Chem. Soc.*, 1987, **109**, 2589.
143. P. E. Hansen, *Ann. Rept NMR Spectrosc.*, 1983, **15**, 105.
144. Y. Nakashima, H. Kanada, M. Fukunaga, K. Suzuki and K. Takahashi, *Bull. Chem. Soc., Jpn*, 1992, **65**, 2894.
145. A. E. Aliev and K. D. M. Harris, *Magn. Reson. Chem.*, 1993, **31**, 54.

146. H. Kunzer, C. E. Cottrell and L. A. Paquette, *J. Am. Chem. Soc.*, 1986, **108**, 8089.
147. A. C. de Dios and C. J. Jameson, unpublished results.
148. T. G. Burlingame and W. H. Pirkle, *J. Am. Chem. Soc.*, 1966, **88**, 1837.
149. W. H. Pirkle, *J. Am. Chem. Soc.*, 1966, **88**, 1837.
150. R. Dyllick-Brenzinger and J. D. Roberts, *J. Am. Chem. Soc.*, 1980, **102**, 1166.
151. L. A. Silks, J. Peng, J. D. Odom and R. B. Dunlap, *J. Chem. Soc., Perkin Trans. 1*, 1991, 2495.
152. A. D. Buckingham, T. Schaefer and W. G. Schneider, *J. Chem. Phys.*, 1960, **32**, 1227.
153. A. D. Buckingham and J. A. Pople, *Discuss. Faraday Soc.*, 1956, **22**, 17.
154. F. H. A. Rummens, in *NMR Basic Principles and Progress*, ed. P. Diehl, E. Fluck and R. Kosfeld, Springer-Verlag, Berlin, 1975, Vol. 10.
155. A. K. Jameson, C. J. Jameson and H. S. Gutowsky, *J. Chem. Phys.*, 1970, **53**, 2310.
156. C. J. Jameson, A. K. Jameson and S. M. Cohen, *J. Chem. Phys.*, 1975, **62**, 4224.
157. C. J. Jameson, A. K. Jameson and H. Parker, *J. Chem. Phys.*, 1978, **68**, 3943.
158. C. J. Jameson, A. K. Jameson and S. M. Cohen, *J. Chem. Phys.*, 1973, **59**, 4540.
159. C. J. Jameson, A. K. Jameson, D. Oppusunggu and S. Wille, *J. Chem. Phys.*, 1982, **76**, 152.
160. K. Jackowski, *Chem. Phys. Lett.*, 1992, **194**, 167.
161. C. J. Jameson, A. K. Jameson and D. Oppusunggu, *J. Chem. Phys.*, 1984, **81**, 2313.
162. C. J. Jameson, A. K. Jameson, S. M. Cohen, H. Parker, D. Oppusunggu, P. M. Burrell and S. Wille, *J. Chem. Phys.*, 1981, **74**, 1608.
163. J. C. Hindman, *J. Chem. Phys.*, 1966, **44**, 4582.
164. A. K. Jameson and C. J. Jameson, *Chem. Phys. Lett.*, 1987, **134**, 461.
165. M. Alei, A. E. Florin, W. M. Litchman and J. F. O'Brien, *J. Phys. Chem.*, 1971, **75**, 932.
166. C. J. Jameson and A. K. Jameson, *J. Chem. Phys.*, 1984, **81**, 1198.
167. C. J. Jameson, A. K. Jameson and D. Oppusunggu, *J. Chem. Phys.*, 1984, **87**, 85.
168. C. J. Jameson, A. K. Jameson and H. Parker, *J. Chem. Phys.*, 1979, **70**, 5916.
169. C. J. Jameson, A. K. Jameson and P. M. Burrell, *J. Chem. Phys.*, 1980, **73**, 6013.
170. G. Heckmann and E. Fluck, *Mol. Phys.*, 1972, **23**, 175.
171. D. Brinkman and H. Y. Carr, *Phys. Rev.*, 1966, **150**, 174.
172. W. W. Warren and R. E. Norberg, *Phys. Rev.*, 1966, **148**, 402.
173. R. K. Mazitov, K. M. Enikeev and A. V. Ilyasov, *Z. Phys. Chem.*, 1987, **155**, 55.
174. P. Diehl, O. Muenster and J. Jokisaari, *Chem. Phys. Lett.*, 1991, **178**, 147.
175. K. W. Miller, N. V. Reo, A. J. M. S. Uiterkamp, D. P. Stengle, T. R. Stengle and K. L. Williamson, *Proc. Natl Acad. Sci. USA*, 1981, **78**, 4946.
176. R. Seydoux, P. Diehl, R. K. Mazitov and J. Jokisaari, *J. Magn. Reson. A*, 1993, **101**, 78.
177. M. Haser, R. Ahlrichs, H. P. Baron, P. Weis and H. Horn, *Theo. Chim. Acta*, 1992, **83**, 455.
178. U. Meier, C. vanWüllen and M. Schindler, *J. Comput. Chem.*, 1992, **13**, 551.
179. P. Pulay, private communication.
180. D. B. Chesnut and K. D. Moore, *J. Comput. Chem.*, 1989, **10**, 648.
181. P. W. Fowler, P. Lazzeretti, M. Malagoli and R. Zanasi, *J. Phys. Chem.*, 1991, **95**, 6404.
182. D. B. Chesnut and C. G. Phung, *Chem. Phys. Lett.*, 1991, **183**, 505.
183. C. E. Dykstra and P. G. Jasien, *Chem. Phys. Lett.*, 1984, **109**, 388.
184. J. G. Pearson, E. Oldfield, F. S. Lee and A. Warshel, *J. Am. Chem. Soc.*, 1993, **115**, 6851.
185. A. D. McLean and G. S. Chandler, *J. Chem. Phys.*, 1980, **72**, 5639.
186. C. C. McDonald and W. D. Phillips, *J. Am. Chem. Soc.*, 1967, **89**, 6332.
187. A. Allerhand, R. F. Childers and E. Oldfield, *Biochemistry*, 1973, **12**, 1335.
188. J. D. Augspurger, C. E. Dykstra, E. Oldfield and J. G. Pearson, in *Nuclear Magnetic Shieldings and Molecular Structure*, ed. J. A. Tossell, NATO ASI Series C Vol. 386, Kluwer, Dordrecht, 1993, pp. 75-94.

189. F. S. Lee, Z. Chu and A. Warshel, *J. Comput. Chem.*, 1993, **14**, 161.
190. C. Lian, H. B. Le, B. Montez, J. Patterson, S. Harrell, D. Laws, I. Matsumura, J. Pearson and E. Oldfield, *Biochemistry*, 1994, **33**, 5238.
191. R. Chattopadhyaya, W. E. Meador, A. R. Means and F. A. Quioco, *J. Mol. Biol.*, 1992, **228**, 1177.
192. P. J. Loll and E. E. Lattman, *Protein Struct. Funct. Genet.*, 1989, **5**, 183.
193. S. J. Weiner, P. A. Kollman, D. T. Nguyen and D. A. Case, *J. Comput. Chem.*, 1986, **7**, 230.

This Page Intentionally Left Blank

***Ab Initio* Calculations of NMR Chemical Shielding**

D. B. CHESNUT

*P. M. Gross Chemical Laboratory, Duke University, Durham,
North Carolina 27708, USA*

1. Introduction	71
2. The general problem	72
3. Basic theory	75
4. Self-consistent field approaches	82
4.1. Theoretical approaches	82
4.2. A large system calculation	84
4.3. The self-consistent reaction field	88
4.4. Locally dense basis sets	90
4.5. An atoms in molecules approach	95
4.6. A water cluster calculation	98
4.7. An orbital shielding analysis	100
5. Effects of correlation	106
5.1. GIAO MP2	107
5.2. SOLO	109
5.3. Multi-configuration IGLO	112
5.4. Density functional theory	115
5.5. Summary of correlation treatments	117
6. Concluding remarks	118
References	119

1. INTRODUCTION

The calculation of nuclear magnetic resonance (NMR) chemical shielding by *ab initio* techniques is a challenging and important problem. It is challenging because of the small nature of NMR chemical shielding, and important because nuclear magnetic resonance spectroscopy is perhaps the most sensitive probe of molecular electronic structure; its understanding on a theoretical base is of great practical utility. The last decade has seen significant improvements in both theoretical techniques and in computer hardware that are allowing us to calculate more accurately magnetic as well as other properties. While shielding calculations were initially performed on molecules containing atoms in the first long row of the Periodic Table, it is becoming commonplace now to treat atoms in the second and higher rows.

Review articles like this have relevance for different people in different ways. Those who practice the art will be aware of most of the many papers published in the field, and draw heavily on the several excellent review articles published yearly by people like Cynthia Jameson in the *Specialized Periodical Reports on Nuclear Magnetic Resonance*¹ that specialize in conveying the essential elements of a large number of published results. While hopefully being of some interest to this group, the current review article is likely more appropriate for the person either just beginning to show an interest in the theoretical determination of chemical shielding or to the scientist in a related theoretical or experimental area who is interested in seeing what can and has been done in this particular field. It is more with this latter group of people that this article has been organized. Rather than looking over a large array of data we will concentrate on a few representative results that indicate the abilities as well as the limitations of present calculations.

A rather general overview is given first, citing some of the limitations and problems one faces in carrying out chemical shielding calculations (and quantum mechanical calculations in general). Then the basics of the theory are presented so that the reader has a feel for where the effect comes from and how it is approached theoretically. The main approaches to the calculations are examined (mainly, various ways of combating the gauge problem), and then are presented what we hope are fairly representative illustrations of shielding calculations, beginning at the Hartree-Fock level and ending with the more recent attempts to include electron correlation. Because a limited number of examples must be presented, much outstanding work is necessarily omitted and not all the many contributors to the field adequately represented. For a more comprehensive coverage of the field the reader is referred to the very useful annual reviews by Jameson.¹

2. THE GENERAL PROBLEM

Quantum mechanics can, in principle, describe all of chemistry. The problem is that the very complicated nature of chemical systems and of quantum mechanics itself presently forces us into a series of approximations that limits the accuracy of our calculations as well as the size of systems we can treat. What are the problems associated with the present approximate theoretical approaches to NMR shielding, and how can they be overcome? What are we able to do now, and what are our limitations? What approximations are necessary at the moment and which can perhaps soon be overcome?

Many of the calculations of chemical shielding we discuss are done at the Hartree-Fock level on rigid, isolated molecules. More than just a few

calculations are beginning to appear in the literature where post-Hartree-Fock treatments (electron correlation) are being performed, achieving notable results. But for the most part at present, current applications of the theory are at the formally uncorrelated, single determinant, Hartree-Fock level. Fortunately for the theoretician, there have been a number of experimental studies establishing absolute shielding scales for carbon,² nitrogen,³ oxygen,⁴ fluorine,⁵ and phosphorus⁶ species in the gas phase low density limit, the best approximation to the rigid isolated molecule theoreticians tend to treat. These studies allow us to test our calculations without the sometimes difficult complications of intermolecular interactions present in liquid and solid phases.

But even here there are effects not easily taken into account theoretically. The gas phase measurements are done at finite temperatures (usually near 300 K), and there are effects of rotation and vibration.⁷ If vibrational potentials were symmetric, the averaged nuclear positions would be independent of the vibrational level occupied. However, anharmonicities are present and lead to a dependence of the nuclear positions—and the wave function and, thus, the chemical shielding—on the vibrational level occupied. Molecular rotation tends to stretch bonds, and rotations and vibrations are coupled. Accordingly, the electronic wave function depends on the rovibrational state occupied, and, thus, on the temperature. It turns out that the largest effect is that of averaging over the ground vibrational state, the molecule's zero-point motion, a contribution that can have a sizeable magnitude. Jameson and Osten report corrections relative to equilibrium vibrationally unaveraged structures containing fluorine at 300 K of -6.8 to -18.0 ppm in some haloethanes⁸ and halomethanes.⁹ Ditchfield¹⁰ calculates an -11.2 ppm correction for fluorine in HF, while Fowler and Raynes¹¹ report a -13.1 ppm zero point correction for oxygen in H₂O. Corrections for carbon are not as large, being, for example, -1.5 ppm in CO₂ and -3.4 ppm in CH₄. More recently Jameson and de Dios¹² have reported a difference of -12.8 between the isotropic shielding for phosphine at room temperature (300 K) and its value for the rigid equilibrium structure. Correcting for such effects is difficult and presently prohibitive for large molecules. A likely simple way to account for such effects is to use structures determined at ambient temperatures where bonds and angles have been thermally modified.

Most NMR measurements are done on liquids or solids. The rovibrational problems are still present, and in addition one must deal with the complicating presence of intermolecular interactions. Intermolecular effects depend on the particular system, but can be quite large when lone pairs are present or when solute-solvent coupling such as hydrogen bonding occurs. In principle one can treat a small "droplet" of material but the current size of systems quantum mechanics can handle severely limits such an approach.

We are just coming to the point of being able to consider small aggregates of molecules as models for studying chemical shielding effects in the liquid and solid phases.

Assuming that the above problems can somehow be handled at the Hartree–Fock level, there still remains the problem of electron correlation. Hartree–Fock theory effectively neglects the instantaneous interaction between electrons, treating each electron in average or mean field of the others. In a number of shielding calculations neglect of electron correlation has, as we shall see, serious consequences; post-Hartree–Fock approaches are thought to be especially important for systems with lone pairs and multiple bonds. While we generally know what to do at the Hartree–Fock level, the situation is much more complicated when trying to treat correlation, and the magnitude of the problem tends to strain today's computational abilities in terms of the size of molecular systems that can presently be treated. We shall illustrate some of the advances being made in this important area by a variety of approaches that appear promising in attacking the problem.

Finally, nearly all treatments, whether correlation is included in some partial way or not, neglect relativistic effects. Relativistic effects become important when velocities approach that of the speed of light, and, while this is not much of a problem with first or second row species, the further down the Periodic Table we move the more noticeable such effects become.¹³

To calculate an electronic property such as chemical shielding a molecular geometry must be specified. One can employ an experimental geometry if known, or find that molecular configuration that provides a minimum energy (an "optimized" structure) from some theoretical standpoint. For small and medium sized molecules, quantum theory can be used to determine structures, usually very accurately. Many times experimental structures are not known, and theoretical means are the only choice.

At extended, post-Hartree–Fock levels, theoretical and experimental structures agree very well. Again, however, as molecular systems become large, the more rigorous quantum techniques become burdensome. Hartree–Fock calculations of structures are often quite adequate, usually agreeing with experiment to within 0.01–0.03 Å and 2–3°. ¹⁴ Hartree–Fock bond lengths tend to be shorter than experiment, and there are pathological cases; one must be circumspect when calculating a Hartree–Fock structure and be aware of these situations.

Rovibrational effects affect molecular geometries as does isotopic substitution. Calculations may be performed at either optimized or experimental configurations. What are the effects of modifying the bond lengths and bond angles in a molecule? The major effects from rovibrational effects and isotopic substitution depend primarily on the first derivatives of the shielding with respect to the pertinent coordinate.⁷ Although extensive

theoretical studies have been performed on first row species with respect to bond length changes,¹⁵ relatively few have been carried out for second row species and relatively little bond angles studies have been performed in general; the work of Jameson and de Dios¹² on phosphorus in PH_3 represents the only current detailed investigation involving a second row element.

As has come to be expected for elements residing in the right hand portion of the Periodic Table, most bond length derivatives are negative;¹⁶ there is as yet no general statement that can be made concerning bond angle changes. Bond length derivatives are relatively small for singly bonded species (a few ppm for a bond length change of 0.01 Å), while the derivatives for multiply bonded atoms are quite significant. The relative insensitivity of the isotropic chemical shielding to single bond modification and the much greater effect with multiple bonds has been noted previously.¹⁵

While these many problems might seem at first discouraging, we can in most cases calculate chemically meaningful shieldings at the Hartree-Fock level and the beginning level of including electron correlation. Although we must learn how to better handle rovibration, correlation, and relativistic effects, the methods currently available do provide answers that are generally *useful* and often essentially quantitatively correct, a major point we hope to make in this review.

Finally, a comment on conventions in reporting NMR shielding data. While experimentalists tend to report relative displacements (relative to some standard) of the NMR lines, normally called "chemical shifts", δ , theoretically one determines an "absolute" displacement, usually referred to as "chemical shielding", σ . This is really a shift with respect to the bare nucleus, and is such that more positive values indicate diamagnetic or upfield shifts, and negative values paramagnetic or downfield shifts. The results here are reported on such an absolute basis and, accordingly, we speak of "shielding"; relative shifts can easily be obtained by taking the appropriate differences with respect to an appropriate standard. The advantage of absolute shifts is that systematic errors are not hidden by a relative comparison, and, of course, relative shifts, if desired, are easily obtained from the absolute values.

3. BASIC THEORY

In discussing the results of *ab initio* calculations of chemical shielding it is helpful to have some notion of the underlying theory. We present the elements of the necessary theory here in a form sufficient to allow the reader to fill in details if desired but hopefully not overwhelming at the same time. It should allow one to realize the physical underpinning of the theory while

at the same time gaining some appreciation of the inherent computational complexity.

The physical notion behind chemical shielding has a classical base and is relatively simple. A particle of mass m and charge q moving with a vector velocity \vec{v} at a vector distance \vec{r} from the origin gives rise to an induced magnetic field $\vec{B}^{(ind)}$ at the origin given by the Biot-Savart law

$$\begin{aligned}\vec{B}^{(ind)} &= \left(\frac{\mu_0}{4\pi} \right) \frac{q}{m} \left(\frac{\vec{r} \times m\vec{v}}{r^3} \right) \\ &= \left(\frac{\mu_0}{4\pi} \right) \frac{q}{m} \left(\frac{\vec{r} \times [\vec{p} - q\vec{A}]}{r^3} \right) \\ &= \left(\frac{\mu_0}{4\pi} \right) \frac{q}{m} \left(\frac{\vec{r} \times \vec{\pi}}{r^3} \right)\end{aligned}\tag{1}$$

where we first express $m\vec{v}$ in terms of its canonical momentum, \vec{p} , and the vector potential, \vec{A} , due to an external magnetic field, $\vec{B} = \nabla \times \vec{A}$, and lastly symbolically redefine these terms as what is often referred to as the kinetic momentum, $\vec{\pi}$. ($\mu_0/4\pi$) is a term required when using the SI system, and would be replaced by c^{-1} in the more sensible cgs system; μ_0 is the absolute permittivity of the vacuum (free space). A prime example of such moving charged particles are the electrons surrounding the nuclei in a rigid (Born-Oppenheimer) molecule; in the presence of an external magnetic field there is a net electronic current which induces additional magnetic fields at all points of the molecular systems, in particular at the sites of the nuclear moments.

Consider a molecule with a single nuclear moment, $\vec{\mu}$, in the presence of an external magnetic field, \vec{B} . The energy levels of the nuclear moment are characterized by an effective or "spin" Hamiltonian given by

$$\begin{aligned}\bar{H}_{\mu}^{spin} &= \sum_{ij} -\mu_i \cdot (1 - \sigma_{ij}) \cdot B_j \\ &= -\vec{\mu} \cdot \vec{B} + \vec{\mu} \cdot \vec{\sigma} \cdot \vec{B}\end{aligned}\tag{2}$$

where the $-\vec{\mu} \cdot \vec{B}$ term is the classical moment-field interaction, and the $\vec{\mu} \cdot \vec{\sigma} \cdot \vec{B}$ term characterizes the dominant interaction of the nuclear moment with the field induced by the electrons' motion, this term being found to be given by $\vec{B}^{(ind)} = \vec{\sigma} \cdot \vec{B}$. $\vec{\sigma}$ is the chemical shielding tensor, a second order, asymmetrical tensor. The nuclear spin Hamiltonian is an effective Hamiltonian for the nuclear moment in that it contains no explicit reference to the other particles in the system; coupling between the nuclear moment and the

electrons is present, of course, and their effect on the nuclear moment is contained (to first order in B) in the shielding tensor term.

Often one sees the shielding tensor defined as

$$\sigma_{ij} = \frac{\partial^2 E}{\partial \mu_i \partial B_j} \quad (3)$$

where E is taken as the electronic energy of the system. Some find this confusing since, while the external field \vec{B} is indeed a parameter in which the electronic energy (and wave function) can be expanded, the nuclear moment $\vec{\mu}$ should really be treated as an operator and it is not immediately clear how one can take a derivative with respect to it. The definition in Eq. (3) does *not* refer to Eq. (2) and is only clear after a more formal derivation, which we now proceed to outline.

In order to proceed, it is necessary to consider the straightforward perturbation treatment of two weakly interacting subsystems, in our case the nuclear moment on the one hand and the electrons and fixed nuclei of the molecule on the other. While our treatment is focused on a nuclear spin system and an electronic system, the approach is general. Suppose the Hamiltonian of the combined system is given by

$$H = H_\mu + H_e + H_{\mu e} \quad (4)$$

where the first two terms are the Hamiltonians of the "isolated" (that is, non-interacting) nuclear and electronic systems, respectively, and the last term represents the coupling between the two. We assume that we know the zeroth order energies (and wave functions) of the isolated systems, and furthermore we shall presume, as is true, that the energy level spacings of the electronic levels are huge compared to those of the nuclear levels. We also take the ground electronic level to be non-degenerate (i.e. an electron closed shell system). The coupling term, $H_{\mu e}$, can be treated as a perturbation on the lowest state(s) of the system, which in the absence of the coupling term are given by the product of the ground electronic wave function, $\psi_{e,g}$, and the $2I + 1$ spin states associated with the nuclear moment, $\vec{\mu}$, of spin I . That is, while there are many $(2I + 1)$ nuclear spin states associated with these lowest levels, the electronic part is characterized by a *unique* wavefunction.

Although the external magnetic field, \vec{B} , will remove the degeneracy of the nuclear spin levels, they are still very close together compared to the electronic splitting. In the case of degeneracy or near-degeneracy, the proper approach is to find the matrix elements of the Hamiltonian in the manifold of these states, and diagonalize the Hamiltonian in this finite (and

usually small) subset. If we denote the various spin functions by s_j , then we need to evaluate integrals of the form

$$\langle s_j, \psi_{e,g} | H_{\mu e} | s_i, \psi_{e,g} \rangle = \langle s_j | \langle \psi_{e,g} | H_{\mu e} | \psi_{e,g} \rangle | s_i \rangle \quad (5)$$

where we have been able to isolate the integration over the electronic coordinates because of the unique nature of $\psi_{e,g}$. That is to say, the spin system "sees" an effective Hamiltonian of the form

$$H_{\mu}^{spin} = -\vec{\mu} \cdot \vec{B} + \int \psi_{e,g}^* H_{\mu e} \psi_{e,g} d\tau_e \quad (6)$$

where the first term in Eq. (6) is H_{μ} and the integral is only over the electron coordinates.

The problem now is to properly determine what $H_{\mu e}$ is. To do this one starts with the full Hamiltonian of the coupled systems

$$H = -\vec{\mu} \cdot \vec{B} + \sum_k \frac{1}{2m} (\vec{p}_k + e\vec{A}_k)^2 + V(\dots, \vec{r}_k, \dots) \quad (7)$$

where $q = -e$ and the vector potential is given by

$$\vec{A}_k = \vec{A}_k^{(B)} + \vec{A}_k^{(\mu)} \quad (8)$$

where

$$\vec{A}_k^{(B)} = \frac{1}{2} \vec{B} \times (\vec{r}_k - \vec{G}) \quad (9)$$

is the contribution from the external field, \vec{B} , and

$$\vec{A}_k^{(\mu)} = \left(\frac{\mu_0}{4\pi} \right) \left(\frac{\vec{\mu} \times \vec{r}_{k\mu}}{r_{k\mu}^3} \right) \quad (10)$$

is that contribution from the nuclear moment itself; $\vec{r}_{k\mu} = \vec{r}_k - \vec{R}_{\mu}$ is the electronic coordinate measured relative to nuclear position, \vec{R}_{μ} . The $e\vec{A}$ term in Eq. (7) would be replaced by $(e/c)\vec{A}$ (and $(\mu_0/4\pi)$ by c^{-1}) in the cgs system. Note that there is an arbitrary constant vector \vec{G} in Eq. (9) which defines the gauge origin of the external field, whereas the electronic coordinate in Eq. (10) is non-arbitrarily defined relative to the origin of the nuclear moment. Usually, the term \vec{G} in Eq. (9) is not explicitly included, and the gauge is tied to the arbitrary origin of the coordinate system chosen. Its presence here is meant to remind us of the arbitrary nature of the vector potential in this regard, an arbitrariness that cannot make any difference in an exact quantum mechanical treatment, but one that does cause difficulties

in the approximate treatments we are almost always forced to perform. The kinetic momentum, $\vec{\pi}_k$, here is

$$\vec{\pi}_k = \vec{p}_k + e\vec{A}_k^{(B)} \quad (11)$$

and the Hamiltonian can be written as

$$\begin{aligned} H = & -\vec{\mu} \cdot \vec{B} + \sum_k \frac{\vec{\pi}_k^2}{2m} + V \\ & + \sum_k \left(\frac{e}{2m} (\vec{\pi}_k \cdot \vec{A}_k^{(\mu)} + \vec{A}_k^{(\mu)} \cdot \vec{\pi}_k) + \frac{e^2}{2m} \vec{A}_k^{(\mu)} \cdot \vec{A}_k^{(\mu)} \right) \end{aligned} \quad (12)$$

The two terms involving the nuclear vector potential, $\vec{A}_k^{(\mu)}$, can be seen to be first ($H_{\mu e}^{\mu(1)}$) and second ($H_{\mu e}^{\mu(2)}$) order in the nuclear moment, $\vec{\mu}$. Because both the nuclear and external field vector potentials individually satisfy the Coulomb gauge, $\nabla \cdot \vec{A} = 0$, the first order terms in Eq. (12) may be put in the form

$$\begin{aligned} H_{\mu e}^{\mu(1)} &= \sum_k \frac{e}{m} \left(\frac{\mu_0}{4\pi} \right) \frac{\vec{\mu} \times \vec{r}_{k\mu}}{r_{k\mu}^3} \cdot \vec{\pi}_k \\ &= \vec{\mu} \cdot \sum_k \frac{e}{m} \left(\frac{\mu_0}{4\pi} \right) \frac{\vec{r}_{k\mu} \times \vec{\pi}_k}{r_{k\mu}^3} \end{aligned} \quad (13)$$

and one sees the classical Biot-Savart law beginning to emerge in our quantum mechanical treatment. To determine the spin Hamiltonian then, we need the integral over the electronic coordinates of

$$\begin{aligned} H_{\mu}^{spin} &= \langle \psi_{e,g} | H | \psi_{e,g} \rangle \\ &= -\vec{\mu} \cdot \vec{B} + E_e^{(0)} + \langle \psi_{e,g} | H_{\mu e}^{\mu(1)} + H_{\mu e}^{\mu(2)} | \psi_{e,g} \rangle \end{aligned} \quad (14)$$

The first two terms correspond to integrating over H_{μ} and H_e , respectively; the second term is a constant for the spin system, will shift all levels by the same amount, and can be dropped. Since we desire only terms first order in $\vec{\mu}$, the last integral can be neglected, and we need only to evaluate

$$\begin{aligned} &\langle \psi_{e,g} | H_{\mu e}^{\mu(1)} | \psi_{e,g} \rangle \\ &= \vec{\mu} \cdot \sum_k \int \psi_{e,g}^* \frac{e}{m} \left(\frac{\mu_0}{4\pi} \right) \frac{\vec{r}_{k\mu} \times \vec{\pi}_k}{r_{k\mu}^3} \psi_{e,g} d\tau_3 \\ &= -\vec{\mu} \cdot \sum_k \int \left(\frac{\mu_0}{4\pi} \right) \frac{\vec{r}_{k\mu} \times}{r_{k\mu}^3} \left[\left(\frac{-e}{2m} \right) (\psi_{e,g}^* \vec{\pi}_k \psi_{e,g} + \psi_{e,g} \vec{\pi}_k^* \psi_{e,g}^*) \right] d\tau_3 \end{aligned}$$

$$\begin{aligned}
&= -\vec{\mu} \cdot \sum_k \int \left(\frac{\mu_0}{4\pi} \right) \frac{\vec{r}_{k\mu} \times \vec{J}_k(\vec{r})}{r_{k\mu}^3} d\tau_3 \\
&= -\vec{\mu} \cdot \vec{B}^{(ind)}
\end{aligned} \tag{15}$$

where the manipulations in Eq. (15) are permitted by the Hermitian character of $\vec{\pi}_k$ and allow us to exhibit the quantum mechanical current density due to electron k , $\vec{J}_k(\vec{r}_k)$. The relationship between the induced field and the Biot-Savart law is now fully transparent. It is from Eq. (15) that we must derive the $\vec{\mu} \cdot \vec{\sigma} \cdot \vec{B}$ term of Eq. (2); we need to find from it those terms linear in the external field, \vec{B} .

We need to realize that $\psi_{e,g}$ is the solution of the uncoupled electron problem in the presence of the external field, \vec{B} . That is,

$$\begin{aligned}
\psi_{e,g} &= \psi_{e,g}(\vec{B}) \\
&= \psi_{e,g}^{(0)} + \sum_{j=x,y,z} B_j \psi_{e,g,j}^{(1)} + \frac{1}{2} \sum_{i,j} B_i B_j \psi_{e,g,i,j}^{(2)} + \dots
\end{aligned} \tag{16}$$

the electronic wave is a function of \vec{B} and, assuming the effect of \vec{B} on the electrons may be treated as a perturbation (our second perturbation), can be expanded in a power series in the various components of \vec{B} . The perturbing coupling term in the electronic system is that between the electrons and the externally applied field given by the usual expression

$$H_e^{pert} = \sum_k \left(\frac{e}{2m} \right) \vec{B} \cdot (\vec{r}_k - \vec{G}_k) \times \vec{p}_k \tag{17}$$

Accordingly, we want to look for terms at most linear in \vec{B} in the wave function expansion (Eq. (16)) or in the operators $\vec{\pi}_k$ (Eq. (15)); the latter will come from the $\vec{A}_k^{(B)}$ part of the operator expression (see Eq. (9)). Using a “ D ” and “ P ” notation to define diamagnetic and paramagnetic contributions, respectively, to the induced field, it is not difficult to show that these two terms are given by

$$\begin{aligned}
\vec{\mu} \cdot \vec{B}_D^{(ind)} &= \vec{\mu} \cdot \langle \psi_{e,g}^{(0)} | \frac{e}{m} \left(\frac{\mu_0}{4\pi} \right) \frac{\vec{r}_{k\mu} \times \vec{A}_k^{(B)}}{r_{k\mu}^3} | \psi_{e,g}^{(0)} \rangle \\
&= \vec{\mu} \cdot \langle \psi_{e,g}^{(0)} | \frac{e}{2m} \left(\frac{\mu_0}{4\pi} \right) \frac{\vec{r}_{k\mu} \times \vec{B} \times (\vec{r}_k - \vec{G})}{r_{k\mu}^3} | \psi_{e,g}^{(0)} \rangle
\end{aligned} \tag{18}$$

and

$$\begin{aligned} \vec{\mu} \cdot \vec{B}_p^{(ind)} = \vec{\mu} \cdot \sum_{j=x,y,z} B_j \langle \Psi_{e,g,j}^{(1)} | \frac{e}{m} \left(\frac{\mu_0}{4\pi} \right) \frac{\vec{r}_{k\mu} \times \vec{p}_k}{r_{k\mu}^3} | \Psi_{e,g}^{(0)} \rangle \\ + (\text{complex conjugate}) \end{aligned} \quad (19)$$

so that finally

$$\mathbf{H}_\mu^{spin} = -\vec{\mu} \cdot \vec{B} + \vec{\mu} \cdot (\vec{B}_D^{(ind)} + \vec{B}_P^{(ind)}) \quad (20)$$

The diamagnetic field, $B_D^{(ind)}$, is associated with the electronic ground state wave function in the absence of an external field, is generally aligned in a direction nearly opposite that of the external field, and tends to cause an upfield shift of the nuclear resonance; the paramagnetic field, $B_P^{(ind)}$, is associated with the perturbed electronic functions, is generally in a direction nearly parallel with the external field, and tends to cause a downfield shift.

Looking back at Eq. (2) we see that the shielding tensor element, σ_{ij} , will be given by the coefficients of $\mu_i B_j$ in Eqs (18) and (19). This involves further straightforward but tedious manipulations and is not done here. The perturbation approach for both the nuclear and electronic systems is well justified, and, once the set of external-field-unperturbed electronic wave functions is known, one can be confident of correctly finding the perturbed set of states. The major problem, of course, is determining how to find the unperturbed states. Our current abilities don't allow us to find the exact solutions, so approximate methods must be invoked. While the employment of perturbation theory implies straightforward application of the necessary quantum mechanics, the shielding effect one is calculating is so small that minor errors in the electronic wave function can have devastating effects on the resulting shielding tensor. The extent, then, to which our estimate of the shielding tensor is good depends critically on how good our approximate approach produces viable *unperturbed* electronic wave functions.

Typically one starts at the coupled perturbed Hartree–Fock level,¹⁷ and for many years this was the sole approach. As was discussed earlier, one must select a basis and a molecular geometry, decide whether or how to deal with rovibrational effects, and how one will attempt to combat the gauge problem; these approaches are described in the following section and in the examples we present. If a post-Hartree–Fock treatment is desired, these same questions must be addressed, and, in addition, one must decide on a particular method for including correlation. Current approaches to this more difficult but more nearly exact treatment of calculating chemical shielding are given toward the end of the review.

4. SELF-CONSISTENT FIELD APPROACHES

4.1. Theoretical approaches

The *ab initio* calculation of chemical shielding is no different than any other problem in quantum mechanics in that some type of approximate treatment must be employed. The effect of electronic currents producing internal fields is a very small one and can be treated by perturbation theory; in particular, as we have just seen, the chemical shielding tensor is defined as that term in the energy expression which is bilinear in the external field and the magnetic moment of the nucleus in question. Although it is a perturbation, perturbation theory is no better than the zeroth-order states from which it derives, and here is where the general computational problem arises. Because of the smallness of the effect, very accurate wave functions are needed. This means that whatever level of theory is used, one needs to employ large basis sets, and with this comes the N^4 problem due to the many two-electron integrals that must be calculated.

Up until just recently nearly all approaches to the determination of chemical shielding were at the Hartree–Fock level or some variant thereof. With the advent of faster and bigger computers we have been able to provide basis sets that take one near the Hartree–Fock limit in chemical shielding calculations. But Hartree–Fock theory is an approximation and achieving the Hartree–Fock limit in calculations is indicative only of doing as well as one can possibly do with this approach, but not necessarily doing well. In fact, one of the more significant advances in the last few years has been the recognition of those cases where correlation (post-Hartree–Fock) appears to be important and, more importantly, the use of techniques that take us beyond Hartree–Fock to include various degrees of correlation in the determination of chemical shielding. In the majority of cases, Hartree–Fock theory yields semi-quantitative results that are typically of the order of 3–4% of the shielding range of the nucleus in question,^{18,19} which in many cases is quite adequate to solve chemical problems. However, there are those cases involving lone pairs and multiple bonds where lack of correlation in the Hartree–Fock approach (by definition) causes severe error and where post-Hartree–Fock approaches are needed. Some examples of the inclusion of correlation in chemical shielding calculations are discussed later.

Chemical shielding calculations do differ from other problems in computational chemistry in that a static magnetic field enters the Hamiltonian. This means that a vector potential must be employed and with this comes the gauge problem in chemical shielding calculations. Maxwell's equations allow us great latitude in the choice of the vector potential and various choices (the particular gauge) are made to simplify the equations. The Coulomb gauge ($\nabla \cdot \vec{A} = 0$) is normally employed, and with that the definition of the vector potential for the k^{th} electron becomes

$$\vec{A}_k = \frac{1}{2} \vec{B} \times \vec{r}_k \quad (21)$$

where \vec{r}_k refers to the coordinate of the k^{th} electron's molecular coordinate. However, this vector potential can just as easily be rewritten as

$$\vec{A}_k = \frac{1}{2} \vec{B} \times (\vec{r}_k - \vec{G}_k) \quad (22)$$

where \vec{G}_k is an arbitrary constant vector; in essence, the vector potential has its own origin defined by the choice of gauge. Of course, in any exact treatment the particular gauge employed cannot affect the results. However, we normally do not carry out exact treatments, and thus the choice of gauge can affect our answers and, in the case of chemical shielding, does so significantly. Even though Hartree-Fock theory in its limit is gauge invariant,²⁰ we normally do not achieve the Hartree-Fock limit in our calculations and problems ensue.

There are a variety of approaches for overcoming the gauge problem. On the one hand, a common gauge origin may be employed (generally the origin of the molecular coordinate system) and one relies on sufficiently large basis sets to approach the Hartree-Fock limit close enough so that the gauge dependence is minimized. However, as we will see in some of our examples, this does not appear to be a viable approach to solving the gauge problem; all of the other approaches that we will shortly discuss are significantly better than the common origin approach.

An alternative to the common origin approach is what may be described as a distributed origin approach where gauge factors are explicitly contained in either the atomic orbitals or the molecular orbitals of the calculation. Ditchfield²¹ introduced the idea of employing atomic orbitals which carry a complex gauge factor referred to the position of the nucleus where the particular orbital is centred. These orbitals, which are now called London orbitals,²² form the basis (literally) for his gauge including atomic orbital (GIAO) approach. Wolinsky, Hinton, and Pulay²³ have recently produced an efficient new implementation of this theory at the Hartree-Fock level which has expanded its applicability significantly.

Kutzelnigg and Schindler^{24,25} designed their individual gauge for localized orbitals (IGLO) coupled Hartree-Fock approach so that the complex gauge factors are contained in and refer to the centroid of localized molecular orbitals. Their approach is particularly nice in that not only does it allow circumvention of the gauge origin problem but it also allows one the ability to characterize atomic and bond contributions to the chemical shielding in terms of the localized molecular orbitals with which chemists feel comfortable. In their theory the complex gauge factors enter only in the form of

developments leading to the working equations and do not introduce the extra bookkeeping required in the GIAO approach.

Hansen and Bouman^{26,27} have also introduced a local origin variant of the coupled Hartree–Fock method in which the random phase approximation is applied. Complex (gauge independent) orbitals are not introduced explicitly, but rather by expanding angular momentum terms relative to a local origin for each orbital and using properties of the random phase approximation they are able to arrive at shielding expressions that contain no reference to an overall gauge origin. This localized-orbital-local-origin (LORG) approach introduces a localization of the molecular orbitals as does the IGLO method of Kutzelnigg and Schindler, and also allows the decomposition of the total shielding into individual local bond contributions and bond-bond contributions involving other bonds. Facelli *et al.*²⁸ have compared the LORG and IGLO methods from both the theoretical and computational viewpoints.

The GIAO, IGLO, and LORG methods are basically equivalent in terms of their calculational ability. The localized orbital IGLO and LORG methods are appealing in terms of their ability to partition the shielding into parts related to specific spatial regions of the molecule, and are thought to be easier than GIAO in terms of computational effort required. On the other hand, Ditchfield's GIAO method appears to be more efficient in terms of convergence of the chemical shielding value as a function of basis set size.²³ As indicated previously, all three methods are superior to the common origin approach. All of these methods, including the common origin approach, are illustrated in the examples we present.

4.2. A large system calculation

A particularly interesting example is that of the estimation of the ¹³C NMR shielding in C₆₀, the now-famous buckminsterfullene (also known as buckyball), the cage-shaped molecule having the form of an Archimedean truncated icosahedron containing 12 pentagonal and 20 hexagonal faces. This example will serve to illustrate both our capabilities and limitations in terms of shielding calculations, as well as providing an interesting extrapolation approach to the determination of NMR shielding. This work was carried out by Fowler, Lazzaretti, Zanasi, and Malagoli^{29,30} and consisted of determining the carbon shielding in this molecule (in which all the carbons are equivalent) using a variety of relatively small basis sets, the size of the basis set being limited here by the huge size of the molecule being studied. Results were obtained using the STO-3G, STO-3G*, 6-31G, and the 6-31G* basis sets.

To appreciate the magnitude of the problem involved, we show in Table 1 for each of these basis sets the number of orbitals involved, the total number

Table 1. Size and timing parameters for Hartree–Fock shielding calculations on C_{60} for a variety of relatively small basis sets. NI (nosymm) is the total number of two electron integrals required for each basis set, NI (unique) is the number of unique symmetry unrelated two-electron integrals, while NI (sig) is the number of unique integrals larger than a threshold of 10^{-10} au. Note that the integrals numbers are expressed in millions (M). The cpu hours are the times required for each basis set.

Basis	STO-3G	STO-3G*	6-31G	6-31G*
No. orbitals	300	660	540	900
NI(nosymm)	1019.3M	23 790.5M	10 668.3M	82 195.1M
NI(unique)	8.5M	199.1M	89.1M	686.4M
NI(sig)	2.6M	28.1M	28.8M	129.9M
cpu hours	6.1	82.4	44.3	232.7

of two-electron integrals for each calculation (NI (nosymm)), the number of symmetry unique two electron integrals (NI (unique)), and the number of significant two-electron integrals (NI (sig)), where the latter is defined by those integrals larger than a 10^{-10} au threshold. Also included in the table is the computer cpu time required for each calculation. With a basis set of size N one must in principle determine approximately $(N^4)/8$ two-electron integrals (more exactly, $(N(N+1)(N(N+1)+2)/8)$); the presence of symmetry reduces this number to a smaller, unique set of integrals, and discarding integrals smaller than some given threshold value reduces this number further.

To appreciate the enormity of this problem, consider those calculations carried out with the 6-31G* basis, the largest basis employed here. Nine hundred orbitals are involved with over 82 *billion* two-electron integrals. Of the total number of integrals *only* some 700 million are unique, and when those of no significance are discarded there still remains the need to handle 129 million of them! While the cpu time for the minimal STO-3G basis was a modest 6 h, that for this larger split valence with polarization set was some 233 h, a quantity which translates into 9.7 days! For those who do not appreciate long cpu times, consider the fact that industrial rates for supercomputing such a single calculation would cost well over \$100 000.

In the type of calculations that these authors carried out where a common gauge origin is employed, one has to decide what and where the gauge origin is to be. Furthermore, one always worries about whether or not the basis is set employed is adequate in terms of convergence or near-convergence to the Hartree–Fock limit. One can get an idea of convergence by looking at the calculated results as a function of ever larger basis sets. The gauge problem (for a common gauge origin) can be examined by carrying out calculations at several different gauge origins. this, indeed is

Table 2. The parameter (p,p) measuring the effective completeness of the basis set and the calculated isotropic shielding for carbon in C_{60} for gauge origins chosen at both at the centre of mass (c.m.) and at the location of one of the carbon atoms (C).

Basis	(p,p)	$\sigma_{C(c.m.)}$	$\sigma_{C(C)}$
STO-3G	90.1	270.4	656.8
STO-3G*	186.4	211.0	447.0
6-31G	176.3	203.8	461.2
6-31G*	243.9	173.2	306.4
Extrapolation	360	97.0	46.2
Experiment ^a		43	43

^aRef. 31.

what these investigators did, with the results shown in Table 2. Lazzeretti and Zanasi³² have shown that the particular quantity

$$(p,p) = \frac{2}{3} \sum_{\alpha} \langle \Psi^{(0)} | p_{\alpha} | \Psi^{(1)}(p_{\alpha}) \rangle \quad (23)$$

is equal to the number of electrons in a system when a complete basis set is employed. Accordingly, it was taken as a measure of the completeness of the basis sets employed in their study. Table 2 shows this quantity along with the isotropic shielding for carbon both in the centre of mass system (c.m.) and for that gauge origin chosen at one of the carbons of the molecule (C). It is evident that the calculated shielding is a sensitive function of the size of the basis set employed, and that even at the 6-31G* level convergence has not been reached.

The approach these investigators took, then, was to use the quantity (p,p) as an indicator of completeness and to perform a linear extrapolation of the calculated results to the known number of electrons for this system (360). This results in a calculated isotropic shielding of 97.0 ppm for the centre of mass gauge origin and 46.3 when the origin is chosen at a carbon atom; this last value agrees quite well with experiment, whereas the centre of mass gauge origin calculation differs from experiment by a large amount based on our current abilities to calculate carbon chemical shifts. Fowler *et al.*³⁰ argue that the carbon gauge origin is a more realistic one to choose since, in this case, the centre of mass origin would be at the centre of the carbon cage far away from the location of any of the atoms in the molecule. The dichotomy of results here does illustrate very well the difficulty of performing shielding calculations with a common gauge origin. The problem is that one doesn't necessarily know the appropriate common gauge to choose before the fact; furthermore, the great sensitivity of the results to choice of gauge origin makes one question the overall validity of the calculated shielding.

Table 3. The number of orbitals, the (p,p) completeness parameter, and the isotropic shifts for carbon in benzene calculated for a variety of basis sets, both small and large, and for gauge origins both at the centre of mass (c.m.) and at a carbon nucleus (C).

Basis	No. orbitals	(p,p)	$\sigma_{\text{C(c.m.)}}$	$\sigma_{\text{C(C)}}$
A.				
STO-3G	36	10.2	138.6	204.7
STO-3G*	72	19.8	122.2	170.8
STO-3G**	90	21.6	118.7	165.5
6-31G	66	19.7	127.1	165.6
6-31G*	102	26.9	115.6	135.2
6-31G**	120	28.1	109.2	130.0
Extrapolation		42	89.7	74.5
B.				
198CTGO	198	40.51	57.39	60.62
252CTGO	252	40.69	57.03	60.00
300CTGO	300	41.34	54.69	56.25
360CTGO	360	41.65	54.05	54.99
396CTGO	396	41.70	54.01	54.83
Extrapolation		42	53.0	53.2
Experiment ^a			57.2	57.2

^aRef. 2

The idea of the extrapolating function, however, is quite interesting. It is further illustrated by calculations carried out on benzene^{30,33} where much larger as well as smaller basis sets can be considered. These results are given in Table 3 for some standard basis sets ranging from the minimal (STO-3G) up to the fully polarized 6-31G** set, as well as sets containing anywhere from 198 to 396 contracted gaussian functions. Table 3 shows the number of orbitals involved for the benzene calculation for each basis, again the quantity (p,p) which is taken as a measure of the completeness of the basis set, and calculated isotropic shieldings both in the centre of mass and at the carbon atom origins. The results of the extrapolation procedure carried out on the smaller sets shown in part A of the table show that the extrapolated value is again far off from that measured experimentally. The use of larger basis sets where one expects to be closer to the Hartree-Fock convergence limit does a much better job, as might be expected, and this is reflected in the figures shown in the table. The two extrapolated values for the larger basis sets are quite close to each other and in quite good agreement with experiment when one takes into account the facts that no influence of vibration or rotation has been taken into account. One lesson from this study, however, seems to be that if the extrapolation procedure as defined here is to be applicable, it apparently cannot be one that is linear in nature.

However, molecules the size of buckyball simply cannot be approached at this time with basis sets of the size of 51 orbitals per carbon, regardless of

one's bank account or unlimited computer access time; a rough estimate reveals that such a calculation would require approximately 2 years of cpu time at a cost of over \$8 000 000. The amazing thing, then, is that a calculation of reasonable magnitude can take place and can with reasonable care yield estimated results which are good indicators of what experimentalists ought to find. Even with the great strides in computing that have been made over the last few years, calculations involving *ab initio* approaches must still rely on approximations, and the extrapolation procedure used here could prove to be quite useful.

Fowler, Lazzeretti, Malagoli, and Zanasi³⁴ went on to calculate the chemical shift tensor in its entirety as well as simply the isotropic shielding (one-third the trace of the shielding tensor). The same extrapolation procedure was involved with the same four basis sets are given in Table 1. The extrapolated principle values were calculated to be 179, 10 and -51 ppm, to be compared to the experimental results of Yannoni *et al.*³⁵ of 146, 0, and -34 when placed on the Jamesons' absolute scale for carbon.² While this is an average discrepancy for the principle values of some 20 ppm per component, it is clear that the ordering of the tensor elements is correct and that a correct assignment in terms of the molecular structure can be made. The calculated paramagnetic (negative) eigenvalue is that associated with the normal to the local mirror plane of symmetry in the molecule, with the large diamagnetic (positive) component being an axis lying in the mirror plane at an angle of approximately 12° to the radius vector of the molecule. As the authors point out, this is broadly compatible with the picture of C₆₀ as a molecule with a surface π -system with diamagnetic circulation induced within the faces of the truncated icosahedron by a magnetic field at right angles to them.

In summary, in this example a clever approach has allowed for at least a semi-quantitative estimation of the carbon shielding in a molecule whose size would cause most computational chemists to hurriedly retreat to the safety of the "simple" 10-50 atom systems.

4.3. The self-consistent reaction field

One of the problems relating theoretically determined shieldings to experiment is that a calculation carried out on a rigid isolated molecule need have no resemblance to experimental results obtained with the molecule in question in a liquid or solid environment. Not only may medium effects arise from interaction of the molecule with its environment for a given nuclear configuration, but the medium effects on the shielding may be indirect in modifying the geometry of the molecule itself.

A method for treating the effects of the environment is that of Onsager's

reaction field treatment of polar materials.³⁶ In this approach, the so-called self-consistent reaction field (SCRF) model, the effects of the liquid or solid environment are modelled by placing a polar molecule in the electric field that it induces in the medium, a field which is taken to be proportional to the molecule's dipole moment. Since the dipole moment is determined by the wave function, the system of molecule and reaction field is solved iteratively in the usual self-consistent way, either at the Hartree-Fock or post-Hartree-Fock level. A nice discussion of the basic ideas behind SCRF is given by Wong, Frisch, and Wiberg.³⁷

The SCRF method in principle should allow one to mimic liquid or solid phases in the calculation of chemical shieldings. The model involves choosing an appropriate dielectric constant as well as a cavity size in which the "solute" is placed. The molecule under investigation should be optimized within the reaction field, since not only is the system's wave function modified by the reaction field for a given nuclear configuration, but the lowest energy nuclear configuration itself may be changed in the field's presence leading to an obvious modification of the chemical shielding.

An application of this technique as applied to structural modification has been given by Bühl, Steinke, von Schleyer, and Boese³⁸ for the simple aminoborane H_3BNH_3 . The BN distance determined in the gas phase by microwave spectroscopy is 1.672 Å,³⁹ more than 0.1 Å longer than that from the X-ray redetermination of the structure by these authors which yielded a value of 1.564 Å. They indicate that optimization of this structure at the MP2(Full)/6-31G* level is in good agreement with the observed gas phase structure, which is, of course, the appropriate comparison for the theoretically rigid and isolated molecule.

It is pointed out that if one looks at the chemical shielding of a large series of borane complexes, agreement is quite satisfactory (a standard deviation of approximately 2.0 ppm) with the exception of H_3BNH_3 whose error relative to experiment⁴⁰ is some 8.1 ppm using the structure in which the BN distance is taken to be 1.66 Å. If the X-ray separation of 1.56 Å is used instead, the error in the IGLO calculation is only 3.3 ppm. This clearly suggests that the geometry of the molecule in question may well depend upon its environment. In order to study this possibility, the SCRF method was employed to find optimized structures using as model solvents hexane and water. The optimization of H_3BNH_3 in the reaction field simulated for hexane at the 6-31G* level results in a reduction of the BN bond length to 1.62 Å; for water, the reduction is even more dramatic, the distance falling to 1.57 Å. The authors conclude that the dipole field in the crystal like the dielectric reaction field of water is likely responsible for the calculated shortening. This argument is supported by the close agreement of the theoretically determined BN distance in the reaction field with the X-ray determined separation, and the significantly better agreement with experiment for the NMR chemical shielding of this species.

The SCRF approach does not, of course, include any specific treatment of hydrogen bonding, an effect one expects to be present in aqueous solution. In order to assess the influence of such interactions with solvent molecules in this case, the H_3BNH_3 molecule was surrounded with three water molecules with an overall C_3 symmetry, a minimum energy configuration at the 6-31G* level. The pertinent molecular and intermolecular distances were then optimized at the MP2/6-31G* level and the chemical shielding of this partially hydrated molecule compared to that of the molecule with the same structure parameters but without the waters of hydration. Just as in the SCRF method, the BN distance was significantly shortened to 1.614 Å and the chemical shielding noticeably modified. However, the difference in shielding between the hydrated molecule and the molecule with the same molecular parameters but without the waters present was only 0.6 ppm, showing that the main effect of solvation is in the geometry modification of the solute and not in any direct solvent-solute interactions, at least in the present case.

It is not apparent in this example that the actual shielding calculation was also carried out in the presence of the reaction field, and one can probably infer that it was not. Strictly speaking, when the system's zeroth order wave function in the SCRF approach is found one should then perform the usual chemical shielding calculation in the reaction field. Although structures may be modified in the reaction field, so too will the system's wave function and, accordingly, its shielding. It will be of interest to compare the contributions of these two effects to the overall shielding.

4.4. Locally dense basis sets

Improvements in both hardware and software have allowed the computational chemist *ab initio* approaches to molecules for ever increasing size such as the previously discussed buckminsterfullene (C_{60}). We are reaching the point where small aggregates of molecules can be studied as a means of understanding intermolecular interactions.^{41,42} Still, there are temporal and spatial limits to the size of systems that can be investigated; approximations which allow one to look at specific properties in an accurate manner continue to be useful. The application of locally dense basis sets to the calculation of NMR shieldings is such an example. The N^4 problem is particularly evident in the determination of chemical shieldings since the small magnitude of this particular effect requires a larger basis set than might otherwise be used in the estimation of other properties like the energy or dipole moment.

Several years ago it was discovered that the use of locally dense basis sets in the calculation of NMR chemical shieldings gave results that were in rather good agreement with the more conventional balanced basis set

approach, with considerable savings of computer time.⁴³ The idea was to use a relatively large (locally dense) set of functions on the resonant atom of interest and considerably smaller or attenuated sets of functions on other atoms in the molecule. In that earlier study it was suggested that for atoms in the first long row of the Periodic Table a dense basis of 6-311G(d,p)¹⁴ and an attenuated set 3-21G¹⁴ worked well together; employing larger dense basis sets appeared to provide relatively little improvement while use of smaller attenuated basis sets considerably worsened the results. A number of applications of this technique have been reported in the literature since then involving the amide group in glycylglycine⁴⁴ and its dihydrate,⁴¹ and the proton anisotropy in (H₂O)₁₇ as a model for ice⁴⁵ (see later section), and more recently a detailed presentation of data concerning its applicability and generalization has been given.⁴⁶ While first efforts were focused on the idea of a single atom being dense, later applications^{41,44-46} showed that one can rather select a multi-atom segment or chemical functional group to be dense in order to obtain considerably improved results using this technique. Following the work of Hansen and Bouman⁴⁷ the single atom or group of atoms taken locally dense is referred to as the "NMR chromophore".

Some elements in general bonding situations can be taken singly dense while others cannot. Hydrogen must have included its singly bonded partner ("XH dense") while species like carbon or phosphorus work well as singly dense species. A plot of singly locally dense phosphorus isotropic shielding versus the balanced isotropic shielding is shown in Fig. 1 for some 26 different phosphorus nuclei.

An investigation of oxygen showed that the agreement is not very good when oxygen is involved as the singly dense species in a double bond to carbon. In addition, if one looked at the carbon species involved in the same double bond, it was noted that those differences also tended to be high compared to those of the other carbon species. This suggested the use of the CO group as the NMR chromophore for such cases. Figure 2 shows singly and CO dense oxygen isotropic shieldings versus the balanced calculated values and the improvement is clear. The root-mean-square differences for oxygen improved from 36.6 ppm in the singly dense approach to 16.5 ppm in the CO dense approach; carbons in carbonyl groups, while acceptable as singly dense species, improved from 5.7 to 1.7 ppm. The results comparing the singly dense and CO (doubly) dense approaches for oxygen are just as striking for the principal values as they are for the isotropic shieldings, the rms differences dropping from 61.0 to 19.5. An examination of the data shows that the more paramagnetic oxygen principal values tend to show the larger difference when treated as a singly dense species; it is not surprising that the more paramagnetic terms are more sensitive to chromophore selection.

Chemical shielding calculations carried out with both a balanced 6-311G(d,p) and locally-dense 6-311G(d,p)/3-21G basis for several model

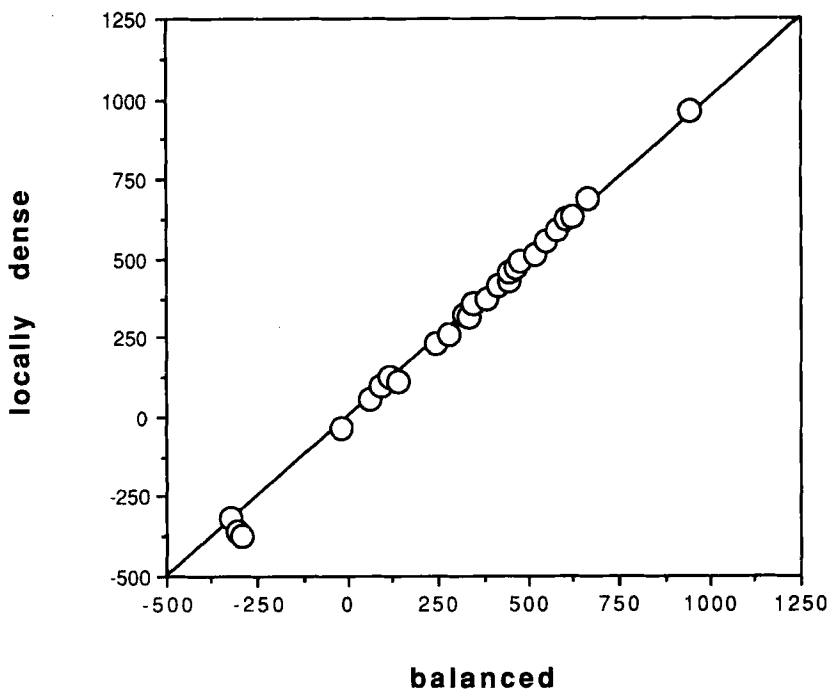


Fig. 1. A comparison of isotropic shieldings (ppm) for balanced and locally dense calculations for (singly dense) phosphorus.

structures of the simple dipeptide glycylglycine were reported some time ago.⁴⁴ In the locally dense approach taken there, the OCNH group fragment was kept locally dense and the remainder of the structure attenuated at the 3-21G level. The pertinent data for both the neutral and zwitterionic forms of glycylglycine are given in Table 4. Because of the mirror plane symmetry of the models, a single Euler angle serves to characterize the tensor orientation for each of the amide group nuclei. This angle, designated θ in the table, is the principal axis direction the in-plane shielding tensor makes that is most nearly aligned with a characteristic bond; for oxygen and carbon this bond is taken to be the CO bond, for nitrogen it is the CN bond, and for hydrogen the NH bond is selected. All of the principal values are given in the table along with the isotropic shielding, σ_{iso} , and the range, R , which is quantitatively defined as the difference between the largest (most positive) and smallest (least positive or most negative) shielding principal values.

With the exception of the hydrogen angle in the neutral species, the differences between locally dense and balanced values are all less than 1° . The reason for the relatively large angle difference in the one bad case most

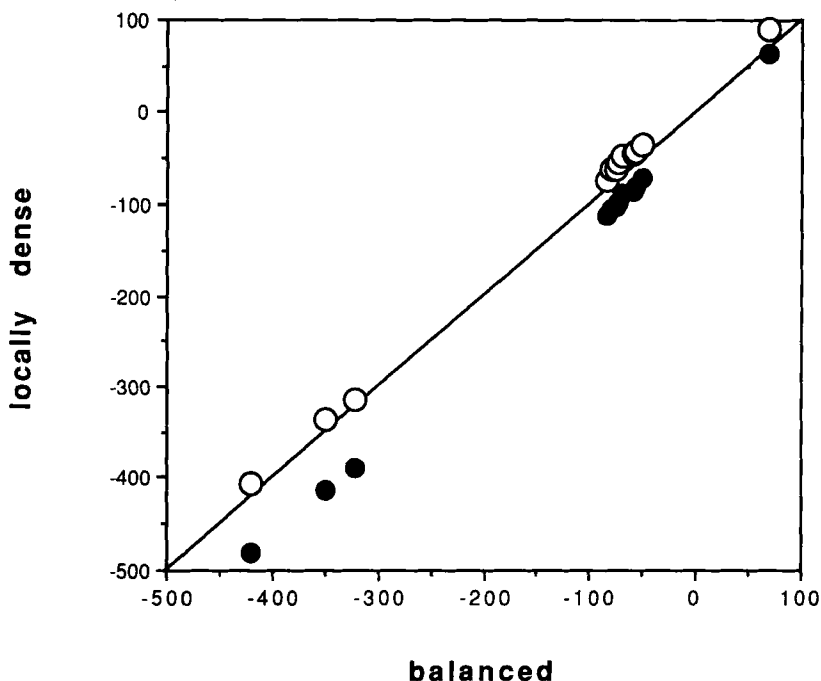


Fig. 2. A comparison of isotropic shielding (ppm) of balanced with locally dense calculations for oxygen in carbonyl groups where the oxygen is singly dense (solid circles) and where the CO group is taken as the NMR chromophore (open circles).

likely lies in the close-to-axial site symmetry shown by the amide group hydrogen in the neutral form; small errors are magnified in such cases. In the zwitterionic species where this close-to-axial symmetry is essentially eliminated, the angle agreement is quite good, and in line with that seen for the general hydrogen XH case as presented earlier. The rmse for the principal values, the isotropic shieldings, and the ranges are in the vicinity of 5–10 ppm for the heavy atoms of the amide group and of the order of 0.3–0.6 ppm for hydrogen, quite in line with previous findings. The proton $\gamma\gamma$ principal value shows the biggest discrepancy, nearly 1.0 ppm in both neutral and zwitterionic cases; the cause of this large difference is presently unknown. The isotropic shielding for the proton agrees quite well between the two approaches.

The balanced calculations for both the neutral and zwitterionic forms of glycylglycine requires 219 orbitals while the locally dense approach uses only 131. Using the amide group locally dense approach, the ratio of the cpu times for the two types of calculations was found to be approximately six, a considerable saving.

Table 4. Shielding tensor data for the amide group nuclei in model neutral and zwitterionic glycylglycine for both 6-311G(d,p) balanced (bal) and 6-311G(d,p)/3-21G (amide group) locally dense (ld) basis sets. The angle θ is in degrees and all the other data in ppm.

	θ	σ_{xx}	σ_{yy}	σ_{zz}	σ_{iso}	R
1. Neutral glygly						
O bal	14.5°	-400.2	-210.1	395.4	-71.6	795.6
ld	14.0°	-399.6	-209.4	390.1	-73.0	789.7
C bal	-4.5°	35.0	-71.9	108.0	23.7	179.9
ld	-4.3°	39.2	-70.3	107.3	25.4	177.6
N bal	6.0°	287.2	94.5	176.7	186.1	192.7
ld	5.8°	288.7	100.2	176.8	188.6	188.5
H bal	34.1°	33.73	30.57	20.09	28.13	13.64
ld	19.6°	33.90	31.54	19.75	28.40	14.15
2. Zwitterionic glygly						
O bal	32.6°	-182.0	-19.2	376.2	58.3	558.2
ld	33.4°	-161.1	-17.0	375.9	66.0	537.0
C bal	22.5°	58.1	-60.7	115.1	37.5	175.8
ld	22.5°	60.8	-59.6	113.5	38.2	173.1
N bal	3.0°	200.9	27.5	181.9	136.8	173.4
ld	2.6°	202.0	35.8	187.2	141.7	166.2
H bal	32.4°	33.77	21.18	13.27	22.74	20.50
ld	32.2°	33.83	22.16	12.88	22.96	20.95

The study of this isolated model dipeptide was the first step in an investigation of the effect of waters of hydration interacting with the amide group nuclei. The relatively good agreement between locally dense and balanced calculations for the unhydrated species and the considerable amount of cpu savings resulting from the locally dense approach led to investigation of glycylglycine with two waters of hydration forming hydrogen bonds at the carbonyl oxygen and amide group hydrogen, respectively.⁴¹ The study of the partially hydrated glycylglycine was done with a variety of orientations of the water and was again carried out with the amide group locally dense and the remainder of the glycylglycine molecule as well as the two waters of hydration attenuated. Use of the locally dense approach allowed the study of many conformations of this system that would otherwise have been very cpu costly had not this approach been used. Significant changes in shielding were noted for the carbonyl oxygen and the amide proton but only small effects were present for carbon and nitrogen. The shift changes for the doubly hydrated species were essentially the sum of those for the monohydrated systems. While the orientation of the shift tensors for oxygen, carbon, and nitrogen were little affected by hydration, that for the amide proton tensor was significant and appeared to follow the orientation of the hydrogen bonding water.

4.5. An atoms in molecules approach

Keith and Bader⁴⁸ have proposed an atoms in molecules approach to the calculation of chemical shielding based on Bader's general theory concerning atoms in molecules.⁴⁹ Bader's theory is based on the premise that the charge density is the principal topological property of an atom or molecule. The charge density exhibits a local maxima at the position of each nucleus, the nuclei being attractors in the gradient vector field of the charge density. One can obtain a disjoint partitioning of the real space of the molecule into so-called atomic basins, by defining each basin to be that region of the space traversed by all the trajectories of the gradient of the charge density that terminate at a given nucleus. Neighbouring basins are separated one from another by trajectories which terminate at what are called the bond critical points located between the atoms. The property of each atomic basin is that it is bounded by a surface of zero flux in the gradient vector field of the electron density. Keith and Bader's IGAIM approach⁴⁸ (individual gauges for atoms in molecules) is based on calculating magnetic properties for a system in terms of the constituent basins. They cite the fact that the nucleus of a ¹S atom acts as a natural gauge origin in that the resulting expressions of the magnetic properties are totally determined by the unperturbed wave function, and, accordingly, they consider a basin's natural gauge to coincide with the nucleus contained.

Taking carbon dioxide as an example, they show that if one chooses the gauge origin at one of the three atoms, the calculated current density is relatively well-behaved within the basin containing that nuclear gauge origin, but can be ill-behaved outside the gauge-origin-containing basin, especially when small basis sets are employed. They suggest, then, that just as the molecular charge distribution can be partitioned into a disjoint set of atomic basins one can partition the chemical shielding calculation in a similar manner. For each nucleus in turn chosen as a gauge origin, the current density within that basin is calculated. At the conclusion of the calculation for each and every basin, a total current density map is derived by summing each basin's separately calculated contribution. From this summed current density the magnetic properties of the molecule, including chemical shielding, are determined.

Using a 6-311++G(2d,2p) basis, Keith and Bader show that chemical shieldings for carbon in a large variety of molecules are much more accurately calculated than they are with a common origin, single calculation approach. Table 5 and Fig. 3 compare experiment with isotropic shifts calculated with IGAIM and common origin coupled Hartree-Fock approaches, along with some GIAO shielding calculations we have performed.⁵⁰ Structures employed were optimized at the 6-311++G(2d,2p) level for the Keith and Bader data, while the GIAO structures were optimized with a 6-311G(d,p) basis; one would not expect significant differences between the two sets of structures.

Table 5. Calculated and observed carbon isotropic shieldings obtained from the summation of basins method⁴⁸ (IGAIM), a common origin coupled Hartree–Fock approach (CPHF), and Ditchfields GIAO method.^{21,50} The statistical summary at the bottom of the table indicates differences of the various theoretical approaches with experiment,^{2,51} the number of data point (N), the mean (\bar{x}), the standard deviation (s.d.), and the root-mean-square error (rmse) are given. All the data are in ppm.

Molecule	σ_{iso} (IGAIM)	σ_{iso} (CPHF)	σ_{iso} (GIAO)	experiment
CH ₄	197.4	198.5	197.4	195.1
C*H ₃ CN	194.7	205.0	194.4	187.7
c-C ₃ H ₆	200.2	211.1	199.7	185.0
C ₂ H ₆	186.3	192.3	186.4	180.9
C*H ₃ CH ₂ CH ₂ CH ₃	179.9		178.7	173.5
C*H ₃ CH ₂ CH ₃	178.7		178.6	170.8
CH ₃ C*H ₂ CH ₃	177.3		177.4	169.1
CH ₃ C*H ₂ OH	178.0		177.5	168.5
CH ₃ C*H ₂ CH ₂ CH ₃	169.5		169.3	160.0
CH ₃ NH ₂	167.0	173.9	167.0	158.3
CH ₃ OH	148.0	155.8	148.9	136.6
C*H ₃ CH ₂ OH	141.0		141.4	127.6
C ₂ H ₂	119.5	127.0	120.3	117.2
CH ₃ F	130.2	140.0	131.8	116.8
C*H ₂ CCH ₂	119.5	130.2	119.5	115.2
HCN	79.9	89.5	81.3	82.1
CH ₃ C*N	72.5	86.8	75.1	73.8
C ₂ H ₄	66.4	73.4	67.8	64.5
CF ₄	86.0	122.3	92.5	64.5
CO ₂	57.9	78.9	62.6	58.8
C ₆ H ₆	61.5	82.1	61.2	57.9
CSO	21.9	78.2	22.0	30.0
HCOOH	32.2	50.2	36.9	23.7
CO	-7.4	-11.9	-7.9	1.0
CS ₂	-41.1	51.9	-47.9	-8.0
CH ₂ C*CH ₂	-34.8	-22.4	-33.2	-29.3
N	26	20	26	
\bar{x}	3.9	20.0	4.5	
s.d.	10.2	17.3	11.6	
rmse	10.9	26.5	12.5	

Table 5 and Fig. 3 reveal a number of pertinent points. Keith and Bader comment that their results are comparable to IGLO results, and we can see here from the indicated root-mean-square errors that they are certainly comparable to the GIAO approach, and that both are significantly better than the common origin approach. The common origin approach simply cannot compete at the same level of basis with theories that contain built-in gauge factors such as GIAO, IGLO, or LORG; even when larger basis sets are used, the common origin approach suffers. A second point to make is

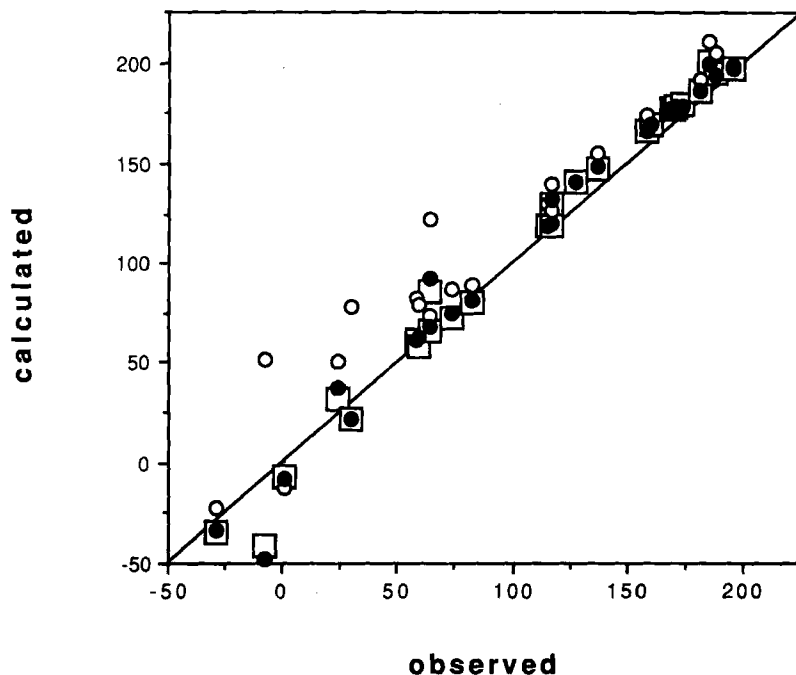


Fig. 3. A comparison of calculated versus observed isotropic shieldings (ppm) for carbon for IGAIM (open squares), common origin coupled perturbed Hartree-Fock (CPHF, open circles), and GIAO (solid circles) approaches.

that GIAO (or IGLO or LORG) is just as good as the IGAIM approach and provides all shifts with one calculation whereas the IGAIM method requires many calculations if all shieldings are desired. If this is to be a practical type of approach to chemical shielding it would be nice to know how the cpu times compare with other, more conventional theories. A third point is that carbon is probably not the best test for a shielding theory, for it tends to be one of the more well-behaved nuclei for shielding determinations. It would be of interest to see how IGAIM compares with the other gauge-including theories for oxygen or nitrogen, or phosphorus in the second long row.

Nevertheless, the IGAIM approach is a novel one and one that is compelling from the standpoint of Bader's atoms-in-molecules description of molecular electronic theory. That fact that the current densities calculated in basins surrounding a gauge-holding nucleus sum to provide a good description of chemical shielding is reflective of the reason why GIAO, where each atom-centred basis function carries its own gauge factor, and IGLO and LORG, where localized molecular orbitals are given separate gauge factors, work.

4.6. A water cluster calculation

Another example of the ability to treat large systems is the locally dense calculation of the chemical shift anisotropy of the hydrogen atom in the $(\text{H}_2\text{O})_{17}$ cluster by Hinton, Guthrie, Pulay, and Wolinski⁵² using their recent efficient implementation of Ditchfield's GIAO method.²³ There are several sets of experimental values for the anisotropy in the literature, at values of approximately 34.1 ppm^{53,54} or 28.6 ppm.^{55,56} This is a significant difference in experimental results (and one which has not been resolved) so the determination of this quantity by *ab initio* methods using a reasonably large water cluster is quite appropriate.

Earlier work of Hinton and Bennett⁵⁷ had been concerned with the calculation of this quantity in small water clusters containing up to five water molecules, employing the relatively small 4-31G split valence basis set. It was felt that larger basis sets would likely yield better results, and that going beyond the first hydration sphere of water (central water plus first hydration sphere of four waters) to a model involving first and second hydration shells (central water, first hydration shell of four waters, and second hydration shell of 12 waters) was necessary. The authors were also interested in further testing their new implementation of the GIAO code.²³ And, of course, it is of some general interest to see the effects of increasing number of neighbours on the calculated shielding properties of the central water molecule. If one is to work with finite clusters of molecules, it is worthwhile knowing how the properties of a central "solute" tend to converge with the cluster size.

Because the experimental measurements were carried out on ice, and because the ice structure is known,⁵⁸ no theoretical geometry optimization was necessary, and the known crystal structure of ice employed. Three types of basis sets were used: balanced 4-31G and 6-311G(d,p) bases, and a locally dense basis where the central water molecule and some of its neighbours were treated at the 6-311G(d,p) level and the rest at the smaller or attenuated 4-31G level.

Table 6 shows the results of the calculations, both of the more recent work as well as those earlier on the smaller water clusters. If one focuses on part A of Table 6 it can readily be seen that at the 4-31G level of basis the various tensor elements of the central proton in the central water as well as its isotropic and anisotropic shifts are quite dependent upon the number of neighbours involved, as well might be expected; the 4-31G calculation of the water pentamer indicates that convergence has not been reached at that level of water cluster. The more recent calculations are shown in part B for both the balanced 6-311G(d,p) level and the locally dense approach in which the central water and its nearest neighbour oxygen atoms were taken as locally dense. Comparison of these balanced and locally dense calculations show that the results were virtually identical to each other; they are also

Table 6. Chemical shieldings (ppm) calculated for various water clusters. The basis sets involved were the 4-31G (S), the 6-311G(d,p) (L), the locally dense set with central H₂O and bonded oxygens dense at 6-311G(d,p) and other atoms at 4-31G (LD-1), and the locally dense set with the central water and its first hydration shell locally dense at 6-311G(d,p) and the second hydration shell at 4-31G (LD-2). $\Delta\sigma$ is the anisotropy which is defined as $(\sigma_{33} - 0.5(\sigma_{22} + \sigma_{11}))$.

Cluster	Basis	σ_{11}	σ_{22}	σ_{33}	σ_{iso}	$\Delta\sigma$
A.						
(H ₂ O) ₁	S	24.77	26.54	41.36	30.89	15.71
(H ₂ O) ₂	S	18.60	19.57	46.07	28.08	26.99
(H ₂ O) ₃	S	17.21	18.36	48.70	28.09	30.92
(H ₂ O) ₅	S	15.77	16.27	48.19	26.74	32.17
B.						
(H ₂ O) ₅	L	12.30	13.32	47.72	24.45	33.92
(H ₂ O) ₅	LD-1	12.35	13.43	47.13	24.30	34.24
C.						
(H ₂ O) ₁₇	LD-1	11.98	12.25	47.28	23.84	35.17
(H ₂ O) ₁₇	LD-2	11.97	12.19	46.91	23.69	34.83
Experiment						34.2 ^a
						34 ^b
						28.5 ^c
						28.7 ^d

^aRef. 53.

^bRef. 54.

^cRef. 55.

^dRef. 56.

significantly different from those obtained for the water pentamer at the 4-31G level, indicating that, indeed, a larger basis is required for an accurate determination of shielding in this system.

Part C of Table 6 shows the two calculations carried out for the cluster of water containing 17 water molecules. These both were locally dense types of calculations where in the first calculation the central water and its two nearest neighbour oxygen atoms were taken as locally dense and the remainder attenuated, and in the second case where all five water molecules of the central water plus first hydration shell were made locally dense. Again, a comparison of these two calculations shows that the results are virtually identical, and that there is a small but significant change in going from the water pentamer to the cluster containing 17 waters.

Table 6 also lists the anisotropies as reported experimentally from four sources. Clearly, the results of Hinton *et al.* favour the anisotropy value near 34 ppm as opposed to that near 29 ppm. The discrepancy between the

experimental results has not been resolved as of this date; in the absence of other information, the results of Rhim and Burum^{55,56} seem most consistent in that their two results, one from a powder study and one from a single crystal investigation, agree with each other. While it is difficult to calculate proton shieldings as precisely as other species, it seems unlikely that one would make an error of the order of 6 ppm; the theoretically determined anisotropies are expected to be essentially correct. While the theoretical calculation is of the Hartree-Fock variety, Hinton *et al.* believed that electron correlation effects for a molecular system such as the water cluster would be unlikely to make a significant contribution to the shielding.

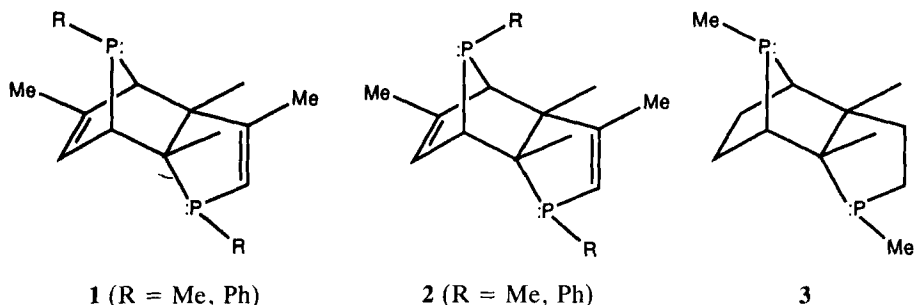
Aside from attempting to clarify the dichotomy of experimental results, the calculations are interesting in their own right in showing both what proper level of basis set is required for shielding calculations (that is, the larger 6-311G(d,p) as opposed to the 4-31G basis) as well as seeing how the various hydration shells affect the properties of a central molecule. The calculations also illustrate the benefits of the locally dense approach. The authors find that taking the central water plus the two hydrogen bonded nearest-neighbour oxygens as locally dense and others attenuated compared to that calculation in which all five waters of the central and first hydration shells were made locally dense took only some 60% of the time, yet provided results which were virtually equal to one another. In terms of the bases employed here, one can estimate that a balanced calculation on the cluster containing 17 water molecules at the 6-311G(d,p) would require 6–8 times longer than that calculation where only the central water and its first hydration partners are made locally dense.

These results illustrate the potential importance of considering long-range solvent effects in chemical shielding calculations. The chemical shift anisotropy more than doubles upon completing the first solvation sphere and increases by about 1 ppm with the addition of the second solvation sphere. Hinton, Guthrie, Pulay, and Wolinski⁵² feel that further addition of a third sphere would probably have very little effect on the chemical shielding parameters.

4.7. An orbital shielding analysis

It is always satisfying when results of a complicated quantum mechanical calculation can be readily understood in terms of the basic facets of the theory. The recent analysis of phosphorus shieldings in the 7-phosphanorbornenes (7-pnb)⁵⁹ is such an example.

Phosphorus-31 NMR shifts cover a very wide range (circa 1415 ppm⁶⁰) and even for similar phosphorus functionalities can exhibit pronounced sensitivity to molecular structural modification. Nowhere are the effects of structure on shifts so pronounced as in the family of bridged unsaturated

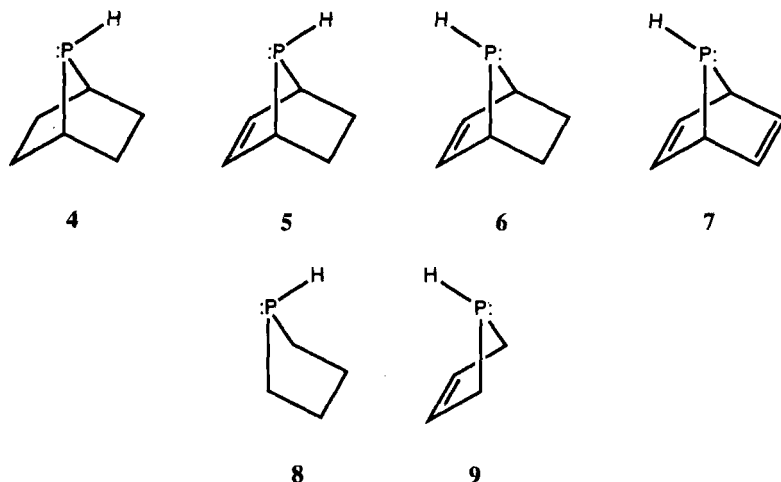


phosphines, where angle and rotational constraints can be strong and atoms can be held in fixed positions that might allow specific orbital interactions to develop. The family of 7-phosphanorbornenes is an excellent case in point. Because of the configurational stability of phosphorus, *syn* and *anti* isomers are possible for this structural type. There is exceptionally strong deshielding in derivatives of both of the isomeric forms, but it is especially pronounced in those with the *syn* structure.^{61,62}

Structures 1, 2, and 3 are illustrative of this *syn*, *anti* effect. The *anti* methyl(phenyl) derivative 2 exhibits a resonance at 301.9 ppm (279.9 ppm), while the *syn* derivative of 1 yields a resonance considerably downfield at 227.6 ppm (208.6 ppm). The contracted bond angle (79°)⁶² in the 7-phosphanorbornenes is clearly not alone the cause of the strong deshielding since in the corresponding saturated structure the angle remains about the same but the shift is in the normal phosphine region. The double bond is therefore clearly implicated in the deshielding effect.

In an effort to understand these effects, shielding calculations were carried out employing Ditchfield's GIAO coupled Hartree-Fock method²¹ on the four biocyclophosphorus compounds 7-phosphabicyclo[2.2.1]heptane (4, ndb), 7-phosphabiocyclo[2.2.1]heptene (5, *anti* and 6, *syn*), and 7-phosphabiocyclo[2.2.1]heptadiene (7, 2db), as well as the saturated five-membered ring phospholane (8, tetrahydrophosphole, thp) and the monocyclic unsaturated five-membered ring 3-phospholene (9, 2,5-dihydrophosphole, 2,5-dhp). The basis sets employed were the valence triple-zeta with polarization (6-311G(d,p)) for carbon and hydrogen⁶³ (a [4s,3p,d/3s,p] basis with six cartesian d functions), and the McLean-Chandler 12s, 9p basis⁶⁴ in the contraction (631111/42111) = [6s,5p] for phosphorus with either one (for optimization) or two (for shielding) sets of (six) d polarization functions. The structures were optimized at this level of basis, and were all required to exhibit C_s symmetry.

Absolute shielding values for phosphorus and all other nuclei in the six molecules studied are given in Table 7 along with pertinent data concerning several important structural angles. The absolute shielding values for the *anti* and *syn* species (5 and 6) may be compared to the experimental results



from the R=methyl derivative of **1** and **2**, where it is seen that the calculated shieldings for both the simple hydrogen derivatives (as well as the methyl derivatives) are some 40 to 50 ppm too high on an absolute basis. The GIAO method in the basis employed here tends to yield phosphorus shieldings that are on average 14–15 ppm high and show a scatter of values of some 25–30 ppm when compared to absolute gas phase measurements.^{19,65} Given this noise level of current Hartree–Fock calculations for phosphorus, the above agreement on an absolute basis can be considered satisfactory. Of greater significance, however, is the change in shielding in moving from the *anti* to *syn* forms. The calculations give a downfield shift of 95.6 ppm to be compared to the experimental results of 74.3 ppm for the methyl derivatives **1** and **2**, and 71.3 ppm for the corresponding phenyl derivatives. Species **3** (with no unsaturation in the bicyclic ring) is shifted upfield by some 118.8 ppm with respect to the (*syn*)

Table 7. Absolute shieldings (ppm) and angles (degrees) for the optimized phosphorus bicyclic (7-phosphanorbornenes) and monocyclic (five-membered-ring) structures.

	ndb	<i>anti</i>	<i>syn</i>	2db	2,5-dhp	thp
A. Absolute shieldings						
P	409.6	365.4	269.5	142.3	434.8	420.0
B. Angle data						
H7PC1	99.1	100.3	99.9	100.7	96.7	97.5
C1PC4	80.0	79.3	79.1	77.7	92.3	89.6
flap-1	126.0	124.5	129.1	125.8	166.6	145.0
flap-2	119.0	120.0	116.4	115.4	—	—

methyl derivative of **1** while the calculated difference between the ndb and *syn* cases is 140.1 ppm. It is apparent that the theoretical calculations are reproducing the effects seen experimentally.

The flap angles serve as an indicator of the underlying cause of the shielding changes. Flap-1 is defined as that flap angle on the side of the CPC bridge that contains the phosphorus hydrogen and flap-2 the flap angle for the opposite side. The sum of the two flap angles is virtually constant for the four bicyclic structures, and the flap-1 angle is always significantly larger than flap-2 by some nine-degrees on average,⁶⁶ clearly suggesting that the interaction of the phosphorus hydrogen with either the double bond or the saturated CC linkage is stronger than that of the lone pair. In the case of the monocyclic compounds (thp and 2,5-dhp, **8** and **9**), the (single) flap angle opens up considerably to relieve the strain forced upon the system in the case of the bicyclic structures; the shieldings in the five-membered rings are moved significantly upfield of the predicted resonances of the bicyclic structures containing one or two double bonds (*anti*, *syn*, and 2db), and is comparable to that of the unsaturated phosphanorbornane (ndb).

As is usually the case, the dominant changes in shielding were found to arise from the paramagnetic terms arising from the external field term ($H \cdot L$) coupling of orbitals unoccupied in the Hartree-Fock ground state and those normally filled. These will be large when rotationally related atomic orbitals have large coefficients in those molecular orbitals which are coupled by this operator, the more localized the MOs containing the rotationally related atomic orbitals tend to be, the larger will be the coupling. Because the theoretical approach involves perturbation theory, the coupling between molecular orbitals also depends upon the difference in orbital energies, so that one might expect that the smaller the homo-lumo gap the more likely strong paramagnetic shielding can be realized. Indeed, this qualitative dependence upon the energy gap is the basis for the old average energy approximation used in shielding calculations 30 years ago.⁶⁷ Application of these basic ideas to the systems being studied is evident when the contribution to the shielding is broken down in terms of the molecular orbitals which are coupled and their relative positions along the orbital energy axis. In the neutral phosphines investigated, one has a lone pair which is going to tend to dominate MOs lying close to the energy gap; likewise, the π orbital will contribute strongly to states close to the gap as will the π^* orbital to the low-lying virtual states. Another aspect found to be important was a strong contribution (along with the π^* orbital) to the low lying unoccupied levels in all the molecules studied of a p orbital on phosphorus lying perpendicular to the C_s plane of symmetry and having the same symmetry as the π^* state. The molecular orbitals which tended to determine the shielding were those dominated by the lone pair and π bonding orbitals of the occupied levels, and the phosphorus (perpendicular) p orbital and π^* orbitals of the unoccupied states. The localized nature of

the molecular orbitals dominated by the phosphorus lone pair, π (and π^*), and the (perpendicular) phosphorus p orbitals and their nearness in energy to each other present a potent combination for deshielding.

For the ndb case (4), a lone-pair-dominated orbital occurs as homo and a mainly Pp orbital as lumo. The addition of a double bond to the system in the *anti* configuration (5) causes both these orbitals to split and to now contain π or π^* components; the homo is raised and the lumo lowered by this coupling and, since these MOs tend to dominate the shielding, a paramagnetic shift in the resonance occurs from 409.6 ppm to 365.4 ppm; see Table 7. The splitting of the levels is relatively small reflecting the fact that the lone-pair double-bond interaction is apparently relatively weak. When the phosphorus hydrogen is placed in a *syn* arrangement (6), the larger interaction of the phosphorus hydrogen with the double bond causes these occupied levels to split further, and the homo level is moved up; there is essentially no lowering of the lumo level since the PH interaction there is absent due to the different symmetry (A' compared to A''). However, the gap energy, $E_g = E[\text{lumo}] - E[\text{homo}]$, is reduced leading to a sizable paramagnetic shift of 269.5 ppm in the *syn* case compared to 365.4 ppm in the *anti* case. The effect of adding a second double bond (the 2db case, 7) is to add additional π - and π^* -dominated occupied states to those previously present. While this doesn't significantly modify the energies of the occupied states (still a strong coupling between the PH and one of the π bonds), it does effect a lowering of the lumo energy, thereby reducing E_g even further. The corresponding result is to further shift the phosphorus resonance downfield from 269.5 ppm in the *syn* molecule to 142.3 ppm in the 2db case.

If the strong PH interaction with the other rings of the bicyclic compounds is permitted by a relatively small flap angle (120 – 130°), opening up this flap angle should reduce or remove the effect. As the data for the optimized monocyclic structures in Table 7 show, removing the constraints present in the bicyclic compounds allows the flap angle to open up to 145.0 and 166.6° in these monocyclic species, the phosphorus hydrogen is moved significantly further away from the opposing carbon portion of the molecules essentially minimizing this interaction, and the shieldings move strongly upfield to 420.0 ppm and 434.8 ppm. To see if an artificial reduction in the flap angle of the monocyclics would lead to the same type of effects as seen in the bicyclic cases where it occurs naturally, the flap angle in the two molecules was modified (without further optimization), and the resulting shieldings are shown graphically in Fig. 4. Indeed, as one closes down the flap angle in both the saturated and unsaturated cases the shieldings move downfield as the earlier rationalization would predict. Figure 4 also includes the *syn* and *anti* bicyclic shielding points. One would expect the *anti* shielding to be more like the saturated (thp) case in that the phosphorus hydrogen in both situations "sees" more strongly the saturated portion of the carbon framework; as shown, the *anti* bicyclic point falls on the curve for the

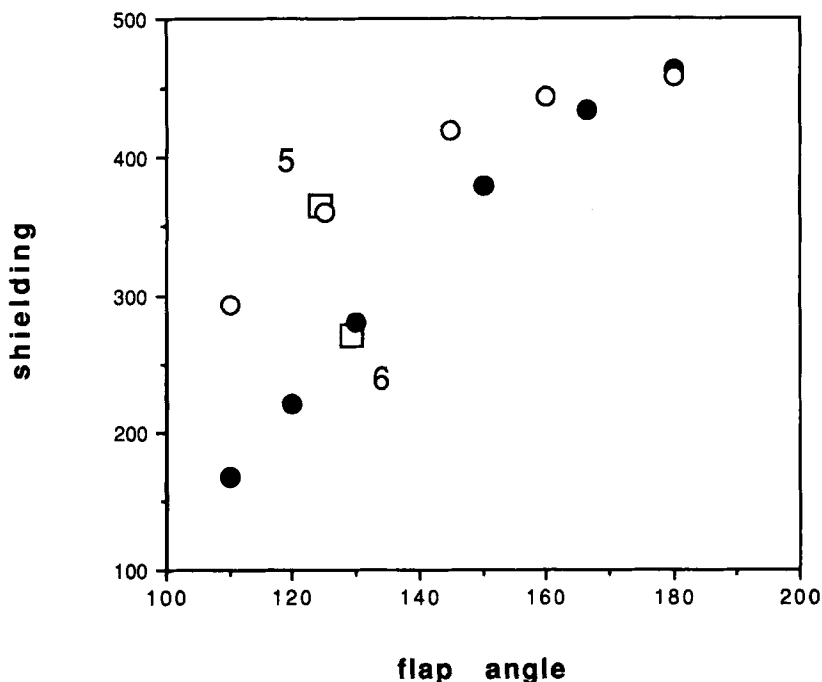


Fig. 4. Phosphorus isotropic shieldings (ppm) as a function of the flap angle (degrees) for the five-membered ring monocyclic (open circles) and 7-phosphanorbornene *anti* (5) and *syn* (6) bicyclic compounds (open squares). See text for abbreviations. \square , 7-pnb; \bullet , 2,5-dhp; \circ , thp.

saturated five-membered ring. Likewise, the *syn* bicyclic shielding should be most like that found for a comparable flap angle for the unsaturated (2,5-dhp) case, and it, too, falls nicely along the appropriate curve.

The parallel between changes in the energy gap and the shieldings in the bicyclic compounds suggests that in these cases one might expect to find a simple relation between these two quantities. Figure 5 shows a plot of shielding versus the inverse of the energy gap, E_g^{-1} , for the four bicyclic compounds as well as the five-membered ring species (in both the optimized and flap-varied species), and the expected simple relation indeed emerges; the negative slope is that expected for the paramagnetic terms. The fact that a single general curve is exhibited is clearly consistent with the same mechanism being in place for all these molecules.

The average energy approximation⁶⁷ was employed out of necessity years ago due to lack of suitable calculation facilities then, and because it led to expressions for shieldings that depended only on a knowledge of the ground state wave function, a quantity that one could obtain through a variety of (often severe) approximations; the predicted shielding varied inversely as

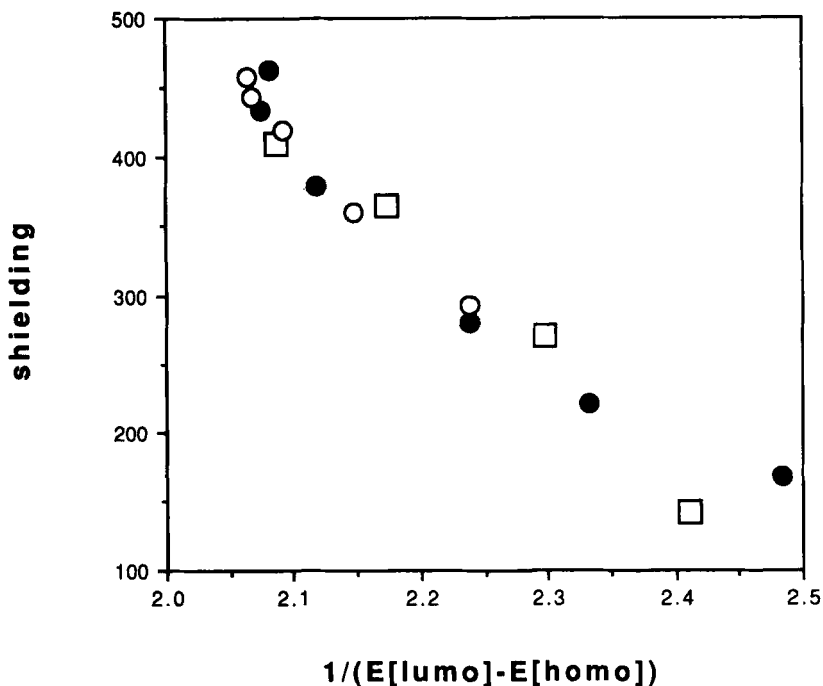


Fig. 5. Phosphorus isotropic shieldings (ppm) as a function of the inverse of the homo-lumo energy gap (inverse au) for the bicyclic (open squares) and all the flap-varied monocyclic species (open and closed circles). See text for abbreviations. \square , 7-pnh; \bullet , 2,5-dhp; \circ , thp.

some “average” excitation energy. But, of course, if shielding in particular cases is dominated by a selected set of orbitals whose orbital energy differences differ very little, the average energy approach is qualitatively correct. Such appears to be the case in the present study as discussed above and as shown by the simple dependence of the shielding on the inverse of the homo-lumo gap energy in Fig. 5.

5. EFFECTS OF CORRELATION

The ability in recent years to carry out coupled Hartree-Fock calculations with fairly large basis sets has allowed us to approach sufficiently close to the Hartree-Fock limit that we are able to spot those problem cases where the inclusion of correlation is necessary in order to calculate good shielding values. Electron correlation appears to be particularly important for shielding in multiple-bonded systems, especially when lone pairs are also involved, and where nearly degenerate or low-lying excited states are

present. In this section we will look at some examples of including correlation in shielding calculations by way of many body of Møller–Plesset⁶⁸ perturbation theory in the GIAO method,^{69,70} the implementation of the second-order polarization propagator (SOPPA) method^{71,72} that incorporates the localized-orbital-local-origin (LORG) methodology called SOLO⁷³ (second-order LORG), a non-perturbative multi-configuration extension of IGLO called MC-IGLO,^{74,75} and finally an example employing density function theory.⁷⁶ In these examples we shall point out the difference that correlation makes in a number of cases as well as identifying those molecular species where its use appears unnecessary or imperative.

5.1. GIAO MP2

Many body perturbation theory starts from the one-electron Fock Hamiltonian as the unperturbed situation and treats to various orders the difference between the true molecular Hamiltonian and the Fock Hamiltonian. This difference is, of course, the difference between the true electron repulsion and the effective or mean field employed in Hartree–Fock theory. Application of Møller–Plesset perturbation theory in first order recovers the Hartree–Fock result, so that the first inclusion of correlation appears at the second-order level. Fukui, Miura, and Matsuda⁶⁹ as well as Gauss⁷⁰ have carried out such second-order many body perturbation theory treatments in the GIAO approach.

The results of Fukui *et al.* for four first-row hydrides using a finite field approach are contained in Part A of Table 8. SCF and MP2 isotropic shieldings are given along with observed values and the difference between the MP2 and SCF calculations. We see in Part A2 of Table 8 that the effects at this level of perturbation theory for hydrogen are small, amounting on average to a decrease in the shielding of a little over 0.1 ppm. Although inclusion of correlation at the MP2 level for this species tends to reduce the average error from 1.52 ppm to 1.38 ppm, the error is still large. Hydrogen, the simplest of all chemical species, appears to be the hardest to calculate accurately in terms of the error as a percentage of the shielding range! An error of 1–2 ppm for hydrogen represents 10–20% of its shielding range, a significantly larger percentage than is observed for other atoms of the first and second long row of the Periodic Table.

The results for the heavy atoms of the four first row hydrides shown in Part A1 of Table 8 are interesting from several perspectives. Here no multiple bonds are involved and the average effect of the inclusion of correlation at the MP2 level is to increase the shieldings by about 11 ppm on average. Fukui *et al.* note that SCF excitation energies are too small, a problem fixed by the inclusion of correlation and which then makes more positive the dominating paramagnetic term. We further note that the

Table 8. Many body perturbation theory (MP2) calculations of some heavy atoms of first-row hydrides by Fukai *et al.*⁶⁹ and some oxygen shieldings by Gauss.⁷⁰ The shieldings are in ppm and are noted as SCF (coupled Hartree-Fock) and MP2 (second-order Møller-Plesset theory).⁶⁸ Except where noted, the experimental results are taken directly from the cited papers.

	SCF	MP2	Observed	MP2-SCF
A1. Heavy atoms of some first-row hydrides				
HF	415.2	427.0	410	11.8
H ₂ O	348.1	359.3	344 ^a	11.2
NH ₃	271.0	286.2	264.5	15.2
CH ₄	194.9	201.5	197.4	6.6
A2. Hydrogen shieldings				
HF	29.68	29.86	28.72	0.18
H ₂ O	31.88	31.70	30.09	-0.18
NH ₃	32.68	32.40	30.68	-0.28
CH ₄	31.92	31.64	30.61	-0.28
B. Oxygen shieldings				
CH ₃ OH	341.6	354.4	345.9 ^b	12.8
H ₂ O	325.7	342.3	344.0	16.6
CO ₂	200.4	236.4	243.4	36.0
N ₂ O	107.5	192.1	200.5	84.6
H ₂ O ₂	139.7	151.4	133.9 ^b	11.7
CO	-177.7	-52.8	-42.3	124.9
H ₂ CO	-482.7	-342.2	-312.1 ^a	140.5
OF ₂	-471.1	-465.5	-473.1	5.6

^aGas phase data of Wasylishen, Moibroek, and Macdonald.⁷⁷

^bLiquid phase data cited by Kitzinger⁷⁸ converted to an absolute shielding using the absolute shielding for liquid water as 307.9.⁷⁷

inclusion of correlation here tends to move the calculated shielding to values which are consistently higher than experiment by about 10–15 ppm. This, however, is a good result when one considers the effect of rovibration on chemical shielding. These calculations, as most, were carried out on rigid, gas-phase-like molecules, whereas experimental results are obtained for species that are rotating and vibrating. The effect of rotation and vibration is generally to lengthen bonds, and it is rather well established now that the change of chemical shielding with bond extension is negative for elements like carbon, nitrogen, oxygen, and fluorine, elements in the right-hand portion of the first long row of the Periodic Table.^{15,16} Accordingly, if one were to correct the rigid-molecule calculated shieldings in these systems for the effects of rovibration, the corrections should be negative and would tend to move the calculated values closer to experiment. The corrections in HF¹⁰ and H₂O¹¹ are calculated to be -11.1 and -13.1 ppm, respectively. The

correction for methane² is small, -3.3 ppm, and a value of -8.8 ppm has been calculated for ammonia.⁷⁹ Applying these rovibrational corrections to the four species in Table A1 reduces the average absolute error from 14.5 to 5.5 ppm, a convincing result. Thus, although in this particular set of examples the effect of correlation is relatively small, it does take the shielding value to that region where it gives considerably better agreement with experiment once rovibrational corrections are included. Fukui, Miura, and Matsuda looked at several basis sets in this work (6-31, 6-31G(d), and 6-311G(d))¹⁴ and noticed that the change from SCF to correlated MP2 shieldings was not a sensitive function of these basis sets. Although certainly a small sample, if this were to be generally true it might offer one the ability to estimate correlation effects at a lower level of basis at lower cpu cost while performing the SCF calculations with a basis set near saturation.

In Part B of Table 8 are calculations by Gauss⁷⁰ on oxygen, again at the MP2 level. Generally speaking, the errors in Hartree-Fock determination of chemical shieldings show up in a paramagnetic contribution that is too negative. Accordingly, one might expect the effects of correlation to show up most visibly for molecules which have a dominant paramagnetic or negative overall shielding. With the exception of OF₂, this is indeed the case. Molecules like methanol, water, and carbon dioxide have corrections which are relatively small (on the scale of oxygen shieldings) while those for species which have more of a downfield shift such as nitrous oxide, carbon monoxide, and formaldehyde have corrections which are of the order of 100 ppm. Actually, Gauss points out that the isotropic shielding change for OF₂ is misleading since the individual principal values change by the considerable amounts of -24.5 , -73.7 and 115.0 ppm. Gauss' results for these species are plotted in Fig. 6 which clearly illustrates the benefits of the inclusion of correlation in the calculated shieldings; indeed, for the eight cases cited in Table 8B the root-mean-square-error (rmse) is reduced from 71 to 15 ppm.

One final note can be made of the data in Table 8 with reference to the two separate calculations on oxygen in water which yield noticeably different results, both for the SCF and MP2 calculations. These have been carried out with different basis sets and different geometries, experimental geometries for Fukui *et al.*⁶⁹ and optimized for Gauss.⁷⁰ Different geometries can make for noticeable differences,¹⁸ and ideally one should carry out correlation treatments with a basis which saturates the SCF calculation.

5.2. SOLO

Bouman and Hansen⁷³ have taken the second order polarization propagator method (SOPPA) of Oddershede and co-workers^{71,72} and combined it with their LORG method^{26,27} to define what they call second-order LORG, or

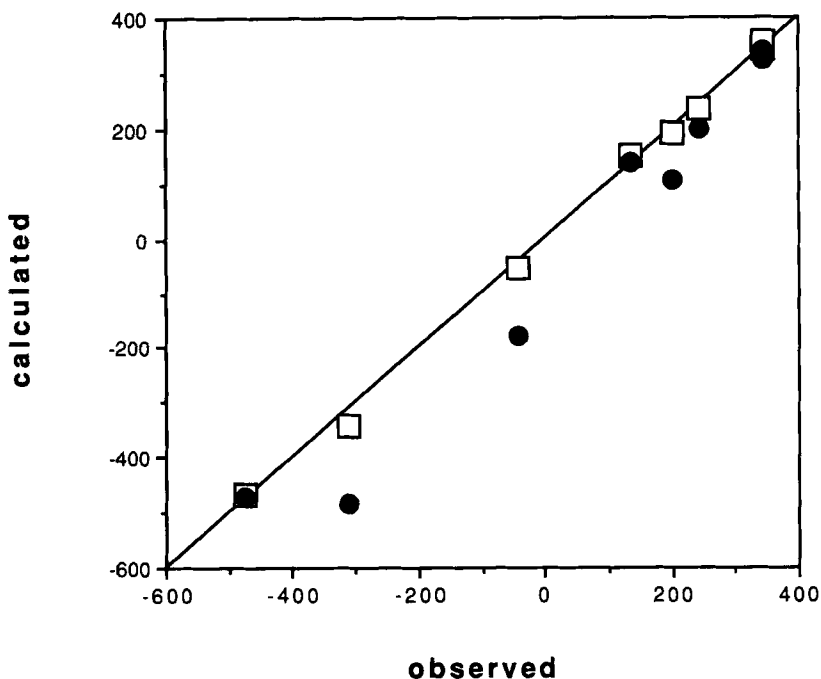


Fig. 6. Calculated and observed isotropic shieldings (ppm) for oxygen in MP2 (open squares) and SCF (closed circles) approaches.

SOLO. As with LORG, they continue to use a compromise gauge origin choice in which orbitals directly associated with the magnetic nucleus have their gauge origins at the nuclear site, while distant orbitals have their gauge origins at their orbital centroids. Hansen and Bouman's treatment in the random phase approximation is much like second-order Møller-Plesset theory.⁶⁸ We illustrate their calculations for two cases, one involving molecules containing phosphorus⁷³ and the other involving shielding calculations on nitrogen in pyridine and the *n*-azines.⁸⁰

The phosphorus calculations are shown in Table 9A both for the SOLO and LORG methods as well as some data from non-correlated GIAO theory. The differences between Hansen and Bouman's SCF and second-order approach (SOLO-LORG in the table) are also given. The changes in going from LORG to SOLO are certainly noticeable, and generally tend to improve agreement between calculated and observed shieldings relative to the errors manifested in the LORG approach. For the data shown in Table 9 the LORG rmse is a little over 100 ppm while that for SOLO is a bit over 60 ppm. The GIAO data,^{19,65} which are for a non-correlated simple Hartree-Fock approach, are comparable in quality for the molecules

Table 9. Phosphorus and nitrogen chemical shieldings in the LORG (Hartree-Fock) and SOLO (post-Hartree-Fock) approaches of Bouman and Hansen.^{73,80} Some coupled Hartree-Fock GIAO¹⁹ and IGLO⁸¹ results are also given for comparison. The shieldings are absolute and in ppm, and the experimental results are those cited by Bouman and Hansen.

A. Phosphorus					
	GIAO	LORG	SOLO	Observed	SOLO-LORG
P ₄	945.7	883	856	880	-27
PH ₃	577.6	598	594	594	-4
(CH) ₂ PH	623.9 ^a	665	637	558	-28
PO ₄ ⁻³	332.9	427	398	328	-29
PF ₃	245.0	284 ^b	210 ^b	223	-74
PN	-15.8	-14	67	53	81
P ₂ H ₂	-294.2	-381	-291	-166	90
B. Nitrogen					
	IGLO	LORG	SOLO	Observed	SOLO-LORG
s-triazine	-41	-33	-28	-39	5
pyrimidine	-71	-58	-45	-51	13
pyridine	-104	-94	-72	-73	22
pyrazine	-121	-136	-102	-90	34
s-tetrazine	-221	-213	-159	-141	54
pyridazine	-240	-235	-197	-156	38
1,2,4-triazine					
N-3	—	-76	-42	-54	34
N-2	—	-171	-151	-134	20
N-1	—	-255	-207	-178	48

^aRef. 65.

^bA somewhat larger basis was required for PF₃.

indicated in Table 9 but do poorly for the PN molecule, a good example of a system containing lone pairs and multiple bonds where correlation is thought to be quite important; the SOLO result in this case is very good.

Table 9B also shows SOLO results for nitrogen in pyridine and the *n*-azines,⁸⁰ cases where the occurrence of multiple bonds and lone pairs indicates correlation effects should be quite important. Again, the non-correlated LORG results as well as some IGLO (again, non-correlated) data⁸¹ are also given. A plot of observed and calculated shieldings for the LORG and SOLO methods for these molecules is shown in Fig. 7 and it is clear from that figure and from the table that inclusion of correlation in second-order significantly improves the results. As noted before, lack of correlation generally tends to force the paramagnetic term in the shielding theory to be too negative so that one would expect a positive change when correlation is included. Such is indeed the case here as can be seen from the

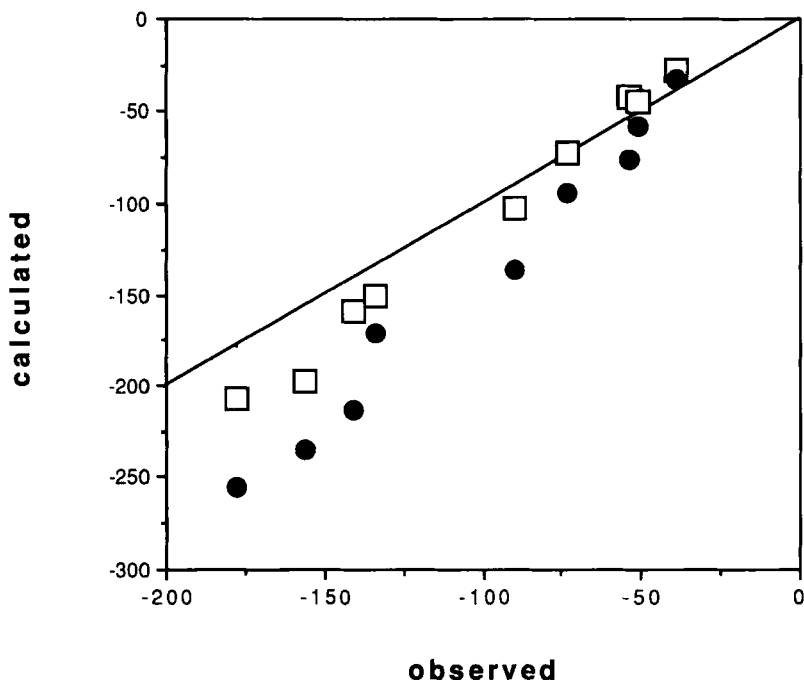


Fig. 7. Comparison of calculate versus observed isotropic shieldings (ppm) for nitrogen in pyridine and the *n*-azines in the SOLO (open squares) and LORG (closed circles) approaches.

SOLO-LORG column for the nitrogen cases where all the differences are positive. Bouman and Hansen⁸⁰ also point out that as correlation tends to make more positive (less negative) the paramagnetic terms, this tends to decrease the shielding anisotropy and range.

The agreement between theory and experiment in the nitrogen case is significantly improved. While the IGLO and LORG approaches have rmse values of 51.3 and 49.2 ppm, respectively, that for SOLO is only 19.9. As in the case of oxygen calculations in the MP2 approach⁷⁰ mentioned previously, this is a convincing demonstration of the need for and the ability to include correlation effects in molecular shielding calculations.

5.3. Multi-configuration IGLO

Once a basis set is chosen for a problem the “space” for the system has been defined. In Hartree–Fock theory there will be a number of molecular orbitals occupied (just enough to hold the electrons), the remaining orbitals

(the virtual orbitals) being empty. The Hartree-Fock wave function is that single configuration that provides the lowest energy for the system in question. If one were to study all configurations in the space defined by the basis, then by definition correlation is included, and the extent to which the calculation is accurate depends upon the completeness of the overall configurational space. Accordingly, another, *non-perturbative* approach to including the effects of correlation is to include more than one configuration in the calculation. Because the number of configurations grows rapidly with the size of the basis set, full configuration interaction (CI) calculations are hardly viable. Often only doubly excited configurations are included (CID) or sometimes both doubly and singly excited configurations (CISD).¹⁴ An alternate approach is the so-called complete active space self consistent field (CASSCF) method.⁸² In the complete active space approach the system's orbitals are divided into internal (inactive and active), and external classes. Orbitals in the inactive class are kept doubly occupied in all the configurational state functions considered, and generally are those orbitals that are likely not to be important in allowing for correlation, such as the core orbitals. Likewise, the external orbital class are those that are never occupied, such as the very high lying virtual orbitals. The most important class is that of the active orbitals which is defined as a finite set of configuration state functions which define a finite set of configurations with the proper space and spin symmetry of the molecular ground state. The approach is a multiconfigurational SCF type of calculation in which one not only optimizes the molecular orbitals involved but also the coefficients relating the admixture of the various configurations. One particular choice for a CASSCF approach is the full valence CASSCF where the active orbitals are those molecular orbitals that arise from the valence orbitals of the atoms that form the molecule.

Kutzelnigg, van Wüllen, Fleischer, Franke, and Mourik^{74,75} have taken this approach to define a multiconfigurational generalization of the Hartree-Fock IGLO method which is called MC-IGLO. Table 10 contains two examples of their calculations, one on some representative molecules (Part A) and one showing a rather detailed study of the parallel and perpendicular shielding in BH as a function of the active space orbitals (Part B). The molecules in Part A are representative of those that might be expected to show small correlation effects (methane and phosphine) as well as those where correlation has in the past been thought to be very important (fluorine, carbon monoxide, and ozone). As we saw earlier in the work of Fukui *et al.*,⁶⁹ there are only very small correlation effects for hydrogen and also for methane and phosphine, molecules that Kutzelnigg *et al.* refer to as "normal" and that are generally well treated by simple SCF theory. The effects on chemical shielding of the other three molecules are quite significant, ranging from a relatively small change of 37 ppm in CO to the amazingly large contribution in ozone of over 2000 ppm! Fluorine is a

Table 10. MC-IGLO shielding calculations of Kutzelnigg, van Wüllen, Fleischer, Franke and Mourik.⁷⁴ The shieldings are absolute (ppm) and the experimental data, except where noted, are as cited in the original paper.

A. Some representative molecules		SCF-IGLO	MC-IGLO	Observed	MC-SCF
CH ₄	(C)	193.8	198.4	198.7	4.6
	(H)	31.22	31.13	30.61	-0.09
PH ₃	(P)	583.4	598.2	594.4	14.8
	(H)	29.43	29.65	29.28	0.22
F ₂		-165.3	-204.3	-192.8	-39.0
CO	(C)	-23.4	13.4	3.0	36.8
	(O)	-83.9	-36.7	-42.3 ^a	47.2
O ₃	(O _c)	-2730.1	-657.7	-724.0	2072.4
	(O _t)	-2816.7	-1151.8	-1290.0	1664.9

B. Parallel and perpendicular shielding in BH as a function of the active space orbitals in a CASSCF approach. The core σ orbital was kept double occupied and represents the "inactive" class of orbitals. The integers in the active space designations represent the number of the various orbital types employed, and n is the total number of "active" orbitals.

Active space			n	$\sigma_{\text{perpendicular}}$	σ_{parallel}
σ	π	δ			
2			2 ^b	-493.71	198.81
3	1		5 ^c	-308.62	199.70
3	1	1	7	-343.55	197.69
5	2	2	13	-325.12	199.67
5	3		11	-368.39	199.68
5	3	2	15	-390.55	199.70
6	3		12	-334.96	199.66
6	3	1	14	-335.14	199.68
9	5		19	-341.04	199.69
9	5	3	25	-361.42	199.72
11	6	3	29	-362.10	199.71

^aGas phase data of Wasylishen, Moibroek and Macdonald.⁷⁷

^bSingle configuration.

^c"Full valence" CASSCF.

somewhat unusual case in that the effect on shielding of correlation in this example is to *decrease* the shielding rather than increase it, as has been the experience for most other molecules. The active spaces for the calculations on these molecules were not indicated, but we presume them to be full valence.

In Part B the shielding in the simple molecule BH is shown both for the

perpendicular and parallel components of the shielding tensor as a function of the orbitals contained in the active space. The active spaces range all the way from the simple Hartree–Fock calculation (2σ , the first entry), to the so-called “full valence” CASSCF ($3\sigma, \pi$, the second entry), all the way up to an active space consisting of 29 molecular orbitals. The parallel component of the shielding tensor shows virtually no change as the active space increases and is evidently associated with the fact that there is no paramagnetic contribution along the molecular axis of symmetry for linear molecules. The perpendicular component changes by almost 200 ppm as the active space increases. The authors consider that the $11\sigma, 6\pi, 3\delta$ active space appears to be close to convergence. It is interesting that the Hartree–Fock calculation and the full valence CASSCF bracket all the calculated values for the perpendicular shielding here. Beyond the full valence active space, the perpendicular shielding varies in a somewhat erratic way. This is somewhat of a disappointing result since, as Kutzelnigg and coworkers point out, one can usually not go beyond full valence CASSCF, and, in those cases where one can, there is no clear recipe how one should extend the active space. The overcompensation of the full valence active space approach may be general in the MC-IGLO approach.

5.4. Density functional theory

Density functional theory is seeing increasing application in computational chemistry.⁸³ In this approach to quantum mechanics one deals directly with the electron density, an intuitive and appealing approach. It is based upon the Hohenberg–Kohn theorem⁸⁴ which states that the external potential of a system is determined by the electron density; since the density determines the number of electrons, it also determines the ground state wave function and all other electronic properties of the system, including chemical shielding. An energy variational principle applies to the energy functional but the difficult and some say challenging aspect of the theory is that the explicit form of the energy functional is not known. None the less, great strides have been made in general and the theory has been shown to apply especially well to large systems where Hartree–Fock theory experiences the N^4 problem, while density functional theory increases only as $c \cdot N^{2.7}$. One of the great advantages of density functional theory, of course, is that it explicitly includes correlation.

Malkin, Malkina, and Salahub⁷⁶ have devised a new approach for NMR shielding calculations in the framework of coupled density functional theory (CDFT) with individual gauges for localized orbitals (the IGLO approach to the gauge problem).^{24,25} In their approach the unperturbed system is described by Kohn–Sham theory⁸⁵ using local or non-local gradient-corrected functionals. The perturbed system is described by coupled

Table 11. Calculated and observed shieldings for a coupled density functional theory (CDFT) approach⁷⁶ on a series of correlation-sensitive molecules. The Becke exchange⁸⁶ and Perdew correlation⁸⁷ potentials were used in the DFT calculation. A comparison with GIAO (SCF) values is given. The observed shieldings are those reported in the original paper except where noted.

Molecule	Atom	GIAO ^a	CDFT	Observed
PN	P	-15.8	42.1	53
	N	-409.4	-347.3	-349
P ₂ H ₂	P	-294.2	-190.9	-166
	C	-8.0	-0.3	1
CO	O	-61.3	-63.4	-42.3
	N _t	89.0	97.0	99.5
NNO	N _c	-2.0	5.9	11.3
	O	219.4	185.4	200.5
	O	191.5	157.2	133.9 ^b
H ₂ O ₂	N	-80.0	-69.3	-61.6
N ₂	C	14.2	-12.3	-1
	O	-406.2	-362.6	-312.1 ^c
H ₂ CO	F	-181.4	-197.8	-192.8

^aCalculated data of Chesnut and Rusiloski (P)¹⁹ and Chesnut and Phung (C,N,O,F).¹⁸

^bLiquid phase data cited by Kitzinger⁷⁸ converted to an absolute shielding using the absolute shielding for liquid water as 307.9.⁷⁷

^cGas phase data of Wasylishen, Moibroek and Macdonald.⁷⁷

equations similar to those found in coupled Hartree-Fock theory. An exchange-correlation potential response linear with respect to the external magnetic field is included using the homogeneous electron gas approximation. Several bases sets and exchange and correlation potentials were investigated, and in general their results are in good agreement with those of the best coupled Hartree-Fock approaches that take into account electron correlation effects.

Table 11 and Fig. 8 show data for a number of correlation-sensitive molecules that Malkin, Malkina and Salahub treated using the Becke exchange⁸⁶ and Perdew correlation⁸⁷ potentials; for comparison, the SCF (no correlation) data from some GIAO calculations of our own are included in the table and figure. The rmse for the uncorrelated GIAO data is 54.7 ppm while that of the CDFT approach is only 19.1. Considering that nuclei with quite large shielding ranges are included in this tabulation, the improved agreement with experiment that CDFT gives is very good. This good agreement with experiment is shown graphically in Fig. 8 where the data for the CDFT approach cluster closely to the 45°-line while the GIAO data points do not.

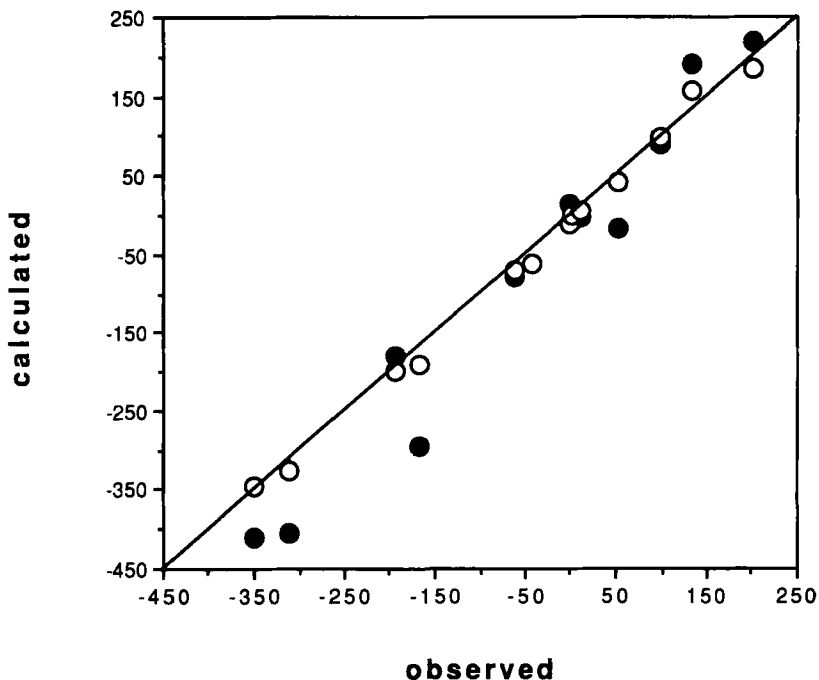


Fig. 8. Comparison of calculated versus observed isotropic shieldings (ppm) for a variety of elements in the coupled density functional theory (CDFT, open circles) and GIAO (closed circles) approaches.

5.5. Summary of correlation treatments

All the current approaches for including correlation in the determination of chemical shielding are generally comparable and yield improved results relative to Hartree–Fock theory. Each has limitations and involves approximations, yet each provides a degree of agreement with experiment for correlation-sensitive molecules that simple Hartree–Fock theory cannot. They provide significant advances in our ability to calculate and understand the important physical property of chemical shielding, and extension of these methods to higher order appears promising. As shown by a number of examples, there are many systems where correlation is apparently not important in chemical shielding and where a self-consistent-field approach is viable; with suitable precaution, Hartree–Fock theory can still be employed in these cases. In general, however, the inclusion of correlation is obviously better than its exclusion with regard to all electronic properties, and one can anticipate that in the near future most shielding calculations will be done with programs that include it.

6. CONCLUDING REMARKS

The purpose of this review has been to give by example an overview of the current state of *ab initio* calculations of NMR chemical shielding. By concentrating on a relatively few cases which are representative of the field, a number of important topics and areas have been neglected, and the reader should be aware of these omissions.

Chemical shielding is a tensor quantity and is generally described in terms of the three principal values of the symmetrized shift tensor and the orientation of its principal axes. There has been no discussion of anisotropy or range (the difference between the largest and smallest principal values); these are important quantities because they provide more information than simply the isotropic shielding. The ability to calculate these quantities from first principles is a much more severe test of theory and this ability should be tested against experiment whenever possible.

The important area of the dependence of chemical shielding on nuclear configuration has barely been touched on and is an important and exciting area of current study. Jameson and de Dios have discussed this problem in several recent articles^{88,89} and in a review article in a recent volume of this series.⁹⁰

In her summary remarks at the 1992 NATO conference on Nuclear Magnetic Shieldings and Molecular Structure, the first conference of its kind, Cynthia Jameson pointed out that there are many unanswered questions in shielding involving elements in the higher rows of the Periodic Table.⁹¹ Phosphorus has been mentioned in this review article and some representative calculations on silicon by Van Wazer, Ewig, and Ditchfield⁹² and on sulphur by Schindler⁹³ are available. Häser, Schneider, and Ahlrichs⁹⁴ have studied a variety of phosphorus clusters up to and including P_{28} and have characterized the more interesting of these by their equilibrium structures and NMR chemical shieldings. The problems extant for elements of atomic number higher than those in the second long row include the fact that there are no absolute shieldings scales as yet and no gas phase data; geometries in solution are generally unknown, and the basis sets for these higher atomic number species are largely untested. For example, Ellis *et al.*^{95,96} have examined some selenium and cadmium chemical shifts from both experimental and theoretical perspectives and discuss the reasons why the chemical shifts cannot be calculated quantitatively at this point. For species of higher atomic number relativistic effects begin to become important,¹³ and we don't yet know how to deal with these in terms of chemical shielding; there is at this time no exact relativistic many-electron Hamiltonian, those we currently work with being defined only to order c^{-2} .

And, of course, there are many other interesting instances of shielding calculations involving species in the first and second long row of the Periodic Table. Tossell has studied applications of NMR shielding in mineralogy and

geochemistry,⁹⁷ and has studied the ²⁹Si shielding tensor in forsterite⁹⁸ showing that the shielding tensors in this silicon-containing material can be explained by simple cluster calculations incorporating only nearest neighbours and simple models for second nearest neighbours. Soderquist *et al.* have put to good use the potent combination of experiment and theory in rationalizing the ¹³C chemical shift tensors in aromatic compounds such as phenanthrene, and triphenylene⁹⁹ and various substituted naphthalenes.¹⁰⁰ De Dios, Pearson, and Oldfield¹⁰¹ show how recent theoretical developments permit the prediction of hydrogen, carbon, nitrogen and fluorine chemical shifts in proteins and suggest new ways of analysing secondary and tertiary structure and probing protein electrostatics. Jackowski¹⁰² has looked at the effects of molecular association in acetonitrile using a simple dimer and trimer model. And finally, Barfield and coworkers continue to probe the ever interesting study of α -, β -, and γ - substituent effects^{103,104} and the important ϕ and ψ angle dependence in a simple model peptide.¹⁰⁵ Generally speaking, a more extended view of the field from both experimental and theoretical perspectives can be seen in the published NATO volume¹⁰⁶ on its Nuclear Magnetic Shieldings and Molecular Structure meeting held at the University of Maryland in the summer of 1992.

Presently, chemical shielding can be calculated to approximately three to four per cent of an element's shielding range on an absolute basis for nuclei of the first and second long rows of the Periodic Table, and somewhat better than this on a relative basis. This is still an order of magnitude away from experimental effects occurring at the 0.1 ppm level, but is good enough to provide in many cases quantitative results and to serve as a predictor as well as a confirming tool in the analysis of molecular electronic structure. The quantitative reliability of calculations in this area and the theoretical ability to study situations experimentally inaccessible are allowing us to gain considerable understanding of electronic structure as probed by NMR.

At the conclusion of the theoretical conference at the University of Colorado in 1960, R. S. Mulliken commented that it seemed safe to say that the chemical bond was not so simple as some people seemed to think.¹⁰⁷ While perhaps a decade ago a similar remark could have been made about chemical shielding, it seems equally safe today to say that our theoretical understanding of the NMR shielding phenomena is on a rather steady and substantial footing.

REFERENCES

1. C. J. Jameson, in *Nuclear Magnetic Resonance*, ed. G. A. Webb (Specialist Periodical Reports), Vols 8–24, 1980–1995, The Royal Society of Chemistry, London.
2. A. K. Jameson and C. J. Jameson, *Chem. Phys. Lett.*, 1987, **134**, 461.
3. C. J. Jameson, A. K. Jameson, D. Oppusunggu, S. Wille, P. M. Burrell and J. Mason, *J. Chem. Phys.*, 1981, **74**, 81.

4. R. E. Wasylshen, S. Moibroek and J. B. Macdonald, *J. Chem. Phys.*, 1984, **81**, 1057.
5. C. J. Jameson, A. K. Jameson and P. Burrell, *J. Chem. Phys.*, 1980, **73**, 6013; C. J. Jameson, A. K. Jameson and J. Honarbakhsh, *J. Chem. Phys.*, 1984, **81**, 5266.
6. C. J. Jameson, A. C. de Dios and A. K. Jameson, *Chem. Phys. Lett.*, 1990, **167**, 575.
7. C. J. Jameson and H. J. Osten, in *Annual Reports on NMR Spectroscopy*, ed. G. A. Webb, Vol. 17, Academic Press, London, 1986, p. 1.
8. C. J. Jameson and H. J. Osten, *J. Chem. Phys.*, 1985, **83**, 5425.
9. C. J. Jameson and H. J. Osten, *Mol. Phys.*, 1985, **55**, 383.
10. R. Ditchfield, *Chem. Phys.*, 1981, **63**, 185.
11. P. W. Fowler and W. T. Raynes, *Mol. Phys.*, 1981, **43**, 65.
12. C. J. Jameson and A. C. de Dios, *J. Chem. Phys.*, 1991, **95**, 9042.
13. See C. J. Jameson and J. Mason, *Multinuclear NMR*, Chap. 3, Plenum, New York, 1987.
14. W. J. Hehre, L. Radom, P. v. R. Schleyer and J. A. Pople, *Ab Initio Molecular Orbital Theory*, John Wiley, New York, 1986.
15. D. B. Chesnut and D. W. Wright, *J. Comp. Chem.*, 1991, **12**, 546.
16. D. B. Chesnut, *Chem. Phys.*, 1986, **110**, 415.
17. W. N. Lipscomb, in *Advances in Magnetic Resonance*, ed. J. S. Waugh, Vol. 2, Academic Press, New York, 1966, p. 137. See also R. Moccia, *Chem. Phys. Lett.*, 1970, **5**, 260, for a clear and concise treatment, including the use of variable bases.
18. D. B. Chesnut and C. G. Phung, *J. Chem. Phys.*, 1989, **91**, 6238.
19. D. B. Chesnut and B. E. Rusiloski, *Chem. Phys.*, 1991, **157**, 105.
20. S. T. Epstein, *J. Chem. Phys.*, 1965, **42**, 2897.
21. R. Ditchfield, *Mol. Phys.*, 1974, **27**, 789.
22. F. London, *J. Phys. Radium*, 1937, **8**, 397.
23. K. Wolinski, J. F. Hinton and P. Pulay, *J. Am. Chem. Soc.*, 1990, **112**, 8251.
24. W. Kutzelnigg, *Israel J. Chem.*, 1980, **19**, 193.
25. M. Schindler and W. Kutzelnigg, *J. Chem. Phys.*, 1982, **76**, 1919.
26. A. E. Hansen and T. D. Bouman, *J. Chem. Phys.*, 1985, **82**, 5035.
27. T. D. Bouman and A. E. Hansen, *Chem. Phys. Lett.*, 1988, **149**, 510.
28. J. C. Facelli, D. M. Grant, T. D. Bouman and A. E. Hansen, *J. Comp. Chem.*, 1990, **11**, 32.
29. P. W. Fowler, P. Lazzeretti and R. Zanasi, *Chem. Phys. Lett.*, 1990, **165**, 79.
30. P. W. Fowler, P. Lazzeretti, M. Malagoli and R. Zanasi, *Chem. Phys. Lett.*, 1991, **179**, 174.
31. R. Taylor, J. G. Hare, A. K. Abdul-Sala and W. H. Kroto, *J. Chem. Soc. Chem. Commun.*, 1990, 1423.
32. P. Lazzeretti and R. Zanasi, *Phys. Rev. A*, 1985, **32**, 2607.
33. P. Lazzeretti, M. Malagoli and R. Zanasi, *J. Mol. Structure (Theochem)*, 1991, **234**, 127.
34. P. W. Fowler, P. Lazzeretti, M. Malagoli and R. Zanasi, *J. Phys. Chem.*, 1991, **95**, 6404.
35. C. S. Yannoni, R. D. Johnson, G. Meijer, D. S. Bethune and J. R. Salem, *J. Phys. Chem.*, 1991, **95**, 9.
36. L. Onsager, *J. Am. Chem. Soc.*, 1936, **58**, 1486.
37. M. W. Wong, M. J. Frisch and K. B. Wiberg, *J. Am. Chem. Soc.*, 1991, **113**, 4776.
38. M. Bühl, T. Steinke, P. von R. Schleyer and R. Boese, *Angew. Chem. Int. Ed. Engl.*, 1991, **30**, 1160.
39. L. R. Thorne, R. D. Suenron and F. J. Lovas, *J. Chem. Phys.*, 1983, **78**, 167.
40. D. F. Gaines and R. Schaefer, *J. Am. Chem. Soc.*, 1964, **86**, 1505.
41. D. B. Chesnut and C. G. Phung, in *Nuclear Magnetic Shieldings and Molecular Structure*, ed. J. A. Tossell, NATO ASI Series, Kluwer, Norwell, MA, 1993, p. 221.

42. D. B. Chesnut and B. E. Rusiloski, *J. Phys. Chem.*, 1993, **97**, 2839.
43. D. B. Chesnut and K. D. Moore, *J. Comp. Chem.*, 1989, **10**, 648.
44. D. B. Chesnut and C. G. Phung, *Chem. Phys. Lett.*, 1991, **183**, 505.
45. J. F. Hinton, P. Guthrie, P. Pulay and K. Wolinski, *J. Amer. Chem. Soc.*, 1992, **114**, 1604.
46. D. B. Chesnut, B. E. Rusiloski, K. D. Moore and D. A. Egolf, *J. Comp. Chem.*, 1993, **14**, 1364.
47. A. E. Hansen and T. D. Bouman, *J. Math. Chem.* 1992, **10**, 221.
48. T. A. Keith and R. F. W. Bader, *Chem. Phys. Lett.*, 1992, **194**, 1.
49. R. F. W. Bader, *Atoms in Molecules—A Quantum Theory*, Oxford University Press, Oxford, 1990.
50. See ref. 18. Some of the GIAO data in Table 5 are previously unreported.
51. C. J. Jameson, *Nucl. Magn. Reson. Spectry Per. Rept*, 1990, 48.
52. J. F. Hinton, P. Guthrie, P. Pulay and K. Wolinski, *J. Am. Chem. Soc.*, 1992, **114**, 1604.
53. L. M. Ryan, R. C. Wilson and B. C. Gerstein, *Chem. Phys. Lett.*, 1977, **52**, 341.
54. A. Pines, D. J. Ruben, S. Vegga and M. Mehreng, *Phys. Rev. Lett.*, 1976, **36**, 110.
55. W. K. Rhim and D. P. Burum, *J. Chem. Phys.*, 1979, **71**, 3139.
56. D. P. Burum and W. K. Rhim, *J. Chem. Phys.*, 1979, **70**, 3553.
57. J. F. Hinton and D. L. Bennett, *Chem. Phys. Lett.*, 1985, **116**, 292.
58. W. W. Peterson and H. A. Levy, *Acta Crystallogr.*, 1957, **10**, 70.
59. D. B. Chesnut, L. D. Quin and K. D. Moore, *J. Am. Chem. Soc.*, 1993, **115**, 11984.
60. J. C. Tebby, *Handbook of Phosphorus-31 Nuclear Magnetic Resonance*, CRC Press, Boca Raton, FL, 1991, p. 8.
61. L. D. Quin, K. C. Caster, J. C. Kisalus and K. A. Mesch, *J. Am. Chem. Soc.*, 1984, **106**, 7021.
62. The various reactions leading to 7-phosphanorbornenes have been discussed by L. D. Quin, *Rev. Heteroatom Chem.*, 1990, **3**, 39.
63. R. Krishnan, J. S. Binkley, R. Seeger and J. A. Pople, *J. Chem. Phys.*, 1980, **72**, 650.
64. A. D. McLean and G. S. Chandler, *J. Chem. Phys.*, 1980, **72**, 5639.
65. D. B. Chesnut and B. E. Rusiloski, in *Phosphorus-31 NMR Spectral Properties in Compound Characterization and Structural Analysis*, eds L. D. Quin and J. G. Verkade, VCH Publishers, Deerfield Beach, FL, 1994, in press.
66. The crystal structure of the phenyl derivative of **2** has been determined (A. T. McPhail, private communication), and exhibits average (of two) flap-1 and -2 angles of $125.8 \pm 0.4^\circ$ and $118.0 \pm 0.6^\circ$, respectively, to be compared to the values of 124.5° and 120.0° calculated for species **5**.
67. M. Karplus and P. T. Das, *J. Chem. Phys.*, 1961, **34**, 1683.
68. C. Möller and M. S. Plesset, *Phys. Rev.*, 1934, **46**, 618.
69. H. Fukui, K. Miura and H. Matsuda, *J. Chem. Phys.*, 1992, **96**, 2039.
70. J. Gauss, *Chem. Phys. Lett.*, 1992, **191**, 614.
71. J. Oddershede, P. Jørgensen and D. L. Yeager, *Computer Phys. Rept*, 1984, **2**, 33.
72. J. Geertsen and J. Oddershede, *Chem. Phys.*, 1984, **90**, 301.
73. T. D. Bouman and A. E. Hansen, *Chem. Phys. Lett.*, 1990, **175**, 292.
74. W. Kutzelnigg, C. v. Wüllen, U. Fleischer, R. Franke and T. v. Mourik, in *Nuclear Magnetic Shieldings and Molecular Structure*, ed. J. A. Tossell, NATO ASI Series, Kluwer, Norwell, MA, 1993, p. 141.
75. C. v. Wüllen and W. Kutzelnigg, *Chem. Phys. Lett.*, 1993, **205**, 563.
76. V. G. Malkin, O. L. Malkina and D. R. Salahub, *Chem. Phys. Lett.*, 1993, **204**, 87.
77. R. E. Wasylishen, S. Moibroek and J. B. Macdonald, *J. Chem. Phys.*, 1984, **81**, 1057.
78. J. P. Kitzinger, *NMR Basic Principles and Progress*, 1982, **17**, 1.
79. C. J. Jameson and A. C. de Dios, *J. Chem. Phys.*, 1991, **95**, 1069.

80. T. D. Bouman and A. E. Hansen, *Chem. Phys. Lett.*, 1992, **197**, 59.
81. M. Schindler, *Magn. Reson. Chem.*, 1988, **26**, 394.
82. B. O. Roos, *Adv. Chem. Phys.*, 1987, **69**, 399.
83. R. G. Parr and W. Yang, *Density Functional Theory of Atoms and Molecules*, Oxford University Press, New York, 1989.
84. P. Hohenberg and W. Kohn, *Phys. Rev.*, 1964, **136**, B864.
85. W. Kohn and L. J. Sham, *Phys. Rev.*, 1965, **140**, A1133.
86. A. D. Becke, *Phys. Rev.*, 1988, **A38**, 3098.
87. J. P. Perdew, *Phys. Rev.*, 1986, **B33**, 8822.
88. C. J. Jameson and A. C. de Dios, in *Nuclear Magnetic Shieldings and Molecular Structure*, ed. J. A. Tossell, NATO ASI Series, Kluwer, Norwell, MA, 1993.
89. C. J. Jameson and A. C. de Dios, *J. Chem. Phys.*, 1992, **97**, 417.
90. A. C. de Dios and C. J. Jameson, *Annual Reports on NMR Spectroscopy*, ed. G. A. Webb, Academic Press, London, 1994 pp. 1-69, this volume.
91. C. J. Jameson, in *Nuclear Magnetic Shieldings and Molecular Structure*, ed. J. A. Tossell, NATO ASI Series, Kluwer, Norwell, MA, 1993, p. 557.
92. J. R. Van Wazer, C. S. Ewig and R. Ditchfield, *J. Phys. Chem.*, 1989, **93**, 2222.
93. M. Schindler, *J. Chem. Phys.*, 1988, **88**, 7638.
94. M. Häser, U. Schneider and R. Ahlrichs, *J. Am. Chem. Soc.*, 1992, **114**, 9551.
95. P. D. Ellis, J. D. Odom, A. S. Lipton, Q. Chen and J. M. Gulick, in *Nuclear Magnetic Shieldings and Molecular Structure*, ed. J. A. Tossell, NATO ASI Series, Kluwer, Norwell, MA, 1993, p. 539.
96. P. D. Ellis, J. D. Odom, A. S. Lipton and J. M. Gulick, *J. Am. Chem. Soc.*, 1993, **115**, 755.
97. J. A. Tossell, in *Nuclear Magnetic Shieldings and Molecular Structure*, NATO ASI Series, Kluwer Academic Publishers, Norwell, MA, 1993, p. 279.
98. J. A. Tossell, *Phys. Chem. Minerals*, 1992, **19**, 338.
99. A. Soderquist, C. D. Hughes, W. J. Horton, J. C. Facelli and D. M. Grant, *J. Am. Chem. Soc.*, 1992, **114**, 2826.
100. A. M. Orendt, N. K. Sethi, J. C. Facelli, W. J. Horton, R. J. Pugmire and D. M. Grant, *J. Am. Chem. Soc.*, 1992, **114**, 2832.
101. A. C. de Dios, J. G. Pearson and E. Oldfield, *Science*, 1993, **260**, 1491.
102. K. Jackowski, *Chem. Phys. Lett.*, 1992, **194**, 167.
103. M. Barfield, in *Nuclear Magnetic Shieldings and Molecular Structure*, ed. J. A. Tossell, NATO ASI Series, Kluwer, Norwell, MA, 1993, p. 523.
104. M. Barfield and S. H. Yamamura, *J. Am. Chem. Soc.*, 1990, **112**, 4747.
105. M. Barfield, private communication, 1993.
106. J. A. Tossell (ed.), *Nuclear Magnetic Shieldings and Molecular Structure*, NATO ASI Series, Kluwer Publishers, Norwell, MA, 1993.
107. As quoted by C. A. Coulson, *Rev. Mod. Phys.*, 1960, **32**, 170.

Structural Biology of Peptides and Proteins in Synthetic Membrane Environments by Solid-state NMR Spectroscopy

T. A. CROSS

*National High Magnetic Field Laboratory, Institute of Molecular Biophysics, and
Department of Chemistry, Florida State University, Tallahassee, Florida 32306, USA*

1. The new frontiers in structural biology	124
1.1. Detailed dynamic characterizations	124
1.2. High resolution structural detail	125
1.3. Protein-solvent interactions	126
1.4. Structure determination in anisotropic environments	128
2. Molecular examples	129
2.1. Bacteriorhodopsin	129
2.2. Filamentous virus coat proteins	130
2.3. Gramicidin A	130
3. Other experimental techniques in structural biology	132
3.1. X-ray crystallography	132
3.2. Solution NMR spectroscopy	132
3.3. High resolution EM	134
4. Solid-state NMR	135
4.1. Introduction and broad range of interactions	135
4.2. Tensors	137
4.2.1. Tensor characterization and orientational anisotropy	137
4.2.2. Tensor sensitivity to chemical modification	139
4.2.3. Tensor averaging	140
4.3. Methods of orientation	142
4.4. Isotopic labelling	144
5. Applications	144
5.1. Bacteriorhodopsin dynamics	144
5.2. Bacteriorhodopsin structural constraints	145
5.3. Coat protein viral studies	146
5.4. Coat protein synthetic membrane studies	146
5.5. Coat protein conformational comparison	147
5.6. Gramicidin structural constraints	148
5.6.1. Gramicidin conformational analysis	150
5.6.2. Gramicidin structural refinement	152
5.7. Gramicidin dynamics	157
5.8. Gramicidin structure-function-dynamic correlations	158

5.9. Gramicidin–lipid interactions	160
5.9.1. Solvent history dependence	160
5.9.2. Effects on lipid phase	161
6. Conclusions	161
Acknowledgements	161
References	161

1. NEW FRONTIERS IN STRUCTURAL BIOLOGY

Structural biology today is at a crossroads. A spectacular view of quaternary and tertiary structure is being achieved via solution NMR studies and X-ray crystallography. The art of crystallization is slowly being replaced with a science and isotopic labelling both by biosynthetic means and chemical synthesis is becoming economically feasible for a wide range of proteins and peptides. Molecular biology and the cloning of a great many proteins is now accomplished resulting in large quantities of proteins that have heretofore been available in only a very limited supply. Classes of protein folds are being identified for many if not most of the cytoplasmic proteins. A new set of frontiers in structural biology where structure, dynamics and functional correlations are sought is now coming into focus.

1.1. Detailed dynamic characterizations

That dynamics are critically important to protein function has been known ever since the crystallographic structure of deoxyhaemoglobin was determined and it was clear that a pathway for O₂ to bind the haeme did not exist. The protein had to be flexible so that a path could be opened for O₂ to bind. Flexibility is characterized by a description of molecular dynamics over a wide range of frequencies, however, the most important frequencies will be those, typically in the microsecond timeframe, that approximate the timeframe of functional processes. For well-studied enzymatic systems details of the reaction kinetics have been worked out. However, an understanding of the rate processes remains vague; when a kinetic process is diffusion limited, what controls the rate of diffusion to the active site? Why does the diffusional rate differ for different substrates?

Answers to such questions will require both experimental and computational efforts. The polypeptide gramicidin A that forms monovalent cation selective channels across lipid bilayers is an ideal system as a meeting ground for computational and experimental structural biologists. This small peptide has a very well-characterized function under a variety of conditions. It is anticipated that local dynamics of the polypeptide backbone play a major role in facilitating this kinetic process. The peptide is small enough so that molecular dynamics of all atoms can be performed and trajectories run

into the nanosecond timescale, even with a substantial aqueous environment. The electrostatics that affect the channel functions are remarkably complicated and a favourite target for theoretical modelling. Experimentally, this system is also tractable from X-ray crystallography, solution and solid-state NMR. To achieve a detailed experimental description of dynamics a very high resolution structure is required.

1.2. High resolution structural detail

Attention is once again being focused on high resolution structural detail. The protein fold does not explain the whole story, in fact, it usually explains little from a functional point of view. Crystallographers and solution NMR spectroscopists know that many imperfections in a protein structural characterization can be concealed at low resolution. Such imperfections become readily apparent at high resolution. Furthermore, with the resolution necessary to achieve the protein fold the conformation for most of the side-chains is not yet well defined. Since the side-chains provide most of the contacts with incoming substrates or for the binding surface with other macromolecules, it is very important to know the conformation of the side-chains and their flexibility. Again, structural details are a prerequisite for a detailed characterization of molecular dynamics and protein-solvent interactions.

X-ray crystallography has been the traditional method for the determination of three dimensional protein conformation. In the past decade solution NMR methods, initially restricted to ^1H NMR, and now extensively utilizing ^{15}N and ^{13}C labelling has become a very successful method for achieving such conformations in solution. Over this same decade, two other techniques have been developing—solid state NMR and high resolution electron microscopy. While a highly competitive spirit between the various technologies has existed, what is emerging today is the recognition of the complementarity of these approaches rather than their overlap. To achieve high resolution structures it may very well be necessary to combine these approaches—the diffraction methods yield low resolution structural solutions initially, while solid-state NMR methods provide high resolution detail and the global conformational information is much harder to achieve. Recently, a protein structure has been refined against a combination of solution NMR constraints and the X-ray structure factors.¹ This level of co-operation to solve not only the structural questions, but also the functional questions represents the future.

Recently, renewed attention has been given to characterizing the dynamics of proteins. From an experimental point of view this requires a description of the global motions; the large amplitude local motions in the side-chains and polypeptide backbone, and librational motions occurring

about all torsion angles to a greater or lesser degree. In each case a structural framework needs to be defined for the motion; that is, the axis about which motion is occurring, its amplitude and a description of the motion, such as, diffusional or discontinuous jumps between substates. Excluded from the following discussion is the wide range of vibrational motions that are typically restricted to high frequency and small amplitude.

1.3. Protein-solvent interactions

Another frontier involves the characterization of protein-solvent interactions. The vast majority of proteins that have been structurally characterized to date have been cytoplasmic and consequently have an aqueous environment. Therefore, despite the natural diversity of protein environments in nature, the protein structural data base has essentially the same environment for all of its proteins. Partly due to the lack of diversity in the data base environments, little is known about the solvent's effect on protein structure and dynamics. However, a few generalities are known about the aqueous environment, such as the marginal structural stability of proteins in this environment.² Often modest changes in temperature, pH or organic denaturants can disrupt the native aqueous conformation. Possibly, such instability is necessary to rapidly achieve the native fold, or the protein structures are unstable so that a constant turnover of proteins in the cell is assured. Moreover, instability suggests flexibility, and flexibility is an essential requirement for enzymatic catalysis. Protein hydrogen bonding sites that are exposed to the solvent are weakened by numerous dipolar interactions that lead to relatively rapid exchange of hydrogen bonds.³⁻⁶ Such exchange rates suggest local unfolding of the protein structure. The pioneering work of Klibanov and others^{7,8} studying enzymes in organic solvents has led to the conclusion that a partial monolayer of water is needed to stimulate dynamics in the protein so that kinetics can occur. In fact, Wu and Gorenstein⁹ have shown in mixed solvents of TFE and D₂O that a restricted film of water on the protein surface enhances dynamic flexibility. The aqueous environment, therefore, appears to play an essential role as a destabilizing (i.e. hydrogen bond exchanging) agent.

Water can also have the role of protecting the protein surface against organic denaturants¹⁰ thereby requiring high concentrations of urea or guanidinium-HCl in order to induce denaturation. Water performs this role by forming a highly structured array of water molecules on the protein surface.¹¹ Furthermore, water has a stabilizing and structural role in some proteins^{11,12} and protein complexes¹³ where individual or small clusters of water molecules form specific and stable electrostatic interactions with the surrounding protein. The characterization of specific water protein interactions has recently become more feasible. The high resolution (0.83 Å)

structure of Crambin¹⁴ has characterized the complete primary hydration shell of this protein in crystalline form. Otting and coworkers¹² have developed an approach for locating the relatively stable waters of hydration on the protein surface by solution NMR methods.

Organic solvents, such as TFE, can be added to aqueous solutions to help stabilize α -helical structures in relatively small peptides.^{15,16} This effect of TFE is considered to be caused by the reduced basicity of TFE compared to water.¹⁷ This results in increased intramolecular hydrogen bonding and decreased intermolecular hydrogen bonding with the solvent.^{15,18} Effectively, TFE stabilizes polypeptide structure by decreasing the efficiency with which water solubilizes protein structure.

Recently, in a study comparing the mirror image crystal structures of HIV-protease synthesized from all D versus all L amino acids, it has been suggested that proof of the long-standing hypothesis that the amino acid sequence is the sole determinant of protein structure has been found.¹⁹ Because water is an achiral solvent it will interact in the same way with each of these proteins and therefore this study does not disqualify the solvent from playing a significant role in structure determination. Clearly, the amino acid sequence plays a central role in structure determination, but it is also well known that non-native solvent environments alter protein structure. What is not known is the role that water plays in determining the native structure and the Milton *et al.* study does not disprove a significant role for the solvent. Furthermore, when the field of structural biology moves into a structural analysis of membrane proteins it will have to consider the chirality of the phospholipid environment. Consequently, if the solvent has a significant effect on conformational determination then the structures with opposite amino acid stereochemistry should not be strict mirror images. Qualitatively, this question has been tested with gramicidin synthesized with amino acids of opposite stereochemistry resulting in a channel conformation of opposite handedness.²⁰ While the functional properties appear to be the same within the error limits of the conductance measurements, the detailed structures have not been achieved for these two conformations and it is entirely possible that differences in the structures may exist for residues at the bilayer surface in the vicinity of the chiral centre of the phospholipids.

Despite our extensive knowledge of water-soluble proteins, the role of water in stabilizing or destabilizing protein structure is unrefined. Worse yet is our knowledge of the membrane environment. Here the environment is heterogeneous extending from the aqueous interface to the hydrophobic interstices of the fatty acyl environment. That water penetrates into the bilayer is well known, but quantitatively not well characterized. It is further complicated when a protein-lipid interface exists. Evidence from fluorescence studies²¹ suggests that the presence of water in the bilayer is increased by incorporating gramicidin. Furthermore, it was suggested that the increase was associated with the protein-lipid interface. A gradient of water

concentration as a function of depth in the bilayer modifies a dielectric gradient. Such heterogeneous properties of the membrane environment for proteins significantly complicates the structural characterization of membrane proteins. Studies of membrane proteins in lipid bilayers are made very difficult by the extensive light scattering of high molecular weight aggregates and the extreme difficulty in forming cocrystals of peptide and lipid. Other than solid-state NMR, very few spectroscopic studies can be performed on such samples. Gramicidin, the filamentous coat proteins and bacteriorhodopsin have all been chosen for subjects of this review because of the extensive solid-state NMR studies that have been done on them. Furthermore, the coat proteins and gramicidin have been studied in multiple solvents and have different native conformations in different environments. The fd coat protein has been studied as part of the virion and in both lipid bilayers and detergent micelles modelling the native membrane conformation of the protein. Interesting similarities and differences have been noted for the protein in these environments. Gramicidin also has more than one native conformation, a protein-bound state and a membrane-bound state. Only this latter conformational state has been studied, but efforts in lipid bilayers, SDS micelles and a variety of organic solvents have led to the beginnings of a detailed understanding of the effects of the membrane environment on peptide conformation and dynamics.

1.4. Structure determination in anisotropic environments

Another frontier is that of determining the structure of proteins in anisotropic environments, environments in which isotropic tumbling of the protein does not occur. Membrane proteins represent a large class of such molecules, but many other proteins that aggregate, such as structural proteins, are also anisotropic. Protein complexes, such as the ribosome or fatty acyl synthetase or viral particles are additional examples. None of these systems is tractable by solution NMR methods. X-ray crystallography is dependent on the formation of crystals that diffract to high resolution. Crystallization is very difficult when two different types of molecules must be ordered simultaneously in the molecular array. Irregular shapes or a large axial ratio also make it difficult. Highly flexible domains that can result in the trapping of numerous conformational substates represent further challenges for the crystallographer. Such heterogeneity greatly impedes the formation of crystals that diffract to high resolution. A different approach is needed that is not dependent on crystallization and which does not have the solution NMR molecular weight limitations. As will be shown here and in a few other recent reviews,²²⁻²⁶ solid state NMR clearly has a role in this new frontier of structural biology. In fact, solid state NMR has a role in all four of these frontier areas in structural biology.

2. MOLECULAR EXAMPLES

Three molecular systems have been chosen for this review, because they represent the most highly developed membrane protein and polypeptide applications of solid-state NMR. Bacteriorhodopsin has been extensively studied by Robert Griffin and colleagues plus contributions from Eric Oldfield and a few others. These efforts have been primarily magic angle spinning studies and powder pattern averaging studies. The coat proteins of the filamentous viruses have been extensively studied by Stanley Opella and colleagues using both magic angle spinning and non-spinning techniques. These proteins have been studied in different environments—as part of the intact virion and in lipid bilayers. Gramicidin is the smallest of these systems and has become the most extensively characterized by solid-state NMR with major efforts by my own research group and those of Bruce Cornell, Antoinette Killian and James Davis, as well as more limited efforts by a variety of others. This system has proven to be ideal from the standpoint of isotopic labelling and orienting lipid bilayers containing the peptide.

2.1. Bacteriorhodopsin

Bacteriorhodopsin (bR) is one of the most extensively characterized membrane-bound proteins. Many biophysical and microbiological techniques have also been brought to bear on this challenging problem.^{27–29} The protein is a light-driven proton pump that naturally occurs in a highly ordered two-dimensional array in *Halobacterium halobium*. The generation of an electrochemical gradient across membranes for synthesis of ATP makes this an exceptionally interesting protein.³⁰ The three-dimensional resolution (3.5 Å parallel to the membrane surface and 10 Å perpendicular to this surface) by cryoelectron microscopy represents one of the major success stories of this relatively new approach for solving macromolecular structure from ordered two-dimensional arrays.³¹ At this level of resolution 7 α helices are defined and the bulky side-chains have been identified. The β -ionone of the retinal chromophore is identified nearer to the extracellular surface than the cytoplasmic side. This chromophore is covalently linked to the protein via a Schiff base to Lys-216. The detailed structure of the retinal, its orientation with respect to the protein and modifications as a function of the photochemical cycle have been the subject of numerous studies. The mechanism is initiated by retinal photo-absorption resulting in conversion of the 13-*cis* form to the all-*trans* configuration. The deprotonation of the Schiff base is involved in the transport of the proton across the membrane and consequently considerable interest has been focused on the retinal chromophore.

2.2. Filamentous virus coat proteins

The filamentous viral coat proteins are small (approximately 50 amino acids) proteins that form a protective sheath about a single-stranded circle of DNA. Prior to viral assembly the protein is stored in the membranes of the host bacterium. As the DNA is extruded through the membrane the protein sheath is formed encapsulating the DNA. Therefore, both the structural and transmembrane forms of this protein are of considerable interest and by studying both it is hoped that inferences about the transition between these two conformations and environments can be elucidated. Opella and coworkers^{22,32,33} have been studying the viral form by solid state NMR of uniformly oriented samples.³⁴ The membrane form has been extensively studied in SDS micelles by both Opella's³⁵⁻³⁸ and Sykes'^{39,41-43} research groups. Recently, considerable progress has been made in studying the membrane bound form in dodecylphosphocholine micelles⁴⁴ and in oriented phospholipid bilayers.^{44,45}

The viral forms of the filamentous coat proteins are primarily α -helical. The Pfl virus is the best characterized of this class of phage particles. Extensive fibre diffraction^{46,47} and neutron diffraction of magnetically aligned gels⁴⁸⁻⁵⁰ have resulted in a well-accepted model for the coat protein conformation and its packing arrangement in the virion.

2.3. Gramicidin A

Gramicidin A is a 15 amino acid residue polypeptide that as a dimer forms a monovalent cation selective channel in lipid bilayers.⁵¹⁻⁵⁴ This peptide has an alternating sequence of amino acid stereochemistry: HCO-Val₁-Gly₂-Ala₃-DLeu₄-Ala₅-DVal₆-Val₇-DVal₈-Trp₉-DLeu₁₀-Trp₁₁-DLeu₁₂-Trp₁₃-DLeu₁₄-Trp₁₅-NHCH₂CH₂OH. This peptide is an enzymatic product of *Bacillus brevis* during the transition from the vegetative to the sporulative phase. The channel activity is thought to promote the bacterium's ability to scavenge amino acids in time of deprivation which triggers sporulation. Gramicidin and various proteases are excreted from the cell at the same time. Presumably the channel conformation induces lysis of cells in the vicinity and the proteases decompose the proteins released by cell lysis so that the *Bacillus* can scavenge for carbon and nitrogen. Interestingly, gramicidin has another native function, presumably with a different structure, that of binding to the sigma subunit of the RNA polymerase causing the vegetative form of this subunit to fall off making way for the new sporulative subunit.⁵⁵ Gramicidin A is very poorly characterized in this latter role and it will not be discussed any further in this review. The channel folding motif, proposed by Urry in 1971⁵⁶ has the channel formed by a single-stranded helical dimer hydrogen bonded in an amino terminus to

amino terminus junction at the bilayer centre. This model is essentially a β -sheet structure in which the side-chains all project from one side of the sheet, thereby forcing the sheet to take on a helical conformation, in this case with 6.3 residues per turn. One of the first success stories for biological solid-state NMR on this system in fully hydrated lipid bilayers was to determine the right-handed helical sense.⁵⁷ In a lipid bilayer the side-chains interact with the lipid and the peptide linkage planes line the pore which has a diameter of approximately 4 Å. This model for the folding motif of the channel is well accepted, but structural detail was absent until recently. Cocystals of gramicidin and lipid have been extant for years,⁵⁸ but the most recent preliminary results from these crystals suggest a very different packing arrangement for the lipid and gramicidin from that of the native arrangement.^{59,60} However, it is known from diffraction studies of oriented bilayers that gramicidin is a single-stranded helix⁶¹ and the separation of monovalent and divalent cation binding sites has also been determined.⁶²

Gramicidin forms a variety of well-defined structures in organic solvents. These dimeric structures are intertwined helices that may be parallel or antiparallel, right-handed or left-handed and they may be staggered.⁶³ This mix of structures is observed in solvents such as methanol and ethanol and the conformers interconvert on approximately the 1 s timescale in this environment. In dioxane and tetrahydrofuran the conformers do not interconvert appreciably on a timescale four orders of magnitude slower, in fact, normal phase HPLC can be used to resolve and isolate the individual conformers in dioxane.⁶⁴ If a few per cent water is added to this conformer trapping solvent a mixture of conformers is regenerated.⁶⁵ Such solvents without water do not have the ability to destabilize protein structure. However, it remains to be seen what the membrane environment is like. The fatty acyl chains clearly have no hydrogen-bonding capability with the exception of their ester linkage at the hydrophilic-hydrophobic interface. However, a considerable concentration of water does penetrate the lipid bilayer environment⁶⁶ and it may be enough to prevent the lipid bilayer from being a conformational trapping environment. In partitioning studies of tryptophan analogues between water and cyclohexane, the *N*-hydrated analogue copartitions into the cyclohexane; that is, the indole is responsible for bringing waters of hydration into the hydrophobic environment.⁶⁷ Similar activity is also possible for gramicidin upon peptide insertion into the lipid bilayer. Furthermore, the addition of gramicidin to lipid bilayers has been shown to significantly increase the water content in the middle of the bilayer.²¹ However, this water content may only be enough to temper the trapping nature of this environment, since it has been shown that the membrane environment can stabilize non-functional states for extensive periods of time above the bilayer gel-liquid crystalline phase transition temperature.⁶⁸⁻⁷⁰ The consequences of this may indeed be far reaching. The trapping of such non-minimum energy conformations in a lipid bilayer

suggests a possible regulatory role for nature to control the functional activity of membrane proteins (Arumugam and Cross, unpublished results).

3. OTHER EXPERIMENTAL TECHNIQUES IN STRUCTURAL BIOLOGY

3.1. X-ray crystallography

X-ray crystallography, which has been the traditional approach for protein structure determination, has been largely ineffective for membrane-bound proteins. Bacteriorhodopsin naturally forms an ordered array and so was one of the first membrane proteins studied by X-ray crystallography. The transmembrane portion of this protein composed of α -helical segments has proved to be quite typical of membrane proteins. While the 7 Å structure was determined in 1975⁷¹ higher resolution detail has become available very slowly and not by X-ray diffraction. Cocrystals of gramicidin and lipid were first prepared and characterized in 1981.⁵⁸ These crystals have a molar ratio for gramicidin to lipid of 1:2 and they diffract to approximately 2 Å. Recently, a possible packing arrangement for this structure has been published and although considerable lipid is present in the crystal the arrangement of lipid and peptide is not consistent with the membrane conformation of the gramicidin channel.⁵⁹ This failure of cocrystals to mimic the membrane conformation is indeed a serious foreboding for this approach. However, a few successes have occurred. The bacterial reaction centre has been solved by X-ray crystallography^{72,73} and a bacterial porin has also been solved.⁷⁴ While it can be anticipated that successes by X-ray crystallography will continue, the progress is anticipated to be very slow due to the difficulty in forming quality three-dimensional crystals.⁷⁵

3.2. Solution NMR spectroscopy

Solution NMR determinations of three-dimensional protein structure require that the nuclear spin interactions that affect the observed spectra must be averaged to their isotropic value. Failing this, the spectral resonances become severely broadened and the number and quality of the structural constraints is decreased. The primary structural constraint in solution NMR methods has been the utilization of homonuclear ¹H NOEs. The nuclear Overhauser effect is mediated by dipolar relaxation between two nuclei with nonzero spin. Consequently, the effect, measured as an intensity, has a distance dependence of r^{-6} reflecting the separation of the two interacting spins. Additional structural constraints have been achieved by the observation of homonuclear J couplings. Such measurements are frequently

restricted to observation of very low molecular weight proteins for which resolution of these small couplings is possible. The observed couplings are dependent on torsion angles between the homonuclear sites by the Karplus relationship.

The strength in this approach is that distances between sites separated by many residues in the primary sequence can be severely constrained by the observation of NOEs. Consequently, the higher orders of protein structure are particularly well defined by this approach. At a very local level of protein structure the torsion angles have a considerable error bar, even in the most well-defined structures.

For membrane proteins and peptides several possibilities exist for solution NMR sample preparation. Most membrane proteins are not soluble in organic solvents because they have substantial hydrophilic domains. However, Girvin and Fillingame⁷⁶ have studied subunit c, the transmembrane component of the F_1F_0 ATP synthase, in a chloroform-methanol-water (4:4:1) solvent mixture. It was found that the subunit formed a hairpin with α -helical segments as previously expected. Despite this apparent success, the use of organic solvents must be approached with caution. Numerous efforts to model the complex of cyclosporin A and cyclophilin failed because the molecular structure of cyclosporin A had been obtained from organic solvents and it was fundamentally different from the cyclosporin structure bound in the complex as recently determined.⁷⁷ Furthermore, all of the structural studies of gramicidin obtained by solution NMR in organic solvents⁷⁸⁻⁸³ or X-ray crystallography with crystals formed out of organic solution⁸⁴⁻⁸⁶ have been very different from the lipid bilayer bound form.⁸⁷ Consequently, lipid micelles or detergent micelles have been used so as to add minimally to the aggregate molecular weight that is undergoing global isotropic motions and to form a better model of the membrane environment.

Solubilization of lipids in vesicles or in liposomes results in spectral quality that is too low for a detailed structural analysis. Neither are micellar structures ideal as models of a lipid bilayer environment. An important characteristic of a phospholipid bilayer is the relatively wide hydrophobic/hydrophilic boundary region in which many of the water molecules are hydrogen bonded with the bilayer surface. These waters contribute substantially to the membrane dipole potential which is the summation of non-random electric dipole moments of the lipid headgroup, ester linkages and the water molecules.⁸⁸ It has been shown that the radii of curvature of the bilayer surface has an influence on the orientation of the water dipole moments.^{89,90} Furthermore, the curvature of the micellar surface will distort how proteins are oriented with respect to the hydrophilic surface. The α helices of membrane proteins are arranged approximately parallel with respect to the bilayer normal. Such an orientation is likely induced, at least in part, by the parallel bilayer surfaces. Moreover, water penetration into

the micelle because of the irregular packing in spherical or obovate structures is likely to be significantly greater than into a bilayer. This could have a serious effect on conformational stability in a micellar environment.

Despite these concerns, the study of membrane proteins and peptides in detergent micelles has been one of the only ways to characterize spectroscopically these very difficult proteins. Numerous proteins and peptides have been studied in detergent micelles, for example, glucagon,⁹¹ calcitonin,⁹² phospholipase A,⁹³ gramicidin⁹⁴ and filamentous viral coat proteins.⁹⁵ Fewer studies have been performed in lysolipids.^{44,96} While the determinations in micelles demonstrated potential for the future, the molecular weights have been severely limited. The coat protein conformational studies of the filamentous viruses, fd and M13, in detergent micelles appear to bear a close resemblance to the available data on the protein conformations in lipid bilayers. Similarly, the structure of gramicidin in SDS micelles^{80,94} represented a major success, because the folding motif has turned out to be the same as the gramicidin channel conformation in a lipid bilayer. This was particularly important because previous studies in organic solvents, both by crystallography⁸⁴⁻⁸⁶ and solution NMR achieved double helical conformations^{64,79,80,82,83,97} that bore little resemblance to the single-stranded channel conformation. Furthermore, this was the first demonstration of the right-handed helical sense of the single-stranded conformation of gramicidin. Later⁵⁷ it was shown that the gramicidin channel conformation in hydrated lipid bilayers formed a right-handed helix. Prior to this it had been generally accepted that the helical sense was left-handed.^{98,99}

3.3. High resolution EM

Cryoelectron microscopy has the potential to be a very useful structural biology tool for membrane proteins. For such an analysis two-dimensional crystals are needed. Numerous electron diffraction patterns are obtained from such crystals in a range of sample orientations to the beam. Interestingly, the formation of two-dimensional crystals represents a very different task than the formation of three-dimensional crystals. In 3-D crystals hydrophilic contacts between macromolecules dominate, but in 2-D crystals the hydrophobic contacts appear to dominate.⁷⁵ Therefore, 3-D crystallization of membrane proteins requires modifying the hydrophobic surface so that it will be camouflaged, whereas for 2-D crystallization the hydrophobic domains are an advantage. Furthermore, the time required for developing 2-D crystals is very short compared with that for 3-D crystals. Already considerable progress has been made with several proteins other than bacteriorhodopsin³¹ such as the plant light-harvesting complex¹⁰⁰ and PhoE porin.¹⁰¹

4. SOLID-STATE NMR

4.1. Introduction and broad range of interactions

The uniqueness of NMR as a form of spectroscopy is founded in the inherent sensitivity of the technique to nuclear environments. Unlike UV/Vis spectroscopy which is sensitive to certain infrequent atomic clusters, NMR can be used to study all atomic sites in a biological macromolecule (Fig. 1). Like IR and Raman spectroscopy, not only can each atomic site give rise to a signal, but it can give rise to a variety of signals through many different interactions or vibrational modes. But IR suffers from many complications, the dominating problem is one of spectral resolution, while it is possible to resolve all of the ^1H NMR resonances in a 10 kD protein, it is only possible, for instance, through factor analysis of the amide I band to estimate percentages of different types of secondary structure.¹⁰²

All of the atomic sites in proteins can be observed by choosing the appropriate isotopic label. For proteins and peptides the frequently used isotopes are ^1H , ^2H , ^{13}C , ^{14}N , ^{15}N , ^{17}O , ^{19}F and ^{31}P . This variety not only allows for the observation of most specific sites, but allows for the observation of numerous interactions and characteristics, such as chemical shift and quadrupole interactions, homonuclear and heteronuclear dipolar interactions, T_1 , T_2 , $T_{1\rho}$, and NOE relaxation properties among others. This wealth of nuclear observations can be translated into a quantitative

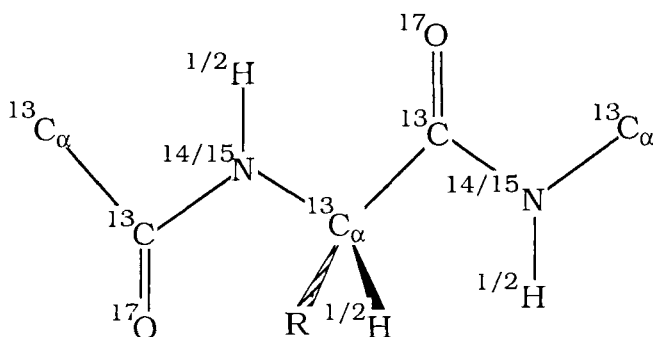


Fig. 1. Every atomic site in proteins can be studied by NMR spectroscopy and for every atomic site there are numerous nuclear spin interactions that can be studied. For instance: ^{15}N and ^{13}C chemical shifts; $^{15}\text{N}-^1\text{H}$, $^{14}\text{N}-^{13}\text{C}$, $^{13}\text{C}-^{13}\text{C}$, $^{13}\text{C}-^{17}\text{O}$ dipolar interactions; ^2H and ^{14}N quadrupolar interactions. Furthermore, there are many relaxation parameters for each site that can be studied.

description of protein and peptide structure and dynamics because of the remarkably detailed theoretical understandings of nuclear spin interactions. This understanding has gaps, but enough is known so that a detailed interpretation of the data is possible.

Solid-state NMR refers to the NMR spectroscopy of atomic sites that are not undergoing isotropic reorientation on the timescale of the particular NMR experiment. This may refer to the magnitude of the chemical shift, dipolar or quadrupolar interaction depending on the specific experiment being conducted. For most of NMR spectroscopy it refers to the Larmor frequency, the resonant frequency of the nucleus being observed. For studies of membrane proteins, their anisotropic motions in hydrated lipid bilayers is an advantage rather than a detriment as in solution NMR methods. There are major challenges to be addressed before a detailed three dimensional structural characterization can be considered. The first challenge involves the isolation and resolution of specific nuclear spin interactions. In solution NMR, sophisticated pulse sequences and the utilization of multiple dimensions has resulted in the resolution of numerous constraints from relatively high molecular weight proteins. In solid state NMR T_2 relaxation is very short and the manipulation of the spins is substantially compromised by the broad resonances. Consequently, an increased reliance on isotopic labelling is required for most of the spectroscopy that will be described here. Methods are currently under development that utilize the high natural abundance of ^{14}N and ^1H s,¹⁰³⁻¹⁰⁵ but to date most of the structural constraints have been achieved by specific site or specific amino acid labelling of the polypeptide or protein.

The second challenge involves the separation of structural and dynamic effects on the nuclear spin interactions. When a motion occurs at a particular site the effect on the observed nuclear spin interactions is the combined effect of motional amplitude and the orientation of the motional axis with respect to the spin interaction tensor, and secondly, uniaxial orientation of the samples with respect to the magnetic field of the NMR spectrometer is required for orientational constraints. It is these orientational constraints that will provide the foundation for the structure determination methods to be described.

The historical strength of solid-state NMR methods for biological samples has not been in structure determination so much as in the characterization of dynamics. NMR has played a major role in correcting the biochemical perception that proteins are rigidly approximated by the crystal structure. This misconception is not restricted to macromolecules, even molecular groups in crystals of small molecules can undergo very substantial motions, such as aromatic ring flips.^{106,107} Despite this strength of the solid-state NMR approach, the full potential for dynamics characterization has only been sampled. It is certainly within our grasp to achieve a very detailed characterization of molecular motions. Typically, in solution NMR relaxa-

tion parameters are observed to gain insight into dynamic properties. For this purpose the nuclear spin interaction that provides the relaxation mechanism is justified and an appropriate spectral density function is assumed. In solid-state NMR similar analyses of relaxation data are frequently made. However, there is another approach for obtaining a more detailed description of the motional model; that is the axis about which motions are occurring, the amplitude for the motion and whether the motion is diffusional or represents a jump between conformational sub-states. For this end, averaging of nuclear spin interaction tensors can be observed by recording powder pattern spectra as a function of temperature (Fig. 2). These spectra record the residual anisotropy after averaging by anisotropic motions. From this latter analysis it is possible to achieve an experimentally determined model of the local motion, thereby allowing for a much more reasonable analysis of relaxation parameters. Such an exacting approach has only recently been attempted.¹⁰⁹ Furthermore, the powder pattern analysis approach can be taken a step further for those motions that occur on the timescale of the interaction being observed. Under these conditions T_2 relaxation becomes orientation dependent and not only can the motional model be structurally characterized as described above, but the frequency of the motion can also be defined with considerable accuracy.¹¹⁰

The analyses of structure and dynamics are intertwined. Without a structural model it is not possible to define accurately local dynamics, without a dynamic characterization only a distorted view of the structure will emerge. In finding solutions to the challenges described above a number of specific issues need to be overcome as are discussed in the following sections.

4.2. Tensors

4.2.1. Tensor characterization and orientational anisotropy

The nuclear spin interactions are characterized by second rank tensors. The magnitudes of the tensor elements for relatively small interactions (i.e. less than the frequency bandwidth of the spectrometer's receiver or power spectrum of the exciting irradiation) can be determined directly from the observation of the spectra of disordered solids. The frequencies of the various spectral discontinuities represent the tensor element magnitudes. For dipolar interactions the magnitude of the axially symmetric tensor elements can be calculated from the identify of the interacting nuclei and a knowledge of the nuclear separation. For other interactions such as the chemical shift it is not possible to calculate the tensor element magnitudes, in fact, the magnitudes vary significantly with the molecular environment. The most striking example of this was given by Hiyama *et al.*¹¹¹ in which two different crystal forms of the same peptide were prepared and the

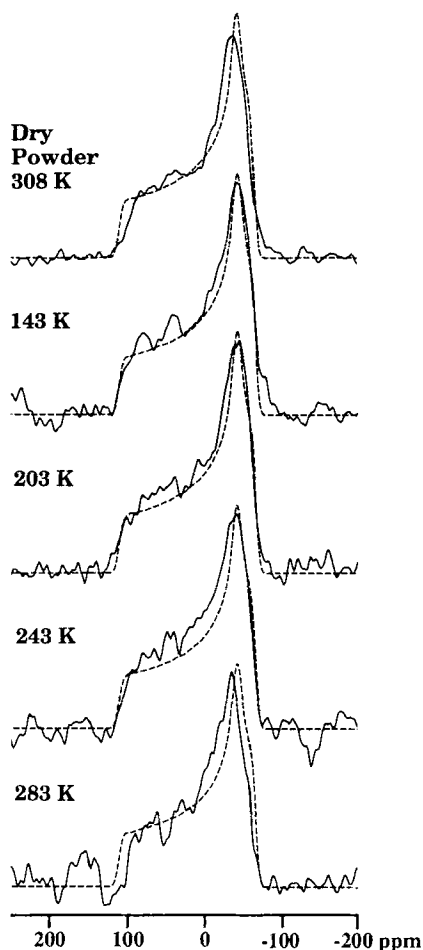


Fig. 2. ^{15}N chemical shift powder pattern spectra obtained from ^{15}N Trp₁₁ labelled gramicidin A in a lipid (dimyristoylphosphatidylcholine) environment. The top spectrum was obtained from a dry sample, the rest were obtained from hydrated (50% by weight) lipid bilayers. Spectra were obtained with cross polarization at 400 MHz for the proton frequency.¹⁰⁸ The dashed line spectra are all the same and represent the best fit to the 143 K spectrum; that is, the static chemical shift spectrum. These spectra show that there is no significant librational averaging of the tensor below 200 K and that there is substantial averaging at 283 K which is 18° below the gel to liquid crystalline phase transition temperature.

magnitudes of the tensor elements for the isotopically labelled site were very different in the two crystal forms. The characterization of such tensors by observing powder pattern spectra is complicated by dynamics in room temperature samples that are either dry or hydrated. Librational motions that occur about the torsion or dihedral angles appear to be quenched by lowering the temperature below 200 K (see Fig. 2) for all sites with the exception of methyl rotation and free amino group rotation.^{108,112,113} Even in dry samples at room temperature it is clear that librational amplitudes on the order of 10–15° are occurring (Fig. 2). Such anisotropic motions significantly alter the tensor element magnitudes. Consequently, the low temperature spectra are important for an accurate interpretation of data from oriented samples. The samples in lipid bilayers that have been rapidly frozen have a single polypeptide conformation and consequently the discontinuities of the powder patterns are very well defined and the tensor element magnitudes can be assessed accurately.^{108,114}

Far fewer experimental descriptions of tensor orientations have been achieved. For dipolar interactions the orientation of the unique tensor element with respect to the molecular frame is equivalent to the internuclear vector. This has been confirmed in two separate studies; a single crystal study¹¹⁵ and a powder determination of three nuclear spin interaction tensors involving a unique nuclear site.¹¹⁶ For axially asymmetric tensors the orientation of the tensor elements is not so clear. Several experimental methods have been developed for orienting the interaction tensor to the molecular frame. Two-dimensional magic angle spinning studies yield a relatively low resolution determination¹¹⁷ and single crystal studies are restricted to model compounds.¹¹⁵ The most successful approach has been to orient the nuclear spin interaction tensor with respect to a dipolar interaction vector that is established within the molecular frame.¹¹⁸ Numerous ¹⁵N amide chemical shift tensors^{111,119–123} (Fig. 3) and a few ¹³C carbonyl chemical shift tensors^{105,116,124–126} have been oriented. The advantage of this latter method is that the tensors can be described for the site of interest, in the molecule of interest and in the environment and conformation of interest^{114,120} (Lazo and Cross, unpublished).

4.2.2. *Tensor sensitivity to chemical modification*

For the quantitative interpretation of resonance frequencies for structural constraints it is essential that the tensors be accurately characterized. ¹⁵N chemical shift tensor element magnitudes have been shown to vary considerably from site to site among a set of amide sites in gramicidin.¹²³ The magnitudes appear to be particularly different for glycine residues which also have unusual isotropic chemical shifts. While these results describe site to site variability, the data have been obtained from dry powders of the polypeptide and considerable conformational heterogeneity

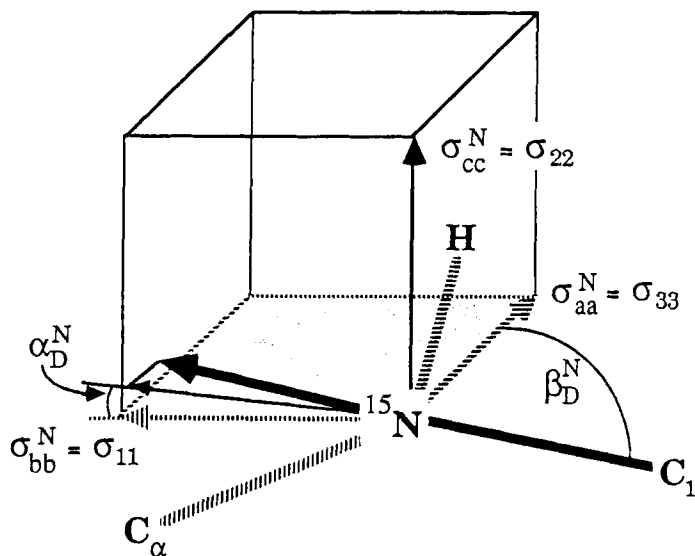


Fig. 3. Definition of the ^{15}N chemical shift tensor elements with respect to the molecular frame. It has become necessary to define a set of labels for the tensor elements that is based in the molecular frame rather than in the context of the chemical shift spectrum. σ_{11} , σ_{22} , and σ_{33} are defined by the frequency magnitudes of the elements. σ_{cc} is defined as the element that is approximately perpendicular to the peptide plane, σ_{aa} is the element to which the azimuthal angle, β_D is defined and σ_{bb} completes the orthogonal set.¹⁰⁵ For most of the amide backbone sites the two sets of definitions correspond as presented in this figure.

may compromise the results. Comparative studies of the static tensors obtained from hydrated fast-frozen bilayers at approximately 125 K is underway (Lazo and Cross, in preparation). Where there is a difference in the covalent chemistry of the site the variability in tensors has been well documented, such as a blocked amino terminus or a proline residue.^{119,123} The model compound studies of Drobny and coworkers also indicate considerable variation among a selection of peptide model compounds for which dipolar coupled data sets had been obtained.^{121,124} The uniformity of the results from gramicidin may simply reflect the uniformity of the backbone conformation along the helical axis. At this time, it is still necessary to characterize the tensors as completely as possible so that the error bar on the structural constraints can be minimized.

4.2.3. Tensor averaging

Molecular motions reduce anisotropy over the timescale of the motion. Global motions of peptides in membranes or even small proteins will average axially asymmetric static tensors to an axially symmetric tensor in

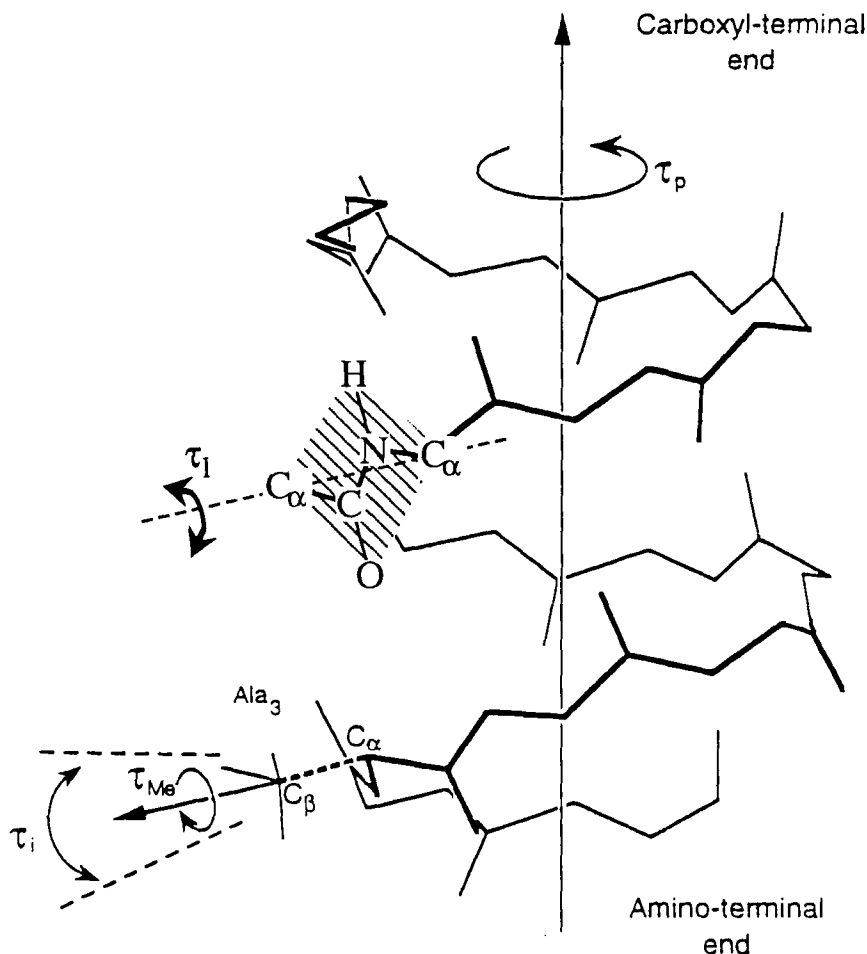


Fig. 4. Definitions of the correlation times for various motions of the gramicidin channel. On this schematic of the gramicidin monomer is illustrated the global correlation time, τ_p , that represents a motion about the channel axis and the bilayer normal. τ_{Me} represents the fast three-state jumping or rapid diffusional motion of the methyl group about its C-C_{Me} axis. Librational motions are described for the C-C_{Me} axis, τ_i and for the polypeptide backbone about the C _{α} -C _{α} axis, τ_l .

which the large tensor element or parallel component is parallel with the motional axis and the bilayer normal (Fig. 4). Relatively small amplitude librational motions will reduce the magnitude of the nuclear spin interactions. These latter motions are often modelled as a wobbling in a cone-shaped volume; that is, with no preferred direction. This results in a relatively uniform averaging of the spin interaction tensors, such that the

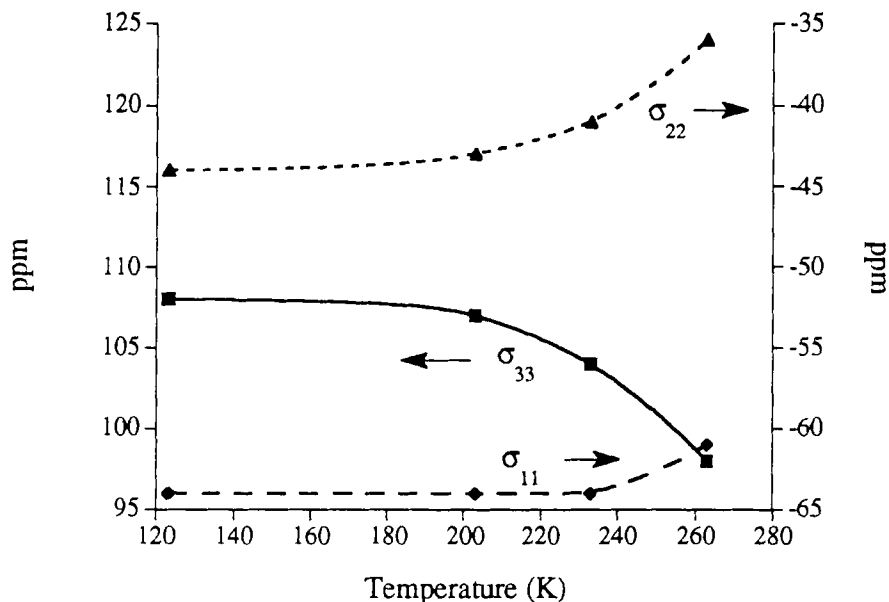


Fig. 5. Data from powder pattern spectral simulations of ^{15}N Ala₃ labelled gramicidin in hydrated bilayers as a function of temperature, similar to the data shown in Fig. 2. The librational averaging of the polypeptide is shown to be largely an effect on the σ_{22} and σ_{33} tensor elements; that is, the librational motions are anisotropic. Once again it is shown that the librational averaging below 200 K is insignificant.

static lineshape asymmetry is unaffected. However, by monitoring the lineshape as a function of temperature from the static librational extreme below 200 K averaging of preferred tensor elements can be observed (Fig. 5). This results in both a change in the spin interaction magnitude and its asymmetry. Large amplitude local motions can also occur such as the flip of benzyl rings in the phenylalanine and tyrosine side-chains.⁴⁵ This rotameric jump motion about the χ_2 torsion angle can also be observed among other side-chains and other torsional sites such as χ_1 angles. In particular low viscosity environments it is also possible to observe examples of rotational diffusion about the χ_2 torsion angle. However, such diffusional motion has not been observed for peptide sites within a bilayer environment. The delineation between such motions is easily recognized by observation of motionally averaged powder pattern lineshapes.^{127,128}

4.3. Methods of orientation

To achieve orientational constraints from solid-state NMR it is necessary to uniformly align the samples in the NMR spectrometer relative to the

magnetic field direction. Considerable effort in recent years has gone into the development of methods for orienting samples, because such samples are useful for a wide range of biophysical methods. Three-dimensional crystallization is not necessary, and moreover it yields samples that are small by NMR standards, is very difficult to achieve for membrane proteins and finally there are typically more than one molecule per unit cell. This latter point results in samples having multiple orientations for each site that is to be studied, thereby complicating the spectra. Two-dimensional crystallization such as that used for cryo-EM yields very small samples. Similarly, it is very difficult to build up large stacks of bilayers using the Langmuir/Blodgett methods.^{129,130}

Diamagnetic anisotropy in liquid crystalline preparations can lead to uniform alignment in the presence of a relatively strong magnetic or electric field. Even in the presence of the strongest NMR magnets, the interaction energy associated with a single molecule is not substantial enough to align the molecules with respect to the field.¹³¹ For lipid bilayers the orientation is with the bilayer normal perpendicular to the field.¹³²⁻¹³⁵ The uniformity of the alignment is dependent on the viscosity of the preparations and whether the field dependent interaction can overcome the viscous drag. In Seelig *et al.*¹³² this was accomplished by generating bilayers containing substantial quantities of charged lipids; in so doing the bilayers swell much more so than in DMPC preparations. Because the susceptibility is so much greater for polypeptides than for lipids, the tendency when gramicidin is present is for the complex to align with the bilayer normal parallel with respect to the magnetic field. This is typical of membrane proteins because transmembrane segments are often α -helical with the peptide planes essentially parallel with the bilayer normal. In fact, bacteriorhodopsin has been aligned with the use of moderate electric fields.¹³⁶

Prestegard, Sanders and coworkers have pioneered the use of a magnetically oriented model membrane composed of DMPC and CHAPSO as an orienting matrix to study the structure of a sialic acid containing glycolipid.¹³⁷⁻¹³⁹ In this preparation of bilayer-like discs the residual anisotropy is so limited that high resolution solution NMR spectra can be obtained. Another novel approach has recently been described as a magnetically oriented ferrofluid consisting of magnetic particles surrounded by a detergent bilayer suspended in an aqueous environment.¹⁴⁰ In this initial study elongated macromolecular structures were aligned for small angle neutron scattering experiments.

A variety of methods have been devised based on shear. For aligning lipid bilayers most of these methods are modifications on shearing samples between two glass plates. To optimize the alignment of samples with a low water content, annealing at high temperature^{141,142} or repeated application of high pressure¹⁴³ has been used. To prepare the sample on a glass plate the lipids are typically solubilized in an organic solvent, the sample is spread

on the plate and thoroughly dried before hydrating.¹⁴⁴ Such samples can be extremely well aligned as demonstrated by analysis of the solid state NMR linewidth.^{145,146} Magnetic field enhancement of the orientation has probably occurred during the NMR characterization of such samples as shown by neutron diffraction of magnetic-field-annealed samples.¹⁴⁷

4.4. Isotopic labelling

Solid phase peptide synthesis is making possible a wide range of solid-state NMR studies of peptides. Previous reliance on biosynthetic methods resulted in very limited approaches and poor incorporation efficiency for specifically labelled amino acids. Systems cloned into an efficient expression system in *E. coli* have generated many useful samples for NMR, but it is not possible to clone all of the desired products into a bacterial system. Furthermore, when trying to incorporate labels with two different amino acids to generate a dipolar coupling the incorporation of the double label is subject to the inefficiency of each amino acid incorporation or scrambling of the label. Even 80% efficiency can result in the single site label having a greater intensity than the dipolar coupled double label. Therefore, there is considerable advantage to solid-phase peptide synthesis where incorporation efficiency of 99% can be readily attained. Furthermore, the percentage of labelled amino acid that is incorporated into the peptide of interest for NMR studies can be as high or higher than 50% for modest sized peptides (15 amino acids).¹⁴⁸ The application of solid-phase peptide synthesis to higher molecular weight peptides and proteins has been demonstrated. Synthesis of 50 amino acid segments and the coupling of segments together has been utilized in synthesizing HIV-protease, 22.5 kD protein composed of two identical 99 amino acid polypeptide chains.¹⁴⁹ Opportunities for incorporating a variety of labels to study the active site of such a protein or to study the entire structure can be envisioned.

For the incorporation of ²H special precautions may need to be taken. For instance, the aromatic C-D bonds in the indole ring are acid labile, even in fairly mild conditions and therefore acid conditions need to be avoided to incorporate ²H successfully into such sites. This has been achieved by using Fluorenylmethoxycarbonyl (Fmoc) chemistry where no acid cleavage steps are utilized.^{146,148,150}

5. APPLICATIONS

5.1. Bacteriorhodopsin dynamics

The combination of a modest molecular weight (26 kD) protein and a lipid environment results in an aggregate that is too large for high resolution

NMR. Early solid-state NMR experiments were utilized primarily to characterize the side-chain dynamics of the protein. ^2H NMR data have shown considerable mobility in the C-terminal side-chains and somewhat less in the loop regions between trans-membrane bilayer segments.^{151–154} Although these results are compelling they have not been universally accepted.^{155,156} Several approaches have been used to obtain the dynamic information. The averaging of the nuclear spin interaction tensors provides models for the amplitude, axis and mode of the dynamic process.^{153,155,156} In solid-state NMR there is a very wide range of spin relaxation properties that can be obtained in the absence of isotropic global motions which often induce efficient relaxation.¹⁵² Related to T_2 relaxation is the observation of homogeneous linewidths for sites that are locally undergoing enough motion to approach an isotropic average. Selective observations of the mobile segments of the protein can thereby be made.¹⁵⁴

5.2. Bacteriorhodopsin structural constraints

More recently structural information has begun to accumulate from solid-state NMR studies. The interpretation of the ^{15}N chemical shift for the Schiff base correlates with colour changes and potentially with the counterion environment.¹⁵⁷ The averaging of the ^{13}C carbonyl tensors by global rotation about the bilayer normal resulted in a very narrow powder pattern as in the studies of gramicidin. Such averaging not only leads to models for the molecular motions, but also to structural constraints with respect to the motional axis.¹⁵⁵ However, because the averaging is so extensive and because there is considerable uncertainty in the carbonyl ^{13}C tensor orientation with respect to the molecular frame^{105,116,124–126} conclusions as to conformation are made difficult. Distance constraints from rotational resonance studies have successfully been applied to constrain the conformation of the retinal.^{158,159} These distance constraints are highly quantitative as opposed to the NOE-derived distance constraints in solution NMR which are typically interpreted in a qualitative fashion. Although there are significant complications with such distance measurements the primary reason for the quantitative nature of the rotational resonance constraints is that the interaction is more successfully restricted to two spins than in the solution NMR experiment. Via these distance measurements it has been definitively shown that the configuration about the Schiff base $\text{C}=\text{N}$ bond changes with the state of bR. The conformation of the retinal has also been constrained in uniformly aligned samples of bR.¹⁶⁰ Deuteration of specific sites in the β -ionone ring allowed for the determination of the ring orientation with respect to magnetic field and the bilayer normal. Furthermore, this ring orientation, constrained the tilt of the retinal alkyl chain with respect to the bilayer normal. These studies were compromised by a 10°

mosaic spread in the bilayer normal orientation with respect to the magnetic field.¹⁶⁰

5.3. Coat protein viral studies

Using uniformly ^{15}N and specific amino acid labelling of the fd and Pf1 coat proteins, considerable solid-state NMR spectroscopy has been performed supporting the α -helical characterization and that the helices are almost parallel with the filamentous axis.^{22,161–163} A variety of nuclear spin interactions have been studied to achieve orientational constraints for this form of the protein. The orientational constraints have been used effectively by observing the overlap in $\alpha\beta$ plots that represents the allowed conformational space in polar angles relative to the axis of orientation. For a single site the $\alpha\beta$ plot for one spin interaction such as the ^{15}N chemical shift is overlapped with a similar plot for the ^{15}N - ^1H dipolar interaction. In the resulting plot only the overlapped regions are retained for consideration with additional data. An advantage to handling the data in this way is that it is relatively straightforward to estimate the margin of error in the measurement and assessment of each orientational constraint.

5.4. Coat protein synthetic membrane studies

The viral particles align remarkably well with respect to the magnetic field in a relatively dilute solution;¹⁶¹ however, it is far more challenging to achieve such uniform orientation for the membrane-bound form of the peptide.^{44,164} Despite this difficulty, very significant structural constraints have been achieved that emphasize the unique properties of orientational constraints. In the membrane form it is clear that the α -helical segments are not parallel, in fact a considerable segment of the α -helix is parallel to the plane of the bilayer, while a second hydrophobic stretch is perpendicular. Each of the structural constraints has a very considerable error bar due to the relatively poor orientation, but because the constraints are absolute, that is, the constraint is relative to the laboratory fixed Z axis of the magnetic field, they are still very informative.

The determination of such tertiary structure by solution NMR methods is far more difficult, because there are no specific contacts between the segments which are tethered together by a short flexible linker. However, the study of the coat protein in lyso-PC micelles has provided detailed secondary structure information that defines the two helical segments.⁴⁴ In order to reduce the spectral overlap in these micellar studies it was necessary to label the protein uniformly with ^2H (at 80%) and ^{15}N (at 98%). The ^2H labelling results in less efficient T_2 relaxation and hence the

resonance linewidths are considerably narrower. Furthermore, it results in less efficient T_1 relaxation, thereby reducing both spin diffusion and spin exchange processes.^{38,165} Of course, the disadvantage is that 80% of the ^1H signal has been eliminated in the process, hence the need for ^{15}N isotopic labelling. The use of partial uniform deuteration has not become a generally accepted technique, however; NMR spectroscopists have exceptionally few opportunities to modify the relaxation behaviour of the nuclear spins and as experiments with proteins having long global correlation times are attempted the relaxation behaviour makes solution NMR very difficult. Partial uniform deuteration has the potential to make a variety of membrane protein studies by solution NMR possible.

A considerable concern among structural biologists is the fidelity with which detergents mimic the membrane environment. The filamentous coat proteins are one of the few macromolecular systems in which studies are being conducted in detergents, lyso-lipids and in lipid bilayers. Early denaturing gel studies suggested that the coat protein in SDS was dimeric. Studies by Henry and Sykes have continued to support that concept.^{41,42} However, similar studies in SDS by two independent groups show that such phenomena are dependent upon the amount of detergent present in the sample and that at sufficient SDS concentrations the M13 and fd coat proteins are monomeric.^{95,166,167} Furthermore, Sykes has emphasized some of the significant differences between the hydrophilic headgroup of sodium dodecyl sulfate and other better models of the lipid headgroup of phosphatidylcholine. Because the positively charged nitrogen is surrounded by four methyl groups in choline headgroups, O'Neil and Sykes¹⁶⁸ have argued that such methyls result in considerable hydrophobic character for the outer surface of the micelle.

5.5. Coat protein conformational comparison

One of the primary conclusions from the solid-state NMR studies is the variability in dynamics along the peptide backbone. From powder pattern analyses of amino acid specific labelled samples it has been possible to identify regions of relatively high and low backbone mobility.^{44,45} In the membrane form two α -helical segments are quite static while the two terminal segments and the intervening segment are substantially more mobile. Because of the mobility in the intervening segment it is very difficult to define the tertiary structure from solution NMR and NOE measurements. However, the orientation constraints for the two helical segments clearly show that one of the helices is parallel to the bilayer normal while the other is perpendicular. Consequently the two segments are perpendicular to each other. The dynamics in the viral form of the protein change significantly.^{33,34} The terminal segments become essentially static, but interestingly the

intervening segment retains considerable dynamic flexibility. Furthermore, the helical segments become essentially parallel to each other in this form of the protein.

5.6. Gramicidin structural constraints

Chemical shift spectra of anisotropic samples that have been uniformly aligned yield a single resonance whose frequency is orientation dependent (Fig. 6). Such data constrain nuclear spin interaction tensors with respect to the bilayer normal and the channel axis. If the orientations of the chemical shift tensors have been determined with respect to the molecular frame it will be possible to constrain the covalent bonds with respect to the channel axis. It is the development of numerous orientational constraints that will be essential for solving the three-dimensional structure. Both dipolar and quadrupolar interactions can be used in a similar fashion for orientational constraints. The dipolar interaction has the advantage that the tensor is axially symmetric and its orientation is generally accepted as having its unique axis along the internuclear vector. Furthermore, the magnitude of this interaction can be determined from a knowledge of the bond length (Fig. 7). Consequently, from an observed dipolar splitting the orientation of a bond such as the peptide N-C or amide N-H bonds can be determined with respect to the channel axis. For C-D groups the ^2H quadrupolar splitting can be analysed in just the same way except that the tensors are typically somewhat asymmetric and the magnitude of the quadrupolar interaction cannot be calculated. As with the chemical shift interaction either the magnitude and asymmetry can be observed from powder pattern spectra or they can be assumed from appropriate literature values.

In 1986 the first prediction of chemical shift orientational constraints for gramicidin¹⁶⁹ and the first such observations in ^{13}C carbonyl labelled gramicidin were published.¹⁷⁰ Numerous ^{13}C constraints have been published since then (Fig. 8).^{126,171-175} These constraints are somewhat less reliable because of the greater uncertainty in the orientation and magnitudes of the tensor elements with respect to the molecular frame. The uncertainty results from residual ^{14}N - ^{13}C dipolar couplings in the powder pattern spectra. These couplings effectively broaden the spectral lineshapes resulting in a poorer definition of the tensor elements.¹⁰⁵ ^{15}N chemical shift constraints have been published for each of the backbone sites.¹²³ Furthermore, tensor element magnitudes have been determined for each site and tensor orientations for many of the sites.^{120,123} Numerous dipolar orientational constraints have been obtained for gramicidin: ^{15}N - ^1H ,^{87,176} ^{15}N - ^{13}C ,^{87,177,178} and ^{13}C - ^{13}C .¹⁷² The ^2H quadrupolar interaction has also been effectively utilized for orientational constraints.^{146,179-182}

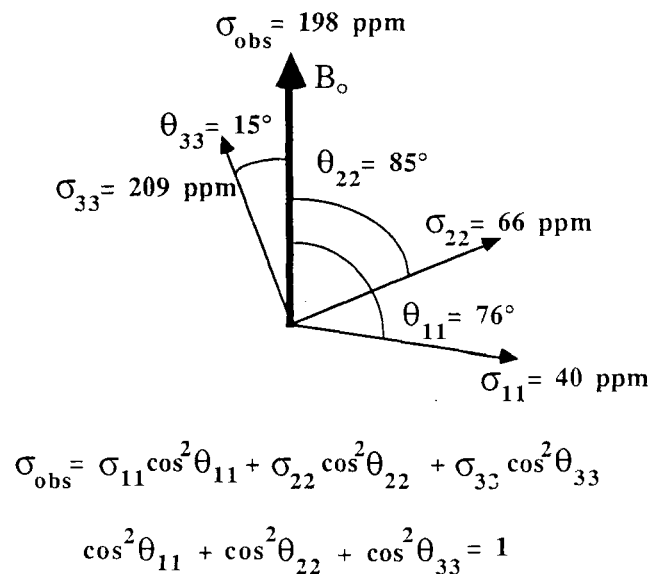
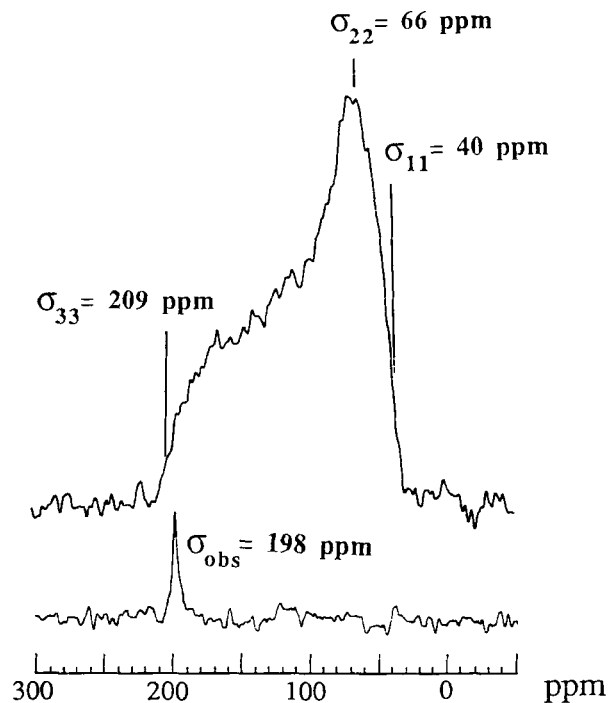


Fig. 6. Interpretation of the ^{15}N chemical shift ($\sigma_{\text{obs}} = 198$ ppm) from ^{15}N Ala₃ labelled gramicidin in uniformly aligned lipid bilayers such that the bilayer normal is parallel with respect to the magnetic field. The dry powder pattern spectrum yields chemical shift tensor element magnitudes of 209, 66 and 40 ppm. The observed chemical shift represents a structural constraint, it does not define a unique orientation for the molecular frame with respect to the magnetic field. A possible orientation for this site relative to the magnetic field is presented.

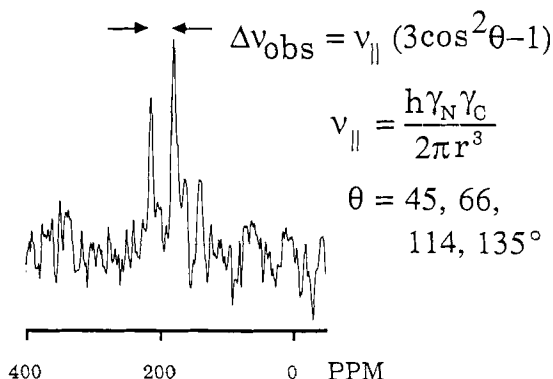


Fig. 7. ^{15}N chemical shift spectra of $^{13}\text{C}_1$ Gly $_2$ - ^{15}N Ala $_3$ gramicidin in oriented bilayers for which the single sharp line at 198 ppm observed in ^{15}N Ala $_3$ gramicidin is split by the dipolar coupling to the carbonyl oxygen of Gly $_2$. Spectra are obtained with cross polarization at a proton frequency of 200 MHz. Because the sign of $\Delta\nu_{\text{obs}}$ is not defined and because of the \cos^2 term there are four possible orientations for this N-C bond axis with respect to the magnetic field and the channel axis.

5.6.1. Gramicidin conformational analysis

An alternative approach is presented here to that of Opella and coworkers^{22,32} that was briefly described above. It is possible to determine analytical solutions for the torsion angles that define the protein conformation. The ^{15}N - ^{13}C and ^{15}N - ^1H dipolar interactions define for each peptide linkage the orientation of the peptide plane with respect to the channel axis (Fig. 9). The orientational constraints do not define a unique orientation for each internuclear vector. Several ambiguities are caused by the $\cos^2\theta$ dependence and by a potential sign ambiguity in the observed dipolar splitting. This leads to multiple possible orientations for each peptide plane. By taking advantage of the known covalent geometry (bond angles) and the observed chemical shift orientational constraints a unique orientation for each peptide plane with respect to the channel axis can be achieved.¹⁸³ The relative orientation of the adjacent planes and hence the ϕ , ψ torsion angles can be determined by taking advantage of the tetrahedral geometry about the α -carbon. Typically two possible solutions result; however, this ambiguity does not propagate with the sequential addition of peptide planes because the orientational constraint for each peptide plane is independent.^{146,177} An initial structure (Fig. 10) for the complete backbone of the gramicidin channel observed in fully hydrated lipid bilayers has recently been achieved.⁸⁷

This initial structure confirmed the β -sheet type of torsion angles, the hydrogen bonds between helical turns, identified the number of residues per

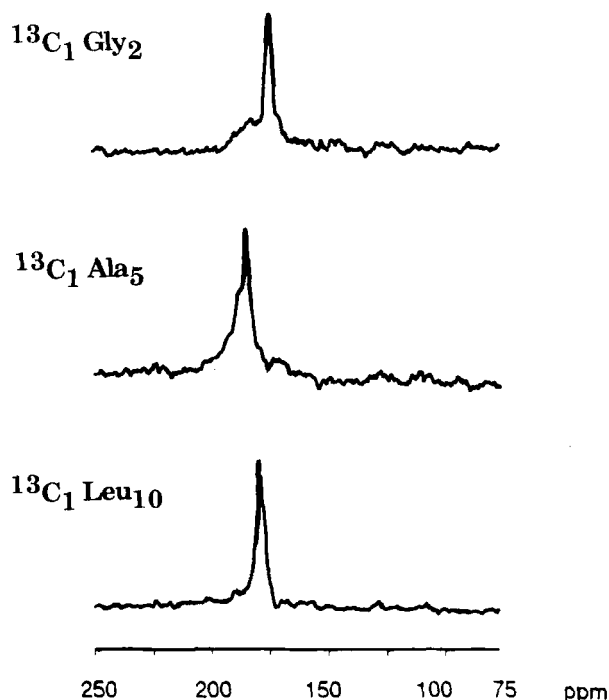


Fig. 8. ^{13}C chemical shift spectra for three different isotopically labelled sites in gramicidin. Spectra were obtained by cross polarization at a proton frequency of 200 MHz. The single sharp line spectra represent clear examples of “self decoupling” from the ^{14}N nucleus that is covalently attached to these carbonyl carbon sites. In dry powder pattern spectra of such sites the dipolar interaction is readily observed, but in these hydrated samples above the lipid phase transition there is no evidence for the dipolar coupling.

turn and confirmed the right-handed helical sense. The difference between the two structures derived from the orientational constraints is subtle. The repeating structural unit in the backbone is a dipeptide. In conformation I the LD planes have the carbonyl oxygens tipped away from the channel pore by approximately 20° while the DL planes have carbonyl groups nearly parallel with the channel axis. In conformation II the DL planes remain nearly parallel while the LD planes are rotated with the carbonyl oxygens in towards the channel axis by approximately 20° . This latter structure is consistent with the cation selective nature of the channel.

In an analogous fashion it is possible to determine the torsion angles of the side-chains. By using the ^2H quadrupolar splitting for five carbon bound sites in each indole ring as well as the ^{15}N chemical shift (Fig. 11) and ^{15}N - ^1H dipolar interaction it has been possible to determine a unique

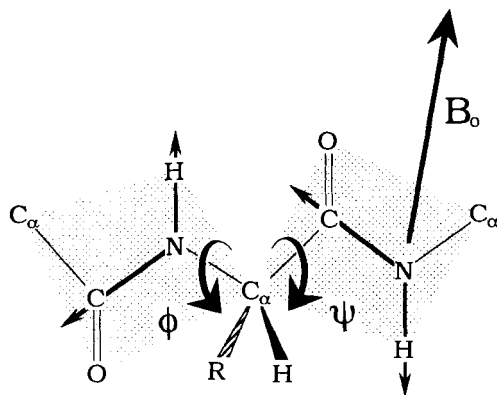


Fig. 9. The orientations of the N-H and N-C₁ bonds are used to define the orientation of the peptide plane with respect to the magnetic field direction, the laboratory Z axis. When the orientations for adjacent peptide planes are determined advantage can be taken of the tetrahedral geometry of the shared alpha carbon so as to determine the ϕ and ψ torsion angles. The solid state NMR data may not only determine the relative orientation of the peptide planes but their absolute orientation with respect to the laboratory frame and the molecular frame of the environment (the lipid bilayer).

orientation of the indole ring with respect to the channel axis and nearly unique χ_1 and χ_2 torsion angles.^{87,150} Finding structural solutions for the valine and leucine side-chains is an even greater challenge because of the potential for large amplitude local motions.¹⁸² Via a combination of powder pattern lineshape spectra and spectra of oriented samples, it has been possible to describe conformational substates about the χ_1 torsional axis and to determine the relative population of these substates.¹⁸⁴

5.6.2. Gramicidin structural refinement

For the backbone structure the hydrogen bonds have been identified from the initial structure, but the hydrogen bond lengths are not ideal and optimal utilization of the chemical shift orientational constraints has not been made. The computational protocol for refinement⁸⁷ represents a form of simulated annealing in which small random changes are made in the ϕ , ψ ($\leq \pm 3^\circ$) and the ω ($\leq \pm 0.1^\circ$) torsion angles. For the initial structure the ω torsion angle had been fixed at 180° , but for the refinement it is introduced as a variable. For each altered conformation the structure was realigned with respect to the lab Z axis and the nuclear spin and hydrogen bond parameters calculated. Comparisons with the observed nuclear spin parameters and ideal hydrogen bond distances were made to generate a penalty function. Through more than 30 000 successful torsion angle modifications for each annealing run, a set of refined structures was achieved with minimal

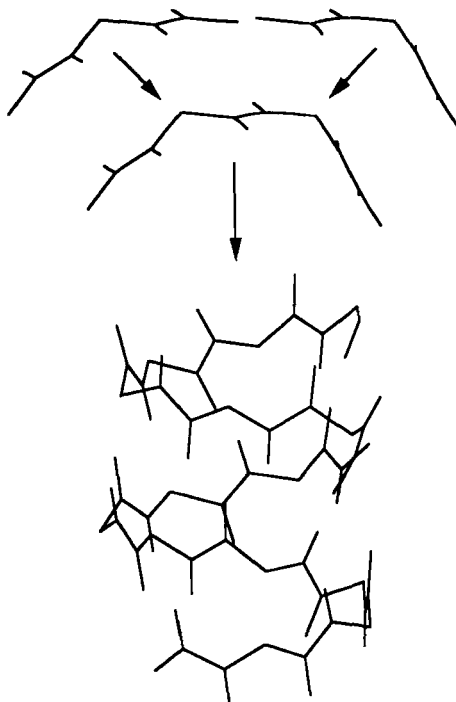


Fig. 10. Determination of the initial polypeptide backbone structure. From the procedure illustrated in Fig. 9 the relative orientation of peptide planes (a diplane) is determined. Here diplanes that share one plane are compared, those that share a common orientation for the shared plane can be combined. This process is continued for the entire backbone of the gramicidin monomer to yield the initial structure shown.

penalty function and retained global structural features of the initial structure. This set of structures (Fig. 12) demonstrates the remarkable fidelity of the orientational constraints. The root-mean square angular deviation among the torsion angles is less than $\pm 3^\circ$. The structure is very well defined because the constraints are quantitative and independent; that is, they are constraints to the laboratory fixed Z axis. Despite the computational search over a large conformational space the refined structure deviates little from the initial structure. The ω torsion angles are confined to values of $\pm 7^\circ$ from the planar initial configuration. When significant changes in the ψ_i angle were observed in the refined set of structures it was typically compensated for by a change in ϕ_{i+1} .

The average values of the refined set of structures have been used to establish a mean structure which is compared here to the torsion angles determined from a solution NMR study in SDS micelles (Fig. 13).^{94,185} Again, because the structural repeat is a dipeptide it is appropriate to

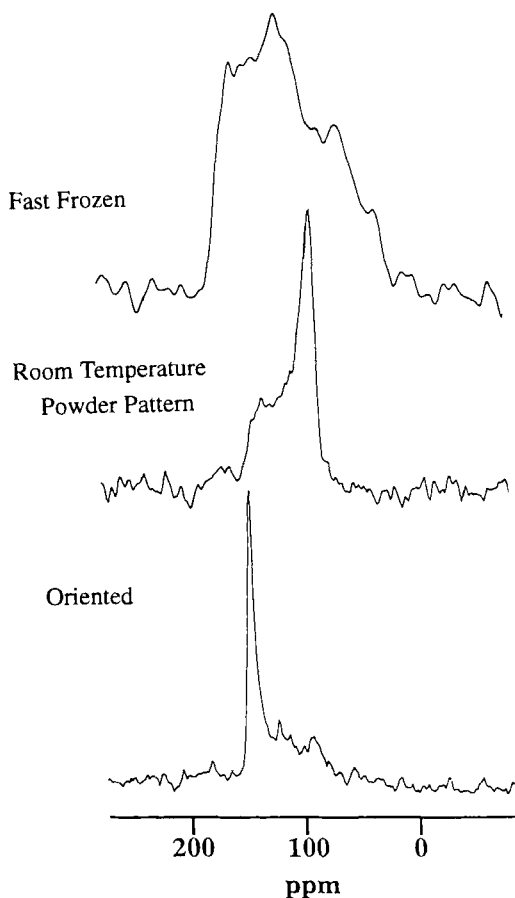


Fig. 11. ^{15}N chemical shift spectra for $^{15}\text{N}_{\epsilon 1}$ Trp₉ labelled gramicidin in hydrated lipid bilayers. The fast frozen sample at 150 K yields the static chemical shift spectrum. At room temperature, near the lipid phase transition axial rotation of the channel dramatically reduces the anisotropy to yield an axially symmetric powder pattern. The spectrum obtained from uniformly aligned bilayers yields a chemical shift that is exactly aligned with the σ_{\parallel} component of the averaged tensor.

separate this comparison of torsion angles for the odd and even residues. Remarkably, the structure at the bilayer surface appears to be very similar for these two environments. However, substantial (30° – 40°) torsion angle differences occur near the monomer–monomer junction and in the monomer centre. A potential explanation for this is the lack of parallel bilayer surfaces in the micellar sample to maintain a linear channel axis through the junction. Other significant differences between the micellar and lipid bilayer bound conformations appear with the indole side-chain orientations. In the

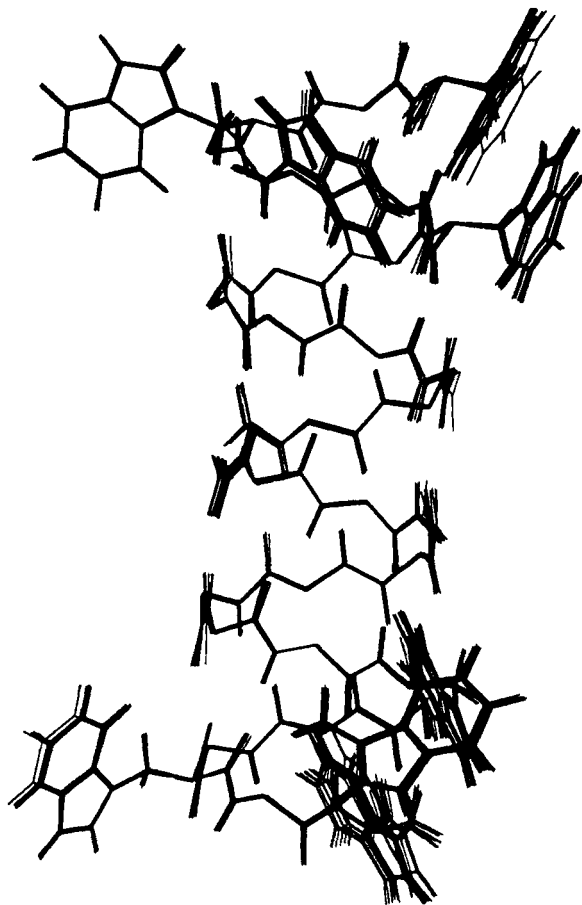


Fig. 12. A set of refined conformations for the gramicidin channel showing the backbone and the indole side-chains. The initial structure was refined against all of the orientational constraints and ideal hydrogen bond geometry. The hydrogen bonds between turns of the helix were clearly identified in the initial structure. In the refinement the assumption of planarity for the peptide linkage was relaxed and significant deviations from planarity were detected. The result of the refinement is a set of structures with a root mean square deviation for the torsion angles of less than 3° .

lipid environment the N-H orientations are all directed toward the bilayer surfaces, but the side-chain torsion angles for Trp₉ and Trp₁₁ are significantly different between these two preparations. Trp₉ by solution NMR is in a different rotameric state that prohibits the stacking interaction that is suggested by the most probable side-chain torsion angles for these residues in the lipid environment.

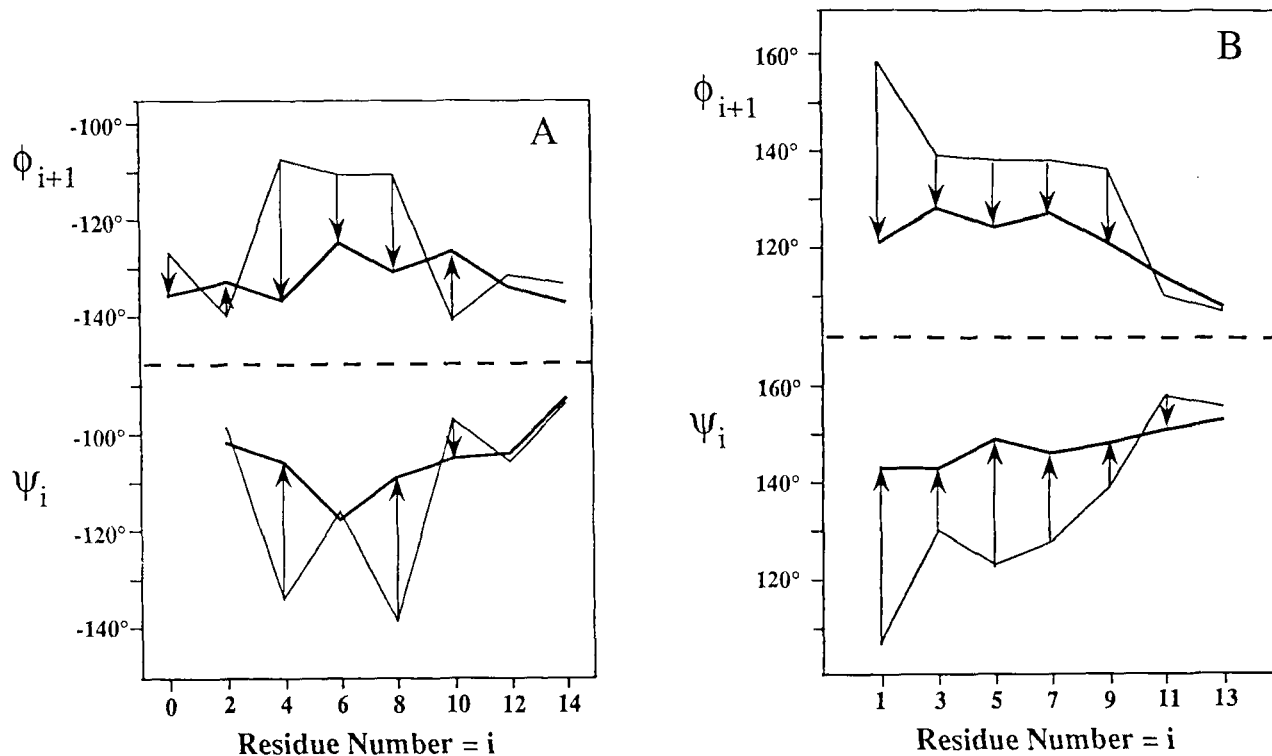


Fig. 13. The torsion angles for the solid state NMR derived conformation determined for gramicidin in lipid bilayers are compared to those for gramicidin in sodium dodecyl sulphate micelles by solution NMR methods. This figure compares the torsion angles for the D residues separately from the L residues. The lipid bilayer conformation (thick line) shows significantly less variability in the torsion angles as compared with the micellar conformation (thin line). The torsion angles at the carboxyl terminus are remarkably similar, but significant differences are apparent at the amino terminus and in the monomer centre.

5.7. Gramicidin dynamics

Not only is there an opportunity to characterize structural detail from the solid-state NMR data, but through a combination of temperature-dependent powder pattern analyses and relaxation studies of oriented samples at different field strengths it has been possible to characterize uniquely the local motions in the backbone.¹⁰⁹ To achieve such a description it is essential that the global motions of the channel be well characterized. From alanine methyl deuterated sites it has been possible to characterize the global correlation time over the temperature range from 279 to 325 K.¹¹⁰ In this temperature range the ^2H powder pattern spectra displayed shapes indicative of motional averaging in the intermediate motional regime. At 309 K where the relaxation studies were performed the global correlation time is in the microsecond timescale and this motion will not contribute significantly to the efficient T_1 relaxation process for the amide nitrogen sites. The averaging of the ^{15}N chemical shift tensors between 120 K and 280 K define an anisotropic librational motion that initiates near 200 K and has an amplitude of approximately $\pm 20^\circ$ at 280 K (Lazo and Cross, in preparation).¹⁰⁸ The axis about which the librational motion occurs is consistent with the $\text{C}_\alpha\text{--C}_\alpha$ axis. By using this model for the local motion it has been possible to interpret the T_1 relaxation data for these same sites. The efficient relaxation is due to motion on the nanosecond timescale as shown for Leu₄ Fig. 14. Similar amplitudes and frequencies have been obtained for a variety of sites along the polypeptide backbone (North and

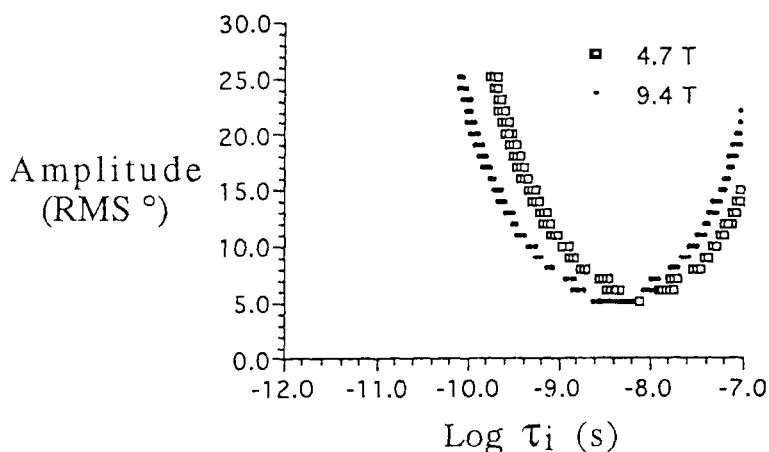


Fig. 14. ^{15}N relaxation data for amide sites in the polypeptide backbone have been analysed in terms of a librational motion about the $\text{C}_\alpha\text{--C}_\alpha$ axis. Very efficient relaxation is induced by motions near the Larmor frequency. The intersection of the two curves indicates that relatively small amplitude motions in nanosecond time-frame are responsible for the relaxation.

Cross, in preparation). The amplitude is much less than the librational amplitude determined from the powder pattern analysis, however librational averaging of the powder patterns will represent all frequencies greater than the 10 kHz timescale, while the motion that will induce efficient T_1 relaxation is in the vicinity of the Larmor frequency. The observation of backbone motions on the nanosecond timescale is not unique.^{186–189} However, it remains unexplained why these motions are so overdamped compared to the expected harmonic frequencies for an oscillator with the moment of inertia of a single peptide plane rotating about the $C_\alpha C_\alpha$ axis (0.5 ps).

5.8. Gramicidin structure–function–dynamic correlations

The backbone folding motif determined from orientational constraints is very similar to the numerous computational models of recent years. The alternating pattern of carbonyl group orientations suggests that every other carbonyl may have a more significant role in solvating cations in the channel. This is consistent with local correlations between neighbouring peptide planes that have been observed in computational studies.^{190–192} The nanosecond motions in the backbone were not anticipated by computational studies, but they have the potential to be very important for channel function. Based on energetic calculations the residence time per dipeptide along the channel is 10 ns.¹⁹¹ From kinetic data and using a four state model the transit time across the channel has been estimated to be 142 ns corresponding to 12 ns per dipeptide.¹⁹³ The observed 10 ns timeframe dynamics in the backbone suggests a direct correlation between the translocation of the cation and the librational frequency of the peptide planes. The mechanism for overdamping is not known but several possibilities exist (Cross and North, in preparation). The motions of the peptide planes (Fig. 15) could be sequentially correlated through the shared α carbons such that all of the peptide planes move in a coherent fashion. This concept has been suggested before through molecular mechanics computational studies.¹⁹⁴ It is also possible that the peptide planes could be correlated through the hydrogen bonds between helical turns. In this way stripes of peptide planes approximately parallel to the channel axis would maintain coherence. A third explanation for overdamping is the influence of the relatively high viscosity of the lipid environment. This environment is expected to overdamp the side-chain dynamics and in turn this could affect backbone dynamics. A fourth possibility is that the backbone motions are mediated by slight changes in helical pitch as a result of collisions between lipid and the bulky indole side-chains that protrude into the lipid environment. Such intermolecular collisional events could be taking place on this timeframe. Whatever, the mechanism for overdamping the possibilities exist

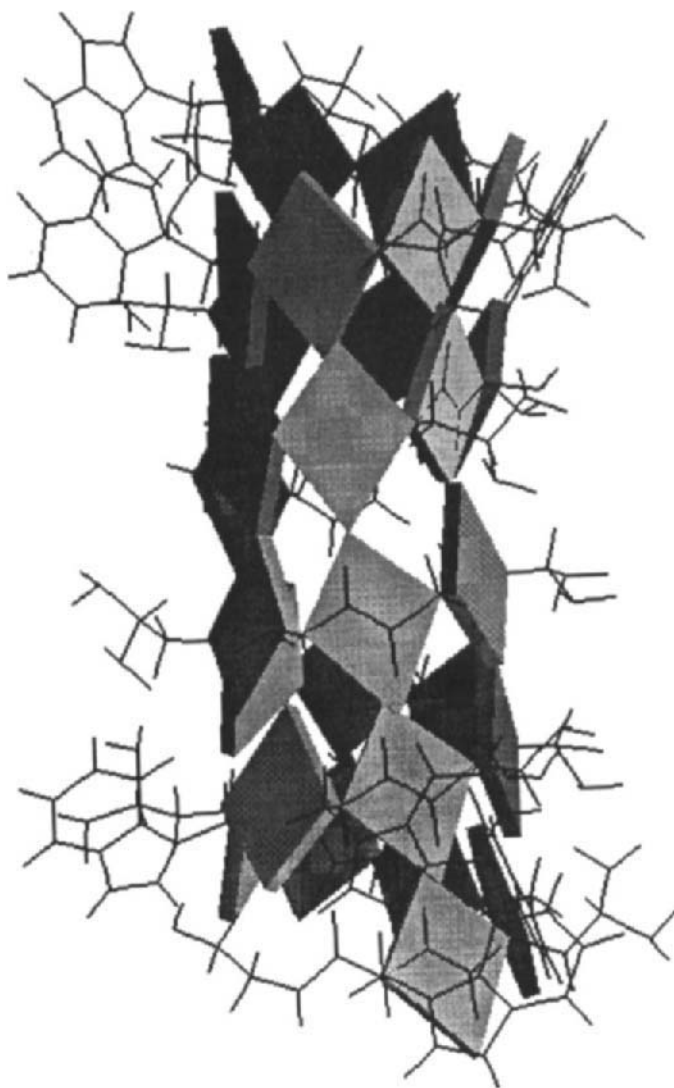


Fig. 15. A line drawing of the entire gramicidin channel is shown based on the solid state NMR structure determination. The peptide planes have been superimposed on this figure with the program GRASP developed by Anthony Nichols (Columbia University). It is suggested here that the low frequency local motions of the backbone arise from correlated motions. Several potential models for correlated motions can be visualized through this illustration of the channel. A sequential correlation would follow the amino acid sequence through the five helical turns. If the correlations were mediated via hydrogen bonds then a nearly vertical stripe of peptide planes would be highly correlated. Correlations could also extend radially in from the viscous environment of the fatty acyl chains. Such overdamped motions may also arise from changes in helical pitch as the indole groups are bumped by the lipid environment. Subtle changes in pitch can significantly affect peptide plane orientations.

for unique structure–dynamic–function correlations that have rarely been obtained for any macromolecular system.

The tryptophans have at least two very important functional roles in the gramicidin channel. Each of the indoles has been uniquely defined with their N–H bond oriented toward the bilayer surface¹⁵⁰ presumably for hydrogen bonding to the hydrophilic interface. Such hydrogen bonds could be to water molecules that occur at the interface or penetrate into the hydrophobic domain along the lipid–peptide surface. Alternatively, the tryptophan could be hydrogen bonded to the lipid molecules themselves.^{114,195–197} In either case the tryptophans orient the channel with respect to the bilayer surface, tethering the structure to the hydrophilic domain. This is consistent with synthetic mutation studies in which tryptophan has been replaced by phenylalanine and it has been shown that the mutants more readily migrate between the bilayer leaflets (Becker and Andersen, personal communication).

The electrophysiologists have also shown that sequential replacement of the tryptophans by phenylalanine results in an incremental decrease in the channel conductance.¹⁹³ Based on these results they predicted that the tryptophan should have similar orientations with respect to the channel such that each indole ring dipole moment would exert a similar influence on conductance. The NMR data are completely consistent with this prediction and furthermore, with Trp₉ and Trp₁₅ having similar orientations there is the potential for substantial ring stacking.⁸⁷ The dipole moment orientations are such that the major component is parallel to the channel axis and oriented toward the bilayer centre in such a way as to reduce the potential energy barrier at the monomer–monomer junction.¹⁵⁰ This provides a possible explanation for both the reduction in conductance when tryptophan is replaced by phenylalanine and for the incremental nature of this reduction as sequentially more of the tryptophans are replaced with phenylalanine.

5.9. Gramicidin–lipid interactions

5.9.1. Solvent history dependence

As noted before, gramicidin can adopt a variety of well-defined conformations in organic solvents.⁶³ Depending on the hydrogen-bonding capabilities of the solvent these structures can be very stable. When phospholipid–gramicidin samples are prepared by cosolubilizing these components in an organic solvent followed by drying and hydration to form bilayers or vesicles, the organic solvent makes a difference in the structural and functional characteristics of the peptide.^{68–70} Through these studies it was suggested that the bilayers were stabilizing non-channel conformations. It was also noted that by heating samples for extended periods of time^{68–70} or by sonicating the samples even in a well-controlled temperature bath^{68,198}

that conversion of the molecule to the channel state could be induced. Fluorescence studies have recently confirmed the solvent history dependence¹⁹⁹ and HPLC studies have confirmed the presence of monomers and intertwined dimers of gramicidin in vesicles shortly after complex formation.^{65,198} This aspect of the lipid environment is consistent with what is known about conformational trapping in organic solvent environments. It has been shown^{64,97} that a sample of mixed conformations can be resolved by normal phase HPLC and that purified conformations are stable for weeks in dioxane or tetrahydrofuran.²⁰⁰ Questions remain as to how effectively the lipid environment can trap non-minimum energy conformations, but it is clear that the absence of a hydrogen-bonding solvent can enhance conformational stability. In a membrane environment significant water penetration, especially at the peptide-lipid interface may be present with the potential to promote conformational interconversion. As a result the extreme trapping behaviour of the organic solvent may not be reproduced in the membrane environment. This catalytic role for water represents a critically important issue in our understanding of the differences between an aqueous and a non-aqueous environment for proteins.

5.9.2. *Effects on lipid phase*

The effects of gramicidin on lipid organization have recently been reviewed by Killian.⁵³ Such organizations are influenced by the shape of the components. Lysolipids favour a highly curved surface such as a micelle due to the small hydrophobic component of the lipid. Conversely, diacylphosphatidylethanolamine favours a hexagonal organization while phosphatidylcholine appears to have a balanced hydrophobic and hydrophilic radius and hence favours a bilayer phase. The gramicidin channel has a fixed length; if the channel is placed into a lipid environment when there is a mismatch between the hydrophobic dimension of the lipid and peptide then curvature in the lipid surface will be induced. Consequently, the incorporation of gramicidin into a lipid environment has a very significant effect on the organizational propensity of numerous lipid classes. In lysolipids gramicidin promotes bilayer formation.²⁰¹⁻²⁰³ The induction of hexagonal phase by gramicidin on diacylphosphatidylcholine was first reported in 1981.²⁰⁴ Numerous studies have been conducted since to investigate the effects of saturation and chain length⁵³ and it has been shown that a mismatch in length is necessary for hexagonal phase induction.²⁰⁵

6. CONCLUSIONS

The utility of both orientational and distance constraints has been demonstrated for membrane proteins and polypeptides. The methods have been

developed to the point where illuminating biochemical information has been obtained. There remains considerable work ahead to make the methods more generally applicable through use of naturally abundant nuclei or uniformly labelled sites.

Not only is solid state NMR effective for describing structural detail, but high resolution dynamics characterizations are leading to important and novel functional understanding. Through high-resolution structure the details of peptide-solvent interactions will be forthcoming. This too will lead to functional understanding at a very fundamental biophysical level. Finally, it is important to recognize that this information is being obtained from just the protein systems for which a new approach for structural elucidation was needed, proteins in an anisotropic environment.

ACKNOWLEDGEMENTS

I am indebted to J. Vaughn, R. Rosanske and T. Gedris of the NMR Facility and to U. Goli and H. Henricks of the Bioanalytical Synthesis and Services Facility for their expertise and help in this effort. The work from my own laboratory represents the accumulated study of many students and postdoctoral researchers over the past 8 years—to them I offer my thanks for all their hard work. TAC gratefully acknowledges National Institutes of Health Support, AI-23007.

REFERENCES

1. B. Shaanan, A. M. Gronenborn, G. H. Cohen, G. L. Gilliland, B. Veerapandian, D. R. Davies and G. M. Clore, *Science*, 1992, **257**, 961.
2. A. J. Doig and D. H. Williams, *Biochemistry*, 1992, **31**, 9371.
3. S. N. Loh, K. E. Prehoda, J. Wang and J. L. Markley, *Biochemistry*, 1993, **32**, 11022.
4. K.-S. Kim, J. A. Fuchs and C. K. Woodward, *Biochemistry*, 1993, **32**, 9600.
5. M.-F. Jeng and S. W. Englander, *J. Mol. Biol.*, 1991, **221**, 1045.
6. C.-L. Chyan, C. Wormald, C. M. Dobson, P. A. Evans and J. Baum, *Biochemistry*, 1993, **32**, 5681.
7. S. Bone, *Biochim. Biophys. Acta*, 1987, **916**, 128.
8. A. Zaks and A. M. Klibanov, *J. Biol. Chem.*, 1988, **263**, 3194.
9. J. Wu and D. G. Gorenstein, *J. Am. Chem. Soc.*, 1993, **115**, 6843.
10. S. N. Timasheff, *Biochemistry*, 1992, **31**, 9857.
11. M. M. Teeter, *Annu. Rev. Biophys. Biophys. Chem.*, 1991, **20**, 577.
12. G. Otting, E. Liepinsh and K. Wuthrich, *Science*, 1991, **254**, 974.
13. J. A. Kornblatt, M. J. Kornblatt, G. H. B. Hoa and A. G. Mauk, *Biophys. J.*, 1993, **65**, 1059.
14. M. M. Teeter, S. M. Roc and N. H. Heo, *J. Mol. Biol.*, 1993, **230**, 292.
15. F. D. Sonnichsen, J. E. Van Eyk, R. S. Hodges and B. D. Sykes, *Biochemistry*, 1992, **31**, 8790.
16. A. L. Breeze, T. S. Harvey, R. Bazzo and I. D. Campbell, *Biochemistry*, 1991, **30**, 575.

17. M. Llinas and M. P. Klein, *J. Am. Chem. Soc.*, 1975, **97**, 4731.
18. J. W. Nelson and N. R. Kallenbach *Proteins*, 1986, **1**, 211.
19. R. C. deL. Milton, S. C. F. Milton and S. B. H. Kent, *Science*, 1992, **256**, 1445.
20. R. E. Koeppe, II, L. L. Providence, D. V. Greathouse, F. Heitz, Y. Trudelle, N. Purdie and O. S. Andersen, *Proteins*, 1992, **12**, 49.
21. C. Ho and C. D. Stubbs, *Biophys. J.*, 1992, **63**, 897.
22. S. J. Opella, P. L. Stewart and K. G. Valentine, *Quart. Rev. Biophys.*, 1987, **19**, 7.
23. S. O. Smith and R. G. Griffin, *Annu. Rev. Phys. Chem.*, 1988, **39**, 511.
24. S. J. Opella, in *Biological Magnetic Resonance*, eds L. J. Berliner and J. Reuben, Plenum Press, New York, 1990, pp. 177–197.
25. L. E. Chirlian and S. J. Opella, *Adv. Magn. Reson.*, 1990, **14**, 183.
26. S. O. Smith and O. B. Peersen, *Annu. Rev. Biophys. Biomol. Struct.*, 1992, **21**, 25.
27. R. A. Mathies, S. W. Lin, J. B. Ames and W. T. Pollard, *Annu. Rev. Biophys. Biophys. Chem.*, 1991, **20**, 491.
28. R. R. Birge, *Biochim. Biophys. Acta*, 1990, **1016**, 293.
29. H. G. Khorana, *J. Biol. Chem.*, 1988, **263**, 7439.
30. W. Stoeckenius and R. A. Bogomolni, *Annu. Rev. Biochem.*, 1982, **52**, 587.
31. R. Henderson, J. M. Baldwin, T. A. Ceska, F. Zemlin, E. Beckmann and K. H. Downing, *J. Mol. Biol.*, 1990, **213**, 899.
32. P. L. Stewart, K. G. Valentine and S. J. Opella, *J. Magn. Reson.*, 1987, **71**, 45.
33. L. A. Colnago, K. G. Valentine and S. J. Opella, *Biochemistry*, 1987, **26**, 847.
34. T. A. Cross and S. J. Opella, *J. Am. Chem. Soc.*, 1983, **105**, 306.
35. T. A. Cross and S. J. Opella, *Biochemistry*, 1981, **20**, 290.
36. M. J. Bogusky, P. Tsang and S. J. Opella, *Biochem. Biophys. Res. Commun.*, **127**, 540.
37. R. A. Schiksnis, M. J. Bogusky, P. Tsang and S. J. Opella, *Biochemistry*, 1987, **26**, 1373.
38. K. Shon and S. J. Opella, *J. Magn. Reson.*, 1989, **82**, 193–197.
39. G. D. Henry, J. H. Weiner and B. D. Sykes, *Biochemistry*, 1987, **26**, 3626.
40. G. D. Henry and B. D. Sykes, *J. Magn. Reson.*, 1993, **102B**, 193.
41. G. D. Henry and B. D. Sykes, *Biochemistry*, 1990, **29**, 6303.
42. G. D. Henry and B. D. Sykes, *Biochemistry*, 1992, **31**, 5284.
43. G. D. Henry and B. D. Sykes, *J. Magn. Reson.*, 1993, **102B**, 193.
44. K. Shon, Y. Kim, L. A. Colnago and S. J. Opella, *Science*, 1991, **252**, 1303.
45. G. C. Leo, L. A. Colnago, K. G. Valentine and S. J. Opella, *Biochemistry*, 1987, **26**, 854–862.
46. L. Makowski, D. L. D. Caspar and D. A. Marvin, *J. Mol. Biol.*, 1980, **140**, 149.
47. D. A. Marvin, *J. Mol. Biol.*, 1966, **15**, 8.
48. W. Stark, M. J. Glucksman and L. Makowski, *J. Mol. Biol.*, 1988, **199**, 171.
49. R. Nambudripad, W. Stark and L. Makowski, *J. Mol. Biol.*, 1991, **220**, 359.
50. R. Nambudripad, W. Stark, S. J. Opella and L. Makowski, *Science*, 1991, **252**, 1305.
51. B. A. Cornell, *J. Bioenerg. Biomemb.*, 1987, **19**, 655.
52. B. A. Wallace, *Annu. Rev. Biophys. Biophys. Chem.*, 1990, **19**, 127.
53. J. A. Killian, *Biochim. Biophys. Acta*, 1992, **1113**, 391.
54. D. D. Busath, *Annu. Rev. Physiol.*, 1993, **55**, 473.
55. R. Fisher and T. Blumenthal, *Proc. Natl Acad. Sci. USA*, 1982, **17**, 451.
56. D. W. Urry, *Proc. Natl Acad. Sci. USA*, 1971, **68**, 672.
57. L. K. Nicholson and T. A. Cross, *Biochemistry*, 1989, **28**, 9379.
58. M. R. Kimball and B. A. Wallace, *Acta Crystallogr., Sec. A*, 1981, **37**, c50.
59. B. A. Wallace and R. W. Janes, *J. Mol. Biol.*, 1991, **217**, 625.
60. R. W. Janes and B. A. Wallace, in *Biomembrane Structure and Function—The State of the Art*, eds B. P. Gaber and K. R. K. Easwaran, Adenine Press, 1992, pp. 245–251.
61. J. Katsaras, R. S. Prosser, R. H. Stinson and J. H. Davis, *Biophys J.*, 1991, **61**, 827.
62. G. A. Olah, H. W. Huang, W. Liu and Y. Wu, *J. Mol. Biol.*, 1991, **218**, 847.
63. W. R. Veatch, E. T. Fossel and E. R. Blout, *Biochemistry*, 1974, **13**, 5249.

64. S. M. Pascal and T. A. Cross, *J. Mol. Biol.*, 1992, **226**, 1101.
65. M. DeC. Bano, L. Braco and C. Abad, *J. Chromatography*, 1988, **458**, 105.
66. A. Blume, W. Hubner and G. Messner, *Biochemistry*, 1988, **27**, 8239.
67. W. C. Wimley and S. H. White, *Biochemistry*, 1992, **31**, 12813.
68. P. V. LoGrasso, F. Moll III and T. A. Cross, *Biophys. J.*, 1988, **54**, 259.
69. J. A. Killian, L. K. Nicholson and T. A. Cross, *Biochim. Biophys. Acta*, 1988, **943**, 535.
70. J. A. Killian, K. U. Prasad, D. Hains and D. W. Urry, *Biochemistry*, 1988, **27**, 4848.
71. P. N. T. Unwin and R. Henderson, *J. Mol. Biol.*, 1975, **94**, 425.
72. J. Deisenhofer and H. Michel, *Science*, 1989, **245**, 1463.
73. H. Michel and J. Deisenhofer, *Curr. Top. Membr. Trans.*, 1990, **36**, 53.
74. M. S. Weiss, U. Abele, J. Weckesser, J. Welte, E. Schiltz and G. E. Schultz, *Science*, 1991, **254**, 1627.
75. W. Kuhlbrandt, *Quart. Rev. Biophys.*, 1992, **25**, 1.
76. M. E. Girvin and R. H. Fillingame, *Biochemistry*, 1993, **32**, 12167.
77. Y. Theriault, T. M. Logan, R. Meadows, L. Yu, T. Olejniczak, T. F. Holzman, R. L. Simmer and S. W. Fesik, *Nature*, 1993, **361**, 88.
78. B. Roux, R. Bruschweiler and R. R. Ernst, *Eur. J. Biochem.*, 1990, **194**, 57.
79. A. S. Arseniev, V. F. Bystrov, V. T. Ivanov and Y. A. Ovchinnikov, *FEBS Letters*, 1984, **165**, 51.
80. A. S. Arseniev, V. F. Barsukov and V. F. Bystrov, in *Chemistry of Peptides and Proteins*, Vol. 3, eds W. Voelter, E. Bayer, Y. A. Ovchinnikov and V. T. Ivanov, Walter de Gruyter & Co., Berlin, 1986, pp. 127-158.
81. V. F. Bystrov and A. S. Arseniev, *Tetrahedron*, 1988, **44**, 925.
82. Z. Zhang, S. M. Pascal and T. A. Cross, *Biochemistry*, 1992, **31**, 8822.
83. S. M. Pascal and T. A. Cross, *J. Biomol. NMR*, 1993, **3**, 495.
84. D. A. Langs, *Science*, 1988, **241**, 188.
85. B. A. Wallace and K. Ravikumar, *Science*, 1988, **241**, 182.
86. D. A. Langs, G. D. Smith, C. Courseille, G. Precigoux and M. Hospital, *Proc. Natl Acad. Sci. USA*, 1991, **88**, 5345.
87. R. R. Ketchum, W. Hu and T. A. Cross, *Science*, 1993, **261**, 1457.
88. K. Gawrisch, D. Ruston, J. Zimmerberg, V. A. Parsegin, R. P. Rand and N. Fuller, *Biophys. J.*, 1992, **6**, 1213.
89. E. G. Finer and A. Drake, *Chem. Phys. Lipids*, 1974, **12**, 1.
90. K. Gawrisch, W. Richter, A. Moeps, P. Balgavy, K. Arnold and G. Klose, *Studia Biophysica*, 1985, **108**, 5.
91. W. Braun, G. Wider, K. H. Lee and K. Wuthrich, *J. Mol. Biol.*, 1983, **169**, 921.
92. M. A. C. Morelli, A. Pastore and A. Motta, *J. Biomol. NMR*, 1992, **2**, 335.
93. A. R. Peters, N. Dekker, L. van den Berg, R. Boelens, R. Kaptein, A. J. Slotboom and G. H. de Hass, *Biochemistry*, 1992, **31**, 10024.
94. A. L. Lomize, V. Yu. Orechov and A. S. Arseniev, *Bioorg. Khim.*, 1992, **18**, 182.
95. P. A. McDonnell and S. J. Opella, *J. Magn. Reson.*, 1993, **102B**, 120.
96. F. Inagaki, I. Shimada, K. Kawaguchi, M. Hirano, I. Terasawa, T. Ikura and N. Go, *Biochemistry*, 1989, **28**, 5985.
97. S. M. Pascal and T. A. Cross, *Life Science Advances : Biophysics*, 1993, **12**, 91.
98. D. W. Urry, *Enzymes Biol. Membr. (2nd Ed.)*, 1985, **1**, 229.
99. D. W. Urry, J. T. Walker and T. L. Trapane, *J. Membr. Biol.*, 1982, **69**, 225.
100. D. N. Wang and W. Kuhlbrandt, *J. Mol. Biol.*, 1991, **217**, 691.
101. B. K. Jap, P. J. Walian and K. Gehring, *Nature*, 1991, **350**, 167.
102. I. Azpiazu, J. C. Gomez-Fernandez and D. Chapman, *Biochemistry*, 1993, **32**, 10720.
103. K. V. Ramanathan and S. J. Opella, *J. Magn. Reson.*, 1990, **86**, 227.
104. B. S. A. Kumar and S. J. Opella, *J. Magn. Reson.*, 1991, **95**, 417.
105. Q. Teng, M. Iqbal and T. A. Cross, *J. Am. Chem. Soc.*, 1992, **114**, 5312.

106. M. H. Frey, J. A. DiVerdi and S. J. Opella, *J. Am. Chem. Soc.*, 1985, **107**, 7311.
107. C. M. Gall, J. A. DiVerdi and S. J. Opella, *J. Am. Chem. Soc.*, 1981, **103**, 5039.
108. N. D. Lazo, W. Hu, K.-C. Lee and T. A. Cross, *Biochem. Biophys. Res. Comm.*, 1993, **197**, 904.
109. C. L. North and T. A. Cross, *J. Magn. Reson.*, 1993, **101B**, 35.
110. K.-C. Lee, W. Hu and T. A. Cross, *Biophys. J.*, 1993, **65**, 1162.
111. Y. Hiyama, C.-H. Niu, J. V. Silverton, A. Bavaso and D. A. Torchia, *J. Am. Chem. Soc.*, 1988, **110**, 2378.
112. J. N. S. Evans, R. J. Appleyard and W. A. Shuttleworth, *J. Am. Chem. Soc.*, 1993, **115**, 1588.
113. A. Christensen and J. Schaefer, *Biochemistry*, 1993, **32**, 2868.
114. N. D. Lazo, W. Hu and T. A. Cross, *J. Chem. Soc., Chem. Commun.*, 1992, 1529.
115. G. Harbison, L. W. Jelinski, R. Stark, D. A. Torchia, J. Herzfeld and R. G. Griffin, *J. Magn. Reson.*, 1984, **60**, 79.
116. C. J. Hartzell, T. K. Pratum and G. P. Drobny, *J. Chem. Phys.*, 1987, **87**, 4324.
117. M. Munowitz, W. P. Aue and R. G. Griffin, *J. Chem. Phys.*, 1982, **77**, 1686.
118. M. Linder, A. Hohener and R. R. Ernst, *J. Chem. Phys.*, 1980, **73**, 4959.
119. K. G. Valentine, A. L. Rockwell, L. M. Gierasch and S. J. Opella, *J. Magn. Reson.*, 1987, **73**, 519.
120. Q. Teng and T. A. Cross, *J. Magn. Reson.*, 1989, **85**, 439.
121. C. J. Hartzell, M. Whitefield, T. G. Oas and G. P. Drobny, *J. Am. Chem. Soc.*, 1987, **109**, 5966.
122. T. G. Oas, C. J. Hartzell, F. W. Dahlquist and G. P. Drobny, *J. Am. Chem. Soc.*, 1987, **109**, 5962.
123. W. Mai, W. Hu, C. Wang and T. A. Cross, *Protein Science*, 1993, **2**, 532.
124. T. G. Oas, C. J. Hartzell, T. J. McMahon, G. P. Drobny and F. W. Dahlquist, *J. Am. Chem. Soc.*, 1987, **109**, 5956.
125. R. E. Stark, L. W. Jelinski, R. J. Ruben, D. A. Torchia and R. G. Griffin, *J. Magn. Reson.*, 1983, **55**, 266.
126. C. Wang, Q. Teng and T. A. Cross, *Biophys. J.*, 1992, **61**, 1550.
127. D. A. Torchia, *Ann. Rev. Biophys. Bioeng.*, 1984, **13**, 125.
128. L. Mueller, M. H. Frey, A. L. Rockwell, L. M. Gierasch and S. J. Opella, *Biochemistry*, 1986, **25**, 557.
129. S. A. Vinogradova, A. O. Golubok, O. V. Kolomytkin and S. Ya. Tipisev, *Jetp Lett.*, 1990, **512**, 581.
130. L. K. Tamm and H. M. McConnell, *Biophys. J.*, 1985, **47**, 105.
131. Y. Kawamura, I. Sakurai, A. Ikegami and S. Iwayanagi, *Mol. Cryst. Liq. Cryst.*, 1981, **67**, 77.
132. J. Seelig, F. Borle and T. A. Cross, *Biochim. Biophys. Acta*, 1985, **814**, 195.
133. C. Rosenblatt, P. Yager and P. E. Schoen, *Biophys. J.*, 1987, **52**, 295.
134. J. B. Speyer, P. K. Sripada, S. K. Das Gupta, G. G. Shipley and R. G. Griffin, *Biophys. J.*, 1987, **51**, 687.
135. F. Scholz, E. Boroske and W. Helfrich, *Biophys. J.*, 1984, **45**, 589.
136. A. K. Dioumaev, D. S. Chernavskii, P. Ormos, G. Varo and L. Keszthelyi, *Biophys. J.*, 1992, **61**, 1194.
137. Y. Aubin and J. H. Prestegard, *Biochemistry*, 1993, **32**, 3422.
138. C. R. Sanders and J. P. Schwonek, *Biochemistry*, 1992, **31**, 8898.
139. C. R. Sanders and J. P. Schwonek, *Biophys. J.*, 1993, **65**, 1460.
140. T. Sosnick, S. Charles, G. Stubbs, P. Yau, E. M. Bradbury, P. Timmins and J. Trehwella, *Biophys. J.*, 1991, **60**, 1178.
141. L. Powers and N. A. Clark, *Proc. Natl Acad. Sci. USA*, 1975, **72**, 840.
142. L. Powers and P. S. Pershan, *Biophys. J.*, 1977, **20**, 137.

143. S. A. Asher and P. S. Pershan, *Biophys. J.*, 1979, **27**, 393.
144. I. C. P. Smith, *Chimia*, 1971, **25**, 349.
145. T. M. Rothgeb and E. Oldfield, *J. Biol. Chem.*, 1981, **256**, 6004.
146. T. A. Cross, R. R. Ketchum, W. Hu, K.-C. Lee, N. D. Lazo and C. L. North, *Bull. Magn. Reson.*, 1992, **14**, 96.
147. J. M. Pachence, R. Knott, I. S. Edelman, B. P. Schoenborn and B. A. Wallace, *Ann. NY Acad. Sci.*, 1984, 566.
148. C. G. Fields, G. B. Fields, R. L. Noble and T. A. Cross, *Int. J. Peptide Protein Res.*, **33**, 298.
149. M. Schnolzer and S. B. H. Kent, *Science*, 1992, **256**, 221.
150. W. Hu, K.-C. Lee and T. A. Cross, *Biochemistry*, 1993, **32**, 7035.
151. M. A. Keniry, H. S. Gutowsky and E. Oldfield, *Nature*, 1984, **307**, 383.
152. M. A. Keniry, A. Kintantar, R. L. Smith, H. S. Gutowsky and E. Oldfield, *Biochemistry*, 1984, **23**, 288.
153. R. A. Kinsey, A. Kintanar, E. Oldfield, *J. Biol. Chem.*, 1981, **256**, 9028.
154. J. L. Bowers and E. Oldfield, *Biochemistry*, 1988, **27**, 5156.
155. B. A. Lewis, G. S. Harbison, J. Herzfeld and R. G. Griffin, *Biochemistry*, 1985, **24**, 4671.
156. J. Herzfeld, C. M. Mulliken, D. Siminovitch and R. G. Griffin, *Biophys. J.*, 1987, **52**, 855.
157. H. J. M. de Groot, S. O. Smith, J. Courtin, E. van den Berg, C. Winkel, J. Lugtenburg, R. G. Griffin and J. Herzfeld, *Biochemistry*, 1990, **29**, 6873.
158. F. Creuzet, A. McDermott, R. Gebhard, K. van den Hoef, M. B. Spijker-Assink, J. Herzfeld, J. Lugtenburg, M. H. Levitt and R. G. Griffin, *Science*, 1991, **251**, 783.
159. L. K. Thompson, A. E. McDermott, J. Raap, C. M. van der Wielen, J. Lugtenburg, J. Herzfeld and R. G. Griffin, *Biochemistry*, 1992, **31**, 7931.
160. A. S. Ulrich, M. P. Heyn and A. Watts, *Biochemistry*, 1992, **31**, 10390.
161. T. A. Cross, P. Tsang and S. J. Opella, *Biochemistry*, 1983, **22**, 721.
162. T. A. Cross and S. J. Opella, *J. Mol. Biol.*, 1985, **182**, 367.
163. D. J. Tobias, M. L. Klein and S. J. Opella, *Biophys. J.*, 1993, **64**, 670.
164. B. Bechinger and S. J. Opella, *J. Magn. Reson.*, 1991, **95**, 585.
165. D. M. LeMaster and F. M. Richards, *Biochemistry*, 1988, **27**, 142.
166. P. A. McDonnell, K. Shon and S. J. Opella, *J. Mol. Biol.*, 1993, **233**, 447.
167. F. J. M. van de Ven, J. W. M. van Os, J. M. A. Aelen, S. S. Wymenga, M. L. Remerowski, R. N. H. Konings and C. W. Hilbers, *Biochemistry*, 1993, **32**, 8322.
168. J. D. J. O'Neil and B. D. Sykes, *Biochemistry*, 1988, **27**, 2753.
169. T. A. Cross, *Biophys. J.*, 1986, **49**, 124.
170. R. Smith and B. A. Cornell, *Biophys. J.*, 1986, **49**, 117.
171. R. Smith, D. E. Thomas, A. R. Atkins, F. Separovic and B. A. Cornell, *Biochim. Biophys. Acta*, 1990, **1026**, 161.
172. R. Smith, D. E. Thomas, F. Separovic, A. R. Atkins and B. A. Cornell, *Biophys. J.*, 1989, **56**, 307.
173. B. A. Cornell, F. Separovic, A. J. Baldassi and R. Smith, *Biophys. J.*, 1988, **53**, 67.
174. B. A. Cornell and F. Separovic, *Eur. Biophys. J.*, 1988, **16**, 299.
175. C. Wang, Master's Thesis, Florida State University, Tallahassee, FL, 1991.
176. P. V. LoGrasso, L. K. Nicholson and T. A. Cross, *J. Am. Chem. Soc.*, 1989, **111**, 1910.
177. Q. Teng, L. K. Nicholson and T. A. Cross, *J. Mol. Biol.*, 1991, **218**, 607.
178. A. W. Hing and J. Schaefer, *Biochemistry*, 1993, **32**, 7593.
179. A. W. Hing, S. P. Adams, D. F. Silbert and R. Norberg, *Biochemistry*, 1990, **29**, 4144.
180. A. W. Hing, S. P. Adams, D. F. Silbert and R. Norberg, *Biochemistry*, 1990, **29**, 4156.
181. R. S. Prosser, J. H. Davis, F. W. Dahlquist and M. A. Lindorfer, *Biochemistry*, 1991, **30**, 4687.
182. J. A. Killian, M. J. Taylor and R. E. Koeppe II, *Biochemistry*, 1992, **31**, 11283.

183. M. T. Brenneman and T. A. Cross, *J. Chem. Phys.*, 1990, **92**, 1483.
184. K.-C. Lee and T. A. Cross, *Biophys. J.*, 1994, **66**, 1380.
185. V. F. Bystrov, A. S. Arseniev, I. L. Barsukov and A. L. Lomize, *Bull. Magn. Reson.*, 1987, **8**, 84.
186. T. A. Cross and S. J. Opella, *J. Mol. Biol.*, 1982, **159**, 543.
187. S. K. Sarkar, C. E. Sullivan and D. A. Torchia, *Biochemistry*, 1985, **24**, 2348.
188. H. B. R. Cole and D. A. Torchia, *Chem. Phys.*, 1991, **158**, 271.
189. M. G. Usha, W. L. Peticolas and R. J. Wittebort, *Biochemistry*, 1991, **30**, 3955.
190. S.-W. Chiu and E. Jakobsson, *Biophys. J.*, 1993, **64**, A301.
191. B. Roux and M. Karplus, *Biophys. J.*, 1991, **59**, 961.
192. B. Roux and M. Karplus, *J. Phys. Chem.*, 1991, **95**, 4856.
193. M. D. Becker, D. V. Greathouse, R. E. Koeppe II and O. S. Andersen, *Biochemistry*, 1991, **30**, 8830.
194. C. M. Venkatachalam and D. W. Urry, *J. Comput. Chem.*, 1983, **4**, 461.
195. G. H. W. M. Meulendijks, T. Sonderkamp, J. E. Dubois, R. J. Nielsen, J. A. Kremers and H. M. Buck, *Biochim. Biophys. Acta*, 1989, **B979**, 321.
196. A. M. O'Connell, R. E. Koeppe II and O. S. Andersen, *Science*, **250**, 1256.
197. S. F. Scarlatta, *Biochemistry*, 1991, **30**, 9853.
198. M. deC. Bano, L. Braco and C. Abad, *FEBS Lett.*, 1988, **250**, 67.
199. K. J. Cox, C. Ho, J. V. Lomardi and C. D. Stubbs, *Biochemistry*, 1992, **31**, 1112.
200. L. Braco, C. Abad, A. Campos and J. E. Figueruelo, *J. Chromatogr.*, 1986, **353**, 181.
201. J. A. Killian, B. de Kruijff, C. J. A. Van Echteld, A. J. Verkleij, J. Leunissen-Bijvelt and J. DeGier, *Biochim. Biophys. Acta*, 1983, **728**, 141.
202. J. A. Killian, F. Borle, B. De Kruijff and J. Seelig, *Biochim. Biophys. Acta*, 1986, **854**, 133.
203. I. Pasquali-Ronchetti, A. Spisni, E. Casali, L. Masotti and D. W. Urry, *Biosci. Rep.*, 1983, **3**, 127-133.
204. C. J. A. Van Echteld, R. Van Stigt, B. De Kruijff, J. Leunissen-Bijvelt, A. J. Verkleij and J. De Gier, *Biochim. Biophys. Acta*, 1981, **648**, 287.
205. J. A. Killian, K. U. Prasad, D. W. Urry, B. De Kruijff, *Biochim. Biophys. Acta*, 1989, **978**, 341.

This Page Intentionally Left Blank

NMR Characterization of Complex Organic Resins

I-SSUER CHUANG and GARY E. MACIEL

*Department of Chemistry, Colorado State University, Fort Collins,
Colorado 80523, USA*

1. Introduction	170
2. Solid-state NMR	171
2.1. High-resolution solid-state NMR of dilute spins	172
2.1.1. Cross-polarization with high-power ^1H decoupling	172
2.1.2. Dynamic nuclear polarization	176
2.1.3. Large-volume magic-angle spinning (MAS) rotors	176
2.1.4. Magic-angle spinning (MAS)	176
2.1.5. ^{14}N - ^{13}C dipolar interaction under MAS	177
2.1.6. Linewidth of CP-MAS spectra of dilute spins	178
2.2. High-resolution solid-state ^1H NMR	178
2.3. Deuterium NMR	179
3. Solid-state NMR characterization of complex organic resins	179
3.1. Furfuryl alcohol resins	180
3.2. Phenol-formaldehyde resins	185
3.2.1. NMR studies of curing of phenolic resins	186
3.2.2. Thermal decomposition of cured phenolic resins	197
3.2.3. Stability of phenolic resin towards formalin, towards base and towards acids	201
3.3. Urea-formaldehyde resins	203
3.3.1. ^{13}C CP-MAS NMR studies of UF resin systems	205
3.3.2. ^{15}N CP-MAS studies of UF resin systems	218
3.3.3. NMR study of the stabilities of UF resin components towards hydrolytic treatments	222
3.4. Resins derived from isocyanates	225
3.4.1. Isocyanurate-rich and biuret-rich MDI-based resins	227
3.4.2. Phase separation and molecular motions in polyurethanes	239
3.5. Nylons	245
3.5.1. Solid-state ^{13}C NMR studies of nylons	245
3.5.2. Solid-state ^{15}N NMR studies of nylons	249
3.5.3. Solid-state ^2H NMR studies of nylons	256
3.6. Epoxy resins	258
3.7. Polyester resins	261
3.8. Cyanate resins	269

4. Resins in polymer blends and composite materials	271
4.1. Resins in polymer blends	272
4.2. Resins in composite materials	273
References	274

1. INTRODUCTION

Prior to the mid-1970s, NMR studies of polymer materials were concentrated mainly in two areas: the high-resolution NMR study of liquid polymer solutions, and broad-line NMR studies of solid polymers. For polymers soluble in liquid solvents and for some elastomers with a high degree of molecular mobility, the power and versatility of high-resolution liquid-sample NMR has contributed to significant advances in understanding polymer structure (e.g. configuration sequence, conformation and the immediate structural environment surrounding a specific nuclear site) and dynamic properties at the molecular level. For polymers with crosslinked networks, the insolubility in suitable solvents placed high-resolution liquid-sample NMR out of reach. The huge anisotropic interactions that are averaged out in the liquid state by rapid isotropic molecular motion are largely preserved in the solid state; hence, the NMR spectra of crosslinked polymers typically consist of broad, often featureless lines in the absence of solid-state line-narrowing techniques, and NMR studies were carried out by broadline and pulse-relaxation techniques prior to the mid-1970s. Even though broadline NMR studies provide some information on structure and mechanism of macromolecular dynamics through the analysis of second moments¹⁻⁴ and the activation energy of molecular motion through variable-temperature relaxation measurements,^{3,4} an understanding of the mechanism of network formation and the detailed chemical structures of crosslinked polymers is largely outside the ability of broad-line NMR techniques.

The combination of cross-polarization (CP)^{5,6} with high-power ¹H decoupling and magic-angle spinning⁷⁻¹² (CP-MAS)¹³ in the mid-1970s rendered the high-resolution solid-state NMR study of solid polymers a reality, especially with ¹³C in natural abundance. In general, NMR spectroscopy of solids has developed into a powerful tool for chemists during the past 10-20 years because of the ability to control (e.g. by pulse sequences) the time evolution of the nuclear spin systems, allowing one to choose the interaction(s) one wishes to highlight in a particular experiment. A recent review of developments in solid-state NMR has been published by Clayden.¹⁴

2. SOLID-STATE NMR

The Hamiltonian, H , of a multinuclear spin system can be expressed as follows:

$$H = H_Z + H_D + H_Q + H_\delta + H_J$$

where

H_Z = the Zeeman interaction of each nuclear spin with the applied static magnetic field;

H_D = the direct dipole-dipole interaction between nuclear spins;

H_Q = the quadrupolar coupling between a nuclear spin with $I > 1/2$ and the local electric field gradient;

H_δ = the chemical shielding caused by field-induced electron circulations near the nucleus;

H_J = the indirect spin-spin coupling (through electronic structure) between nuclear spins.

The dipolar interactions, quadrupolar coupling (for $I > 1/2$), chemical shielding and indirect spin-spin coupling are all orientation-dependent (anisotropic) interactions, although the anisotropy of the last of these is typically small for ^1H and ^{13}C . In the liquid state, the dipolar and quadrupolar interactions are averaged essentially to zero due to rapid isotropic molecular motion, giving rise to high-resolution spectra in which the isotropic chemical shifts (the time average of chemical shielding) and indirect spin-spin coupling (J-coupling) can be observed.^{3,4,15-21} The chemical shift of a specific nuclear site in a molecule and its J-coupling to other nuclei can provide a wealth of information, enabling one to determine the nuclear position and environment in that molecule, for example the configurational sequence and conformation.¹⁵⁻³¹ For a molecule undergoing chemical exchange, lineshape analysis provides information on the mechanism and rate of chemical exchange.³²⁻³⁵ Furthermore, the dipolar interactions can be manifested through relaxation, providing information on molecular motion^{3,4,18-22,35-38} and internuclear distances.^{19,20,31,39,40} Modern liquid-sample NMR spectroscopy uses versatile pulse sequences^{19,20,41-43} to explore various specific nuclear spin interactions and elucidates molecular structure and dynamics through a wide range of ingenious techniques, some of which can be extrapolated into high-resolution solid-state NMR.

Molecular mobilities are much less extensive in the solid state than in the liquid state, and residual anisotropic interactions such as dipolar interactions and chemical shift anisotropy are preserved in the solid state. In this regard, the information content is richer in solid-state NMR than in liquid-state NMR. However, "conventional" (prior to the mid-1970s) solid-state NMR spectra of even spin- $1/2$ nuclei are extremely broad because of dipolar

interactions and chemical shift anisotropy, and the valuable fine structure resulting from isotropic chemical shifts is obscured. In order to retrieve isotropic chemical shifts, the dipolar interactions and chemical shift anisotropies must first be removed. Furthermore, one can manipulate the spin system by various solid-state pulse sequences to retrieve specific anisotropic interactions and relate them to structure.¹⁴ There are many published articles^{5-14,44-57,59-63} and books^{3,4,19,21,26,58,64-73} that deal with solid-state NMR; here we summarize only some topics that are especially relevant to crosslinked polymers.

2.1. High-resolution solid-state NMR of dilute spins

For dilute spins such as ^{13}C (natural abundance 1.1%) and ^{15}N (natural abundance 0.37%), there are two difficulties to overcome, namely, the sensitivity and resolution. The development of Fourier transform (FT) NMR in the early 1970s^{19,20,74-78} resulted in a significant increase in NMR sensitivity relative to the continuous wave (CW) method, generating great advances in ^{13}C NMR spectroscopy. FT NMR not only boosts the sensitivity in NMR spectroscopy, but also dramatically enhances the versatility of time-domain experiments through various pulse sequences,^{19,20,41-43} a factor that accounts for a major part of the development in modern NMR spectroscopy. However, the FT NMR sensitivities of rare spins such as ^{13}C and ^{15}N still suffer from low natural abundance, low magnetogyric ratios and often long T_1 's. The application of cross-polarization (CP)⁶ by Pines, Gibby and Waugh in 1973 opened up a new avenue for solid-state ^{13}C NMR, an approach that was strengthened by Schaefer and Stejskal in 1976¹³ by combining CP with magic-angle spinning (MAS).

2.1.1. Cross-polarization with high-power ^1H decoupling

In the usual cross-polarization strategy the sensitivity of the dilute spin (e.g. ^{13}C), is enhanced by a process that transfers polarization from the abundant ^1H spin reservoir to ^{13}C spins by application of two resonant rf fields, $\mathbf{B}_{1\text{H}}$ and $\mathbf{B}_{1\text{C}}$, which satisfy the Hartmann-Hahn condition:⁵

$$\omega_{1\text{H}} = \omega_{1\text{C}}, \quad \text{where } \omega_{1\text{H}} = \gamma_{\text{H}}B_{1\text{H}} \text{ and } \omega_{1\text{C}} = \gamma_{\text{C}}B_{1\text{C}} \quad (1)$$

The pulse sequence for CP is shown in Fig. 1. After a 90° ^1H pulse, the ^1H spin system is "spin locked" along the direction of the ^1H rf field, $\mathbf{B}_{1\text{H}}$, by a 90° phase shift, and another rf field, $\mathbf{B}_{1\text{C}}$, is applied at the ^{13}C resonance frequency under the Hartmann-Hahn condition. During the CP contact period, τ , energy exchange takes place between ^1H and ^{13}C spin systems via the ^1H - ^{13}C dipolar coupling, and ^{13}C magnetization builds up along the

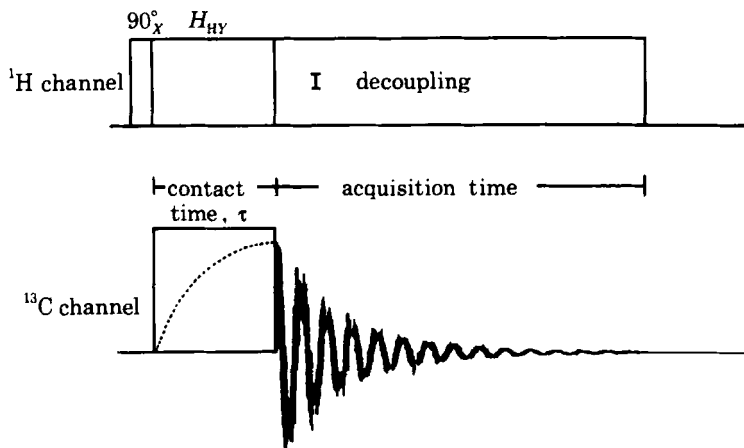


Fig. 1. Pulse diagram of the single-contact $^1\text{H} \rightarrow ^{13}\text{C}$ cross-polarization experiment. After a ^1H 90° pulse, ^1H magnetization is spin-locked by a 90° phase shift of the ^1H rf field, B_{1H} . During the CP contact period, $t_{cp} = \tau$, both sets of ^1H and ^{13}C spins are spin-locked with spin-locking fields B_{1H} and B_{1C} , respectively, under Hartmann–Hahn condition (see text). After the cross-polarization contact period, ^{13}C is monitored with ^1H decoupling.⁴⁶

direction of B_{1C} . The magnetization generated along B_{1C} is observed as a free induction decay (FID) by turning off B_{1C} . During acquisition of the ^{13}C signal, ^1H decoupling power is on.

Cross-polarization efficiency from the ^1H spin system to the ^{13}C spin system depends on the strength of ^1H – ^{13}C dipolar interaction, the duration of the CP contact time (τ) between ^1H and ^{13}C spins, and the rotating-frame ^1H spin-lattice relaxation time ($T_{1\rho}^H$). It is also found that the cross-polarization efficiency may depend on the magic-angle spinning rate (*vide infra*).⁷⁹ With ^{13}C in 1.1% natural abundance (or 0.37% for ^{15}N) and the rather high-density ^1H milieu in most organic polymers, and under the Hartmann–Hahn match condition (Eq. (1)), the cross-polarized ^{13}C NMR magnetization $I(\tau)$ after a CP contact time τ can be described by Eq. (2):⁶⁸

$$I(\tau) = \frac{I^*}{1 - \lambda} (1 - e^{-(1 - \lambda)\tau/T_{CH}}) e^{-\tau/T_{1\rho}^H} \quad (2)$$

where I^* is the ideal (full) cross-polarized ^{13}C magnetization and $\lambda = T_{CH}/T_{1\rho}^H$. T_{CH} is the ^1H – ^{13}C cross-polarization rate constant, which depends on the strengths of the ^1H – ^{13}C and ^1H – ^1H dipolar interactions and is roughly proportional to the inverse sixth power of ^1H – ^{13}C internuclear distances.^{68,80–84} T_{CH} and $T_{1\rho}^H$ values vary with different samples and they may have different values for different sets of ^{13}C and ^1H within each

sample; therefore, for a quantitative analysis, T_{CH} and $T_{1\rho}^H$ must be determined.

There are two common ways to measure $T_{1\rho}^H$ through ^{13}C magnetization in a CP experiment. In the first method, one measures ^{13}C magnetization generated in a set of experiments with different ^1H spin-lock times before performing cross-polarization,^{85,86} as shown in Fig. 2.⁸⁵ This method of measuring $T_{1\rho}^H$ is very straightforward and the results are easily extracted from the data. The second method is called the variable contact-time (VCT) experiment.^{86,87} In this approach, one monitors ^{13}C magnetization in a set of experiments with different CP contact times and then uses curve fitting to Eq. (2) to determine I^* , T_{CH} and $T_{1\rho}^H$. The advantage of the VCT experiment in obtaining $T_{1\rho}^H$ is that all three parameters, I^* , T_{CH} and $T_{1\rho}^H$, can be determined in the same set of experiments; the disadvantage of the VCT approach is that it can be difficult to extract the results from a computer fit of Eq. (2), if there is more than one structural component contributing to a given peak.

One of the important features of Eq. (2) is that I^* for ^{13}C is approximately four times what one would obtain at thermodynamic equilibrium via direct polarization (DP) by ^{13}C spin-lattice relaxation. That is, one can enhance ^{13}C magnetization ideally by a factor of four (the ratio of magnetogyric ratios of ^1H to ^{13}C). Another important feature of cross-polarization is that one can repeat the CP pulse sequence after five times T_1^H , because all of the ^{13}C polarization originates from ^1H reservoirs. For direct polarization (DP) ^{13}C NMR, that is, the acquisition of ^{13}C magnetization after a 90° pulse, one needs to wait five times T_1^C for the ^{13}C spin system to return to its thermodynamic equilibrium state. In general, T_1^C is much larger than T_1^H and is a bottleneck for ^{13}C sensitivity in DP ^{13}C NMR. If one wants only to achieve maximum signal-to-noise ratio within a fixed time, the optimal repetition time for the pulse sequence shown in Fig. 1 is roughly $1.25 \times T_1^H$.⁸⁵

For natural-abundance organic materials, the major dipolar interactions of dilute spins (e.g. ^{13}C and ^{15}N) are the heteronuclear dipole-dipole

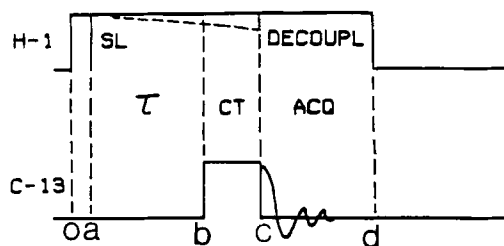


Fig. 2. Pulse diagram for the proton $T_{1\rho}$ relaxation experiment.⁸⁵

couplings with abundant spins (usually ^1H). The dipolar interactions between ^{13}C and ^1H can yield a field-independent linewidth of tens of kHz. High-power CW irradiation at the ^1H Larmor frequency during the detection of ^{13}C magnetization can remove the major dipolar interaction. Once the various dipolar couplings to and between ^1H spins are removed by high-power ^1H decoupling, the remaining dipolar interactions can be removed by magic-angle spinning in most cases (Section 2.1.4.), with the exception of the quadrupole-modulated ^{14}N - ^{13}C dipolar interaction (Section 2.1.5.).

Opella and coworkers⁸⁸ advanced a dipolar-dephasing pulse sequence to distinguish ^{13}C nuclei with weak ^1H - ^{13}C dipolar interactions from ^{13}C 's with strong ^1H - ^{13}C dipolar interactions. Figure 3 shows the pulse sequence for the dipolar-dephasing (interrupted-decoupling)^{88,89} CP experiment. During the dipolar-dephasing period (e.g. $50\ \mu\text{s}$), the ^1H rf field is off and the ^{13}C spin system is modulated by ^1H - ^{13}C dipolar interactions before the measurement of ^{13}C magnetization under high-power ^1H decoupling. For those ^{13}C spins with directly bonded protons in a rigid segment, the ^{13}C magnetization will decay dramatically before data acquisition, whereas for ^{13}C spins without directly bonded ^1H or for those ^{13}C spins with directly bonded ^1H but in a rather mobile moiety (such as rapidly rotating $-\text{CH}_3$), the ^{13}C magnetization will largely survive the dipolar-dephasing period. Comparison between CP spectra obtained with and without dipolar dephasing provides important structural information. There are several examples in

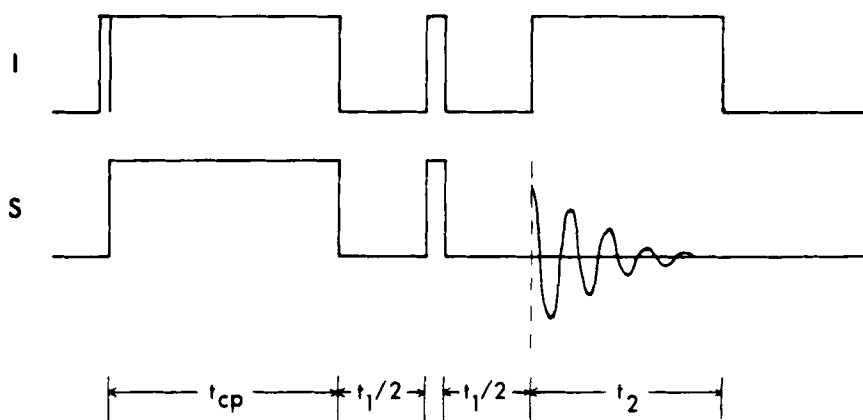


Fig. 3. Pulse sequence for the dipolar-dephasing CP-MAS NMR experiment. After a cross-polarization contact period $t_{\text{cp}} = \tau$ under the Hartmann-Hahn condition, both rf fields are turned off for a time t , in the middle of which a 180° pulse is applied to each channel; and finally, S-spin data acquisition with I decoupling occurs during t_2 .⁸⁹

later parts of this review demonstrating the power of the dipolar-dephasing CP experiment in elucidating the structures of complex polymers. Recent elaborations of ^1H - ^{13}C CP and depolarization strategies show excellent progress for distinguishing between rigid >C-H and >CH_2 moieties, that is, spectral editing.⁹⁰

2.1.2. *Dynamic nuclear polarization*

In some cases, a polymer system may contain unpaired electron spins. In this case it is possible to transfer the polarization from electron spins to ^1H spins and then apply ^1H - ^{13}C cross-polarization, or to transfer the polarization from electron spins to ^{13}C spin directly. The transfer of unpaired electron magnetization to nuclear spins involves the application of microwave irradiation at or near the electron-spin Larmor frequency; the process is called dynamic nuclear polarization (DNP).⁹¹⁻⁹³ In favourable cases, the gain in ^{13}C intensity from DNP far exceeds that obtained from just ^1H - ^{13}C cross-polarization. DNP has been utilized to investigate coals,⁹⁴ polymers,⁹⁵ polymer blends,⁹⁵⁻¹⁰¹ and chemical-vapour-deposited films.¹⁰²

2.1.3. *Large-volume magic-angle spinning (MAS) rotors*

Due to ^{15}N 's low natural abundance (0.37%) and low magnetogyric ratio (about 0.1 that of ^1H), ^{15}N is in most cases not suitable for CP-MAS studies unless ^{15}N -enriched materials are employed.¹⁰³⁻¹¹⁸ However, there are fragmentary recent reports of examples of natural-abundance ^{15}N CP-MAS measurements on some nitrogen-rich samples.^{106,119-121}

Large-volume ($2.5\text{--}6.5\text{ cm}^3$) magic-angle spinning (MAS) systems^{119,122-129} have made natural-abundance ^{15}N CP-MAS studies of urea-formaldehyde,¹²³ polyurethane¹²⁴ and hydridopolysilazane (HPZ) resins¹²⁵ possible within a reasonable experiment time.

2.1.4. *Magic-angle spinning (MAS)*

The magnetic shieldings of nuclear spins generated by field-induced circulations of electrons are anisotropic, and the anisotropy manifested in the solid state is proportional to the applied static magnetic field, \mathbf{B}_0 . For ^{13}C nuclei involved in π -bonds in hydrocarbons, the anisotropy of magnetic shielding (chemical shift anisotropy, or CSA) can extend to 200 ppm in width;¹³⁰ therefore, the ^{13}C NMR spectrum of a static hydrocarbon powder can have a width up to 10 kHz at a static magnetic field strength of 4.7 T. Typically, CSA powder patterns for ^{13}C in different structural environments within a given polymer overlap in the absence of MAS and cannot be unravelled clearly without this technique. When a solid sample is spun around an axis at an angle θ relative to the external magnetic field \mathbf{B}_0 , the chemical shift

anisotropy is scaled down to $(1/2)(3\cos^2\theta - 1)$. If θ is equal to $(\cos^{-1}1/\sqrt{3})$, the magic angle, then the chemical shift anisotropy is averaged to zero and the chemical shift tensor averages to the isotropic chemical shift. The setting of the spinning angle within $\pm 0.1^\circ$ of the magic angle (about 54.7°) can be achieved by using the ^{79}Br NMR signal of KBr ;¹³¹ therefore, the residual linebroadening introduced by an error in the magic-angle setting is usually insignificant for polymers, in comparison to other sources of broadening, for example dispersion of isotropic chemical shifts due to structural heterogeneities.

If the MAS rate is smaller than the width (in Hz) of the chemical shift anisotropy, the signal due to the isotropic chemical shift of each nuclear spin environment will be accompanied by spinning sidebands, which result from a modulation of the CSA by MAS. Even though the spinning sideband patterns of a MAS NMR spectrum can be used to determine the principal values of chemical shielding tensors in favourable (simple) cases,^{132,133} in most MAS NMR applications to resins, spinning sidebands are either suppressed by various pulse sequences¹³⁴⁻¹³⁸ or moved totally out of the region of interest by sufficiently rapid MAS. For a static magnetic field strength of 4.7 T, a MAS spinning rate of about 6.5 kHz is needed for most ^{13}C MAS NMR experiments of organic solids that contain unsaturated moieties, if one wishes to move the sidebands out of harm's way. Accordingly, at a strength higher than 4.7 T, a spinning rate higher than 6.5 kHz is needed. Even though it is possible to perform MAS at much higher spinning rates,¹³⁹ there are uncertainties associated with obtaining quantitative CP-MAS NMR spectra at high MAS spinning rates.⁷⁹ However, there have been recent developments, especially modulated CP match conditions,^{140e} that appear to alleviate this problem.¹⁴⁰ In any case, fast MAS usually requires small samples, which reduces the anticipated sensitivity advantage associated with using the higher magnetic fields that require faster MAS speeds.

2.1.5. ^{14}N - ^{13}C dipolar interaction under MAS

Qualitatively speaking, when the quadrupole coupling constant of a nuclear spin with $I \geq 1$ is substantial in comparison to the Larmor frequency of the quadrupolar nucleus, then the quantization of this quadrupolar nucleus is no longer exactly along \mathbf{B}_0 , and MAS does not completely average dipolar interactions between other nuclear spins and this nucleus. The nuclear electric quadrupole effect on dipolar interactions has been described in detail both for static samples¹⁴¹⁻¹⁴³ and for magic-angle spinning.¹⁴⁴⁻¹⁵⁶ One finds that there is a residual linebroadening or splitting in the MAS spectrum due to this quadrupolar effect, which becomes smaller at a higher applied magnetic field, because the quadrupolar effect is a perturbation. This problem is most often encountered in the effects of ^{14}N ($I = 1$) on ^{13}C

spectra. As will be seen below (Sections 3.3. and 3.4.) in some examples, a field of 4.7 T is a reasonable compromise field for most nitrogen-containing organic polymers. Of course, one can substitute ^{14}N by ^{15}N ($I = 1/2$) synthetically, but this process is practical only if one also wants to perform ^{15}N CP-MAS NMR experiments.

2.1.6. Linewidth of CP-MAS spectra of dilute spins

The linewidths of ^{13}C CP-MAS spectra of organic solids are roughly 10 to 100 times larger than those typically achieved in liquid-sample ^{13}C NMR.¹⁵⁷ VanderHart, Earl and Garroway have discussed the linebroadening mechanisms of ^{13}C CP-MAS spectra in great detail.¹⁵⁷ Macromolecules may exist as mixtures of a large number of conformers of comparable energies and the spectrum obtained may represent the superposition of the resonances of all the various conformers in the case of molecular motion that is slow on the NMR timescale.¹⁵⁸ Molecular packing in the solid state may modify bond angles or alter hydrogen bonding, which can produce sizeable chemical shift effects.¹⁵⁹ Furthermore, in cross-linked polymers, there is a substantial heterogeneity in configurational sequences. Because isotropic chemical shifts are sensitive to such issues as conformation, bond angles and configurational sequences,^{21-24,27-31,69,70,158} the linewidths of ^{13}C NMR spectra of solid polymers are generally large (e.g. 5–500 Hz) even under well-executed high-power ^1H decoupling and magic-angle spinning. For nitrogen-containing polymers, we expect to see some additional ^{13}C linewidth contribution from residual ^{14}N – ^{13}C dipolar interactions under magic-angle spinning (Section 2.1.5.).

2.2. High-resolution solid-state ^1H NMR

The dominant non-Zeeman interaction for ^1H spins in solid samples is the homonuclear ^1H – ^1H dipolar interaction. The counterpart of heteronuclear dipolar decoupling for homonuclear ^1H – ^1H dipole couplings is an appropriate multiple-pulse sequence of the type first introduced by Waugh and coworkers, for example WAHUA,¹⁶⁰ MREV-8,^{161,162} and BR-24,¹⁶³ among many others. The combination of MAS (for averaging the ^1H CSA) and one of these multiple-pulse sequences is referred to as CRAMPS (for combined rotation and multiple-pulse spectroscopy);^{164–168} this is a high-resolution ^1H solid-state NMR technique, which yields isotropic ^1H chemical shift spectra with linewidths in Hz that are comparable to those achieved in ^{13}C CP-MAS experiments. Equipped with this high-resolution ^1H CRAMPS approach, it is possible to study ^1H spin diffusion in polymers (and therefore the domain size or intimacy between polymers in polymer blends) by one-dimensional (1D) or 2D techniques.^{169–173}

2.3. Deuterium NMR

Nuclei with $I > 1/2$ have nonzero nuclear electric quadrupole moments, and the quadrupole coupling to the electric field gradient at the nuclear site typically produces a large linebroadening in the NMR spectrum of a static powder. The full linewidth of the deuterium (^2H) NMR spectrum of a solid powder can go up to 250 kHz, yielding an effect that is a sensitive measure of molecular orientation, order and motion. Since ^2H has a very low natural abundance of 0.015%, it requires isotopic enrichment in almost all ^2H NMR applications. On the other hand, this low natural abundance can be an advantage in the selectivity that can be achieved: with ^2H enrichment at only a specific site, one can probe individual groups or segments of microscopic domains. In contrast to other spectroscopic labelling methods, for example based on ESR or fluorescence observation, selective ^2H enrichment has a negligible effect on the properties of the sample.

Molecular geometry or orientation and the type and rate of molecular motion determine the dominating ^2H quadrupole coupling, which can be directly related to specifically labelled C- ^2H bonds in organic materials.^{49,57,121,174-181} Because the linewidth and lineshape of a ^2H NMR spectrum are sensitive to the type and rate of molecular motion, broadband ^2H NMR spectroscopy has become a prominent technique for examining the molecular motions of both small molecules and polymers. The usual strategy is to compare the observed ^2H line shape to those calculated for specific, trial motional models. In the past several years, ^2H NMR spectroscopy has found a variety of applications in the study of polymer blends,¹⁸² hard and soft segments of block copolymers,¹⁸³⁻¹⁸⁵ polymer chain orientation¹⁸⁶ and partially ordered systems.¹⁸⁷⁻¹⁸⁹

3. SOLID-STATE NMR CHARACTERIZATION OF COMPLEX ORGANIC RESINS

In preparing this review, we have used the following description as a working definition of an "organic resin": a macromolecular organic system synthesized by condensation polymerization of a specific set of monomers, with perhaps some diversity in the primary structure, including various degrees of crosslinking. The properties of solid polymers depend on their molecular structures, phase behaviour, morphology, molecular order and molecular motions, and the end use of most complex organic polymer materials is in the solid state. Information on the structure of a cured resin and the curing process of a resin is important for understanding its performance and improvement. Reactions during the curing process may differ from those observed in the early stages of resin formation because of different conditions (e.g. the presence of a curing agent, catalysis and heat

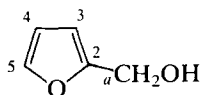
during the curing), and it is important to have reliable non-destructive techniques for probing the microscopic and molecular structural parameters of such polymers in the solid state. For polymer blends and composite materials, the proximity of the components at the molecular level is one of the most important factors in determining their properties; therefore, the most reliable techniques for the investigation of such materials must be based on measurements in the solid states. For all of these reasons, one needs reliable techniques to investigate the structure and formation of a cured resin.

^{13}C (and/or ^{15}N) CP-MAS NMR spectroscopy provides high-resolution solid-state techniques that can accurately determine ^{13}C chemical shifts, which can be correlated with molecular structure in the solid state. T_1 and $T_{1\rho}$ measurements provide information on motion in the ranges of 50–200 MHz (from T_1 measurement) or 30–100 kHz (from $T_{1\rho}$)^{3,4,18–22,35–38,56,70,85,174,190–194} that can be attributed to some specific segment of the polymer molecule through the observed ^{13}C chemical shift. The influence of ^1H spin diffusion on the T_1 and $T_{1\rho}$ values of different components of a polymer blend can provide very useful information regarding the intimacy of these components.^{51,195–208} Recently, ^{13}C NMR under rotor-synchronized magic-angle spinning has provided an opportunity to study molecular order and dynamics of partially ordered polymer samples.^{57,209–216} High-resolution solid-state NMR is one of the very few techniques that one can use to characterize the type, number and distribution of crosslinks in a complex resin and details of the curing process.

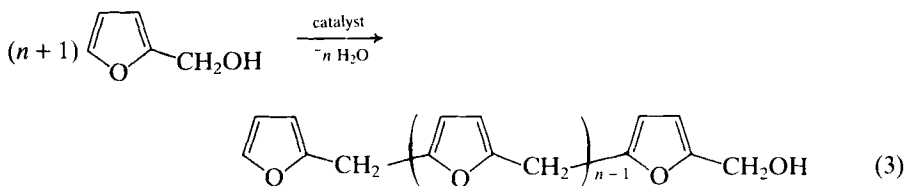
Because of the wide scope of organic resins, we restrict our attention in this review to relatively detailed discussions of the NMR study of eight resin systems and a few examples of resins in polymer blends and composite materials. For convenience, some of the detailed discussions are based on studies from this laboratory. This review is meant to be *representative*, rather than *comprehensive*; we hope we have *represented* all of the most important types of NMR studies of organic resins.

3.1. Furfuryl alcohol resins

Resins prepared from furfuryl alcohol (I) are of considerable technological interest.^{217–220} The initial formation of uncured furfuryl alcohol resins is believed^{217–219} to occur via the formation of methylene linkages ($-\text{CH}_2-$ of II) according to Eq. (3),

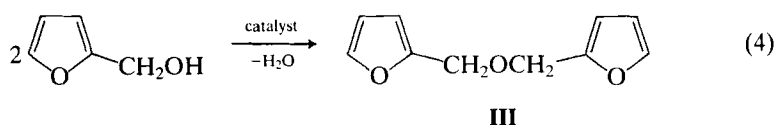


I



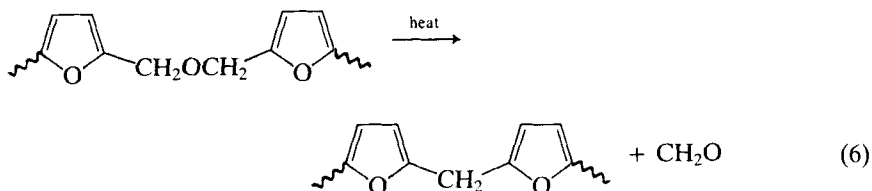
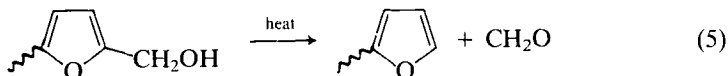
II

and/or the formation of dimethylene ether linkages ($\text{-CH}_2\text{OCH}_2\text{-}$ of **III**) according to Eq. (4).

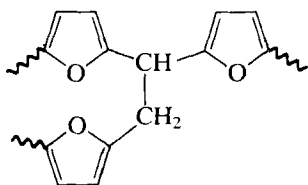


III

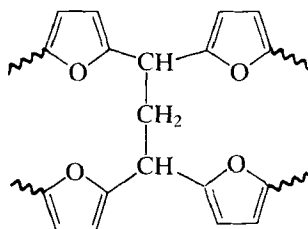
However, the curing process(es) of uncured furfuryl alcohol resins initiated by heating is more poorly understood. During the curing of furfuryl alcohol resins, formaldehyde is evolved, as indicated by Eqs (5) and (6).^{220,221}



In 1963, based on evidence from IR spectroscopy, Conley and Metil²²² suggested that crosslinking reactions in the curing can occur via the coupling of methylol groups ($\text{-CH}_2\text{OH}$) or formaldehyde with methylene linkages **II**, forming structures **IV** and **V**.

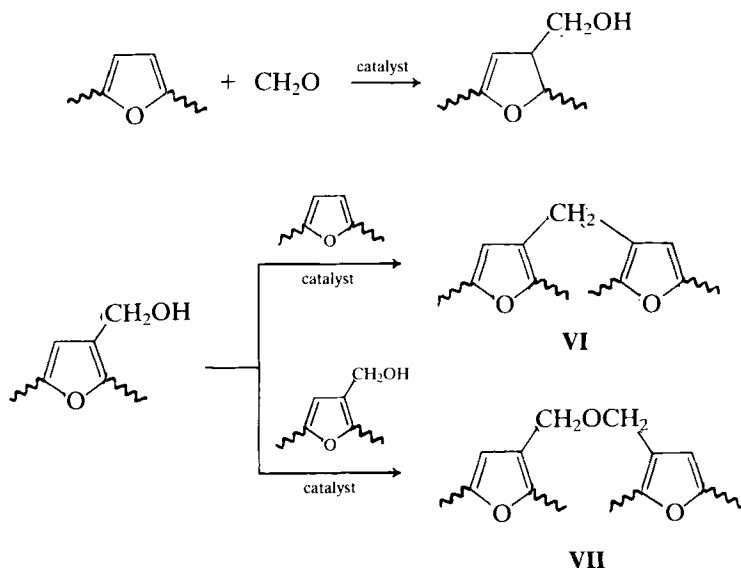


IV



V

On the other hand, in 1971 Wewerka²²¹ suggested that the curing process involves the 3,4 positions of the furan rings of the furfuryl alcohol resins as follows:



Because of the insoluble character of cured furfuryl alcohol resins, it had been difficult to provide clear-cut evidence on the Wewerka or Conley and Metil models.

In 1982, Maciel, Chuang and Myers²²³ utilized the ^{13}C CP-MAS technique to investigate a cured furfuryl alcohol resin. Figure 4 shows ^{13}C CP-MAS spectra of the resin with and without a $100\ \mu\text{s}$ interrupted-decoupling period. Peaks at about 29, 109 and 151 ppm were assigned to methylene linkages, unsubstituted 3,4 positions, and substituted 2,5 positions of **II**, **IV** and **V**, respectively. The peak at about 38 ppm can be assigned to >C-H moieties of **IV** and **V**. Resonances of the substituted 3 or 4 position of **VI** or **VII** would have a ^{13}C chemical shift of about 120 ppm and could survive a $100\ \mu\text{s}$ interrupted-decoupling (Fig. 4b). The results of Fig. 4 clearly rule out the possible existence of **VI** and **VII** in this cured furfuryl alcohol resin. Figure 4 also indicates that there are no methylol groups or dimethylene ether linkages in this cured furfuryl alcohol resin (*vide infra*). Therefore, the ^{13}C CP-MAS technique provides strong evidence in support of the curing process of furfuryl alcohol resins suggested by Conley and Metil.²²²

In a follow-up experiment, Chuang, Maciel and Myers²²⁴ examined the furfuryl alcohol resin polymerized from furfuryl alcohol (**I**) under nitrogen with a 0.42% solution of H_3PO_4 in H_2O as the polymerization catalyst. The ^{13}C CP-MAS spectrum of this uncured furfuryl alcohol resin is shown in Fig.

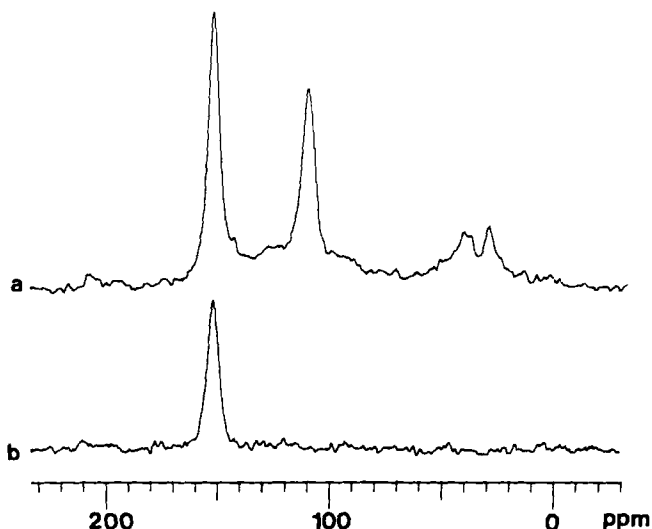
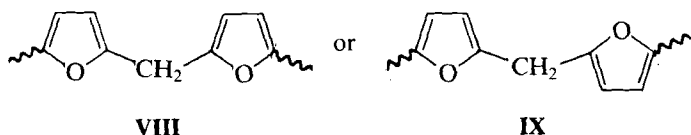


Fig. 4. (a) 15.0 MHz ^{13}C CP-MAS spectrum of a cured furfuryl alcohol resin. (b) ^{13}C CP-MAS spectrum of the same resin obtained with a $100\ \mu\text{s}$ dipolar-dephasing period.²²³

5a. This uncured furfuryl alcohol resin does not contain any appreciable concentrations of methylol groups ($-\text{CH}_2\text{OH}$, liquid-sample ^{13}C chemical shift: 57 ppm)²²⁵ or dimethylene ether linkages ($-\text{CH}_2\text{OCH}_2-$, liquid-sample ^{13}C chemical shift: 64 ppm).²²⁵ Therefore, the polymerization of furfuryl alcohol occurs mainly by the formation of methylene linkages under acidic conditions (Eq. (3)). The formation of dimethylene ether linkages (Eq. (4)) is either unimportant, or the disappearance of dimethylene ether linkages (Eq. (6)) is at least as fast as its formation. Figure 5a shows only slight evidence of the existence of methylene glycol (HOCH_2OH) and its oligomers (84–92 ppm region); however, ^{13}C CP-MAS NMR is not an efficient way to observe mobile species such as methylene glycol or its small oligomers.

The spectrum in Fig. 5a also shows doublet patterns around 108 ppm and 151 ppm. These doublet patterns can be explained in terms of the two different ring-to-ring conformations shown as structures **VIII** and **IX**. This kind of conformational differentiation is absent in short chains that have



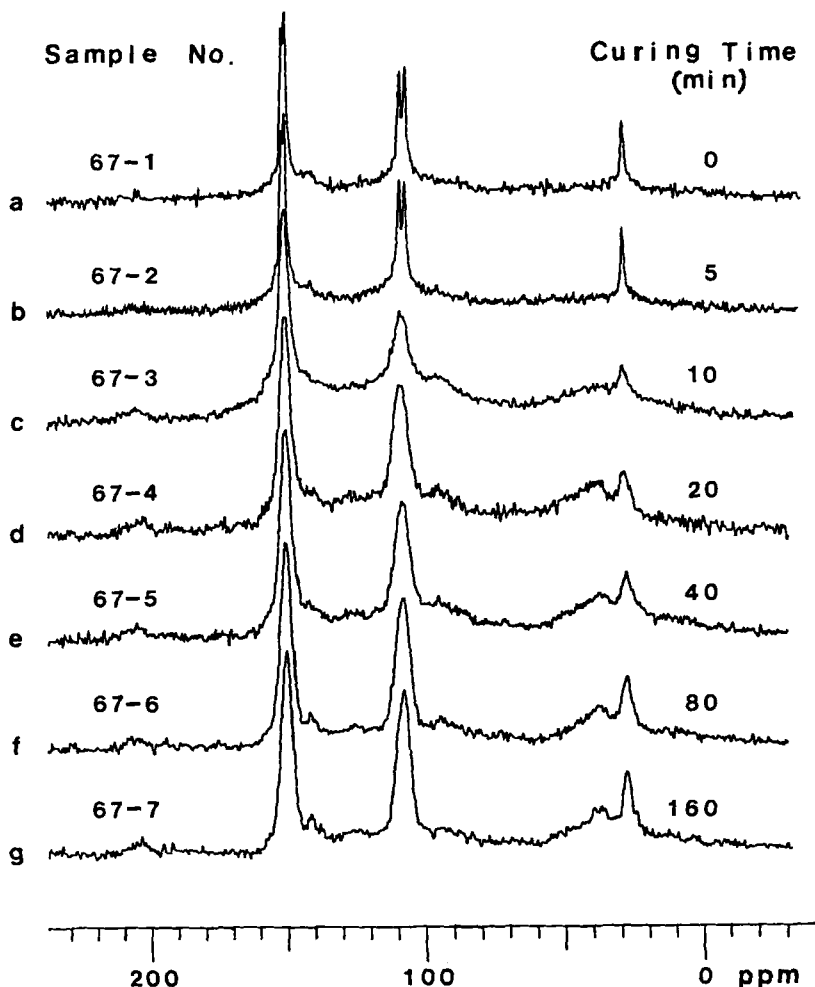


Fig. 5. 15.0 MHz ^{13}C CP-MAS spectra of furfuryl alcohol resins with seven different curing times as shown. CP contact time = 1 ms; repetition time = 1 s.²²⁴

been studied in the liquid state, where rapid conformational exchange that cannot occur in more rigid solids is present.

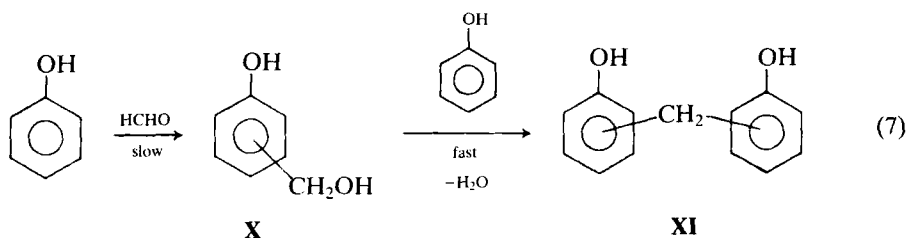
The uncured furfuryl alcohol resin represented in Fig. 5a was neutralized by addition of a 0.20% aqueous solution of NaOH and then cured to varying extents by adding 3% $\text{BF}_3 \cdot \text{NH}_2\text{C}_2\text{H}_5$ to the resin and heating under nitrogen at 100°C for varying times. ^{13}C CP-MAS spectra of six different furfuryl alcohol resins with different curing times are shown in Fig. 5b-g. The two main spectral trends from Fig. 5a-g are: (a) as curing proceeds, all peaks start to broaden and the doublets around the 108 and 151 ppm peaks

start to merge, which reflects the increasing structural heterogeneity brought about by the crosslinking process; (b) as curing progresses, a broad peak at about 36–44 ppm starts to appear. The appearance of ^{13}C NMR intensity in the 36–44 ppm region in Fig. 5c and d indicates that the main crosslinking process is the formation of $\geq\text{CH}$ moieties of species **IV** and/or **V**, a conclusion suggested by Conley and Metil²²² and confirmed by Maciel *et al.*²²³

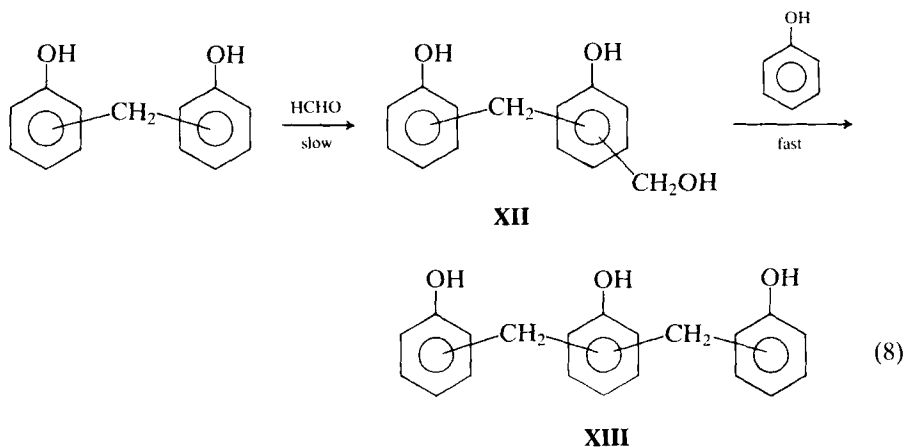
3.2. Phenol-formaldehyde resins

Phenol-formaldehyde (or phenolic) resins^{226–228} prepared from the condensation of phenol and formaldehyde are apparently the very first completely synthetic polymers ever intentionally synthesized. Although the curing of phenol-formaldehyde resins has received a great deal of attention, most of the studies prior to 1980 suffered from experimental limitations, chiefly due to solubility limitations for liquid-sample analysis. Solution-state ^{13}C NMR has proved to be a useful tool for the determination of structures of *soluble* phenolic resins^{229–240} and related materials.^{241–243}

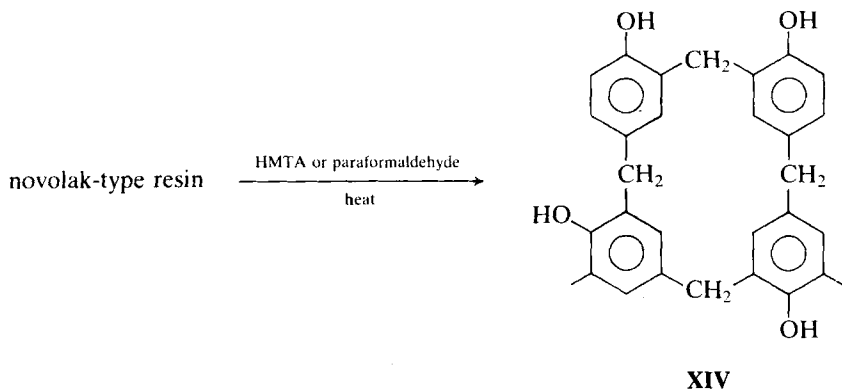
In general, there are two types of precured phenolic resins, the difference depending on the feed ratio of phenol to formaldehyde and on the pH of the preparation. Novolak resins are obtained by the reaction of phenols and formaldehyde under acidic conditions with molar excess of phenols. Due to the slowness of the addition of formaldehyde to phenols, novolaks contain no reactive methylol ($-\text{CH}_2\text{OH}$) groups and therefore cannot readily condense by themselves on heating. When mixed and heated with hexamethylenetetramine (HMTA, structure of the adamantane type with $\geq\text{N}$ -replacing $\geq\text{C}-\text{H}$), or paraformaldehyde, they become crosslinked, insoluble cured resins. The formation of cured novolak resins was proposed as follows:



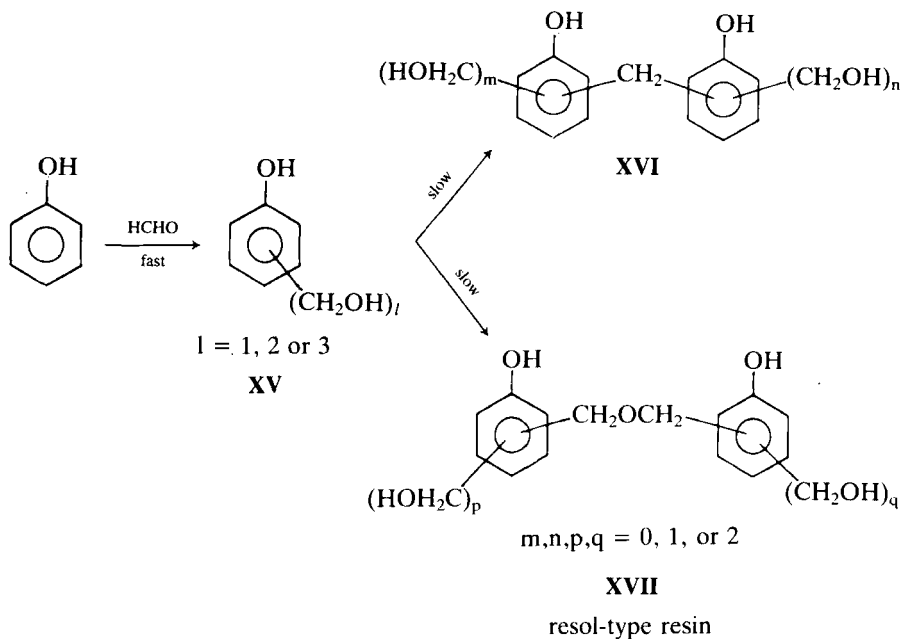
Owing to the orientation effect of hydroxyl groups in substitution reactions on phenols, the methylol groups and methylene linkages in **X–XIV** are *ortho* or *para* to the hydroxyl groups on the ring.



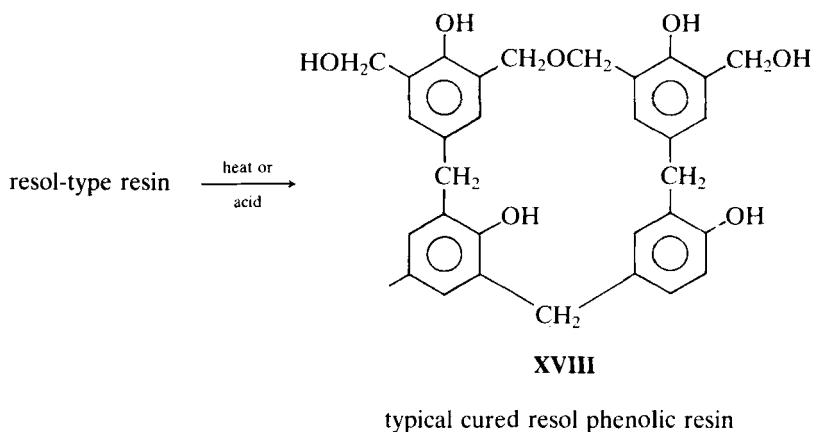
typical novolac-type resin



Resol-type phenolic resins are obtained by the reaction of phenols and excess formaldehyde under basic conditions. The initial substitution reaction with phenols is faster than the subsequent condensation reaction between substituted phenol rings:



Resol-type resins contain methylol ($-\text{CH}_2\text{OH}$) groups, methylene linkages and occasionally some dimethylene ether linkages ($-\text{CH}_2\text{OCH}_2-$) at positions *ortho* or *para* to the hydroxyl groups of phenolic rings. The curing of resol-type phenolic resins is carried out by heating or acidification:



3.2.1. NMR studies of curing of phenolic resins

In 1980, Fyfe, Rudin and Tchir²⁴⁴ prepared cured resol-type phenolic resins from phenol and natural-abundance formaldehyde, and from phenol and

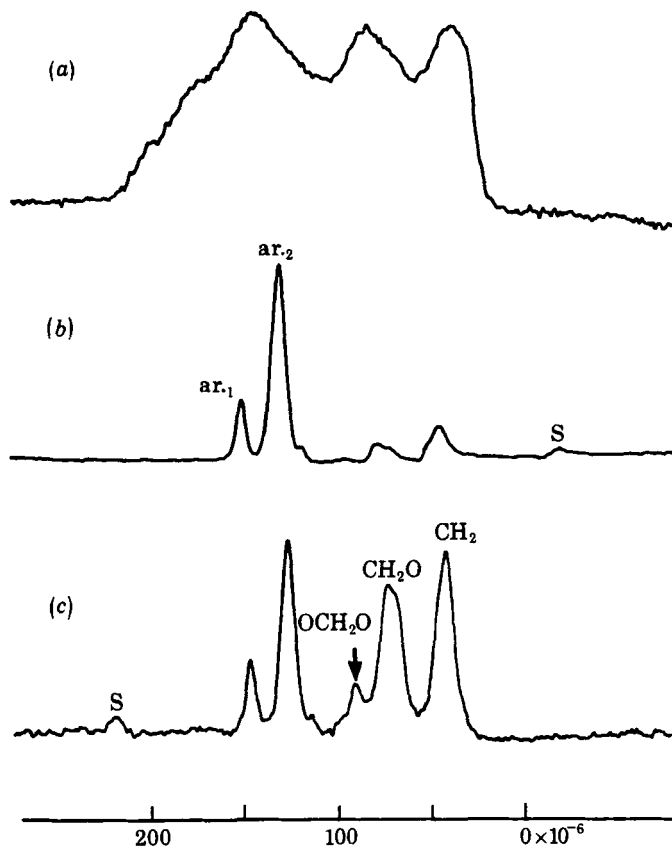


Fig. 6. 22.6 MHz ^{13}C NMR spectra of a cured, solid phenolic resin. (a) Static sample; CP contact time = 1 ms; repetition time = 2 s; number of accumulations = 3000. (b) Magic-angle spinning at 3.6 kHz; CP contact time = 1 ms; repetition time = 2 s; number of accumulations = 2000. (c) Conditions as in (b) except that 500 accumulations were averaged and the sample was prepared by using formaldehyde ^{13}C enriched to *c.* 5%. The small peaks marked S denote spinning sidebands. The chemical shifts are relative to TMS.⁴⁶

$\sim 5\%$ ^{13}C -enriched formaldehyde under the same conditions. Solid-state CP ^{13}C NMR spectra of these resins are shown in Fig. 6. The resolution achieved by magic-angle spinning (cf. Fig. 6a and b) allows the assignment of the resonances in Fig. 6b. The resonances due to carbons of phenolic rings (Ar_1 is for the carbon bearing the phenol hydroxyl group and Ar_2 for the remaining ring carbons) are well separated from those assigned to the aliphatic carbons. The assignment of the high-shielding (low-frequency) signals to the formaldehyde-derived groups is confirmed by the use of 5%

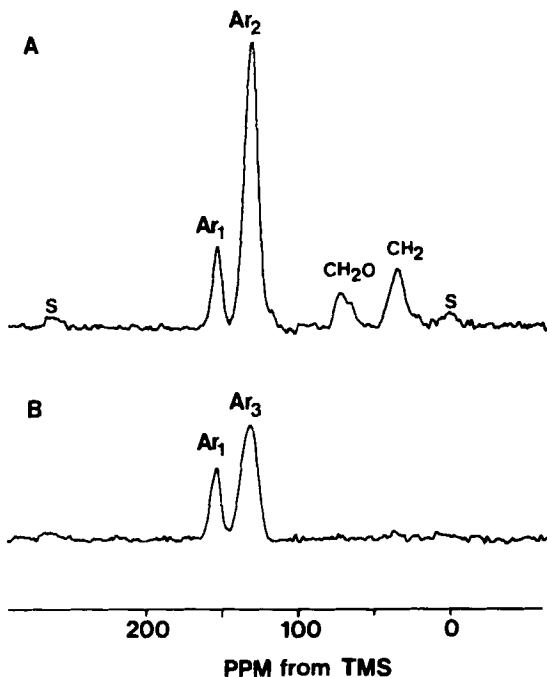


Fig. 7. Solid-state ^{13}C NMR spectra of a solid rotor of a cured resol-type phenolic resin similar to that used for Fig. 6. (A) Magic-angle spinning, 1-ms cross-polarization time, 2-s repetition time, 500 accumulations. (B) Conditions as in (A) except that during the 50- μs period before data acquisition, the proton decoupler was gated off for the first 40 μs .²⁴⁴

enriched $^{13}\text{CH}_2\text{O}$ as a starting material and is indicated in Fig. 6c. The ^{13}C CP-MAS spectra give a direct measure of the nature and the extent of the crosslinking in the cured phenolic resin network.

Fyfe *et al.*²⁴⁴ used the dipolar-dephasing ^{13}C CP-MAS technique to measure the total substitution in the phenol rings and the extent of crosslinking. Figure 7 shows the ^{13}C CP-MAS spectra of a cured resol-type phenolic resin with and without a 40 μs dipolar-dephasing time before ^{13}C signal acquisition. The peak arising from substituted aromatic carbons—Ar₁ for the hydroxyl-bearing phenol carbon and Ar₃ for *ortho*- and/or *para*-substituted phenol ring carbons—can survive the 40 μs dipolar-dephasing period, as indicated in Fig. 7b. A comparison of the intensities assigned to Ar₂ and Ar₃ in Fig. 7a and b gives an NMR measure of the total substitution in the phenol ring.

Fyfe and coworkers^{46,244} also employed ^{13}C CP-MAS NMR to investigate a series of phenolic resins with increasing degree of cure, and concluded

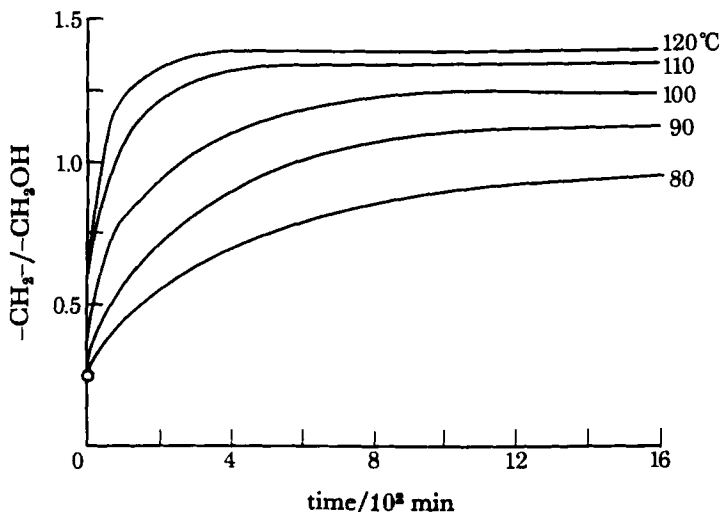


Fig. 8. The curing process of solid phenolic resins as monitored by the ratio of methylene ($-\text{CH}_2-$) to methylol ($-\text{CH}_2\text{OH}$) peaks in the ^{13}C CP-MAS spectrum as a function of curing time and temperature. The sample was cured as a thin film between plates to ensure accurate temperature control.⁴⁶

qualitatively that the curing process involves the conversion of methylol groups to methylene linkages; that is, Eqs (7) and (8). Figure 8 shows the progress of curing of a solid phenolic resin as monitored by the ratio of methylene to methylol peaks as a function of curing time and curing temperature. The degree of crosslinking cannot be accurately determined by this ratio (*vide infra*).

Maciel and coworkers²⁴⁵ investigated novolak-type phenolic resins by ^{13}C CP-MAS at three different static magnetic field strengths—1.41, 2.35 and 4.70 T. They found that there was no substantial gain in resolution with increasing field strength; therefore, the broad lines of these spectra reflect the heterogeneous nature of conformations and linkages in the resins. Spectra obtained with 1, 2 and 4 ms CP contact times show that the *relative* peak intensities within each spectrum are independent of CP contact time over this range. Bryson *et al.*²⁴⁵ also investigated the curing of two novolak resins with 10% HMTA by ^{13}C CP-MAS. Figure 9 shows the effect of curing time on the ^{13}C CP-MAS spectrum of a novolak phenolic resin. As discussed above, novolak resins do not contain methylol groups ($-\text{CH}_2\text{OH}$, ^{13}C chemical shift 62 ppm). Each spectrum in Fig. 9 shows a peak at about 117 ppm that is assigned to unsubstituted carbons *ortho*- and/or *para*- to the phenolic hydroxyl group, and a peak centred at about 130 ppm that is assigned to methylene-substituted carbons *ortho* and/or *para* to a phenolic hydroxyl or unsubstituted carbons *meta* to a phenolic hydroxyl. From the

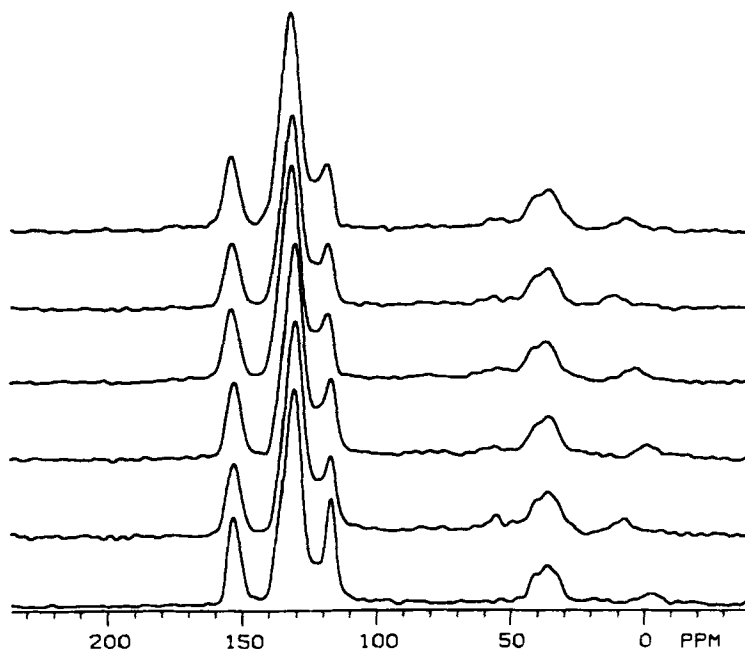
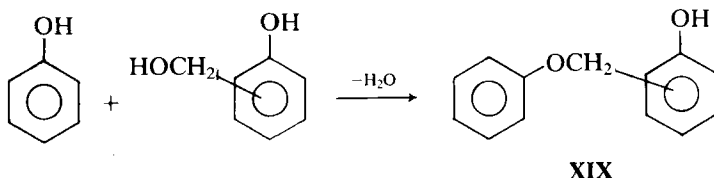


Fig. 9. Effect of cure time on the 25 MHz ^{13}C CP-MAS spectrum of a "random" novolak phenolic resin. Cure times from bottom to top are 0, 0.25, 0.5, 1, 4 and 24 h. All spectra were obtained with a 2-ms CP contact time and a 1-s repetition time.²⁴⁵

deconvoluted spectra (not shown) corresponding to Fig. 9, it is clear that the 117 ppm peak decreases in integrated intensity and increases in linewidth with increasing curing time. The decrease in intensity indicates more substitution in phenolic rings and the increase in linewidth reflects the increase in the number of different conformations and configurations assumed by the phenolic moieties with increasing crosslinking.

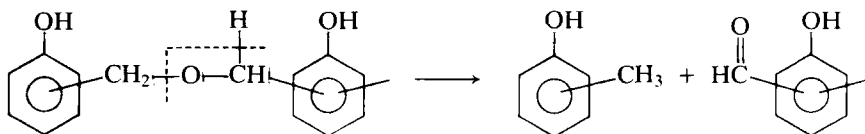
The disappearance of $-\text{CH}_2\text{O}-$ units in the phenolic resins during the curing process does not necessarily lead to the formation of methylene linkages, because the evolution of formaldehyde may occur at high curing temperatures. Therefore, the ratio of $-\text{CH}_2\text{O}-$ to $-\text{CH}_2-$ does not necessarily reflect the extent of crosslinking in a phenolic resin. Instead, So and Rudin²⁴⁶ used the peak intensity at 152 ppm (Ar_1 in Fig. 6, assigned to a phenolic carbon bearing the hydroxyl group) and at about 35 ppm (assigned to methylene linkages) to determine the extent of curing and crosslinking. They used 2 ms for the CP contact time and several different delay times between successive CP sequences and concluded that a 2 ms CP contact time and 8 s repetition delay time are the "optimum" parameters for the quantization of peak intensities at about 152 ppm and 35 ppm.

Maciel, Chuang and Gollob²⁴⁷ used more than eight CP contact times, ranging from 30 μ s to 10 ms, to investigate 16 different resol-type phenolic resins. Owing to rapid ^1H spin diffusion in these phenolic resins, which have high proton densities, $T_{1\rho}^{\text{H}}$ is essentially the same for all protons in a given sample. $T_{1\rho}^{\text{H}}$ values of these 16 resin samples were found to range from 3 to 10 ms from sample to sample. For each sample, the peak around 152 ppm (assigned to hydroxyl-bearing phenolic carbons) has the largest T_{CH} value, ranging from 60 to 350 μ s; the peak around 130 ppm (assigned to aromatic carbons other than hydroxyl-bearing carbons) has the second-largest T_{CH} value for each given sample, ranging from 60 to 300 μ s in different samples. On this basis, the 2 ms CP contact time used by Fyfe *et al.*,²⁴⁴ Bryson *et al.*²⁴⁵ and So and Rudin²⁴⁶ for quantitative measurements seems justified. Based on a shoulder at about 160 ppm and a peak at about 73 ppm in the ^{13}C CP-MAS spectra of four cured phenolic resins, Maciel and coworkers²⁴⁷ speculated that, in addition to crosslinking through methylene linkages during the cure of a phenolic resin, crosslinking through the hydroxyl groups of phenolic rings is another possibility:



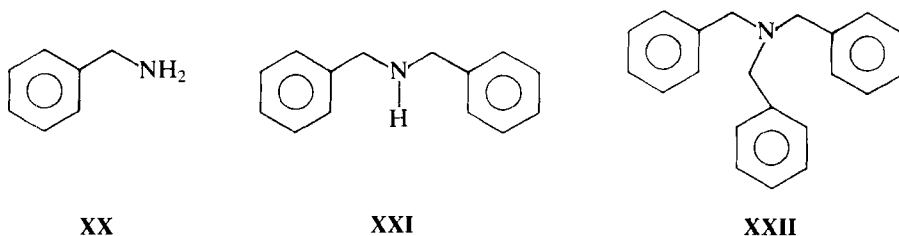
However, none of the 12 uncured phenolic resin samples investigated by Maciel *et al.*²⁴⁷ showed substantial evidence of this type (XIX) of species in the ^{13}C CP-MAS spectra. This study²⁴⁷ also found that there were substantial amounts of methylol groups and dimethylene ether linkages in the cured resol-type phenolic resins, in contrast to the cured novolak-type phenolic resins (*vide supra*) and furfuryl alcohol resins (Section 3.1.).

The ^{13}C CP-MAS spectra of all four cured phenolic resins investigated by Maciel *et al.*²⁴⁷ show a pronounced intensity at about 18 ppm and a weak intensity at about 194 ppm, which can be assigned to methyl carbons directly attached to the phenol ring at the ortho position (relative to the phenolic hydroxyl group) and to $-\text{CHO}$ carbons directly attached to the phenol ring, respectively. These two types of structures can be formed by the following routes suggested by Zinke:²⁴⁸



As mentioned above, novolaks do not contain reactive methylol groups. For the curing of novolak-type phenolic resins, HMTA or para-formaldehyde is mixed with the resin and the mixture is heated. HMTA is the most common curing agent used in the manufacture of phenolic resins. It has been known that curing with HMTA results in increased crosslinking. However, despite years of study, the detailed role of this key substance in the curing process remained vague before 1987.

A thorough solution-state ^{13}C NMR study of the reaction between phenol and HMTA by Sojka, Wolfe and Guenther²³⁹ revealed the presence of primary, secondary and tertiary hydroxy-benzylamines (XX–XXII) as reaction intermediates, strongly suggesting that the various benzylamines are central to the curing mechanism of solid phenolic resins.



Hatfield and Maciel¹⁰⁸ utilized 99% ^{13}C -labelled or ^{15}N -labelled HMTA as a curing agent for novolak resin studies. A mixture of 10% HMTA and 90% phenolic resin was heated at nine different temperatures for 1 h at each temperature. The ^{13}C CP-MAS spectra of this phenolic resin system with different degrees of curing are shown in Fig. 10. These spectra provide the first unequivocal proof of the reasonable assumption that the carbons of HMTA eventually become methylene linkages ($-\text{CH}_2-$, ^{13}C chemical shift: 30–40 ppm) in the resin and are therefore responsible for the observed increase in crosslinking. Figure 10 indicates that curing at 100°C does not bring about appreciable change; however, curing at 120°C starts to bring about some dramatic changes: (a) the peak at about 30–40 ppm assigned to methylene linkages grows substantially; (b) the observed intensities at 55 and 83 ppm reveal the presence of at least one intermediate formed from HMTA during the cure; and (c) another peak at about 167 ppm appears during the cure. The intensities at about 30–40 ppm continue to grow up to a curing temperature of 180°C; however, the growth of peak intensity at about 167 ppm stops at the 150°C cure and remains essentially constant thereafter. In Fig. 10 the peak intensity at 55 and 83 ppm grows very fast after curing at 130°C and remains almost constant up to a curing temperature of 150°C, then starts to decay with curing at 160, 170 and 180°C. Intensity of the peak at 75 ppm assigned to 99% ^{13}C -labelled HMTA decreases gradually and continuously over a wide temperature range.

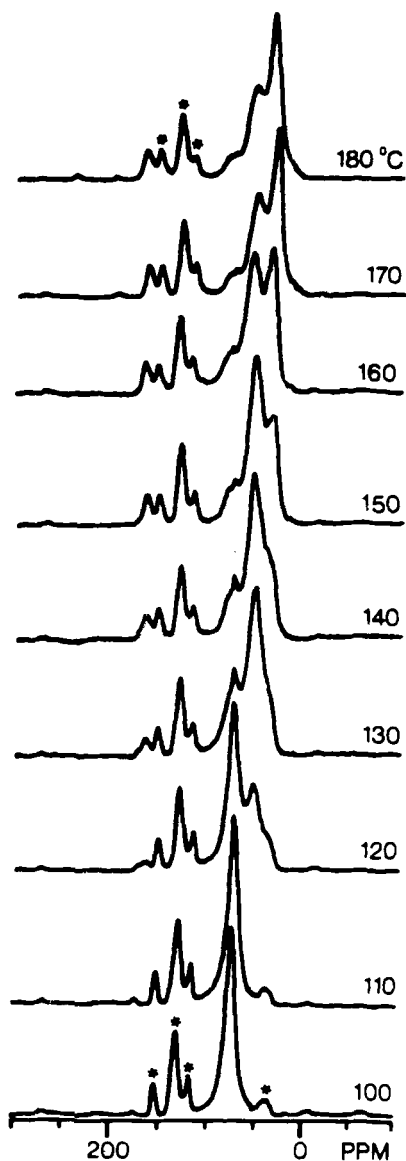
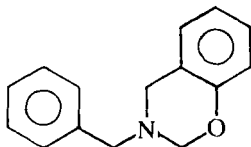


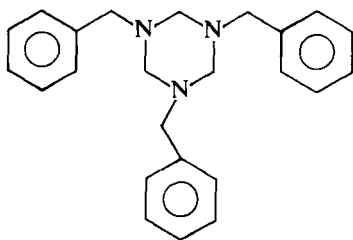
Fig. 10. ^{13}C CP-MAS spectra of a phenolic resin cured with ^{13}C -labelled HMTA for 1 h at the temperatures indicated. Asterisks in the top and bottom spectra denote natural-abundance peaks.¹⁰⁸

Based on the behaviour of the ^{13}C peaks with chemical shifts of 55 and 83 ppm shown in Fig. 10, and the virtual absence of certain other peaks in the spectra, several previously proposed species were eliminated from further consideration as substantially important intermediates for the curing of phenolic resins by HMTA. The ^{13}C peak intensities at 55 and 83 ppm in Fig. 10 are strongly correlated; this fact indicates the presence of structures of the benzoxazine (**XXIII**) type throughout the cure. This type of structure,

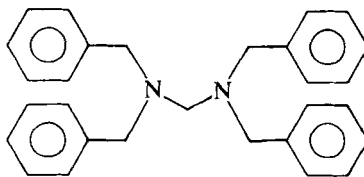


XXIII

along with hydrogen-bonded HMTA (*vide infra*), also accounts for the ^{15}N NMR intensity at 41 ppm in Fig. 11, which shows the ^{15}N CP-MAS spectra of a phenolic resin cured with 99% ^{15}N -enriched HMTA. If the benzoxazine (**XXIII**) structure were the only HMTA-derived intermediate present in the curing process, the intensity ratio of peaks at 55 and 83 ppm would be 2:1. Intensity at 55 ppm is much higher in Fig. 10 than this ratio; therefore, another intermediate must also be present in the curing process. After checking the information obtained from a solution NMR study²³⁹ on proposed intermediates for the curing of phenolic resin by HMTA, Hatfield and Maciel assigned the extra peak intensity at about 55 ppm to tribenzylamine (**XXII**), benzyl-substituted triazines (**XXIV**) or diamines (**XXV**).¹⁰⁸



XXIV



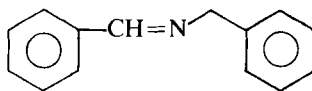
XXV

Before a detailed consideration of the evidence from ^{15}N CP-MAS regarding structures **XXII**, **XXIV** and **XXV** as possible intermediates in the curing of phenolic resin by HMTA, it is relevant to note that Hatfield and Maciel¹⁰⁸ noticed that ^{13}C intensity corresponding to HMTA (75 ppm) decreases gradually over a wide temperature range (Fig. 10), whereas ^{15}N

intensity corresponding to HMTA (44 ppm) disappears essentially completely in the 110°C curing (see the expanded version in Fig. 11). The disappearance of the 44 ppm peak intensity in the ^{15}N spectrum is accompanied by the appearance of a ^{15}N peak at 41 ppm, as shown in the expanded version in Fig. 11. This apparent anomaly means that certain changes that occur during the cure are observable in the ^{15}N NMR experiment but not in the ^{13}C NMR experiment. After performing ^{15}N CP-MAS experiments on model systems, Hatfield and Maciel¹⁰⁸ concluded that the formation of hydrogen bonds between HMTA and a phenol-formaldehyde resin is responsible for a change in ^{15}N chemical shift of HMTA from 44 to 41 ppm, and that ^{15}N CP-MAS NMR establishes that HMTA is hydrogen bonded to the phenolic resin in the very early stages of curing.

Based on the broad shoulder from 47 to 53 ppm in the ^{15}N CP-MAS spectrum shown in Fig. 11 and the intensity ratio of the 55 and 83 ppm peaks in the ^{13}C CP-MAS spectra for samples cured at various temperatures (Fig. 10), Hatfield and Maciel¹⁰⁸ concluded that structures of the types, tribenzylamine (XXII), benzoxazine (XXIII), 1,3,5-tribenzylhexahydrotriazine (XXIV) and tetrabenzylidiaminomethane (XXV) are the major intermediates of HMTA in the curing of phenolic resins. It was also concluded that side reactions that produce amide moieties of the type $\text{R}-\text{NH}-\text{CHO}$ during the curing process are responsible for the peak at 167 ppm in the ^{13}C CP-MAS spectra (Fig. 10) and the peak at 154 ppm in the ^{15}N CP-MAS spectra (Fig. 11).

The most striking difference between the solid-state NMR results of HMTA curing of a phenolic resin¹⁰⁸ and those of solution-state model studies²³⁹ is the absence of appreciable concentrations of intermediates of the benzylamine (XX), dibenzylamine (XXI), and azomethine (XXVI) types



XXVI

in the solid-state curing. The ultimate fate for most of the nitrogen atoms originating from HMTA is evolution as ammonia gas (3 ppm peak in Fig. 11). According to Hatfield and Maciel,¹⁰⁸ it seems plausible that the transformation steps leading from the tribenzylamine-type structure (XXII) to ammonia include steps that involve analogous benzylamine (XX) and dibenzylamine (XXI) structures. If this is the case, these intermediates (XX; XXI) must be sufficiently reactive that their concentrations do not build up enough to permit direct observation in the ^{13}C CP-MAS or ^{15}N CP-MAS spectra.

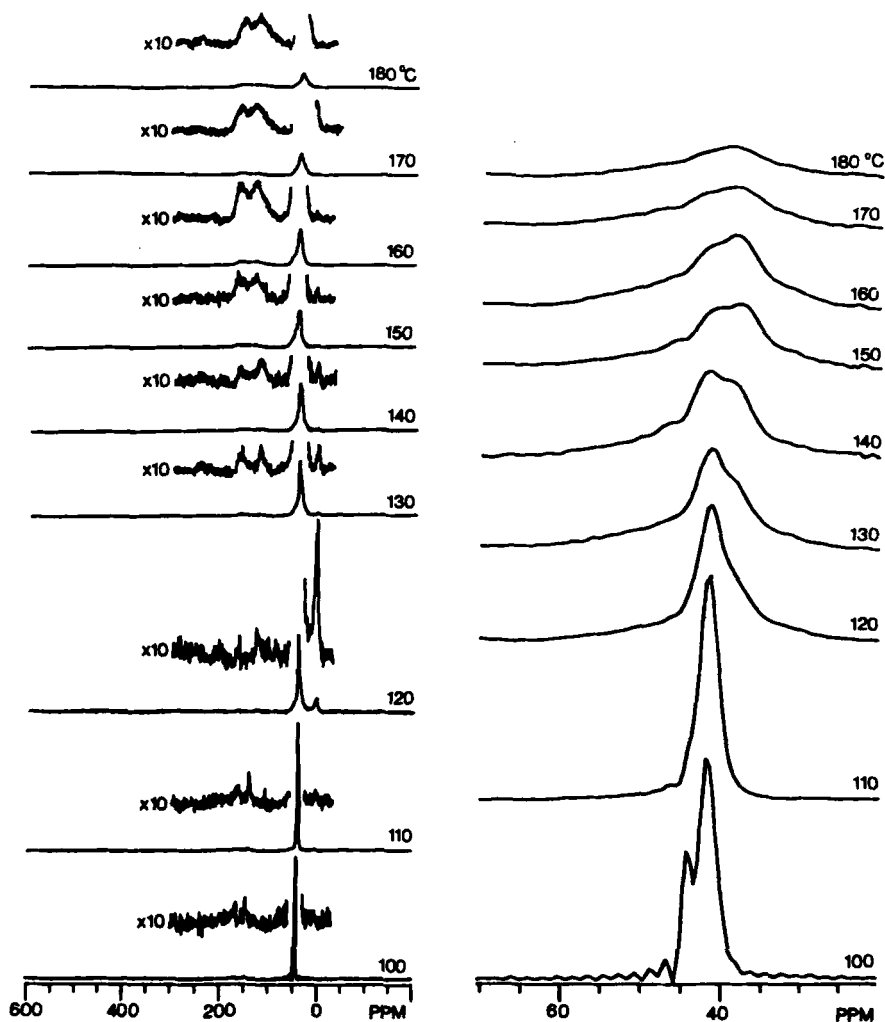
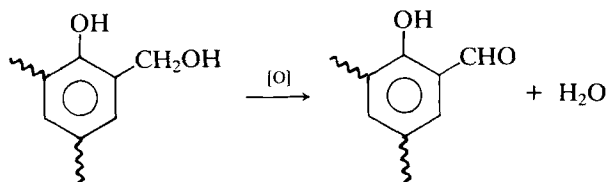


Fig. 11. ^{15}N CP-MAS spectra of phenolic resin cured with ^{15}N -labelled HMTA for 1 h at the temperatures indicated. Left column: full spectra; right column: expanded.¹⁰⁸

3.2.2. Thermal decomposition of cured phenolic resins

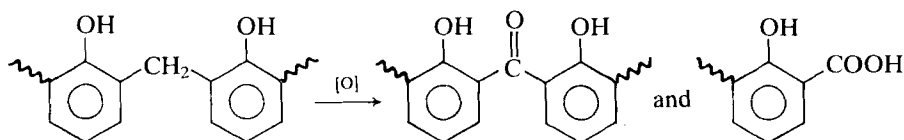
Because phenolic resins can be used as high-temperature polymers,²²⁶ it is important to understand their thermal stabilities at high temperatures. Fyfe and coworkers²⁴⁹ employed ^{13}C CP-MAS NMR to study the thermal decomposition of cured phenolic resins in air at 220, 300 and 400°C; they also investigated the thermal decomposition of the same phenolic resins in vacuum at 400°C. The results obtained for the air and vacuum decompositions are quite different.

Fyfe *et al.*²⁴⁹ prepared resins from phenol and natural-abundance formaldehyde or 5% ^{13}C -enriched formaldehyde under the same conditions, and then cured their resins at 180°C for 160 min. Their ^{13}C CP-MAS results, some of which are shown in Fig. 12, indicate that the main effect of heating the cured phenolic resins to 220°C for 15 min is a marked decrease in the relative concentration of methylol groups ($-\text{CH}_2\text{OH}$, 70 ppm) and a corresponding increase in the peak intensity for methylene linkages between two phenolic rings: the normal curing process of converting methylol groups to methylene linkages by utilizing the remaining unsubstituted *ortho* and *para* sites relative to the hydroxyl-substituted ring carbon. They also observed peaks at 190 and 15 ppm in their ^{13}C CP-MAS spectra of phenolic



resins heated at 220°C, which they assigned to aldehyde groups formed (presumably) by the direct oxidation of methylol groups and to methyl groups attached to phenolic rings, respectively. The formation of methyl groups attached to phenolic rings turned out to be the major $-\text{CH}_2-$ conversion occurring when the resins were heated in vacuum (*vide infra*).

Fyfe and coworkers²⁴⁹ concluded that their phenolic resin lost all methylol groups (70 ppm) when heated at 300°C for 15 min (Fig. 12); this loss of methylol groups was accompanied by only a small amount of oxidation to carbonyl moieties (e.g. the carboxy group of a hydrobenzoic acid, 172 ppm; or the ketone moiety of a dihydroxybenzophenone, 195 ppm) as indicated by Fig. 12. They therefore reasoned that the substantial degree of oxidation which took place subsequently cannot be via methylol groups. When resin heating at 300°C was continued for another 75 min, the spectra of Fig. 12 showed a marked decrease in the concentration of methylene linkages, with the simultaneous formation of a number of carbonyl groups. Comparing the ^{13}C CP-MAS spectra (not shown here) of phenolic resins prepared from non-enriched and 5% ^{13}C -enriched formaldehyde, both having been heated at 300°C for 90 min, Fyfe and coworkers²⁴⁹ concluded that the main source of the carbonyl functionalities is the formaldehyde-derived aliphatic groups in the original resins. In very good agreement with previous IR studies by Conley and coworkers,²⁵⁰ Fyfe *et al.* confirmed the oxidative degradation at 300°C as follows:



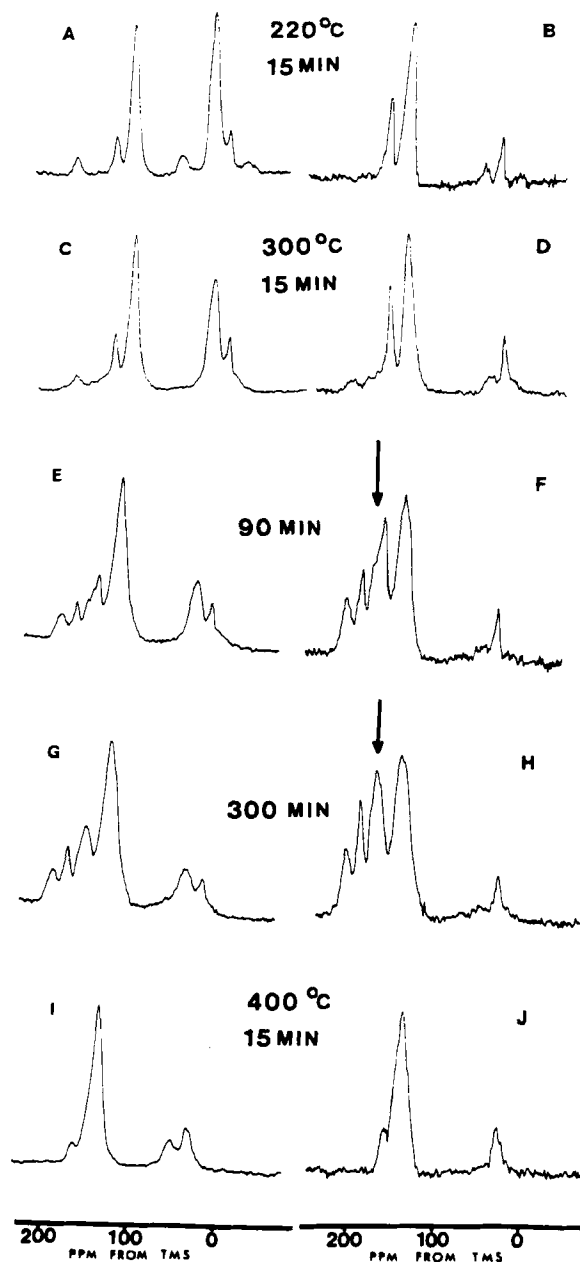
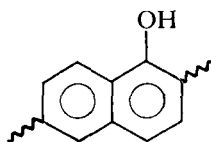
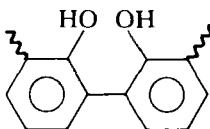
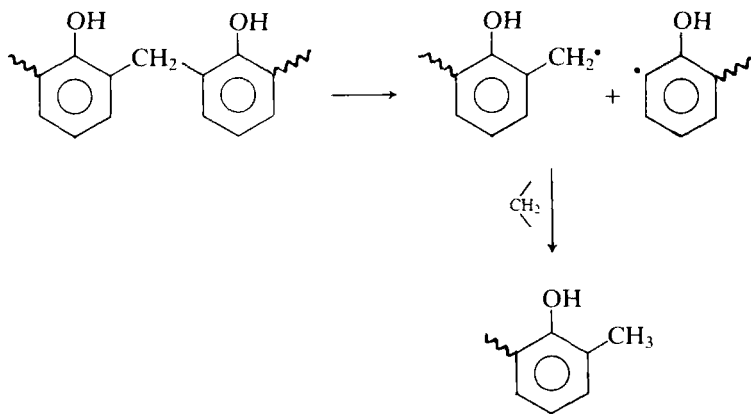


Fig. 12. ^{13}C CP-MAS spectra (left column) and the corresponding $50\ \mu\text{s}$ dipolar-dephasing ^{13}C CP-MAS spectra of various heat-treated resols. Resins were prepared from phenol (P) and 5% ^{13}C -enriched formaldehyde (F) with $\text{P/F/NaOH} = 1/2/0.01$ and cured at 180°C for 160 min under 15-psi nitrogen. The temperature and duration of heat treatments as shown.²⁴⁹

When phenolic resins were heated at 400°C, there was a considerable loss in material (43% after 15 min and 52% after 30 min) and drastic changes in ^{13}C CP-MAS spectra of the phenolic resins.²⁴⁹ Fyfe *et al.* identified the structural nature of the degradative products but did not imply a particular mechanism for their formation. The products they identified include structures of types **XXVII** and **XXVIII**, among others.

**XXVI****XXVII**

From their ^{13}C CP-MAS study, Fyfe *et al.*²⁴⁹ observed that the major degradative process of phenolic resins heated at 400°C under vacuum was the loss of methylol groups and the formation of substantial amounts of methyl groups, with little other structural change in the sample. The methyl groups may be formed as follows:²⁴⁹



They observed two methyl signals in their ^{13}C CP-MAS spectra, which they attributed to methyl groups attached to *ortho* and *para* positions with respect to the hydroxyl-bearing phenolic carbons. As mentioned above, phenolic resins degraded in air produce some methyl groups attached to phenolic rings, probably via the same pathway as in vacuum. Fyfe *et al.* concluded that phenolic resins are much more stable under vacuum than in air and confirmed the oxidative nature of the degradative process of phenolic resins.

3.2.3. Stability of phenolic resin towards formalin, towards base and towards acids

Phenolic resins are relatively resistant to non-oxidizing inorganic or organic acids at elevated temperature, and to moisture, as well as various other chemicals.^{226,227} However, to understand and possibly to improve the chemical stability of phenolic resins, it is desirable to characterize degradation that does occur. Accordingly, Chuang and Maciel²⁵¹ used ^{13}C CP-MAS NMR to study the effects of formalin, base, non-oxidizing acid and oxidizing acid on a cured resol-type phenolic resin. The major change observed by ^{13}C CP-MAS NMR (see Fig. 13) in the cured phenolic resin after treatment with 1 N aqueous NaOH solution or nonoxidizing 1 N aqueous sulfuric acid solution under N_2 (g) at 65°C for 3 days, followed by distilled water washing, is simply neutralization of the resin. Some of the dimethylene ether linkages ($-\text{CH}_2\text{OCH}_2-$) that connect two phenolic rings of the cured phenolic resin are cleaved by 1 N NaOH to produce two corresponding methylol groups ($-\text{CH}_2\text{OH}$), whereas these linkages are stable towards the treatment with 1 N sulfuric acid. The linkages through phenolic hydroxyl groups observed previously²⁴⁷ (XIX, Section 3.2.1.) are stable towards 1 N NaOH or 1 N sulfuric acid treatment. Understandably, the etherification of the phenolic hydroxyl group (*O*-alkylation) has been used to improve alkali resistance of phenolic resins.²²⁶

Chuang and Maciel²⁵¹ treated a cured resol-type phenolic resin with 36.8% formalin (containing 8% methanol for stabilization) under N_2 (g) at 25°C for 1 day, and evacuated the treated phenolic resin at 10^{-2} torr after washing with distilled water. Their ^{13}C CP-MAS results (Fig. 13) indicate that, in addition to the neutralization effect, formalin interacts with phenolic resin to produce more methylol groups at originally unsubstituted *ortho*- or *para*- positions (with respect to the hydroxyl-bearing phenolic carbon) and produce more *p,p'*-methylene linkages between two phenolic rings. Methylene linkages, methylol groups, $-\text{CHO}$ groups and $-\text{CH}_3$ groups attached to phenolic rings of cured phenolic resin, as well as $\text{Ar}-\text{O}-\text{CH}_2-\text{Ar}'$ (XIX) species, are all stable towards the treatments of 1 N NaOH, 1 N sulfuric acid and 36.8% formalin, as seen in Fig. 13.

Based on their ^{13}C CP-MAS NMR results,²⁵¹ Chuang and Maciel observed that almost all of the methylol groups and dimethylene ether linkages in their cured phenolic resin were eliminated by treatment with concentrated (36 N) sulfuric acid under N_2 (g) at 25°C or at 65°C for 1 day. Some of the dimethylene ether linkages were cleaved to produce $-\text{CHO}$ and $-\text{CH}_3$ moieties, whereas methylene linkages, $-\text{CHO}$ groups, $-\text{CH}_3$ groups attached to phenolic rings of cured phenolic resins, and $\text{Ar}-\text{O}-\text{CH}_2\text{Ar}'$ moieties in the resin are stable with these 36 N sulfuric acid treatments (see Fig. 13). Concentrated sulfuric acid was also found to sulfonate some of the aromatic carbons at positions *ortho* to the phenolic hydroxyl groups of a

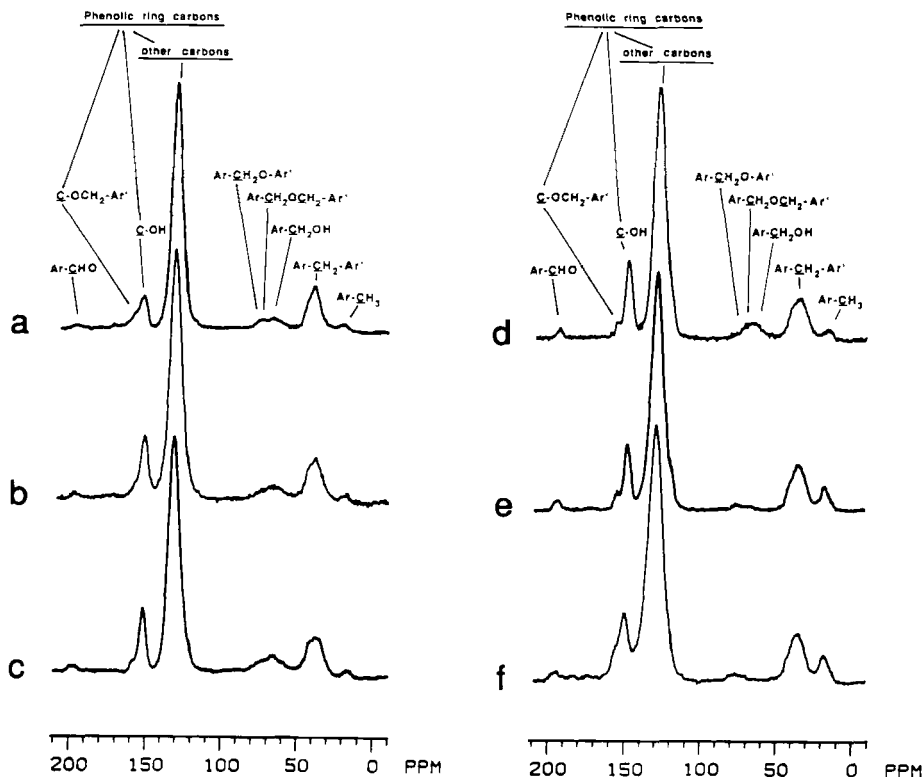


Fig. 13. 15.1 MHz ^{13}C CP-MAS NMR spectra of (a) a resol-type PF resin (cured PF 50 resin), (b) cured PF resin after treatment with 0.1 N sodium hydroxide solution under $\text{N}_2(\text{g})$ at 65°C for 3 days, (c) cured PF 50 resin after treatment with 36.8% formalin under $\text{N}_2(\text{g})$ at 25°C for 1 day, (d) cured PF 50 resin after treatment with 1.0 N sulfuric acid solution at 65°C for 3 days, (e) cured PF 50 resin after treatment with 36 N sulfuric acid at 25°C for 1 day and (f) cured PF 50 resin after treatment with 36 N sulfuric acid at 65°C for 1 day. CP contact time = 1 ms; repetition time = 1 s.²⁵¹

cured phenolic resin at room temperature and to sulfonate some aromatic carbons *ortho* and/or *para* to phenolic hydroxyl groups of the cured phenolic resin at 65°C , as seen in Fig. 13.

Chuang and Maciel²⁵¹ found a drastic change in their ^{13}C CP-MAS NMR spectrum of a cured phenolic resin upon treatment with 15 N nitric acid in air at 25°C for 1 day, as seen in Fig. 14. This reagent oxidizes some of the phenolic rings to cyclic ketones and nitrates some of the phenolic rings. Most of the methylene linkages and $-\text{CHO}$ groups in the cured phenolic resin were unaffected, whereas methylol groups and $-\text{CH}_3$ groups were eliminated, nitrated or oxidized by 15 N nitric acid (see Fig. 14).

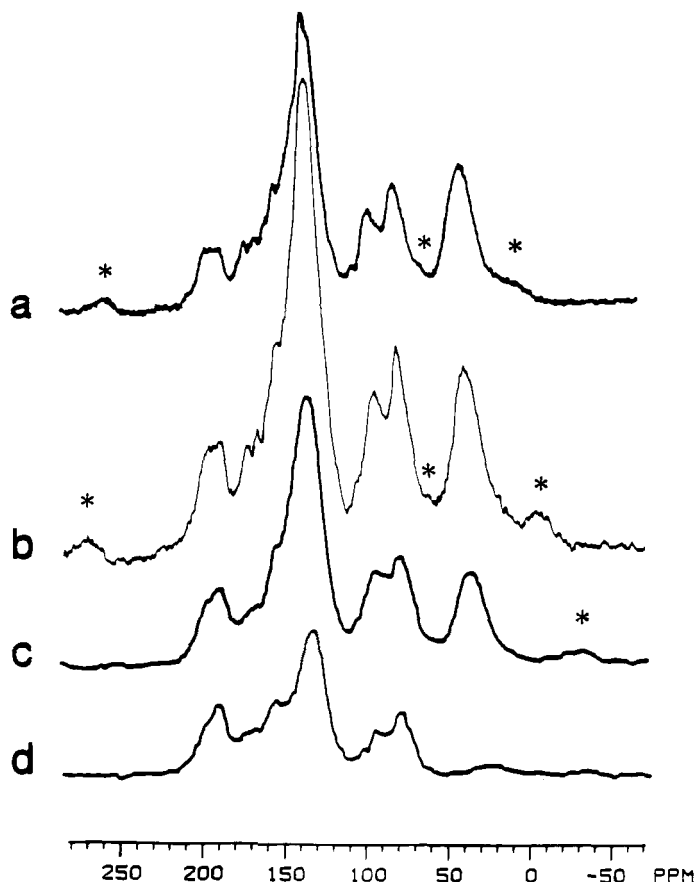


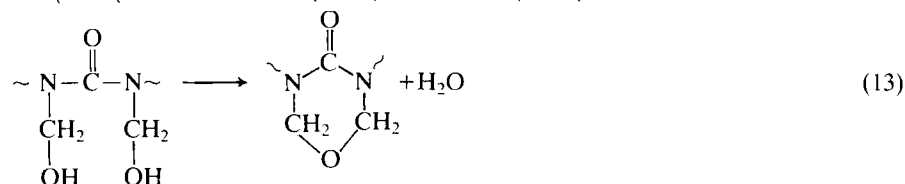
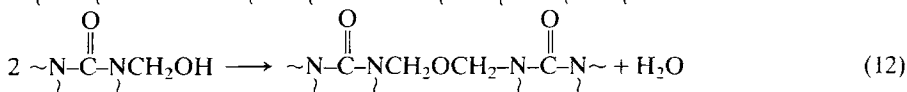
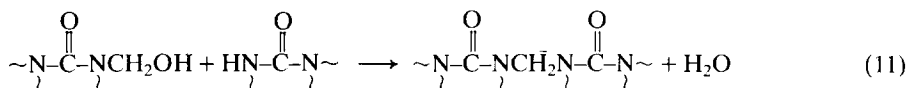
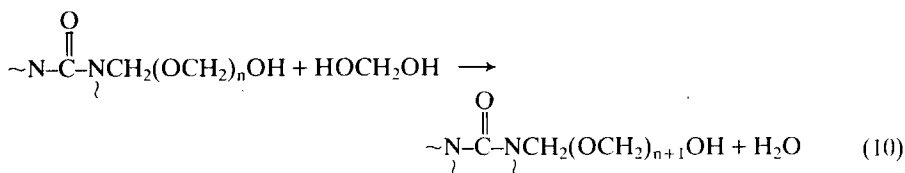
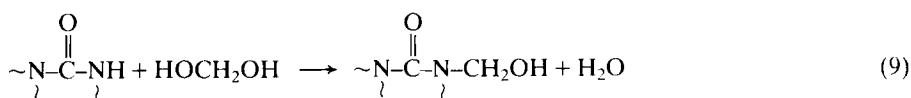
Fig. 14. ^{13}C NMR spectra of the residue of cured PF 50 resin after treatment with 15 N nitric acid in air at 25°C for 1 day (CP contact time = 1 ms; repetition time = 1 s): (a) 50.3 MHz CP-MAS spectrum; (b) 22.6 MHz CP-MAS spectrum; (c) 15.1 MHz CP-MAS spectrum; (d) 15.1 MHz 50- μs dipolar-dephasing CP-MAS spectrum. Spinning sidebands are indicated by asterisks.²⁵¹

3.3. Urea-formaldehyde resins

Urea-formaldehyde (UF) resins²⁵² have long been used in technological applications of coatings, adhesives, castings, moulding compounds and textile auxiliaries. UF resins are especially important as adhesives for various wood products. From the 1940s to the 1970s, a large volume of information was published on the kinetics and synthetic pathways of the initial reaction involved in the preparation of UF resin systems.^{252,253} Among the methods of investigation, liquid-sample ^1H NMR^{254–260} provides some direct and useful information. Liquid-sample ^{13}C NMR^{261–272} has

emerged as a powerful technique for studying UF resins in their early stages of formation and has provided the most detailed information on the reactions and structures of UF resins that can be dissolved in suitable solvents. However, the structures of insoluble resin fractions and the nature of the curing processes of UF resins, which are very important issues concerning the performance characteristics of UF resins, are out of the range of liquid-state ^{13}C NMR.

The formation of a UF polymer is believed to occur via some combination of the following reactions:^{252,253}



Urea has four N-H bond sites available for interaction with formaldehyde, which in turn has two atomic sites available in the carbonyl group for interaction. Therefore, the reaction products between urea and formaldehyde can range from the very simple one, monomethylolurea, $\text{H}_2\text{NC}(\text{O})\text{NHCH}_2\text{OH}$, to very complicated, widely crosslinked three-dimensional products.²⁵² The reaction conditions that lead to soluble UF resins are very limited. Hence, UF resins prepared by a large range of reaction conditions, and especially the curing process and final cured UF resin products, cannot be studied by liquid-sample analytical techniques, such as ^{13}C NMR spectroscopy.

High-resolution solid-state NMR spectroscopy is a powerful tool for the investigation of structural details and the formation processes of complicated UF resin systems. In the past 10 years, ^{13}C CP-MAS techniques have been utilized to study uncured²⁷³ and cured UF resins (Section 3.3.1.),²⁷⁴⁻²⁷⁶ and

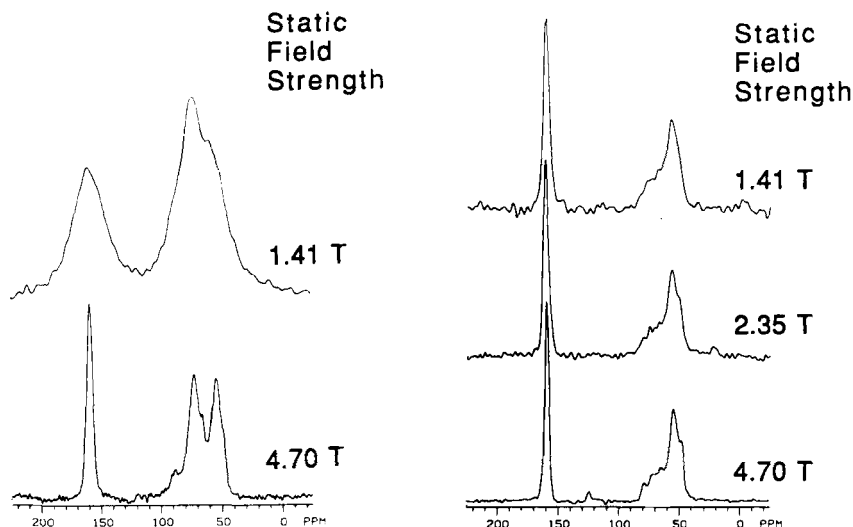


Fig. 15. Static field dependence of the ^{13}C CP-MAS spectra of urea-formaldehyde resins. Left column, natural abundance. Right column, 99.7% ^{15}N -labelled UF resin.²⁷⁴

the hydrolytic stabilities of UF resin components (Section 3.3.3.).²⁷⁷ ^{15}N CP-MAS studies of ^{15}N -enriched UF resin¹⁰⁶ and natural-abundance UF resins (Section 3.3.2.)¹²³ provide very useful supplements to ^{13}C CP-MAS studies. ^{13}C CP-MAS techniques have also been used to investigate polymer blends of furfuryl alcohol and urea-formaldehyde resins (Section 4.1.1.).²⁷⁸

3.3.1. ^{13}C CP-MAS NMR studies of UF resin systems

Maciel *et al.*²⁷⁴ investigated four sets of UF resins and the model compound, *N,N'*-dimethylolurea, by ^{13}C CP-MAS NMR in 1982. Due to the ^{14}N quadrupolar effect on MAS averaging of the ^{14}N - ^{13}C dipolar interaction (see Section 2.1.5.), the ^{13}C CP-MAS spectra of UF resins prepared from natural-abundance urea show a strong static magnetic field dependence, as indicated in the left column of Fig. 15. In contrast, there is only a weak static magnetic field dependence of the ^{13}C CP-MAS spectra of a 99.7% ^{15}N -enriched UF resin sample, as shown in the right column of Fig. 15. Because of the field dependence shown in Fig. 15, Maciel *et al.* employed a 50.3 MHz ^{13}C CP-MAS spectrometer for investigating the structure and curing of natural-abundance UF resins in spite of the difficulty of dealing with spinning sidebands with 1981 MAS technology.^{279,280} The major chemical conclusions of these early ^{13}C CP-MAS studies are: (a) the synthesis of UF resins with excess urea and under acidic conditions produces

a linear chain with little tertiary nitrogen and dimethylene ether linkages ($-\text{CH}_2\text{OCH}_2-$) between two urea units; and (b) the concentration of methylol groups ($-\text{CH}_2\text{OH}$) on secondary nitrogen decreases, while the concentration of branching tertiary nitrogens increases, with increasing degree of cure.

Jada²⁷³ used a 150 MHz spectrometer (with a ^{13}C Larmor frequency of 37.7 MHz) to investigate uncured UF resins. The linewidths of ^{13}C CP-MAS spectra of those uncured prepolymers are generally broad, partly due to the residual ^{14}N - ^{13}C dipolar interactions unaveraged by MAS (Section 2.1.5.). Jada observed that the major methylene component in the base-catalysed UF prepolymer is methylol units connected to secondary amides, whereas the major methylene component in the acid-catalysed UF prepolymer is methylene linkages connecting a tertiary amide and a secondary amide. He did not identify methanol, methoxy groups, or cyclic ethers in his UF prepolymers by ^{13}C CP-MAS.

The factors that affect the component of UF resin products include the concentration of the main reaction components (urea and formaldehyde), pH, temperature, and duration of reaction.²⁵² Studies of the structures of UF resin systems in the past had been largely fragmentary, mainly because various reaction conditions were deliberately avoided in many past studies in order to provide a soluble product that could be examined by liquid-sample techniques. Chuang and Maciel²⁷⁵ adopted a systematic approach to the study of UF resin systems by ^{13}C CP-MAS techniques. They focused on the effects of urea concentration, formaldehyde-to-urea molar ratio and pH on the structures of UF resins. The duration of reactions was fixed at 12 h. Most of the reactions were conducted at room temperature ($23 \pm 2^\circ\text{C}$), except for a few cases in which the control of the temperature was difficult within the short time period of a rapidly exothermic reaction. The extensive investigation covered four different formaldehyde-to-urea molar ratios (1.00, 1.50, 2.00, 3.00) at three different concentrations, and all these systems were reacted at six different pH values (1; 3; 5; 7; 9; 12). With a MAS speed of about 6.5 kHz, the spinning sidebands are outside the central region of the 50.3 MHz ^{13}C CP-MAS spectra of UF resins; therefore, the spinning sideband suppression technique practised by Maciel *et al.*²⁷⁴ in 1982 was avoided in this later study. Quantitative aspects of the ^{13}C CP-MAS approach were examined by variable contact-time experiments^{86, 87} on a range of UF resin samples.²⁷⁵

Table 1 lists the ^{13}C chemical shifts of some of the important structural fragments that possibly or likely occur in UF resins. The assignments are based on liquid-state ^{13}C NMR studies,^{261-272,276} and ^{13}C CP-MAS studies²⁷³⁻²⁷⁶ of model compounds and UF resin systems.

Chuang and Maciel^{275,276} observed the formation of urons (Eq. (13)) in some of their UF resin systems (*vide infra*) based on ^{13}C CP-MAS spectra (e.g. third and fourth rows of Fig. 19). In contrast to the observation by

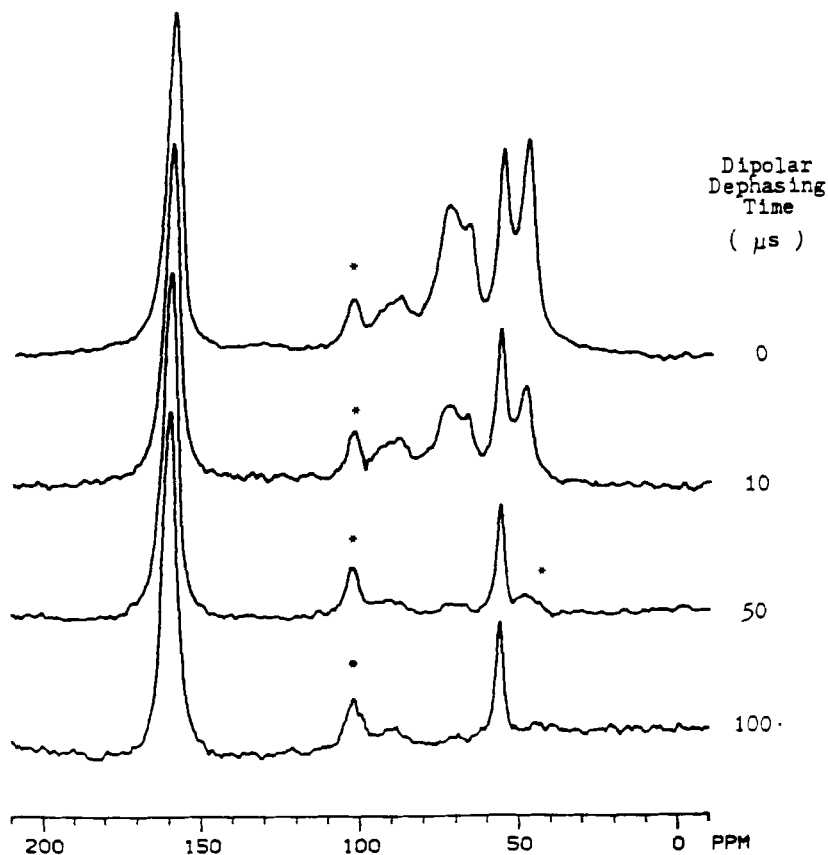


Fig. 16. 50.3 MHz ^{13}C CP-MAS spectra of a urea-formaldehyde (UF) resin obtained with four different dipolar-dephasing times.²⁷⁵

Jada,²⁷³ Chuang and Maciel²⁷⁵ detected methoxy groups in some of their UF resin systems (e.g. Fig. 16). Both methoxy groups and methylene linkages between a secondary amide on one end and a tertiary amide on the other end have a ^{13}C chemical shift of about 55 ppm. One way to distinguish between contributions of these two types of moieties to the ^{13}C CP-MAS spectra is to perform dipolar-dephasing ^{13}C CP-MAS experiments.^{88,89} Owing to rapid rotation around the O-C bond, the resonance arising from -OCH₃ groups survives dipolar dephasing much better than other resonances arising from ^{13}C spins with directly bonded protons and in a more rigid moiety, as indicated in Fig. 16. By using this dipolar-dephasing approach, Chuang and Maciel²⁷⁵ estimated that roughly 54% of the 55 ppm peak in the sample represented in Fig. 16 is due to methoxy groups.

Chuang and Maciel²⁸¹ also observed a strong static field strength

dependence on their ^{13}C CP-MAS spectrum of the model compound, *N,N'*-dimethylolurea ($\text{HOCH}_2\text{NHC(O)NHCH}_2\text{OH}$), due to the residual ^{14}N - ^{13}C dipolar interaction under MAS. They found that the quadrupolar effect on MAS averaging of the ^{14}N - ^{13}C dipolar interaction in the ^{13}C CP-MAS spectrum has been quenched to a degree that no characteristic splittings are observed in the 160 and 65 ppm peaks in the ^{13}C CP-MAS spectrum of *N,N'*-dimethylolurea taken on a 260 MHz spectrometer. Figure 17 shows the ^{13}C CP-MAS spectra of *N,N'*-dimethylolurea at four different static fields. In the 50.3 MHz spectrum (Fig. 17c), one can observe the splittings that are due to crystallographic effects in highly crystalline *N,N'*-dimethylolurea (Section 3.2.2.). These splittings are not observed in the 160 and 65 ppm regions of the spectra of complex UF resins largely because of the lack of crystallographic order and effects and the chemical shift dispersion associated with structural heterogeneity in amorphous resins.

The most obvious pH effect in the syntheses of UF resins Chuang and Maciel²⁷⁵ found in their ^{13}C CP-MAS investigation is that the formation of methylene linkages (Eq. (11)) is catalysed only by acids, at least when the reaction is conducted at 23°C. As seen in Fig. 18, the major constituents of a UF resin prepared at pH 7 and pH 9 are monomethylolurea and *N,N'*-dimethylolurea. The major constituents of a UF resin prepared at pH 12 are methylolurea and dimethylene ether linkages connecting two urea units, as seen in Fig. 18. Due to the overlap of the splitting pattern centred at 65 ppm with the CH_2 peak of dimethylene ether linkages at 69 ppm in the 50.3 MHz spectra, a more quantitative discussion is deferred to Section 3.3.2., which presents ^{15}N CP-MAS results. In this section, we concentrate the discussion on the effect of pH values, concentrations and formaldehyde-to-urea molar ratios on the UF resins prepared under acidic conditions (pH = 1, 3, 5).

Because the rate and equilibrium constants for the formation of asymmetrical *N,N*-dimethylolurea are far smaller than the corresponding quantities for monomethylolurea and/or symmetrical *N,N'*-dimethylolurea,²⁵⁶ Chuang and Maciel found that the ^{13}C CP-MAS spectra of UF resins prepared at pH 1, 3 and 5 from mixtures with a formaldehyde-to-urea ratio of 1.00 are very similar to each other due to the limited supply of formaldehyde with this formaldehyde-to-urea ratio. As seen in the spectra of the top rows of Figs 19–21, the main constituents of these samples are carbonyl groups, linear-chain methylene linkages, and some crosslinking methylene linkages. The spectra in the top rows of Figs 19–21 show that, except for the formation of methoxy groups, the concentration effect on the UF resin prepared with a 1.00 formaldehyde-to-urea ratio is small. With the increasing amount of formaldehyde available in a reaction mixture with an F/U molar ratio of 1.50 (relative to the case of an F/U molar ratio of 1.00), pH and concentration effects on the methylation rate (Eq. (9)) and on the formation rates of methylene linkages (Eq. (11)) play larger roles in

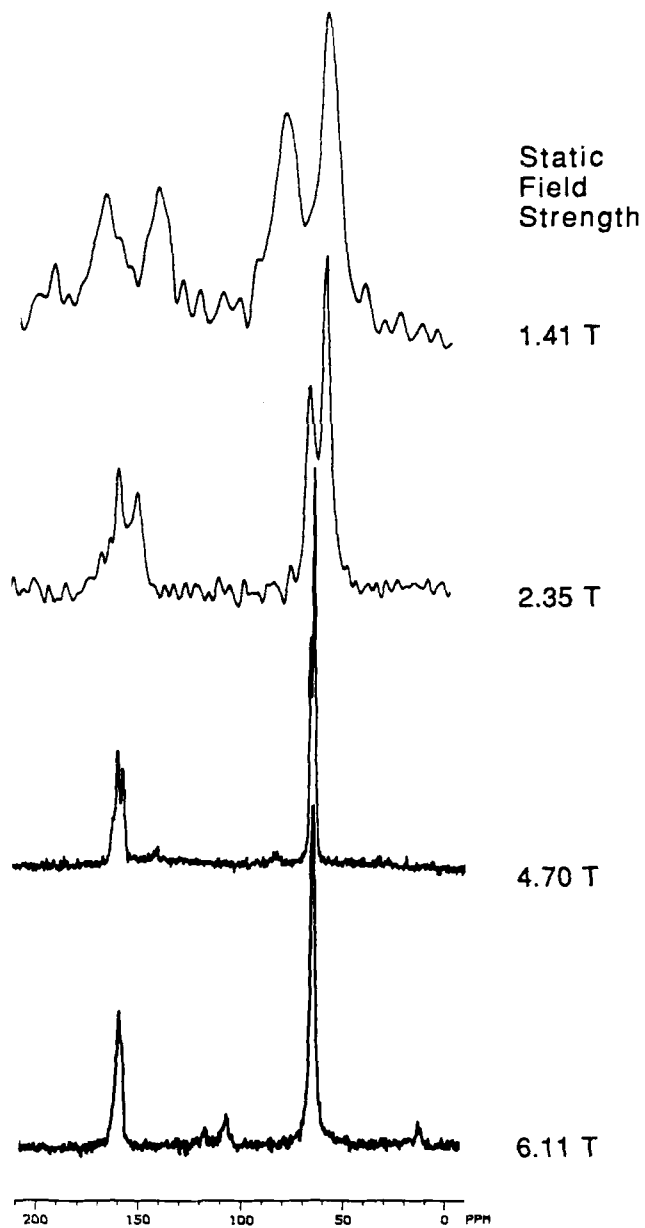


Fig. 17. ^{13}C CP-MAS spectrum of an N,N' -dimethylolurea powder taken at four different static fields indicated.

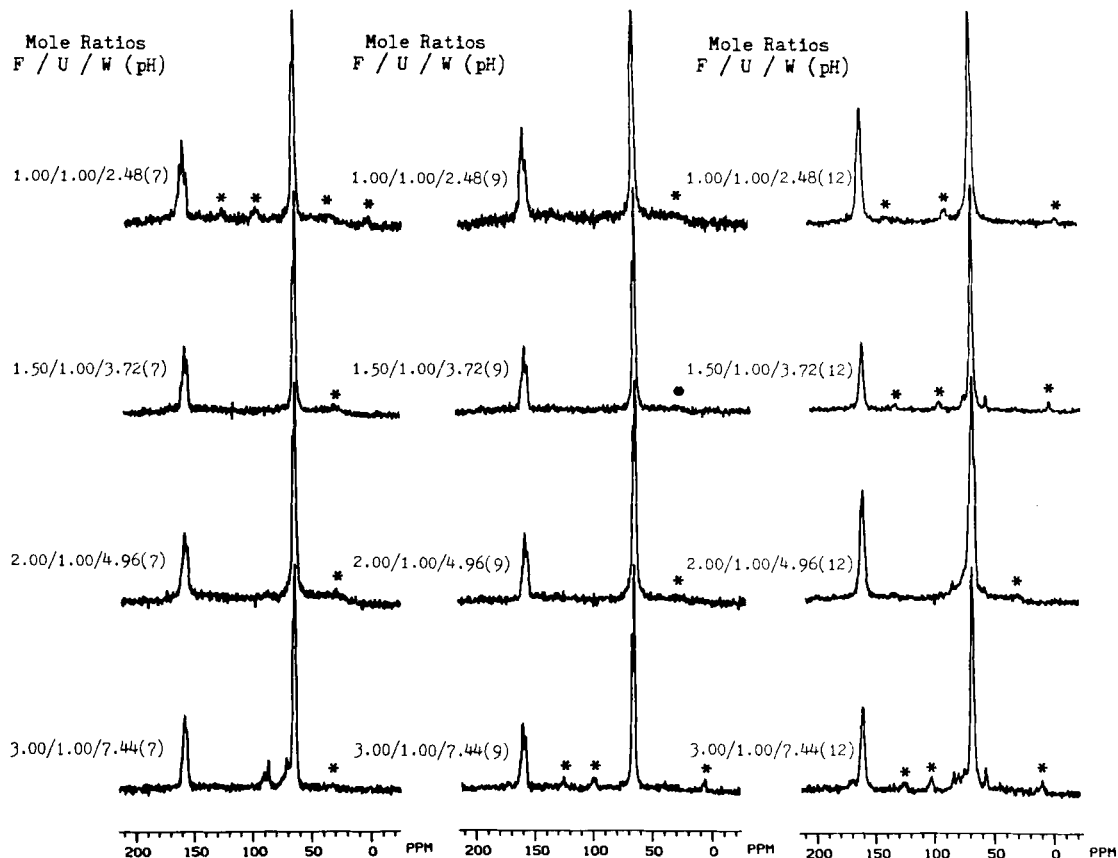


Fig. 18. 50.3 MHz ^{13}C CP-MAS NMR spectra of UF resin samples prepared under concentrated conditions from mixtures with four different formaldehyde/urea/water (F/U/W) molar ratios: 1.00/1.00/2.48, 1.50/1.00/3.72, 2.00/1.00/4.96, and 3.00/1.00/7.44. Left column pH 7; middle column pH 9; right column pH 12. CP contact time = 1 ms; repetition time = 1 s. Spinning sidebands are indicated by asterisks.

Concentrated

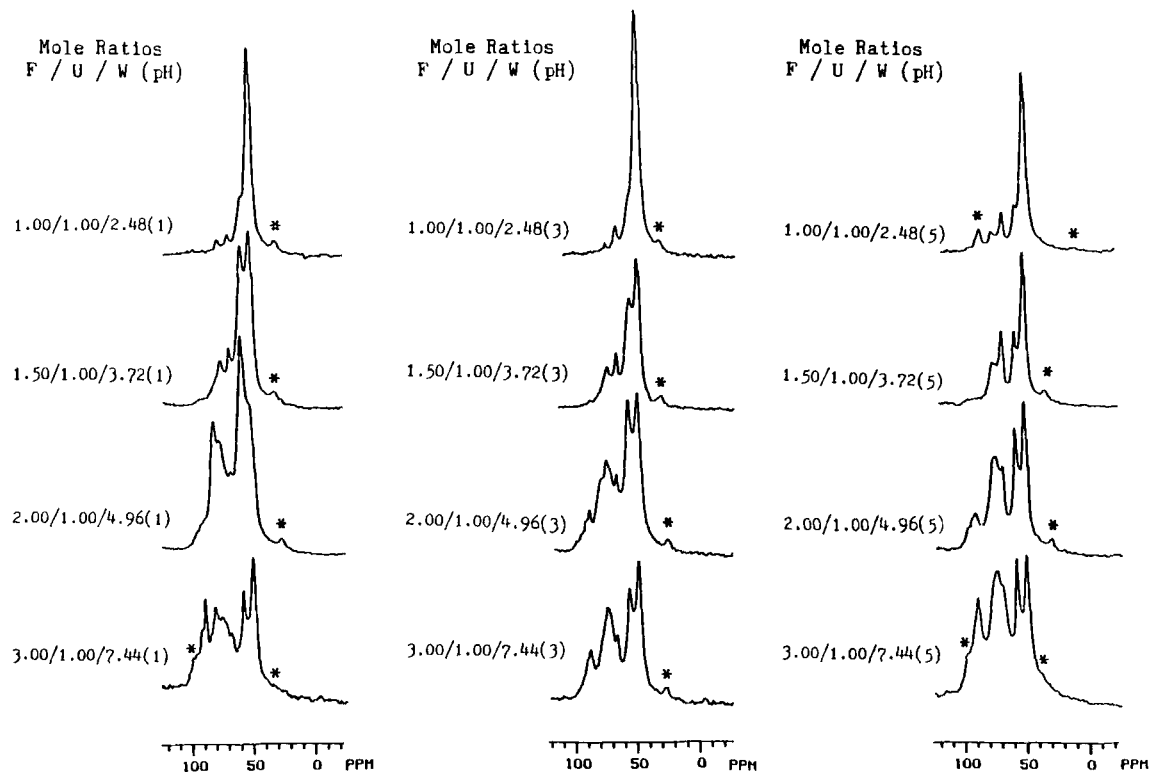


Fig. 19. 50.3 MHz ^{13}C CP-MAS NMR spectra of UF resin samples prepared under concentrated conditions with four different F/U/W molar ratios: 1.00/1.00/2.48, 1.50/1.00/3.72, 2.00/1.00/4.96 and 3.00/1.00/7.44. Left column pH 1; middle column pH 3; right column pH 5. CP contact time = 1 ms; repetition time = 1 s. The spectra are plotted with the same height for peaks assigned to carbonyl carbons; only the spectral regions assigned to aliphatic carbons are shown here. Spinning sidebands are indicated by asterisks.²⁷⁵

Intermediate

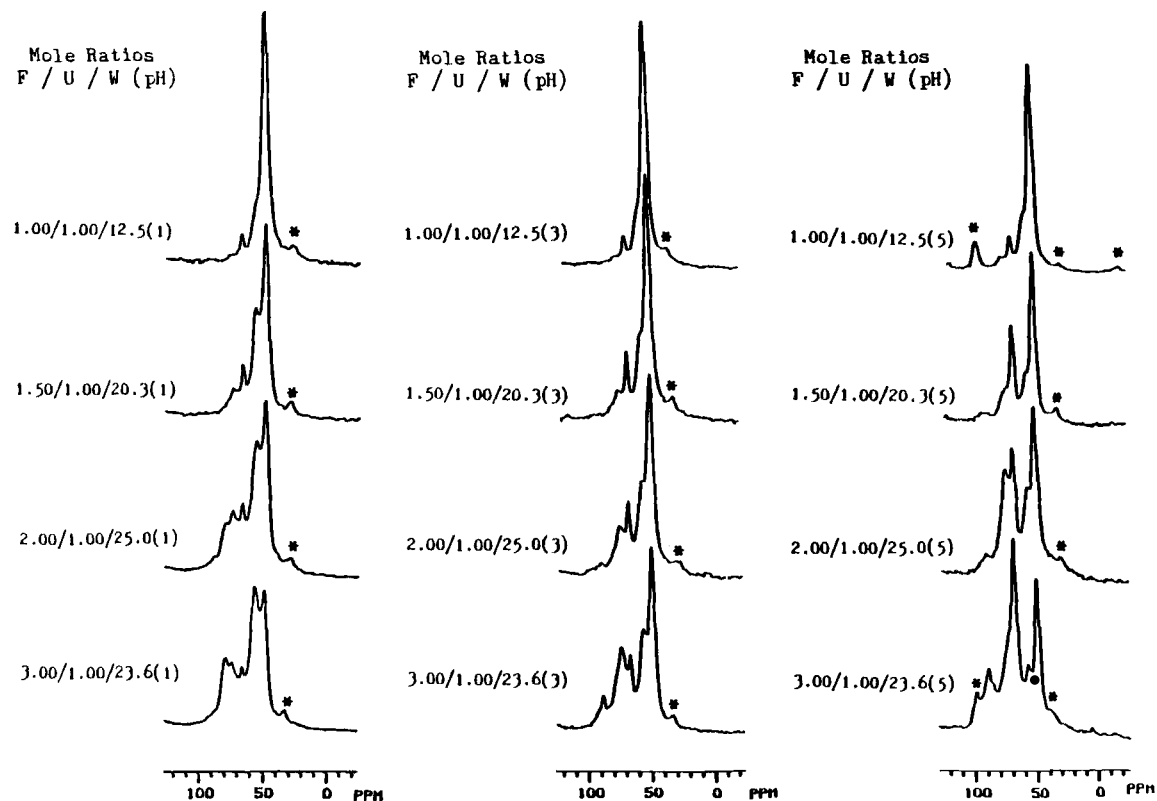


Fig. 20. 50.3 MHz ^{13}C CP-MAS NMR spectra of UF resin samples prepared at intermediate concentrations from mixtures with four different F/U/W molar ratios, 1.00/1.00/12.5, 1.50/1.00/20.3, 2.00/1.00/25.0 and 3.00/1.00/23.6. Left column pH 1; middle column pH 3; right column pH 5. CP contact time = 1 ms; repetition time = 1 s. The spectra are plotted with the same height for peaks assigned to carbonyl carbons; only the spectral regions assigned to aliphatic carbons are shown here. Spinning sidebands are indicated by asterisks.²⁷⁵

Dilute

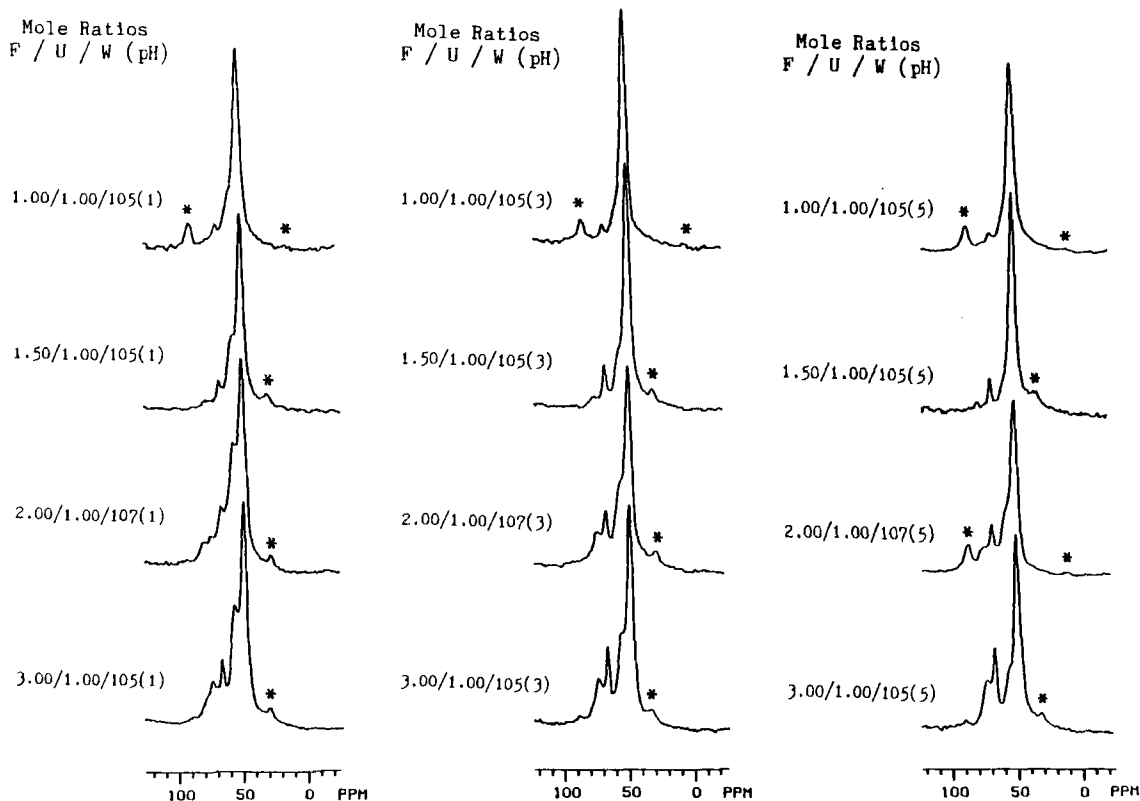


Fig. 21. 50.3 MHz ^{13}C CP-MAS NMR spectra of UF resin samples prepared under dilute conditions from mixtures with four different F/U/W molar ratios, 1.00/1.00/105, 1.50/1.00/105, 2.00/1.00/107 and 3.00/1.00/105. Left column pH 1; middle column pH 3; right column pH 5. CP contact time = 1 ms; repetition time = 1 s. The spectra are plotted with the same height for peaks assigned to carbonyl carbons; only the spectral regions assigned to aliphatic carbons are shown here. Spinning sidebands are indicated by asterisks.²⁷⁵

determining the structures of UF products. The second row of Fig. 19 shows the ^{13}C CP-MAS spectra of three UF resins prepared with an F/U molar ratio of 1.50 under the most concentrated reagent conditions at pHs 1, 3 and 5. Dipolar-dephasing results show that about 40% of the ^{13}C intensity at about 55 ppm and 70% of the intensity at 73 ppm in the 1.50/1.00/3.72(5) spectrum of Fig. 19 are attributed to the methylene methyl ethers ($-\text{CH}_2-\text{OCH}_3$) attached to secondary amides of urea units. The total amount of methylene methyl ethers is highest in the sample prepared at pH 5 and is negligible in the sample prepared at pH 3. After taking into account the contribution of methoxy groups to the peak at 55 ppm, the other most obvious effect indicated in the second row of Fig. 19 is a drastic decrease in the formation of crosslinking methylene linkages (54 ppm peak) with increasing pH value. The spectra in the second row of Fig. 19 show that there is a substantial amount of methylol groups (65 ppm peak) left in the resin prepared at pH 5 (1.50/1.00/3.72(5) spectrum in Fig. 19); therefore, one can conclude that the formation of methylene linkages from methylol groups (Eq. (11)) is not as favourable at pH 5 as it is at pH 3 and pH 1. The effect of pH on the structure of UF resins decreases with increasing dilution of the reaction mixture (cf. second rows of Figs 19–21).

Concentration effects on the UF resins prepared from mixtures with an F/U molar ratio of 1.50 at pH 3 are manifested in the ^{13}C CP-MAS spectra of Figs 19–21 (second row, second spectrum). The degree of crosslinking through methylene linkages (54 ppm peak) and the amount of methylol groups attached to tertiary amides (72 ppm peak) are seen to decrease with increasing dilution of the reaction mixture. Figures 19–21 (second row, first spectrum) show that concentration effects on the UF resins prepared at pH 1 are very similar to the case at pH 3, whereas concentration effects on the UF resins prepared at pH 5 are much smaller, with the exception of the formation of methylene methyl ethers; there are negligible amounts of methylene methyl ethers in all the UF resins prepared under dilute conditions, while the formation of methylene methyl ether groups is most favourable under concentrated conditions at pH 5.

With an F/U molar ratio of 2.00, the formation of dimethylene ether linkages (Eq. (12)) and of urons (Eq. (13)) adds some more complexity into the UF reaction systems, as seen in the third row of Fig. 19. This figure shows that, in addition to those pH effects and concentration effects observed in the UF resin systems with an F/U molar ratio of 1.50, the formation of dimethylene ether linkages connecting one tertiary amide and one secondary is most favourable at pH 5, whereas the formation of dimethylene ether linkages connecting two tertiary amides is most favoured at pH 1. The third row of Fig. 19 also shows that the proportion of urons (79 ppm) decreases dramatically by going from pH 1 to 3 and from pH 3 to 5, and the third row of Figs 19–21 shows that the formation of various ethers decreases drastically with increasing dilution of the reaction mixtures.

With an F/U molar ratio of 3.00, there is more than enough formaldehyde available in the concentrated reaction mixtures for bonding to each amino group of urea moieties. Chuang and Maciel learned from their ^{13}C CP-MAS spectra that, in addition to substantial amounts of methylene linkages, poly(oxymethylene)glycols, hemiformals and their methyl ethers, resins prepared at pH 1, 3 or 5 also contain major portions of urons, dimethylene ether linkages and methylol groups. Effects of pH on the structure of a UF resin is small for the most concentrated reaction mixture with an F/U molar ratio of 3.00 (fourth row of Fig. 19); however, the pH effects become large if the reaction mixture is moderately diluted by water, and structure-vs.-pH relationships that are similar to those observed in UF resin systems prepared with F/U molar ratios of 1.50 and 2.00 are seen in the fourth row of Fig. 20. In the most dilute reaction mixture with an F/U molar ratio of 3.00 they investigated, pH effects on the UF resin products are again diminished in comparison to the moderately dilute reaction mixtures (see fourth row of Fig. 21).

The most drastic concentration effects on structure of UF resins occur when the most concentrated reaction mixture with an F/U molar ratio of 3.00 is moderately diluted (cf. fourth rows of Figs 19 and 20). In this case formaldehyde is liberated from dimethylene ether linkages and simple methylene linkages become major components in these UF resin systems. With further dilution, the concentration effects are similar to those of the reaction mixtures with F/U molar ratios of 1.50 and 2.00.

Based on their ^{13}C CP-MAS spectra, Chuang and Maciel²⁷⁵ concluded that the degree of crosslinking through methylene linkages increases with increasing F/U molar ratios from 1.00 to 1.50 and from 1.50 to 2.00 in the UF resins, as seen in the spectra of Fig. 19. These spectra also show that the amounts of dimethylene ether linkages, urons and poly(oxymethylene)glycols also increase with increasing F/U molar ratios from 1.50 to 2.00 and from 2.00 to 3.00. The effects of F/U molar ratios of the structures of UF resins increases with increasing concentrations and decreasing pH values. For those UF resins prepared at pH 5, the amount of methylol groups in a resin increases with increasing F/U molar ratios, especially at intermediate and high reagent concentrations.

In order to obtain additional information on the mechanisms of various reactions in the complicated UF resin systems, Chuang and Maciel²⁷⁶ also used *N,N'*-dimethylolurea instead of formalin as a source of methylene groups in the UF resins. Figure 22 (left and middle columns) shows that the formation of methylene linkages (Eq. (11)) from *N,N'*-dimethylolurea and urea is so favourable and quick at pH 1 and pH 3 that the low solubilities of *N,N'*-dimethylolurea and UF resins do not hinder the progress of the reaction under even the most concentrated conditions (Fig. 22a and d). In contrast to that, as seen in Fig. 22g, due to a less favourable and slower reaction between *N,N'*-dimethylolurea and urea, the low solubilities of

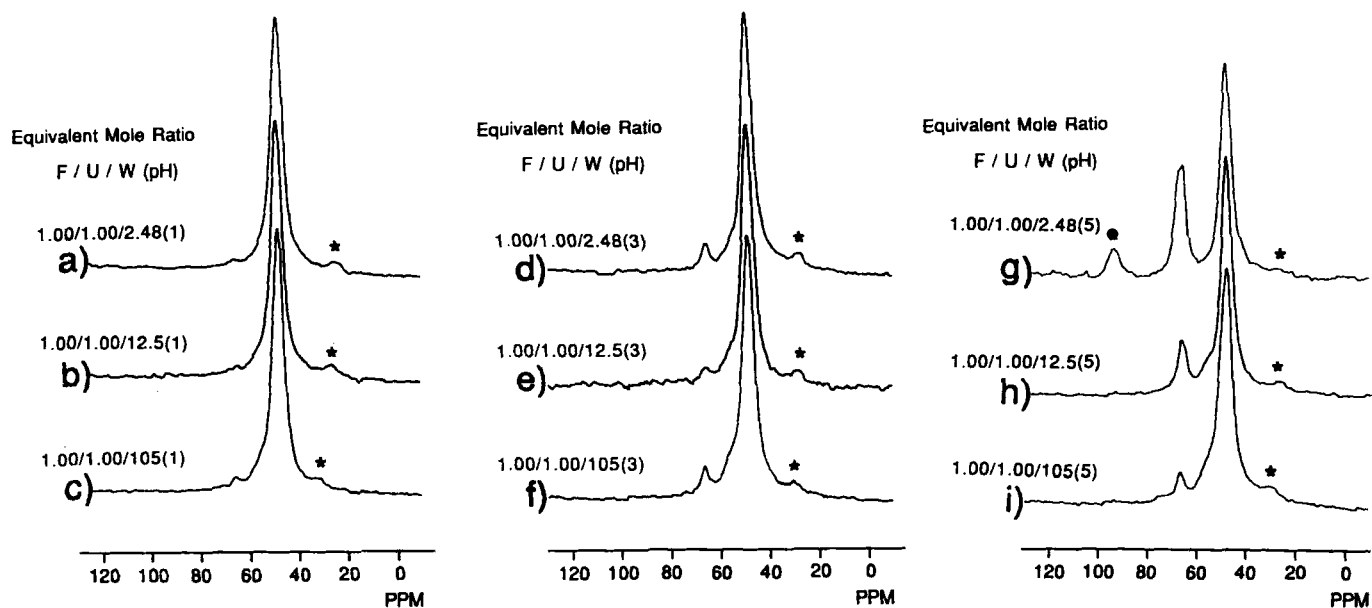


Fig. 22. 50.3 MHz ^{13}C CP-MAS spectra of nine UF resins prepared from *N,N'*-dimethylolurea, urea and water at three different concentrations and at pHs 1 (left column), 3 (middle column) and 5 (right column) as indicated. The spectra are plotted with the same height for peaks assigned to carbonyl carbons; only the spectral regions assigned to aliphatic carbons are shown here. Spinning sidebands are indicated by asterisks.

N,N'-dimethylolurea and UF resins leave some unreacted methylol groups (65 ppm peak) in the most concentrated reaction mixture (designated 1.00/1.00/2.48(5) for the indicated F/U/H₂O molar ratios and (pH)). With some dilution, the amounts of unreacted methylol groups in the 1.00/1.00/12.5(5) and 1.00/1.00/105(5) reaction mixtures diminished dramatically (Fig. 22h and i).

Chuang and Maciel²⁷⁶ observed that the reactions among *N,N'*-dimethylolurea molecules themselves proceed so well at pH 1 that the low solubilities of *N,N'*-dimethylolurea and UF resins play only a small role in determining the structures of UF resins, as indicated by Fig. 23 (left column). The major components in these three UF resins are crosslinking methylene linkages, linear methylene linkages, methylol groups and urons. The amounts of methylol groups and urons decrease with decreases in reagent concentrations, implying that the reaction is more complete at lower concentrations. Figure 23 (middle column) indicates that the reactions among *N,N'*-dimethylolurea molecules themselves are less favourable and slower at pH 3 than at pH 1. The low solubilities of *N,N'*-dimethylolurea and UF resins play a big role in determining the structures of UF resins, and the reaction at pH 3 is much more complete at lower concentrations. The rates of reactions among *N,N'*-dimethylolurea molecules themselves at pH 5 are so low that the reactions are far from complete under concentrated conditions (Fig. 23 g and h). There is still a large amount of unreacted methylol groups (65 ppm and 72 ppm peak) left even in the most dilute reaction mixture (Fig. 23i).

3.3.2. ¹⁵N CP-MAS studies of UF resin systems

As nitrogen is another element that is comparable in occurrence to carbon in UF resins, Chuang *et al.*¹⁰⁶ examined ¹⁵N-enriched UF resins by ¹⁵N CP-MAS NMR. Distinctions between secondary and tertiary amide nitrogens were made partly on the basis of chemical shift differences and partly on the basis of dipolar-dephasing experiments,^{88,89} as tertiary amide nitrogens have no directly attached hydrogen. Chuang *et al.* concluded that a lower level of structural detail is usually obtained by ¹⁵N CP-MAS NMR than what is provided by corresponding ¹³C CP-MAS experiments on the two UF resin samples examined, even though ¹⁵N data provide a useful supplement to ¹³C data in the elucidation of structure in cured resins.

Equipped with a large-volume (2.5 cm³) MAS spinner system,^{119,122} Chuang and Maciel¹²³ later utilized the ¹⁵N CP-MAS technique to investigate an extensive series of UF resins in natural abundance. For UF resins prepared under acidic conditions, ¹⁵N CP-MAS NMR spectra provide clean evidence for the existence of unreacted primary amide sites and crosslinking tertiary amide sites in UF resins with some structural detail; ¹³C CP-MAS experiments on the same samples had been shown^{275,276} to be powerful for studying details of these structurally complicated resins (Section 3.3.1.).

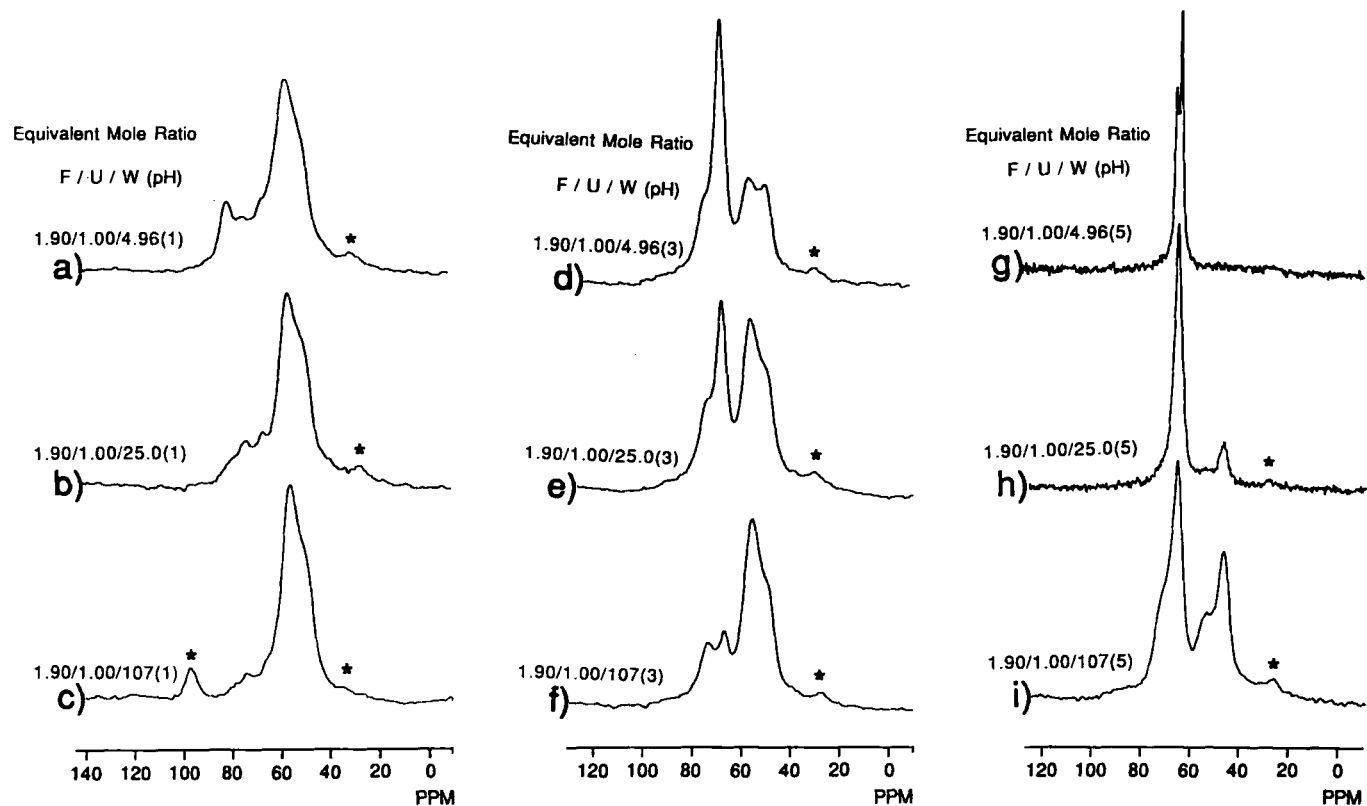


Fig. 23. 50.3 MHz ^{13}C CP-MAS spectra of nine UF resins prepared from *N,N'*-dimethylolurea reagent and water at three different concentrations and at pHs 1 (left column), 3 (middle column) and 5 (right column) indicated. The spectra are plotted with the same height for peaks assigned to carbonyl carbons; only the spectral regions assigned to aliphatic carbons are shown here. Spinning sidebands are indicated by asterisks.

As indicated above, the combination of residual ^{14}N quadrupolar effects on MAS averaging of the ^{14}N - ^{13}C dipolar interaction and primarily inhomogeneous line broadening due to chemical shift dispersion prevents the 50.3 MHz ^{13}C CP-MAS NMR spectra from providing a clear distinction between dimethylene ether linkages and methylol groups in methylol-rich UF resins (Section 3.3.1.). Chuang and Maciel¹²³ found that ^{15}N CP-MAS NMR clearly distinguishes between such linkages in UF resins prepared under neutral or basic conditions. The ^{15}N CP-MAS spectrum of a resin sample designated 1.00/1.00/12.5(9),¹²³ shown in Fig. 24a, indicates that this resin sample, obtained from a clear solution after vacuum drying, has *N,N'*-dimethylolurea (102 ppm peak) as its major constituent, with some monomethylolurea (102 and 78 ppm peaks) and/or urea (78 ppm) as a minor constituent. The ^{15}N CP-MAS spectrum of Fig. 24b shows that a resin sample (designated 1.00/1.00/12.5(9 \rightarrow 7)) prepared from an identical mixture, but neutralized to pH 7 before vacuum drying, has a smaller relative intensity at 102 ppm and additional peaks at 94 and 90 ppm. During neutralization of the reaction mixture with an F/U/W molar ratio of 1.00/1.00/12.5 from pH 9 to pH 7, some portion of the solution may briefly have been under acidic conditions, and formation of methylene linkages (94 ppm peak in the ^{15}N CP-MAS spectrum) and dimethylene ether linkages (90 ppm peak) occurred. Furthermore, the formation of dimethylene ether linkages (*vide infra*) is more feasible at pH 7 than at pH 9 during the vacuum drying period.

Chuang and Maciel also investigated the distribution of methylene linkages and dimethylene ether linkages in the 1.00/1.00/12.5(9 \rightarrow 7) UF resin by ^{15}N CP-MAS NMR. Figure 24b and c shows ^{15}N CP-MAS spectra of this resin taken at two different repetition rates, 30 s and 1 s. These two spectra indicate that protons that contribute via cross-polarization to ^{15}N peaks at 90 and 94 ppm have about the same T_1 of ~ 2 s, and protons generating cross-polarized ^{15}N peaks at 78 ppm and 102 ppm have about the same T_1 of ~ 8 s. Clearly, ^1H spin diffusion between these two proton sets with different T_1 values is too slow to yield a uniform T_1 . They also used a previously reported CP-detected ^1H spin diffusion technique¹²⁶ to establish that ^1H spin diffusion is efficient *within* each proton set and the cause of the inefficient ^1H - ^1H spin diffusion *between* two proton sets with different T_1 values must be spatial segregation. They estimated the domain size of the aggregate to be larger than 300 Å, on the basis of an equation of McBrierty and coworkers:^{197,204} $\langle r^2 \rangle^{1/2} = (6D\tau)^{1/2}$, where $\langle r^2 \rangle^{1/2}$ is the root-mean-square diffusive path, D is the spin-diffusion coefficient (for protons, $D \sim 10^{-12} \text{ cm}^2 \text{ s}^{-1}$) and τ is the time over which proton spin-diffusion produces a universal relaxation time (e.g. T_1). They also observed a common spectral feature that is prominent in the ^{15}N CP-MAS spectra of all the UF resin samples that display this kind of spatial segregation in T_1^{H} behaviour; this feature is strong intensity at 102 ppm, a peak that arises from

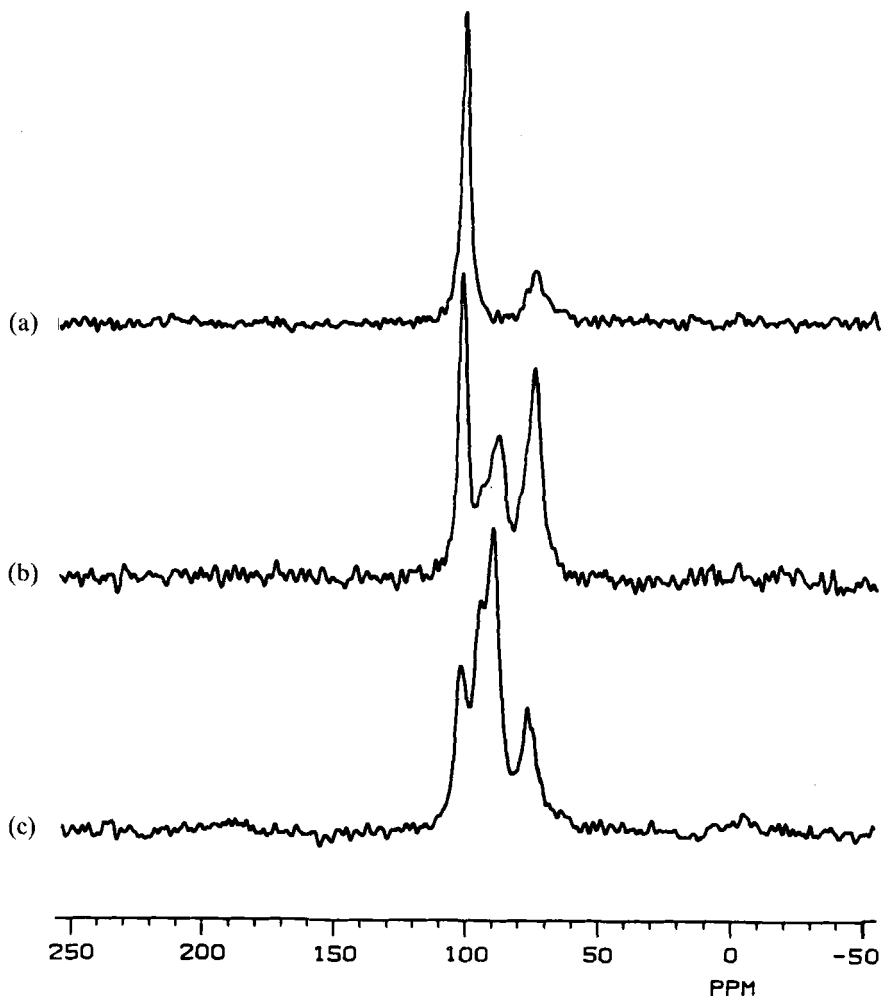


Fig. 24. 20.3 MHz natural-abundance ^{15}N CP-MAS NMR spectra of a UF resin prepared with an F/U/W molar ratio of 1.00/1.00/12.5 at pH 9. UF resin solids were obtained by (a) vacuum drying at 10^{-2} torr and -5°C the clear 1.00/1.00/12.5 solution at pH 9; (b) and (c) vacuum drying at 10^{-2} torr and -5°C the clear 1.00/1.00/12.5 solution after neutralization to pH 7. CP contact time = 1 ms; repetition time = 30 s for (a) and (b), 1 s for (c).

secondary amides attached to methylol groups. It was speculated that the cause of this segregation may be the aggregation of methylol-containing resin units, probably because of hydrogen bonding. Proton T_1 values of several UF resins prepared under acidic conditions and UF resins without large amounts of methylol groups were measured, and a uniform T_1^{H} value was found within each sample.

Based on their ^{15}N CP-MAS studies, represented in Fig. 25, Chuang and Maciel¹²³ concluded that the formation of dimethylene ether linkages is most favourable at pH 12 and least favourable at pH 9, among the three pH values of 7, 9 and 12.

3.3.3. *NMR study of the stabilities of UF resin components towards hydrolytic treatments*

Both poor durability and the emission of formaldehyde^{252,282–288} are important drawbacks to the use of cured UF resin products. It has been widely believed that these deficiencies are due in considerable degree to hydrolytic degradation of UF resins, according to the back reactions represented in Eqs (9)–(12), especially under warm conditions of high humidity and high acidity.

Chuang and Maciel²⁷⁷ carried out a ^{13}C CP-MAS NMR characterization of the solid residues of nine UF resins after hydrolytic treatment at pH 4 and 86°C for 20 h and the solid residues of one UF resin after eight different hydrolytic treatments. For UF resins prepared from a mixture with an F/U molar ratio of 1.00, all the major components, including linear methylene linkages, crosslinking methylene linkages and terminal methylols, show a high degree of stability towards hydrolytic treatment at pH 4 and 86°C for 20 h, whereas crosslinking methylene linkages in UF resins show a higher susceptibility towards this hydrolytic treatment than do linear methylene linkages. UF resins prepared with an F/U molar ratio of 2.00/1.00 under acidic conditions contain a wide variety of components;²⁷⁵ and some of these components are susceptible to hydrolytic degradation at pH 4 and 86°C.²⁷⁷ As seen in Fig. 26 for a typical example, these include dimethylene ether linkages (69 and 76 ppm), polyoxymethylene glycols (88–92 ppm), and methylol groups attached to tertiary amides (72 ppm). These hydrolytically susceptible components are probably the main formaldehyde emitters in UF resin products. Linear methylene linkages and crosslinking methylene linkages are relatively stable towards hydrolytic treatments at pH 4 and 86°C in these 2.00/2.00 UF resins, as seen in Fig. 26 for a typical example.

^{13}C CP-MAS studies of the hydrolytic treatments of a UF resin with an F/U/W molar ratio of 2.00/1.00/4.96 at 25°C indicate²⁷⁷ that most of the dimethylene ether linkages and short-chain polyoxymethylene glycols are susceptible to hydrolysis at pH 4. Figure 26 shows some typical results. Even though methylol groups attached to tertiary amides are relatively stable to 25°C hydrolytic treatment at pH 4, they display a high susceptibility to hydrolytic treatment at the same temperature and pH 1, as seen by comparing spectra in Fig. 26 (left column). The ^{13}C CP-MAS spectra of samples obtained by subjecting the same 2.00/1.00/4.96 UF resin to hydrolytic treatments at five different pH values at 86°C are shown in Fig. 26 (right column).²⁷⁷ These spectra indicate that both dimethylene ether

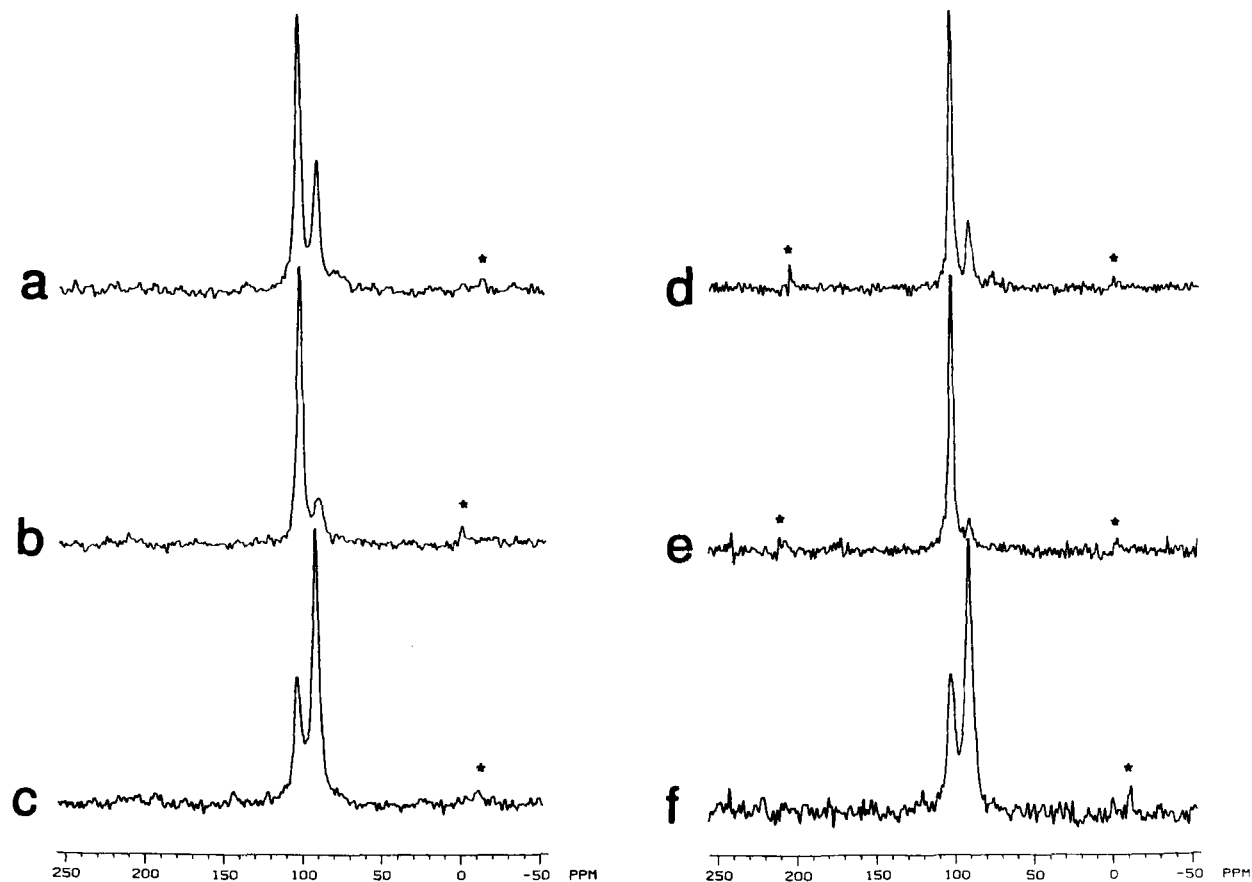


Fig. 25. 20.3 MHz natural-abundance ^{15}N CP-MAS NMR spectra of UF resins prepared with an F/U/W molar ratio of 2.00/1.00/4.96 at three different pH values: (a) and (d) pH 7; (b) and (e) pH 9; (c) and (f) pH 12. CP contact time = 1 ms; repetition time = 3 s (left column) and 30 s (right column). Spinning sidebands are indicated by asterisks.¹²³

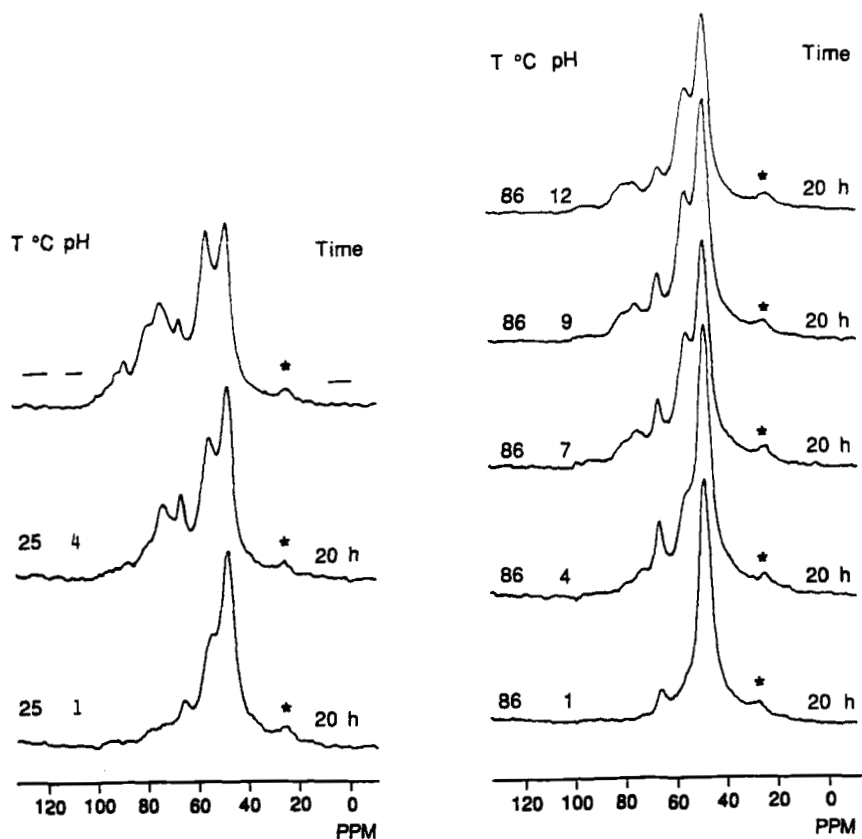
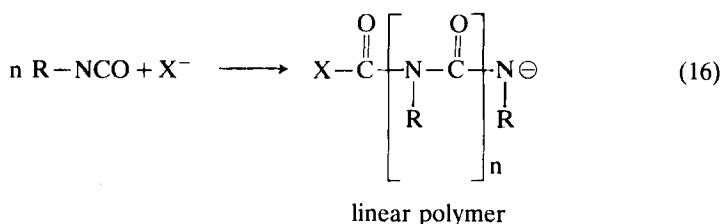
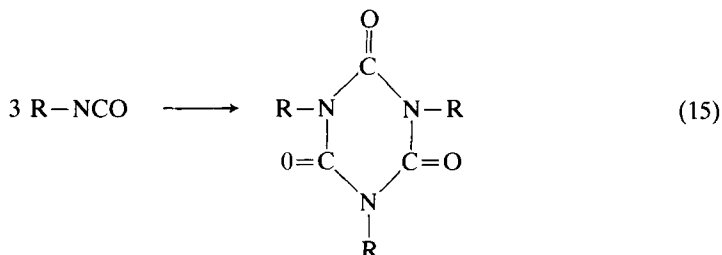
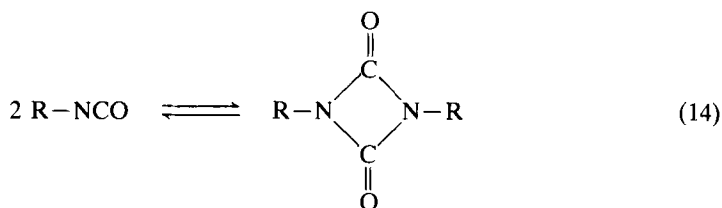


Fig. 26. 50.3 MHz ^{13}C CP-MAS spectra of a UF resin sample prepared from a mixture of formalin and urea with an equivalent F/U/W molar ratio of 2.00/1.00/4.96 at pH 3 (top spectrum, left column) and its solid residues after hydrolytic treatments at 25°C and at pHs 4 and 1 (left column) and its solid residues after hydrolytic treatments at 86°C and at five different pH values indicated for 20 h (right column). The spectra are plotted with the same height for peaks assigned to carbonyl carbons; only the spectral regions assigned to aliphatic carbons are shown here. Spinning sidebands are indicated by asterisks.

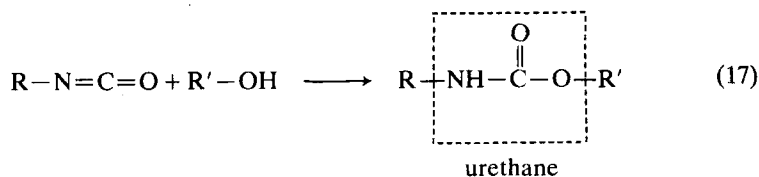
linkages and methylol groups attached to tertiary amides are susceptible to hydrolytic treatments at 86°C, especially at high pH or low pH values; the former moieties are especially susceptible to 86°C hydrolytic treatments under acidic conditions. Crosslinking methylene linkages are seen to show some degree of susceptibility to 86°C hydrolytic treatment at pH 1, but less susceptibility at the higher pH values investigated.

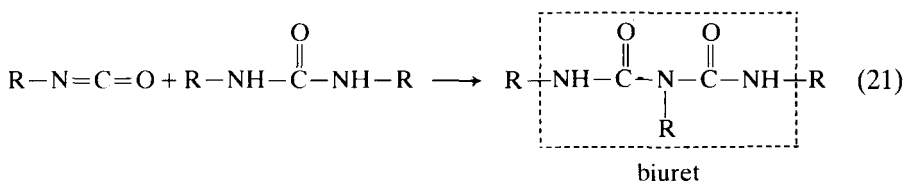
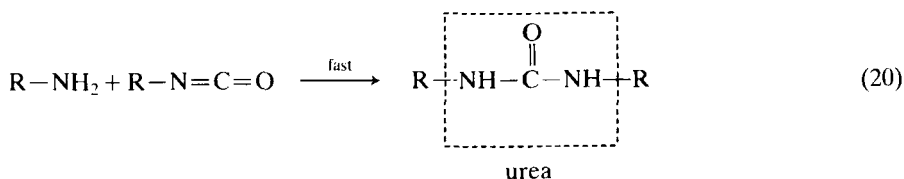
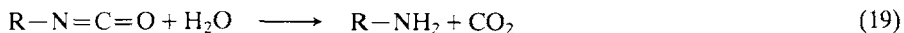
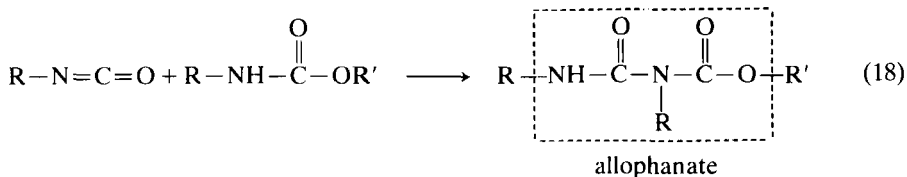
3.4. Resins derived from isocyanates

Isocyanates ($R-N=C=O$) can undergo a wide variety of reactions.²⁸⁹ In the presence of a suitable Lewis acid, such as stannous octoate, isocyanates polymerize to form several products,²⁸⁹⁻²⁹¹ such as cyclic dimers (uretidiones; Eq. (14)), cyclic trimers (isocyanurates; Eq. (15)) and linear polymers (Eq. (16)).



Isocyanates can react with compounds containing active hydrogen to form various kinds of linkages, for example urethanes, allophanates, ureas and biurets.²⁸⁹





Because of their high reactivities towards compounds containing active hydrogen, isocyanates have been used as adhesives.²⁹²⁻²⁹⁴

Polyurethanes prepared from diisocyanates and diols possess an excellent range of properties and are the materials of choice for many applications. The outstanding and versatile properties are due to the variety of their chemical structures (Eqs (14)–(21)) and the formation of multiblock copolymers with alternating soft and hard segments.^{295,296} The soft segments can be either long-chain flexible polyethers or polyesters, and the hard segments can be either urethanes or ureas. Because urethanes or ureas of one hard segment can participate in hydrogen bonding with urethanes or ureas of another segment,²⁹⁷⁻²⁹⁹ the hard segments can segregate from the soft segments to form a microheterogeneous composite and behave like the crosslinking points of an elastomer.³⁰⁰⁻³⁰⁶

Solid-state NMR studies have made some important contributions to the understanding of isocyanate-based polymer chemistry,^{113-116,307-310} especially in phase separation in polyurethanes,^{307,311-316} molecular motions in the hard segments of polyurethanes,^{184,185,317} extension effects on the phase structure of polyurethane elastomers^{318,319} and the interpenetration of polyurethanes in polymer networks.^{320,321}

3.4.1. Isocyanurate-rich and biuret-rich MDI-based resins

4,4'-Methylenebis(phenyl isocyanate) (MDI, see Table 2 for structure) is a difunctional monomer with widespread application in the foam, adhesive, construction and related industries.^{292,295,296} The modification of polyurethanes with isocyanurate crosslinks can produce materials with enhanced thermal and dimensional stabilities.³²²⁻³²⁷ Duff and Maciel¹¹³ employed ^{13}C (natural abundance) and ^{15}N (enriched) CP-MAS techniques to characterize MDI-based polyisocyanurate resin systems. Several such resins were prepared under a variety of reaction conditions from natural-abundance MDI and from ^{15}N -enriched MDI, using stannous octoate as catalyst. Pertinent ^{13}C and ^{15}N chemical shifts are shown in Table 2. Figure 27 shows the effects of static magnetic field strength on the ^{13}C CP-MAS spectra of an MDI-polyisocyanurate resin cured with stannous octoate for 2 h at 120°C. The resonances of ^{13}C nuclei that are located near ^{14}N nuclei are broadened by the interference of MAS averaging of the ^{14}N - ^{13}C dipolar interaction by the ^{14}N quadrupole effect (see Section 2.1.5.); this broadening decreases with increasing field strength. The resolution of the isocyanurate resonance (150 ppm) is excellent at 90.5 MHz, but the spectrum shown is severely complicated by spinning sidebands (MAS speed was only 3.2 kHz). Because of the uncertainties associated with the cross-polarization efficiencies at the highest available spinning speeds⁷⁹ (see also Section 2.1.4.), Duff and Maciel studied the MDI-polyisocyanurate systems at the compromise field of 4.7 T (50.3 MHz for ^{13}C).

The spectra in Fig. 28 show that ^{13}C CP-MAS NMR can identify the isocyanurate carbonyl carbon (150 ppm), but cannot cleanly distinguish an unreacted isocyanate carbonyl carbon (125 ppm) from aromatic carbons at positions *ortho* and/or *meta* relative to isocyanate-substituted aromatic carbons. Therefore, the use of relative ^{13}C CP-MAS intensities of resonances due to isocyanurate carbonyl carbons and unreacted isocyanate carbonyl carbons for the estimation of the concentration of isocyanurate crosslinks was only qualitative. Even though the dipolar-dephasing ^{13}C CP-MAS technique can qualitatively distinguish unreacted isocyanate carbonyl carbons from unsubstituted aromatic carbons at *ortho* and/or *meta* positions relative to an isocyanate-substituted carbon, the resulting intensities of the spectrum cannot be treated in a quantitative manner without extensive characterization of the relevant spin dynamics. Based on the ^{13}C results on MDI-polyisocyanurate resins cured at five different temperatures, shown in Fig. 28, Duff and Maciel concluded *qualitatively* that the relative amount of unreacted isocyanate appears to be greatest for the cure temperatures of 100 and 160°C, while the corresponding ^{13}C intensity is lowest at 120°C. On the other hand, the relative amount of the isocyanurate reaches a maximum value for the cure temperature of 120°C. The ^{13}C CP-MAS spectra of the resin cured at 80°C show that some other chemical

Table 2. Structures and key NMR data on MDI-based model compounds^a (taken from Ref. 113).

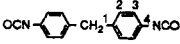
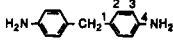
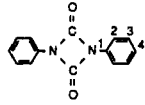
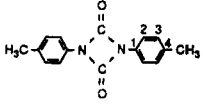
Prototype structure	Carbon or nitrogen	¹³ C chemical shift, ppm	¹⁵ N chemical shift, ppm	Description ^b
MDI 	CH ₂	41 ^c	—	Methylene carbons
	1	138	—	Methylene-substituted <i>para</i> carbons
	2	130 (130) ^d	—	Unsubstituted <i>meta</i> carbons
	3	125 (125)	—	Unsubstituted <i>ortho</i> carbons
	4	132	—	Isocyanate-substituted carbons
	CO	125 (125)	—	Isocyanate carbonyl carbons
	N	—	46 ^e (46) ^f	Isocyanate nitrogens
MDA 	CH ₂	41 ^g	—	Methylene carbons
	1	130	—	Methylene-substituted <i>para</i> carbons
	2	129	—	Unsubstituted <i>meta</i> carbons
	3	114	—	Unsubstituted <i>ortho</i> carbons
	4	146	—	Amino-substituted carbons
	N	—	52 ^g (56) ^h	Amino nitrogens
Phenyl uretidione 	1	135 ^{i,j} (136) ^k	—	Nitrogen-substituted carbons
	2	117 (117)	—	Unsubstituted <i>ortho</i> carbons
	3	129 (130)	—	Unsubstituted <i>meta</i> carbons
	4	125 (124)	—	Unsubstituted <i>para</i> carbons
	CO	151 (151)	—	Uretidione carbonyl carbons
	N	—	145 ^j	Uretidione nitrogens
<i>p</i> -tolyl uretidione 	1	134 ^{i,j}	—	Nitrogen-substituted carbons
	2	117	—	Unsubstituted <i>ortho</i> carbons
	3	130	—	Unsubstituted <i>meta</i> carbons
	4	132	—	Methyl-substituted <i>para</i> carbons
	CH ₃	21	—	Methyl carbons
	CO	151	—	Uretidione carbonyl carbons
	N	—	145 ^j (145) ^l	Uretidione nitrogens

Table 2—*contd.*

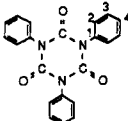
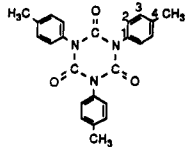
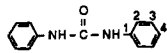
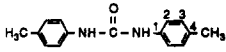
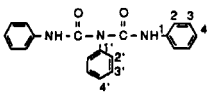
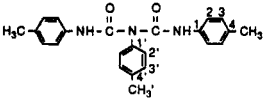
Prototype structure	Carbon or nitrogen	¹³ C chemical shift, ppm	¹⁵ N chemical shift, ppm	Description ^b	
Phenyl isocyanurate 	1	134 ^{m,n} (133) ^o	—	Nitrogen-substituted carbons	
	2	128	(129)	—	Unsubstituted <i>ortho</i> carbons
	3	129	(129)	—	Unsubstituted <i>meta</i> carbons
	4	129	(129)	—	Unsubstituted <i>para</i> carbons
	CO	149	(150)	—	Isocyanurate carbonyl carbons
	N	—	149 ⁿ	—	Isocyanurate nitrogens
<p><i>p</i>-tolyl isocyanurate</p> 	1	134 ^{m,n} (133) ^p	—	Nitrogen-substituted carbons	
	2	130	(130)	—	Unsubstituted <i>ortho</i> carbons
	3	130	(130)	—	Unsubstituted <i>meta</i> carbons
	4	139	(138)	—	Methyl-substituted <i>para</i> carbons
	CH ₃	21	(22)	—	Methyl carbons
	CO	150	(149)	—	Isocyanurate carbonyl carbons
	N	—	149 ⁿ (149) ^q	—	Isocyanurate nitrogens
Phenyl urea 	1	140 ^{r,s} (139) ⁱ	—	Nitrogen-substituted carbons	
	2	118	—	—	Unsubstituted <i>ortho</i> carbons
	3	129	(130)	—	Unsubstituted <i>meta</i> carbons
	4	122	—	—	Unsubstituted <i>para</i> carbons
	CO	153	(156)	—	Urea carbonyl carbons
	N	—	106 ^s (106) ^u	—	Urea nitrogens
<p><i>p</i>-tolyl urea</p> 	1	137 ^{r,s}	—	Nitrogen-substituted carbons	
	2	118	—	—	Unsubstituted <i>ortho</i> carbons
	3	129	—	—	Unsubstituted <i>meta</i> carbons
	4	131	—	—	Methyl-substituted <i>para</i> carbons
	CH ₃	20	—	—	Methyl carbons
	CO	153	—	—	Urea carbonyl carbons
	N	—	107 ^s	—	Urea nitrogens

Table 2—*contd.*

Prototype structure	Carbon or nitrogen	¹³ C chemical shift, ppm	¹⁵ N chemical shift, ppm	Description ^b
Phenyl biuret 	1	139 ^{v,w}	—	Amide-substituted carbons
	2	122	—	Unsubstituted <i>ortho</i> (to NH) carbons
	3	130	—	Unsubstituted <i>meta</i> (to NH) carbons
	4	125	—	Unsubstituted <i>para</i> (to NH) carbons
	1'	138	—	Imide-substituted carbons
	2'	131	—	Unsubstituted <i>ortho</i> (to N) carbons
	3'	131	—	Unsubstituted <i>meta</i> (to N) carbons
	4'	130	—	Unsubstituted <i>para</i> (to N) carbons
	CO	155	—	Carbonyl carbons
	NH	—	116 ^w	Amide nitrogens
	N	—	143	Imide nitrogens
<i>p</i> -tolyl biuret 	1	140 ^{v,w} (141) ^x	—	Amide-substituted carbons
	2	122 (120)	—	Unsubstituted <i>ortho</i> (to NH) carbons
	3	130 (131)	—	Unsubstituted <i>meta</i> (to NH) carbons
	4	134 (134)	—	Methyl-substituted <i>para</i> (to NH) carbons
	CH ₃	21 (21)	—	<i>para</i> methyl (to NH) carbons
	1'	137 (136)	—	Imide-substituted carbons
	2'	131 (132)	—	Unsubstituted <i>ortho</i> (to N) carbons
	3'	131 (132)	—	Unsubstituted <i>meta</i> (to N) carbons
	4'	135 (136)	—	Methyl-substituted <i>para</i> (to N) carbons
	CH ₃ '	20 (21)	—	<i>para</i> methyl (to N) carbons
	CO	155 (155)	—	Carbonyl carbons
	NH	—	114 ^w	Amide nitrogens
	N	—	143	Imide nitrogens

^aParenteses indicate chemical shifts obtained from ¹³C and ¹⁵N CP/MAS or single-pulse MAS experiments. ^b*Ortho*, *meta* and *para* designations are relative to the nitrogen-substituted carbon. ^cDelides, C.; Pethrick, R. A.; Cunliffe, A. V.; Klein, P. G. *Polymer* **1981**, 22, 1205. ^d37.5 MHz ¹³C single-pulse MAS experiment repetition delay = *t*_d = 55 s. ^eSibi, M.P.; Lichter, R. L. *J. Org. Chem.* **1979**, 44, 3017. ^fCP contact time = *τ* = 6 ms; repetition delay = *t*_d = 30 s. ^g1.5 g in 8 ml of dimethylsulphoxide. ^h*τ* = 1 ms; *t*_d = 200 s. ⁱPrepared as in: Raiford, L. C.; Freyermuth, H. B. *J. Org. Chem.* **1943**, 8, 230. ^j0.5 g in 10 ml of benzene. ^k*τ* = 3 ms; *t*_d = 30 s. ^l*τ* = 6 ms; *t*_d = 30 s. ^mPrepared as in Ref. 4. ⁿ1.0 g in 8 ml of acetone. ^o*τ* = 3 ms; *t*_d = 30 s. ^p*τ* = 3 ms; *t*_d = 30 s. ^q*τ* = 6 ms; *t*_d = 10 s. ^rPrepared as in Ref. 36. ^s1.0 g in 8 ml of dimethylsulphoxide. ^t*τ* = 3 ms; *t*_d = 30 s. ^u*τ* = 1 ms; *t*_d = 100 s. ^vPrepared as in Ref. 40. ^w0.5 g in 8 ml of acetone. ^x37.5 MHz ¹³C CP/MAS experiment, *τ* = 1.5 ms; *t*_d = 10 s.

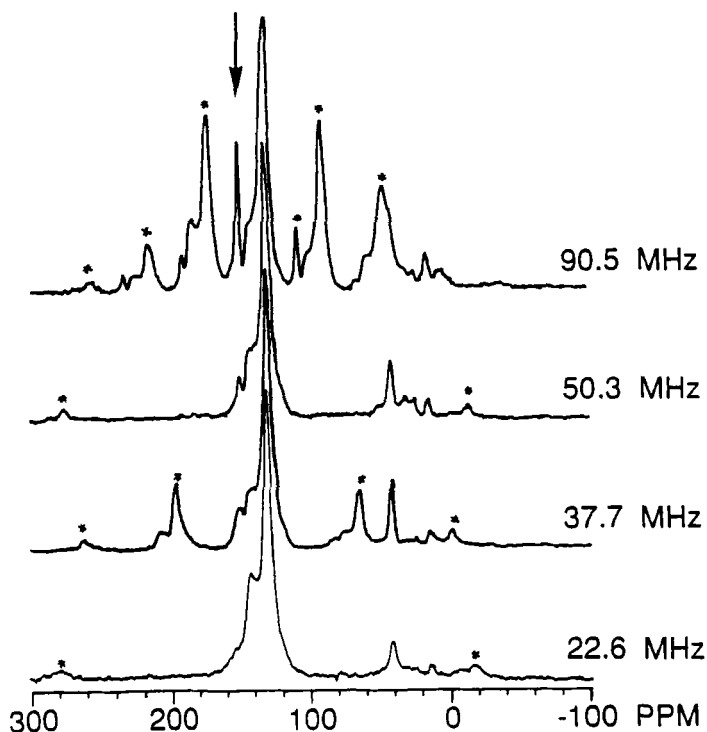


Fig. 27. Effects of static magnetic field strength on the ^{13}C CP-MAS spectra of an MDI-polyisocyanurate resin cured with stannous octoate for 2 h at 120°C . The ^{15}C Larmor frequency is indicated on the right side of each spectrum. The arrow indicates the position of the isocyanurate carbonyl resonance. Asterisks indicate positions of spinning sidebands.¹¹³

species are formed in this resin. Even with the aid of spectra from an MDI-polyurea and MDI-based biuret resin system, Duff and Maciel could only tentatively suggest that the formation of biuret and/or urea linkages is competitive with isocyanurate formation and that the combination of these pathways results in an increased consumption of isocyanate cured at 100°C , where the formation of biuret and/or urea linkages is not prevalent.

In comparison to their ^{13}C CP-MAS counterparts, ^{15}N CP-MAS spectra¹¹³ (Fig. 29) of ^{15}N -enriched MDI-polyisocyanurate resins cured at 100, 120 and 160°C are simpler, and minor products can be clearly identified in the spectra. From determinations of T_{ρ}^{H} and T_{NH} values from variable contact-time ^{15}N CP-MAS experiments (Section 2.1.1. and Eq. (2)), quantitative results were obtained. Duff and Maciel concluded that isocyanurate crosslinks are favoured most at 120°C , among the temperatures examined, followed by 160°C and 100°C , and that the amount of unreacted

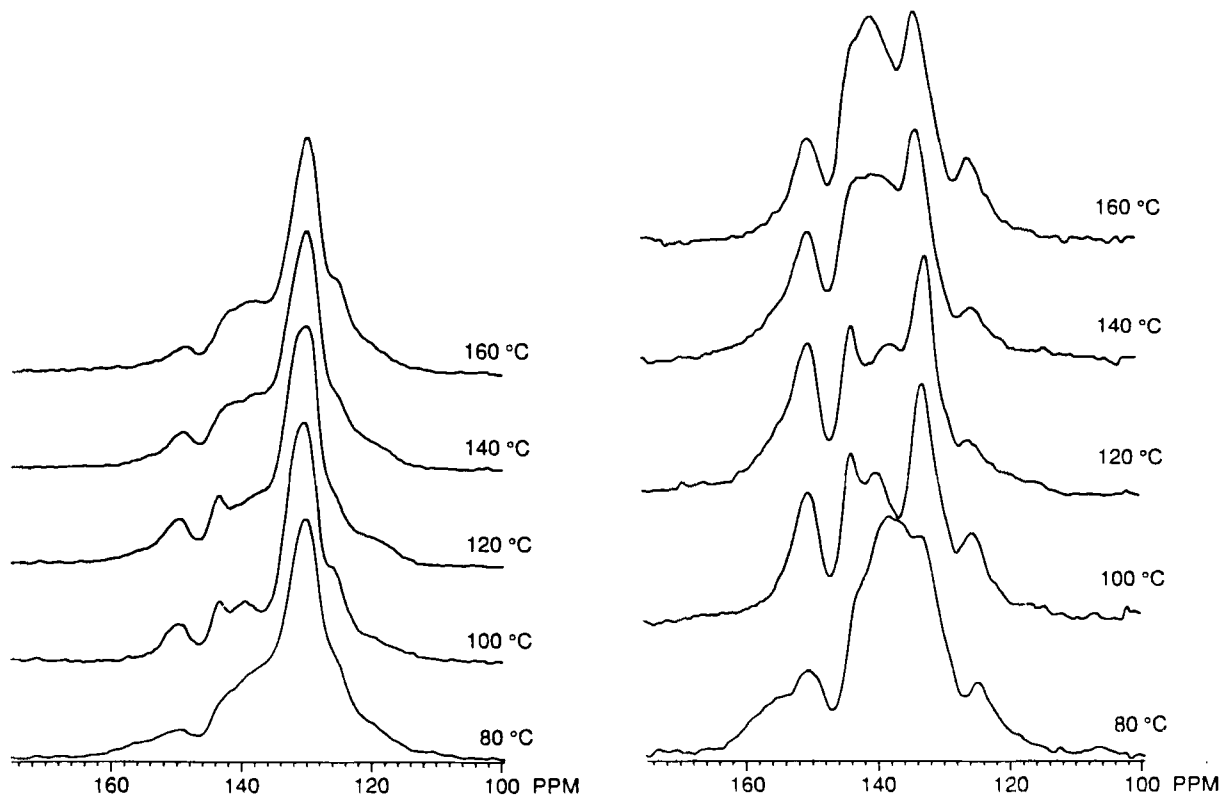


Fig. 28. 50.3 MHz ^{13}C CP-MAS spectra (left column) and dipolar-dephasing (70 μs) ^{13}C CP-MAS spectra (right column) of MDI-polyisocyanurate resins prepared at different temperatures. The spectra are expanded to show the pertinent chemical shift range, excluding the methylene carbon resonance at 41 ppm.¹¹³

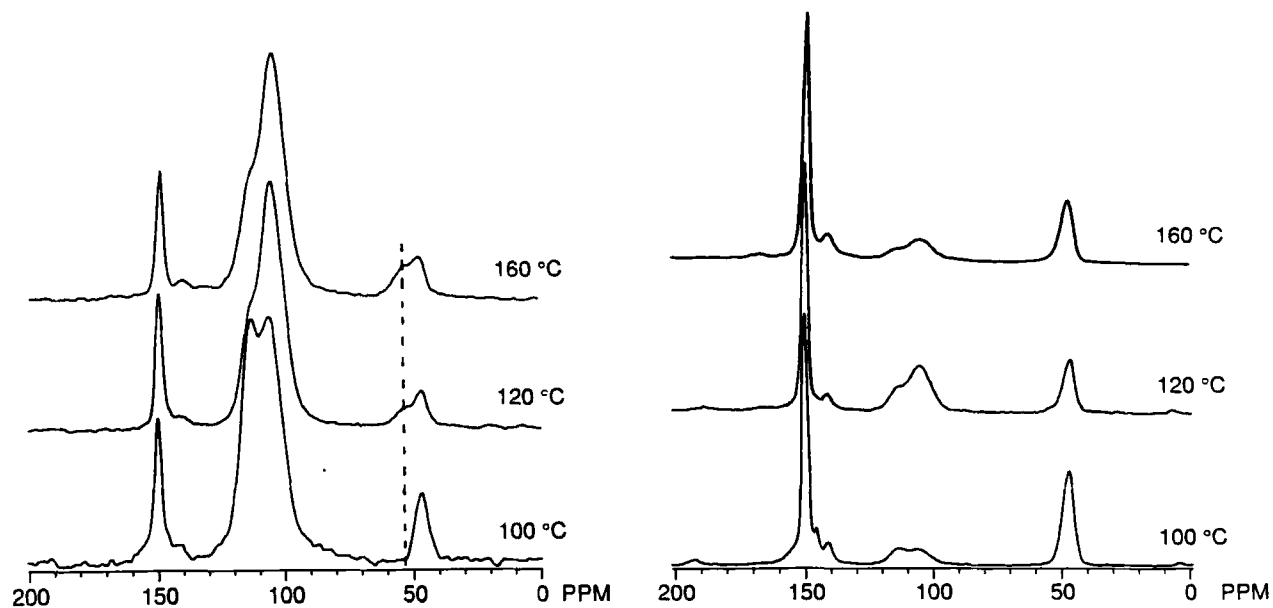


Fig. 29. 20.3 MHz ^{15}N CP-MAS spectra of three ^{15}N -enriched MDI-polyisocyanurate resins prepared at three different temperatures. CP contact time: 0.4 ms (left column) and 6 ms (right column).¹¹³

isocyanate was considerably larger (c. 38%) for the lowest cure temperature examined (100°C) than the highest cure temperature of 160°C (c. 30%). Figure 29 clearly indicates the formation of urea linkages (104 ppm), biuret-type networks (114 ppm and 141 ppm peaks) and amines (53 ppm peak) in the MDI-polyisocyanurate resin systems.

Duff and Maciel¹¹⁵ utilized both ^{15}N and ^{13}C CP-MAS NMR to monitor the fate of residual isocyanate groups in three ^{15}N -enriched MDI-polyisocyanurate resins cured at 100, 120 and 160°C¹¹³ after exposure to air for 7 months. The isocyanurate linkages are thermodynamically and hydrolytically stable and are not expected to degrade appreciably after curing.^{328, 329} Therefore, Duff and Maciel expected and confirmed that the solid-state post-cure reaction chemistry in those three MDI-based isocyanurate resins exposed to air for 7 months is essentially that originating from residual isocyanate groups still present after the initial cure. The consumption of isocyanate and the subsequent formation of urea linkages (Eqs (19) and (20)) during this 7-month period are clearly evident from changes in the ^{15}N CP-MAS spectra shown in Fig. 30. These ^{15}N CP-MAS NMR results readily identify the consumption of isocyanate to form amine (Eq. (19)) as the product of isocyanate hydrolysis. In addition, the formation of urea linkages (104 ppm) from the reaction of amine and isocyanate (Eq. (20)) was clearly shown. No significant reaction of urea linkages with isocyanate groups to form biuret linkages (Eq. (21)) is detected in the ^{15}N CP-MAS spectra of air-exposed samples shown in Fig. 30. Analysis of the variable contact-time ^{15}N CP-MAS spectra yielded estimates for the extent of the various types of isocyanate post-cure reaction chemistry for each resin. Again, Duff and Maciel demonstrated that ^{15}N CP-MAS was especially suited for monitoring solid-state reaction chemistry of the isocyanate group. Based on similar T_1^{N} and $T_{1\rho}^{\text{H}}$ values for isocyanate groups and isocyanurate moieties, and the significant differences between T_1^{N} and $T_{1\rho}^{\text{H}}$ values for other structures, Duff and Maciel concluded that isocyanate groups and isocyanurate moieties are closely associated and form distinct domains separated from other structures.

Duff and Maciel¹¹⁶ investigated the thermal decomposition of isocyanurate-rich MDI-based resins in successive heating experiments by ^{15}N and ^{13}C CP-MAS NMR. Representative spectra are shown in Figs 31 and 32. The ^{15}N CP-MAS results, corrected for spin dynamics, yield semiquantitative information on the concentrations of the various local nitrogen-atom environments during the thermal decomposition process. Once again, the ^{15}N CP-MAS and dipolar-dephasing ^{15}N CP-MAS experiments yielded simpler spectra than their ^{13}C CP-MAS counterparts in monitoring the thermal decomposition of MDI-polyisocyanurate resin. Even structures in low concentration, such as biuret and uretidione linkages, are clearly identified in the ^{15}N CP-MAS spectra (Fig. 32). Detailed changes in the chemical structure and constituency of the resin upon increasing heating

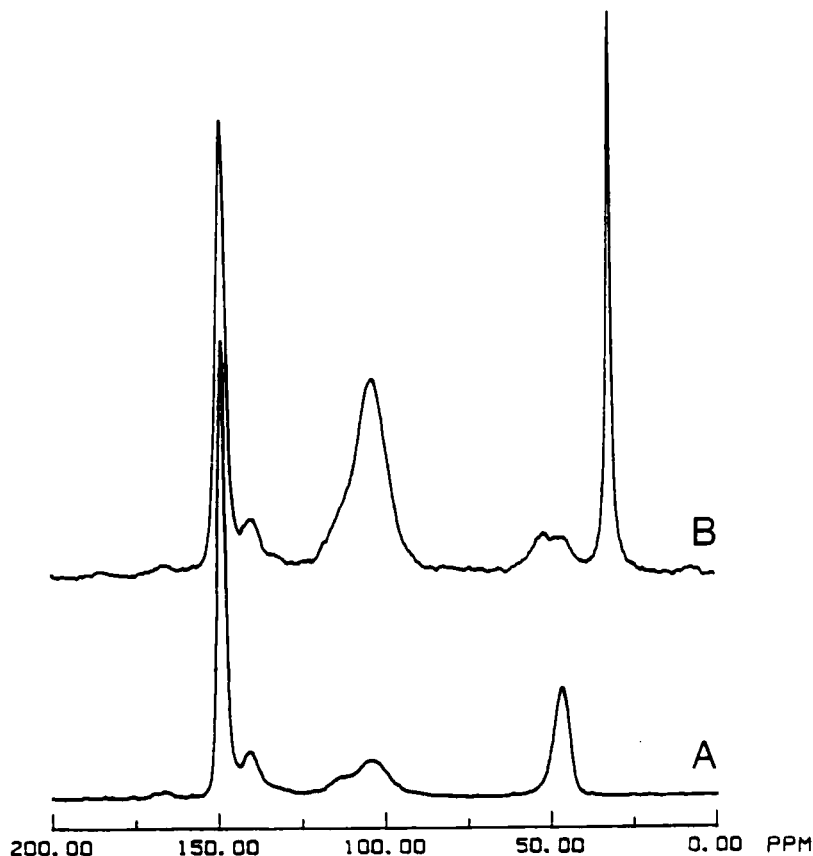


Fig. 30. (A) 20.3 MHz ^{15}N CP-MAS spectrum of a ^{15}N -enriched MDI-polyisocyanurate resin initially cured at 160°C . (B) 26.4 MHz ^{15}N CP-MAS spectrum of MDI-polyisocyanurate resin initially cured at 160°C after 7-month exposure to air. CP contact time = 6 ms; repetition time = 6 s.¹¹⁵

temperature were characterized from the ^{15}N CP-MAS results. ^{15}N CP-MAS and dipolar-dephasing ^{15}N CP-MAS experiments also verified that the increased linewidth of the urea peak (104 ppm) upon heating at 340°C or above is not due to carbodiimide structures ($\text{RN}=\text{C}=\text{NR}$). Also, on the basis of ESR results on similar samples prepared from ^{14}N -containing MDI-based resins, Duff and Maciel concluded that the concentration of free radicals is not high enough to account for the significant "broadening" observed in the ^{15}N CP-MAS spectrum of a ^{15}N -enriched sample heated at 340°C , attributing this "broadening" instead to an increased chemical shift dispersion for the urea linkages.

The formation of biuret linkages through combinations of reactions

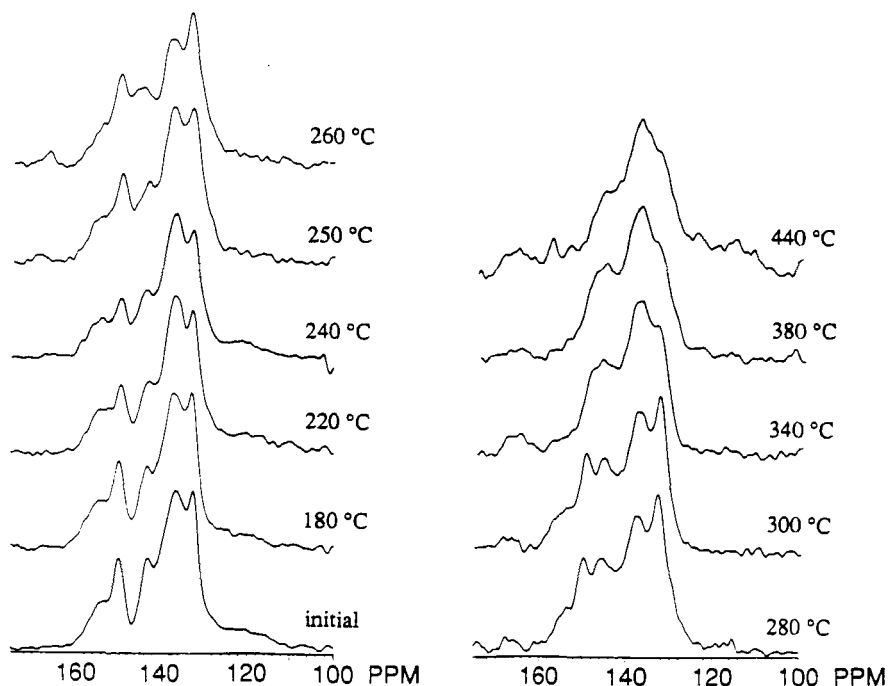


Fig. 31. 50.3 MHz ^{13}C CP-MAS dipolar-dephasing spectra of a ^{15}N -enriched isocyanurate-rich MDI-based resin heated at the temperatures indicated. CP contact time = 4 ms; repetition time = 6 s; dipolar-dephasing time = 70 μs .¹¹⁶

represented in Eqs (19)–(21) is regarded as a side reaction in the preparation of isocyanurate linkages^{113,289} or polyurethanes.²⁸⁹ One alternative pathway to the biuret linkages is the reaction of diisocyanates with carboxylic acids.^{330, 331} Duff and Maciel¹¹⁴ used ^{15}N and ^{13}C CP-MAS techniques to characterize cured $\text{HCO}_2\text{H}/\text{MDI}$ -based resin systems tailored with a high concentration of biuret linkages, and prepared under a variety of reaction conditions from MDI and formic acid. The ^{13}C CP-MAS and dipolar-dephasing ^{13}C CP-MAS results shown in Fig. 33 indicate that the concentration of biuret linkages is essentially constant in resins prepared from the same formal $\text{HCO}_2\text{H}/\text{MDI}$ molar ratio for curing temperatures between 120°C and 160°C, but is larger for larger formal $\text{HCO}_2\text{H}/\text{MDI}$ molar ratios for a given cure temperature. The ^{15}N CP-MAS spectra are shown in Fig. 34, which again are simpler and easier to interpret than their ^{13}C CP-MAS counterparts. From these spectra Duff and Maciel found that the major reaction between formic acid and MDI is the formation of MDI-based urea linkages (104 ppm) and formic acid anhydride, which react further with isocyanate groups to yield biuret linkages (114 ppm) and perhaps diformyl imide moieties.

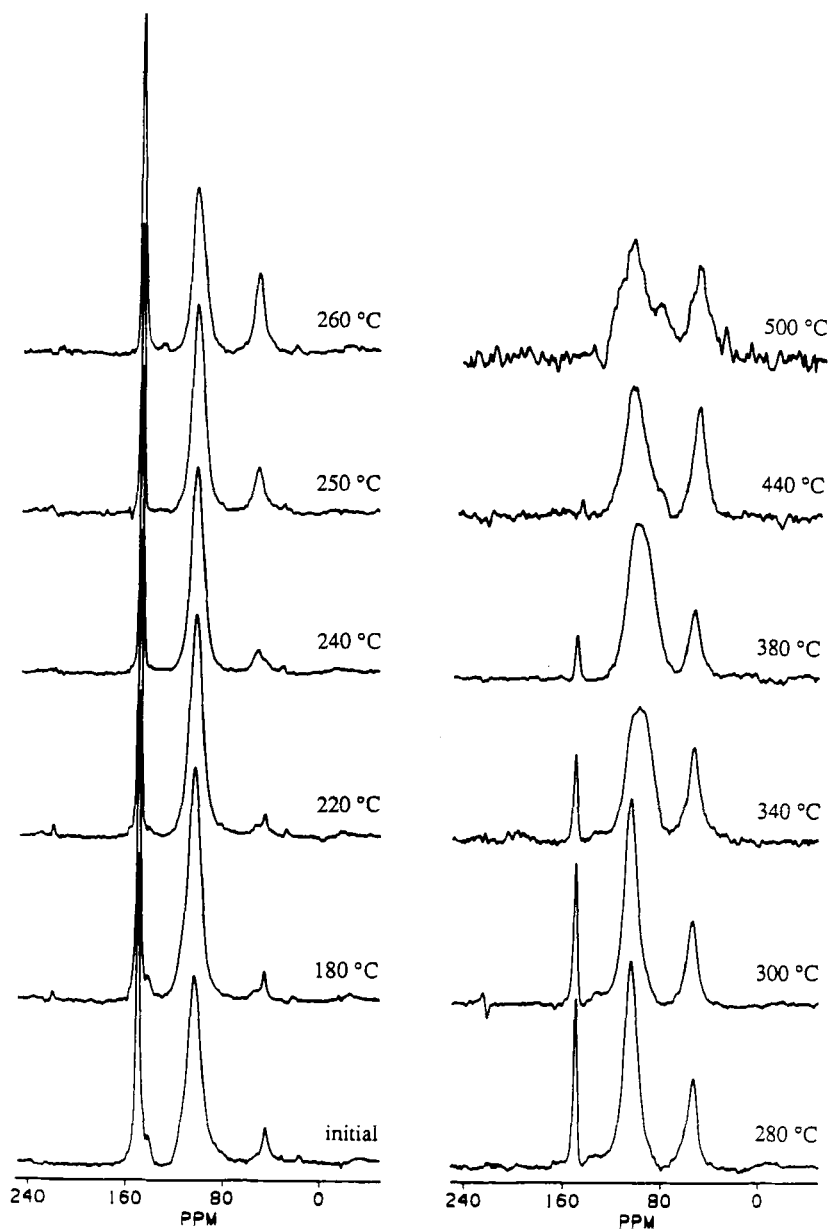
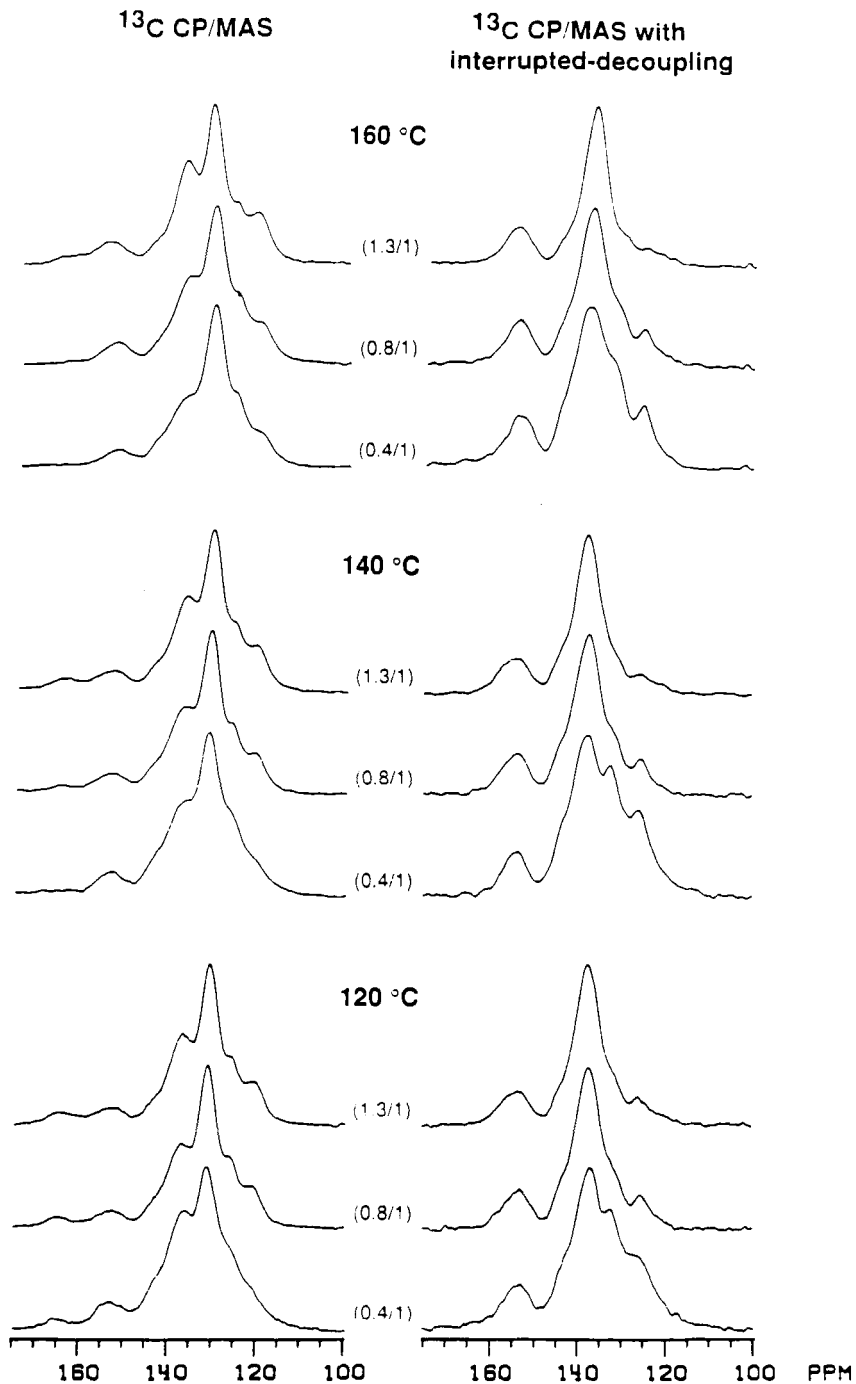


Fig. 32. 26.5 MHz ^{15}N CP-MAS spectra of a ^{15}N -enriched isocyanurate-rich MDI-based resin heated at the temperatures indicated.¹¹⁶



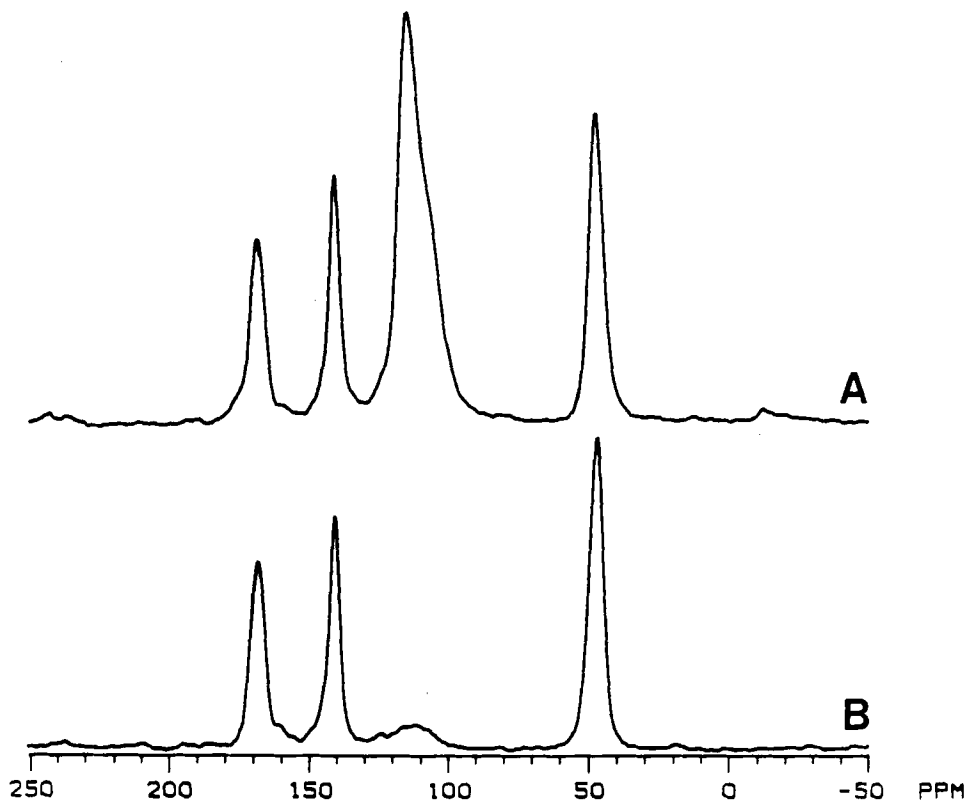


Fig. 34. 20.3 MHz ^{15}N CP-MAS spectra of ^{15}N -enriched $\text{HCO}_2\text{H}/\text{MDI}$ resin prepared from a reaction mixture having a formal $\text{HCO}_2\text{H}/\text{MDI}$ molar ratio of 0.4/1 and cured at 140°C for 3 h: (A) normal CP-MAS; (B) 70- μs dipolar-dephasing CP-MAS. CP contact time = 4 ms; repetition time = 6 s.¹¹⁴

3.4.2. Phase separation and molecular motions in polyurethanes

As indicated above, the excellent physical properties of polyurethanes are now generally attributed to phase separation of hard segments from soft segments, and it is important to characterize the nature of the phase separation in detail. Assink³¹¹ and Assink and Wilkes³¹² have shown that the ^1H -pulse free-induction decay (FID) of several polyurethanes consists of

Fig. 33. 50.3 MHz ^{13}C CP-MAS spectra (left column) and ^{13}C CP-MAS dipolar-dephasing spectra (right column) of $\text{HCO}_2\text{H}/\text{MDI}$ -based biuret resins cured for 3 h at the temperatures indicated. The fraction in parentheses indicates the formal $\text{HCO}_2\text{H}/\text{MDI}$ molar ratio of the reactants. CP contact time = 2 ms; repetition time = 6 s; dipolar-dephasing time = 70 μs .¹¹⁴

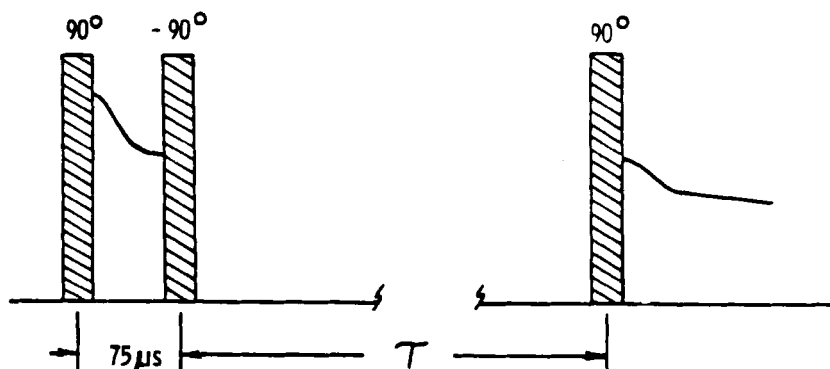


Fig. 35. Pulse sequence used for the Goldman-Shen experiment. The time during which the spin energy diffuses to reach an internal equilibrium is denoted τ .³³⁷

fast and slow components. The fast Gaussian decay component can be attributed to the rigid hard domains and the slow exponential decay component can be attributed to the flexible soft domains of polyurethanes.^{332,333} However, there are other possibilities, such as a very broad distribution of correlation times,³³⁴ and cross-correlation effects^{335,336} can cause a multiple-component FID.

In order to examine these two alternatives, Assink³¹³ performed a Goldman-Shen³³⁸ type of experiment, for which the pulse sequence is shown in Fig. 35: after a 90° pulse, the fast component of the FID is eliminated (dephased) within $75\ \mu\text{s}$, while the slow component still retains a significant portion of its magnetization; this remaining magnetization is tipped back to the direction of the magnetic field, where the longitudinal magnetization is allowed to approach an internal equilibrium through spin exchange for a duration, τ ; and finally the spin-exchanged magnetization is detected after another 90° pulse. From the Goldman-Shen data on polyurethanes, Assink concluded that the spin-diffusion rate is fast enough to establish only one proton T_1 value for each sample and that the contribution from spin-lattice relaxation to the magnetization equilibrium can be neglected for the τ values he employed. From the measurements of the ^1H spin-diffusion rate for each polyurethane he investigated, Assink confirmed the interpretation that there are two distinct spin systems in a phase-separated polyurethane, with the rigid domain that comprise the hard segments giving rise to the fast component of the FID and the flexible portion of soft segments giving rise to the slow component of FID. Based on a coplanar model equivalent to a rigid sphere surrounded by a uniform layer of mobile material, Assink estimated the domain size of the hard segment, obtaining results that are consistent with small-angle X-ray scattering measurements.^{339, 340} Assink also observed that the decay rate of the soft

phase appeared to vary with τ in his Goldman-Shen experiment and attributed the variation in decay rate to domain inhomogeneity or interface effects.

Eisenbach and Gronski³⁰⁷ used ^{13}C CP-MAS NMR, direct-polarization (DP) ^{13}C -MAS NMR and FT-IR spectroscopy to study hydrogen bonding and phase separation in polyurethane elastomers. They observed that there is only one $-\text{HN}-\text{C} \begin{array}{c} \text{---} \text{O} \text{---} \\ \text{---} \text{C} \text{---} \end{array}$ signal in their solid-state ^{13}C spectra and that signal is shifted by 17 ppm to lower shielding (137.5 ppm) as a result of hydrogen bonding. The fact that there is only one $-\text{HN}-\text{C} \begin{array}{c} \text{---} \text{O} \text{---} \\ \text{---} \text{C} \text{---} \end{array} ^{13}\text{C}$ signal in the solid-state ^{13}C spectra implies that all $-\text{NH}-$ groups form hydrogen bonds of similar strength, either with carbonyl oxygen atoms of other urethane groups or with ether oxygen atoms of soft segments, an interpretation in complete agreement with conclusions from IR-measurements.²⁹⁸ Based on differences in the linewidths of signals arising from carbonyl carbons in their ^{13}C CP-MAS and DP-MAS spectra, Eisenbach and Gronski asserted that there are two kinds of $>\text{C}=\text{O}$ groups in the hard segments: hydrogen-bonded carbonyl groups in the rigid domain and non-hydrogen-bond carbonyl groups of isolated hard segment surrounded by soft segments, which cannot provide hydrogen to carbonyl groups for hydrogen bond formation. They also used cross-polarization to partially deuterated material of the hard segment to probe the interface region between the hard phase and the soft phase.

Nierzwicki³¹⁴ utilized ^1H FIDs to study microphase separation and interfaces in urethane elastomers. In one series of polyurethanes that has a high degree of phase separation, the ^1H FID can be fit to a combination of one fast Gaussian decay component and one slow Lorentzian decay component. In two other series of polyurethanes, the ^1H FID has three components: two Gaussian decay components and one slow Lorentzian component. Nierzwicki attributed the faster Gaussian decay component to protons of the hard domain and the slower Gaussian decay to protons in the interface region between hard and soft domains. Of course, he attributed the slow Lorentzian decay component to protons of soft domains. The fraction of the material engaged in the interface was calculated by the initial amplitudes of each component in the ^1H FID.

Figure 36 shows models of the fully extended³⁰¹ and folded configurations³⁰⁴ of the hard segments of polyurethanes^{306,315} studied by Jelinski and coworkers.³¹⁵ They performed solid-state deuterium NMR experiments on a series of specifically deuterated polyurethanes that contain 100, 70, 60 and 50 wt % hard segment. Because the polyurethanes are deuterated specifically at the butanediol moiety of the hard segment, the deuterium NMR spectra reflect the motional environment of this group only. The deuterium NMR spectra, shown in Fig. 37d-f, of the all-hard

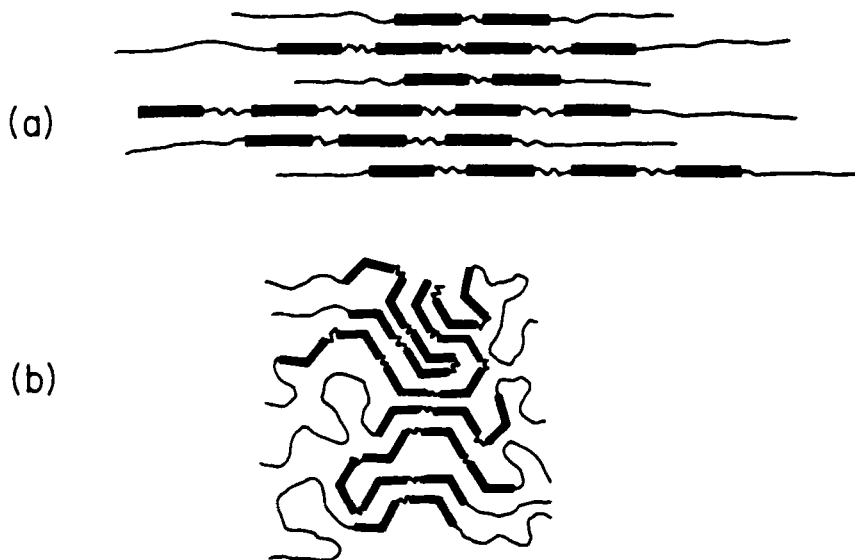


Fig. 36. The fully extended (A) and folded configuration (B) models for the hard segments of polyurethanes.³¹⁵

polyurethane sample indicate that *gauche*–*trans* conformational jumps in the hard segments occur at an intermediate rate on the ^2H NMR timescale. This result suggests that the hard segments assume not an extended, all-*trans* configuration, but one in which kink motions can occur. All the ^2H NMR spectra of polyurethanes containing 70, 60 and 50 wt % hard segments have both a broad and a sharp component, as seen in Fig. 37a–c. Jelinski and coworkers attributed the broad component to those hard segments that manifest molecular motion that is identical with that of the all-hard polyurethane. They also attributed the sharp component to those hard segments that dissolve in the soft-rich microdomains and/or reside in the diffuse boundary region between the hard- and soft-segment microdomains. From the simulated spectra composed of appropriate fractions of the all-hard spectrum and the narrow spectrum, they estimated the fraction of hard segments that are dissolved in soft-rich microdomains and/or reside in the interfacial region. Their NMR results provide support to the validity of the Koberstein–Stein³⁰⁴ hard-segment model of polyurethanes (Fig. 36b).

Jelinski and coworkers also used ^2H NMR to investigate the complex molecular motions in two bulk hard-segment polyurethanes.¹⁸⁵ These two polyurethanes were prepared from MDI with extender butanediol-2,2,3,3- d_4 (BDO), and from 2,4-toluenediyl diisocyanate (TDI) with the same extender. ^2H NMR line shapes and T_1 values of these two polyurethanes were obtained as a function of temperature. The spectra are shown in Fig. 38 for

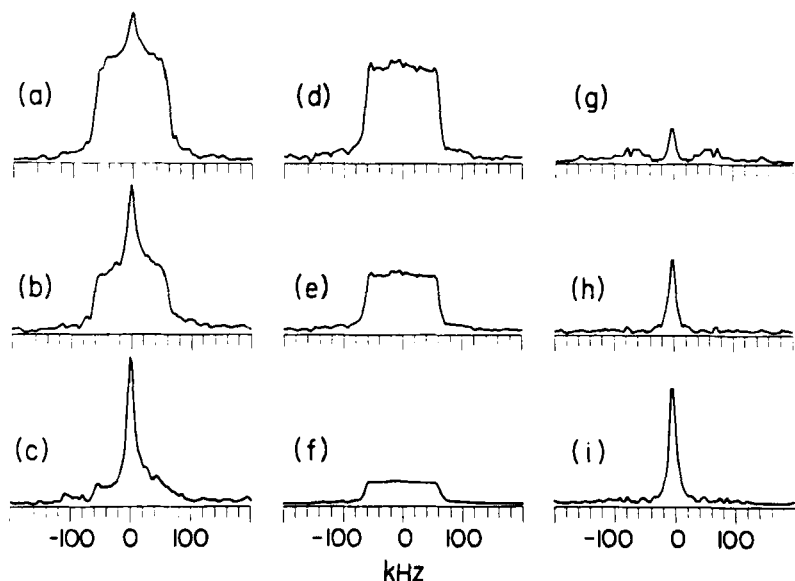


Fig. 37. Solid-state quadrupole echo ^2H NMR spectra of hard segment labelled polyurethanes obtained at 22°C and 55.26 MHz. Spectra of (a) 70, (b) 60, and (c) 50 wt % hard segment. Spectra (d)–(f) are of the all-hard segment material reported at different vertical gains. Spectra (g)–(i) were obtained by subtracting an appropriate amount of the symmetrized spectra in the center column from those in the left column. All spectra were obtained with a 2-s recycle delay.³¹⁵

MDI-BDO polymers. These results indicate a broad distribution of motional correlation times. For semicrystalline MDI-BDO polyurethane, the distribution divides cleanly into two components that are attributable to the crystalline and amorphous regions of the materials, whereas for the amorphous TDI-BDO polyurethanes there is only a single broad distribution, in keeping with the completely amorphous nature of this material. The ^2H NMR lineshape of the crystalline region of MDI-BDO polyurethane indicates that the C–D bonds may be considered static on the ^2H NMR timescale. However, the T_1 data indicate that there are high-frequency librational motions of the labelled methylene groups in these relatively rigid regions. In the amorphous regions of MDI-BDO and in the amorphous TDI-BDO polyurethanes, the broad range of motional correlation times extends five orders of magnitude (from 10^{-5} to 10^{-9} s) at room temperature. By comparing experimental spectra and computer simulations, it was concluded that the molecular motions in these amorphous regions are mainly *gauche*–*trans* conformational hops between two equally populated sites separated by a dihedral angle of $\sim 114^\circ$.

Meadows and coworkers³¹⁷ investigated the molecular motions and phase

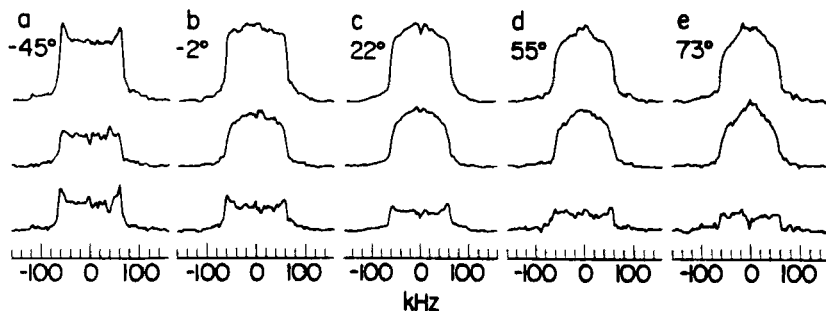


Fig. 38. Solid-state ^2H NMR spectra (55.26 MHz) of the hard-segment MDI-BDO polymer obtained with the amorphous quadrupole echo pulse sequence. Top row: spectra obtained with an equilibrium delay time of 2–4 s after the saturating “comb” of pulses. Middle row: spectra obtained with a delay time of 100–160 ms. Bottom row: difference spectra of an equilibrium and fast-recycle spectra. Spectra within a column (a–e) were obtained at the same temperature. The experimental temperatures are (a) -45°C , (b) -2°C , (c) 22°C , (d) 55°C , and (e) 73°C .¹⁸⁵

separation in two model urethane elastomers by ^{13}C CP-MAS NMR. $T_{1\rho}$ values were determined for the aromatic and butanediol carbons of hard segments as a function of ^{13}C rf field strength and temperature. They correlated the $T_{1\rho}$ values of the aromatic carbons to the observed high-temperature behaviour of the elastomer as determined by dynamic mechanical spectroscopy. The biexponential behaviour of $T_{1\rho}$ measurements of the butanediol carbons in one of the model urethanes indicated that two types of motional populations can be associated with hard segments in the hard domains and in the phase-mixed domains.

Spieß and coworkers¹⁸⁴ used wideline ^2H NMR on a model polyurethane that was specifically labelled with ^2H to measure the variation of molecular motion from the core of the hard phase to the interphase between the hard and soft phases over a broad temperature range. These results could be fitted satisfactorily to a model in which 85% of the hard segments exist in the hard phase with low mobility at temperatures below 410 K (10 K below the melting point) and the rest of the hard segments are dispersed in the soft phase with high mobility at temperatures above 260 K (about 60 K above the glass transition temperature). The strong similarity between the broad line due to the hard phase of the polyurethane and the hard-segment oligomer deuterated at the outmost and centre positions suggests that the hard phase of the multiblock polyurethane and the crystalline hard-segment oligomer are very similar on a local scale. A gradient of mobility from the centre (smaller molecular mobility) to the exterior (greater molecular mobility) of the hard segments exists in both the hard phase of polyurethanes and model oligomers between 300 and 410 K. After comparing the variation in molecular mobility and storage modulus as a function of temperature, they

concluded that (a) as the temperature increases from 200 °K to 280 °K, the increasing mobility of the soft phase correlates with a 100-fold decrease in the modulus over this temperature range; (b) as the temperature increases to 400 K, the increase in mobility at the exterior of the hard phase correlates with the gradual decrease in the modulus; and (c) at temperatures around 410 K, the onset of high mobility at the centre of hard segments in the hard phase correlates with the loss of mechanical integrity of the polyurethanes.

Dickinson, Shi and Chien^{318,319} used both CP-MAS and DP-MAS ¹³C NMR to study the effects of extension on the molecular dynamics and morphology of polyurethane elastomers. T_{CH} , $T_{1\rho}^H$, T_1^H and T_1^C values were measured. The results were interpreted in terms of crystalline and amorphous domain sizes and the relative amounts of each. Effects of spin-diffusion on various relaxation parameters were used to provide evidence of incomplete phase separation.

3.5. Nylons

One of the dominant characteristics of nylons is their intermolecular hydrogen bonding, which provides a driving force for crystallization. Nylon crystals may exist in different forms (e.g. α -, β - and γ - forms), depending on the preparation conditions. During the past several years, there has been a surge of solid-state NMR studies on various nylons. Solid-state ¹³C NMR^{120,341–350} and solid-state ¹⁵N NMR^{119–121,349–357} techniques have successfully identified various crystalline and amorphous forms of nylon. Deuterium NMR provides a deep insight into molecular motions in nylons.^{121,180,181, 358} The effect of water on the structure of nylons has been investigated by ¹³C NMR³⁴⁵ and ²H NMR.^{180, 181} Fyfe *et al.*³⁵⁹ employed NMR microscopy to study the absorption, desorption and exchange of water in nylon-6,6. Veeman and coworkers^{341–343} used solid-state NMR to investigate glass-filled polyamide-6 composites. The following is a brief review of some ¹³C, ¹⁵N and ²H solid-state NMR studies of various nylons.

3.5.1. Solid-state ¹³C NMR studies of nylons

As shown in Fig. 39, hydrogen bonding in the α crystalline form of polyamide-6 (nylon 6, $[-(CH_2)_5CONH-]_n$) is between antiparallel adjacent chains, and in the γ -form the hydrogen bonding is between parallel chains. In the α -form of nylon 6, the amide linkage lies in the plane of the methylene zigzag structure, whereas the amide linkage of the γ -form is rotated by approximately 60° relative to the methylene zigzag plane. Veeman and coworkers³⁴¹ observed that the carbons on either side of the amide group, C1 and C5, have a chemical shift of about 3 ppm to higher

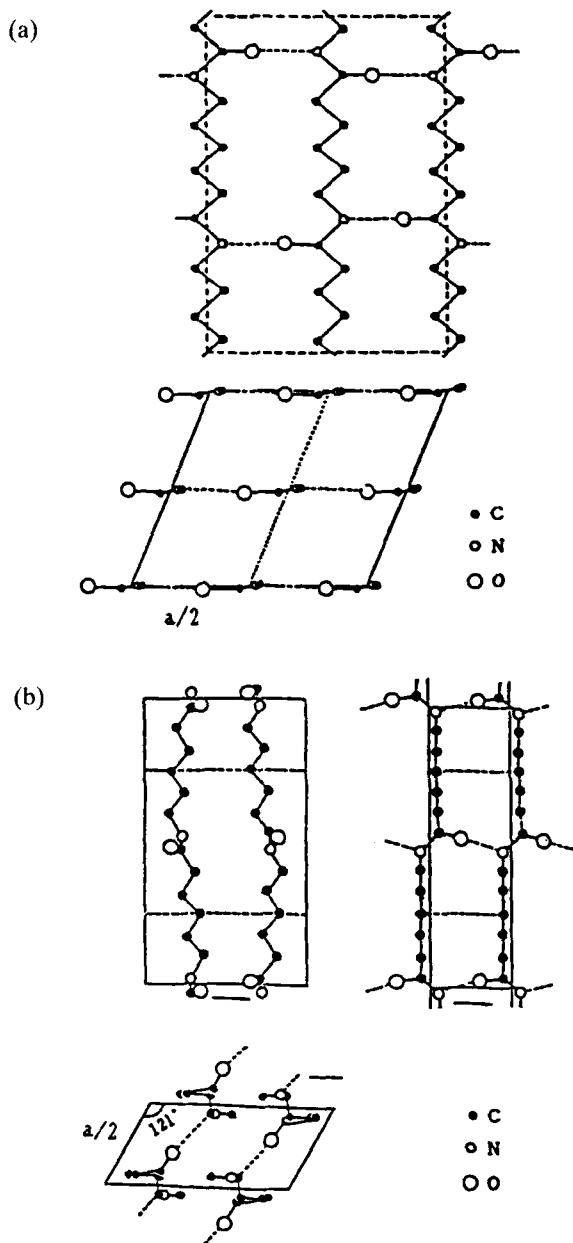


Fig. 39. Crystal structures of nylon 6: (a) α -form; (b) γ -form.³⁴⁶

shielding in the γ -form of nylon 6 relative to the α -form, and they attributed this shift to subtle differences in hydrogen bonding and density between the α and γ forms. They also utilized the fact that ^{13}C nuclei in the amorphous fraction of nylon 6 have much smaller T_1^C values than do the carbons in the crystalline fraction and obtained a ^{13}C NMR spectrum of the predominantly amorphous fraction by the application of closely spaced (1 s) ^{13}C 90° pulses that saturate ^{13}C nuclei in the crystalline fraction.

Ketels *et al.*³⁴⁵ investigated the effects of sorbed water, fast cooling of the nylon 6 melt and addition of ethylene-vinyl alcohol copolymer to nylon 6 on the ^{13}C CP-MAS spectra and T_1^C values of nylon 6 and found that the sorbed water did not affect either significantly. They also observed that fast cooling of a nylon 6 melt, and probably the presence of ethylene-vinyl alcohol copolymers in a blend with nylon-6, enhances the formation of γ -crystallites. Okada *et al.*³⁴⁶ also observed ^{13}C NMR chemical shift differences between the α - and γ -forms of nylon 6. However, their assignments of ^{13}C CP-MAS spectra are different from the assignments of Weeding *et al.*³⁴¹ and Ketels *et al.*³⁴⁵ Okada *et al.* attributed differences between the ^{13}C chemical shifts of the α - and γ -forms of nylon to differences in hydrogen bond strengths and the involvement of intramolecular hyperconjugation. Their interpretation of a weaker hydrogen bond in the α -form in comparison to the γ -form was supported by their FT-IR results and by X-ray results reported by Malta *et al.*³⁶⁰ Kubo *et al.*³⁴⁷ used ^{13}C MAS techniques to investigate samples of nylon 6 crystallized under various conditions. They also studied a drawn nylon 6 at various temperatures by ^{13}C CP-MAS techniques. Based on ^{13}C chemical shifts of the α -form and the amorphous fraction of nylon 6, they concluded that methylenes in the α -crystallites of nylon 6 are in the *trans* zigzag structure, and methylene carbons in the amorphous fraction, as well as in the liquid solution state, undergo rapid transitions between the *trans* and *gauche* conformations. In a subsequent article,³⁴⁸ Kubo *et al.* investigated nylon 4 ($[-(\text{CH}_2)_3\text{NHCO-}]_n$), nylon 6 and nylon 66 ($[-\text{NH}(\text{CH}_2)_6\text{NHCO}(\text{CH}_2)_4\text{CO-}]_n$) by solid-state ^{13}C NMR spectroscopy over a range of temperature from 20 to 100°C. Figure 40 shows the $-\text{CH}_2-$ region of the ^{13}C CP-MAS spectra of a nylon 4 single-crystal sample as a function of temperature. As represented in Fig. 40, the lineshapes and ^{13}C chemical shifts of the ^{13}C CP-MAS peaks assigned to the crystalline fraction (α -form) of these nylons do not change significantly between 20 and 100°C. This result shows that the structure of the crystalline component does not change substantially within this temperature range. Based on the ^{13}C chemical shifts of the α -forms and the amorphous fractions of nylons 4, 6 and 66, these authors also concluded that methylene carbons in the amorphous fractions of these three nylons, as well as in their liquid-solution states, undergo rapid transitions between the *trans* and *gauche* conformations. The ^{13}C chemical shift behaviours of the CH_2 peaks of the non-crystalline fractions of these nylons were explained by Kubo *et al.*³⁴⁸ in terms of γ and δ effects.²⁷

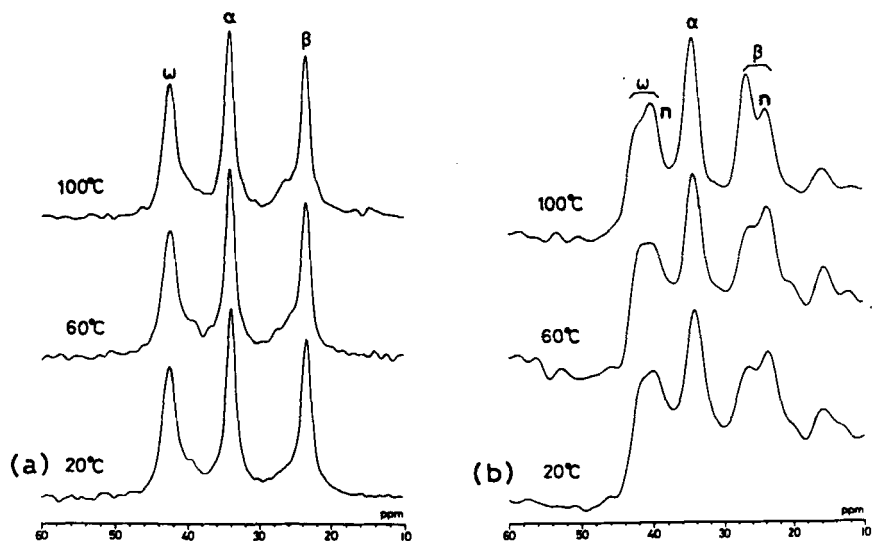


Fig. 40. The aliphatic regions of the ^{13}C NMR spectra of nylon 4 single crystal sample as a function of temperature: (a) ^{13}C CP-MAS, (b) ^{13}C DP-MAS.⁵⁴⁸

Based on their own solid-state ^{13}C and ^{15}N NMR results of ^{15}N -labelled nylon 6 polymer, as well as supporting infrared and X-ray diffraction studies, Hatfield and coworkers³⁴⁹ determined that "highly amorphous" nylon 6 contains low fractions of α and γ phases and a sample that is "high in α crystallinity" contains a substantial amorphous fraction, but no γ content. Similarly, they found that nylon 6 "high in γ crystallinity" contains a substantial fraction of the amorphous phase but no α content. Utilizing the fact that ^{13}C 's in the amorphous fraction of nylon 6 have much smaller T_1 values than do ^{13}C 's in the crystalline phases, Hatfield *et al.* obtained ^{13}C DP-MAS spectra that discriminate in favour of the amorphous phase for three nylon 6 samples that were predominantly amorphous, high in α crystallinity and high in γ crystallinity; these spectra are shown in Fig. 41. They noticed that these three ^{13}C DP-MAS spectra are essentially the same and concluded that the structure of the amorphous phase of nylon 6 (as measured by DP-MAS) is not sensitive to the composition of the accompanying crystalline phase in these three samples. They also used the T1CP experiment of Torchia³⁶¹ and differences between T_1^C values for carbons in amorphous regions and crystalline regions³⁴⁹ to obtain ^{13}C CP-MAS spectra that discriminate in favour of crystalline phases for two nylon 6 samples that were high in α crystallinity and high in γ crystallinity. In this way, they obtained ^{13}C CP-MAS spectra of the α phase and of the γ phase without much interference from the amorphous phase. Based on the ^{13}C and ^{15}N

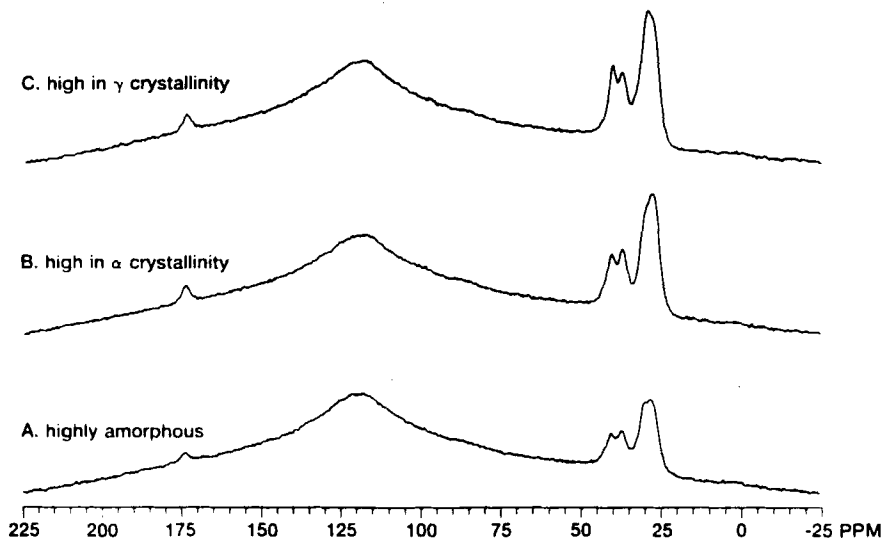


Fig. 41. ^{13}C DP-MAS spectra that discriminate in favour of the amorphous phase of samples that are (A) predominantly amorphous, (B) high in a α -crystallinity, and (C) high in γ -crystallinity.³⁴⁹

chemical shifts (Section 3.5.2.) of the α , γ and amorphous phases, they suggested that the strength of hydrogen bonding is greatest in the γ phase, followed by the amorphous phase and then the α phase of nylon 6. This same conclusion had also been inferred from infrared and X-ray data by Murthy *et al.*³⁶² This result suggests that the γ and amorphous phases of nylon 6 are more strongly hydrogen bonded than the more thermodynamically stable α phase, and implies that the thermodynamic stability of the α phase relative to the γ phase arises from interactions other than hydrogen bonding.

Mathias and Johnson³⁵⁰ used solid-state ^{13}C and ^{15}N NMR to investigate ^{15}N -labelled nylon 12 ($[-\text{CH}_2]_{11}\text{NHCO-}]_n$). The discussion of ^{15}N results is deferred to Section 3.5.2. Mathias and Johnson observed clear differences in peak intensities, positions, and sharpness in the ^{13}C CP-MAS NMR spectra of various nylon 12 samples they prepared. Figure 42 shows spectra of three crystalline forms. The difference between the amide and the zigzag methylene plane orientation in the various crystal forms is reflected in differences in the chemical shift values in both ^{13}C and ^{15}N CP-MAS spectra.

3.5.2. Solid-state ^{15}N NMR studies of nylons

Solid-state ^{15}N NMR not only provides information on the structure of nylons that is complementary to that provided by ^{13}C NMR, it also offers

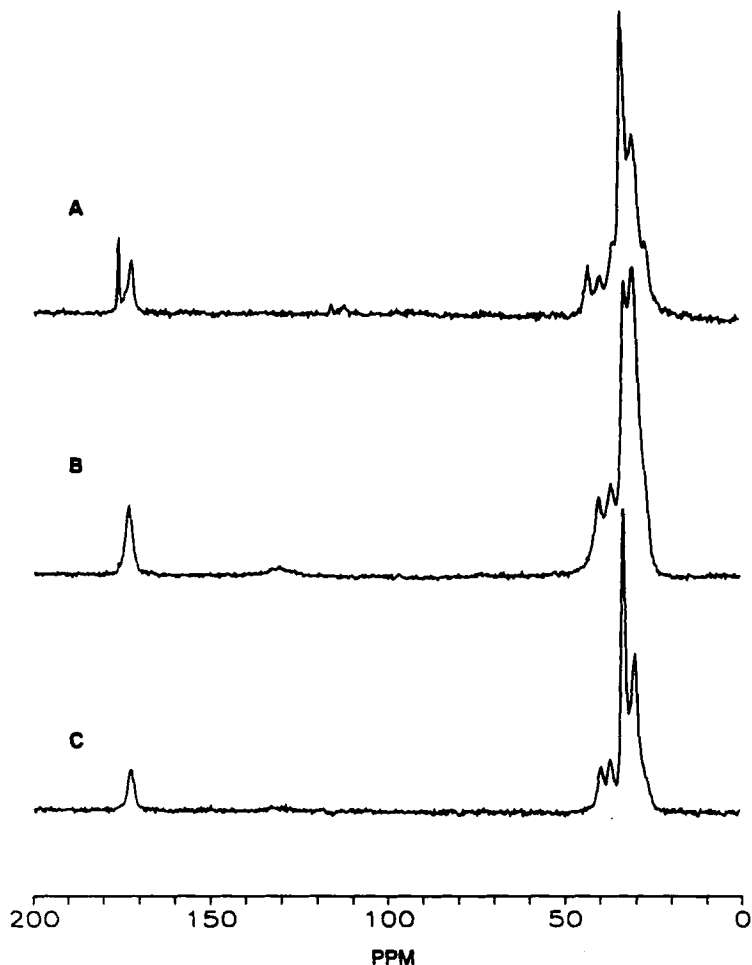


Fig. 42. ^{13}C CP-MAS NMR spectra of ^{15}N -labelled nylon 12: (A) α -plus γ -forms, (B) γ' -form, and (C) γ -form.^{35b}

several advantages over ^{13}C NMR, because ^{15}N chemical shifts are extremely sensitive to the conformation about the amide group and there is only one chemically distinct nitrogen in each polyamide repeat unit. Furthermore, this unique nitrogen can be involved in hydrogen bonding. One big disadvantage of solid-state ^{15}N NMR is the low sensitivity. However, Mathias and coworkers^{120,121,350-352} showed that natural-abundance ^{15}N CP-MAS NMR analysis of nitrogen-containing polymers is not only feasible but is sensitive to composition, conformation and crystalline form. Zhang and Maciel¹¹⁹ obtained a very high-quality natural-abundance ^{15}N CP-MAS spectrum of nylon 66 in 8000 s by using a 2.5 cm³ spinner.

Mathias *et al.*³⁵¹ used natural-abundance ^{15}N CP-MAS NMR to evaluate crystalline composition and conformation in nylons 6–10 ($[\text{NH}(\text{CH}_2)_6\text{NHCO}(\text{CH}_2)_8\text{CO-}]_n$), 11 and 12. They observed characteristic peaks for the amide units in α -crystalline domains at 83–85 ppm to lower shielding than the glycine peak and in γ -crystalline domains at 88–90 ppm to lower shielding than glycine. They also observed peaks which appear to correspond to amorphous groups and/or amide units in intermediate or crystal-blend forms which had not been observed or conclusively identified by other techniques. Mathias and coworkers³⁵² also reported natural-abundance ^{15}N CP-MAS results on aramid-containing nylon 6, copolyamides and model amides. They concluded that solid-state ^{15}N NMR is a better tool for differentiating the α and γ crystal forms of nylon 6 than solid-state ^{13}C NMR. Their ^{15}N CP-MAS spectra indicate that the nylon 6 blocks in the copolymers are mostly of the γ form. In order to characterize the previously unobserved non-crystalline and amorphous regions in polyamides by ^{15}N CP-MAS relaxation studies, Mathias and coworkers³⁵³ prepared ^{15}N -labelled (20% enrichment) nylon 6. With the good quality ^{15}N CP-MAS spectrum obtained on this ^{15}N -labelled nylon 6, they deconvoluted the spectrum into two peaks, as shown in Fig. 43. The high-shielding resonance in Fig. 43 is located at 84.2 ppm with a line width of 2.4 ppm, and is correlated with the α crystalline form of nylon 6. The broader (6.3 ppm line width) lower-shielding resonance at 87.2 ppm had not been observed in their previous natural-abundance ^{15}N CP-MAS studies of polyamides, but is clearly seen in the spectrum shown in Fig. 43. They assigned the broader peak to the non-crystalline or “amorphous” fraction of the nylon sample, since its chemical shift is midway between those of the α and γ resonances observed for nylon 6 and other nylons.³⁵²

In order to evaluate the mobility of each region in nylon 6 and more conclusively identify the broader low-shielding peak in Fig. 43, Mathias and coworkers³⁵³ measured the ^{15}N T_1 value (T_1^{N}) at 300 K for the peaks at 84.2 and 87.2 ppm. The crystalline component at 84.2 ppm manifested a T_1^{N} value of 416 s and the 87.2 ppm peak showed two components, with T_1^{N} s of 29.6 and 1.9 s. The two smaller T_1^{N} values of the 87.2 ppm peak indicate that this peak is not associated with the rigid γ crystalline form of nylon 6 (with a chemical shift of 88.5 ppm),³⁵¹ but rather arises from an amorphous fraction with much greater mobility than in the crystalline fractions of the sample. From the fact that there are two T_1^{N} s for the peak at 87.2 ppm, they concluded that there are two types of non-crystalline regions: a bulk amorphous fraction with liquid-like mobility and a non-crystalline “interphase” region with restricted motion. They further took advantage of the difference in T_1^{N} values between the crystalline and amorphous phases to observe directly the amorphous fraction. The ^{15}N DP-MAS spectrum of this ^{15}N -labelled nylon 6, obtained with a recycle delay of 5–10 s, is nearly

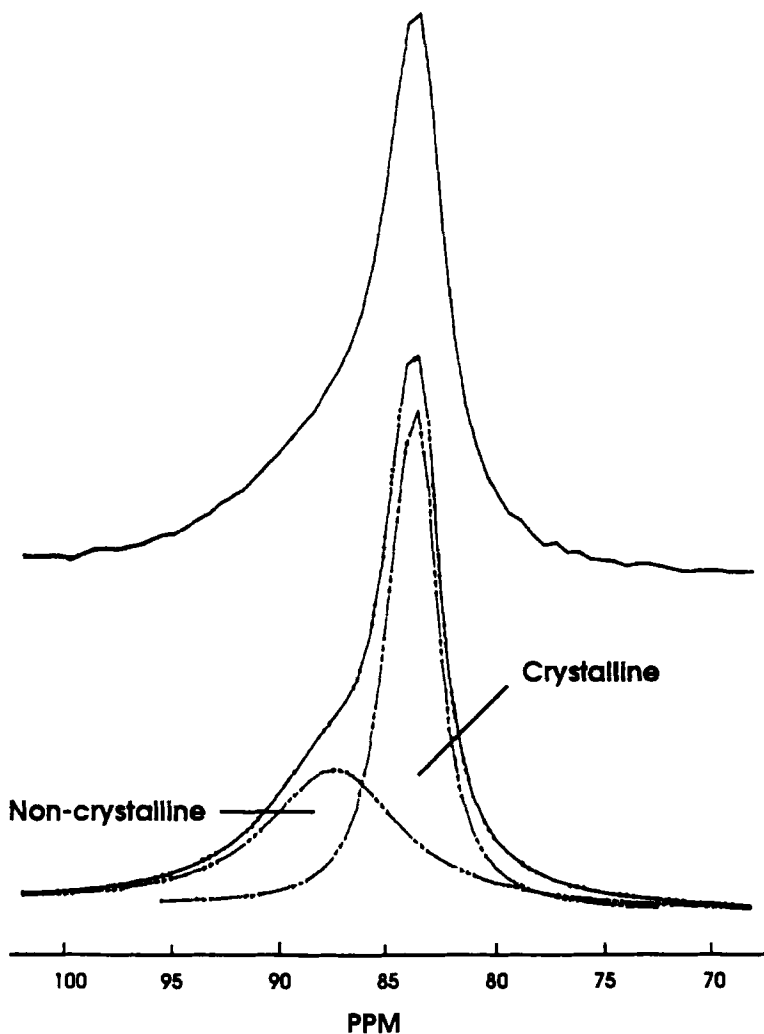


Fig. 43. ^{15}N CP-MAS spectrum of nylon 6. The bottom traces show the TENSOR calculated fit along with the individual (crystalline and non-crystalline) components.³⁵³

identical with the broad, low-shielding peak in the deconvoluted CP-MAS spectrum (Fig. 43).

In another article, Mathias *et al.*³⁵⁴ utilized proton T_1 discrimination via the T1CP experiment of Torchia³⁶¹ to obtain the solid-state ^{15}N spectrum of mainly the α crystalline component of nylon 6. Mathias *et al.* also determined ^{15}N chemical shift anisotropy (CSA) of nylon 6 at different temperatures (27–150°C). The CSA powder patterns of nylon 6 show the

signal growth of an amorphous fraction at elevated temperature, with a chemical shift near the isotropic value obtained with MAS. The σ_{33} component becomes less prominent with increasing temperature and finally disappears above 115°C. They speculated that motion involving vibration or libration of the hydrogen atoms in the still immobile hydrogen-bonded crystalline portion of the sample causes disappearance of this tensor component. Mathias *et al.* also measured T_1^H of various samples of nylon 6 at 300 and 350 K, obtaining about 1 s for each sample, and concluded that there is rapid ^1H spin diffusion between phases.

In their ^{15}N CP-MAS studies of various samples of ^{15}N -enriched nylon 6, Hatfield and coworkers³⁴⁹ obtained ^{15}N CP-MAS spectra of samples that were predominantly (a) amorphous, (b) high in α crystallinity, or (c) high in γ crystallinity. They also used the T1CP experiment of Torchia³⁶¹ to obtain ^{15}N NMR spectra that discriminate in favour of the crystalline phase for samples that were high in α crystallinity or high in γ crystallinity. Based on ^{15}N chemical shifts of the α , γ and amorphous phases in nylon 6, they concluded that the strength of hydrogen bonding is greatest in the γ phase, followed by the amorphous phase and then the α phase in their samples, in agreement with conclusions from their ^{13}C results (Section 3.5.1.).

In their studies of natural-abundance^{120,351} and ^{15}N -enriched^{120,354,355} nylon 11 by solid-state ^{15}N NMR, Mathias and coworkers identified the α , γ and amorphous phases by means of ^{15}N chemical shifts and T_1^N . They also confirmed the existence of the δ form of nylon 11 at temperatures above 95°C, as shown in Fig. 44.³⁵⁵ Various solid-state ^{15}N NMR techniques were used, including static-sample ^{15}N CSA measurements at different temperatures and T_1^N , T_1^H and $T_1^H\rho$ measurements by ^{15}N CP-MAS. The ^{15}N CSA pattern of the crystalline component of nylon 11 shows no evidence of narrowing at the 95°C α - δ transition. This crystalline-component CSA pattern failed to narrow even at 147°C. Based on ^{15}N CSA results, they confirmed the stability of hydrogen-bonded sheets in the crystalline domain and proposed that the crystal-to-crystal transition occurs without disruption of in-plane hydrogen bonding, involving rapid methylene-segment librations (see Section 3.5.3.) that expand the crystal structure from the triclinic α form to the pseudohexagonal δ form.

Mathias and coworkers also investigated natural-abundance^{120,350,351} and ^{15}N -labelled³⁵⁰ nylon 12 by ^{15}N DP-MAS and ^{13}C CP-MAS NMR techniques (Section 3.5.1.). They observed ^{15}N CP-MAS spectra (Fig. 45) of various samples of nylon 12 that contain different crystalline forms and different degrees of crystallinity. They saw a shoulder appearing at 90.3 ppm in the spectrum of the ^{15}N -labelled γ -rich materials (Fig. 45) and interpreted that shoulder as due not to some amorphous conformation, but arising from some other rigid or crystalline component(s) with an amide bond twist of more than 60°. They also found that the T_1^N values of the γ -rich materials have at least three components. They attributed the intermediate T_1^N value

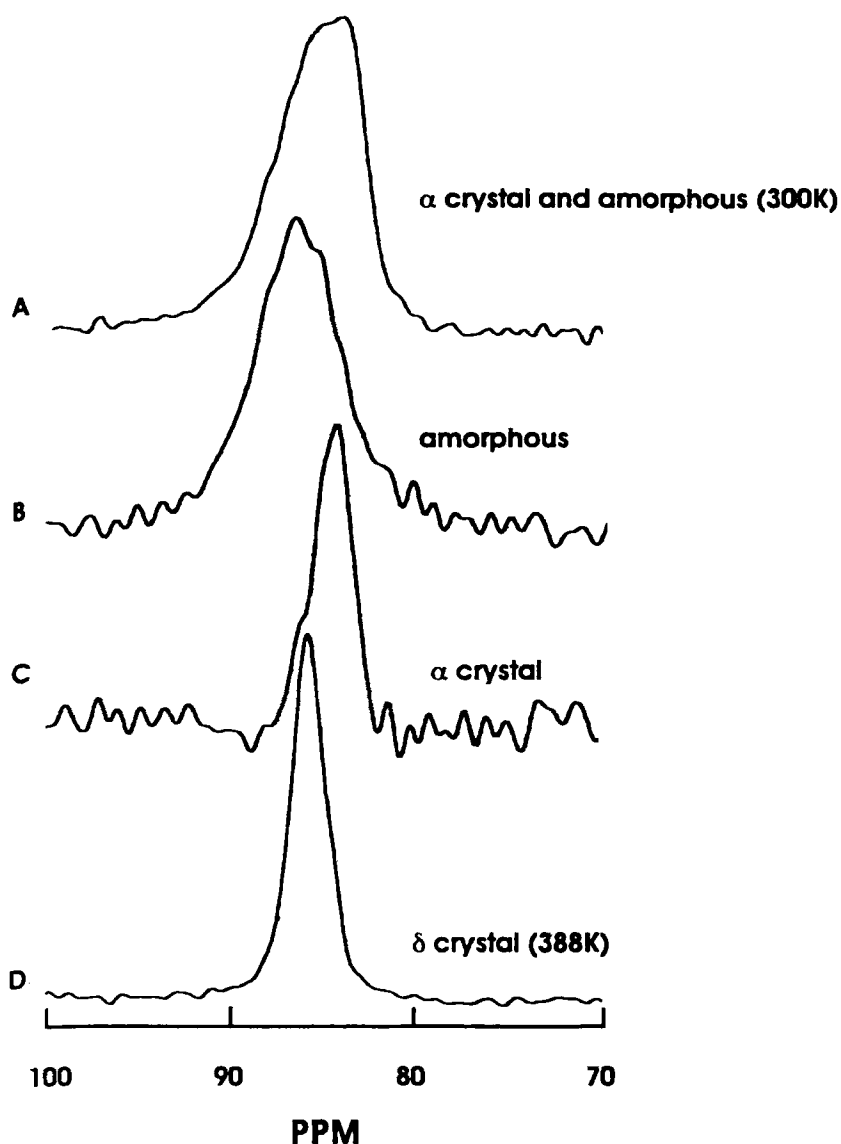


Fig. 44. ^{15}N NMR spectra of a ^{15}N -enriched isothermally annealed nylon 11. Trace A is the CP-MAS spectrum obtained at 300 K. Trace B was obtained by applying a 90° ^{15}N pulse with proton decoupling to saturate the crystal-component resonance. Trace C is the difference between spectra A and B, showing only the α -crystal resonance at 84.2 ppm. The α -crystal resonance disappears on heating above the α - δ transition temperature (368 K) to give the δ form seen in trace D at 388 K.³⁵⁵

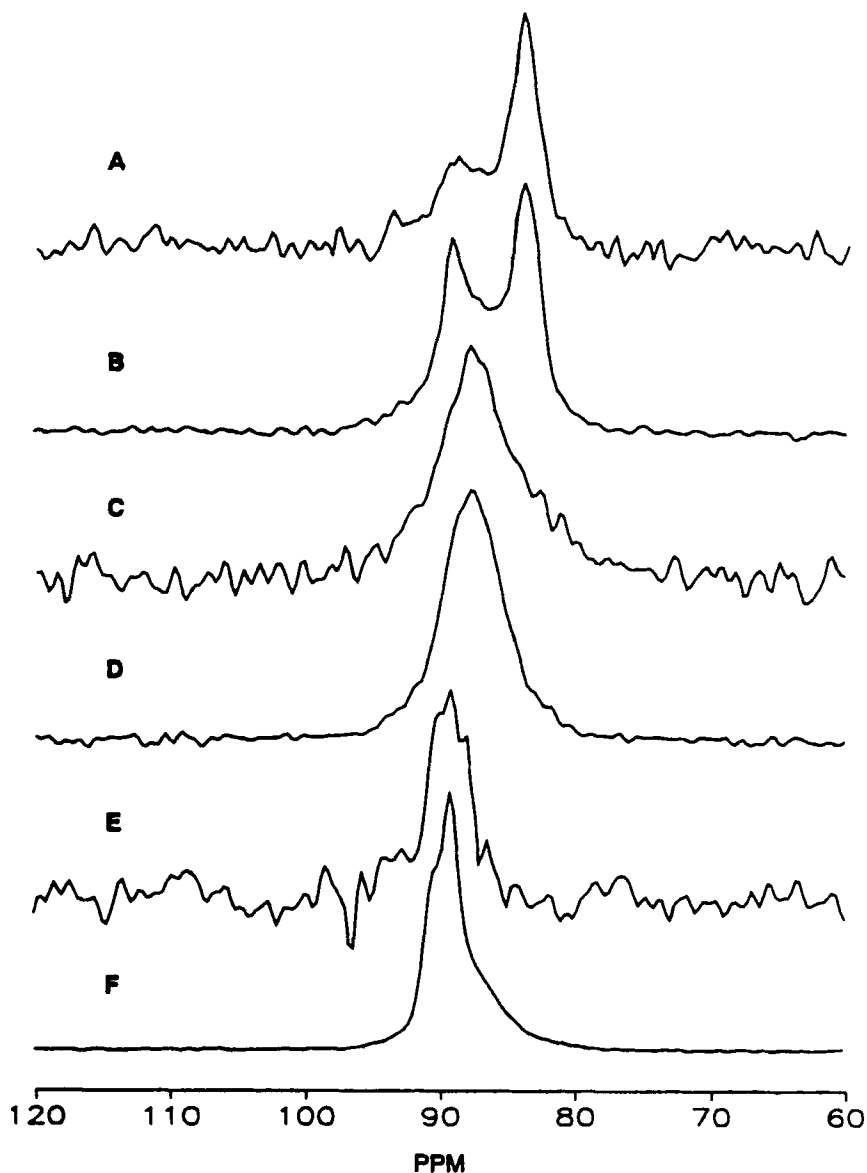


Fig. 45. ^{15}N CP-MAS spectra of a ^{15}N -enriched (l) and commercially available (c) nylon 12: (A) α - plus γ -form (c), (B) α - plus γ -form (l), (C) γ' -form (c), (D) γ' -form (l), (E) γ -form (c), (F) γ -form (c), (l).^{35b}

to an ordered interphase region joining the amorphous phase (smallest T_1^N) and crystalline phase (largest T_1^N).

3.5.3. Solid-state ^2H NMR studies of nylons

English and coworkers have reported studies of the segmental dynamics of nylon 66 by solid-state ^2H NMR in a series of articles.^{180,181,358} Because the ^2H spin-lattice relaxation time of the crystalline domains are 24–100 times larger at each temperature than that in non-crystalline domains, they were able to study the segmental dynamics in the crystalline phase^{180,358} and in the amorphous phase¹⁸¹ of nylon 66 separately.

In the crystalline phase of nylon 66,^{180,358} the mobility of the N–D bond is expected to be greatly constrained by hydrogen bonding between the carbonyl oxygen and the N–D hydrogen. The experimental ^2H NMR line shapes illustrate that only a minor amount of motional averaging takes place up to the highest temperature examined (228°C). Below 180°C, the line shapes are nicely fitted by a “rigid lattice” simulation. Above 180°C, an inhomogeneous distribution of small librational motion about the N–C axis accounts very well for observed changes in the experimental spectra. The mobilities of C–D sites are much higher than those of N–D sites. Furthermore, the line shapes and spin-lattice relaxation data together indicate that the motion in these C–D systems is not one that may be described as jumps between discrete sites (such as *trans*–*gauche* isomerization) with the rate increasing with temperature in the usual fashion for a thermally activated process, but rather is one in which the rate of motion ($\approx 10^{11}$ Hz) shows only very weak temperature dependence and the angular amplitude increases substantially with temperature. This latter type of motion is denoted a libration. English *et al.* also observed that there is more motion in the shorter (adipoyl) moiety than in the longer (hexamethylenediamine) moiety of nylon 66 at room temperature, whereas at high temperature, the amplitude of motion is quite comparable in both moieties.

In the amorphous phase of nylon 66,¹⁸¹ the ^2H NMR line shapes of the N–D labelled polymer below $\sim 100^\circ\text{C}$ are quite close to the rigid pattern for the crystalline phase at a similar temperature and indicate that there is very little motional averaging taking place. In contrast to the very limited amount of motional averaging observed for the N–D lineshapes, the C–D lineshapes are indicative of a very substantial amount of motional averaging for a large fraction of each methylene site at temperatures above -70°C , as shown in Fig. 46. English and coworkers proposed a bimodal model to explain their ^2H NMR results on C–D sites. In this model, mode I (libration) is operative in both free and constrained domains and mode II motion (an inhomogeneous distribution of *trans*–*gauche* jumps of the type usually ascribed to methylene segments) is operative only in the free domains. At temperatures of 118°C and higher, a narrow component appears in the line

Noncrystalline Nylon 66 Below T_g
 (3,3,4,4 d₄ Diacid)
²H - 30.7 MHz, τ₁ = 20 μs

Noncrystalline Nylon 66 Above T_g
 (3,3,4,4 d₄ Diacid)
²H - 30.7 MHz, τ₁ = 20 μs

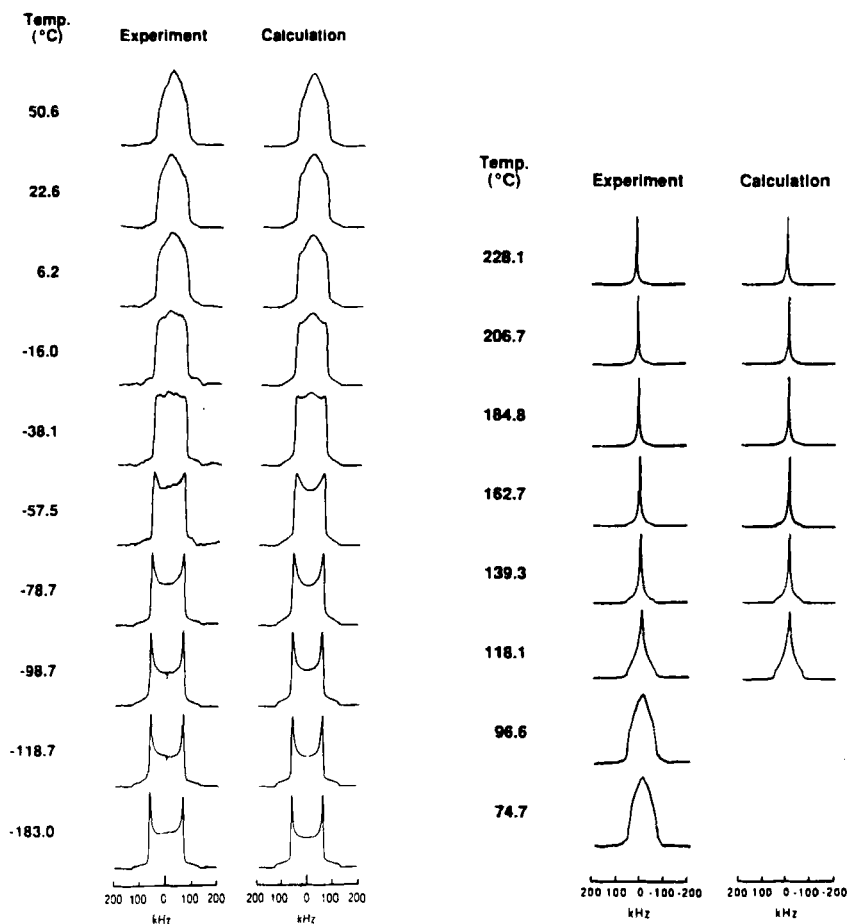


Fig. 46. Experimental and calculated ²H NMR line shapes of a nylon-66 sample as a function of temperature below the glass transition temperature (left set of spectra) and above the glass transition temperature (right set of spectra).¹⁸¹

shapes for all of the labelled samples (e.g. Fig. 46) and is attributable to rapid ($\nu_c \gg 10^5$ Hz), nearly isotropic motion. The fraction of the line shape represented by this narrow component increases with increasing temperature and represents more than 78% of the line shape above 200°C. Mathias and coworkers¹²¹ investigated the motions of nylons 6 and 11 by solid-state ²H NMR. Their observations are similar to those of English and coworkers.

3.6. Epoxy resins

Epoxy resins are used in composite materials, protective coatings, adhesives, castings, flooring^{363–366} and encapsulation materials for many electronic components.³⁶⁷ The properties and structures of epoxy resins are determined by the choice of co-monomers, initiators and a variety of possible polymerization schemes. The insoluble nature of an epoxy resin product makes high-resolution solid-state NMR spectroscopy a valuable technique to study the structure–property relationships and curing processes of these resins.^{368–385} Havens and Koenig,³⁷³ Mertz and Koenig,³⁷⁴ and Andreis and Koenig⁵⁵ have published reviews on NMR studies of epoxy resins; therefore, we provide just an update on this subject and briefly review NMR studies of epoxy resins in composite materials in Section 4.2.

Koenig and coworkers³⁸⁰ utilized ^{13}C CP-MAS techniques to characterize the networks formed by a tetrafunctional epoxide (tetraglycidyl(diaminodiphenyl)methane, TGDDM) reacting with a tetrafunctional amine hardener (diaminodiphenylsulfone, DDS). ^{13}C chemical shifts provide a tool for distinguishing intramolecular ether linkages (cyclic ether formation, an ineffective crosslink) from intermolecular ether linkages; the peak for the two carbons involved in intramolecular ether groups appears at 68 ppm, while peaks for the two carbons involved in intermolecular ether groups appear at 75 ppm for $\geq\text{CH}$ groups and 63 ppm for $\geq\text{CH}_2$ groups. They also used dipolar-dephasing ^{13}C CP-MAS experiments to separate the carbons involved with rigid junction points (tertiary amine sites) from those carbons which are more mobile (secondary amine sites). Based on their ^{13}C CP-MAS results, they found that intramolecular cyclic ether formation increases with an increase in the concentration of amines and that the per cent of secondary amines reacting to form tertiary amines increases with a decrease in the concentration of amine hardener. The results of their ^{13}C CP-MAS study of epoxy resins are consistent with results of their computer modelling.³⁸⁶

Lonikar *et al.*³⁸⁷ have shown that incorporation of masked isocyanates (chemically blocked isocyanates) in an epoxy resin system significantly decreases equilibrium moisture adsorption by reacting irreversibly with residual functional groups ($-\text{OH}$, $>\text{NH}$ and oxirane groups). The reactivity of an isocyanate is suppressed in its masked form at temperatures well above room temperature. But, at sufficiently high temperatures, either the parent isocyanate is regenerated by decomposition (removal) of the masking moiety, or the masked isocyanate itself undergoes reactions similar to those of the parent isocyanate. In either case the above-mentioned residual functional groups are consumed. Sankar *et al.*³⁸¹ demonstrated with ^{13}C CP-MAS experiments that reactions between the epoxy and masked isocyanates indeed occur. They were also able to identify intermediates and by-products in those reactions. Attias *et al.*³⁸² studied the chemical structure

of networks resulting from curing of *N,N*-diglycidylaniline-type resins with aromatic amines by ^{13}C CP-MAS NMR. Because all of the reactions involve aliphatic carbons, they focused only on the aliphatic part of the ^{13}C spectra. The ^{13}C CP-MAS spectra of the epoxy resin systems consist mainly of broad and poorly resolved peaks that are too complex to be interpreted directly; therefore, they used the ^{13}C chemical shifts corresponding to the products expected for six possible reaction pathways in various proportions to simulate the spectra. Figure 47 shows their simulation of the ^{13}C CP-MAS spectrum of the products of epoxy-amine reactions. Based on this kind of simulation, they found that for a stoichiometric TGDDM (*N,N,N',N'*-tetraglycidyl-4,4'-diaminodiphenylmethane)/DDS (4,4'-diaminodiphenylsulfone) resin, 65% of the epoxy groups are involved in reactions leading to cyclic structures and for a non-stoichiometric TGDDM/DDS resin, 70% of the epoxy groups contribute to the formation of cyclic structural units. With the highly reactive hardener DDM (4,4'-diaminodiphenyl methane), 55% of the total epoxy groups in the stoichiometric TGDDM/DDM resin are engaged in epoxy-amine reactions leading to the formation of $-\text{CH}_2\text{CH}(\text{OH})-\text{CH}_2-$ bridges, instead of 35% in the case of the TGDDM/DDS system.

Both Udagawa *et al.*³⁸³ and Egger *et al.*³⁸⁴ employed ^{13}C CP-MAS NMR to investigate the UV-induced and heat-induced curing of epoxy resins by sulfonium salt initiators. Udagawa *et al.* found that the ^{13}C CP-MAS spectra of cured resins are the same irrespective of the initiator concentration and the type of curing process used. They also studied the molecular dynamics of the UV-cured and heat-cured resins by measuring T_1^{C} and $T_{1\rho}^{\text{C}}$. Based on their ^{13}C CP-MAS results, Egger *et al.* found that the reaction of the epoxide without flexibilizer proceeds very rapidly to its gel point. But after 1 day, a total conversion to resin product of only 50% is reached. The epoxide content (51 ppm in Fig. 48) decreases to zero in a period of over 9 months, which demonstrates the rare case of a living cationic polymerization. They also used a "dipolar filter" multiple-pulse sequence (in which the τ windows between the pulses are not kept short as usual, but are set to the rather long values of 7–20 μs) to destroy ^1H magnetization of protons with strong dipolar couplings and then performed a ^1H spin-diffusion experiment detected by ^{13}C CP-MAS to determine the spin-diffusion rate. From these data they estimated the domain size. In all samples they investigated, the experimentally determined phase sizes indicate that the mobile phases consist only of one or a few polyol chains.

To avoid the uncertainty associated with commercial epoxy resin networks, Gallouedec *et al.*³⁸⁵ used a pure diamine, a mixture of diamine/monoamine or a pure monoamine as the curing agent to prepare "model" networks based on a diglycidyl ether of bisphenol A (DGEBA) or of butanediol (DGEPU). Observations from the FTIR spectra and ^{13}C CP-MAS spectra show that the cured resins based on DGEBA and

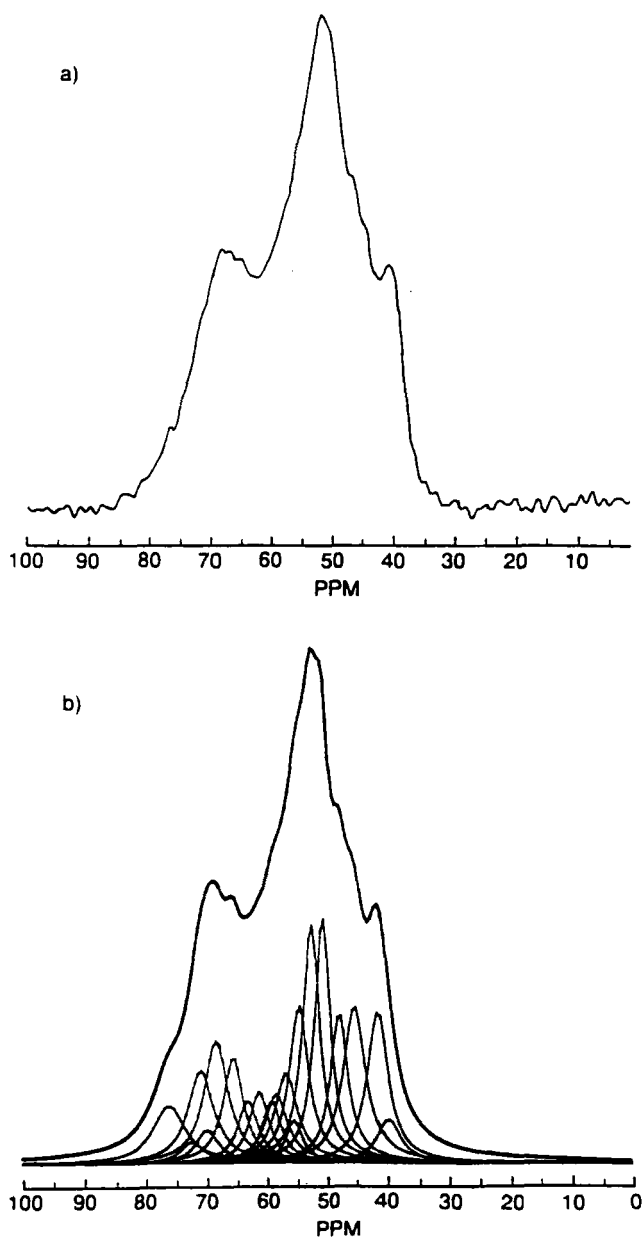


Fig. 47. Simulation of a solid-state ^{13}C NMR spectrum taking into account six possible reactions leading to the epoxy resin: (a) original spectrum, (b) reconstructed spectrum.³⁸²

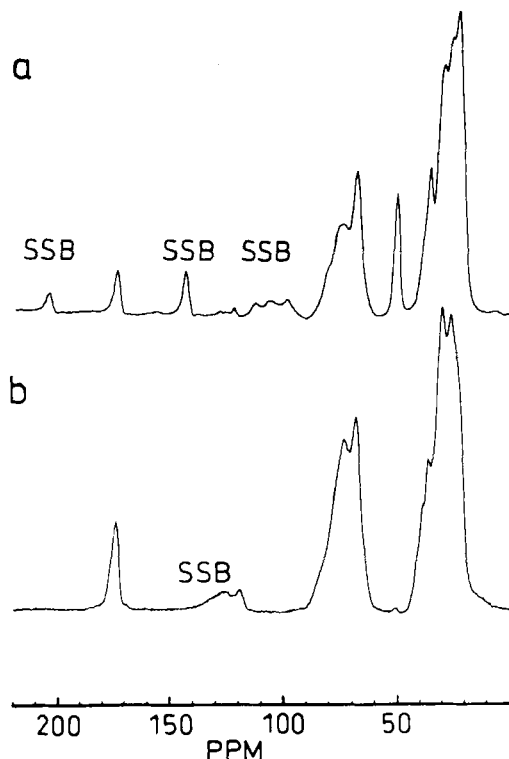
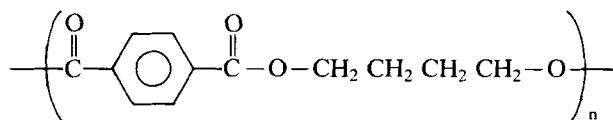


Fig. 48. ^{13}C CP-MAS spectra of curing epoxy resins. (a) Two weeks after preparation; at 51 ppm the signal of the unreacted epoxide is visible. (b) Nine months after preparation; the signal of the unreacted epoxide has disappeared.³⁸⁴

$\text{C}_6\text{H}_{13}\text{NH}_2/\text{H}_2\text{NC}_6\text{H}_{12}\text{NH}_2$ mixtures are largely formed by epoxy-amine additions, without detectable residual epoxy groups and without ether formed by secondary reactions.

3.7. Polyester resins

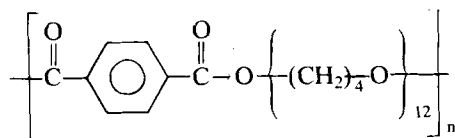
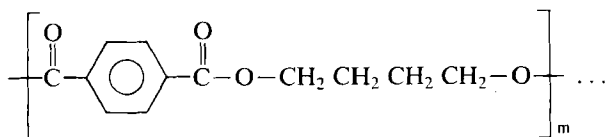
Various solid-state NMR techniques have been employed to study the motions,^{388–408} structures^{408–421} and domain sizes^{199,205} in polyesters. Jelinski *et al.*³⁸⁸ utilized solid-state deuterium NMR to study three-bond motion in the alkyl portion of deuterium-labelled poly(butylene terephthalate) (PBT) homopolymer, **XXIX**. They provided evidence for the occurrence of *gauche-trans* isomerization as an isolated motional mode for the alkyl portion of PBT. Jelinski and coworkers³⁸⁹ then studied phenyl ring motions



XXIX

that occur in semicrystalline PBT (aromatic- d_4) polymer by solid-state deuterium NMR. From lineshape simulations they concluded that there are three distinct motional regimes, consisting of (a) the crystalline regions with static phenyl rings, (b) a region of intermediate mobility with phenyl rings undergoing slow 180° ring flips, and (c) amorphous regions in which the phenyl rings undergo 180° flips ($\tau_c = 1.8 \times 10^{-6}$ s at 70°C) superimposed on rapid, low-angle librational motions. They determined that the 180° ring-flip process has an activation energy of $5.9 \text{ kcal mol}^{-1}$.

Jelinski, Schilling and Bovey³⁹⁰ used ^{13}C NMR to characterize the molecular motions which occur in the mobile regions of solid Hytel thermoplastic elastomer. Hytel, XXX, is a segmented block copolymer



XXX

available in compositions ranging from 0.80 to 0.96 mole fraction PBT "hard" segments, copolymerized with poly(tetramethylenoxy)terephthalate "soft" segments. They selectively observed contributions of the mobile domains to their ^{13}C NMR spectra by using low-power proton decoupling (1 G, or 4 kHz). The fraction of each sample that contributes to their low-power-decoupled ^{13}C NMR spectra was found to consist of all of the aliphatic carbons of the soft segments and $\sim 10\%$ of the terephthalate and hard-segment carbons. The soft-segment aliphatic carbon line widths were found to be a linear function of the average hard-block length of the polymer, but are essentially independent of temperature over the range $30\text{--}110^\circ\text{C}$. The T_1^C values for both aliphatic carbon peaks are independent of the hard-segment length of the polymer and increase with increasing field strength and with increasing temperature. From the results of T_1^C and NOE measurements of aliphatic carbons, these authors concluded that there is

phase separation, with negligible mixing of the two phases at the domain boundaries.

Jelinski³⁹¹ utilized the Herzfeld–Berger spinning sideband method¹³³ to obtain ^{13}C NMR chemical shift tensor parameters for PBT and Hytrel. She concluded that the aliphatic carbons in PBT move between lattice positions at a rate which is fast compared to the methylene chemical shift anisotropy.³⁹¹ She also found that the full width of the chemical shift anisotropy for hydrogen-bearing aromatic carbons is less for the “softest” segment copolymer than that of the other samples. Jelinski *et al.*³⁹² also performed variable contact-time ^{13}C CP-MAS experiments on Hytrel. They found that the decay of the CP signals as a function of contact time has two components, and concluded that Hytrel has two phases. They also obtained chemical shift tensors from the spinning sideband method¹³³ and attributed the reduced CSA in the Hytrel sample with the largest mole fraction of soft segments to small-angle excursions of the aromatic ring about the 1,4-phenylene axis.

Jelinski *et al.*^{393,394} continued to utilize solid-state ^{13}C NMR to characterize the nature of the molecular motions for every carbon of the segmented Hytrel copolymer. Relaxation time measurements, low-temperature MAS, off-axis sample spinning and static powder-pattern difference spectroscopy were used. The results suggest that (a) the aromatic rings undergo 180° ring flips at 22°C in the copolymer with 0.80 mole fraction hard segments, (b) the soft-segment $-\text{CH}_2-$ carbons exhibit dipolar broadening at temperatures just below the glass transition temperature, and (c) substantial molecular motions of the alkyl carbons occur in the hard-segment regions at 34°C .

Jelinski and coworkers^{395–399} also performed solid-state deuterium NMR studies on the Hytrel copolyesters, XXX. As seen in Fig. 49, they found that the deuterium NMR lineshape observed for the segmented copolymer in which only the hard segments are labelled can be deconvoluted into two components; one component is identical to that observed in the PBT homopolymer and the other component is very sharp and displays more nearly isotropic motion. They concluded that most of the hard segments are incorporated into phase-separated lamellae and that some of the hard segments are dissolved in the soft-segment matrices or situated at domain interfaces. They were able to quantify the amounts of these two components and they determined that 9% of the hard segments are involved in essentially isotropic motions in the segmented copolyester containing 0.87 mole fraction of hard segments.

Fyfe *et al.*⁴⁰⁹ used ^{13}C CP-MAS NMR experiments to explore the insoluble, highly crystalline homopolymer of *p*-hydroxybenzoic acid, two methoxy derivatives of this polymer, and two copolymers with biphenylene terephthalate. Resolution of their ^{13}C CP-MAS spectra is sufficient for them to identify the structures of these aromatic polyesters, as seen in Fig. 50. Havens and Koenig⁴¹⁰ utilized the ^{13}C CP-MAS approach to characterize

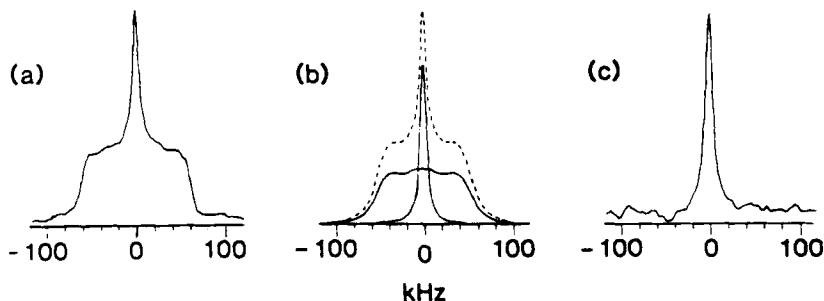


Fig. 49. Experimental (a), calculated (b), and difference (c) solid-state ^2H NMR spectra of the copolyester Hytrel, specifically deuterated in the hard segment. This Hytrel contains 0.87 mole fraction of hard segments. The spectrum in (c) is the difference obtained by subtracting the spectrum of PBT from the segmented copolymer spectrum.³⁹⁷

PBT, **XXIX**, and model compounds. They found that the chemical shifts of the α -crystalline (relaxed) form of PBT are different from those of the β -crystalline (uniaxial stretching) form of PBT, and interpreted the differences in terms of conformational differences in the tetramethylene segments. Perry, Koenig and Lando⁴⁰⁰ utilized ^{13}C CP-MAS to measure $T_{1\rho}^{\text{C}}$ and T_1^{C} values in these polymers. From the $T_{1\rho}^{\text{C}}$ and T_1^{C} values for each ^{13}C peak in the polymer spectrum, they concluded that the β phase manifests more molecular motion than does the α phase and that the interior methylenes have motions of greater frequency and/or amplitude than do the exterior methylenes in both phases.

Davidson, Manuel and Ward⁴¹¹ studied the α and β crystalline forms of PBT by broad-line ^1H NMR. The second moment was determined as a function of specimen orientation for the polymers in the α and β forms. The NMR results for the stretched (β) form are consistent with a model in which the molecular conformation is close to full extension. However, the result of comparing the observed anisotropy of the ^1H NMR second moment with the predicted values for various proposed structures of α form indicates that the conformation and orientation of the central methylene pairs in the glycol residue must remain substantially unchanged in the transformation from the α to the β form, a conclusion in opposition to that drawn by Havens and Koenig.⁴¹⁰

Grenier-Loustalot and Bocelli⁴¹² used high-resolution solid-state ^{13}C NMR to study PBT model compounds and PBT polymers. They observed the fact that the ^{13}C NMR peaks of those central methylene carbons *gauche* to the ester oxygens occur 3.0–3.7 ppm to higher shielding than the peak from central methylene carbons in the *trans* arrangement. Owing to the breadth of the central methylene resonance in the ^{13}C NMR spectrum of

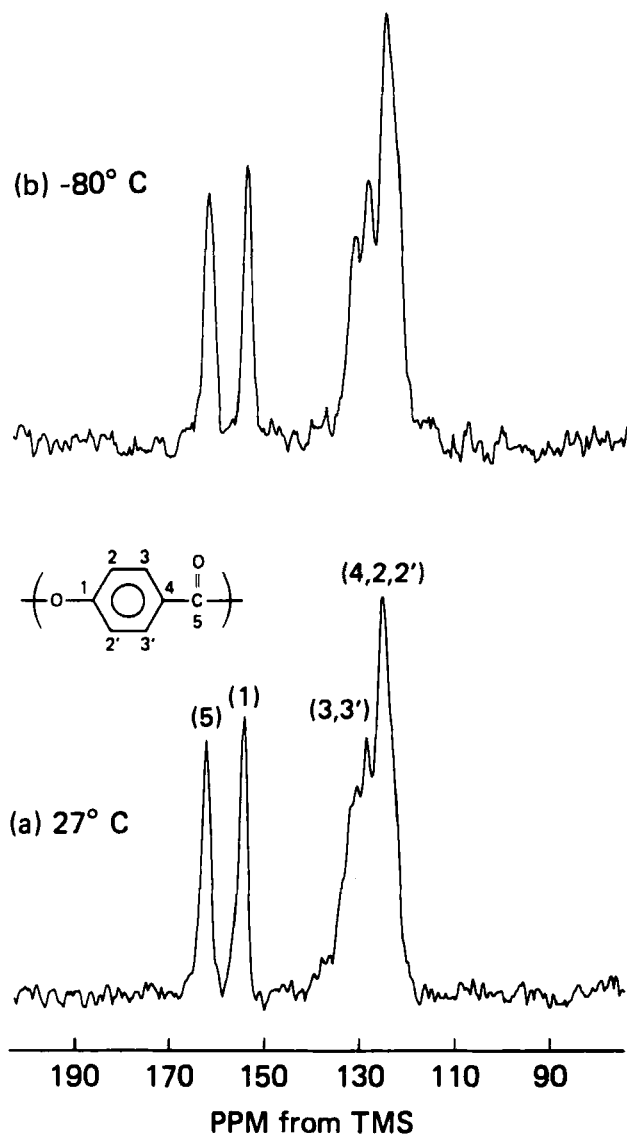


Fig. 50. ^{13}C CP-MAS spectrum of the homopolymer of *p*-hydroxybenzoic acid at (a) 27°C and (b) -80°C. CP contact time = 1.5 ms; repetition time = 3.5 s.⁴⁰⁹

PBT, they were unable to draw conclusions regarding the conformation of the glycol residue in the α form of PBT. In order to overcome the uncertainty brought about by peak breadth, Tonelli and coworkers⁴¹³ employed variable-temperature ^{13}C CP-MAS NMR to study PBT. They found that above about 100°C the spectra are significantly better resolved than at room temperature, with resonance line widths not exceeding 1–2 ppm. They attributed the narrowing of the peaks to the removal of contributions made by amorphous components, which no longer cross-polarize efficiently at temperatures well above the glass transition of PBT because of motional averaging of dipolar interactions. They observed that aside from the hydrogen-bearing aromatic carbons, carbon nuclei in α - and β -PBT resonate at nearly identical frequencies. They concluded that in both the α - and β -crystals the glycol residues of the PBT chains adopt a *trans-trans-trans* conformation and that the main difference between the α and β forms of PBT is the relative orientation of the carbonyl groups in the terephthaloyl residues.

Garbow and Schaefer⁴⁰¹ explored the main-chain motions of PBT by solid-state ^{13}C NMR. They measured T_1^C and T_{ρ}^C values of the ring and aliphatic carbons of quenched and annealed PBT. These authors also employed two-dimensional dipolar rotational spin-echo ^{13}C NMR^{422,423} to determine the ^{13}C - ^1H dipolar coupling strength. These relaxation and dipolar rotational spin-echo ^{13}C results indicate that the phenyl rings in a fraction of the amorphous regions undergo large-amplitude motions consistent with 180° flips superimposed on wiggles and oscillations at room temperature.

Schaefer and coworkers⁴⁰² measured T_{ρ}^C from ^{13}C CP-MAS spectra of various poly(ethylene terephthalate) (PET) samples. They showed that T_{ρ}^C relaxation is a spin-lattice process for amorphous PET materials. In this work they studied the effects of annealing on molecular motions in the low-to-mid-kilohertz frequency range and the relationship between microscopic molecular motions and the transition from ductile to brittle mechanical behaviour resulting from the annealing. Cheung *et al.*¹⁹⁹ utilized a number of transient NMR techniques, including CRAMPS, to elucidate possible domain structures and morphologies in PET. From ^1H spin-diffusion measurements, they indicated that there are two spatially separated phases in PET and that communication between phases can occur via spin-diffusion processes. Havens and VanderHart²⁰⁵ employed multiple-pulse ^1H NMR to probe the morphology of PET fibres by ^1H spin-diffusion measurements. They used a three-domain model (mobile non-crystalline, constrained non-crystalline and crystalline domains) to describe the observed spin diffusion. They estimated the surface areas of crystallites from the initial rates of the measured spin diffusion. Based on their spin-diffusion results, they concluded that annealing causes the system to convert both non-crystalline domains into crystalline materials. Gerstein⁴²⁴ has reviewed the

investigations of both Cheung *et al.*¹⁹⁹ and Havens and VanderHart²⁰⁵ in great detail.

Veregin, Fyfe and Marchessault⁴¹⁴ obtained ¹³C CP-MAS spectra of α , β and γ polymorphs of polypivalolactone, $(-\text{CH}_2\text{C}(\text{CH}_3)_2\text{C}(\text{O})\text{O}-)_n$. ¹³C CP-MAS spectra of the α and γ forms are identical, and a characteristic 1:1 doublet is observed for the two chemically "equivalent" methyl carbons (22.4 and 23.5 ppm), in agreement with the well-established 2_1 -helical conformation of the polymer chain in the α form. In contrast, the ¹³C spectrum of the β form shows a single peak for the two methyl carbons because of the planar zigzag molecular conformation of the polymorph. Figure 51 shows ¹³C CP-MAS spectra of polypivalolactones with various contents of α and β forms. Ritcey and Prud'homme⁴¹⁵ used ¹³C CP-MAS NMR to investigate the similar but optically active poly(α -methyl- α -*n*-ethyl- β -propiolactone) (PMEPL). The solid-state ¹³C NMR spectra of PMEPL revealed that isotactic PMEPL crystallizes in two forms, which can be easily distinguished by the chemical shifts of the α -methyl and main-chain methylene carbon atoms. Morin and Marchessault⁴⁰³ performed a ¹³C CP-MAS NMR study of the molecular dynamics in amorphous and crystalline poly(β -hydroxyalkanoate). The temperature dependence of the T_1 s of the side-chain and backbone carbons clearly reveals that these two moieties undergo very different dynamics, with the former being on the fast-motion side of the T_1 minimum, while the latter is on the slow-motion side. Stark and Garbow⁴⁰⁴ employed both ¹³C CP-MAS and ¹³C DP-MAS approaches to study the dynamics of polyester in suberized potato cell wall. Bergmark and Flodin⁴¹⁶ utilized ¹³C CP-MAS NMR to monitor the curing of unsaturated polyester by styrene.

Thermotropic polyesters have attracted much attention because of their potential as high-performance materials. Due to the extensive investigation of thermotropic polyesters by various solid-state NMR techniques in many laboratories, we note here just a few of the many publications in this area. Volksen *et al.*⁴¹⁷ employed ¹³C CP-MAS dynamics to study copolymer morphology in liquid-crystalline copolyesters based on poly(*p*-oxybenzoate) and poly(*p,p*-biphenylene terephthalate). Laupretre *et al.*⁴⁰⁵ studied the relaxation processes in a liquid-crystalline polyester, $(-\text{OC}(\text{Ph})_3-\text{CO}-\text{O}-[\text{CH}_2-\text{CH}_2-\text{O}-]_n)$, by dielectric relaxation, ESR, and ¹³C CP-MAS NMR. Uryu and Kato⁴¹⁸ used ¹³C CP-MAS to investigate conformation in the thermotropic ester, 4'-cyanopheny-4-*n*-pentoxybenzoate; they observed that the resonance of aromatic carbons *ortho* to the pentoxy group at 114.5 ppm in solution was separated into a doublet (111.4 ppm and 117.8 ppm) in the solid state because of configurational site differences. They also used ¹³C CP-MAS approaches to investigate a thermotropic polyester containing a flexible spacer based on terephthalic acid and 4,4'-dihydroxy-1,6-diphenoxyhexane, using ¹³C chemical shifts to determine the conformations of spacers.⁴¹⁹

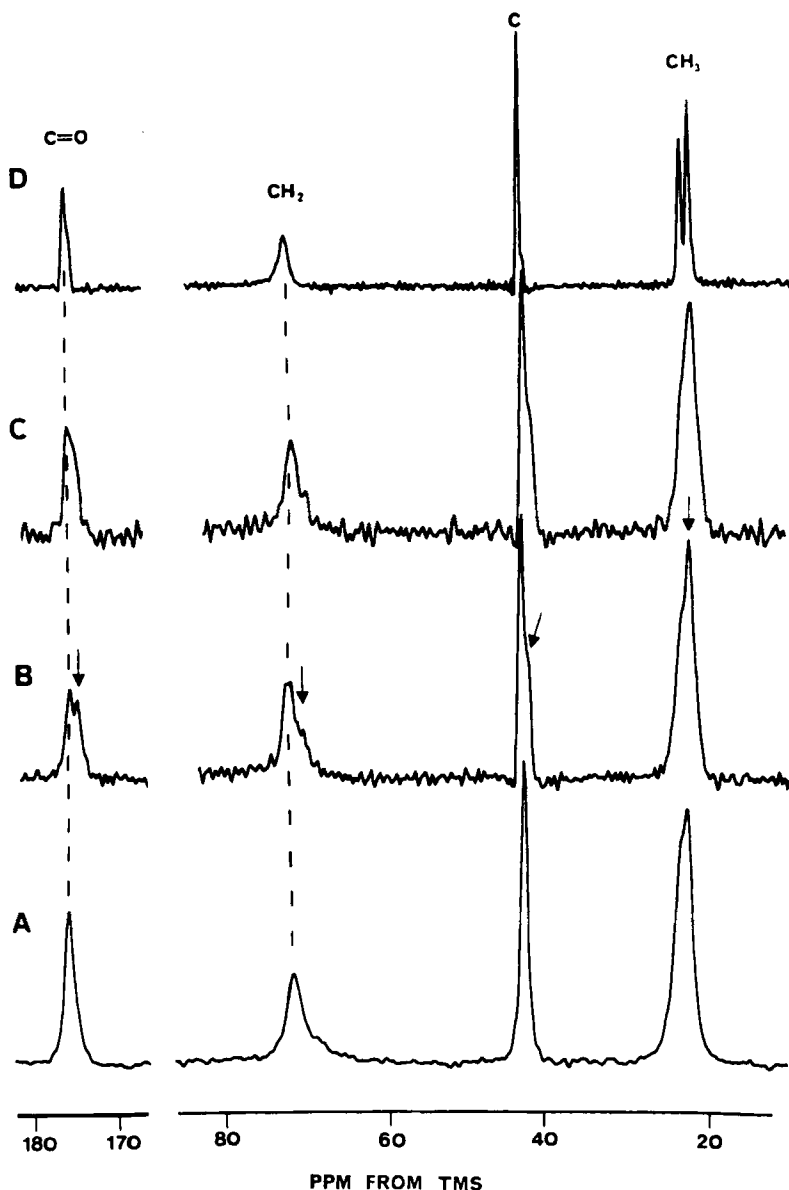


Fig. 51. ^{13}C CP-MAS NMR spectra of polypivalolactone fibres: (A) untreated fibres (α form); (B) stretched fibres (mixture of α and β); (C) stretched fibres, allowed to stand 1 week with no tension (mixture of α and β form); (D) stretched, then annealed fibres (α form). CP contact time = 1 ms; repetition time = 1 s. The spectra were all plotted with -20 Hz Gaussian resolution enhancement. Arrows denote the presence of peaks assigned to resonances arising from the β polymorph.⁴¹⁴

Polyesters based on 2,6-disubstituted naphthalene show unique thermotropic properties and possess very significant applications as high-strength plastics and fibres. Uryu and coworkers⁴²⁰ employed ^{13}C CP-MAS to study naphthalene-based thermotropic polyesters and model compounds. Fyfe *et al.*⁴⁰⁶ utilized both ^{13}C CP (without MAS) and wide-line deuterium NMR to study the molecular dynamics of naphthalene-base polyesters, *p*-hydroxybenzoic acid-base polyesters, and their copolyesters in a magnetic field. Laupretre and coworkers⁴⁰⁷ investigated the local motions in a mesomorphic main-chain copolyester based on hydroquinone, hydrobenzoic acid, and isophthalic acid units by ^{13}C CP-MAS NMR. They also obtained ^{13}C chemical shift tensor parameters from the spinning sideband intensities, and found that partial motional averaging of the chemical shift tensors of the aromatic carbons is due to oscillations for both *para*- and *meta*-substituted rings at temperatures below the glass transition temperature (405 K). The amplitude of these oscillations increases with increasing temperature. Allen and Ward⁴⁰⁸ studied the structures and chain motions of highly oriented liquid crystalline copolyesters of 4-hydroxybenzoic acid and 2-hydroxy-6-naphthoic acid by modelling the second moment anisotropies from their ^1H NMR lineshapes. Rutledge and Ward⁴²¹ used the ^1H second moment to investigate the segmental orientation in several aromatic polyesters.

3.8. Cyanate resins

Cured cyanate resins have been considered for electronic packing and structural materials applications,⁴²⁵ because of good thermal, mechanical and insulating characteristics. Bisphenol A dicyanate (BPACN, **XXXI**) is one of the resins most often used for the preparation of cured cyanate resins. The curing reaction is postulated to proceed by reaction of three cyanate ($-\text{OCN}$) groups to form a triazine ring (**XXXII**) as shown in Eq. (22)

Fyfe *et al.*⁴²⁶ used high-resolution ^{13}C and ^{15}N NMR spectroscopy in both the solution and solid states to investigate the mechanism of the curing reactions of cyanate-based polymer resins. The starting BPACN (**XXXI**) was separately enriched with ^{13}C and ^{15}N to clearly monitor reactive functional groups during the curing process. Both ^{13}C and ^{15}N liquid-sample NMR results indicate the formation of triazine rings (**XXXII**), as well as structures of the type **XXXIII**. Compound **XXXIII** is postulated to be formed by the addition of water to the cyanate groups, as shown in Eq. (23). The solution-state ^{13}C and ^{15}N NMR results also rule out the possibility of the formation of substantial amounts of any long-lived intermediate "dimer" species on route to triazine ring formation.

Fyfe *et al.*⁴²⁶ performed ^{13}C and ^{15}N CP-MAS NMR experiments on two cured cyanate resins obtained from solution curing and solid-state curing.

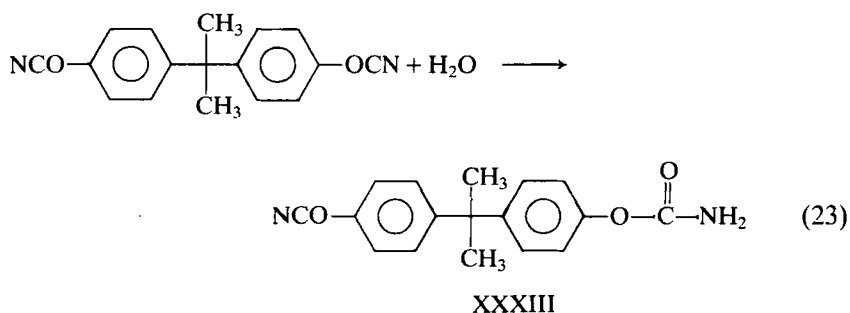
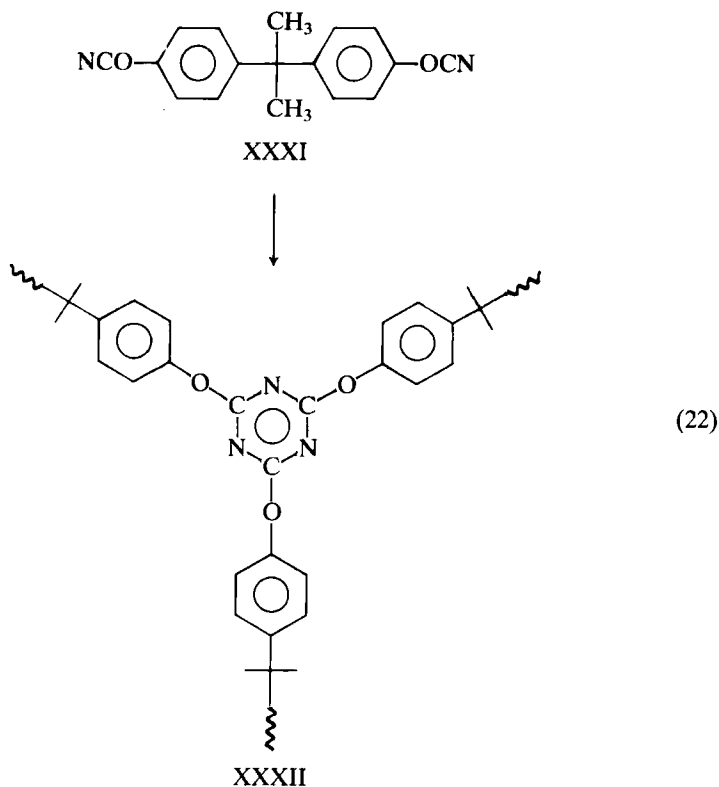


Figure 52 shows the 100.6 MHz ^{13}C CP-MAS spectra of both cured cyanate resins. The spectra clearly indicate that the cyanate resin obtained from solution curing contains both triazine rings (XXXII) and species XXXIII, while the cyanate resin obtained from solid-state curing is a clean product containing only triazine rings. From their ^{15}N CP-MAS results, they confirmed the conclusions drawn from ^{13}C CP-MAS.

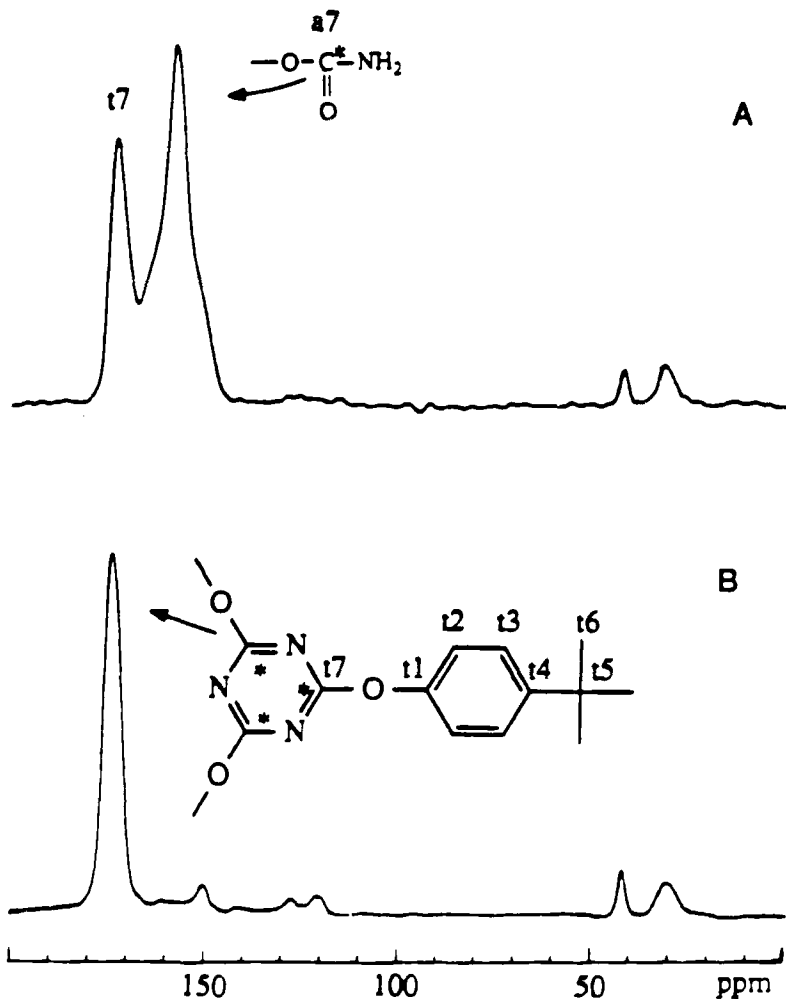


Fig. 52. 100.6 MHz ^{13}C CP-MAS TOSS NMR spectra of (A) the solid sample obtained by evaporation of the solvent after curing a ^{13}C -enriched BPACN in MEK and acetone- d_6 with 200 ppm zinc octanoate as catalyst; (B) the solid sample obtained from bulk curing of the ^{13}C -enriched BPACN at 250°C for 15 min.⁴²⁶

4. RESINS IN POLYMER BLENDS AND COMPOSITE MATERIALS

Solid-state NMR provides a unique tool to probe the microstructures and dynamics of materials down to the molecular levels with a wide range of dimensional scales accessible;^{51,169-173,195-208} therefore, this approach is powerful in the investigation of composite materials and of compatibility in

polymer blends. Recently, the solid-state version of ^{13}C - ^1H heteronuclear chemical shift correlation spectroscopy (HETCOR) has been applied successfully to the study of polymer blends,^{427,428} and the application of this approach can be expected to grow in popularity. Owing to the large scope of the subject of polymer blends and composites, we restrict our review to a very brief description of a few publications.

4.1. Resins in polymer blends

Kwei and coworkers⁴²⁹ employed ^{13}C CP-MAS NMR to study the complexation of poly(*N,N*-dimethylacrylamide) and phenol-formaldehyde resins. From the low-shielding shift of 3 ppm of a hydrogen-bonded carbonyl from the "free" carbonyl position at 174 ppm, they confirmed the observation by glass-transition data that the fraction of hydrogen-bonded carbonyl groups increases in the order blend < annealed blend < complex. Slonim *et al.*⁴³⁰ utilized ^{13}C CP-MAS experiments on urea-formaldehyde resins modified by furfuryl alcohol to confirm the incorporation of furfuryl alcohol into the resins.

Shukla *et al.*⁴³¹ utilized ^{13}C CP-MAS NMR to study the structure and dynamics of starch crosslinked with urea-formaldehyde polymers. ^{13}C linewidth and T_2 measurements of starch carbons show that a maximum degree of crosslinking is obtained at a urea-to-starch (W/W) ratio of 0.6. Increasing the urea-to-starch ratio beyond 0.6 leads to competing self-condensation of dimethylolurea. Their NMR results also establish that chemical crosslinking occurs through the primary hydroxyl groups located at the C-6 position of starches.

Eisenberg and coworkers⁴³² measured $T_{1\rho}^{\text{H}}$ and T_1^{H} through the resolved ^{13}C CP-MAS spectra of blends of polyamide-6 and sulfonated polystyrene. On the basis of $T_{1\rho}^{\text{H}}$ and T_1^{H} behaviour under the influence of ^1H spin diffusion they were able to estimate the domain sizes of various blends. Belfiore⁴³³ used ^{13}C CP-MAS to study polyether-polyester block copolymers by examining cross-polarization between a proton-rich component and a proton depleted (deuterium substituted) component, and found that the block copolymers are incompletely phase-separated. Henrichs and coworkers⁴³⁴ measured ^{13}C - ^{13}C nuclear spin diffusion for the study of the miscibility of polymer blends of poly(ethylene terephthalate) (PET) and bisphenol-A polycarbonate (BPAPC) labelled at either the CH_2 groups in PET or the carbonyl carbon in BPAPC. The basis of their approach is that ^{13}C - ^{13}C nuclear spin diffusion strongly depends on internuclear distance. ^{13}C - ^{13}C nuclear spin diffusion was detected in the laboratory frame in a two-dimensional experiment.^{435,436} Their ^{13}C NMR results clearly show that the PET/BPAPC blends studied are homogeneously mixed at distances of 4.5–6 Å. Henrichs *et al.*⁴³⁷ reinvestigated the blend miscibility of BPAPC

and PET by ^{13}C CP-MAS spin-diffusion measurements. They concluded that, in the absence of chemical reactions, mixtures of PET and BPAPC appear to be immiscible. Extensive heating results in a homogeneous system; the chemical reactions that result in polymer homogenization include a loss of the BPAPC carbonyl group.

Okamoto, Cooper and Root⁴³⁸ performed a series of NMR relaxation experiments on a poly(urethane-urea) system through ^{13}C CP-MAS. T_1^{C} and $T_{1\rho}^{\text{H}}$ measurements were able to distinguish between the hard-segment and the soft-segment carbons, but not the interfacial region between them. Natansohn *et al.*³⁰⁹ used ^{13}C CP-MAS NMR to study polyurethane-lignin blends. $T_{1\rho}^{\text{H}}$ values obtained from variable contact-time experiments^{86,87} for protons in polyurethane (70 ms) and in lignin (16 ms) are the same in pure states or in blends, an indication that polyurethane and lignin are well separated in blends.³⁰⁷

Ku *et al.*⁴³⁹ studied the structure-property relationships of simultaneous interpenetrating networks from castor-oil-based polyurethane and polystyrene by ^{13}C CP-MAS. Based on $T_{1\rho}^{\text{H}}$ values determined by variable contact-time experiments,^{86,87} they found that the size of the microphase structures ($\sim 100 \text{ \AA}$) estimated by $T_{1\rho}^{\text{H}}$ values under ^1H spin-diffusion is 2–3 orders of magnitude smaller than the domain ($0.1\text{--}1 \mu\text{m}$) observed by the electron microscopic method, and they concluded that a high degree of heterogeneity is present in the macroscopic domain.

4.2. Resins in composite materials

Veeman and coworkers investigated glass-filled polyamide-6 (PA6) composites by ^{13}C CP-MAS^{341–343} and ^{29}Si CP-MAS.³⁴² Their ^{13}C NMR results³⁴¹ indicate the presence of α and γ crystallites, as well as an amorphous phase, in the PA6 composites. These ^{13}C NMR results also show that the PA6 composites contain more γ crystalline PA6 than does the original sample of pure PA6. The ^{13}C CP-MAS spectra³⁴² of three different samples of glass microspheres isolated from the PA6 composites show that the bonding between the glass microsphere and PA6 is enhanced by the action of the coupling agent, γ -aminopropyltriethoxysilane (γ -APS), although there are still strong interactions between the surfaces of the glass microspheres and PA6 even in the absence of coupling agent. In the solid-state ^{13}C NMR study of the PA6 composite with a ^{13}C -labelled γ -APS as the coupling agent,³⁴³ there is some indication of amide formation between the PA6 carboxylic acid end groups and the amine groups of γ -APS. They have determined T_1^{C} , T_2^{C} , $T_{1\rho}^{\text{H}}$, $T_{1\rho}^{\text{C}}$ and T_{CH} values for various sample compositions, and interpreted the results on the basis of the presence of entanglements and interpenetration of the polysiloxane (formed from γ -APS after hydrolysis) and polyamide networks. From these results,^{341–343} they con-

cluded that the interpenetrating network mechanism, and presumably also chemical bonding, contribute to the adhesion between the PA6 matrix and γ -APS.

Jenneskens³⁴⁴ reported ^{13}C CP-MAS results on glassbead/polyamide-6 composites with selectively ^{13}C -enriched γ -aminopropyltriethoxysilane (APS) as coupling agent. Happe *et al.*⁴⁴⁰ used ^1H , ^{19}F and ^{11}B NMR to characterize the curing of carbon-fibre-epoxy prepregs by BF_3 :amine catalysts. Hoh, Ishita and Koenig⁴⁴¹ employed ^{13}C CP-MAS to study the gradient of chemical composition in the silane coupling agent/matrix interface in glass-fibre-reinforced epoxy resin. They also utilized ^{29}Si CP-MAS to study the types of structures and bonds that are formed with silicon at the composite interfaces between the glass and the silane coupling agent and between the silane coupling agent and the epoxy matrix.⁴⁴² They used ^{13}C CP-MAS, ^{29}Si CP-MAS and ^1H NMR imaging to study the effect of water on the silane coupling agent/epoxy resin interface in glass-fibre-reinforced composites,⁴⁴³ and found that water can react with the silane coupling agent and affect its T_{C}^1 and $T_{\text{Si-H}}$ values. Their ^1H NMR imaging results provide information on the amount of water, as well as the location of water in the composite.

Grenier-Loustalot and Grenier⁴⁴⁴ used solid-state ^{13}C NMR, as well as liquid-state ^1H and ^{13}C NMR, to study the mechanism of epoxy resin curing in the presence of glass and carbon fibres. Jackson⁴⁴⁵ utilized ^1H NMR imaging to study the curing of carbon-fibre-reinforced epoxy resin, finding that empirical relationships may be established between the imaging intensity observed and the internal viscosity of the polymer phases. His results show that NMR imaging may be useful in optimizing both the processing conditions and performance of such materials by enabling the measurement of curing characteristics during manufacture. Grenier-Loustalot and Grenier⁴⁴⁶ used ^{13}C CP-MAS to study organic matrices of composite materials. They presented several examples of solid-state ^{13}C CP-MAS structural analyses of epoxide resins polycondensed with aromatic amines.

REFERENCES

1. J. H. Van Vleck, *Phys. Rev.*, 1948, **74**, 1168.
2. H. S. Gutowsky and G. E. Pake, *J. Chem. Phys.*, 1950, **18**, 162.
3. A. Abragam, *The Principles of Nuclear Magnetism*, Clarendon Press, Oxford, 1961.
4. C. P. Slichter, *Principles of Magnetic Resonance*, 3rd edn, Springer-Verlag, Berlin, 1990.
5. S. R. Hartmann and E. L. Hahn, *Phys. Rev.*, 1962, **128**, 2042.
6. A. Pines, M. G. Gibby and J. S. Waugh, *J. Chem. Phys.*, 1973, **59**, 569.
7. E. R. Andrew, A. Bradbury and R. G. Eades, *Nature (London)*, 1958, **182**, 1659.
8. I. J. Lowe, *Phys. Rev. Lett.*, 1959, **2**, 285.
9. H. Kessemeier and R. E. Norberg, *Phys. Rev.*, 1967, **155**, 321.

10. E. R. Andrew, *Prog. Nucl. Magn. Reson. Spectrosc.*, 1972, **8**, 1.
11. E. R. Andrew, *Phil. Trans. Roy. Soc. Lond.*, 1981, **A299**, 505.
12. E. R. Andrew, *Int. Rev. Phys. Chem.*, 1981, **1**, 195.
13. J. Schaefer and E. O. Stejskal, *J. Am. Chem. Soc.*, 1976, **98**, 1031.
14. N. J. Clayden in *Annual Reports on NMR Spectroscopy*, Vol. 24 (ed. G. A. Webb), Academic Press, London, 1992, pp. 1-86.
15. J. A. Pople, W. G. Schneider and H. J. Bernstein, *High Resolution Nuclear Magnetic Resonance*, McGraw-Hill, New York, 1959.
16. P. L. Corio, *The Structure of High-Resolution NMR Spectra*, Academic Press, New York, 1966.
17. R. K. Harris and B. E. Mann, *NMR and the Periodic Table*, Academic Press, New York, 1978.
18. E. D. Becker, *High Resolution NMR: Theory and Chemical Applications*, 2nd edn, Academic Press, New York, 1980.
19. R. R. Ernst, G. Bodenhausen and A. Wokaun, *Principles of Nuclear Magnetic Resonance in One and Two Dimensions*, Clarendon Press, Oxford, 1987.
20. A. E. Derome, *Modern NMR Techniques for Chemistry Research*, Pergamon Press, Oxford, 1988.
21. F. A. Bovey, *Nuclear Magnetic Resonance Spectroscopy*, 2nd edn, Academic Press, New York, 1987.
22. E. Breitmaier and W. Voelter, *¹³C NMR Spectroscopy*, 2nd edn, Verlag Chemie, New York, 1978.
23. F. W. Wehrli and T. Wirthlin, *Interpretation of Carbon-13 NMR Spectra*, Heyden, London, 1978.
24. G. C. Levy, R. L. Lichter and G. L. Nelson, *Carbon-13 Nuclear Magnetic Resonance Spectroscopy*, 2nd edn, Wiley-Interscience, New York, 1980.
25. G. C. Levy and R. L. Lichter, *Nitrogen-15 Nuclear Magnetic Resonance Spectroscopy*, Wiley-Interscience, New York, 1979.
26. J. Mason (ed.), *Multinuclear NMR*, Plenum Press, New York, 1987.
27. (a) A. E. Tonelli and F. C. Schilling, *Acc. Chem. Res.*, 1981, **14**, 233.
(b) S. H. Grover, J. P. Guthrie, J. B. Stothers and C. T. Tan, *J. Magn. Reson.*, 1973, **10**, 227.
28. A. E. Tonelli, *NMR Spectroscopy and Polymer Microstructure: The Conformation Connection*, VCH, New York, 1989.
29. J. A. Tossell (ed.), *Nuclear Magnetic Shieldings and Molecular Structure*, NATO ASI Series, Kluwer, Boston, 1993.
30. D. G. Gadian, *Nuclear Magnetic Resonance and Its Applications to Living Systems*, Clarendon Press, Oxford, 1982.
31. K. Wüthrich, *NMR of Proteins and Nucleic Acids*, Wiley-Interscience, New York, 1986.
32. L. M. Jackman and F. A. Cotton (ed.), *Dynamic Nuclear Magnetic Resonance Spectroscopy*, Academic Press, New York, 1975.
33. A. Steigel, *NMR: Basic Principles and Progr.*, 1979, **15**, 1.
34. J. I. Kaplan and G. Fraenkel, *NMR of Chemically Exchanging Systems*, Academic Press, New York, 1980.
35. S. Szymánski and G. Binsch in *Annual Reports on NMR Spectroscopy*, Vol. 23 (ed. G. A. Webb), Academic Press, London, 1991, p. 209.
36. F. Noack, *NMR: Basic Principles and Progr.*, 1971, **3**, 83.
37. J. Kowalewski in *Annual Reports on NMR Spectroscopy*, Vol. 22 (ed. G. A. Webb), Academic Press, London, 1990, p. 307.
38. J. Kowalewski in *Annual Reports on NMR Spectroscopy*, Vol. 23 (ed. G. A. Webb), Academic Press, London, 1991, p. 289.
39. J. H. Noggle and R. E. Schirmer, *The Nuclear Overhauser Effect: Chemical Applications*, Academic Press, New York, 1971.

40. D. Neuhaus and M. P. Williamson, *The Nuclear Overhauser Effect*, VCH, Weinheim, 1989.
41. W. McFarlane and D. S. Rycroft in *Annual Reports on NMR Spectroscopy*, Vol. 16 (ed. G. A. Webb), Academic Press, London, 1985, pp. 293–364.
42. D. L. Turner, *Prog. Nucl. Magn. Reson. Spectrosc.*, 1985, **17**, 281.
43. D. L. Turner in *Annual Reports on NMR Spectroscopy*, Vol. 21 (ed. G. A. Webb), Academic Press, London, 1989, pp. 161–208.
44. C. S. Yannoni, *Acc. Chem. Res.*, 1982, **15**, 201.
45. J. R. Lyerla, C. S. Yannoni and C. A. Fyfe, *Acc. Chem. Res.*, 1982, **15**, 208.
46. C. A. Fyfe, L. Bemis, R. Childs, H. C. Clark, D. Curtin, J. Davies, D. Drexler, R. L. Dudley, G. C. Gobbi, J. S. Hartman, P. Hayes, J. Klinowski, R. L. Lenkinski, C. J. L. Lock, I. C. Paul, A. Rudin, W. Tchir, J. M. Thomas, F. R. S. and R. E. Wasylshen, *Phil. Trans. R. Soc. Lond.*, 1982, **A305**, 591.
47. G. E. Maciel, *Science*, 1984, **226**, 282.
48. J. J. Lindberg and B. Hortling, *Adv. Polym. Sci.*, 1985, **66**, 1.
49. H. W. Spiess, *Adv. Polym. Sci.*, 1985, **66**, 23.
50. M. Möller, *Adv. Polym. Sci.*, 1985, **66**, 59.
51. R. Voelkel, *Angew. Chem. Int. Ed. Engl.*, 1988, **27**, 1468.
52. B. Blümich and H. W. Spiess, *Angew. Chem. Int. Ed. Engl.*, 1988, **27**, 1655.
53. B. F. Chemelka and A. Pines, *Science*, 1989, **246**, 71.
54. H. Saito and I. Ando in *Annual Reports on NMR Spectroscopy*, Vol. 21 (ed. G. A. Webb), Academic Press, London, 1989, pp. 209–290.
55. M. Andreis and J. L. Koenig, *Adv. Polym. Sci.*, 1989, **89**, 69.
56. V. D. Fedotov and H. Schneider, *Structure and Dynamics of Bulk Polymers by NMR Methods, NMR: Basic Principles and Prog.*, Vol. 21. Springer-Verlag, Berlin, 1989.
57. (a) H. W. Spiess, *Chem. Rev.*, 1991, **91**, 1321. (b) H. W. Spiess, *Ann. Rev. Mater. Sci.*, 1991, **21**, 131.
58. J. L. Koenig, *Spectroscopy of Polymers*, American Chemical Society, Washington, DC, 1992.
59. R. K. Harris and P. Jackson, *Chem. Rev.*, 1991, **91**, 1427.
60. A. E. Derome and S. Bowden, *Chem. Rev.*, 1991, **91**, 1307.
61. J. Klinowski, *Chem. Rev.*, 1991, **91**, 1459.
62. C. A. Fyfe, Y. Feng, H. Grondey, G. T. Kokotailo and H. Gies, *Chem. Rev.*, 1991, **91**, 1525.
63. T. M. Adam and G. P. Drobny, *Chem. Rev.*, 1991, **91**, 1545.
64. U. Haeblerlen, *High Resolution NMR in Solids: Selective Averaging, Adv. Magn. Reson. Suppl. 1* (ed. J. S. Waugh), Academic Press, New York, 1976.
65. E. Fukushima and S. B. W. Roeder, *Experimental Pulse NMR*. Addison-Wesley, London, 1981.
66. R. K. Harris, *Nuclear Magnetic Resonance*, Pitman, London, 1983.
67. C. A. Fyfe, *Solid State NMR for Chemists*, CFC Press, Guelph, 1983.
68. M. Mehring, *Principles of High Resolution NMR in Solids*, 2nd edn, Springer-Verlag, Berlin, 1983.
69. Y. Takeuchi and A. P. Marchand (ed.), *Applications of NMR Spectroscopy to Problems in Stereochemistry and Conformational Analysis*. VCH, Deerfield Beach, Florida, 1986.
70. R. A. Komoroski (ed.), *High Resolution NMR Spectroscopy of Synthetic Polymers in Bulk*, VCH Publishers, Deerfield Beach, Florida, 1986.
71. W. S. Warren (ed.), *Adv. Magn. Reson.*, 1989, **13**.
72. W. S. Warren (ed.), *Adv. Magn. Reson.*, 1990, **14**.
73. L. J. Mathias (ed.), *Solid State NMR of Polymers*, Plenum Press, New York, 1991.
74. R. R. Ernst and W. A. Anderson, *Rev. Sci. Instrum.*, 1966, **37**, 93.
75. R. R. Ernst, *Adv. Magn. Reson.*, 1966, **2**, 1.

76. T. C. Farrar and E. D. Becker, *Pulse and Fourier Transform NMR*, Academic Press, New York, 1971.
77. D. Shaw, *Fourier Transform NMR Spectroscopy*, 2nd edn, Elsevier, Amsterdam, 1984.
78. W. R. Croasmun and R. M. K. Carlson (ed.), *Two-Dimensional NMR Spectroscopy: Applications For Chemists and Biochemists*, VCH, Deerfield Beach, Florida, 1987.
79. R. A. Wind, S. F. Dec, H. Lock and G. E. Maciel, *J. Magn. Reson.*, 1988, **79**, 136.
80. D. E. Demco, J. Tegenfeldt and J. S. Waugh, *Phys. Rev.*, 1975, **B11**, 4133.
81. M. H. Levitt, D. Suter and R. R. Ernst, *J. Chem. Phys.*, 1986, **84**, 4243.
82. C. H. Klein Douwel, W. E. J. R. Maas, W. S. Veeman, G. H. W. Buning and J. M. J. Vankan, *Macromolecules*, 1990, **23**, 406.
83. N. Zumbulyadis and J. M. O'Reilly, *Macromolecules*, 1991, **24**, 5294.
84. A. P. A. M. Eijkelenboom, W. E. J. R. Maas, W. S. Veeman, G. H. W. Buning and J. M. J. Vankan, *Macromolecules*, 1992, **25**, 4511.
85. M. J. Sullivan and G. E. Maciel, *Anal. Chem.*, 1982, **54**, 1615.
86. E. O. Stejskal, J. Schaefer, M. D. Sefcik and R. A. McKay, *Macromolecules*, 1981, **14**, 275.
87. G. E. Maciel and D. W. Sindorf, *J. Am. Chem. Soc.*, 1980, **102**, 7606.
88. (a) S. J. Opella and M. H. Frey, *J. Am. Chem. Soc.*, 1979, **101**, 5854. (b) S. J. Opella, M. H. Frey and T. A. Cross, *J. Am. Chem. Soc.*, 1979, **101**, 5856.
89. L. B. Alemany, D. M. Grant, T. D. Alger and R. J. Pugmire, *J. Am. Chem. Soc.*, 1983, **105**, 6697.
90. (a) X. Wu, S. Zhang and X. Wu, *J. Magn. Reson.*, 1988, **77**, 343. (b) X. Wu, S. Zhang and X. Wu, *Phys. Rev.*, 1988, **B37**, 9827. (c) X. Wu and K. W. Zilm, *J. Magn. Reson.*, 1993, **A102**, 205. (d) X. Wu and K. W. Zilm, *J. Magn. Reson.*, 1993, **A104**, 109.
91. A. Abragam, *The Principles of Nuclear Magnetism*, Chap. IX, Clarendon Press, Oxford, 1961.
92. R. A. Wind, M. J. Duijvestijn, C. Van der Lugt, A. Manenshijn and J. Vriend, *Prog. Nucl. Magn. Reson. Spectrosc.*, 1985, **17**, 33.
93. R. A. Wind, L. Li, H. Lock and G. E. Maciel, *J. Magn. Reson.* 1988, **79**, 577.
94. R. A. Wind, M. J. Duijvestijn, C. Van der Lugt, J. Smidt and J. Vriend, *Fuel*, 1987, **66**, 876.
95. G. G. Maresch, R. D. Kendrick, C. S. Yannoni and M. E. Galvin, *J. Magn. Reson.*, 1989, **82**, 41.
96. G. G. Maresch, R. D. Kendrick, C. S. Yannoni and M. E. Galvin, *Macromolecules*, 1988, **21**, 3523.
97. R. A. Wind, N. Zumbulyadis, R. H. Young, Y. Hung, L. Li, R. H. D. Nuttall and G. E. Maciel, *Solid State Nucl. Magn. Reson.*, 1992, **1**, 55.
98. M. Afeworki, R. A. McKay and J. Schaefer, *Macromolecules*, 1992, **25**, 4084.
99. M. Afeworki and J. Schaefer, *Macromolecules*, 1992, **25**, 4092.
100. M. Afeworki and J. Schaefer, *Macromolecules*, 1992, **25**, 4097.
101. M. Afeworki, S. Vega and J. Schaefer, *Macromolecules*, 1992, **25**, 4100.
102. H. Lock, G. E. Maciel and C. E. Johnson, *J. Mater. Res.*, 1992, **7**, 2791.
103. J. A. Ripmeester, *J. Am. Chem. Soc.*, 1983, **105**, 2925.
104. G. E. Maciel, J. F. Haw, I. Chuang, B. L. Hawkins, T. A. Early, D. R. McKay and L. Petrakis, *J. Am. Chem. Soc.*, 1983, **105**, 5529.
105. J. F. Haw, I. Chuang, B. L. Hawkins and G. E. Maciel, *J. Am. Chem. Soc.*, 1983, **105**, 7206.
106. I. Chuang, B. L. Hawkins, G. E. Maciel and G. E. Myers, *Macromolecules*, 1985, **18**, 1482.
107. P. D. Majors and P. D. Ellis, *J. Am. Chem. Soc.*, 1987, **109**, 1648.
108. G. R. Hatfield and G. E. Maciel, *Macromolecules*, 1987, **20**, 608.
109. D. G. Powell and L. J. Mathias, *Macromolecules*, 1989, **22**, 3812.

110. D. G. Powell and L. J. Mathias, *J. Am. Chem. Soc.*, 1990, **112**, 669.
111. L. J. Mathias, D. G. Powell, J.-P. Autran and R. S. Porter, *Macromolecules*, 1990, **23**, 963.
112. G. R. Hatfield, J. H. Glans and W. B. Hammond, *Macromolecules*, 1990, **23**, 1654.
113. D. W. Duff and G. E. Maciel, *Macromolecules*, 1990, **23**, 3069.
114. D. W. Duff and G. E. Maciel, *Macromolecules*, 1990, **23**, 4367.
115. D. W. Duff and G. E. Maciel, *Macromolecules*, 1991, **24**, 387.
116. D. W. Duff and G. E. Maciel, *Macromolecules*, 1991, **24**, 651.
117. M. D. Lumsden, G. Wu, R. E. Wasylshen and R. D. Curtis, *J. Am. Chem. Soc.*, 1993, **115**, 2825.
118. S. J. Opella, P. L. Steward and K. G. Valentine, *Quart. Rev. Biophys.*, 1987, **19**, 7.
119. M. Zhang and G. E. Maciel, *Anal. Chem.*, 1990, **62**, 633.
120. D. G. Powell, A. M. Sikes and L. J. Mathias, *Polymers*, 1991, **32**, 2523.
121. R. F. Colletti and L. J. Mathias in *Solid State NMR of Polymers* (ed. L. J. Mathias), Plenum Press, New York, 1991, pp. 23–60.
122. M. Zhang and G. E. Maciel, *J. Magn. Reson.*, 1989, **85**, 156.
123. I. Chuang and G. E. Maciel, *Polymer*, 1994, **35**, 1621.
124. I. Chuang, G. E. Maciel and H. Yue, unpublished results.
125. R. H. Lewis, I. Chuang and G. E. Maciel, manuscript in preparation.
126. I. Chuang, D. R. Kinney, C. E. Bronnimann, R. C. Zeigler and G. E. Maciel, *J. Phys. Chem.*, 1992, **96**, 4027.
127. G. E. Maciel, C. E. Bronnimann, R. C. Zeigler, I. Chuang, D. R. Kinney and E. A. Keiter, *Adv. Chem. Ser. No. 234*, 1994, pp. 269–282.
128. I. Chuang, D. R. Kinney and G. E. Maciel, *J. Am. Chem. Soc.*, 1993, **115**, 8695.
129. M. Zhang and G. E. Maciel, *Fuel*, 1990, **69**, 557.
130. W. S. Veeman, *Prog. Nucl. Magn. Reson. Spectrosc.*, 1984, **16**, 193.
131. J. S. Frye and G. E. Maciel, *J. Magn. Reson.*, 1982, **48**, 125.
132. M. M. Maricq and J. S. Waugh, *J. Chem. Phys.*, 1979, **70**, 3300.
133. J. Herzfeld and A. E. Berger, *J. Chem. Phys.*, 1980, **73**, 6021.
134. W. T. Dixon, *J. Chem. Phys.*, 1982, **77**, 1800.
135. W. T. Dixon, J. Schaefer, M. D. Sefcik, E. O. Stejskal and R. A. McKay, *J. Magn. Reson.*, 1982, **49**, 341.
136. W. T. Dixon, *J. Magn. Reson.*, 1985, **64**, 332.
137. (a) D. P. Raleigh, E. T. Olejniczak, S. Vega and R. G. Griffin, *J. Magn. Reson.*, 1987, **72**, 238. (b) D. P. Raleigh, A. C. Kolbert and R. G. Griffin, *J. Magn. Reson.*, 1990, **89**, 1.
138. N. C. Nielsen, H. Bildsoe and H. J. Jakobsen, *J. Magn. Reson.*, 1988, **80**, 149.
139. S. F. Dec, R. A. Wind, G. E. Maciel and F. E. Anthonio, *J. Magn. Reson.*, 1986, **70**, 355.
140. (a) M. Sardashti and G. E. Maciel, *J. Magn. Reson.*, 1987, **72**, 467. (b) R. C. Zeigler, R. A. Wind and G. E. Maciel, *J. Magn. Reson.*, 1988, **79**, 299. (c) Y. Sun and G. E. Maciel, *J. Magn. Reson.*, 1993, **105A**, 145. (d) S. Zhang, X. Wu and M. Mehring, *Chem. Phys. Lett.*, 1990, **166**, 92. (e) O. B. Peersen, X. Wu, M. Han, G. P. Metz and S. O. Smith, 35th Rocky Mountain Conf. on Anal. Chem., Denver, CO, July 25, 1993.
141. D. L. VanderHart, H. S. Gutowsky and T. C. Farrar, *J. Am. Chem. Soc.*, 1967, **89**, 5056.
142. M. E. Stoll, R. W. Vaughan, R. B. Saillant and T. Cole, *J. Chem. Phys.*, 1974, **61**, 2896.
143. H. W. Spiess, U. Haeberlen and H. Zimmermann, *J. Magn. Reson.*, 1977, **25**, 55.
144. E. Lippmaa, M. Alla, H. Raude, R. Telaar, I. Heinmua and E. Kundla, *Proc. 20th Cong. Ampere*, Tallinn, Springer-Verlag, Berlin, 1979, p. 87.
145. E. Kundla and M. Alla, *Proc. 20th Cong. Ampere*, Tallinn, Springer-Verlag, Berlin, 1979, p. 92.
146. S. Opella, M. H. Frey and T. A. Cross, *J. Am. Chem. Soc.*, 1979, **101**, 5856.
147. C. J. Groombridge, R. K. Harris, K. J. Packer, B. J. Say and S. F. Tanner, *J. Chem. Soc. Chem. Commun.*, 1980, pp. 174–175.

148. A. Naito, S. Ganapathy and C. A. McDowell, *J. Chem. Phys.*, 1981, **74**, 5393.
149. N. Zumbulyadis, P. M. Henrichs and R. H. Young, *J. Chem. Phys.*, 1981, **75**, 1603.
150. J. G. Hexem, M. H. Frey and S. J. Opella, *J. Am. Chem. Soc.*, 1981, **103**, 224.
151. J. G. Hexem, M. H. Frey and S. J. Opella, *J. Chem. Phys.*, 1982, **77**, 3847.
152. R. K. Harris, P. Jonsen and K. J. Packer, *Org. Magn. Reson.*, 1984, **22**, 784.
153. R. K. Harris, P. Jonsen and K. J. Packer, *Magn. Reson. Chem.*, 1985, **23**, 565.
154. R. K. Harris, P. Jonsen, K. J. Packer and C. Campbell, *Magn. Reson. Chem.*, 1986, **24**, 977.
155. A. C. Olivieri, L. Frydman and L. E. Diaz, *J. Magn. Reson.*, 1987, **75**, 50.
156. R. K. Harris and A. C. Olivieri, *Prog. Nucl. Magn. Reson. Spectrosc.*, 1992, **24**, 435.
157. D. L. VanderHart, W. L. Earl and A. N. Garroway, *J. Magn. Reson.*, 1981, **44**, 361.
158. I. Ando, T. Yamanobe, H. Kurosu and G. A. Webb in *Annual Reports on NMR Spectroscopy*, Vol. 22 (ed. G. A. Webb), Academic Press, London, 1990, pp. 205-248.
159. E. Lippmaa, M. A. Alla, T. J. Pehk and G. Engelhardt, *J. Am. Chem. Soc.*, 1978, **100**, 1929.
160. J. S. Waugh, L. M. Huber and H. Haeberlen, *Phys. Rev. Lett.*, 1968, **20**, 180.
161. P. Mansfield, *J. Phys. C*, 1971, **4**, 1444.
162. W. K. Rhim, D. D. Elleman and R. W. Vaughan, *J. Chem. Phys.*, 1973, **58**, 1772.
163. D. P. Burum and W. K. Rhim, *J. Chem. Phys.*, 1979, **71**, 944.
164. B. C. Gerstein, R. G. Pembleton, R. C. Wilson and L. M. Ryan, *J. Chem. Phys.*, 1977, **66**, 361.
165. L. M. Ryan, R. E. Taylor, A. J. Paff and B. C. Gerstein, *J. Chem. Phys.*, 1980, **72**, 508.
166. C. E. Bronnimann, B. L. Hawkins, M. Zhang and G. E. Maciel, *Anal. Chem.*, 1988, **60**, 1743.
167. G. E. Maciel, C. E. Bronnimann and B. L. Hawkins, *Adv. Magn. Reson.*, 1990, **14**, 125.
168. R. K. Harris, P. Jackson and G. J. Nesbitt, *J. Magn. Reson.*, 1989, **85**, 294.
169. P. Caravatti, P. Neuenschwander and R. R. Ernst, *Macromolecules*, 1985, **18**, 119.
170. P. Caravatti, P. Neuenschwander and R. R. Ernst, *Macromolecules*, 1986, **19**, 1889.
171. L. A. Belfiore, T. L. Lutz, C. Cheng and C. E. Bronnimann, *J. Polym. Sci. Part B: Polym. Phys.*, 1990, **28**, 1261.
172. G. C. Campbell and D. L. VanderHart, *J. Magn. Reson.*, 1992, **96**, 69.
173. D. L. VanderHart, G. C. Campbell and R. M. Briber, *Macromolecules*, 1992, **25**, 4734.
174. F. A. Bovey and L. W. Jelinski, *J. Phys. Chem.*, 1985, **89**, 571.
175. L. W. Jelinski, *Annu. Rev. Mater. Sci.*, 1985, **15**, 359.
176. K. Müller, P. Meier and G. Kothe, *Prog. Nucl. Magn. Reson. Spectrosc.*, 1985, **17**, 211.
177. R. L. Vold, R. R. Vold and N. J. Heaton, *Adv. Magn. Reson.*, 1989, **13**, 17.
178. F. D. Blum, B. Durairaj and A. S. Padmanabhan, *Macromolecules*, 1984, **17**, 2837.
179. R. Brandes, R. R. Vold, R. L. Vold and D. R. Kearns, *Biochem.*, 1986, **25**, 7744.
180. J. Hirschinger, H. Miura, K. H. Gardner and A. D. English, *Macromolecules*, 1990, **23**, 2153.
181. H. Miura, J. Hirschinger and A. D. English, *Macromolecules*, 1990, **23**, 2169.
182. C. J. Landry and P. M. Henrichs, *Macromolecules*, 1989, **22**, 2157.
183. L. W. Jelinski, J. J. Dumais, A. L. Cholli, T. S. Ellis and F. E. Karasz, *Macromolecules*, 1985, **18**, 1091.
184. (a) J. A. Kornfield, H. W. Spiess, H. Nefzger, H. Hayen and C. D. Eisenbach, *Macromolecules*, 1991, **24**, 4787. (b) A. D. Meltzer, H. W. Spiess, C. D. Eisenbach and H. Hayen, *Macromolecules*, 1992, **25**, 993.
185. A. Kintanar, L. W. Jelinski, I. Gancarz and J. T. Koberstein, *Macromolecules*, 1986, **19**, 1876.
186. H. W. Spiess, *Colloid Polym. Sci.*, 1983, **261**, 193.
187. J. Seeling and A. Seeling, *Quart. Rev. Biophys.*, 1980, **13**, 19.
188. P. Meier, E. Ohms and G. Kothe, *J. Chem. Phys.*, 1986, **85**, 3598.
189. J. H. Davis, *Adv. Magn. Reson.*, 1989, **13**, 195.

190. H. W. Spiess, *NMR: Basic Principles and Progress*, 1979, **15**, 55.
191. R. Kitamaru in *Applications of NMR Spectroscopy to Problems in Stereochemistry and Conformational Analysis* (eds Y. Takeuchi and A. P. Marchand), VCH, Deerfield Beach, Florida, 1986, p. 75.
192. D. W. McCall, *Acc. Chem. Res.*, 1971, **4**, 223.
193. J. Schaefer, E. O. Stejskal and R. Buchdahl, *Macromolecules*, 1977, **10**, 384.
194. X. Zhang, K. Takegoshi and K. Hikichi, *Macromolecules*, 1991, **24**, 5756.
195. D. C. Douglass and V. J. McBrierty, *Macromolecules*, 1978, **11**, 766.
196. R. A. Assink, *Macromolecules*, 1978, **11**, 1233.
197. V. J. McBrierty, *Faraday Disc. Chem. Soc.*, 1979, **68**, 78.
198. E. O. Stejskal, J. Schaefer, M. D. Sefcik and R. A. McKay, *Macromolecules*, 1981, **14**, 275.
199. T. T. P. Cheung, B. C. Gerstein, L. M. Ryan, R. E. Taylor and D. R. Dybowski, *J. Chem. Phys.*, 1980, **73**, 6059.
200. T. T. P. Cheung, *J. Chem. Phys.*, 1982, **76**, 1248.
201. V. J. McBrierty and D. C. Douglas, *J. Polym. Sci. Macromol. Rev.*, 1981, **16**, 295.
202. B. Albert, R. Jerome, P. Teyssie, G. Smyth and V. J. McBrierty, *Macromolecules*, 1984, **17**, 2552.
203. K. J. Packer, J. M. Pope and R. R. Yeung, *J. Polym. Sci. Polym. Phys. Ed.*, 1984, **22**, 589.
204. B. Albert, R. Jerome, P. Teyssie, G. Smyth, N. G. Boyle and V. J. McBrierty, *Macromolecules*, 1985, **18**, 388.
205. J. R. Havens and D. L. VanderHart, *Macromolecules*, 1985, **18**, 1663.
206. P. M. Henrichs, J. Tribone, D. J. Massa and J. M. Hewitt, *Macromolecules*, 1988, **21**, 1282.
207. C. Marco, J. G. Fatou, M. A. Gomez, H. Tanaka and A. E. Tonelli, *Macromolecules*, 1990, **23**, 2183.
208. T. Kimura, K. Neki, N. Tamura, F. Horii, M. Nakagawa and H. Odani, *Polymer*, 1992, **33**, 493.
209. G. S. Harbison and H. W. Spiess, *Chem. Phys. Lett.*, 1986, **124**, 128.
210. G. S. Harbison, V.-D. Vogt and H. W. Spiess, *J. Chem. Phys.*, 1987, **86**, 1206.
211. P. Tang, R. A. Santos and G. S. Harbison, *Adv. Magn. Reson.*, 1989, **13**, 225.
212. V.-D. Vogt, M. Dettenmaier, H. W. Spiess and M. Pietralla, *Colloid Polym. Sci.*, 1990, **268**, 22.
213. Y. Yang, A. Hagemeyer, K. Zemke and H. W. Spiess, *J. Chem. Phys.*, 1990, **93**, 7740.
214. A. Hagemeyer, K. Schmidt-Rohr and H. W. Spiess, *Adv. Magn. Reson.*, 1989, **13**, 85.
215. J. J. Titman, Z. Luz and H. W. Spiess, *J. Am. Chem. Soc.*, 1992, **114**, 3756.
216. J. J. Titman, Z. Luz and H. W. Spiess, *J. Am. Chem. Soc.*, 1992, **114**, 3765.
217. A. Dunlop and F. N. Peters, *The Furans*, Reinhold, New York, 1953.
218. C. R. Schmitt, *Polym. - Plast. Technolog. Eng.*, 1974, **3**, 121.
219. A. Gandini, *Adv. Polym. Sci.*, 1977, **25**, 47.
220. J. Milkovic, G. E. Myers and R. A. Young, *Cellul. Chem. Technol.*, 1979, **13**, 651.
221. E. M. Wewerka, *J. Polym. Sci. Part A-1*, 1971, **9**, 1703.
222. R. T. Conley and I. Metil, *J. Appl. Polym. Sci.*, 1963, **7**, 37.
223. G. E. Maciel, I. Chuang and G. E. Myers, *Macromolecules*, 1982, **15**, 1218.
224. I. Chuang, G. E. Maciel and G. E. Myers, *Macromolecules*, 1984, **17**, 1087.
225. A. H. Fawcett and W. Dadamba, *Makromol. Chem.*, 1982, **183**, 2799.
226. A. Knop and L. A. Pilato, *Phenolic Resins*, Springer-Verlag, New York, 1985.
227. A. A. K. Whitehouse, E. G. K. Pritchett and G. Barnett, *Phenolic Resins*, Iliffe, London, 1967.
228. R. H. Young and J. M. Tancrede in *Adhesives in Manufacturing* (ed. G. L. Schneberger), Marcel Dekker, New York, 1983.

229. Y. Mukoyama, T. Tanno, H. Yokokawa and J. Fleming, *J. Polym. Sci. Polym. Chem. Ed.*, 1973, **11**, 3193.
230. M. I. Siling, Y. G. Urman, I. V. Adorova, S. G. Alekseyeva, O. S. Matyukhina and I. Y. Slonim, *Polym. Sci. U.S.S.R.*, 1977, **19**, 358.
231. A. J. J. deBreet, W. Dankelman, G. B. Huysman and J. deWitt, *Angew. Makromol. Chem.*, 1977, **62**, 7.
232. E. Dradi, G. Casiraghi, G. Sartori and G. Casnati, *Macromolecules*, 1978, **11**, 1295.
233. E. Dradi, G. Casiraghi and G. Casnati, *Chem. Ind. (London)*, 1978, **Aug. 19**, 627.
234. K. Kamide and Y. Miyakawa, *Makromol. Chem.*, 1978, **179**, 359.
235. S. A. Sojka, R. A. Wolfe, E. A. Deitz and B. F. Dannels, *Macromolecules*, 1979, **12**, 767.
236. M. G. Kim, G. T. Tiedeman and L. W. Amons, *Weyerhaeuser Science Symposium (1979)*, 1981, **2**, 263.
237. G. Casiraghi, G. Sartori, F. Bigi, M. Cornia, E. Dradi and G. Casnati, *Makromol. Chem.*, 1981, **182**, 2151.
238. G. Casiraghi, G. Casnati, M. Cornia, G. Satori and F. Bigi, *Makromol. Chem.*, 1981, **182**, 2973.
239. S. A. Sojka, R. A. Wolfe and G. D. Guenther, *Macromolecules*, 1981, **14**, 1539.
240. R. Pethrick and B. Thompson, *British Polym. J.*, 1986, **18**, 380.
241. E. Fitzgerald, *J. Appl. Polym. Sci.*, 1990, **41**, 1809.
242. E. A. Fitzgerald, S. P. Tadros, R. F. Almeida, G. A. Sienko, K. Honda and T. Sarubbi, *J. Appl. Polym. Sci.*, 1992, **45**, 363.
243. L. E. Bogan, Jr, *Macromolecules*, 1991, **24**, 4807.
244. C. A. Fyfe, A. Rudin and W. Tchir, *Macromolecules*, 1980, **13**, 1320.
245. R. L. Bryson, G. R. Hatfield, T. A. Early, A. R. Palmer and G. E. Maciel, *Macromolecules*, 1983, **16**, 1669.
246. S. So and A. Rudin, *J. Polym. Sci. Polym. Lett. Ed.*, 1985, **23**, 403.
247. G. E. Maciel, I. Chuang and L. Gollob, *Macromolecules*, 1984, **17**, 1081.
248. A. Zinke, *J. Appl. Chem.*, 1951, **1**, 257.
249. C. A. Fyfe, M. S. McKinnon, A. Rudin and W. J. Tchir, *Macromolecules*, 1983, **16**, 1216.
250. H. W. Lochte, E. L. Strauss and R. T. Conley, *J. Appl. Polym. Sci.*, 1965, **9**, 2799.
251. I. Chuang and G. E. Maciel, *Macromolecules*, 1991, **24**, 1025.
252. B. Meyer, *Urea-Formaldehyde Resin*. Addison-Wesley, Reading, MA, 1979.
253. G. Widmer in *Encyclopedia of Polymer Science and Technology*, Vol. 2 (eds H. F. Mark, N. G. Gaylord and N. M. Bikales), Interscience, New York, 1965.
254. S. M. Kambanis and R. C. Vasishth, *J. Appl. Polym. Sci.*, 1971, **15**, 1911.
255. M. Chiavarini, N. Del Fanti and R. Bigatto, *Angew. Makromol. Chem.*, 1975, **46**, 151.
256. B. Tomita and Y. Hirose, *J. Polym. Sci. Polym. Chem. Ed.*, 1976, **14**, 387.
257. M. Chiavarini, R. Bigatto and N. Conti, *Angew. Makromol. Chem.*, 1978, **70**, 49.
258. I. Y. Slonim, S. G. Alekseyeva, Y. G. Urman, B. M. Arshava and B. Y. Aksel'rod, *Polym. Sci. USSR*, 1979, **20**, 1598.
259. K. Kumlin and R. Simonson, *Angew. Makromol. Chem.*, 1978, **72**, 67.
260. K. Kumlin and R. Simonson, *Angew. Makromol. Chem.*, 1981, **93**, 27.
261. R. M. Rammon, W. E. Johns, J. Magnuson and A. K. Dunker, *J. Adh.*, 1986, **19**, 115.
262. M. G. Kim and L. W. Amos, *Ind. Eng. Chem. Res.*, 1990, **29**, 208.
263. A. J. J. de Breet, W. Dankelman, W. G. B. Huysmans and J. de Wit, *Angew. Makromol. Chem.*, 1977, **62**, 7.
264. I. Y. Slonim, S. G. Alekseyeva, Y. G. Urman, B. M. Arshava, B. Y. Aksel'rod and I. M. Gurman, *Polym. Sci. USSR*, 1977, **19**, 899.
265. I. Y. Slonim, S. G. Alekseyeva, Y. G. Urman, B. M. Arshava, B. Y. Aksel'rod and L. N. Smirnova, *Polym. Sci. USSR*, 1977, **19**, 920.
266. J. R. Ebdon and P. E. Heaton, *Polymer*, 1977, **18**, 971.
267. B. Tomita and S. Hatono, *J. Polym. Sci. Polym. Chem. Ed.*, 1978, **16**, 2509.

268. I. Y. Slonim, S. G. Alekseyeva, Y. G. Urman, B. M. Arshava and B. Y. Aksel'rod, *Polym. Sci. USSR*, 1979, **20**, 1661.
269. I. Y. Slonim, S. G. Alekseyeva, Y. G. Urman, B. M. Arshava, B. Y. Aksel'rod, I. M. Gurman and L. N. Smirnova, *Polym. Sci. USSR*, 1979, **20**, 2569.
270. A. Sebenik, U. Osredkar, M. Zigon and I. Vizovisek, *Angew. Makromol. Chem.*, 1982, **102**, 81.
271. H. Pasch, I. S. Dairanieh and B. Al-Tahou, *J. Polym. Sci. Polym. Chem.*, 1990, **28**, 2049.
272. H. Pasch, G. Hovakeemian and S. Lahalih, *J. Polym. Sci. Polym. Chem.*, 1991, **29**, 525.
273. S. S. Jada, *J. Macromol. Sci.-Chem.*, 1990, **A27**, 361.
274. G. E. Maciel, N. M. Szeverenyi, T. A. Early and G. E. Myers, *Macromolecules*, 1983, **16**, 598.
275. I. Chuang and G. E. Maciel, *Macromolecules*, 1992, **25**, 3204.
276. I. Chuang and G. E. Maciel, *Polymer*, 1994, **35**, 1602.
277. I. Chuang and G. E. Maciel, *J. Appl. Polym. Sci.*, 1994, **52**, 1637.
278. I. Y. Slonim, S. G. Alekseyeva, B. M. Arshava, S. L. Pokrovskii and P. A. Okunev, *Polym. Sci. USSR*, 1985, **27**, 1993.
279. W. T. Dixon, *J. Magn. Reson.*, 1981, **44**, 220.
280. W. T. Dixon, J. Schaefer, M. D. Sefcik, E. O. Stejskal and R. A. McKay, *J. Magn. Reson.*, 1981, **45**, 173.
281. I. Chuang and G. E. Maciel, unpublished results.
282. G. E. Myers and M. Nagaoka, *Wood Sci.*, 1981, **13**, 140.
283. G. E. Myers, *Wood Sci.*, 1982, **15**, 127.
284. G. E. Myers, *Forest Prod. J.*, 1984, **34(5)**, 35.
285. G. E. Myers, *Forest Prod. J.*, 1983, **33(4)**, 49.
286. G. E. Myers, *Forest Prod. J.*, 1985, **35(6)**, 57; **35(9)**, 20.
287. G. E. Myers and J. A. Koutsky, *Forest Prod. J.*, 1987, **37(9)**, 56.
288. B. Meyer, B. A. K. Andrews and R. M. Reinhardt (eds), *Formaldehyde Release from Wood Products*, ACS Symposium Series No. 316, American Chemical Society, Washington, DC, 1986.
289. K. C. Frisch and L. P. Ruma, *J. Macromol. Sci. - Revs. Macromol. Chem.*, 1970, **C5**, 103.
290. V. E. Shashoua, *J. Am. Chem. Soc.*, 1959, **81**, 3156.
291. J. W. Britain and P. G. Gemeinhardt, *J. Appl. Polym. Sci.*, 1960, **4**, 207.
292. C. S. Schollenberger in *Handbook of Adhesives* (ed. I. Skeist), Van Nostrand Reinhold, New York, 1977.
293. M. E. Kimball, *Polym. News*, 1984, **9**, 198.
294. S. G. Abbott and N. Brumpton, *J. Adhesion*, 1981, **13**, 41.
295. J. H. Saunders and K. C. Frisch, *Polyurethanes: Chemistry and Technology*, Wiley Interscience, New York, 1962.
296. K. N. Edwards (ed.), *Urethane Chemistry and Applications*, American Chemical Society, Washington, DC, 1981.
297. R. Bonart, *J. Macromol. Sci. Phys.*, 1968, **2**, 115.
298. R. W. Seymour, G. M. Estes and S. L. Cooper, *Macromolecules*, 1970, **3**, 579.
299. R. Bonart, *Angew. Makromol. Chem.*, 1977, **58/59**, 259.
300. J. Blackwell and K. H. Gardner, *Polymer*, 1979, **20**, 13.
301. R. Bonart and E. H. Müller, *J. Macromol. Sci. Phys.*, 1974, **B10**, 177 and 345.
302. J. Blackwell and C. D. Lee, *J. Polym. Sci., Polym. Phys. Ed.*, 1983, **21**, 2169.
303. J. W. C. Van Bogart, P. E. Gibson and S. L. Cooper, *J. Polym. Sci., Polym. Phys. Ed.*, 1983, **21**, 65.
304. J. T. Koberstein and R. S. Stein, *J. Polym. Sci., Polym. Phys. Ed.*, 1983, **21**, 1439.
305. C. B. Wang and S. L. Cooper, *Macromolecules*, 1983, **16**, 775.
306. L. M. Leung and J. T. Koberstein, *J. Polym. Sci., Polym. Phys. Ed.*, 1985, **23**, 1883.
307. C. D. Eisenbach and W. Gronski, *Makromol. Chem., Rapid Commun.*, 1983, **4**, 707.

308. S. S. Sankar, S. V. Lonikar, R. D. Gilbert, R. E. Fornes and E. O. Stejskal, *J. Polym. Sci. Part B: Polym. Phys.*, 1990, **28**, 293.
309. A. Natansohn, M. Lacasse, D. Banu and D. Feldman, *J. Appl. Polym. Sci.*, 1990, 899.
310. P. Jackson and R. H. Carr, *Magn. Reson. Chem.*, 1991, **29**, 1061.
311. R. A. Assink, *J. Polym. Sci., Polym. Phys. Ed.*, 1977, **15**, 59.
312. R. A. Assink and G. L. Wilkes, *Polym. Eng. Sci.*, 1977, **17**, 606.
313. R. A. Assink, *Macromolecules*, 1978, **11**, 1233.
314. W. Nierzwicki, *J. Appl. Polym. Sci.*, 1984, **29**, 1203.
315. J. J. Dumais, L. W. Jelinski, L. M. Leung, I. Gancarz, A. Galambos and J. T. Koberstein, *Macromolecules*, 1985, **18**, 116.
316. D. S. Idiyatullin, V. S. Smirnov, M. P. Letunovskii and V. V. Strakhov, *Polym. Sci. USSR*, 1989, **31**, 813.
317. M. D. Meadows, C. P. Christenson, W. L. Howard, M. A. Harthcock, R. E. Guerra and R. B. Turner, *Macromolecules*, 1990, **23**, 2440.
318. L. C. Dickinson, J. Shi and J. C. W. Chien, *Macromolecules*, 1992, **25**, 1224.
319. J. Shi, L. C. Dickinson and J. C. W. Chien, *Macromolecules*, 1992, **25**, 3278.
320. W. Ku, J. Liang, K. Wei, H. Liu, C. Huang, S. Fang and W. Wu, *Macromolecules*, 1991, **24**, 4605.
321. T. P. Russell, D. S. Lee, T. Nishi and S. C. Kim, *Macromolecules*, 1993, **26**, 1922.
322. S. R. Sandler, *J. Appl. Polym. Sci.*, 1967, **11**, 811.
323. K. C. Frisch, K. J. Patel and R. D. Marsh, *J. Cell. Plast.*, 1970, **6**, 203.
324. H. E. Reymore, Jr, P. S. Carleton, R. A. Kolakowski and A. A. R. Sayigh, *J. Cell. Plast.*, 1975, **11**, 328.
325. C. L. Wang, D. Klempner and K. C. Frisch, *J. Appl. Polym. Sci.*, 1985, **30**, 4337.
326. Y. Imai, T. Hidai, T. Inukai and T. Nakanishi, *Cell. Polym.*, 1986, **5**, 13 and 25.
327. M. Barikani and C. Hepburn, *Cell. Polym.*, 1986, **5**, 169.
328. W. E. Johns, *J. Adhes.*, 1982, **15**, 59.
329. M. Shindo, *Polym. Mater. Sci. Eng.*, 1983, **49**, 169.
330. M. W. Ranney, *Isocyanates Manufacture*, Chemical Process Review No. 63, Noyes Data Corp., Park Ridge, New Jersey, 1972, p. 217.
331. R. G. Arnold, J. A. Nelson and J. Verbanc, *Chem. Rev.*, 1957, **57**, 47.
332. R. A. Assink, *J. Polym. Sci., Polym. Phys. Ed.*, 1977, **15**, 59.
333. R. A. Assink and G. I. Wilkes, *Polym. Eng. Sci.*, 1977, **17**, 606.
334. H. A. Resing, *Adv. Mol. Relaxation Processes*, 1972, **3**, 199.
335. P. S. Hubbard, *J. Chem. Phys.*, 1969, **51**, 1647.
336. M. F. Baud and P. S. Hubbard, *Phys. Rev.*, 1968, **170**, 384.
337. R. A. Assink, *Macromolecules*, 1978, **11**, 1233.
338. M. Goldman and L. Shen, *Phys. Rev.*, 1966, **144**, 321.
339. R. R. Lagasse, *J. Appl. Polym. Sci.*, 1977, **21**, 2489.
340. R. R. Lagasse, Sandia Laboratories Report SAND 77-0822.
341. T. L. Weeding, W. S. Veeman, H. Angad Gaur and W. G. B. Huysmans, *Macromolecules*, 1988, **21**, 2028.
342. T. L. Weeding, W. S. Veeman, L. W. Jenneskens, H. Angad Gaur, H. E. C. Schuurs and W. G. B. Huysmans, *Macromolecules*, 1989, **22**, 706.
343. T. P. Huijgen, H. Angad Gaur, T. L. Weeding, L. W. Jenneskens, H. E. C. Schuurs, W. G. B. Huysmans and W. S. Veeman, *Macromolecules*, 1990, **23**, 3063.
344. L. W. Jenneskens in *Interfacial Phenomena in Composite Materials '91* (eds I. Verpoest and F. Jones), Butterworth Heinemann, Oxford, 1991, pp. 11-16.
345. H. Ketels, L. van de Ven, A. Aerdt and G. van der Velden, *Polym. Commun.*, 1989, **30**, 80.
346. A. Okada, M. Kawasumi, I. Tajima, T. Kurauchi and O. Kamigaito, *J. Appl. Polym. Sci.*, 1989, **37**, 1363.

347. K. Kubo, T. Yamanobe, T. Komoto, I. Ando and T. Shiibashi, *J. Polym. Sci. Part B: Polym. Phys.*, 1989, **27**, 929.
348. K. Kubo, I. Ando, T. Shiibashi, T. Yamanobe and T. Komoto, *J. Polym. Sci. Part B: Polym. Phys.*, 1991, **29**, 57.
349. G. R. Hatfield, J. H. Glans and W. B. Hammond, *Macromolecules*, 1990, **23**, 1654.
350. L. J. Mathias and C. G. Johnson, *Macromolecules*, 1991, **24**, 6114.
351. L. J. Mathias, D. G. Powell and A. M. Sikes, *Polym. Commun.*, 1988, **29**, 192.
352. D. G. Powell, A. M. Sikes and L. J. Mathias, *Macromolecules*, 1988, **21**, 1533.
353. D. G. Powell and L. J. Mathias, *Macromolecules*, 1989, **22**, 3812.
354. L. J. Mathias, D. G. Powell, J.-P. Autran and R. S. Porter, *Mater. Sci. Eng.*, 1990, **A126**, 253.
355. L. J. Mathias, D. G. Powell, J.-P. Autran and R. S. Porter, *Macromolecules*, 1990, **23**, 963.
356. D. G. Powell and L. J. Mathias, *J. Am. Chem. Soc.*, 1990, **112**, 669.
357. D. G. Powell and L. J. Mathias, *Polym. Commun.*, 1990, **31**, 58.
358. J. J. Wendoloski, K. H. Gardner, J. Hirschinger, H. Miura and A. D. English, *Science*, 1990, **247**, 431.
359. C. A. Fyfe, L. H. Randall and N. E. Burlinson, *J. Polym. Sci. Part A: Polym. Chem.*, 1993, **31**, 159.
360. V. Malta, G. Cojazzi, A. Fichera, D. Ajo and R. Zannetti, *Eur. Polym. J.*, 1979, **15**, 765.
361. D. A. Torchia, *J. Magn. Reson.*, 1978, **30**, 613.
362. N. S. Murthy, M. Stamm, J. P. Sibilia and S. Krimm, *Macromolecules*, 1989, **22**, 1261.
363. H. Lee and K. Neville, *Handbook of Epoxy Resins*, McGraw-Hill, New York, 1967.
364. R. S. Bauer (ed.), *Epoxy Resin Chemistry*, ACS Symposium Series 114, American Chemical Society, Washington, DC, 1979.
365. R. S. Bauer (ed.), *Epoxy Resin Chemistry II*, ACS Symposium Series 221, American Chemical Society, Washington, DC, 1983.
366. C. A. Harper (ed.), *Handbook of Plastics, Elastomers, and Composites*, 2nd edn, McGraw Hill, New York, 1992.
367. N. Kinjo, M. Ogata, K. Nishi and A. Kaneda, *Adv. Polym. Sci.*, 1989, **88**, 1.
368. A. N. Garroway, W. B. Moniz and H. A. Resing, *Faraday Symp. Chem. Soc.*, 1978, **13**, 63.
369. A. N. Garroway, W. B. Moniz and H. A. Resing, *ACS Symp. Series*, 1979, **103**, 67.
370. R. K. Harris, K. J. Packer and B. J. Say, *Makromol. Chem. Suppl.*, 1981, **4**, 117.
371. G. E. Balimann, C. J. Groombridge, R. K. Harris, K. J. Packer, B. J. Say and S. F. Tanner, *Phil. Trans. Roy. Soc. Lond.*, 1981, **A299**, 643.
372. A. N. Garroway, W. M. Ritchey and W. B. Moniz, *Macromolecules*, 1982, **15**, 1051.
373. J. R. Havens and J. L. Koenig, *Appl. Spectrosc.*, 1983, **37**, 226.
374. E. A. Mertz and J. L. Koenig, *Adv. Polym. Sci.*, 1986, **75**, 73.
375. A. Cholli, W. M. Ritchey and J. L. Koenig, *ACS Symp. Series*, 1984, **243**, 233.
376. M.-F. Grenier-Loustalot and P. Grenier, *Eur. Polym. J.*, 1986, **22**, 457.
377. M.-F. Grenier-Loustalot, F. Cazaux, J. Berecoechea and P. Grenier, *Eur. Polym. J.*, 1986, **22**, 471.
378. A. A. Chalmers and P. Perlstein, *Eur. Polym. J.*, 1987, **23**, 887.
379. J. F. Haw and N. A. Johnson, *Anal. Chem.*, 1986, **58**, 3254.
380. E. A. Mertz, D. R. Perchak, W. M. Ritchey and J. L. Koenig, *Ind. Eng. Chem. Res.*, 1988, **27**, 586.
381. S. S. Sankar, S. V. Lonikar, R. D. Gilbert, R. E. Fornes and E. O. Stejskal, *J. Polym. Sci. Part B: Polym. Phys.*, 1990, **28**, 293.
382. A. J. Attias, B. Bloch and F. Laupretre, *J. Polym. Sci. Part A: Polym. Chem.*, 1990, **28**, 3445.
383. A. Udagawa, Y. Yamamoto, Y. Inoue and R. Chûjô, *Polymer*, 1991, **32**, 2947.

384. N. Egger, K. Schmidt-Rohr, B. Blümich, W.-D. Domke and B. Stapp, *J. Appl. Polym. Sci.*, 1992, **44**, 289.
385. F. Gallouedec, F. Costa-Torro, F. Laupretre and B. Jasse, *J. Appl. Polym. Sci.*, 1993, **47**, 823.
386. E. A. Mertz, D. R. Perchak, W. M. Ritchey and J. L. Koenig, *Ind. Eng. Chem. Res.*, 1988, **27**, 580.
387. S. V. Lonikar, N. Rungsimuntakul, R. D. Gilbert and R. E. Fornes, *J. Polym. Sci. Part A: Polym. Chem.*, 1990, **28**, 759.
388. L. W. Jelinski, J. J. Dumais and A. K. Engel, *Macromolecules*, 1983, **16**, 492.
389. A. L. Cholli, J. J. Dumais, A. K. Engel and L. W. Jelinski, *Macromolecules*, 1984, **17**, 2399.
390. L. W. Jelinski, F. C. Schilling and F. A. Bovey, *Macromolecules*, 1981, **14**, 581.
391. L. W. Jelinski, *Macromolecules*, 1981, **14**, 1341.
392. L. W. Jelinski, J. J. Dumais, F. C. Schilling and F. A. Bovey in *NMR Spectroscopy: New Methods and Applications*, ACS Symposium Series 191 (ed. G. C. Levy), American Chemical Society, Washington, DC, 1982, p. 345.
393. L. W. Jelinski, J. J. Dumais and A. K. Engel, *Macromolecules*, 1983, **16**, 403.
394. L. W. Jelinski, J. J. Dumais, P. I. Watnick, A. K. Engel and M. D. Sefcik, *Macromolecules*, 1983, **16**, 409.
395. L. W. Jelinski, J. J. Dumais and A. K. Engel, *Org. Coat. Appl. Polym. Sci. Proc.*, 1983, **248**, 102.
396. L. W. Jelinski, J. J. Dumais and A. K. Engel, *ACS Symp. Ser.*, 1984, **247**, 55.
397. F. A. Bovey and L. W. Jelinski, *J. Phys. Chem.*, 1985, **89**, 571.
398. L. W. Jelinski in *Developments in Block Copolymers—2* (ed. I. Goodman), Applied Science, London, 1986.
399. L. W. Jelinski in *High-Resolution NMR Spectroscopy of Synthetic Polymers in Bulk* (ed. R. A. Komoroski), VCH, Deerfield Beach, Florida, 1986, p. 335.
400. B. C. Perry, J. L. Koenig and J. B. Lando, *Macromolecules*, 1987, **20**, 422.
401. J. R. Garbow and J. Schaefer, *Macromolecules*, 1987, **20**, 819.
402. M. D. Sefcik, J. Schaefer, E. O. Stejskal and R. A. McKay, *Macromolecules*, 1980, **13**, 1132.
403. F. G. Morin and R. H. Marchessault, *Macromolecules*, 1992, **25**, 576.
404. R. E. Stark and J. R. Garbow, *Macromolecules*, 1992, **25**, 149.
405. F. Laupretre, C. Noël, W. N. Jenkins and G. Williams, *Faraday Discuss. Chem. Soc.*, 1985, **79**, 191.
406. C. A. Fyfe, B. J. Fahie, J. R. Lyster, J. Economy, N. Niessner, A. Mühlebach and G. A. Facey, *Macromolecules*, 1992, **25**, 1623.
407. A. Gérard, F. Laupretre and L. Monnerie, *Macromolecules*, 1993, **26**, 3313.
408. R. A. Allen and I. M. Ward, *Polymer*, 1991, **32**, 202.
409. C. A. Fyfe, J. R. Lyster, W. Volksen and C. S. Yannoni, *Macromolecules*, 1979, **12**, 757.
410. J. R. Havens and J. L. Koenig, *Polym. Commun.*, 1983, **24**, 194.
411. I. S. Davidson, A. J. Manuel and I. M. Ward, *Polymer*, 1983, **24**, 30.
412. M.-F. Grenier-Loustalot and G. Bocelli, *Eur. Polym. J.*, 1984, **20**, 957.
413. M. A. Gomez, M. H. Cozine and A. E. Tonelli, *Macromolecules*, 1988, **21**, 388.
414. R. P. Veregin, C. A. Fyfe and R. H. Marchessault, *Macromolecules*, 1986, **19**, 2379.
415. A. M. Ritchey and R. E. Prud'homme, *Macromolecules*, 1992, **25**, 972.
416. P. Bergmark and P. Flodin, *Polymer*, 1987, **28**, 1657.
417. W. Volksen, J. R. Lyster, J. Economy and B. Dawson, *J. Polym. Sci. Polym. Chem. Ed.*, 1983, **21**, 2249.
418. T. Uryu and T. Kato, *Chem. Lett.*, 1987, PP 211–214.
419. T. Uryu and T. Kato, *Macromolecules*, 1988, **21**, 378.
420. T. Kato, G. M. A. Kabir and T. Uryu, *J. Polym. Sci. Part A: Polym. Chem.*, 1989, **27**, 1447.

421. G. C. Rutledge and I. M. Ward, *J. Polym. Sci. Part B: Polym Phys.*, 1993, **31**, 513.
422. J. Schaefer, R. A. McKay, E. O. Stejskal and W. T. Dixon, *J. Magn. Reson.*, 1983, **52**, 123.
423. (a) J. Schaefer, M. D. Sefcik, E. O. Stejskal, R. A. McKay, W. T. Dixon and R. E. Cais, *Macromolecules*, 1984, **17**, 1107. (b) J. Schaefer, E. O. Stejskal, R. A. McKay and W. T. Dixon, *Macromolecules*, 1984, **17**, 1479.
424. B. C. Gerstein in *High-Resolution NMR Spectroscopy of Synthetic Polymers in Bulk* (ed. R. A. Komoroski), VCH, Deerfield Beach, Florida, 1986, p. 307.
425. G. W. Bogan, M. E. Lyssy, G. A. Monnerat and E. P. Woo, *SAMPE J.*, 1988, **24**, 19.
426. C. A. Fyfe, J. Niu, S. J. Rettig, N. E. Burlinson, C. M. Reidsema, D. W. Wang and M. Poliks, *Macromolecules*, 1992, **25**, 6289.
427. A. Bielecki, D. P. Burum, D. M. Rice and F. E. Karasz, *Macromolecules*, 1991, **24**, 4820.
428. S. Kaplan, *Macromolecules*, 1993, **26**, 1060.
429. T. P. Yang, E. M. Pearce, T. K. Kwei and N. L. Yang, *Macromolecules*, 1989, **22**, 1813.
430. I. Y. Slonim, S. G. Alekseyeva, B. M. Arshava, S. L. Pokrovskii and P. A. Okunev, *Polym. Sci. U.S.S.R.*, 1985, **27**, 1993.
431. P. G. Shukla, S. Sivaram and B. Mohanty, *Macromolecules*, 1992, **25**, 2746.
432. Z. Gao, A. Molnár, F. G. Morin and A. Eisenberg, *Macromolecules*, 1992, **25**, 6460.
433. L. A. Belfiore, *Polymer*, 1986, **27**, 80.
434. M. Linder, P. M. Henrichs, J. M. Hewitt and D. J. Massa, *J. Chem. Phys.*, 1985, **82**, 1585.
435. N. M. Szevereniy, M. J. Sullivan and G. E. Maciel, *J. Magn. Reson.*, 1982, **47**, 462.
436. P. Caravatti, J. A. Deli, G. Bodenhausen and R. R. Ernst, *J. Am. Chem. Soc.*, 1982, **104**, 5506.
437. P. M. Henrichs, J. Tribone, D. J. Massa and J. M. Hewitt, *Macromolecules*, 1988, **21**, 1282.
438. D. T. Okamoto, S. L. Cooper and T. W. Root, *Macromolecules*, 1992, **25**, 1068.
439. W.-H. Ku, J.-L. Liang, K.-T. Wei, H.-T. Liu, C.-S. Huang, S.-Y. Fang and W.-G. Wu, *Macromolecules*, 1991, **24**, 4605.
440. J. A. Happe, R. J. Morgan and C. M. Walkup, *Polymer*, 1985, **26**, 827.
441. K.-P. Hoh, H. Ishita and J. L. Koenig, *Polym. Compos.*, 1988, **9**, 151.
442. K.-P. Hoh, H. Ishita and J. L. Koenig, *Polym. Compos.*, 1990, **11**, 121.
443. K.-P. Hoh, H. Ishita and J. L. Koenig, *Polym. Compos.*, 1990, **11**, 192.
444. M.-F. Grenier-Loustalot and P. Grenier, *Polymer*, 1992, **33**, 1187.
445. P. Jackson, *J. Mater. Sci.*, 1992, **27**, 1302.
446. M.-F. Grenier-Loustalot and P. Grenier, *Eur. Polym. J.*, 1986, **22**, 457.

Applications of Labelling and Multidimensional NMR in the Characterization of Synthetic Polymers

GRAEME MOAD

*CSIRO, Division of Chemicals and Polymers, Private Bag 10, Clayton,
Victoria 3168, Australia*

1. Introduction	287
2. Chemical microstructure of polymer chains	288
2.1 Tacticity of homopolymers	288
2.2 Monomer sequence distribution in copolymers	293
3. Syntheses of labelled monomers	296
4. Detection and quantitation of polymer end-groups	297
4.1. Initiation mechanisms and chain end structures	303
4.2. Initiator breakdown, mechanisms for radical-radical reactions	307
4.3. Kinetics and efficiency of initiation	308
4.3.1. Comparison with non-NMR methods for ascertaining initiator efficiency	310
4.4. Relative reactivity of monomers in copolymerization	312
4.4.1. Comparison with non-NMR methods for measuring relative reactivities	315
4.5. Polymer properties	316
5. Syntheses of labelled initiators	318
Acknowledgements	318
Abbreviations	318
References	319

1. INTRODUCTION

The field of NMR and its application to synthetic polymers has advanced rapidly over the past few years with dramatic improvements in spectrometer technology and many exciting developments in the types of experiments that can be carried out.¹⁻⁶

The sensitivity of NMR signals to the environment of the observed atoms puts NMR methods amongst the most powerful for obtaining structural information on polymers. It is the method of choice for determining chain tacticity, monomer sequence distribution in copolymers, and chemical defect structures within or attached to polymer chains (defect structures are defined as those which differ from the normal repeat units). It is also one of

the most effective and informative methods for evaluating the kinetics and mechanism of the polymerization processes.

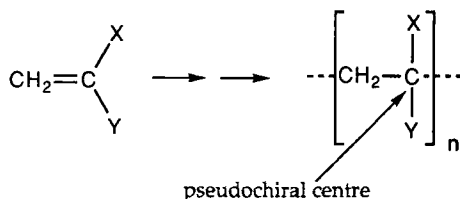
The aim of this review, a much shorter version of which appeared in *Chemistry in Australia*,⁷ is to demonstrate some of the recent developments in the application of high resolution 1D and 2D NMR to synthetic polymers formed by chain polymerization, paying particular attention to the advances made with the use of polymers prepared with specifically labelled initiators or monomers.

2. CHEMICAL MICROSTRUCTURE OF POLYMER CHAINS

The physical and mechanical properties of synthetic polymers formed by chain polymerization depend critically on the arrangement and relative configuration of monomer units within the chains. This section details how labelling and NMR can be applied to establish the chemical microstructure of polymers. As this area has already been dealt with in general terms by several recent reviews^{1,4-6} only two aspects are given detailed consideration in the present work. These are the tacticity of homopolymers (Section 2.1) and monomer sequence distribution of copolymers (Section 2.2) prepared from 1- or 1,1-disubstituted olefins.

2.1. Tacticity of homopolymers

Most common monomers, $\text{CH}_2=\text{CXY}$, are asymmetrically substituted (i.e. $\text{X} \neq \text{Y}$) and addition to their carbon-carbon double bond establishes a pseudo-chiral centre (Scheme 1).



Scheme 1

Possibilities for stereosequence isomerism therefore arise due to variations in the relative configuration of such centres along the polymer chain.^{5,8} The chains are said to have tacticity.

It should be stressed that in this discussion on polymer stereochemistry,

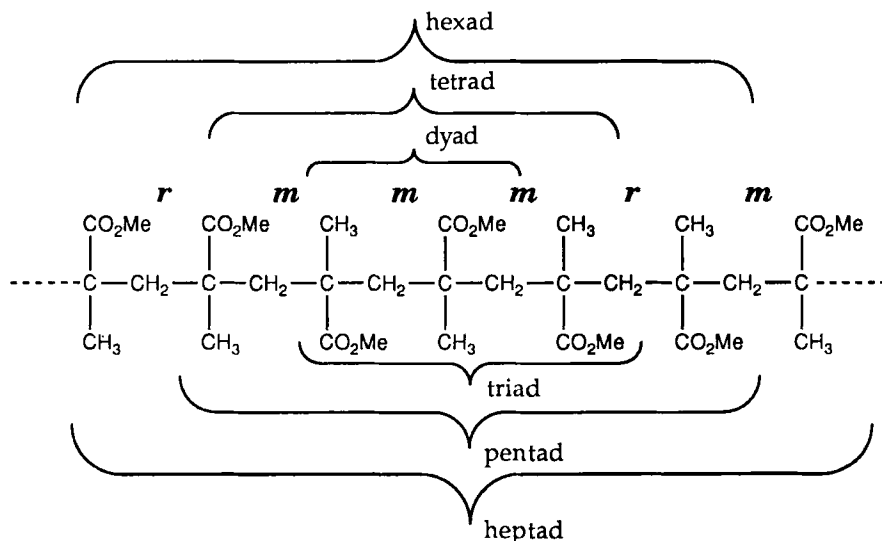


Fig. 1. Definition of terminology used to describe polymer stereochemistry.

only relative configurations are considered (i.e. whether a substituent is “up or down” with respect to that on a neighbouring unit—see Fig. 1). Therefore, the smallest structural unit with stereochemical information is the dyad. There are two types of dyad, meso (*m*), where the two chiral centres have like relative configuration, and racemic (*r*), where the centres have opposite relative configuration. Higher order ‘*n*-ads’ (triads, tetrads, etc. see Fig. 1) can be defined in terms of their component dyads.

There have been many studies on the NMR of polymers with the aim of ascertaining the tacticity of the polymers prepared under various conditions. One of the most widely studied polymers is PMMA. In the case of PMMA, the chemical shifts of certain protons⁹ and carbons¹⁰ within the chain are sensitive to their environment up to at least the hexad (–CH₂–) or heptad level (–CXY–) (cf. Fig. 1). The advantages of preparing polymers from precursors that are specifically enriched in ¹³C will be demonstrated by examining the NMR of PMMA prepared from MMA-carbonyl-¹³C—see Fig. 2.¹⁰

The first and most obvious benefit of using an isotopically labelled material is higher sensitivity. The natural abundance of ¹³C is only *c.* 1%. Thus, ¹³C-labelling can give up to two orders of magnitude increase in effective concentration with corresponding benefits in the signal to noise ratio for the enriched carbons. Other benefits follow:

1. Use of an enriched monomer allows NMR experiments to be performed on more dilute polymer solutions. Therefore, the problem of peak broadening due to excessive solution viscosity is reduced.

2. Since spectra can be obtained more quickly with labelled than with unlabelled materials, the opportunities for correctly optimizing the acquisition parameters for the NMR experiment are greatly enhanced.
3. The intensities of signals due to the remaining (i.e. unlabelled) carbons of the polymer are very weak by comparison to those of the enriched carbons. This means that narrow spectral widths selecting the area of interest can be employed without incurring the problems of spectrum foldover. High data point resolution can, therefore, be achieved without the need to resort to enormous data block sizes.

With few exceptions,¹¹ NMR studies on the tacticity of PMMA prepared by radical polymerization have concluded that the relative peak intensities in the ^{13}C or ^1H NMR spectra can be interpreted, within experimental error, by Bernoullian statistics for chain growth.⁸ That experimental error may, however, be sufficient to hide a significant departure from the Bernoullian model.

The spectrum shown in Fig. 2 was obtained on PMMA prepared from 10% enriched MMA-*carbonyl*- ^{13}C by radical polymerization at 60°C with benzene as solvent and AIBN as initiator.¹⁰ In this case a low enrichment level is desirable to avoid any line broadening that might arise due to coupling between the carbonyls of adjacent monomer units. The excellent signal to noise ratio obtained in Fig. 2 allowed a precise and reliable integration. The spectrum demonstrated that, for this polymer, a higher order model was necessary to explain the relative concentrations of the various tactic sequences displayed in the spectrum. A statistically significant correlation, found between measured and expected peak intensities, was obtained based on a first order Markov model for propagation.¹⁰ Recently a Japanese group have reached a similar conclusion.¹²⁻¹⁴

Signal assignment in NMR has often involved a purely statistical approach, where measured signal intensities were compared with those expected on the basis of a given polymerization mechanism.^{8,10,15} This approach was used in the above-mentioned study on PMMA tacticity.¹⁰ However, ambiguities in peak assignment can arise if:

1. There is uncertainty about the polymerization mechanism. It should also be noted that a fit of experimental data to a simple model does not invalidate more complex models. Ockham's Razor should not be applied in assigning polymerization mechanisms.¹⁶
2. There is imprecision in the absolute peak intensities, there are peaks of similar intensity in the spectrum, or signals are not completely resolved. In this context, a variety of factors can complicate quantitative measurements of the NMR of polymers. They include: inappropriate use of line shape fitting methods on incompletely resolved signals, impurities in the polymer or polymer end-groups,¹⁷ and badly designed

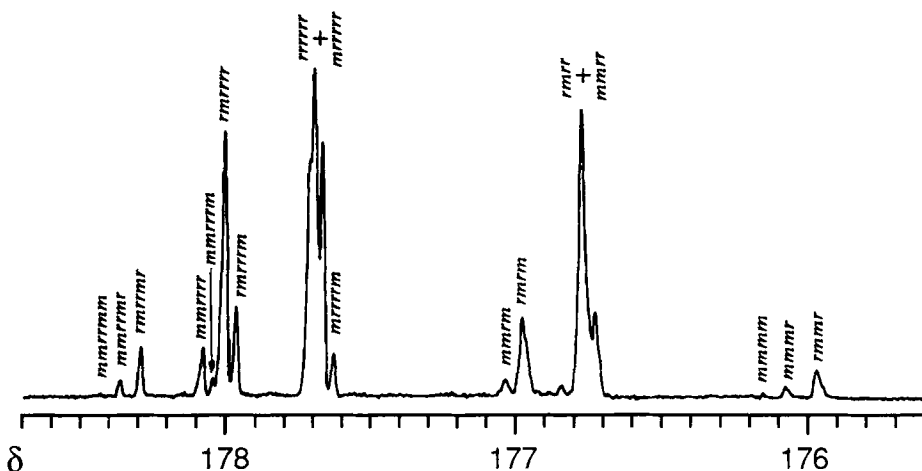


Fig. 2. Carbonyl region of the 62.9 MHz ^{13}C NMR spectra (toluene- d_8 , 297 K) of PMMA-carbonyl- ^{13}C .¹⁰

NMR experiments. A Japanese group has recently examined the effects of acquisition parameters, spectrometer frequency, and other factors on quantitation of NMR spectra of PMMA.¹²⁻¹⁴

The availability of appropriate model compounds or polymers of defined stereochemistry, and theoretical calculations can help assign resonances and resolve ambiguities in peak assignments in many cases.⁵ However, the required experimental effort associated with these approaches can be formidable.

2D NMR methods offer the opportunity of making unambiguous peak assignments on the basis of a single NMR experiment.^{9,18} Although 2D NMR techniques have been known for some time, and many applications to synthetic polymers have appeared,^{1,5,6, 19} applications to polymers involving less abundant nuclei (e.g. ^{13}C) have been limited by the considerable investment in NMR instrument time that is necessary for these experiments. ^{13}C - ^1H correlation spectroscopy has been applied to synthetic macromolecules^{20,21} and has been used to assign resonances to tactic sequences in the case of polyolefins,²²⁻²⁴ poly(vinyl alcohol) and derivatives,^{25,26} poly(vinylamine),²⁷ and poly(vinyl chloride).^{28,29} There have been fewer applications of long-range ^{13}C - ^1H correlation spectroscopy to macromolecules. These experiments have only recently been rendered practicable through the use of polymers specifically labelled with ^{13}C ¹⁸ or by the use of inverse detection methods (see below).

A contour plot from long range ^{13}C - ^1H heteronuclear correlation spectrum for PMMA-carbonyl- ^{13}C is shown in Fig. 3.¹⁸ The standard

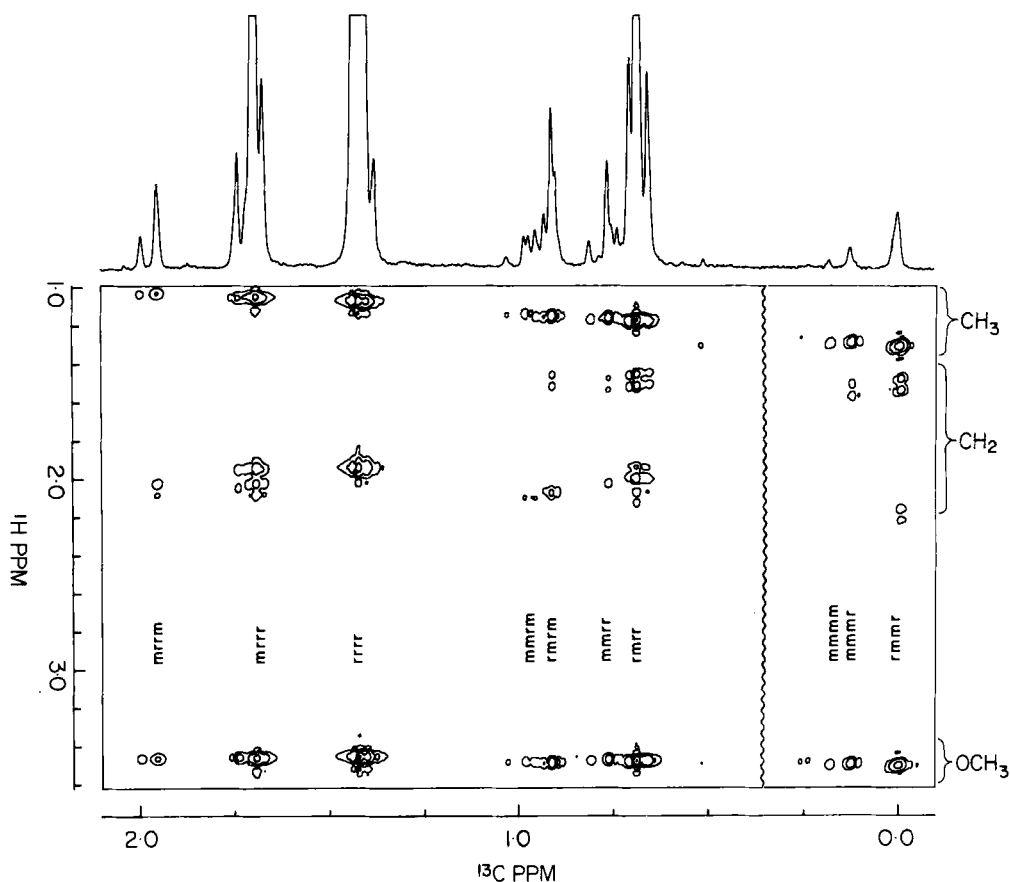


Fig. 3. Contour plot from the ^{13}C - ^1H heteronuclear correlated 2D NMR experiment (chlorobenzene- d_5 at 381 K) on 90% enriched PMMA-carbonyl- ^{13}C . The rightmost part of the spectrum has been displayed with an additional lower contour. The ^{13}C NMR axis is referenced with respect to the most upfield $^{13}\text{C}=\text{O}$ resonance.¹⁸

Freeman-Morris sequence was employed.³⁰ a number of other pulse sequences for long-range ^{13}C - ^1H correlation spectroscopy have been reported (e.g. COLOC, XCORFE)³⁰ which offer a number of advantages when applied to small molecules or oligomers. However, in selecting a sequence for a high molecular weight polymer sample, these advantages must be weighed against any increase in the duration of the pulse sequence and the consequent effect on the signal to noise ratio for the resonances of interest.

Nuclei in polymer chains possess much faster relaxation times (T_1 and T_2) than their low molecular weight analogues. For ^{13}C nuclei in polymer chains, relaxation times typically lie in the range 100 ms (most primary, secondary, and tertiary carbons) to 1 s (quaternary carbons). Thus, the

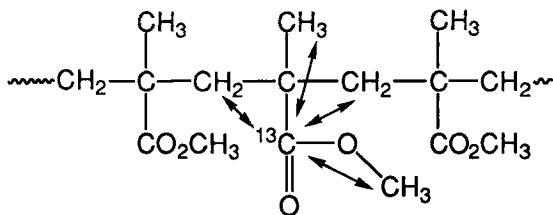


Fig. 4.

number of $1/2J$, $1/4J$ and other such delays in the pulse sequence (see above) must be kept to a minimum so as to maximize the signal to noise ratio. This is particularly important when coupling constants are small as is the case in long-range correlation spectroscopy (e.g. see below).

All protons in PMMA-*carbonyl*- ^{13}C are vicinal to a carbonyl and the magnitude of the 4-bond couplings is *c.* 10 Hz (Fig. 4).¹⁸ The precise magnitude of the vicinal couplings is subject to a Karplus relationship,³¹ and is thus dependent of conformation of the polymer molecule. The benefits of the correlation experiment is graphically illustrated in Fig. 5. By taking cross-sections through the carbonyl resonances parallel to the ^1H axis, ^1H NMR spectra of the coupled hydrogens are obtained. Since all protons in PMMA-*carbonyl*- ^{13}C are vicinal to a carbonyl, the experiment provides complete ^1H NMR spectra of the individual pentads which make up the PMMA sample. These spectra can be assigned to specific tactic sequences working from first principles without the need to make any assumptions. The analysis thus enables a completely unambiguous assignment of all the hydrogens and carbonyls in PMMA at the pentad level.¹⁸ Assignment of other carbons can then be made by correlating these with the carbonyl carbons.

Recently a new method for obtaining enhanced sensitivity in long-range ^{13}C - ^1H heteronuclear correlation spectroscopy has emerged. The work described above and in most literature examples of long range ^{13}C - ^1H correlation spectroscopy has involved ^{13}C detection. Bax and Summers³² demonstrated that considerable sensitivity enhancement could be obtained with "reverse detected" NMR. The ^1H nucleus is substantially more sensitive in NMR terms than the ^{13}C nucleus.³⁰

Proton-detected long-range ^{13}C - ^1H heteronuclear correlation spectroscopy has been successfully applied to provide absolute configurational assignments for the carbons and hydrogens of PMMA^{33,34} and PAMS.³³

2.2. Monomer sequence distribution in copolymers

The arrangement of monomer units in copolymer chains is determined by the copolymerization conditions, the inherent reactivity of the monomers

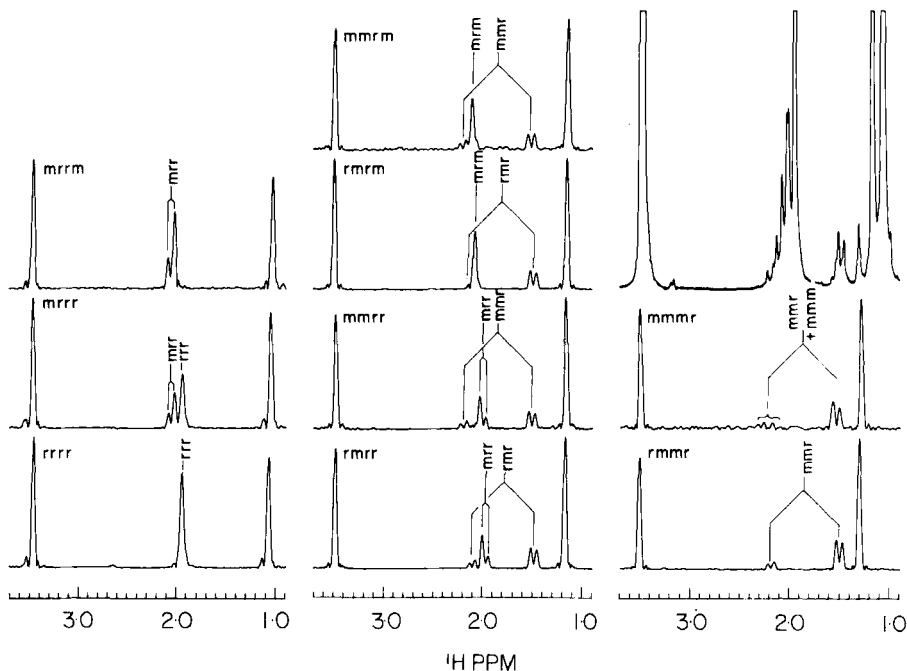


Fig. 5. Cross-sections taken from the 2D NMR spectrum of 90% enriched PMMA-carbonyl- ^{13}C parallel to the ^1H axis and passing through the most intense of the ^{13}C resonances within the region assigned to the indicated C=O pentad (cf. Fig. 3). The intensity of the spectrum due to the *mmmm* pentad was too small to be extracted from the 2D NMR spectrum (cf. Fig. 2). The amplitudes of the spectra have been normalized with respect to the largest peak in each spectrum.¹⁸ The ^1H NMR spectrum (chlorobenzene- d_5 381 K) of 10% enriched PMMA-carbonyl- ^{13}C is shown in the top right corner.

and their concentration. A knowledge of the monomer sequence distribution in copolymers is important both to provide information on the kinetics and mechanism of copolymerization and to understand the properties of the copolymers. NMR is usually the most effective and the most used technique for determination of monomer sequence distribution in copolymers.^{8,15}

The NMR chemical shifts of carbons in or adjacent to the polymer backbone are sensitive to the nature of the monomer units. It is generally assumed that chemical shift changes induced by monomer sequence are less than those induced by tactic sequence. However, as discussed below, this need not always be the case.

Problems often arise in assigning signals to monomer sequences due to the coincidence of signals. The usual experiment is to prepare a series of copolymers each containing a different ratio of the monomers. A correlation of expected and measured peak intensities may then enable peak

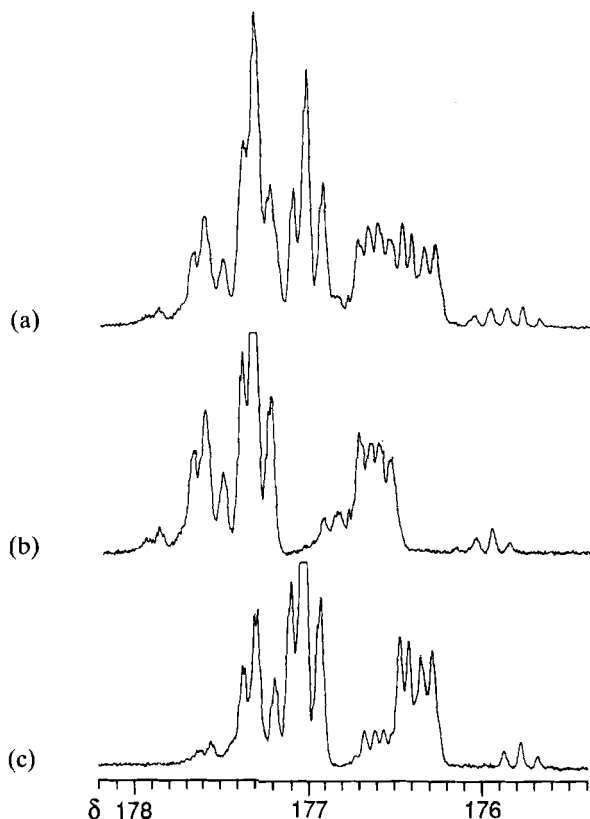
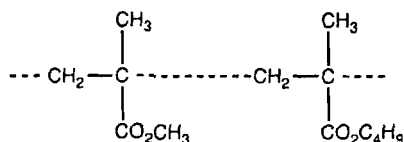


Fig. 6. Carbonyl region of the 62.9 MHz ^{13}C NMR spectra (chlorobenzene- d_5 , 373 K) of (a) P(BMA)-carbonyl- ^{13}C -co-MMA-carbonyl- ^{13}C ; (b) P(BMA-carbonyl- ^{13}C -co-MMA); and (c) P(BMA-co-MMA-carbonyl- ^{13}C).³⁹

assignment.^{35,36} The use of special pulse sequences may help resolve signals in special circumstances.³⁷ However, ambiguities in peak assignment may still remain. When there is no direct proof of the assignments, a new proposed mechanism or a spectrum with improved resolution can see reassignment of signals. Papers offering reassignment of signals are not uncommon in the polymer literature.³⁸

The benefits of employing a labelled monomer in the study of the NMR of copolymers are illustrated in Fig. 6a-c. The P(BMA-co-MMA) was prepared with the carbonyl of either or both monomer units 90% enriched in ^{13}C .³⁹



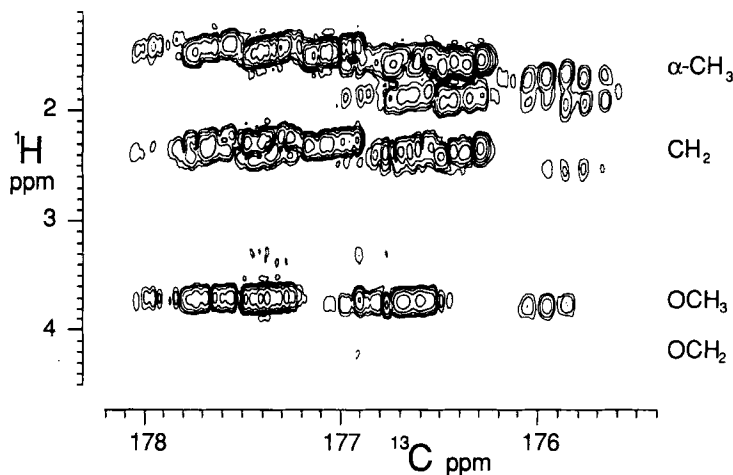


Fig. 7. Contour plot from the long range ^{13}C - ^1H correlation NMR (chlorobenzene- d_5 , 373 K) of P(BMA-carbonyl- ^{13}C -co-MMA-carbonyl- ^{13}C).³⁹

Figure 6a shows the relatively complicated spectrum of the copolymer in which both carbonyls are ^{13}C -labelled (a similar spectrum can be obtained, after significantly longer time, on an unenriched copolymer). Figure 6b and c shows the spectra of the copolymer in which only one of the monomers is labelled. This enables a quick assessment of what signals are due to which monomer residue and, furthermore, demonstrates that, for this copolymer, the chemical shifts are more sensitive to tacticity than they are to the monomer sequence distribution. The result indicates that previous assignments for this copolymer⁴⁰ are in error.

It is not necessary to make all three copolymers to demonstrate these assignments. Figure 7 shows the long range ^{13}C - ^1H correlation spectrum for the doubly labelled copolymer.³⁹ A cross-section through the methoxyl hydrogen region (3.6–3.9) affords a spectrum similar to Fig. 6b. Note that cross peaks due to the butyl $-\text{OCH}_2-$ are not seen in this spectrum. None the less, with a single copolymer and a single NMR experiment, those resonances attributable to MMA vs. BMA centred sequences can be unambiguously identified.

3. SYNTHESSES OF LABELLED MONOMERS

In deciding whether to embark on NMR experiments using labelled monomers, the synthetic work and initial expense incurred in the use of

labelled precursors should be balanced against the need to prepare more polymer samples and greater amount of NMR instrument time required to get the same information using unlabelled materials. Some of the experiments discussed above would not be possible with unlabelled materials.

The syntheses of many of the monomers commonly used in chain polymerizations that are specifically ^{13}C -labelled have been reported in the literature and are summarized in Table 1. For general guidance on the synthesis of ^{13}C -labelled compounds a number of texts can be consulted.^{41,42} It should also be noted that synthesis of carbon-14 labelled monomers can usually be readily adapted to the synthesis of the corresponding ^{13}C -labelled compounds.

4. DETECTION AND QUANTITATION OF POLYMER END-GROUPS

A quantitative determination of the polymer end-groups can give a wealth of information on the polymerization process used in its preparation. It provides a chemical probe of the detailed polymerization mechanism and can afford a greater understanding of polymer properties.

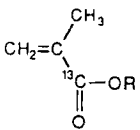
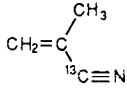
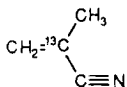
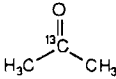
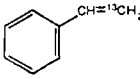
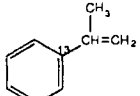
Various methods have been utilized for the determination of the polymer end-groups.⁵³⁻⁵⁵ These include chemical analysis, various forms of spectroscopy (UV, IR, NMR), pyrolysis- gas chromatography, and radioisotope labelling (some of these methods are mentioned in greater detail in the subsequent text). Methods for determination of initiator-derived ends can be divided into two categories: (a) those which involve direct determination of the polymer end-groups; and (b) those which involve use of an initiator which is specifically labelled to aid detection of derived end groups.

The sensitivity of modern NMR allows initiator residues and other minor defect structures to be determined directly in special cases where the desired signals are discrete from those due to the backbone carbons.⁵⁶⁻⁶⁰ However, the sensitivity and the dynamic range of the NMR instrument places limits on the molecular weight of the polymers that can be examined. For precise quantitation most work has been carried out on polymers with $M_n < 3000$.

In some cases it may be possible to suppress NMR signals due to backbone carbons or hydrogens, thus improving the visibility of end-group resonances and allowed obscured signals to be observed. This can be done through application of the following procedures:

1. by spectral subtraction. This method has the disadvantage that noise is added to the spectrum in the subtraction process and, moreover, may require (see also (4) below) preparation of an exactly similar polymer but without the defect structures being sought.^{61,62} Note that this method does not alleviate the dynamic range problem mentioned above.

Table 1. Syntheses of ^{13}C -enriched monomers.

Monomer	Enriched precursor	Overall yield (steps) ^a	Reference synthesis	Reference applications
 RMA-carbonyl- ^{13}C	$^{13}\text{CO}_2$	80% (2 steps) ^b	10	10,18,39
 MAN-nitrile- ^{13}C	K^{13}CN	42% (2 steps)	43	—
 MAN-2- ^{13}C		42% (2 steps)	43	—
ethene-1- ^{13}C	—	—	—	44-46
propene-1- ^{13}C	$^{13}\text{CH}_3\text{I}$	90% (2 steps)	47	47,48
propene-2- ^{13}C	—	—	—	48
propene-3- ^{13}C	$^{13}\text{CH}_3\text{I}$	~70% (1 step)	48	48
butene-3- ^{13}C	$\text{CH}_3^{13}\text{CH}_2\text{I}$	^c (1 step)	49	49
butene-4- ^{13}C	$^{13}\text{CH}_3\text{I}$	^c (1 step)	49	49
butadiene-1- ^{13}C	K^{13}CN	73% (3 steps)	43	—
butadiene-2- ^{13}C	$\text{CH}_3^{13}\text{CO}_2\text{H}$	20% (11 steps)	43	—
 S- β - ^{13}C	$^{13}\text{CO}_2$	15% (6 steps)	50	—
 AMS-1- ^{13}C	$\text{CH}_3^{13}\text{CO}_2\text{H}$	51% (8 steps)	43	51
<i>p</i> -DVB- $\alpha\alpha$ - $^{13}\text{C}_2$	$^{13}\text{CO}_2$	26% (7 steps)	52	52

^aYield based on enriched reagent (number of steps after use of the enriched reagent given in parentheses).

^bMethyl, ethyl and butyl esters have been prepared by this route in similar yields.

^cYield not explicitly stated.

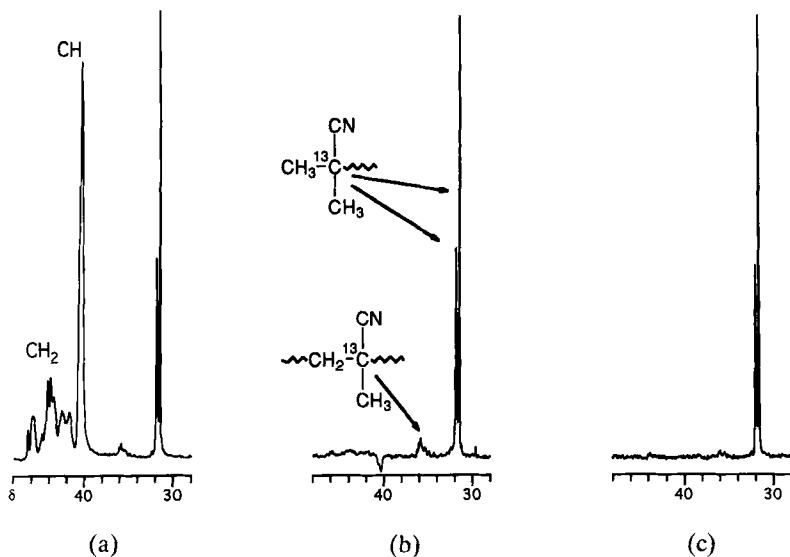


Fig. 8. Sections of the 62.9 MHz ^{13}C NMR spectra of PS (\bar{M}_n 48 000) prepared with AIBN- α - ^{13}C : (a) normal spectrum; (b) spectrum obtained using “quaternary only” sequence; (c) spectrum obtained using Hahn spin echo sequence.⁶⁴ The signals centred at δ 31 and 36 are assigned to the labelled carbons of the end groups (5) and copolymerized MAN respectively. The signals labelled CH and CH_2 are due to the methine and methylene hydrogens of the polystyrene backbone.

2. with the Hahn spin echo experiment. Johns *et al.*⁶³ and Moad *et al.*⁶⁴ demonstrated that end-group signals typically persist longer than backbone signals by virtue of their longer T_2 relaxation times (see Fig. 8c).
3. through the use of deuterium-enriched monomers. Kashiwagi *et al.*⁶⁵ have demonstrated how ^1H NMR can be used successfully to determine initiator-derived end-groups in polymers prepared from perdeuterated monomer. Similarly, the use of ^{12}C -enriched monomers has been envisaged as an aid in detecting end-groups in ^{13}C NMR experiments.⁶⁶
4. with the aid of pulse sequences that select for the number of attached hydrogens. For example, in PS prepared with AIBN a “quaternary only” pulse sequence⁶⁷ can be used to emphasize signals due to the quaternary carbons of the AIBN-derived residues (see Fig. 8b).⁶⁴ The non-aromatic repeat unit carbons in PS are methines or methylenes.
5. with 2D NMR methods. For example, ^{13}C - ^1H correlation spectroscopy might be used to advantage when ^{13}C signals are discrete yet ^1H signals are overlapping.⁶⁸

The above techniques all rely on suppressing signals due to the backbone carbons. In the case of the methods (2)–(3) above this will allow acquisition at higher spectrometer gain settings and help in overcoming spectrometer dynamic range problems. However, sensitivity problems associated with detecting end-groups in high molecular weight polymers are not entirely solved. It should also be noted that after applying some of these techniques, quantitation is not a straight-forward exercise.

Selective labelling of the initiator, on the other hand, provides substantial enhancement of the NMR signals due to the initiator residues. A number of stable isotopes have been employed in this context (including D, F, and ^{15}N); however, most work has involved use of ^{13}C -labelling. Many of the initiators that have been synthesized for this application are summarized in Section 5 and the polymerizations and copolymerizations that have been studied are summarized in Tables 2–4.

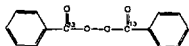
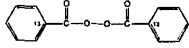
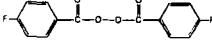
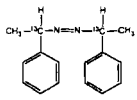
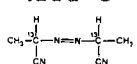
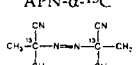
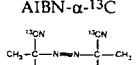
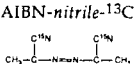
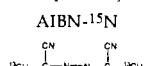
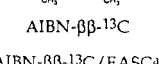
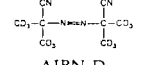
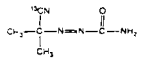
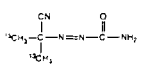
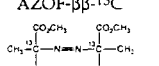
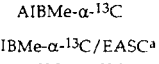
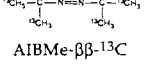
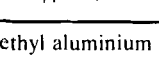
For precise quantitation of polymer end-groups, it is necessary to take many factors into account including all of those necessary for quantitation of any NMR spectrum. A number of parameters require particular attention.

The pulse delays used in the acquisition of the NMR spectrum must be chosen so as to be appropriate for the relaxation times of the end or other groups of interest. Particular attention must be paid to this when quantitative information on residual initiator, initiator-derived by-products, etc. is also required. Relaxation times (T_1 and T_2) for these low molecular weight compounds are usually substantially longer than those for the polymer end-groups. For example, in benzene- d_6 at 30°C , the labelled carbons in the products formed during polymerization of **5** initiated by AIBN- α - ^{13}C (see Scheme 2) have T_1 relaxation times ranging from *c.* 120 s (low molecular weight by-products—**2**, **3**) to *c.* 5 s (cyanoisopropyl end-groups **5**, $M_n = 48\,000$).⁶⁹ Note that the relaxation times of the end-groups are dependent on the molecular weight of the polymer (a pentamer has $T_1 \sim 9$ s) and yet are still very much greater than those of the PS backbone carbons ($T_1 < 1$ s) or of quaternary carbon of the MAN unit in P(MAN-*co*-**5**) ($T_1 \sim 1.5$ s).⁶⁴

In any quantitative work, it is also important that the NOE factors for the resonances of interest should either be removed (by inverse gated decoupling) or be accurately known and allowed for. Usually the latter strategy is employed since, even when labelled initiators are used, it is usually imperative to maximize signal-to-noise for the end-group resonances. It is noteworthy that the quaternary carbons of the cyanoisopropyl end-groups in PS (**5**), even though they have no directly attached hydrogens, experience a 2.7-fold NOE.⁶⁹ This is similar to that reported for the methyl carbons.⁶⁶

In the following sections the various experiments that can be carried out based on analysis of polymer end-groups using NMR and isotopically labelled initiators are discussed and compared critically with other methods for obtaining similar information. The NMR method has provided a means

Table 2. Radical polymerizations studied with labelled initiators.

Initiator	Polymer
 BPO-carbonyl- ¹³ C	S, ⁷¹ MMA, ⁷² MMA-co-S, ⁷² other ⁷³⁻⁸²
 BPO-α- ¹³ C	S, ⁸³ MMA ⁸⁴
 BPO-F	MMA-co-S, ⁸⁵ other ⁸⁶
 APE-α- ¹³ C	MA, ⁶¹ MMA, ⁶¹ MPK, ⁶¹ VAc, ⁶¹ AN-co-S, ⁸⁷ other ^{88,89}
 APN-α- ¹³ C	AN-co-S ⁹⁰
 AIBN-α- ¹³ C	MMA, ⁹¹ S, ^{64,69,91} VAc, ⁹¹ MMA-co-S, ^{54,91} MMA-co-VAc ⁹¹
 AIBN-nitrile- ¹³ C	VAc, ⁹² VF ⁹²
 AIBN- ¹⁵ N	MMA-co-S, ⁹³ other ⁹⁴
 AIBN-β- ¹³ C	AMS, ⁹⁵ EA, ⁹⁶ MMA, ^{97,98} MAN, ⁹⁷ S, ^{97,98} VC, ⁹⁹ VP, ⁷⁷ AN-co-MMA, ¹⁰⁰ EA-co-S, ⁹⁶ MAN-co-S, ⁹⁷ MMA-MPK, ¹⁰¹ MMA-MVK, ¹⁰¹ MMA-co-S, ⁹⁷ MMA-co-VC, ⁹⁹ S-co-VC, ⁹⁹ other ^{77,89,102,103}
 AIBN-β- ¹³ C/EASC ^a	MMA-co-S ¹⁰⁴
 AIBN-D	EA, ⁹⁶ EA-co-S, ⁹⁶ MMA-co-S ⁹³
 AZOF-nitrile- ¹³ C	VAc ⁹²
 AZOF-β- ¹³ C	MMA-co-S, ¹⁰⁵ MAN-co-S, ¹⁰⁶ S-co-VAc ¹⁰⁶
 AIBMe-α- ¹³ C	MMA, ⁹¹ S, ⁹¹ VAc, ⁹¹ MMA-co-S, ^{91,107,108} MMA-co-VAc ⁹¹
 AIBMe-α- ¹³ C/EASC ^a	MMA-co-S ¹⁰⁸
 AIBMe-β- ¹³ C	AN, ¹⁰⁹ MA, ¹⁰⁹ MMA, ¹⁰⁹ S, ¹⁰⁹ MMA-co-S ¹⁰⁴
 AIBMe-β- ¹³ C/EASC ^a	MMA-co-S ¹⁰⁴

^aEASC = ethyl aluminium sesquichloride.

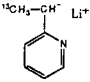
Table 3. Co-ordination polymerizations studied with labelled initiators.

Initiator	Polymer
$\delta\text{TiCl}_3\text{-Al}(^{13}\text{CH}_3)_3\text{-Zn}(^{13}\text{CH}_3)_2$	$\text{S},^{110} \text{VCH},^{110} \text{P},^{111,112} \text{E-co-P}^{113}$
$\delta\text{TiCl}_3\text{-Al}(^{13}\text{CH}_3)_2\text{I}$	P^{114}
$\delta\text{TiCl}_3\text{-Al}(^{13}\text{CH}_3)_2\text{Cl}$	P^{111}
$\delta\text{TiCl}_3\text{-Al}(^{13}\text{C}_2\text{H}_5)_3\text{-Zn}(^{13}\text{C}_2\text{H}_5)_2$	$\text{P}^{111,112}$
$\delta\text{TiCl}_4\text{-MgCl}_2\text{-ethyl benzoate-}$ $\text{Al}(^{13}\text{C}_2\text{H}_5)_3\text{-Zn}(^{13}\text{C}_2\text{H}_5)_2$	P^{111}
$[\text{Al}(^{13}\text{CH}_3)_3, \text{Al}(^{13}\text{CH}_2\text{CH}_3)_3]^a$	$\text{P},^{115} \text{B}^{115}$
$[\text{Al}(^{13}\text{CH}_3)_3, \text{Al}(^{13}\text{CH}_2\text{CH}_3)_3]^b$	$\text{P},^{116} \text{B}^{116}$

^aHomogeneous catalyst system: bis(cyclopentadienyl)titanium diphenyl/methyl alumoxane/trialkyl aluminium.

^bHomogeneous catalyst system: ethylenediindenyl dimethyltitanium/methyl alumoxane/trialkyl aluminium.

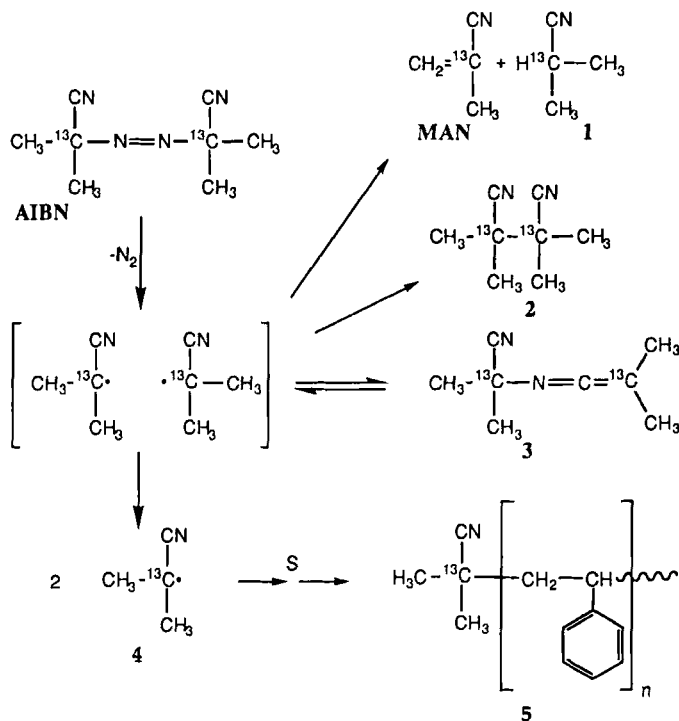
Table 4. Anionic polymerizations studied with labelled initiators and/or terminators

Initiator ^a	Terminator	Polymer
	CH_3OH	$2\text{-VP},^{117,118} 4\text{-VP},^{118}$ $\text{isopropenylpyridine}^{118}$
R^-M^+ R^-M^+	$^{13}\text{CH}_3\text{I}$ $^{13}\text{CH}_3\text{I}$	$2\text{-VP},^{b,117,119} \text{isopropenylpyridine}^{c,120}$ $\text{MMA},^{d,121,e122}$

^aInitiator has structure analogous to monomer structure (structure used with 2-VP shown).

^bM = Li, Na, K, Rb. ^cM = Li, K, Cs. ^dM = Li, Na. ^eM = Li, Cs.

of examining the mechanism of the initiation process and determining the nature and stereochemistry of the polymer end-groups (see Section 4.1), for establishing the rate and efficiency of initiation (see Section 4.3), for measuring rate constants for initiator breakdown and determining the mechanisms for radical-radical reactions (see Section 4.2), for evaluating the relative reactivity of monomers towards initiator-derived radicals (many initiator-derived radicals can be viewed as model propagating species—see Section 4.4), and for establishing polymer structure-property relationships (see Section 4.5). Several reviews have appeared on the use of labelled initiators and on NMR as a means of detecting polymer end-groups.^{7,60,66,70} This review will, for the most part, concentrate on areas not covered by those works.



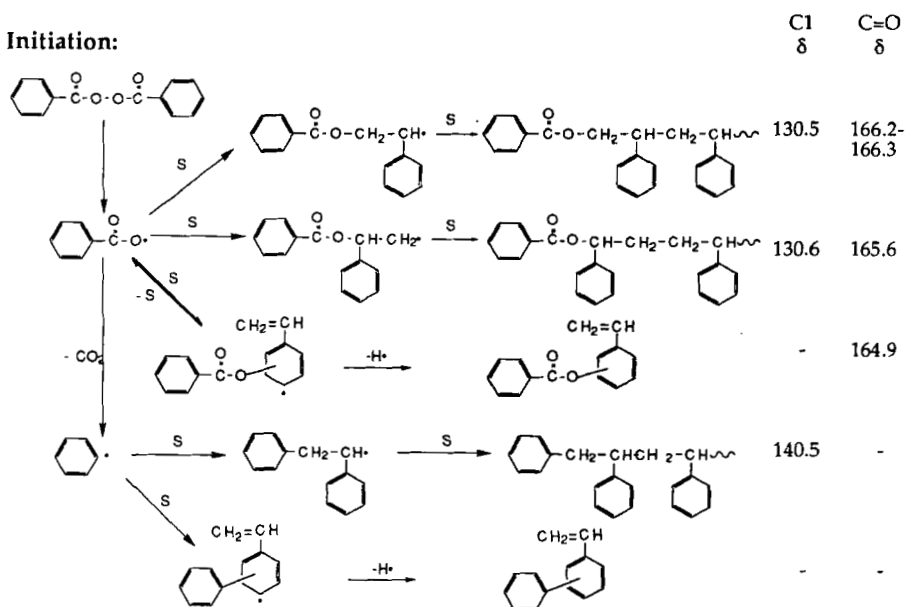
Scheme 2

4.1. Initiation mechanisms and chain end structures

One of the main reasons for conducting experiments on polymer end-group determination is to unravel the details of the initiation mechanism and establish the nature of the chain ends. Most work has been carried out on polymers formed by radical polymerization (see Table 2) though studies on co-ordination (Table 3) and anionic polymerization (Table 4) have also appeared.

The main advantage of NMR methods over alternative techniques for initiator residue detection is that NMR signals are extremely sensitive to the structural environment of the initiator residue. For example, it was demonstrated for polymerizations initiated by BPO-carbonyl- ^{13}C that it was possible to distinguish the carbonyl resonances in primary, secondary, tertiary and aromatic benzoate groups (see Figs 9, 10a). Furthermore, the carbonyls of various secondary benzoates formed by head addition and transfer to initiator or primary radical termination also give rise to discrete signals in the ^{13}C NMR spectrum.⁷¹ These chain ends were unambiguously identified on the basis of the NMR chemical shifts of model compounds and

Initiation:



Transfer to Initiator/Primary Radical Termination:

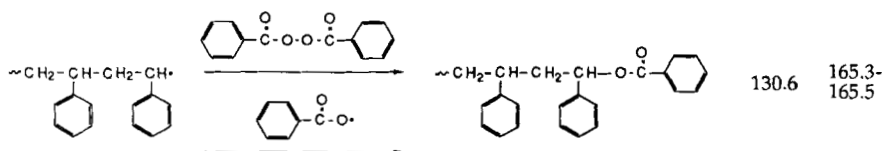


Fig. 9. Origin and ^{13}C chemical shifts of the benzyloxy end-group aromatic C1⁸³ and C=O⁷¹ carbons in PS prepared with BPO.

the dependence of their relative concentrations of the various chain ends on the polymerization conditions. The chemical shifts of the end-groups are also distinct from the initiator and a potential initiator by-product, benzoic acid.

The end-group signals are often also sensitive to the presence and stereochemistry of the more remote monomer units.⁶⁶ The chemical shifts of the labelled carbons of the end-groups in PS prepared with AIBN- α - ^{13}C (6) are dependent on the presence and configuration of carbons eight or more monomer units removed from the end-group (Fig. 11).⁶⁴ Assignments of resonances to specific configurational sequences have not been made at this stage.

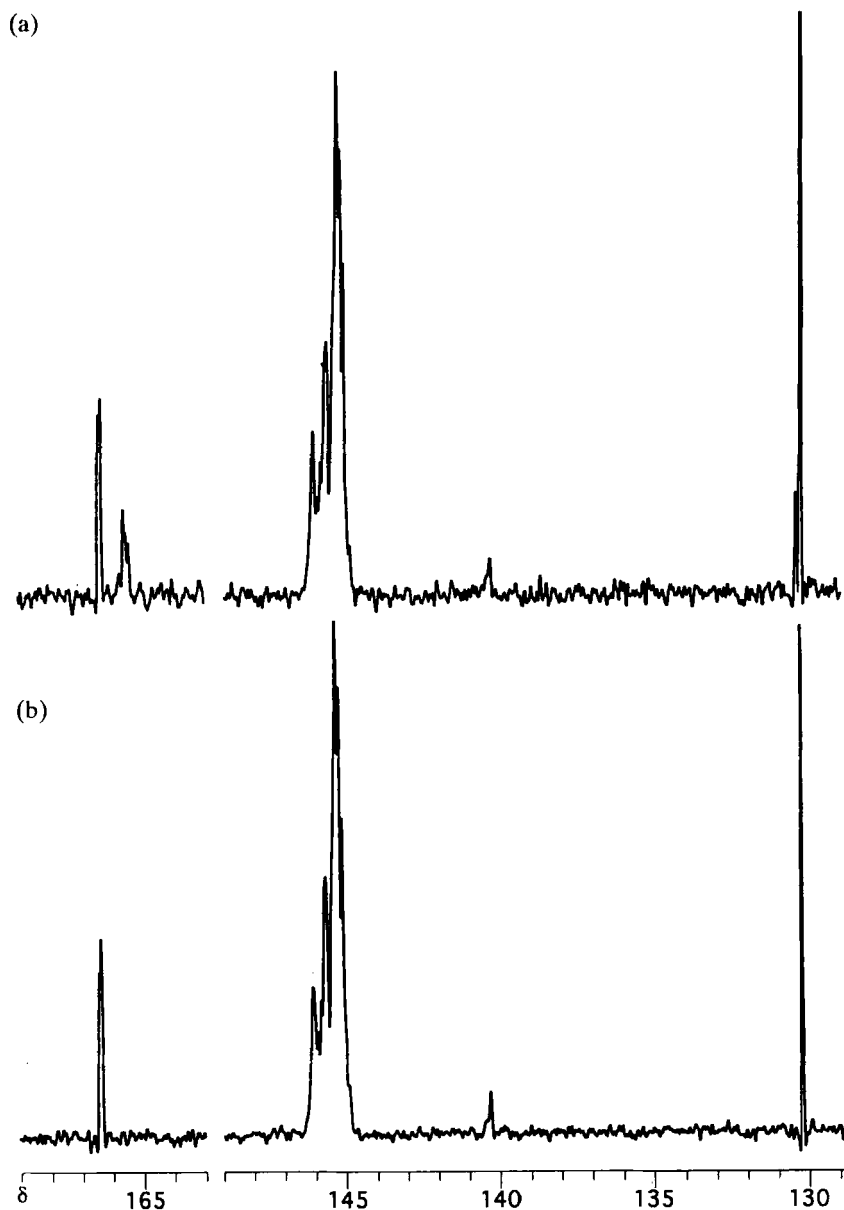


Fig. 10. Sections of the 62.9 MHz ^{13}C NMR spectrum of PS prepared with a 1:1 mixture of BPO-*carbonyl*- ^{13}C and BPO- α - ^{13}C (a) as prepared, (b) after heating at 300°C for 4 h under nitrogen.⁸³ Signal assignments for initiator fragments are given in Fig. 9. The envelope at δ 145 is due to the PS aromatic C1 carbon.

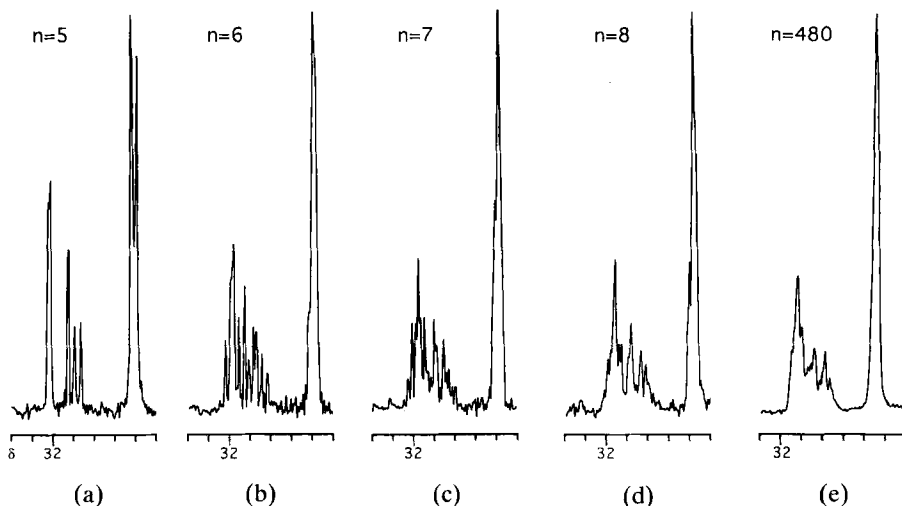
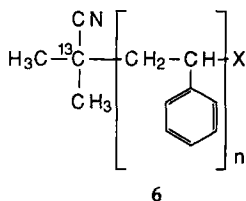


Fig. 11. Section of the 62.9 MHz ^{13}C NMR spectrum of oligostyrenes **6** ($n = 5-8$, $\text{X}=\text{Cl}$) and PS prepared with AIBN- α - ^{13}C as initiator.⁶⁴

In other cases, the NMR spectra of the chain ends of polymers have been successfully deconvoluted to establish the stereospecificity of the initiation process and, by inference, mechanisms for stereoregulation in propagation and their dependence on initiator and reaction conditions.^{66,110-118,122} There has been greater success in identifying the chain end stereochemistry in anionic^{117, 118, 122} and co-ordination polymerizations.¹¹⁰⁻¹¹⁶ This can be attributed to these polymerizations showing generally greater chemo- and stereospecificity.

The absolute concentration of the initiator-derived end-groups can be estimated by integration of the end-group signals relative to backbone signals and comparing this with the number average molecular weight of polymer.^{64,66,71} This information can be used *either* to confirm that all end-groups can be seen or, if this is known to be the case, it can be used to infer the mechanism of termination. Given spectra of good signal to noise (usually readily obtainable for polymers of molecular weight $<100\,000$ and assuming other criteria (see above) for successful quantitation are met, the



precision of this form of quantitative end-group determination is limited mainly by the accuracy of molecular weight measurement.

4.2. Initiator breakdown, mechanisms for radical-radical reactions

Studies on the thermal or photochemical decomposition of ^{13}C -labelled initiators have provided rate constants and mechanisms for initiator decomposition and have also allowed a detailed examination of the reactions of the initiator-derived radicals. In that the latter may often be simple models for the propagating species in radical polymerization, a knowledge of their behaviour can provide an insight into the mechanisms of chains termination processes. The decompositions of $\text{AIBN-}\alpha\text{-}^{13}\text{C}^{69,123}$ and $\text{AIBMe-}\alpha\text{-}^{13}\text{C}^{84}$ have been studied with these objectives in mind. Rate constants for initiator disappearance (k_d) measured by the NMR technique generally agree with those obtained by other methods.

The principle advantage of this NMR method over most other methods for following initiator decomposition is that it simultaneously provides detailed information on product formation without need for isolation or chromatography of those products. This is a particularly important consideration when the products of initiator decomposition are themselves labile.¹²³ This is true of the ketenimines **3** and **7** which are formed when AIBN is decomposed in benzene. The mechanism for AIBN decomposition is shown in Scheme 3 (refer also Scheme 2). The labelled carbons of $\text{AIBN-}\alpha\text{-}^{13}\text{C}$ and all of its major decomposition products, **2**, **3**, **7**, **9** and **MAN**, have discrete and characteristic chemical shifts thus allowing ready quantitation (see Fig. 12).

The use of labelled initiators also allows a variety of other experiments:¹²³

1. If a 1:1 mixture of the doubly labelled $\text{AIBN-}\alpha\text{-}^{13}\text{C}$ and unlabelled AIBN is used, then amount of products (e.g. **2** and **3**) formed by cage vs. encounter reaction can be determined by examining their labelling pattern. The products (**2** and **3**) formed by cage recombination will have the same labelling pattern as the initiator from which they are derived (i.e. labelled **4** can only react with labelled **4**). On the other hand, in the encounter process, **4** formed by $\text{AIBN-}\alpha\text{-}^{13}\text{C}$ has an equal likelihood of combining with **4** from the unlabelled initiator.
2. Quantitation of the oligomeric products enables absolute rate constants for the first few propagation steps to be determined.
3. The mechanisms whereby the various radical species react can be established.
4. The ratio of combination and disproportionation for initiator-derived and oligomeric radicals can be measured.

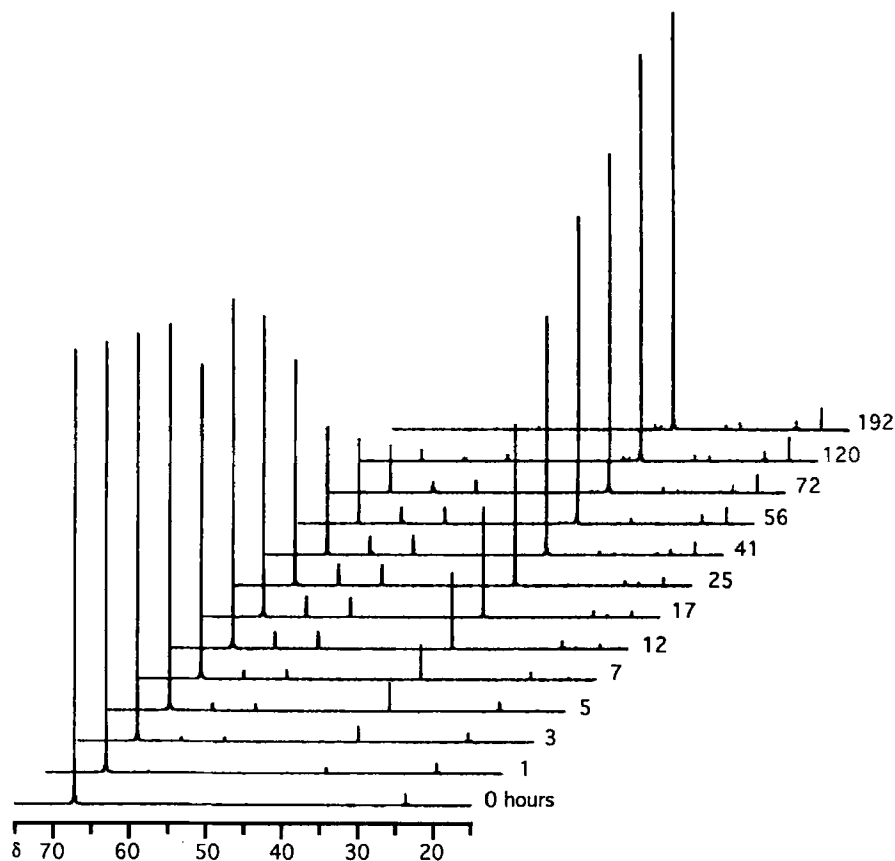


Fig. 12. Sections of the 62.9 MHz the ^{13}C NMR spectra of a 1:1 mixture of AIBN- α - ^{13}C and AIBN after heating at 60°C for the times indicated. Signal assigned to the labelled carbons of AIBN, 1, 2, and 3 are indicated on the spectrum. Other signals are attributable to labelled carbons of 7 (δ 55.7, 61.3 and 30.7) and 9 (δ 40.3, 39.3, 28.7), and the methyls of AIBN (δ 23.6) and 2 (δ 21.7).¹²³

4.3. Kinetics and efficiency of initiation

A further use of ^{13}C -labelled initiators is in assessing the kinetics and efficiency of initiation.^{54,69,107} This application requires that the polymer end-groups, residual initiator, and various initiator-derived by-products should each give rise to discrete signals in the NMR spectrum. This has been demonstrated for homo- and copolymerizations of S and MMA prepared with AIBN- α - ^{13}C , AIBMe- α - ^{13}C , or BPO-carbonyl- ^{13}C as initiator.

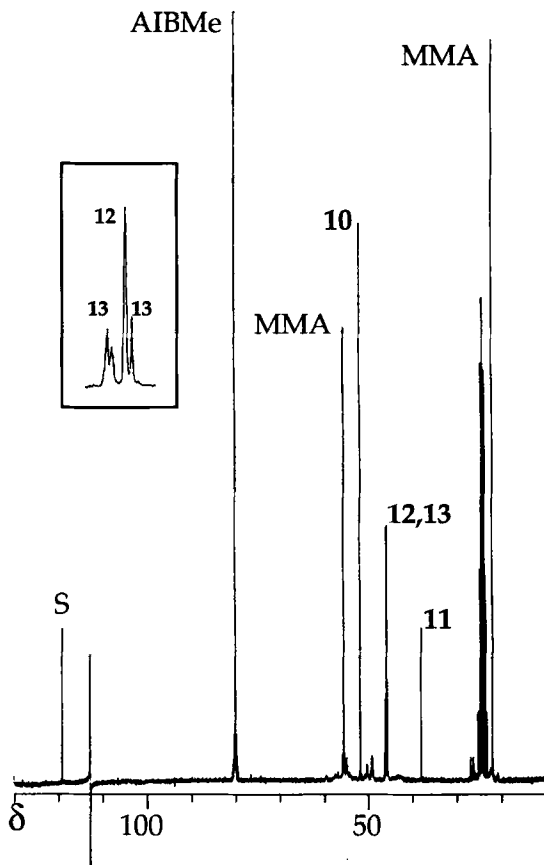
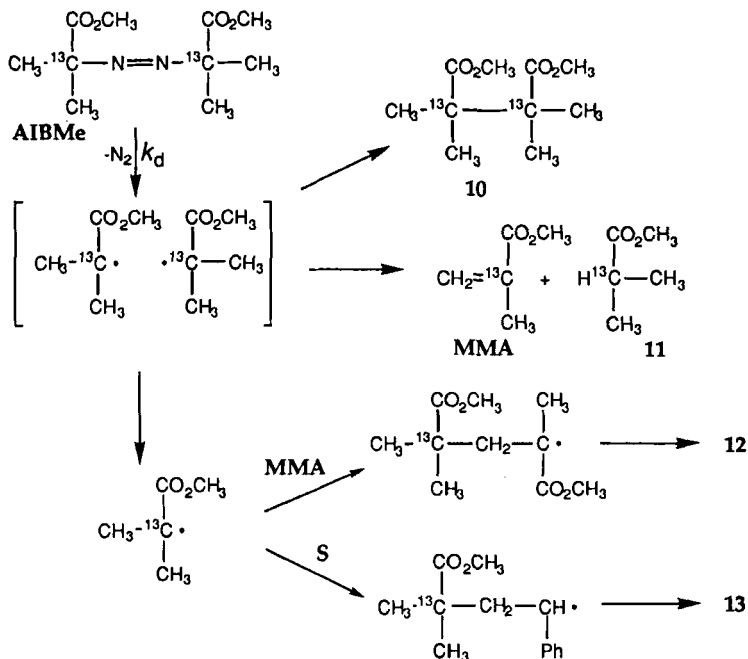


Fig. 13. Sections of the 62.9 MHz ^{13}C NMR spectrum of copolymerization reaction mixture prepared in toluene- d_8 solvent with AIBMe- α - ^{13}C as initiator after 14 h at 60°C. Assignments of major peaks are indicated on the spectrum. Signal at 27.5 ppm is due to the methyl of toluene- d_8 . Small unlabelled signals are due to P(MMA-co-S). The inset shows an expansion of the portion of the spectrum containing signals due to the polymer end groups (12, 13). The large central peak is attributed to labelled carbons of the end groups 12 formed by addition to MMA. The remaining signals are attributable to 13 formed by addition to styrene (cf. Scheme 4).¹⁰⁷

4.3.1. Comparison with non-NMR methods for ascertaining initiator efficiency

Various other methods have been applied to measure initiator efficiency.^{124,125} Perhaps the most common method for determining initiator efficiency in radical polymerization is the inhibitor method.¹²⁶ In this case a radical scavenger is added to a polymerization reaction mixture to determine



Scheme 4

the number of initiating radicals that would otherwise have initiated radical polymerization. The method has the disadvantage that it can only be readily applied at zero conversion.

If radioisotope-labelled initiators are employed for polymerization, the polymer may be isolated and analysed to determine the concentration of end-groups in the polymer sample and the initiator efficiency calculated.^{127,128} While offering greater sensitivity than other methods, the technique has the disadvantage that end-groups formed by initiation cannot be distinguished from those formed by other processes or from residual initiator. The method gives the total initiator residues in the polymer. Other processes leading to end-group formation include transfer to initiator, primary radical termination and copolymerization of initiator byproducts (see above). Analysis of the kinetics of polymerization can help resolve these problems. A further disadvantage is that polymer isolation and purification is required.

UV^{129,130} and IR spectroscopy¹³¹ have been used to study the kinetics and efficiency of initiation of polymerization. The IR method¹³¹ is in many ways analogous to that of the NMR method. No labelling is required. However, the end-group must contain a chromophore that absorbs a clear region of

the IR or near IR spectrum and must be sufficiently sensitive to its environment that end-groups can be distinguished from residual initiator, etc.

It is also possible to infer the initiator efficiency from an analysis of polymerization kinetics.¹³² With this method uncertainties are introduced along with the assumptions that are required to analyse the polymerization kinetics.

4.4. Relative reactivity of monomers in copolymerization

The use of labelled initiators to evaluate the relative reactivity of monomers towards radicals was pioneered by Bevington *et al.*⁹⁷ There have since been many applications of this technique. The method involves determination of the relative concentrations of the end-groups formed by addition to two monomers (e.g. **14** and **15**) in a binary copolymer formed with use of a labelled initiator (cf. Scheme 5). For example, when AIBMe- α - ^{13}C is used to initiate copolymerization of MMA and VAc (see Fig. 14),⁹¹ the following simple relationship (Eq. (1)) gives the relative rate constants for addition to the two monomers.

$$\frac{k_{\text{MMA}}}{k_{\text{VAc}}} = \frac{[\text{VAc}] \cdot [\text{14}]}{[\text{MMA}] \cdot [\text{15}]} \quad (1)$$

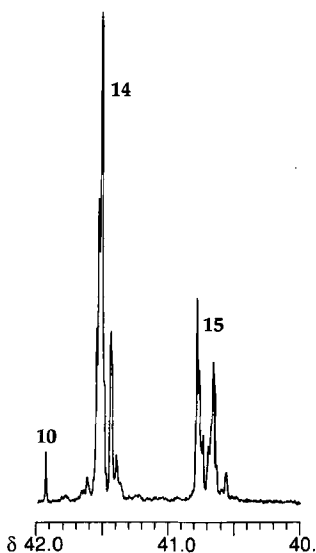
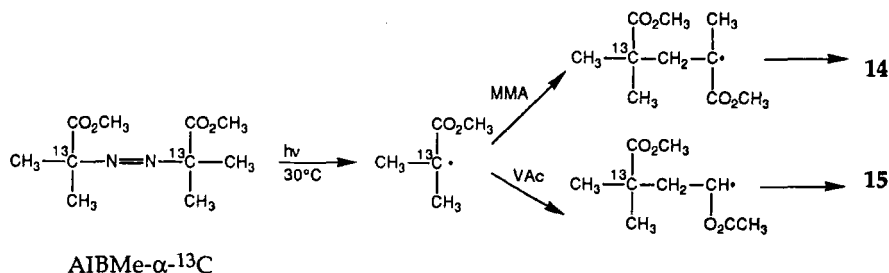


Fig. 14. Section of the 62.9 MHz ^{13}C NMR spectrum of MMA-VAc copolymer prepared in benzene solvent with AIBM- α - ^{13}C as the initiator. Signals are assigned to the labelled carbons of **10**, **14**, and **15**.



Scheme 5

However, a number of cautions need to be taken into consideration when applying this technique:

1. The end-groups formed by primary radical termination, transfer to initiator, etc. must be resolved from those formed by addition to monomer or it must be proven (or assumed) that these reactions do not occur.
2. The simple expression (Eq (1)) is valid only for polymerizations carried out at low (effectively zero) conversion. Kinetic modelling can be used to allow for the effects of conversion.
3. The relative reactivity of radicals towards monomer may be dependent on the reaction medium.⁹¹

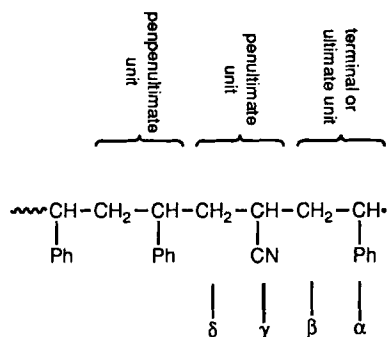
There are several driving forces for accumulating this information. Perhaps the most important is to enable the prediction of polymerization kinetics and polymer structure. As well as simply determining the nature of the polymer end-groups, it has been demonstrated that the effect of specificity in the initiation process can have a significant influence on the overall composition and sequence distribution of polymer chains up to 15 or more units removed from the initiator residue.¹³³ Data obtained on relative reactivity of radicals towards some of the more common monomers have been summarized in Table 5. Various other substrates have also been studied. Reference to these are found in Table 2.

A further use of relative reactivity data is to provide insight into polymerization mechanisms. The initiator-derived radicals may be simple models for the propagating species in radical polymerization. However, there are several factors that may cause the relative reactivities for model radicals to be different from those of the propagating species they resemble. These include: (a) medium effects, and (b) penultimate unit effects.

Recent studies have shown that the effect of reaction solvent on the relative reactivities of initiator-derived radicals towards monomers is small

Table 5. Relative reactivities of monomers towards initiator-derived radicals.

Monomer	Radical						
	30°C	(Me) ₂ (CN)C• 60°C	100°C	(Me) ₂ (CO ₂ Me)C• 30°C	60°C	PhCO ₂ • 60°C	(Me)PhCH• 100°C
Ace	—	2.2 ¹⁰²	—	—	—	—	2.9 ⁸⁸
MAN	—	0.34 ⁹⁷	0.49 ¹⁰⁶	—	—	—	—
AN	—	0.44 ¹⁰⁰	—	—	—	—	5.0 ⁶²
MMA	0.56 ⁹¹	0.56 ⁹⁷	0.56 ¹⁰⁵	—	0.7 ¹⁰⁹	0.11 ^{72,75}	1.9 ^{62,88}
MA/EA	—	0.34 ⁹⁶	—	—	—	—	1.5 ⁶²
AMS	1.06 ^{95,a}	0.95 ⁹⁵	0.87 ⁹⁵	—	—	—	1.1 ⁸⁸
S	1.0	1.0 ⁹⁷	1.0	1.0	1.0 ¹⁰⁹	1.0	1.0 ⁸⁸
MPK	—	1.34 ¹⁰¹	—	—	—	—	5.8 ⁸⁸
MVK	—	0.78 ¹⁰¹	—	—	—	—	4.2 ⁸⁸
VAc	0.02 ⁹¹	0.03 ¹⁰⁶	0.05 ¹⁰⁶	0.03 ⁹¹	—	—	—
VC	—	0.04 ^{99,b}	—	—	—	—	—

^a40°C.^b45°C.

compared with that observed for propagating radicals in copolymerization of MMA and S or MMA and VAc.⁹¹

The most ambitious use of labelled initiators was reported by Cywar and Tirrell¹³⁴ who were interested in testing penultimate unit effects. These authors investigated the relative reactivity of S and AN towards various γ -substituted propyl radicals (see Table 6). The initiators **16** and **17** were

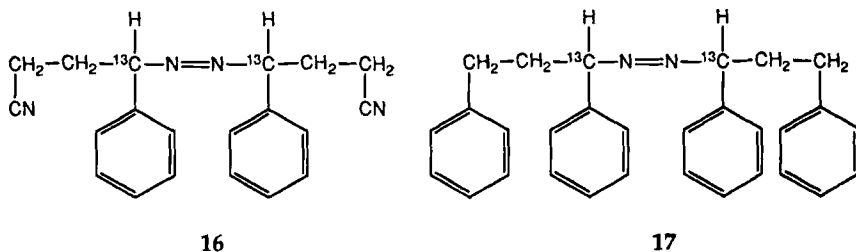
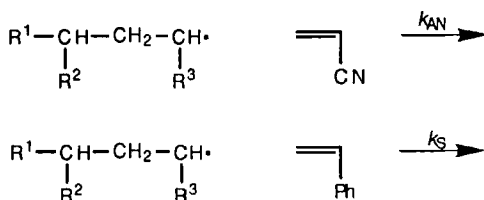


Table 6. Relative rates for addition of substituted propyl radicals to S and AN.

R ¹	R ²	R ³	k_{AN}/k_S	γ^a
H	CH ₃	H	24.5 ± 1.1 ¹³⁵	1.08
H	C ₃ H ₇	H	26.2 ± 2.4 ¹³⁵	1.16
H	Ph	H	22.6 ± 2.0 ¹³⁵	1.0
H	CN	H	6.8 ± 0.6 ¹³⁵	0.30
H	Ph	Ph	4.8 ± 0.3 ¹³⁴	1.0
H	CN	Ph	1.9 ± 0.1 ¹³⁴	0.40
"Polymer"	Ph	Ph	4.2 ³⁶	1.0
"Polymer"	CN	Ph	1.7 ³⁶	0.40

^a γ -substituent effect = k_{AN}/k_S for radical relative to that for analogous radical with R² = Ph.

prepared by multistep syntheses from barium carbonate.¹³⁴ The relative reactivities of the initiator-derived radicals determined by studying the decomposition of these initiators in S and AN mixtures were found to correlate well with those estimated from copolymerizations data by assuming a penultimate model (see Table 6).³⁶



4.4.1. Comparison with non-NMR methods for measuring relative reactivities

Other forms of end-group analysis have been used to assess relative reactivities of radicals towards monomers. Since these techniques (e.g. radiolabelling) usually offer no information regarding the environment of the end-group, the methods involve conducting homopolymerizations and using a side reaction leading to loss of label as a reference.

Relative reactivities of monomers can also be reliably established using radical trapping techniques.⁵⁴ These methods involve analysis of low molecular weight products formed by trapping the product of one monomer addition. The most popular methods are the "nitroxide trapping technique", the "mercury method" and "spin trapping". The nitroxide trapping technique was developed by Rizzardo and Solomon and makes use of stable nitroxide radicals as radical traps.¹³⁶ The method has been applied to establish the initiation mechanisms and relative reactivities for a wide range

of heteroatom-centred and more reactive carbon-centred radicals.⁵⁴ The mercury method¹³⁷ is generally limited to carbon-centered radicals and works best with more electrophilic monomers (e.g. acrylic monomers). In spin trapping, nitroso-compounds or nitrones are used to trap radicals as nitroxides which can be detected by ESR.¹³⁸

The main advantages of the NMR method over the non-NMR methods is that no product isolation is required and that "standard" polymerization reaction conditions can be employed (i.e. no additional reagents and few limitations on reaction media or polymerization conditions).

4.5. Polymer properties

Radical polymerization is a chain reaction involving initiation, propagation and termination, and chain transfer steps. One can define a defect group as any unit in the chain that differs from the standard repeat unit $(\text{CH}_2\text{-CXY})_n$. The end-groups must then be considered as defect structures and, clearly, each initiation, termination, and chain transfer step will result in the formation of defect structures.

Thus, it has long been recognized that initiation would lead to formation of structural units different from those which make up the bulk of the chain and there has been some speculation on whether initiator-derived functionality, by-products, and residual initiator might act as defect sites to initiate degradation.¹³⁹⁻¹⁴² However, when considered as a fraction of the total polymer, the initiator-derived groups seem insignificant. For example, in PS, the end-groups will account for *c.* 0.2% of units in a sample of molecular weight 100 000. This accounts for the assumption that initiator-derived defects will have no direct influence on the physical and chemical properties of polymers.

The recent development of techniques, in particular NMR spectroscopy, whereby details of the initiation and other stages of polymerization can be studied in depth has brought about a revision in this thinking. As discussed above, by preparing a polymer with a ^{13}C -labelled initiator it is possible to identify and quantify the initiator-derived functionality and by-products in high molecular weight polymers (M_n up to or greater than 200 000) by ^{13}C NMR. These labelled polymers may then be used to establish what happens to the initiator-derived groups during subsequent processing (e.g. thermal degradation) and thereby establish whether they play a role in initiating chain degradation. In recent studies the thermal degradation of PS prepared with labelled BPO^{83,143} or AIBN⁸³ as initiator has been examined. With the aid of the labelled polymers, it was possible to establish the relative liability of the various initiator-derived end-groups and propose a connection between polymerization reaction conditions and the thermal stability of the polymers (compare Fig. 10a and b).

Table 7. Syntheses of ^{13}C -enriched initiators.

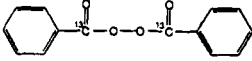
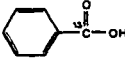
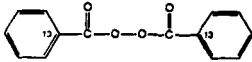
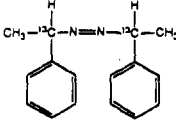
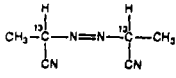
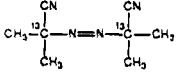
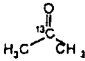
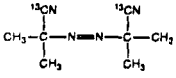
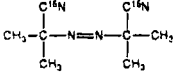
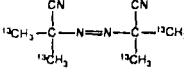
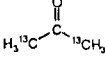
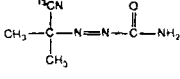
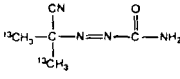
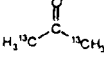
Initiator	Enriched precursor	Overall yield (steps)	Reference ^a
 BPO-carbonyl- ^{13}C		76% (2 steps)	71
 BPO- α - ^{13}C	$\text{CH}_3^{13}\text{CO}_2\text{Na}$	22% (6 steps) ^b	83
 APE- α - ^{13}C	$\text{CH}_3^{13}\text{CO}_2\text{H}$	15% (5 steps)	87
 APN- α - ^{13}C	$^{13}\text{CH}_3\text{CHO}$	35% (2 steps)	90
 AIBN- α - ^{13}C		90% (2 steps)	64,145,146
 AIBN-nitrile- ^{13}C	$\text{K } ^{13}\text{CN}$	^c (2 steps)	92
 AIBN- ^{15}N	$\text{K } ^{15}\text{N}$	^c (2 steps)	93
 AIBN- β - ^{13}C		^c (2 steps)	98
 AZOF-nitrile- ^{13}C	$\text{K } ^{13}\text{CN}$	^d (2 steps)	92
 AZOF- β - ^{13}C		^d (2 steps)	105

Table 7—*contd.*

Initiator	Enriched precursor	Overall yield (steps)	Reference
$\begin{array}{c} \text{CO}_2\text{CH}_3 \quad \text{CO}_2\text{CH}_3 \\ \quad \quad \\ \text{CH}_3-\text{C}^{13}-\text{N}=\text{N}-\text{C}^{13}-\text{CH}_3 \\ \quad \quad \\ \text{CH}_3 \quad \quad \text{CH}_3 \end{array}$ <p>AIBN-α-^{13}C</p>	AIBN- α - ^{13}C	68% (1 step)	107,147
$\begin{array}{c} \text{CO}_2\text{CH}_3 \quad \text{CO}_2\text{CH}_3 \\ \quad \quad \\ ^{13}\text{CH}_3-\text{C}-\text{N}=\text{N}-\text{C}-^{13}\text{CH}_3 \\ \quad \quad \\ ^{13}\text{CH}_3 \quad \quad ^{13}\text{CH}_3 \end{array}$ <p>AIBMe-α-^{13}C</p>	AIBN- β - ^{13}C	" (2 steps)	109
AIBMe- β - ^{13}C			

^aReference is to synthesis used for producing labelled material. Where no detailed synthetic method has been reported a reference to the first reported use is given in parentheses.

^bBenzoic- α - ^{13}C acid was prepared by modification of the scheme described by Ott⁴¹ and converted to the peroxide in a manner analogous to that used for BPO-*carbonyl*- ^{13}C .⁸⁴

^cYield not stated. Synthesis should be similar to that used for AIBN- α - ^{13}C .

^dYield not stated.

^eYield not stated. Synthesis should be similar to that used for AIBMe- α - ^{13}C .

5. SYNTHESSES OF LABELLED INITIATORS

In the context of the above experiments it is important to make an appropriate choice of labelled initiator. For most initiators several options are available and a number of factors come into play.

It is very important to have some knowledge of the available initiation pathways. For example, does the primary radical undergo reactions that might lead to loss of label as volatile products? These reactions include β -scission (e.g. BPO-*carbonyl*- ^{13}C —see Section 4.1) and hydrogen abstraction (t-butoxy radical).¹⁴⁴ In many cases potential side reactions can be identified by consulting the literature.⁵⁴

A second important consideration is that the chemical shifts of the labelled carbons of the end-groups should be separate from signals due to backbone carbons and also that the various types of end-groups that may be formed and other initiator-derived products give rise to discrete signals. The proximity of the label to the site of difference is an important consideration in this context. For example, it may be tempting (despite the additional expense) to use BPO- α - ^{13}C rather than BPO-*carbonyl*- ^{13}C , in studies of polymerization. When the former initiator is used, both phenyl and benzoyloxy end-groups (cf. Figs 11, 12) can be determined.⁸³ However, when BPO- α - ^{13}C is used, the end-groups formed by head addition to monomer cannot be distinguished from those formed by primary radical termination or transfer to initiator.

Once the above-mentioned problems are resolved, other factors to consider are the relaxation times, multiplicities, and perhaps the NOE

factors for the labelled carbons in the various initiator-derived products (see Section 4).

In Table 7 syntheses of ^{13}C -enriched initiators are summarized—for references on their application see Table 2. The general comments made in Section 4 about the synthesis of isotopically labelled compounds also apply here.

ACKNOWLEDGEMENTS

I am grateful to those who have contributed to the work carried out at CSIRO; their names are indicated in the references. Particular thanks go to Ian Willing, Julia Krstina, David Solomon (now at Melbourne University), and Ezio Rizzardo.

ABBREVIATIONS

Ace	Acenaphthalene
AIBN	azo-bis(isobutyronitrile)
AIBMe	azo-bis(methyl isobutyrate)
AMS	α -methylstyrene
AN	acrylonitrile
B	but-1-ene
BPO	benzoyl peroxide
BMA	n-butyl methacrylate
DVB	divinylbenzene
E	ethene
EA	ethyl acrylate
\bar{M}_n	number average molecular weight
MA	methyl acrylate
MMA	methyl methacrylate
MAN	methacrylonitrile
MPK	methyl isopropenyl ketone
MVK	methyl vinyl ketone
P	propene
S	styrene
VAc	vinyl acetate
VC	vinyl chloride
VCH	vinyl cyclohexane
VF	vinyl fluoride
VP	vinyl pyridine

Polymers are abbreviated by prefixing the corresponding monomer abbreviation with a P; for example, PMMA = poly(methyl methacrylate), P(BMA-*co*-MMA) = poly(*n*-butyl methacrylate-*co*-methyl methacrylate).

REFERENCES

1. F. A. Bovey and P. A. Mirau, *Acc. Chem. Res.*, 1988, **21**, 37.
2. G. Moad and R. I. Willing, in *Nuclear Magnetic Resonance—Specialist Periodical Reports*, ed. G. A. Webb, Vol. 19, Chem. Soc., London, 1990; p. 311.
3. A. H. Fawcett, in *Nuclear Magnetic Resonance—Specialist Periodical Reports*, ed. G. A. Webb, Vol. 20, Chem. Soc., London, 1991, p. 317.
4. I. Ando, T. Yamanobe and T. Asakura, *Prog. Nucl. Magn. Reson. Spectrosc.*, 1990, **22**, 349.
5. A. E. Tonelli, *NMR Spectroscopy and Polymer Microstructure*, VCH, New York, 1989.
6. J. L. Koenig, *Spectroscopy of Polymers*, Am. Chem. Soc., Washington, 1992.
7. G. Moad, *Chem. Aust.*, 1991, **58**, 122.
8. F. A. Bovey, *Chain Structure and Conformation of Macromolecules*, Wiley, New York, 1982.
9. F. C. Schilling, F. A. Bovey, M. D. Bruch and S. A. Kozlowski, *Macromolecules*, 1985, **18**, 1418.
10. G. Moad, D. H. Solomon, T. H. Spurling, S. R. Johns and R. I. Willing, *Aust. J. Chem.*, 1986, **39**, 43.
11. M. Reinmoller and T. G. Fox, *Polym. Prepr.*, 1966, **1**, 999.
12. R. Chujo, K. Hatada, R. Kitamaru, T. Kitayama, H. Sato and Y. Tanaka, *Polym. J. (Tokyo)*, 1987, **19**, 413.
13. R. Chujo, K. Hatada, R. Kitamaru, T. Kitayama, H. Sato, Y. Tanaka, F. Horii and Y. Terawaki, *Polym. J. (Tokyo)*, 1988, **20**, 627.
14. R. Chujo, K. Hatada, R. Kitamaru, T. Kitayama, H. Sato, Y. Tanaka, F. Horii and Y. Terawaki, *Makromol. Chem., Macromol. Symp.*, 1990, **34**, 59.
15. J. C. Randall, *Polymer Sequence Determination*, Academic Press, New York, 1977.
16. G. Moad, D. H. Solomon, T. H. Spurling and R. A. Stone, *Macromolecules*, 1989, **22**, 1145.
17. K. Hatada, T. Kitayama, Y. Terawaki and R. Chujo, *Polym. J. (Tokyo)*, 1988, **19**, 1127.
18. G. Moad, E. Rizzardo, D. H. Solomon, S. R. Johns and R. I. Willing, *Macromolecules*, 1986, **19**, 2494.
19. F. A. Bovey and P. A. Mirau, *Makromol. Chem. Macromol. Symp.*, 1990, **34**, 1.
20. S. Macura, J. Bremer and L. R. Brown, *J. Magn. Res.*, 1985, **62**, 328.
21. S. Macura, J. Bremer and L. R. Brown, *J. Magn. Res.*, 1985, **63**, 484.
22. H. N. Cheng and G. H. Lee, *Polym. Bull.*, 1984, **12**, 463.
23. H. N. Cheng and G. H. Lee, *Polym. Bull.*, 1985, **13**, 549.
24. H. N. Cheng and G. H. Lee, *J. Polym. Sci., Part B: Polym. Phys.*, 1985, **25**, 2355.
25. K. Hikichi and M. Yasuda, *Polymer Journal*, 1987, **19**, 1003.
26. M. D. Bruch and J. K. Bonesteel, *Macromolecules*, 1986, **19**, 1622.
27. C. Chang, D. D. Muccio and T. St Pierre, *Macromolecules*, 1985, **19**, 2334.
28. M. W. Crowther, N. M. Szeverenyi and G. C. Levy, *Macromolecules*, 1986, **19**, 1333.
29. P. A. Mirau and F. A. Bovey, *Macromolecules*, 1986, **19**, 210.
30. G. E. Martin and A. S. Zektzer, *Magn. Reson. Chem.*, 1988, **26**, 631.
31. J. L. Marshall, *Carbon—Carbon and Carbon—Proton NMR Couplings*, Verlag Chemie, Deerfield Beach, 1983.
32. A. Bax and M. F. Summers, *J. Am. Chem. Soc.*, 1986, **108**, 2093.
33. P. A. Berger, J. J. Kotyk and E. E. Remsen, *Macromolecules*, 1992, **25**, 7227.
34. J. J. Kotyk, P. A. Berger and E. E. Remsen, *Macromolecules*, 1990, **23**, 5167.
35. D. J. T. Hill, J. H. O'Donnell and P. W. O'Sullivan, *Macromolecules*, 1982, **15**, 960.
36. D. J. T. Hill, A. P. Lang, J. H. O'Donnell and P. W. O'Sullivan, *Eur. Polym. J.*, 1989, **25**, 911.
37. D. J. T. Hill, J. T. H. O'Donnell and P. W. O'Sullivan, *Macromolecules*, 1985, **18**, 9.

38. L. T. Kale, K. F. O'Driscoll, F. J. Dinan and J. J. Eubel, *J. Polym. Sci. Part A*, 1986, **24**, 3145.
39. G. Moad and R. I. Willing, *Polym. J. (Tokyo)*, 1991, **23**, 1401.
40. A. S. Brar and G. S. Kapur, *Polym. J. (Tokyo)*, 1988, **20**, 811.
41. D. G. Ott, *Syntheses with Stable Isotopes of Carbon. Nitrogen and Oxygen*, Wiley, New York, 1981.
42. M. Calvin, C. Heidelberger, J. C. Reid, B. M. Tolbert and P. F. Yankwich, *Isotopic Carbon*, Wiley, New York, 1949.
43. B. Stuetzel, W. Ritter and K. F. Elgert, *Angew. Makromol. Chem.*, 1976, **50**, 21.
44. G. Fink, W. Fenzl and R. Mynott, *Z. Naturforsch.*, 1985, **40B**, 158.
45. G. Fink and R. Rottler, *Angew. Makromol. Chem.*, 1981, **94**, 25.
46. A. Grassi, P. Ammendola, P. Longo, E. Albizzati, L. Resconi and R. Mazzocchi, *Gazz. Chim. Ital.*, 1988, **118**, 539.
47. A. Zambelli, P. Locatelli and E. Rigamonti, *Macromolecules*, 1979, **12**, 157.
48. G. Ferraris, C. Corno, A. Priola and S. Cesca, *Macromolecules*, 1980, **13**, 1104.
49. A. Priola, C. Corno and S. Cesca, *Macromolecules*, 1980, **13**, 1110.
50. O. L. Chapman and U. E. Tsou, *J. Am. Chem. Soc.*, 1984, **106**, 7974.
51. K. F. Elgert, R. Wicke, B. Stuetzel and W. Ritter, *Polymer*, 1975, **16**, 465.
52. M. Periyasamy, W. T. Ford and F. J. McEnroe, *J. Polym. Sci., Part A: Polym. Chem.*, 1989, **27**, 2357.
53. J. C. Bevington, *Radical Polymerization*, Academic Press, London, 1961.
54. G. Moad and D. H. Solomon in *Comprehensive Polymer Science*, eds G. C. Eastmond, A. Ledwith, S. Russo and P. Sigwalt, Vol. 3, Pergamon, London, 1989.
55. W. Kern, *Chem. Ztg.*, 1976, **100**, 401.
56. W. H. Starnes, I. M. Plitz, F. C. Schilling, G. M. Villacorta, G. S. Park and A. H. Saremi, *Macromolecules*, 1984, **17**, 2507.
57. K. R. Carduner, R. O. Carter, M. Zinbo, J. L. Gerlock and D. R. Bauer, *Macromolecules*, 1988, **21**, 1598.
58. T. Kodaira, K. Ito and S. Iyoda, *Polym. Commun.*, 1988, **29**, 83.
59. T. Kitayama, K. Ute, M. Yamamoto, N. Fujimoto and K. Hatada, *Polym. Bull. (Berlin)*, 1991, **25**, 683.
60. K. E. Axelson and K. E. Russell, *Prog. Polym. Sci.*, 1985, **11**, 221.
61. J. C. Bevington, D. A. Cywar, T. N. Huckerby, E. Senogles and D. A. Rittell, *Eur. Polym. J.*, 1988, **24**, 699.
62. J. C. Bevington, D. A. Cywar, T. N. Huckerby, E. Senogles and D. A. Tirrell, *Eur. Polym. J.*, 1990, **26**, 41.
63. S. R. Johns, E. Rizzardo, D. H. Solomon and R. I. Willing, *Makromol. Chem., Rapid Commun.*, 1983, **4**, 29.
64. G. Moad, D. H. Solomon, S. R. Johns and R. I. Willing, *Macromolecules*, 1984, **17**, 1094.
65. T. Kashiwagi, A. Inaba, J. E. Brown, K. Hatada, T. Kitayama and E. Masuda, *Macromolecules*, 1986, **19**, 2160.
66. J. C. Bevington, J. R. Ebdon and T. N. Huckerby, *Eur. Polym. J.*, 1985, **21**, 685.
67. M. R. Bendall, D. T. Pegg, D. M. Doddrell, S. J. Johns and R. I. Willing, *J. Chem. Soc., Chem. Commun.*, 1982, 1138.
68. J. C. Bevington and T. N. Huckerby, *Polymer*, 1992, **33**, 1323.
69. G. Moad, E. Rizzardo, D. H. Solomon, S. R. Johns and R. I. Willing, *Makromol. Chem., Rapid Commun.* 1984, **5**, 793.
70. J. C. Bevington, *Makromol. Chem., Macromol. Symp.*, 1988, **20/21**, 59.
71. G. Moad, D. H. Solomon, S. R. Johns and R. I. Willing, *Macromolecules*, 1982, **15**, 1188.
72. G. Moad, E. Rizzardo and D. H. Solomon, *Polym. Bull. (Berlin)*, 1984, **12**, 471.
73. C. A. Barson, J. C. Bevington and S. W. Breuer, *Eur. Polym. J.*, 1989, **25**, 259.
74. C. A. Barson, K. Behari, J. C. Bevington and T. N. Huckerby, *J. Macromol. Sci., Chem.*, 1988, **25**, 1137.

75. J. C. Bevington, S. W. Breuer and T. N. Huckerby, *Macromolecules*, 1989, **22**, 55.
76. C. A. Barson, J. C. Bevington and T. N. Huckerby, *Polym. Bull. (Berlin)*, 1991, **25**, 83.
77. J. C. Bevington, T. N. Huckerby and S. C. Varma, *Eur. Polym. J.*, 1987, **19**, 319.
78. C. A. Barson, J. C. Bevington and T. N. Huckerby, *Polym. Bull.*, 1989, **22**, 131.
79. J. C. Bevington and T. N. Huckerby, *Macromolecules*, 1985, **18**, 176.
80. C. A. Barson, J. C. Bevington and T. N. Huckerby, *Polymer*, 1991, **32**, 3415.
81. C. A. Barson, J. C. Bevington, S. W. Breuer and T. N. Huckerby, *Eur. Polym. J.*, 1989, **25**, 527.
82. C. A. Barson, J. C. Bevington, S. W. Breuer and T. N. Huckerby, *Makromol. Chem., Rapid Commun.*, 1992, **13**, 97.
83. J. Krstina, G. Moad and D. H. Solomon, *Eur. Polym. J.*, 1989, **25**, 767.
84. J. Krstina, G. Moad and D. H. Solomon, 1993, in preparation.
85. J. C. Bevington, T. N. Huckerby and N. Vickerstaff, *Makromol. Chem., Rapid Commun.*, 1983, **4**, 349.
86. J. C. Bevington, T. N. Huckerby and N. Vickerstaff, *Makromol. Chem. Rapid Commun.*, 1988, **9**, 791.
87. D. A. Cywar and D. A. Tirrell, *Macromolecules*, 1986, **19**, 2908.
88. J. C. Bevington, D. A. Cywar, T. N. Huckerby, E. Senogles and D. A. Tirrell, *Eur. Polym. J.*, 1990, **26**, 871.
89. J. C. Bevington, B. F. Bowden, D. A. Cywar, R. A. Lyons, E. Senogles and D. A. Tirrell, *Eur. Polym. J.* 1991, **27**, 1239.
90. G. S. Prementine and D. A. Tirrell, *Macromolecules*, 1987, **20**, 3034.
91. J. Krstina, G. Moad and D. H. Solomon, *Eur. Polym. J.*, 1992, **28**, 275.
92. J. C. Bevington, S. W. Breuer, E. N. J. Heseltine, T. N. Huckerby and S. C. Varma, *J. Polym. Sci., Polym. Chem. Ed.*, 1987, **25**, 1085.
93. J. C. Bevington, T. N. Huckerby and N. W. E. Hutton, *Eur. Polym. J.*, 1982, **18**, 963.
94. T. Kitayama, S. Kishiro, E. Masuda and K. Hatada, *Polym. Bull. (Berlin)*, 1991, **25**, 205.
95. K. Behari, J. C. Bevington and T. N. Huckerby, *Makromol. Chem.*, 1987, **188**, 2441.
96. J. C. Bevington, T. N. Huckerby and N. W. E. Hutton, *Eur. Polym. J.*, 1984, **20**, 525.
97. J. C. Bevington, T. N. Huckerby and N. W. E. Hutton, *J. Polym. Sci., Polym. Chem. Ed.*, 1982, **20**, 2655.
98. J. C. Bevington, J. R. Ebdon, T. N. Huckerby and N. W. E. Hutton, *Polymer*, 1982, **23**, 163.
99. G. Ayrey, K. Jumangat, J. C. Bevington and T. N. Huckerby, *Polym. Commun.*, 1983, **24**, 275.
100. C. A. Barson, J. C. Bevington and T. N. Huckerby, *Polym. Bull. (Berlin)*, 1986, **16**, 209.
101. K. Behari, J. C. Bevington and T. N. Huckerby, *Polymer*, 1988, **29**, 1867.
102. J. C. Bevington and T. N. Huckerby, *J. Macromol. Sci., Chem.*, 1983, **20**, 753.
103. J. C. Bevington, T. N. Huckerby and B. J. Hunt, *Br. Polym. J.*, 1985, **17**, 43.
104. R. A. Lyons, G. Moad and E. Senogles, *Eur. Polym. J.*, 1993, **29**, 389.
105. J. C. Bevington, S. W. Breuer and T. N. Huckerby, *Polymer Commun.*, 1984, **25**, 260.
106. J. C. Bevington, T. N. Huckerby and S. C. Varma, *Eur. Polym. J.*, 1986, **22**, 427.
107. T. H. Spurling, M. Deady, J. Krstina and G. Moad, *Makromol. Chem., Macromol. Symp.*, 1991, **51**, 127.
108. J. Krstina, G. Moad and D. H. Solomon, *Polym. Bull.*, 1992, **27**, 425.
109. J. C. Bevington, R. A. Lyons and E. Senogles, *Eur. Polym. J.*, 1992, **28**, 283.
110. P. Ammendola, T. Tancredi and A. Zambelli, *Macromolecules*, 1986, **19**, 307.
111. A. Zambelli, P. Locatelli, M. C. Sacchi and I. Tritto, *Macromolecules*, 1982, **15**, 831.
112. A. Zambelli, M. C. Sacchi, P. Locatelli and G. Zannoni, *Macromolecules*, 1982, **15**, 211.
113. P. Ammendola, A. Vitagliano, L. Oliva and A. Zambelli, *Makromol. Chem.*, 1984, **185**, 2421.
114. A. Zambelli, P. Locatelli, M. C. Sacchi and E. Rigamonti, *Macromolecules*, 1980, **13**, 798.

115. A. Zambelli, P. Ammendola, A. Grassi, P. Longo and A. Proto, *Macromolecules*, 1986, **19**, 2703.
116. P. Longo, A. Grassi, C. Pellicchia and A. Zambelli, *Macromolecules*, 1987, **20**, 1015.
117. S. S. Huang and E. T. E. Hogen, *J. Polym. Sci. Polym. Chem. Ed.*, 1985, **23**, 1203.
118. A. H. Soum and E. T. E. Hogen, *Macromolecules*, 1985, **18**, 690.
119. S. S. Huang, A. H. Soum and E. T. E. Hogen, *J. Polym. Sci., Polym. Lett. Ed.*, 1983, **21**, 559.
120. K. Hashimoto and E. T. E. Hogen, *Macromolecules*, 1983, **16**, 1809.
121. R. Volpe and E. T. E. Hogen, *Macromolecules*, 1990, **23**, 4196.
122. R. Volpe, E. T. E. Hogen, F. Gores and A. H. E. Mueller, *Macromolecules*, 1992, **25**, 3553.
123. J. Krstina, G. Moad and D. H. Solomon, *Eur. Polym. J.*, 1993, **29**, 379.
124. M. Buback, L. H. Garcia-Rubio, R. G. Gilbert, D. H. Napper, J. Guillot, A. E. Hamielec, D. Hill, K. F. O'Driscoll, O. F. Olaj, J. Shen, D. H. Solomon, G. Moad, M. Stickler, M. Tirrell and M. A. Winnick, *J. Polym. Sci., Polym. Lett. Ed.*, 1988, **26**, 293.
125. M. Buback, R. G. Gilbert, G. T. Russell, D. J. T. Hill, G. Moad, K. F. O'Driscoll, J. Shen and M. A. Winnick, *J. Polym. Sci., Part A: Polym. Chem.*, 1992, **30**, 851.
126. T. Fukuda, Y.-D. Ma and H. Inagaki, *Macromolecules*, 1985, **18**, 17.
127. J. C. Bevington and T. D. Lewis, *Polymer*, 1960, **1**, 1.
128. J. C. Bevington, *Trans. Faraday Soc.*, 1955, 1392.
129. S. Shetty and R. L. H. Garcia, *Polym. Mater. Sci. Eng.*, 1991, **65**, 103.
130. L. H. Garcia-Rubio and J. Mehta, *ACS Symp. Series.—Computer Applications in the Polymer Laboratory*, 1986, 202.
131. M. Buback, *Makromol. Chem., Rapid Commun.*, 1992, **12**, 1.
132. K. F. O'Driscoll and J. Huang, *Eur. Polym. J.*, 1989, **7/8**, 629.
133. M. N. Galbraith, G. Moad, D. H. Solomon and T. H. Spurling, *Macromolecules*, 1987, **20**, 675.
134. D. A. Cywar and D. A. Tirrell, *J. Am. Chem. Soc.*, 1989, **111**, 7544.
135. S. A. Jones, G. S. Prementine and D. A. Tirrell, *J. Am. Chem. Soc.*, 1985, **107**, 5275.
136. E. Rizzardo and D. H. Solomon, *Polym. Bull.*, 1979, **1**, 529.
137. G. S. Prementine and D. A. Tirrell, *Macromolecules*, 1989, **22**, 52.
138. T. Sato and T. Otsu, *Makromol. Chem.*, 1977, **178**, 1941.
139. D. H. Solomon, P. Cacioli and G. Moad, *Pure Appl. Chem.*, 1985, **57**, 985.
140. E. F. J. Hwang and E. M. Pearce, *Polym. Eng. Rev.*, 1983, **2**, 319.
141. I. Mita in *Aspects of Deregulation and Stabilization of Polymers*, ed. H. H. G. Jellinek, Elsevier, Amsterdam, 1978; p. 247.
142. D. H. Solomon, *J. Macromol. Sci., Chem.*, 1982, **A17**, 337.
143. G. Moad, D. H. Solomon and R. I. Willing, *Macromolecules*, 1988, **21**, 855.
144. D. Bednarek, G. Moad, E. Rizzardo and D. H. Solomon, *Macromolecules*, 1988, **21**, 1522.
145. C. G. Overberger, P. T. Huang and M. B. Berenbaum, *Org. Syn.*, 1963, **4**, 274.
146. C. G. Overberger, P. T. Huang and M. B. Berenbaum, *Org. Syn.*, 1963, **4**, 66.
147. S. Bizilj, D. P. Kelly, A. K. Serelis, D. H. Solomon and K. E. White, *Aust. J. Chem.*, 1985, **38**, 1657.

This Page Intentionally Left Blank

^{13}C NMR Assignments of Polyolefines and Olefine Copolymers Based on the ^{13}C NMR Chemical Shift Calculations and 2D INADEQUATE NMR

TETSUO ASAKURA, MAKOTO DEMURA

*Department of Biotechnology, Tokyo University of Agriculture and Technology,
Koganei, Tokyo 184, Japan*

TETSUO HAYASHI

*Plastics Research Laboratory, Tokuyama Corp. Ltd, 1-1, Harumi-chou, Tokuyama,
Yamaguchi 745, Japan*

1. Introduction	326
2. Calculation	328
2.1. Empirical chemical shift calculation	328
2.1.1. Lindeman-Adams method	328
2.1.2. Cheng method	329
2.2. Chemical shift calculations based on conformational analysis	331
2.2.1. Rotational isomeric state (RIS) model	331
2.2.2. Chemical shift calculations based on γ -shielding effect and RIS model	333
2.3. Polymerization mechanism	335
2.4. Peak simulation	336
3. NMR observation	338
3.1. Usual observations including sample preparation	338
3.2. INEPT	338
3.3. INADEQUATE	338
4. Polyolefines	339
4.1. Polypropylene, PP	339
4.1.1. Stereoirregularity	339
4.1.2. Regioirregularity	345
4.1.3. Chain end	352
4.2. Poly(1-butene), PB	354
4.2.1. Stereoirregularity	354
4.2.2. Regioirregularity	360

4.3. Poly(1-pentene) (PPE), poly(1-hexene) (PHEX), Poly(1-heptene) (PHEP), poly(1-octene) (PO), poly(1-nonene) (PN)	363
4.4. Poly(3-methyl-1-butene)	365
5. Ethylene-olefine copolymers	370
5.1. E-P copolymers	370
5.1.1. Comonomer sequence	370
5.1.2. Stereoirregularity	387
5.2. B-P copolymers	391
6. Conclusion	401
Acknowledgements	401
References	401

1. INTRODUCTION

Initially, ^1H NMR spectroscopy has made major contributions to our understanding of the primary structures such as stereochemical configuration of polyolefines, especially polypropylene, PP.^{1,2} In the case of PP, a major commercial polymer, despite its apparent structural simplicity, the ^1H NMR spectra are complex because the methyl protons couple strongly to the methine protons, and the chemical shift differences among the methine, methylene and methyl protons are relatively small. Therefore, selectively deuterated PP samples as well as high magnetic fields have been used to simplify the ^1H NMR spectra and to make the tacticity assignments easy.³⁻⁵ For other polyolefines with longer side-chains than PP, the ^1H NMR spectra are more complex because of the strong spin-spin coupling and relatively small chemical shift difference among the protons in the side-chain. Thus, precise assignment of the peaks is difficult.¹

With the innovation of ^{13}C NMR, the measurement of the primary structure of polyolefines improved greatly. The greater simplicity and resolution of the ^{13}C NMR spectra through ^1H heteronuclear decoupling without selective deuterations have largely eclipsed the use of ^1H NMR spectroscopies.⁶⁻⁹ Information concerning subtle structural features, not detected or readily apparent by any other spectroscopic technique, are often obvious in ^{13}C NMR spectra.

The empirical method for predicting alkane ^{13}C chemical shifts based on carbon skeleton arrangements developed by Grant and Paul,¹⁰ and modified by Lindeman and Adams,¹¹ has proven valuable in ^{13}C NMR polyolefine spectra for distinguishing carbons of the same type but located in different structural environments. There is, however, no applicable approach to the assignment of the ^{13}C NMR peaks to the stereochemical configuration of polyolefines because such configurational contributions to carbon chemical shifts have not yet been included among the empirical parameter terms. The assignment of the stereochemical configuration of polyolefines is a difficult problem. For the case of PP, the experimentally most successful approach to the assignment is a well-planned synthesis of the model compounds,

3,5,7,9,11,13,15-heptamethylheptadecanes with ^{13}C labelled central methyl group carbons.¹² However, this approach is very time consuming and is not generally used for the assignments of other polyolefines. The syntheses of polyolefines with greatly differing tacticity and the examination on the relationships among the ^{13}C peak intensities, by assuming the mechanism of polymerization,^{1,13} are useful for the assignments and actually have been used in a complementary manner, but it is essentially difficult to make stereochemical assignments of polyolefines using only these data.

Two approaches have been developed and applied successfully to the assignment of ^{13}C NMR spectra of polyolefines. The first is the calculation of ^{13}C chemical shifts on the basis of γ -effects on the ^{13}C chemical shift,¹⁴⁻¹⁶ using the rotational isomeric state, RIS, model.¹⁷⁻²⁰ The tacticity assignment of PP reported experimentally has been well reproduced by such a ^{13}C chemical shift calculation.^{21,22} On the other hand, in the case of poly(1-butene), PB, only a brief and incomplete tacticity assignment had been reported experimentally prior to the calculation of the ^{13}C chemical shift.²³ Thus, the assignment of PB is a good example for judging the potential of such a theoretical approach to assignment. Through the calculation, the dramatic change in the observed ^{13}C NMR spectra of the backbone methylene carbons between PP and PB could be well interpreted. In addition, the detailed tacticity assignments of all of the carbons were reported.^{24,25} This success has demonstrated the usefulness of such a calculation for the purposes of assignment. It also affords a proof of a satisfactory representation of the conformational characteristics of polyolefines on the basis of the conformational energy calculation, since the method of the chemical shift calculation is developed originally from the conformational energy calculation through the RIS model. For the case of methyl-substituted olefine compounds, the empirical rule proposed by Cheng and Bennett has also proved useful.^{26,59}

The second approach involves the application of two-dimensional NMR techniques, especially the 2D INADEQUATE (Incredible Natural Abundance Double Quantum Transfer Experiment) technique²⁷ to the stereochemical ^{13}C assignments of polyolefines. In this method, we can obtain information concerning ^{13}C - ^{13}C connectivities in the polymer chain and assign the spectra to the ^{13}C nuclei according to the tacticity of the polymer, in principle. At present, however, a detailed tacticity assignment of polyolefines using only the 2D INADEQUATE method is impossible²⁸ but this is extremely useful in the ^{13}C NMR assignments of ethylene-olefine copolymers²⁹⁻³¹ and regioirregular polyolefines³² where the spectra are very complex because of the presence of several kinds of sequences.

In this chapter, recent ^{13}C NMR assignments of polyolefines and olefine copolymers in solution based on ^{13}C NMR chemical shift calculations and 2D INADEQUATE methods are reviewed with the emphasis being placed on revealing primary structures such as stereochemical configuration,

branching, regioregularity and comonomer sequence. Most of the examples are taken from the works of the present authors and their colleagues.

2. CALCULATION

2.1. Empirical chemical shift calculation

2.1.1. Lindeman–Adams method

Lindeman and Adams¹¹ proposed the empirical rule for the estimation of the chemical shifts of paraffins by improving and extending the chemical shift prediction parameters of Grant and Paul.¹⁰ According to the Lindeman–Adams method, the chemical shift of the carbon atom of interest is presented by:

$$\delta(Ck) = B_S + D_2A_{S2} + D_3A_{S3} + D_4A_{S4} + C_SN_3 + E_SN_4 \quad (1)$$

where $\delta(Ck)$ is the ^{13}C chemical shift value of the k th carbon atom, B_S , A_{SM} , C_S , and E_S are constants; N_3 and N_4 are the numbers of carbon atoms three and four bonds away from the k th carbon atom, respectively, subscript S is the number of carbon atoms attached to the k th carbon atom, D_M is the number of carbon atoms which have M attached carbon atoms and are bonded to the k th carbon atom. The A_{SM} values are used to describe the steric configuration of the next-nearest neighbour carbon atom. The parameters of the Lindeman–Adams method are shown in Table 1. For example, the ^{13}C NMR chemical shifts calculated according to this method by assuming several sequences in regiorregular PP and PB are shown in Sections 4.1.2. and 4.2.2. However, this method is not applicable to the ^{13}C

Table 1. The parameters used in the Lindeman–Adams method for the estimation of chemical shifts.

Parameter	Value (ppm)	Parameter	Value (ppm)
B ₁	6.80	A ₁₂	9.56
B ₂	15.34	A ₁₃	17.83
B ₃	23.46	A ₁₄	25.48
B ₄	27.77	A ₂₂	9.75
C ₁	−2.99	A ₂₃	16.70
C ₂	−2.69	A ₂₄	21.43
C ₃	−2.07	A ₃₂	6.60
C ₄	0.68	A ₃₃	11.14
E ₁	0.49	A ₃₄	14.70
E ₂	0.25	A ₄₂	2.26
		A ₄₃	3.96
		A ₄₄	7.35

NMR chemical shift assignments of stereochemical configurations of polyolefins.

2.1.2. Cheng's method

Recently, Cheng and Bennett^{26,59} have proposed the additivity rules for ¹³C NMR chemical shifts of methyl-substituted alkanes and ethylene-propylene, E-P copolymers. The rules are applicable to multiply substituted methylalkanes and specifically take stereochemical configuration into account. In the interest of better accuracy, different substituent values are provided for methyl, methine, and methylene carbons. The shift equations for the methyl and methylene carbons are as follows:

$$(\text{methyl carbon}) \delta\text{CH}_3 = 19.99 + \sum_i A_i + \sum_{ij} B_{ij} + \sum_{ij} C_{ij} \quad (2)$$

$$(\text{methine carbon}) \delta\text{CH} = 33.26 + \sum_i A_i + \sum_{ij} B_{ij} + \sum_{ij} C_{ij} \quad (3)$$

where A_i is the substituent parameter for position i and B_{ij} is the correction term corresponding to the configurations of the methyl groups at i and j on the same side of the methyl group, and C_{ij} is to be used for methyls at positions i and j on opposite sides of the carbon in question. The parameters of Cheng's method for the estimation of ¹³C chemical shifts of methyl and methine carbons are shown in Tables 2 and 3, respectively. The additive rule for methylene carbon is as follows:

$$\delta\text{CH}_2 = 29.9 + \sum_i A_i + \sum_{ij} B_{ij} + \sum_{ij} C_{ij} + \sum_k D_k \quad (4)$$

Table 2. Parameters used in Cheng's method for the estimation of ¹³C chemical shifts (ppm) of methyl carbons.

A_i	γ	δ	ϵ	ζ
<i>m</i>	-3.05	0.77	0.16	0.05
<i>r</i>	-4.83	0.22	0.03	-0.03

$i \ j$	$B_{\delta\zeta}$	$B_{\delta\epsilon}$	$B_{\gamma\delta}$	$B_{\gamma\epsilon}$	$B_{\epsilon\zeta}$	$C_{\gamma\gamma}$
<i>m m</i>	0.02	0.17	0.75	-0.12	0	-1.7
<i>m r</i>	-0.10	-0.06	0.75	-0.40	0	0
<i>r m</i>	-0.15	-0.33	0.05	-0.14	0	0
<i>r r</i>	-0.20	-0.39	0.05	-0.52	0	1.1

Table 3. Parameters used in Cheng's method for the estimation of ^{13}C chemical shifts (ppm) of methine carbons.

A_i	β	γ	δ	ϵ
<i>m</i>	4.9	-2.38	0.36	0.04
<i>r</i>	4.2	-2.46	0.27	0.00

$i\ j$	$B_{\gamma\epsilon}$	$B_{\gamma\delta}$	$B_{\beta\gamma}$	$B_{\beta\delta}$	$B_{\delta\epsilon}$	$B_{\beta\epsilon}$	$C_{\beta\beta}$
<i>m m</i>	0.043	0.2	-0.8	-0.5	0	-0.01	0.8
<i>m r</i>	0.033	0.02	-1.4	-0.1	0	-0.01	-0.5
<i>r m</i>	-0.057	0	-1.0	-0.1	0	0	-0.5
<i>r r</i>	-0.078	0	-1.5	-0.4	0	0	-1.2

Table 4. Parameters used in Cheng's method for the estimation of ^{13}C chemical shifts (ppm) of methylene carbons.

A_i	β	γ	δ	ϵ	ζ
	7.57	-2.56	0.40	0.05	0

$B_{i\ j}$	$B_{\beta\gamma}$	$B_{\beta\delta}$	$B_{\beta\epsilon}$	$B_{\gamma\delta}$	$B_{\gamma\epsilon}$	$B_{\delta\epsilon}$	$B_{\delta\zeta}$
<i>m</i>	-1.5	-0.34	-0.25	0.4	-0.16	0	0
<i>r</i>	0.3	0.51	0	-0.1	-0.10	0	0

$C_{i\ j}$	$C_{\beta\beta}$	$C_{\beta\gamma}$	$C_{\beta\delta}$	$C_{\beta\epsilon}$	$C_{\beta\zeta}$	$C_{\gamma\gamma}$	$C_{\gamma\delta}$
<i>m</i>	0.54	-0.001	-0.04	-0.107	0	-0.023	-0.017
<i>r</i>	0.34	-0.059	0	-0.072	0	0	0

$D_{\delta\beta\beta}$:	<i>mm</i> = 0.516	$D_{\zeta\delta\beta}$:	<i>mm</i> = -0.164
	<i>mr</i> = 0.196		<i>mr</i> = 0.152
	<i>rm</i> = 0.018		<i>rm</i> = -0.006
	<i>rr</i> = 0.007		<i>rr</i> = 0.004

The term D_k is designed to take into account the effect of three consecutive propylene units. The parameters for methylene carbons are shown in Table 4.

The calculated chemical shifts of the methyl carbons in *mmmm* and *mrrm* sequences of PP are 21.57 and 20.03 ppm, respectively. Since the former is the highest and the latter is the lowest shift values, the predicted chemical shift range roughly corresponds with the observed one from 19.9 to 21.8 ppm.^{33,34} The calculated chemical shifts for the carbon $S_{\gamma\alpha\beta\gamma}$ in the sequence 1-*r* presented in regioirregular PP with this method are listed in Section 4.1.2. (Table 10).

2.2. Chemical shift calculation based on conformational analysis

2.2.1. Rotational isomeric state (RIS) model

A polyolefine chain in solution is generally flexible and can take various time-averaged conformations. In the case of PP, the three-state, and more realistic, five-state RIS models afford a satisfactory representation of the preferred conformations around the backbone bonds.

Let's describe how to make the five-state RIS model for PP.²⁰ The discrete nature of the rotational potential has been recognized and in the RIS approximation, each bond in the backbone is assumed to occur in any one of a small number of discrete rotational states.^{17,18} In addition, not only is each bond in a polymer chain usually restricted to a few discrete rotational states, but also the probability of occurrence of any rotational state about a given bond depends on the rotational states of its nearest-neighbour bonds. This is derived from the conformational energy calculation of *n*-pentane as a function of the torsion angles around two C–C bonds, where the total conformational potential energy is assumed to be the sum of interactions between non-bonded atoms separated by more than two bonds and from the intrinsic torsional energy.³⁵ A similar calculation was performed for *meso* (isotactic) and racemic (syndiotactic) dyads of PP for constructing a RIS scheme which may be expected to represent the PP chain with high accuracy. Figure 1 shows potential energy contours for the bond pair ϕ_i, ϕ_{i+1} of a *meso* dyad, expressed in kcal mol⁻¹ relative to racemic; *trans* (*t*) (the most stable conformation). On the basis of the contours map, the five RIS states centred at 15, 50, 70, 105 and –115° as measured from *t* in the right- or the left-handed sense, depending on the chirality of the skeletal bonds, are selected for bond *i* as shown in Fig. 2. These five states are noted by *t*, *t**, *gauche*(*g*)*, *g*, and \bar{g} , respectively. The statistical weights corresponding to the first-order interactions (i.e. those determined by rotation about one bond) of the five states are included in Fig. 2. The same statistical weight ω may be used for all second-order interactions between the pairs of groups CH₂ and CH₂, CH₃ and CH₂, CH₃ and CH₃ separated by four C–C bonds.

The features of the conformational energy surfaces for the bond pair *i, i* + 1 of a *meso* dyad as shown in Fig. 1 and similarly, of a racemic dyad are well represented by the statistical weight matrices Eqs (5) and (6), respectively:

$$\mathbf{U}\mathbf{m}'' = \begin{bmatrix} 0 & \eta\eta^*\omega & 0 & \eta & 0 \\ \eta\eta^*\omega & 0 & 0 & 0 & \eta^*\tau\omega \\ 0 & 0 & 0 & \eta^*\omega & \eta^*\tau\omega \\ \eta & 0 & \eta^*\omega & 0 & 0 \\ 0 & \eta^*\tau\omega & \eta^*\tau\omega & 0 & 0 \end{bmatrix} \quad (5)$$

$$\mathbf{U}\mathbf{r}'' = \begin{bmatrix} \eta^2 & 0 & \eta\eta^*\omega & 0 & 0 \\ 0 & 0 & 0 & \eta^*\tau\omega & \eta^*\omega \\ \eta\eta^*\omega & 0 & 0 & 0 & \eta^*\omega \\ 0 & \eta^*\omega & 0 & 1 & 0 \\ 0 & \eta^*\tau\omega & \eta^*\tau\omega & 0 & 0 \end{bmatrix} \quad (6)$$

where the elements are indexed in the order t , t^* , g^* , g , \bar{g} and $\eta = 1.0 \exp(-60/RT)$, $\tau = 0.4 \exp(-500/RT)$ and $\eta^*\omega = \omega^* = 0.9 \exp(-1600/RT)$.

The matrix of second-order statistical weights appropriate for the inter-dyad bond pair takes the form given by Eq. (7):

$$\mathbf{U}' = \begin{bmatrix} 1 & 1 & 1 & 1 & 1 \\ 1 & 1 & 1 & 1 & 1 \\ 1 & 1 & 0 & 0 & 1 \\ 1 & 1 & 0 & 0 & 1 \\ 1 & 1 & 1 & 1 & 0 \end{bmatrix} \quad (7)$$

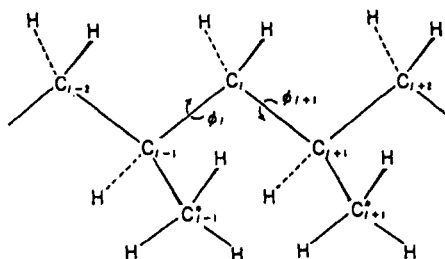
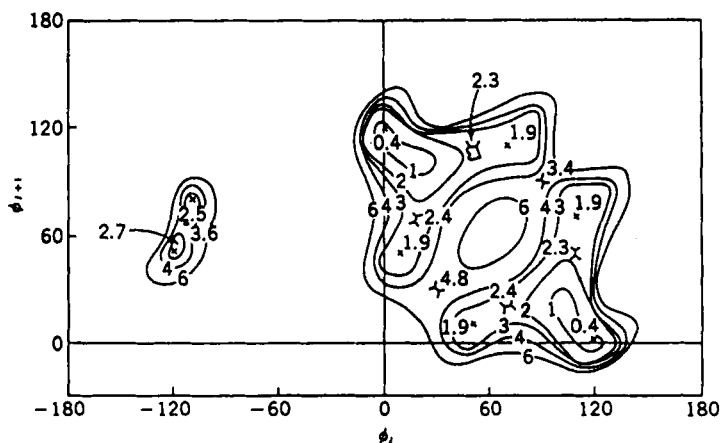


Fig. 1. Potential energy contours for bond pair $i, i+1$ of a *meso* dyad, expressed in kcal mol^{-1} relative to racemic; tt. Methyl rotations χ_{i-1} and χ_{i+1} take on values that minimize the energy for each ϕ_i, ϕ_{i+1} . The X denote local minima, and $><$ denote cols in the surface.

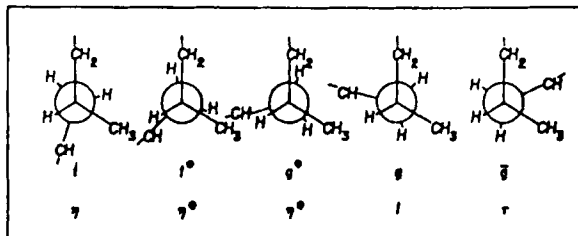


Fig. 2. Newman projections along bond *i* illustrating the basic first-order interactions.

Thus, the statistical weight matrices of order 5×5 for PP chain are formulated, one for the pair of bonds flanking the substituted carbon centre and one for the dyad pair between successive substituted centres; the form of the latter matrix depends on the *meso* or racemic character of the dyad.

These matrices can also be used for representation of the conformational characteristics of polyolefines with more bulky side-chains than PP except for an additional repulsive interaction between the bulky group of the side-chain and backbone.¹⁸ Such an additive interaction occurs when both adjacent backbone bonds are *t* and therefore, the introduction of τ^* (< 1) instead of 1 at only the 1,1 element in the matrix, U' is required.²⁴ The RIS models for PB, poly(1-pentene), poly(4-methyl-1-pentene), and poly[(S)-4-methyl-1-hexene] are also proposed, based on the five states PP model, and assuming mutually independent side groups.³⁶ For the E-P copolymer³⁷ and regioirregular PP,³⁸ the three state RIS models have been proposed and used for chemical shift calculations.

2.2.2. Chemical shift calculation based on γ -shielding effect and RIS model

The γ -effect is recognized in ¹³C NMR studies of paraffinic hydrocarbons as a shielding increase of *c.* -5 ppm accompanying a γ arrangement of carbon atoms separated by three bonds (γ substituents) relative to their *t* arrangements.¹⁴ The actual magnitude of the γ -effect will depend on the probability of the averaged bond conformation and therefore, the probability must be determined in the chemical shift calculation on the basis of the γ -effect. In the case of stereoirregular PP, the five-state RIS model²⁰ can be used for this purpose. Let's explain how to calculate the bond probability for a PP chain and then the ¹³C chemical shifts.

The partition function for the *x*-meric chain comprising *x*-1 dyads of which *x*-3 are subject to diastereoisomerism is conveniently expressed as the following serial product:

$$Z = U_0 U_1^{(2)} \left(\prod_{k=2}^{x-2} U_k^{(2)} \right) U_{x-1}^{(2)} U_x \quad (8)$$

where $U_k^{(2)}$ is either $U_m^{(2)} = U'U_m''$ or $U_r^{(2)} = U'U_r''$, depending on the stereochemical character of the k -th dyad. The terminal operators are:

$$U_0 = [1, 0, 0, 0, 0] \quad (9)$$

and

$$U_x = \text{col}(1, 1, 1, 1, 1) \quad (10)$$

The matrices for the terminal dyads 1 and $x-1$ are:

$$U_1^{(2)} = U' \text{diag}(1, 1, 1, \eta, 1) U'' \quad (11)$$

and

$$U_{x-1}^{(2)} = U''' \text{diag}(1, 1, 1, \eta, 1) \quad (12)$$

where it is immaterials where U'' is identified with U_m'' or U_r'' . Then, the probability, $P_{\beta:j}$ of one bond of the j -th dyad being in the β rotational state is given by:

$$P_{\beta:j} = Z^{-1} U_0 U_1^{(2)} \left(\prod_{h'=2}^{j-1} U_{h'} \right) (U'_{\beta:j} U''_j) \left(\prod_{h=j+1}^{x-2} U_h \right) U_{x-1}^{(2)} U_x \quad (13)$$

in which Z is the partition function, $U'_{\beta:j}$ is the statistical weight matrix, U'' of the dyad j by the replacement of zero in all elements except the column β . A more detailed explanation is given elsewhere.^{20, 39, 40} In Table 5 are

Table 5. Conformational probabilities of 6–11 bonds of 2,4,6,8,10,12,14,16,18-nonamethylnonadecane.

Pentad	<i>t</i> -6 ^a	<i>g</i> -6 ^b	<i>t</i> -7	<i>g</i> -7	<i>t</i> -8	<i>g</i> -8	<i>t</i> -9	<i>g</i> -9	<i>t</i> -10	<i>g</i> -10	<i>t</i> -11	<i>g</i> -11
<i>mmmm</i>	0.495	0.340	0.448	0.381	0.463	0.366	0.469	0.360	0.441	0.388	0.510	0.329
<i>mmmr</i>	0.550	0.033	0.444	0.394	0.466	0.372	0.514	0.330	0.395	0.449	0.660	0.214
<i>mmrr</i>	0.715	0.171	0.391	0.461	0.517	0.335	0.512	0.339	0.395	0.456	0.706	0.179
<i>mmrm</i>	0.424	0.423	0.639	0.231	0.549	0.321	0.556	0.314	0.634	0.237	0.443	0.408
<i>mmrr</i>	0.502	0.348	0.560	0.295	0.464	0.391	0.613	0.259	0.633	0.240	0.587	0.283
<i>rmrr</i>	0.533	0.334	0.593	0.281	0.582	0.292	0.577	0.297	0.590	0.284	0.550	0.320
<i>rmrr</i>	0.647	0.234	0.552	0.318	0.566	0.304	0.561	0.308	0.550	0.320	0.659	0.222
<i>rmrm</i>	0.440	0.414	0.665	0.213	0.651	0.229	0.654	0.226	0.669	0.210	0.431	0.422
<i>rrrr</i>	0.521	0.344	0.645	0.234	0.638	0.242	0.633	0.246	0.640	0.239	0.585	0.331
<i>rrrr</i>	0.632	0.247	0.617	0.261	0.618	0.260	0.615	0.262	0.614	0.264	0.640	0.240

^a *t*-6 indicates *trans* conformation of 6 bond.

^b *g*-6 indicates *gauche* conformation of 6 bond.

summarized the conformational probabilities of 6–11 bonds of 2,4,6,8,10,12,14,16,18-nonamethylnonadecane (NMND) determined with the five-state RIS model for PP at 100°C which are used for the chemical shift calculation of PP.²⁵ The probabilities of *t* and *g* conformations are listed where a sum of the probabilities of *g* and \bar{g} conformations is noted as *g*. The *t** and *g** conformations (Fig. 2) are not taken into account in the chemical shift calculation and, therefore, the probabilities are not listed. The chemical shift difference relative to the ^{13}C chemical shift of the ^{13}C nuclei in the isotactic sequence can be calculated⁴¹ with Eq. (14).

$$\Delta\delta = \sum \gamma P_{\beta ij} \quad (14)$$

2.3. Polymerization mechanism

Recently, multisite models for olefine (co)polymerization mechanism with a number of heterogeneous Ziegler–Natta catalytic systems have been proposed and their applicability has been proven on the basis of the sequence distribution data given by ^{13}C NMR. In order to confirm the validity of sequence assignments, it is very useful to calculate the relative peak areas by the propagation statistics and to compare them with those observed.

As for propylene polymerization, single-site models, neither a symmetric Bernoullian model,⁴² nor first- and second-order Markovian models,⁴³ can predict the sequence distribution data of PP.^{21,33,34,44–46} The two-site model proposed by Chûjô⁴⁷ and Zambelli *et al.*⁴⁶ provides a good prediction of the pentad sequence distribution.^{33,34} In this model, at one site, propylene polymerization proceeds under the control of symmetric Bernoullian statistics (selection between *meso* and *racemo*), and at the other side under the control of an enantiomorphic model⁴⁸ (asymmetric Bernoullian statistics : selection between *dextro* and *levo*). As shown in Table 6, triad and pentad tacticities can be described with three parameters.³³ Here, α is the probability to select a *d*-unit at a *d*-preferring site in the enantiomorphic site, σ is the probability to select a *meso* configuration in the Bernoullian site, and ω is the weight fraction of the polymer produced at the enantiomorphic site. For convenience the term $\alpha(1-\alpha)$ is replaced by β .

Multisite models have been proposed also for the E–P copolymerization with heterogeneous Ziegler–Natta catalytic systems. In these models, each site is statistically independent and obeys Bernoullian (B) or first-order Markovian (M) models. The model MM (combination of independent first-order Markovian models) has also been applicable for the E–P copolymerization with $\delta\text{-TiCl}_3\text{-Et}_2\text{AlCl}$ and $\text{MgCl}_2/\text{TiCl}_3\text{-Et}_3\text{Al}$ catalytic systems.⁴⁹ The parameters of the model MM are two pairs of P_{11} and P_{22} , corresponding to two independent sites, and the fraction (fp) of a polymer produced at one site. (In general, P_{mm} means the probability of *n*-monomer

Table 6. Description of triad and pentad fractions by the two-site model.^a

	Weight fraction	
	ω	$1 - \omega$
triad		
[<i>mm</i>]	$1 - 3\beta$	σ^2
[<i>mr</i>]	2β	$2\sigma(1 - \sigma)$
[<i>rr</i>]	β	$(1 - \sigma)^2$
pentad		
[<i>mmmm</i>]	$1 - 5\beta + 5\beta^2$	σ^4
[<i>mmm</i> <i>r</i>]	$2\beta - 6\beta^2$	$2\sigma^3(1 - \sigma)$
[<i>rm</i> <i>mm</i>]	β^2	$\sigma^2(1 - \sigma)^2$
[<i>mm</i> <i>rr</i>]	$2\beta - 6\beta^2$	$2\sigma^2(1 - \sigma)^2$
[<i>m</i> <i>m</i> <i>r</i> <i>m</i>]	$2\beta^2$	$2\sigma^3(1 - \sigma)$
[<i>r</i> <i>m</i> <i>r</i> <i>r</i>]	$2\beta^2$	$2\sigma(1 - \sigma)^3$
[<i>r</i> <i>m</i> <i>r</i> <i>m</i>]	$2\beta^2$	$2\sigma^2(1 - \sigma)^2$
[<i>r</i> <i>r</i> <i>r</i> <i>r</i>]	β^2	$(1 - \sigma)^4$
[<i>m</i> <i>r</i> <i>r</i> <i>r</i>]	$2\beta^2$	$2\sigma(1 - \sigma)^3$
[<i>m</i> <i>r</i> <i>r</i> <i>m</i>]	$\beta - 3\beta^2$	$\sigma^2(1 - \sigma)^2$

^a $\beta = \alpha(1 - \alpha)$.

adding to an *m*-monomer-ended chain, where 1 and 2 represents ethylene and propylene, respectively.)

Recently, Cheng and Kakugo⁵⁰ confirmed the site-multiplicity from the ¹³C NMR analysis of the E-P copolymers fractionated by TREF (Temperature Rising Elution Fractionation) experiment. Their results suggest that the E-P copolymer with a heterogeneous Ti-based catalyst is made up from three or four components, each of which obeys Bernoullian statistics.

2.4. Peak simulation

For the confirmation of the assignments produced by a polymerization mechanism, relative peak areas must be accurately obtained. For this purpose, a peak simulation program⁵¹ on a microcomputer has been developed by means of the principle of curve resolution.⁴⁵ In Fig. 3 are shown the *rr*-centred methyl region of the observed ¹³C NMR spectrum of isotactic PP(a), results of curve resolution(c), and the reproduced spectrum(b). This figure indicates the good applicability of the peak simulation program.⁵¹ The program used for this simulation includes the optimization process of the intensities, chemical shifts and the line widths of NMR peaks of Lorentzian distribution functions. Non-linear least-square methods was used in the final step of the optimization.

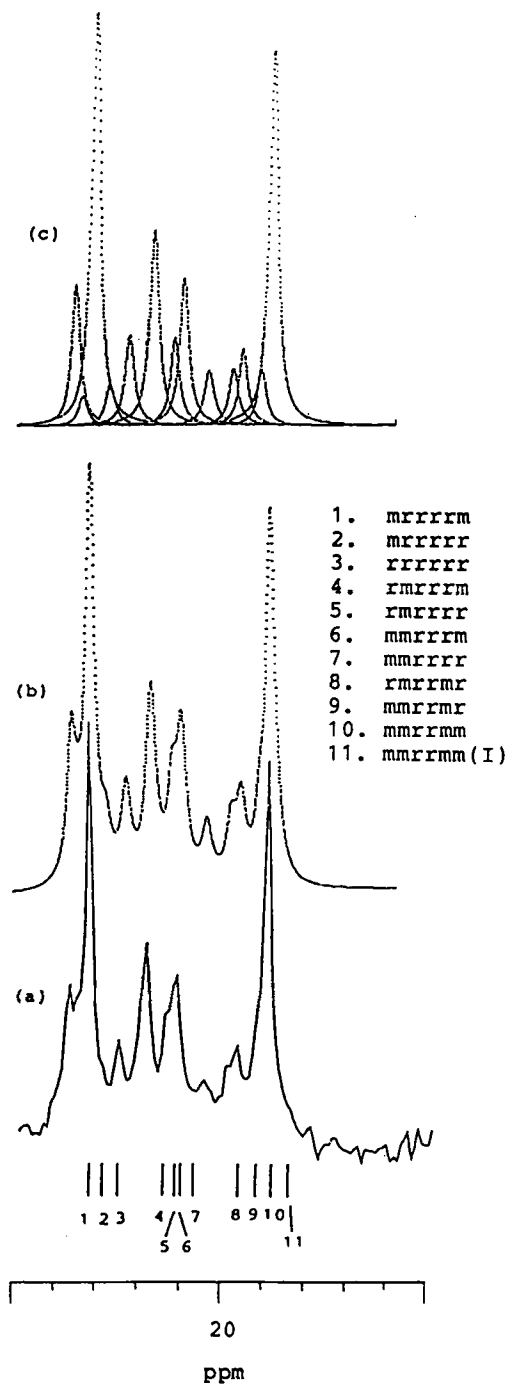


Fig. 3. *rr*-Centred methyl region of the ^{13}C NMR spectrum of isotactic polypropylene. (a) Observed spectrum. (b) Reproduced spectrum. (c) Results of curve resolution.

3. NMR OBSERVATION

3.1. Usual observations including sample preparation

Usual NMR experimental conditions for high-resolution ^1H noise decoupled ^{13}C NMR spectra of polyolefins are as follows.

The sample was dissolved in a 10 mm o.d. glass tube with a mixture of *o*-dichlorobenzene (90 vol%) and benzene- d_6 (10 vol%) in an atmosphere of nitrogen gas. Benzene- d_6 provides the signal for the NMR ^2H internal lock. The concentration of a sample solution is usually 0.10–0.15 g (polymer) cm^{-3} (solvent). As for the ultra-high molecular weight (co)polymers ($\bar{M}_w > 10^6$) and the highly isotactic polymers, the desirable concentration is 0.02–0.07 g (polymer) cm^{-3} (solvent). Hexamethyldisiloxane (about 0.1 cm^3) is added to a sample solution as an internal reference (2.03 ppm, to high frequency of the resonance of tetramethylsilane).

^{13}C NMR spectra were recorded on an NMR spectrometer at high temperatures, 100–150°C. The pulse repetition time (t_r) was set to be at least five times longer than the longest spin-lattice relaxation time of the carbons of interest for the quantitative measurement. For example, t_r was 15 s for the methyl carbon (main chain) of isotactic PP(51), and 25 s for the analysis of chain-end structure of low-molecular weight PP at 120°C.⁵² It is necessary to provide enough high digital resolution for the spectrum.

3.2. INEPT

The ^1H decoupled INEPT (Insensitive Nuclei Enhanced by Polarization Transfer) method^{53,54} is useful for removing ambiguities in the assignments of closed methyl, methine and methylene peaks. The INEPT experiment with a delay time (Δ) of $3/4J^*$ (J^* is the coupling constant between ^{13}C and ^1H) prior to data acquisition distinguishes the methylene peaks from the methine and methyl peaks by the difference of the sign of methylene and other carbon peaks. Only methine peaks, and methyl, methine, and methylene peaks with the same sign are observed when Δ is set to be $2/4J^*$ and $1/4J^*$, respectively. For example, Fig. 7 in Section 4.1.2. shows the distinction between the CH and CH_2 peaks in the ^{13}C spectra of regioirregular PP with the INEPT method.

3.3. INADEQUATE

The 2D INADEQUATE procedure has been developed as a reliable method to determine the connectivity of carbon atoms.^{27,55,56} The carbon-carbon connectivities of a (co)polymer is revealed by a pair of ^{13}C doublets

symmetrically disposed relative to the row frequencies in the 2D-spectrum. By using this method, Hikichi *et al.*²⁹ confirmed the validity of the ^{13}C NMR chemical shift assignments of various types of carbons in the stereoirregular E-P copolymer proposed by Randall.⁵⁷ In Fig. 4 are shown the connectivities of methyl carbons ($P_{\beta\beta}$, $P_{\beta\delta}$, and $P_{\delta\delta}$) with methine carbons ($T_{\beta\beta}$, $T_{\beta\delta}$, and $T_{\delta\delta}$) in the 2D INADEQUATE spectrum of the stereoregular E-P copolymer.³⁰ Pentad comonomer sequence assignments of methine carbons were provided through these connectivities by referring to the methyl pentad assignments, which were made by chemical shift calculations via the γ -effect. The significance of the chemical shift calculation consists in providing the references for the assignments of unidentified peak splittings, because the 2D INADEQUATE spectrum does not directly determine the assignments of peaks but absolutely determines the carbon-carbon connectivities.

The pulse sequence (58) used was $90^\circ\text{-}1/4J\text{-}180^\circ\text{-}1/4J\text{-}90^\circ\text{-}t_1\text{-}135^\circ\text{-acquisition}$ (t_2), where J is a $^{13}\text{C}\text{-}^{13}\text{C}$ coupling. The delay time $1/4J$ was set to be 7.18 ms corresponding to the $^{13}\text{C}\text{-}^{13}\text{C}$ coupling constant of 34.8 Hz. For example, in the 2D INADEQUATE spectrum shown in Section 4.2.2 (Fig. 16), the repetition time of each pulse sequence is 4.5 s. The free induction decays are accumulated 256 times at each mixing time (t_1) and stored in a matrix of 4096×128 . The data matrix was expanded to 8192×256 by zero filling for t_1 and t_2 , and multiplied by the exponential window function prior to the double Fourier transform. The row and column frequencies are 2100 and 4200 Hz with 128, and 4096 data points, respectively.

4. POLYOLEFINES

4.1. Polypropylene, PP

4.1.1. Stereoirregularity

PP is a very important polymer commercially. The tacticity in the chain is most clearly observed in the methyl region of the ^{13}C NMR spectra where the signals are assigned to pentad peaks experimentally as described in the Section 1. It has been demonstrated that such stereosequence-dependent ^{13}C NMR chemical shifts of PP, and the model compounds, can be satisfactorily explained in terms of γ -effects on the ^{13}C chemical shift using the RIS model. Details of the chemical shift calculations of PP and the model compounds are described in Section 2.2. For example, let's describe the heptad assignments of the methyl peaks on the basis of chemical shift calculations.⁵¹

The ^{13}C NMR spectrum of the isotactic PP prepared with $\delta\text{-TiCl}_3/\text{Et}_2\text{AlCl}$ catalytic system (methyl region only) is shown in Fig. 5.⁵¹ The heptad

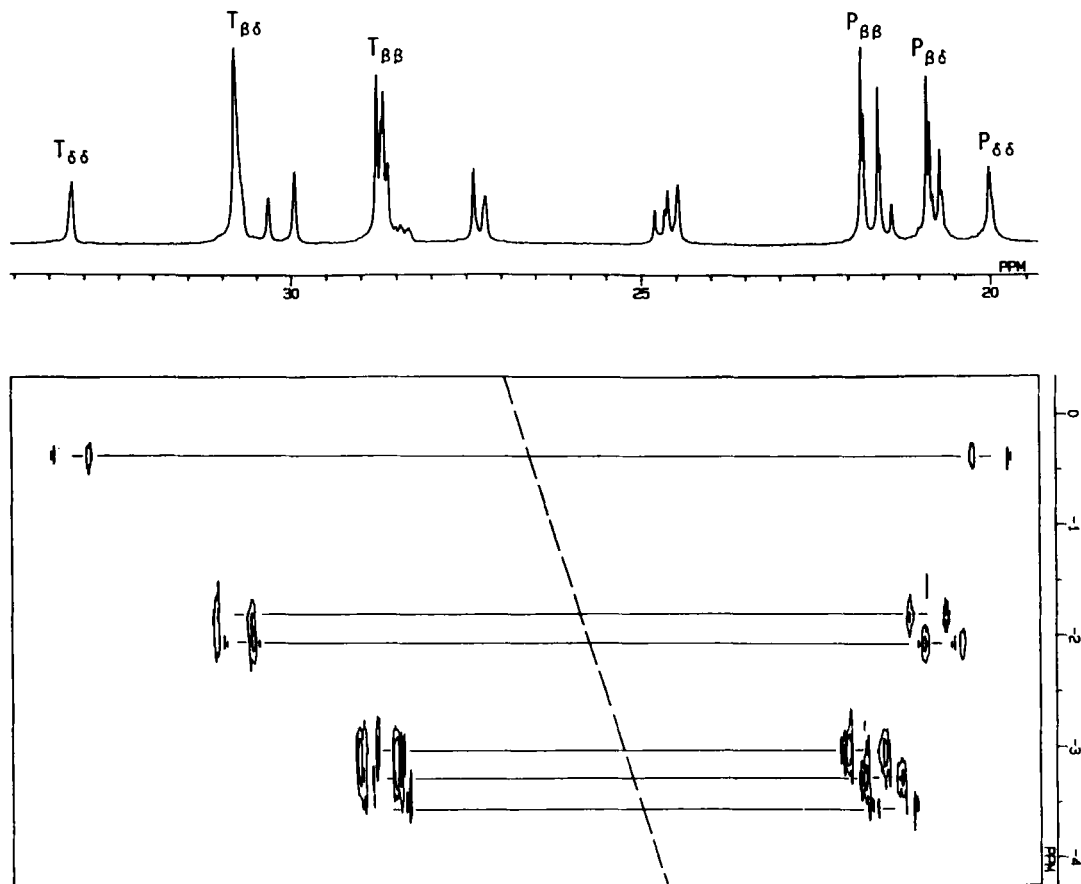


Fig. 4. Resonance regions of methyl and methine carbons in the 2D INADE-QUATE spectrum of the stereoregular ethylene-propylene copolymer.

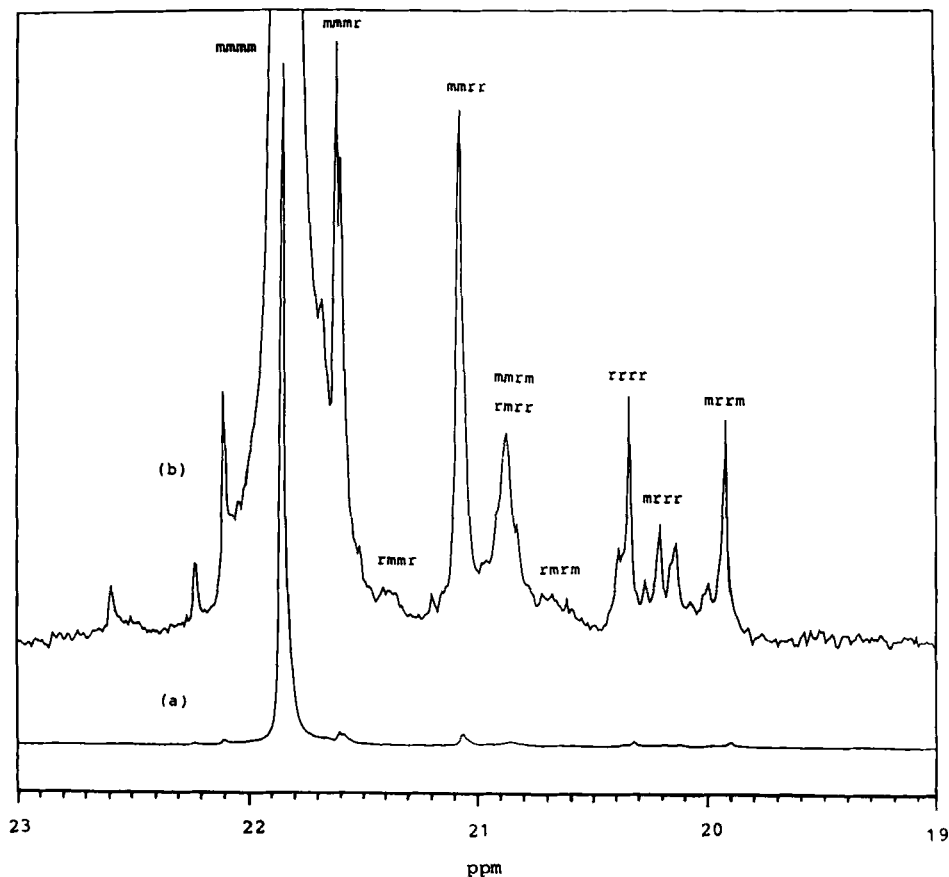


Fig. 5. (a) Methyl resonance region of the ^{13}C NMR spectrum of isotactic polypropylene at 120°C . (b) Expanded spectrum of (a) and pentad assignments.

splittings of the methyl carbon resonances are seen in the expanded spectrum in which the pentad assignments are designated based on those proposed by Zambelli *et al.*¹² On the basis of these pentad assignments, the pentad sequence distribution was obtained. As shown in Table 7, the calculated result by the two-site model (see Section 2.3) agrees well with the observed one. The optimized values of the parameters of the two-site model are as follows: $\alpha = 0.990$, $\omega = 0.938$, $\sigma = 0.351$.

These values indicate that there are isotactic PP (IPP) and atactic PP (APP) chains in this sample. The heptad chemical shifts should be calculated for the stereoisomers in the IPP and APP chains. In Table 8 are listed the values of the chemical shifts calculated for the methyl heptads and pentads at 120°C using the Suter-Flory RIS model²⁰ of PP conformations. The value of -5.3 ppm was taken as the γ -effect of the methine carbon on the

Table 7. Triad and pentad tacticities of the isotactic polypropylene.

Triad	<i>mm</i>	<i>mr</i>	<i>rr</i>
Obsd	0.917	0.048	0.035
Calcd	0.918	0.047	0.035

Pentad	<i>mmmm</i>	<i>mmmr</i>	<i>rmmr</i>	<i>mmrr</i>	<i>mmrm</i> + <i>rmrr</i>	<i>rmrm</i>
Obsd	0.895	0.020	0.002	0.027	0.017	0.005
Calcd	0.893	0.021	0.003	0.024	0.016	0.007

Pentad	<i>rrrr</i>	<i>mrrr</i>	<i>mrrm</i>
Obsd	0.012	0.011	0.012
Calcd	0.011	0.012	0.012

shielding of the methyl carbon.⁶⁰ Calculations were performed for heptad stereoisomers surrounded by isotactic sequences consisting of 30 *meso* dyads and for those by atactic sequences consisting of 30 dyads. To produce the model of atactic sequences, averaging was done after the generation of a Monte Carlo Simulation with a probability of *meso*-selection of 0.5. The calculated chemical shifts of the heptad stereoisomers in the atactic chains agree with the results by Schilling and Tonelli.²¹ The calculated chemical shift differences of the stereoisomers between the IPP and APP chains are from 0.012 to 0.056 ppm. These differences should be considered for the heptad assignments, since the digital resolution of the spectrum is 0.0092 ppm (see typical experimental conditions in Section 3.1). From the calculation of relative peak areas based on $\alpha = 0.990$ and $\omega = 0.938$, it is expected for the IPP sequences that only five heptad peaks should have detectable intensities. The five expected heptads are *mmmmmm*(I) ((I) indicates stereoisomers in IPP chains), *mmmmmr*(I), *mmmmrr*(I), *mmmrmm*(I), and *mmrrmm*(I). In Fig. 3 are shown the *rr*-centred methyl region of the observed spectrum and the calculated chemical shifts (stick spectrum) of heptad sequences. The calculated spectrum well reproduces the profile of the observed heptad splittings. The peak at the lowest frequency is assigned to *mmrrmm*(I) on the basis of the calculated chemical shifts and the other peaks are assigned to heptad resonances in APP chains. The assignments of *mm*- and *mr*-centred heptads are provided similarly. The resultant heptad assignments are shown in Table 9 with the observed and calculated relative peak areas. The good agreement of the calculated relative peak areas with the observed ones indicates the validity of these heptad assignments.

Table 8. Calculated ¹³C chemical shifts^a for the methyl carbon atoms in the heptad stereoisomers situated in the atactic and isotactic chains at 120°C.

Stereoisomer	Atactic chain		Isotactic chain		$\Delta\nu^b$
	ν_A		ν_I		$\nu_A - \nu_I$
	Calcd (heptad)	Calcd (pentad)	Calcd (heptad)	Calcd (pentad)	Calcd (heptad)
<i>m(mmmm)m</i>	-0.047		0.0	0.0	-0.047
<i>m(mmmm)r</i>	-0.094	-0.155	-0.093		-0.001
<i>r(mmmm)r</i>	-0.150		-0.185		0.035
<i>m(mmmr)m</i>	-0.304		-0.301	-0.301	-0.003
<i>m(mmmr)r</i>	-0.269		-0.232		-0.037
<i>r(mmmr)m</i>	-0.360	-0.304	-0.393		0.033
<i>r(mmmr)r</i>	-0.325		-0.323		-0.002
<i>m(rmmr)m</i>	-0.569		-0.602	-0.602	0.033
<i>m(rmmr)r</i>	-0.534	-0.487	-0.532		-0.002
<i>r(rmmr)r</i>	-0.492		-0.463		-0.029
<i>m(mmrm)m</i>	-0.937		-0.932	-0.932	-0.005
<i>m(mmrm)r</i>	-0.909		-0.875		-0.034
<i>r(mmrm)m</i>	-0.996	-0.949	-0.1028		0.032
<i>r(mmrm)r</i>	-0.968		-0.971		0.003
<i>m(mmrr)m</i>	-0.768		-0.734	-0.734	-0.034
<i>m(mmrr)r</i>	-0.793		-0.783		-0.010
<i>r(mmrm)m</i>	-0.826	-0.849	-0.828		0.002
<i>r(mmrm)r</i>	-0.860		-0.878		0.018
<i>m(rmrm)m</i>	-1.220		-1.253	-1.253	0.033
<i>m(rmrm)r</i>	-1.190		-1.193		0.003
<i>r(rmrm)m</i>	-1.174	-1.143	-1.177		0.003
<i>r(rmrm)r</i>	-1.145		-1.118		-0.027
<i>m(rmrr)m</i>	-1.043		-1.044	-1.044	0.001
<i>m(rmrr)r</i>	-1.069		-1.096		0.027
<i>r(rmrr)m</i>	-0.999	-1.040	-0.962		-0.037
<i>r(rmrr)r</i>	-1.024		-1.023		-0.001
<i>m(mrrm)m</i>	-1.977		-2.014	-2.014	0.037
<i>m(mrrm)r</i>	-1.941	-1.892	-1.941		0.0
<i>r(mrrm)r</i>	-1.896		-1.868		-0.028
<i>m(mrrr)m</i>	-1.761		-1.759	-1.759	-0.002
<i>m(mrrr)r</i>	-1.792		-1.821		0.029
<i>r(mrrr)m</i>	-1.719	-1.766	-1.691		-0.028
<i>r(mrrr)r</i>	-1.749		-1.752		0.003
<i>m(rrrr)m</i>	-1.551		-1.523	-1.523	-0.028
<i>m(rrrr)r</i>	-1.580	-1.619	-1.581		0.001
<i>r(rrrr)r</i>	-1.616		-1.640		0.024

^aAll chemical shift values are expressed by ppm relative to that which appeared at the highest frequency, which is set to be 0.00 ppm.

^bNegative values of $\Delta\nu$ indicate that the resonance of the carbon atom in the heptad stereoisomer situated in the atactic chain will occur upfield from its value in the isotactic chain.

Table 9. Assignments and relative peak areas of methyl heptad resonances for highly isotactic polypropylene.

Peak	Assignment		Relative peak area	
	Atactic chain (calcd chemical shift)	Isotactic chain	Obsd	Calcd
0.0	<i>mmmmmr</i> (−0.094) <i>rmmmmr</i> (−0.150)	<i>mmmmmm</i> (0.0) <i>mmmmmr</i> (−0.093) <i>mmmmrr</i> (−0.232)	0.895	0.8926
−0.249			0.014	0.0177
−0.271 ^b	<i>mmmmrr</i> (−0.269) <i>mmmmrm</i> (−0.304) <i>rmmmr</i> (−0.325)		0.004	0.0027
−0.359	<i>rmmmr</i> (−0.360)		0.002	0.0008
−0.495	<i>rrmmrr</i> (−0.492)		0.001	0.0013
−0.520	<i>mrmmrr</i> (−0.534)		0.001	0.0015
−0.546	<i>mrmmrm</i> (−0.569)		0.001	0.0004
−0.793	<i>mmmrmm</i> (−0.768) <i>mmmr</i> (−0.793) <i>rrmmrr</i> (−0.826)	<i>mmmrmm</i> (−0.737)	0.026	0.0215
−0.893	<i>rrmmrr</i> (−0.860)		0.002	0.0027
−0.916	<i>mmmrmm</i> (−0.909)		0.002	0.0008
−0.963	<i>mmmrmm</i> (−0.937) <i>rrmmrr</i> (−0.968)		0.003	0.0019
−0.993	<i>rrmmrr</i> (−0.996) <i>rrmmrr</i> (−0.999) <i>rrmmrr</i> (−1.024)		0.008	0.0077
−1.041	<i>rrmmrr</i> (−1.043) <i>rrmmrr</i> (−1.069)		0.004	0.0042
−1.151	<i>rrmmrr</i> (−1.145)		0.001	0.0027
−1.194	<i>rrmmrr</i> (−1.174)		0.001	0.0015
−1.219	<i>rrmmrr</i> (−1.190)		0.001	0.0015
−1.258	<i>rrmmrr</i> (−1.220)		0.001	0.0008
−1.485	<i>rrmmrr</i> (−1.551)		0.003	0.0013
−1.502 ^c	<i>rrmmrr</i> (−1.580)		0.001	
−1.530	<i>rrmmrr</i> (−1.580) <i>rrmmrr</i> (−1.616)		0.008	0.0096
−1.567 ^c	<i>rrmmrr</i> (−1.616)		0.001	
−1.613	<i>rrmmrr</i> (−1.719)		0.002	0.0027
−1.670	<i>rrmmrr</i> (−1.749)		0.004	0.0050
−1.720	<i>rrmmrr</i> (−1.761)		0.002	0.0015
−1.742	<i>rrmmrr</i> (−1.792)		0.003	0.0027
−1.802	<i>rrmmrr</i> (−1.896)		0.001	0.0013
−1.860 ^c	<i>rrmmrr</i> (−1.941)		0.001	
−1.883	<i>rrmmrr</i> (−1.941)		0.001	0.0015
−1.927	<i>rrmmrr</i> (−1.977)		0.001	0.0004
−1.953		<i>rrmmrr</i> (−2.014)	0.007	0.0088

^aAll chemical shift values are expressed by p.p.m. relative to that which appeared at the highest frequency, which is set to be 0.00 p.p.m.

^b¹³C-satellite overlaps the peak of heptad resonances.

^cAttributable to the nonad peak.

4.1.2. Regioirregularity

^{13}C NMR analysis of regioirregular PP is important because many catalyst systems are known to be non-regiospecific, and head-to-head (H-H) and tail-to-tail (T-T) structures invariably occur to some extent. The ^{13}C NMR chemical shifts of regioirregular PP containing *isolated* H-H and T-T units have been calculated on the basis of the ^{13}C NMR γ -effect and application of the RIS model, taking into account the effect of tacticity.⁶¹ The calculated chemical shifts have been used successfully for the peak assignments.

The assignment of the ^{13}C NMR spectrum of regioirregular PP containing many inverted units is extremely difficult because the spectrum becomes very complex. This is due to the coexistence of several kinds of sequences containing inverted units and also the fine splitting of each carbon peak due to tacticity. Figure 6 shows the ^{13}C NMR spectrum of regioirregular PP containing approximately 40 mol% inverted units with the stick spectra calculated according to the Lindeman-Adams empirical rule.^{11,62} Here, the terminology of Carman *et al.*,⁷⁶ as expanded by Doi⁹⁸ and Smith,⁹⁹ is used for the designation of the carbons. S, T, and P which refers respectively to secondary (CH_2), tertiary (CH), and primary (CH_3) carbons. Two Greek subscripts are used, referring to the distances of the nearest CH groups from the carbon in question. Where four Greek subscripts appear, they refer to the distances of the two nearest CH carbons on each side of the given carbon. Tacticity is also represented by *m(meso)* or *r(racemic)* with a subscript corresponding to the number of CH_2 units between the CH_3/CH units. In addition, in order to avoid confusion, the number of the given carbon in Fig. 6 is designated in parentheses; for example, $\text{T}_{\alpha\beta}(5)$ refers to the "5" carbon in the structure in Fig. 6. The sample is atactic judging from the peak patterns of the carbons, $\text{P}_{\beta\beta}$ and $\text{S}_{\gamma\alpha\alpha\gamma}$.^{21,22} ^{13}C NMR spectral assignments are not easy because of overlapping of the peaks, especially in the region from 30 to 40 ppm. One of the reasons for the complexity of this spectral region, 30–40 ppm, is due to the overlapping of the CH and CH_2 peaks. Therefore, the assignments of these peaks to the CH and CH_2 peaks are performed with the INEPT technique (see Section 3.2), as shown in Fig. 7. The INEPT ($\Delta = 2/4J^*$, where J^* is the ^{13}C - ^1H direct spin-spin coupling) observation gives only the CH spectrum, B. Then, only the CH_2 spectrum, C was obtained from the difference between the ^1H -decoupled, A and INEPT ($\Delta = 2/4J^*$), B spectra. Here, the peak of the CH carbon in the successive head-to-tail (H-T) units, $\text{T}_{\beta\beta}$ was used as a reference. From these spectra, it is observed that all peaks at 36.8–39 ppm are clearly assigned to the CH carbons, and the peaks at 32.6 and 33.4 ppm to the CH_2 carbons. The CH and CH_2 peaks overlap in the spectral region, 34–36.5 ppm, and are assigned to each carbon by the INEPT technique. In addition, small CH_2 peaks which overlap with the CH peak of 31 ppm are detected in the difference spectrum, C. Thus, all of the peaks are classified into the CH,

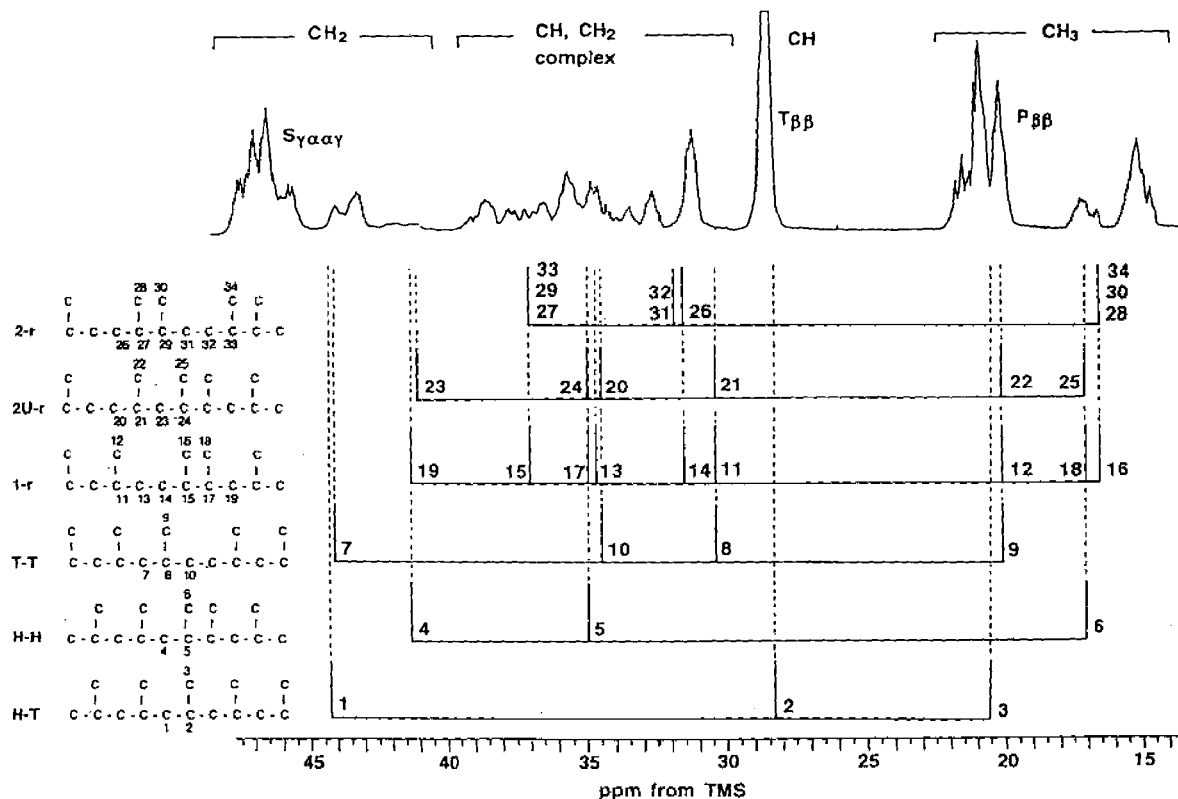
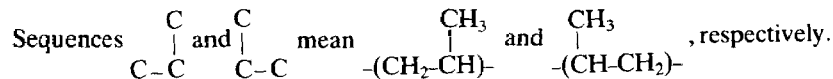


Fig. 6. ^{13}C NMR spectrum of regiorregular PP containing a lot of inverted propylene units (sample concentration 12% (w/v), 15 254 pulses). The stick spectra calculated using the Lindeman-Adams chemical shift empirical rules¹¹ by assuming the presence of several kinds of the sequences in the chain are also shown.



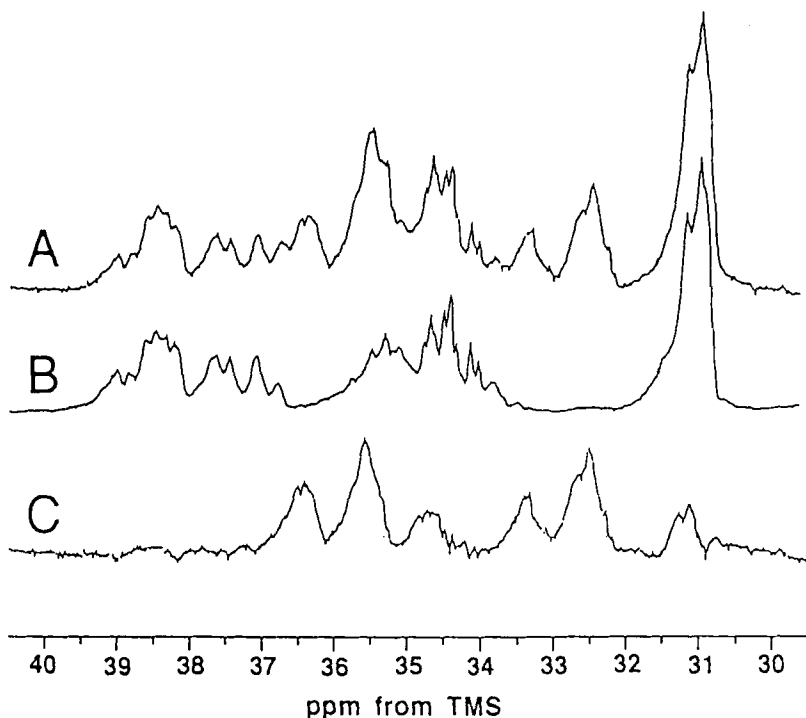


Fig. 7. ^{13}C NMR spectra of regioirregular PP. The spectral region, 29.5–40 ppm, is expanded. (A) ^1H completely decoupled, (B) INEPT ($\Delta = 2/4J^*$, 17 497 pulses) CH only, and (C) differences (A–B), CH_2 only spectra. The CH peak $\text{T}_{\beta\beta}$ carbon in head-to-tail units was used as a reference to obtain the difference spectrum, C.

CH_2 , and CH_3 carbons. In order to continue the assignments, the ^{13}C NMR chemical shifts are calculated according to the Lindeman–Adams empirical rule by assuming the presence of five kinds of sequences containing H–H and/or T–T units in the sample. The calculated results are shown in Fig. 6 as stick spectra. However, it is difficult to assign these peaks to the individual carbons of the sequences assumed although it is possible to speculate on the presence of several kinds of sequences from a comparison of the calculated and observed chemical shifts. Thus, 2D INADEQUATE (see Section 3.3) observation is applied to the peak assignment.

Figure 8 shows the 2D INADEQUATE spectrum of the regioirregular PP. The ^{13}C – ^{13}C connectivities of the carbons in the isolated H–H and T–T units are shown as solid and broken lines, respectively. The assignment of the peaks, which are attributable to the carbons in these units, is relatively easy. The assignments due to the tacticity are also possible at the dyad level. In the region 14.5–17.8 ppm the low frequency peak at 14.7–15.1 ppm has been assigned to be the carbon, $r_0\text{-P}_{\alpha\beta}$, and the high frequency peak at

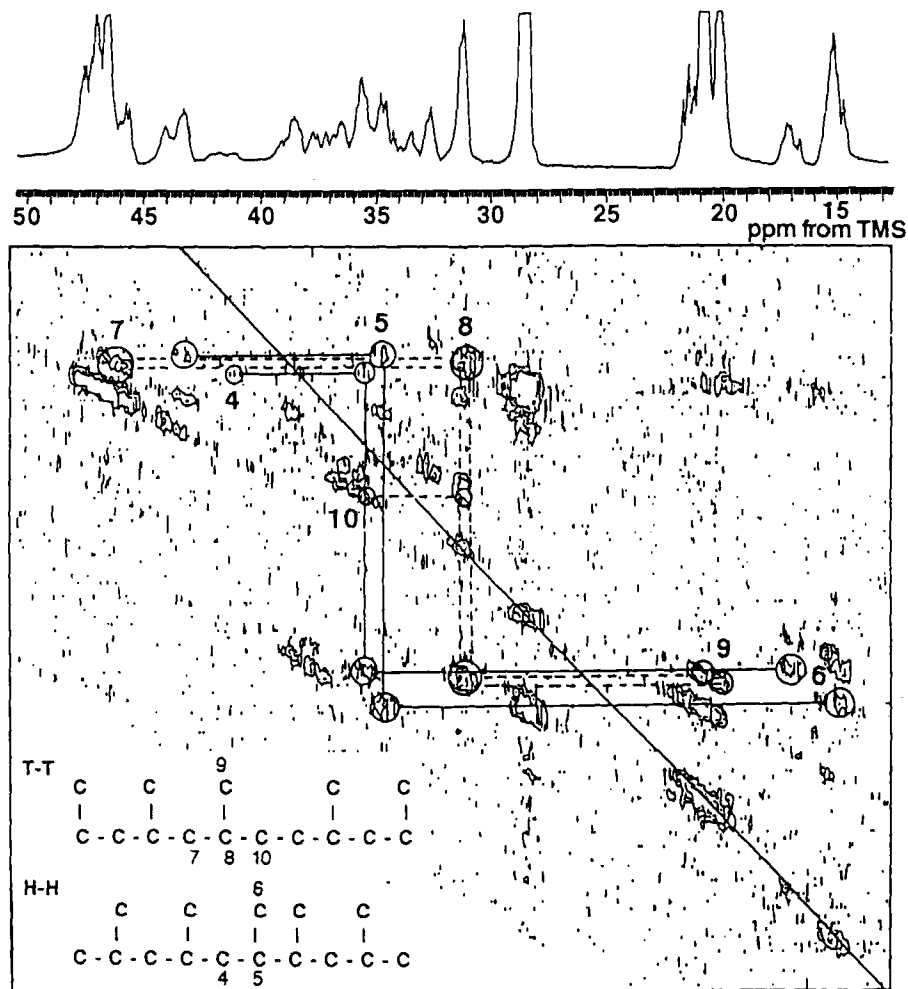


Fig. 8. The 2D INADEQUATE ^{13}C NMR spectrum of regioirregular PP. The ^{13}C - ^{13}C connectivities of the carbons in the isolated head-to-head and tail-to-tail units are shown as solid and broken lines, respectively.

16.6–17.2 ppm is assigned to $m_0\text{-P}_{\alpha\beta}$ in the H-H unit of PP.^{61,64} Therefore, in the CH spectrum of Fig. 6 B, the spectral region 34.2–35.6 ppm is assigned to the carbon, $\text{T}_{\alpha\beta}(5)$ in the H-H units from the ^{13}C - ^{13}C connectivities (solid lines). The peaks at 34.2–34.8 ppm are assigned to the $r_0\text{-T}_{\alpha\beta}$ carbon and the peaks, 35.4–35.6 ppm to $m_0\text{-T}_{\alpha\beta}$ carbon. Similarly, in the region of 40–45 ppm, the peaks at 40.9–42.3 ppm are assigned to $m_0\text{-S}_{\beta\alpha\gamma}$,⁴² and the ones at 43.3–44.1 ppm to $r_0\text{-S}_{\beta\alpha\gamma}$, which are surely observed in the spectrum of the PP sample with predominantly isolated

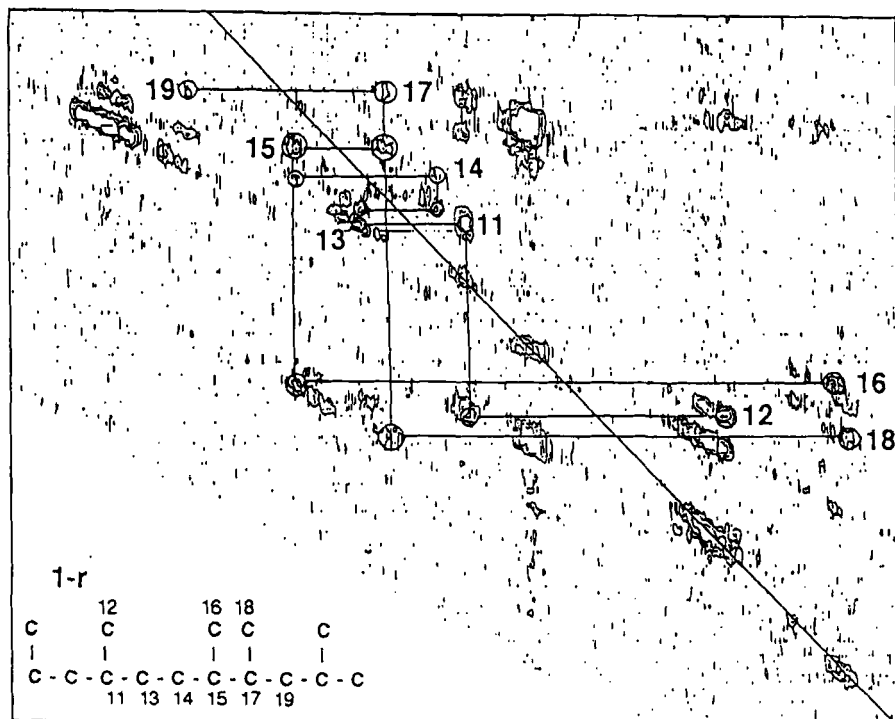


Fig. 9. The 2D INADEQUATE ^{13}C NMR spectrum of regioirregular PP. The ^{13}C - ^{13}C connectivities of the carbons in the sequence 1-r, where a single inverted unit in the successive head-to-tail units is shown as solid line.

H-H and T-T units.⁶¹ Further splittings of these peaks are due to the tacticity and also the presence of other carbons in the sequences which do not contain the isolated H-H and T-T units. The assignments of the peaks of the carbons in the isolated T-T unit are also performed by the 2D INADEQUATE method. However, there are many other ^{13}C - ^{13}C connectivities, clearly indicating the presence of other sequences containing H-H and T-T units.

The appearance of the peak at 32.6 ppm, assigned to the $S_{\delta\beta\alpha\beta}$ (14) carbon, indicates the presence of the sequence 1-r (see Fig. 6). This is supported by the ^{13}C - ^{13}C connectivities of the 2D INADEQUATE spectrum (solid line in Fig. 9). Grassi *et al.*⁶⁵ have reported the ^{13}C NMR spectrum of *isotactic* regioirregular PP containing exclusively the sequence, 1-r in the successive H-T units. Their data constitute a reference for the chemical shifts of the isotactic peaks of the sequence 1-r. By comparison, the absence of the m_0 - $S_{\delta\beta\alpha\beta}$ peak in the spectrum of Fig. 6 is clearly indicated because there are no peaks around 30.4 ppm. Thus, there are

^{13}C - ^{13}C connectivities between $r_0\text{-P}_{\alpha\beta}$ and $r_0\text{-S}_{\beta\alpha\alpha\gamma}$, but no connectivities between the $m_0\text{-P}_{\alpha\beta}$ and $r_0\text{-S}_{\beta\alpha\alpha\gamma}$ peaks.

Nine kinds of carbons, 11–19 in the sequence, 1-*r* can be assigned through the ^{13}C - ^{13}C connectivities (Fig. 9). The peaks of three kinds of CH carbons, $\text{T}_{\delta\beta\gamma\delta}$ (11), $\text{T}_{\delta\gamma\alpha\gamma}$ (15), and $\text{T}_{\delta\alpha\beta\delta}$ (17) are observed. The peak position of the $\text{T}_{\delta\beta\gamma\delta}$ carbon in the sequence 1-*r* coincides with that of the $\text{T}_{\delta\beta\gamma\delta}$ carbon in the isolated T-T unit. In addition, the peak of the $r_0\text{-T}_{\delta\alpha\beta\delta}$ carbon, which is separated from the CH_2 peaks by the INEPT technique (Fig. 7), appears at 34.5 ppm, the same region as the peak of the carbon, $r_0\text{-T}_{\alpha\beta}$ in the H-H unit.

There are also three kinds of CH_2 carbons, $\text{S}_{\gamma\alpha\beta\gamma}$ (13), $\text{S}_{\delta\beta\alpha\beta}$ (14), and $\text{S}_{\beta\alpha\alpha\gamma}$ (19), in the sequence, 1-*r*. The peak at 32.6 ppm is assigned to the $r_0\text{-S}_{\delta\beta\alpha\beta}$ carbon as mentioned above. In the resonance region, 34–36.7 ppm, three CH_2 peaks are observed (Fig. 6). The most shielded peak has already been assigned to the $m_1\text{-S}_{\gamma\beta\beta\delta}$ carbon and the centre peak to the $r_1\text{-S}_{\gamma\alpha\beta\delta}$ carbon. The ^{13}C NMR chemical shifts of the $\text{S}_{\gamma\alpha\beta\gamma}$ carbons in the sequence, 1-*r*, are calculated on the basis of the γ -shielding effect and the RIS model. The chemical shifts of the same carbons are also calculated with the empirical rules reported by Cheng and Bennett (details are shown in Section 2.1.2). The results are listed in Table 10. Both calculated results indicate that the peak of the $r_1\text{-S}_{\gamma\alpha\beta\gamma}$ carbon should be deshielded by *c.* 0.6–1 ppm from the peak of $m_1\text{-S}_{\gamma\alpha\beta\gamma}$ carbon, where m_1 and r_1 mean the tacticity indicated by the arrow in Table 10. Thus, the CH_2 peak at 36.5 ppm is assigned to the $r_1\text{-S}_{\gamma\alpha\beta\gamma}$ (13) carbon in the sequence 1-*r*. The peak at

Table 10. ^{13}C chemical shifts of the carbon $\text{S}_{\gamma\alpha\beta\gamma}$ in the sequence 1-*r* calculated in the pentad level on the basis of the ^{13}C γ -effect and RIS model, A, and with the empirical additive rules proposed by Cheng and Bennett, B [in ppm from $m_1m_1m_2r_0$ (assumed to be 0 ppm)].

	$ \begin{array}{ccccccc} & m_1 & & m_1 & & m_2 & & m_0 \\ & r_1 & & r_1 & & r_2 & & r_0 \\ \text{C} & & \text{C} & & \text{C} & & \text{C} & \text{C} \\ & & & \downarrow & & & & \\ \text{C}-\text{C}-\text{C}-\text{C}-\text{C}-\text{C}-\text{C}-\text{C} \\ & & & & & & \text{S}_{\gamma\alpha\beta\gamma} & \end{array} $			
Sequence	A		B	
$m_1m_1m_2r_0$	0.00		0.00	
$m_1m_1r_2r_0$	-0.09		-0.08	
$m_1r_1r_2r_0$	0.86		1.07	
$m_1r_1m_2r_0$	0.92		1.18	
$r_1r_1m_2r_0$	0.75		1.04	
$r_1r_1r_2r_0$	0.68		0.92	
$r_1m_1r_2r_0$	0.13		0.08	
$r_1m_1m_2r_0$	0.22		0.16	

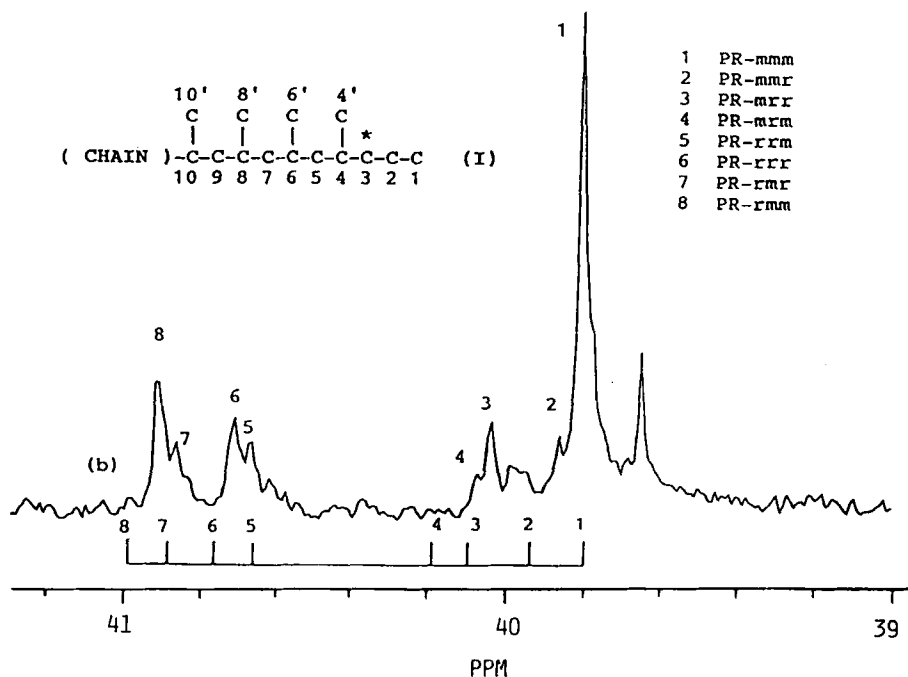


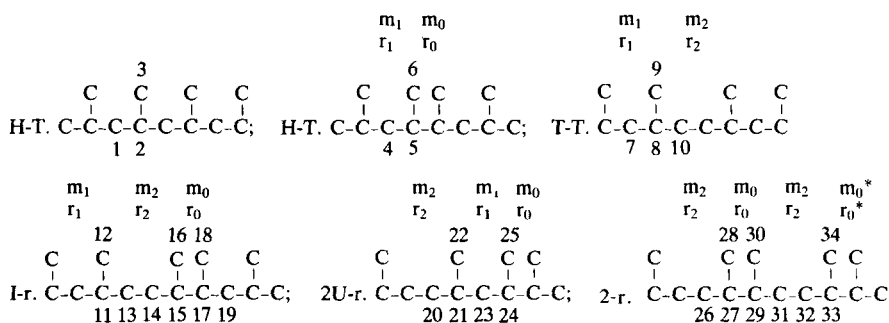
Fig. 10. Resonance region from 39 to 41 ppm in the ¹³C NMR spectrum of boiling heptane soluble fraction of isotactic polypropylene prepared with δ-TiCl₃/Et₂AlCl catalytic system. The predicted chemical shifts of carbon 3-(I) are shown as the stick spectrum at the bottom of the observed spectrum.

35.5 ppm, which is already assigned to the r_1 -S_{γαβδ} carbon in the isolated T-T unit, might contain the m_1 -S_{γαβγ} carbon in the sequence, 1-*r*. The peak of the r_0 -S_{βααγ}(19) carbon is observed at 43–44 ppm, where the peak of the r_0 -S_{γααβ} carbon in the H-H unit also appears. The CH₃ peaks of the carbons, r_0 -P_{δγαγ}(16) and r_0 -P_{δαβδ}(18) in the sequence 1-*r* coincide with the peak of the r_0 -P_{αβ} carbon in the isolated H-H unit. There still remain other ¹³C-¹³C connectivities and therefore it is necessary to consider the presence of other sequences in this regioirregular PP. The peaks of the carbons in the sequence 2U-*r*, where two successive inverted units in the H-T units are involved, and in the sequence 2-*r*, where an inversion occurs, followed by a second inversion are also assigned. The chemical shifts and final assignments are summarized in Table 11. The terminology of Cheng⁴² is used for the designation of the carbons.

Table 11. ^{13}C chemical shift assignments of regioirregular polypropylene.

Chemical shift (ppm from TMS)	H-T	H-H	T-T	1-r	2U-r	2-r
45.7–47.7	$S_{\gamma\alpha\gamma}(1)$					
45.7–46.5			$S_{\gamma\alpha\delta}(7)$			
43.3–44.1		$r_0-S_{\beta\alpha\gamma}(4)$		$r_0-S_{\beta\alpha\gamma}(19)$	$S_{\beta\alpha\beta}(23)$	
40.9–42.3		$m_0-S_{\beta\alpha\gamma}(4)$				
36.8–39.1				$r_0-T_{\delta\gamma\gamma}(15)$		$T_{\delta\alpha\gamma\delta}$ (27 and 29) $T_{\delta\gamma\alpha\gamma}(33)$
36.5				$r_1-S_{\gamma\alpha\beta\gamma}(13)$		
35.4–35.6		$m_0-T_{\alpha\beta}(5)$	$r_1-S_{\gamma\alpha\beta\delta}(10)$	$m_1-S_{\gamma\alpha\beta\gamma}(13)$	$r^1-S_{\gamma\alpha\beta\delta}(20)$	
34.2–34.8		$r_0-T_{\alpha\beta}(5)$	$m_1-S_{\gamma\alpha\beta\delta}(10)$	$r_0-T_{\delta\alpha\beta\delta}(17)$	$m_0-T_{\alpha\beta}(24)$ $m_1-S_{\gamma\alpha\beta\delta}(20)$ $r_0-T_{\alpha\beta}(24)$	
33.4						$r_0-S_{\beta\alpha\beta\gamma}(31)$
32.6				$r_0-S_{\delta\beta\alpha\beta}(14)$		$r_0-S_{\delta\beta\alpha\beta}(26)$
31.1–31.3			$T_{\delta\beta\gamma\delta}+(8)$	$T_{\delta\beta\gamma\delta}(11)$	$T_{\delta\gamma\beta\gamma}(21)$	$m_0^*-S_{\gamma\beta\alpha\beta}(32)^a$
28.3–28.4	$T_{\beta\beta}(2)$					
20.1–21.7	$P_{\beta\beta}(3)$					
20.1–20.9			$m_1-P_{\beta\gamma}(9)$	$m_1-P_{\delta\beta\gamma\delta}(12)$	$m_1-P_{\delta\gamma\beta\gamma}(22)$	
16.6–17.2		$m_0-P_{\alpha\beta}(6)$	$r_1-P_{\beta\gamma}(9)$	$r_1-P_{\delta\beta\gamma\delta}(12)$	$r_1-P_{\delta\gamma\beta\gamma}(22)$	$m_0-P_{\delta\gamma\alpha\gamma}(34)$
14.7–15.1		$r_0-P_{\alpha\beta}(6)$		$r_0-P_{\delta\gamma\alpha\gamma}(16)$	$m_0-P_{\delta\beta\alpha\gamma}(25)$ $r_0-P_{\delta\beta\alpha\gamma}(25)$	$r_0-P_{\delta\alpha\gamma\delta}$ (28 and 30)

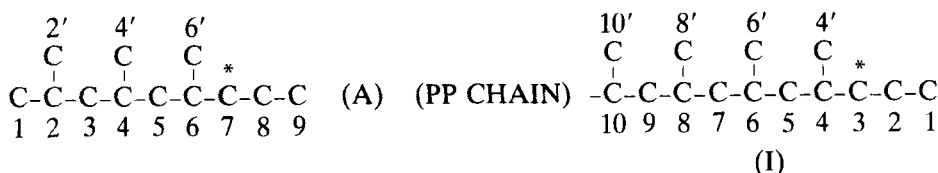
See structure below

^aTentative assignment

4.1.3. Chain end

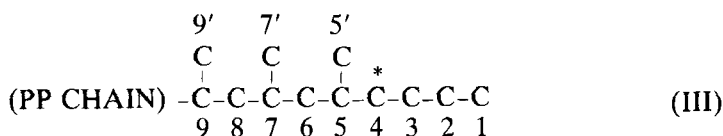
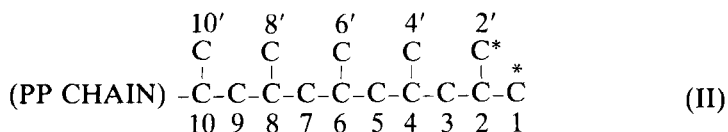
Tactic structures at the chain-end of PP have been investigated by the chemical shift calculation via the γ -effect.⁶⁶ In Fig. 10 is shown the region from 39 to 41 ppm in the spectrum of the boiling heptane soluble fraction of isotactic PP prepared with $\delta\text{-TiCl}_3/\text{Et}_2\text{AlCl}$ catalytic system. By referring to

the chemical shifts of carbon 7 in the *m* and *r* forms of compound (A)(67), the observed peak at 39.8 ppm is assigned to carbon 3(3-I)) in the chain-end structure (I).



(The chemical shifts of carbon 7 in the *m*- and *r*-forms in compound (A) are 40.19 and 40.92 ppm, respectively.⁶⁷⁾

However, the assignments of a number of split peaks in this spectrum from the chemical shifts of model compound (A) are impossible, because it is expected that the chemical shift of carbon-3(I) is affected by a configurational sequence longer than the dyad. The chemical shift calculation via the γ -effect was therefore performed on carbon 3-(I) in the tactic tetrads, which are determined by the configurational relationships among the methine carbons 4, 6, 8, and 10. The isotactic polypropylene chain including structure (I) is simplified to be composed of 20 m dyads followed by the chain-end C10-C1 carbons. Mark's RIS model⁶⁸ was used and the value of -3.7 ppm was taken as the γ -effect of the methyl and methylene carbons on the chemical shift of the methylene carbon. The calculated results are shown in Table 12. The designation, PR-tetrad, means *n*-propyl chain-end group and the following tetrad sequence. The peak observed at 39.8 ppm is assigned to carbon 3-(I) of PR-*mmm* tetrad, because this peak is predicted to be the most highly shielded as illustrated by a stick spectrum (calculated). By comparison between the observed and calculated spectra, the assignments of the split peaks, numbered 1-8, are provided as shown in Table 12. Tacticities in chain-end structures (II) and (III) were similarly evaluated from the split peaks of the methyl carbons 1 and 2' (structure (II)) and from the methylene carbon 4 (structure(III)), respectively.⁶⁶⁾



These results provide information of steric control of the initiation and termination reactions of propylene polymerization.

Table 12. The observed and calculated chemical shift differences ($\Delta\nu$) of carbon 3 in structure (I) and the chemical shifts (ν) observed in the spectrum of boiling heptane soluble fraction of isotactic polypropylene.

					10'	8'	6'	4'						
					C	C	C	C						
(PP CHAIN)					-C-	C-	C-	C-	C-	C-	C-	C-	C-	(I)
					10	9	8	7	6	5	4	3	2	1

Sequence	Peak no.	ν_{Obsd} (ppm)	$\Delta\nu^a_{\text{Obsd}}$ (ppm)	$\Delta\nu^a_{\text{Calcd}}$ (ppm)
PR-tetrad				
PR- <i>mmm</i>	1	39.80	0.0	0.0
PR- <i>mmr</i>	2	39.86	0.06	0.141
PR- <i>mrr</i>	3	40.03	0.23	0.299
PR- <i>rrm</i>	4	40.07	0.27	0.400
PR- <i>rrr</i>	5	40.66	0.86	0.872
PR- <i>rrr</i>	6	40.71	0.91	0.958
PR- <i>rmr</i>	7	40.86	1.06	1.085
PR- <i>rrm</i>	8	40.91	1.11	1.191

^aAll chemical shift values are expressed by ppm relative to that of the appeared at the highest frequency, which is set to be 0.00 ppm.

4.2. Poly(1-butene), PB

4.2.1. Stereoirregularity

The success of the calculations of the γ -effects on the ^{13}C chemical shift, using the RIS model for four kinds of carbons in PB, has underlined the usefulness of such calculations as described in Section 1. Especially, the dramatic change in the observed ^{13}C NMR spectra of the backbone methylene carbons between PP and PB can be interpreted very well in terms of the chemical shift calculation.

The chemical shifts of the methylene C9 and methine C10 of the backbone chain, methylene C10 and methyl C10 of the side-chain of the diastereomers of 2,4,6,8,10,12,14,16,18-nonaethylnonadecane (NEND) as a PB model are calculated on the basis of the γ -effect and the five-state RIS model for PP except for the presence of additional repulsive interactions between the ethyl group of the side-chain and backbone when both adjacent backbone bonds are *t*.²⁴ The statistical weight of such interactions is introduced as a term of τ^* (<1) (Section 2.2.1). Figure 11 shows the observed spectra of the methylene carbons of the side-chain of PB and the methyl carbons of PP at 100°C along with the calculated stick spectra of the C10 methylene carbon of NEND and C10 methyl carbon of NMND at the pentad level. The spread of the methylene peak of PB, due to the tacticity, is well reproduced when τ^* is equal to 0.6. Thus, it is possible to assign easily the peak by pentad tacticity. The assigned order of the pentad

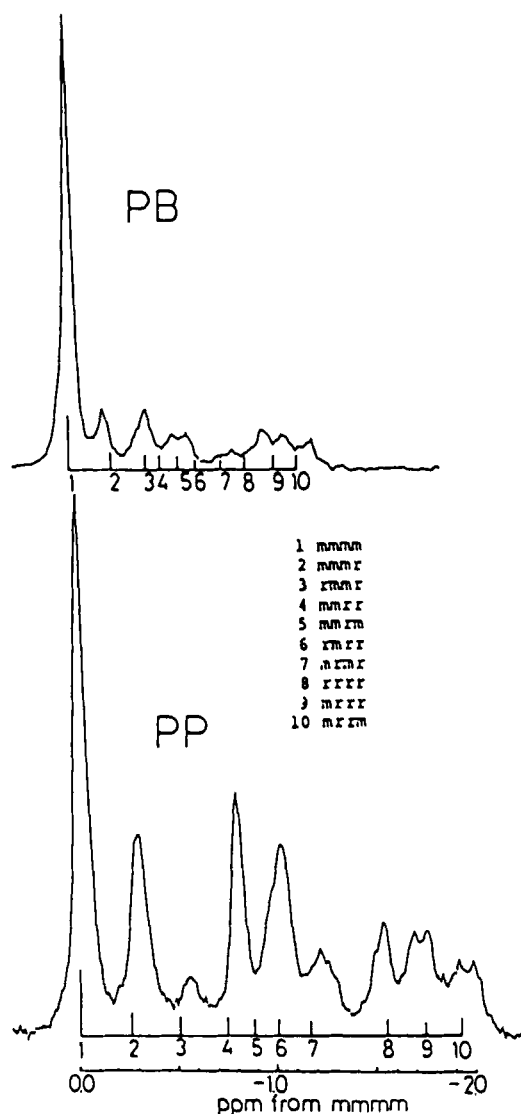


Fig. 11. ^{13}C NMR spectra of the methylene carbon of the side chain of isotactic PB and the methyl carbon of atactic PP at 100°C at the pentad level for the C_{10} methylene carbon of NEND and the C_{10} methyl carbon of NMND appear below. These spectra are expressed relative to the mmmm pentad (most deshielded stereoisomer) set at 0.0 ppm.

chemical shifts of PB is in agreement with that of PP, while the spread of chemical shifts is small in the former.

However, a dramatic change in the ^{13}C NMR spectra of the methylene backbone carbons is observed between PP and PB. The observed spread of the methylene chemical shifts of PP exceeds 2 ppm, while that of PB is only 0.2 ppm as shown in Fig. 12. On the basis of the calculated stick spectra for the C9 carbon of NMND, as shown in Fig. 12, the methylene peak of PP can be interpreted in terms of the hexad tacticity. In the case of PB, if only the chemical shift contribution of the γ shielding effect from the carbons of the backbone chain on the specified methylene carbon is taken into account, then the peak spread of the hexad level splitting should be still large (approximately 2 ppm). However, in contrast to the case of PP, there is an additional γ -shielding effect between the methylene backbone and methyl side-chain carbons. The contribution from the side-chain methyl carbons can be evaluated in addition to that of the backbone carbons to the ^{13}C chemical shifts of the methylene carbons of the backbone chain. The most striking aspect is the compensation of the γ -effect contribution to the specified methylene carbon from the backbone methylene carbons and the side-chain methyl carbons as shown in Fig. 13. As a result, the sum of these two contributions reflects the remarkable decrease of the chemical shifts due to the stereochemical configuration of the chain, as observed in the spectra. According to the calculated chemical shift data, the observed doublet peaks are assigned to *r* (deshielded) and *m* (more shielded) dyads. Thus, in order to interpret the origin of the ^{13}C chemical shifts of the backbone methylene carbons consistently for both PP and PB, we must examine the origin in the hexad level.

This theoretical assignment of PB is confirmed from the agreement of the relative intensities of each of the four carbon peaks in PB (25). Figure 14(a) shows the observed and simulated ^{13}C NMR spectra of the methylene carbon in the backbone chain of PB, together with the decomposed spectra assuming a Lorentzian shape. The fractions of *m* and *r* dyads were determined from the relative intensities in the resonance region split into two peaks, although a slightly asymmetric *r* peak implies the appearance of tetrad splitting. The fraction of *meso* is 0.753, which leads to isotacticity of this PB sample. The ^{13}C NMR spectrum of the methylene carbon of the side-chain makes it possible to evaluate the pentad tacticity of the PB chain as shown in Fig. 14b. The only overlapped pentad peak is *rmmr* + *mmrr*; however, the individual intensities can be evaluated with the aid of the following relations (1):

$$mmmr + 2rmmr = mmrm + mmrr \quad (15)$$

$$mrrr + 2mrrm = rrmr + mmrr \quad (16)$$

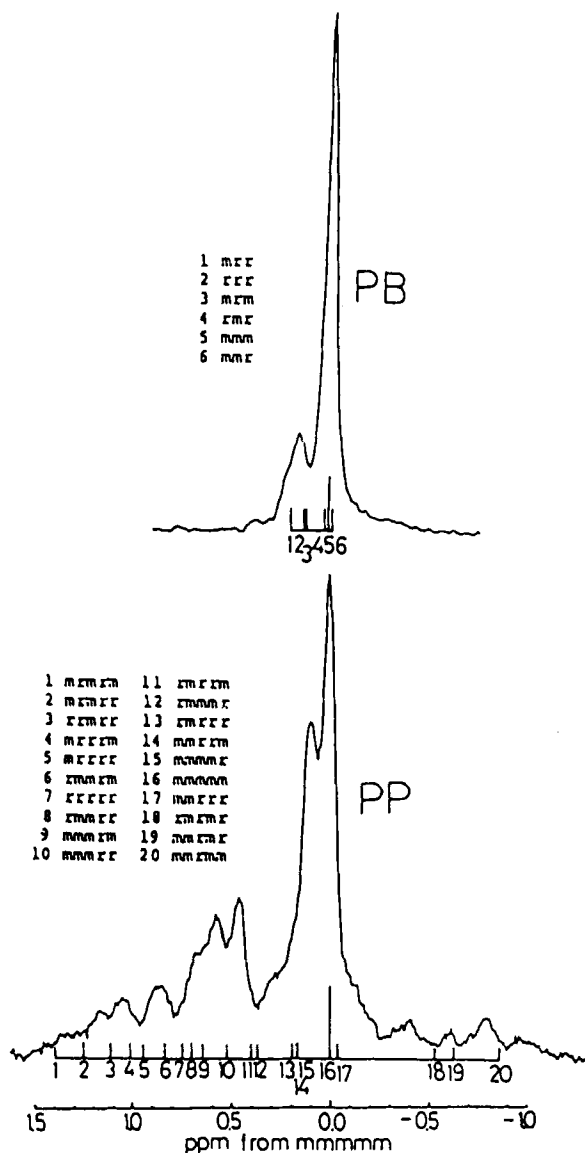


Fig. 12. ^{13}C NMR spectra of the methylene carbons of the backbones of isotactic PB and atactic PP at 100°C . Stick spectra calculated at 100°C at the tetrad (C9 methylene carbon on NMND) levels are also shown below. These spectra are expressed relative to the isotactic peaks (*mmm* tetrad for NEMD and *mmmm* pentad for NMND) set at 0.0 ppm.

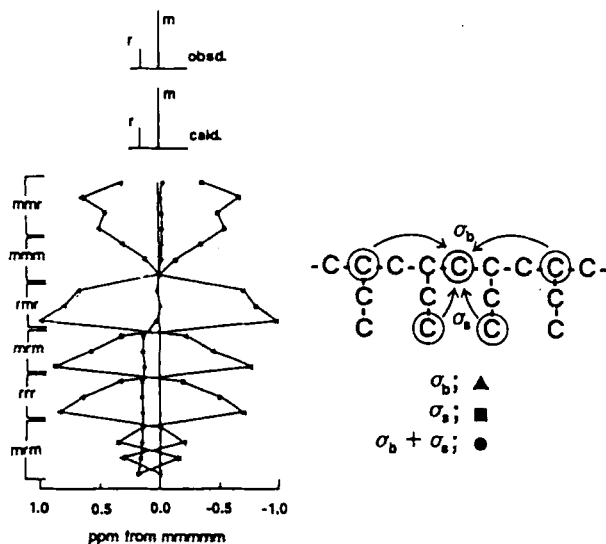


Fig. 13. Calculated hexad chemical shifts for the C1 carbon of PB relative to *mmmmm*. The observed and calculated chemical shifts are shown as stick spectra.

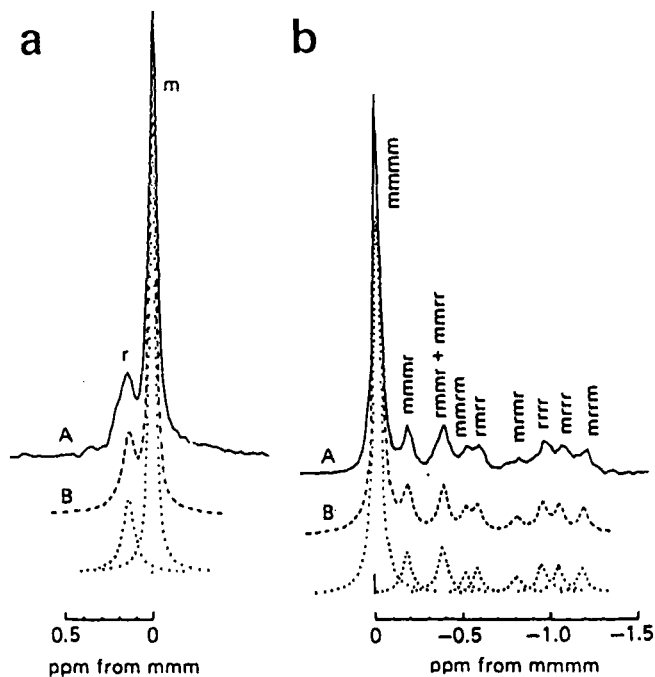


Fig. 14. ^{13}C NMR spectra of methylene carbon of the backbone (a) and the side-chain (b) of PB. A, observed spectrum; B, simulated spectra assuming Lorentzian line shapes.

Table 13. Analysis of ¹³C data of poly(1-butene). Dyad: *m* 0.753, *r* 0.247; Triad: *mm* 0.669, *mr* 0.188, *rr* 0.143.

Pentad	Obsd	Bernoulli trial ^a	Error	First- order Markov ^b	Error	Second- order Markov ^c	Error	Bicatalytic sites model ^d	Error
<i>mmmm</i>	0.583	0.321	0.262	0.514	0.069	0.580	0.003	0.585	-0.002
<i>mmm</i> <i>r</i>	0.079	0.211	-0.132	0.145	-0.066	0.097	-0.018	0.079	0.000
<i>rm</i> <i>mr</i>	0.007	0.035	-0.028	0.007	0.000	0.004	-0.003	0.019	-0.012
<i>mm</i> <i>rm</i>	0.036	0.211	-0.175	0.065	-0.029	0.038	-0.002	0.032	0.004
<i>mm</i> <i>rr</i>	0.078	0.069	0.009	0.099	-0.021	0.070	0.008	0.085	-0.007
<i>rm</i> <i>rr</i>	0.032	0.069	-0.037	0.009	0.023	0.027	0.005	0.038	-0.006
<i>rm</i> <i>rr</i>	0.042	0.023	0.019	0.065	-0.023	0.050	-0.008	0.046	-0.004
<i>m</i> <i>rr</i> <i>m</i>	0.043	0.035	0.008	0.022	0.021	0.028	0.015	0.042	0.001
<i>m</i> <i>rr</i> <i>r</i>	0.045	0.023	0.022	0.068	-0.023	0.069	-0.024	0.046	-0.001
<i>r</i> <i>rr</i> <i>r</i>	0.055	0.004	0.051	0.052	0.003	0.043	0.012	0.054	0.001
SD ^e			0.117		0.037		0.013		0.005

^a $4 \cdot mm \cdot rr / (mr)^2 = 10.9$, $Pm = 0.753$.

^b $P(m/r) = 0.123$, $P(r/m) = 0.359$.

^c $Pmm/m = 0.931$, $Pmr/m = 0.362$, $Prr/m = 0.553$, $Prr/m = 0.441$.

^d $\alpha = 0.041$, $\sigma = 0.453$, $\omega = 0.705$

^eStandard deviation.

The individual pentad intensities are listed in Table 13 as well as the tacticities obtained from the other carbon peaks.

The peaks of the methyl carbons of the side-chains are also assigned to pentad on the basis of the chemical shift calculations.²⁵ Although greater overlap of the pentad peaks was observed than for the methylene carbon of the side-chain, the pentad intensities evaluated from the peak simulation are in excellent agreement with the methylene (side-chain) pentad. Similarly, the methine carbon peaks are assigned to triad, partially pentad.²⁵ The relative intensities for dyad, triad and pentad level (Table 13) are evaluated from the methylene (main-chain), methine (main-chain) and methylene (side-chain) carbon resonances, respectively. The tacticities of PB determined from the four kinds of carbon peaks agreed very well with each other, supporting the validity of the assignment performed on the basis of the chemical shift calculations.

Using the relative intensities at the pentad level, the polymerization mechanism (Section 2.3) of PB can be examined. Fitting to symmetric Bernoullian, first- and second-order Markovian polymerization models¹ was tried. In addition, the bicatalytic sites model of Pino⁶⁹ was examined. The calculated values are summarized in Table 5 together with the optimum values of the probability. Among Bernoullian, first- and second-order Markovian models, the last model with a standard deviation, SD, of 0.013 is

the most appropriate. The bicatalytic sites model with an σ_D of 0.005 is, however, better than any Markovian model. Therefore, the polymerization mechanism of this PB can be described with the bicatalytic sites model as well as PP.³⁴

4.2.2. Regioirregularity

A large number of ^{13}C NMR peaks are observed in the ^{13}C NMR spectrum of regioirregular PB because of the coexistence of several kinds of sequences containing inverted monomer units and the splitting due to the tacticity. In this sample, the assignments are performed by the ^{13}C NMR Lindeman–Adams empirical rule, INEPT and two-dimensional INADEQUATE ^{13}C NMR techniques.⁷⁰

Figure 15 shows the ^{13}C NMR spectrum of the regioirregular PB sample with a large number of chemical inversion units. The ^{13}C chemical shifts calculated according to the ^{13}C NMR Lindeman–Adams empirical rule¹¹ for the prediction of ^{13}C chemical shifts of alkanes are also shown as stick spectra by assuming the presence of several kinds of sequences containing the chemical inversion units.⁶² This sample is atactic judging from the relative peak intensities of the carbons located at the regular head-to-tail (H–T) sequence of the chain.^{24,25} From a comparison of the calculated and observed chemical shifts, it is clear that there are some sequences other than H–T and isolated H–H or T–T units.

In order to separate the CH and CH_2 peaks, the INEPT spectrum was observed.⁶¹ Two peaks at 36 and 36.5 ppm, and the peaks at 24–34 ppm, are assigned to the CH_2 carbons. The peak at 43 ppm, two peaks at ~ 38 ppm and the peak at 35 ppm are a mixture of the CH and CH_2 carbons which are separated by the INEPT observation. The peaks at 11–13 ppm are assigned to the CH_3 carbons. In order to assign these peaks to the carbons located in several kinds of sequences, the 2D INADEQUATE spectrum is observed.

Figure 16 shows the 2D INADEQUATE spectra of regioirregular PB. The ^{13}C – ^{13}C connectivities of the carbons located at the sequences which contain the isolated H–H and T–T units are shown for the region from 22 to 45 ppm. Unassigned peaks still remain. To assign these peaks, other irregular sequences, 1-*r*, 2-*r*, 2U-*r*, are taken into account and the ^{13}C – ^{13}C connectivities are also made in the 2D INADEQUATE spectrum. On the basis of these considerations, all of the peaks are assigned to each carbon in the sequences (Table 14), where the nomenclature proposed by Carman and Wilkes⁶³ is used for the designation of carbon types. This is similar to the case of the ^{13}C NMR spectrum of regioirregular PP with a large amount of chemical inversion³² (Section 4.2.1). The 2D INADEQUATE procedure is especially useful to assign each peak to carbon atoms located in several kinds of sequences in the chain.

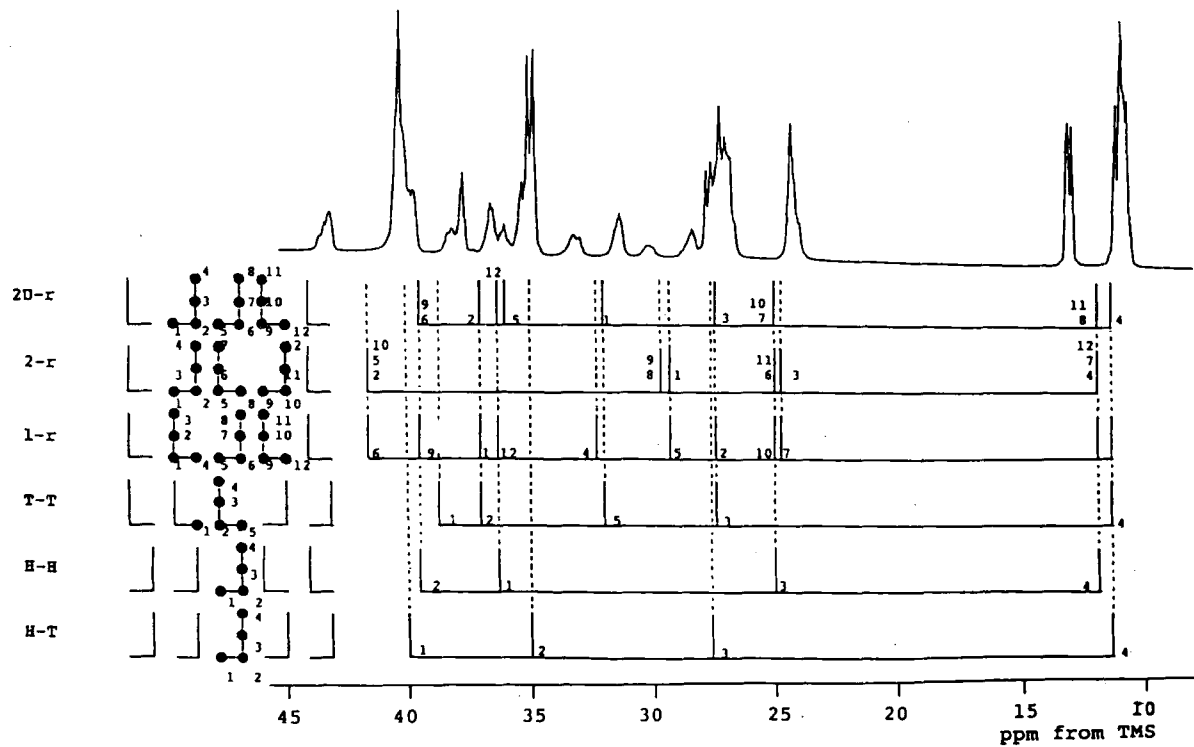


Fig. 15. ^{13}C NMR spectrum of regioirregular PB. The stick spectra are calculated using the Lindeman-Adams ^{13}C NMR chemical shift empirical rule¹¹ those obtained by assuming the presence of several kinds of sequences in the chain are also shown.

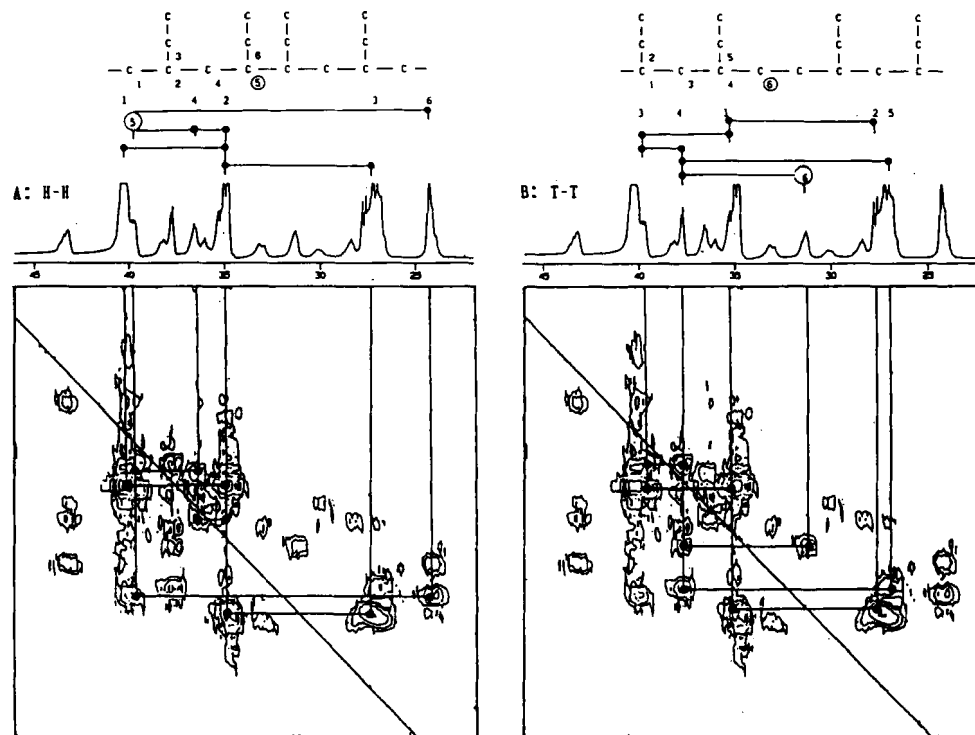


Fig. 16. 2D INADEQUATE ^{13}C NMR spectra of regioirregular PB. The region 22–45 ppm is expanded. The ^{13}C – ^{13}C connectivities of the sequences containing isolated (A) head-to-head and (B) tail-to-tail units are shown as solid lines.

Table 14. ¹³C chemical shift assignment for regioirregular poly(1-butene).

Chemical shift (ppm)	H-T	H-H	T-T	1-r	2-r	2U-r
43.6-43.0	—	—	—	Tδγαγ	Tδαγδ	—
40.1-39.4	m-Sαα	Tδβαγ	m-Sγααδ	Tδαβδ	—	Tδ ⁺ βαγ
38.2-37.5	—	—	Tδβγα	—	—	Tδ ⁺ γβγ
36.4	—	m-Sγααβ	—	—	—	—
35.9	—	—	—	—	—	m-Sδααβ
35.2-34.6	Tββ	Tδββγ	—	—	—	—
33.1-32.8	—	—	—	—	m-Sγαβγ	—
31.2	—	—	m-Sγαβδ	—	—	m-Sδβαγ
30.1-29.9	—	—	—	—	m-Sβαβγ	—
28.3	—	—	—	m-Sδβαβ	—	—
27.7-26.5	s-Sββ	—	s-Sδβγδ	—	—	s-Sδ ⁺ δβγ
24.2-23.7	—	s-Sδβαγ	—	s-Sδγαγ	s-Sδαγδ	s-Sδ ⁺ βαγ
13.0-12.8	—	Pδγαγ	—	Pδγαγ	Pδαγδ	Pδ ⁺ βαγ
11.0-10.5	Pββ	—	Pδβγδ	—	—	Pδ ⁺ γβγ

4.3. Poly(1-pentene) (PPE), poly(1-hexene) (PHEX), poly(1-heptene) (PHEP), poly(1-octene) (PO), poly(1-nonene) (PN)

The tacticity assignments of ¹³C NMR spectra of a series of polyolefines with longer linear side-chains than PB: PPE, PHEX, PHEP, PO and PN, are performed from the ¹³C NMR γ-effect and application of the five-state RIS model. Since no detailed tacticity assignments have been reported for these polyolefins with a longer side-chain than PB, to assign their tacticity is the first step.⁷¹

On the basis of the Lindeman–Adams empirical rule concerning aliphatic ¹³C chemical shifts, the main peaks of the polyolefines are assigned to each carbon. In order to assign the C3 peaks to the tacticities of five polyolefines, the ¹³C NMR chemical shifts were calculated at the pentad level. The value of 0.5 was used for τ* (the additional repulsive interaction between the side-chain and backbone when both adjacent backbone bonds are t as described in Section 4.2.) in the RIS matrix, which was slightly smaller than τ* = 0.6 for PB. When τ* = 0.5 is adapted, the spread of the calculated chemical shifts, due to the tacticity, becomes slightly narrower than that of PB. This is in agreement with the observed tendency of the C3 peaks. By taking into account the calculated chemical shift and the relative intensities of *mm* and *mr* + *rr* triads evaluated from the C2 peaks of the main-chain, the pentad assignments are performed for the C3 peaks of five polyolefines as summarized in Fig. 17 and Table 15. The stick spectrum that appears in the bottom of Fig. 15 represents the calculated pentad chemical shifts. Thus, the order of the pentad C3 chemical shifts of five polyolefines from PPE to

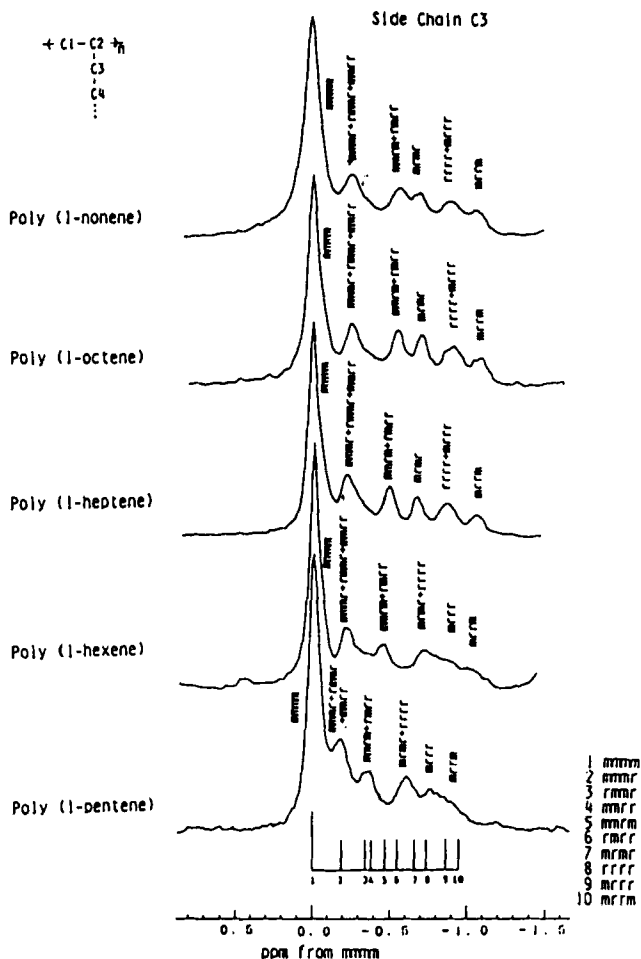


Fig. 17. Pentad assignments of the C3 carbons of five polyolefines. The assignments are performed by taking into account the calculated chemical shift and the relative intensities of the *mm* and *mr + rr* triads evaluated from the C2 peaks of the main chain.

PN are essentially the same as those reported for PP and PB, although some peaks are overlapping. The polymerization mechanism of these polyolefines is discussed through the determination of the parameters of the bicatalytic sites model, which has been used successfully to analyse the PP and PB polymerization mechanism.

However, the tendency of the shift of the C1 peak is very complex as shown in Fig. 18. The dramatic change between PP and PB has been well

Table 15. Observed chemical shifts of C3 carbons of isotactic polyolefines (in ppm relative to the chemical shift of *mmmm*).

Pentad	PPE	PHEX	PHEP	PO	PN
<i>mmmm</i>	0.00	0.00	0.00	0.00	0.00
<i>mmmr</i>	-0.18	-0.21	-0.22	-0.24	-0.25
<i>rmmr</i>	-0.18	-0.21	-0.22	-0.24	-0.25
<i>mmrr</i>	-0.18	-0.21	-0.22	-0.24	-0.25
<i>mmrm</i>	-0.35	-0.46	-0.50	-0.54	-0.55
<i>rmrr</i>	-0.35	-0.46	-0.50	-0.54	-0.55
<i>mrmm</i>	-0.59	-0.72	-0.67	-0.69	-0.69
<i>rrrr</i>	-0.59	-0.72	-0.86	-0.89	-0.88
<i>mrrr</i>	-0.8	-0.9	-0.87	-0.89	-0.88
<i>mrmm</i>	-0.9	-1.0	-1.06	-1.06	-1.04

interpreted on the basis of the chemical shift calculations. However, in the case of five polyolefines from PPE to PN, some new peaks appear and the spread of the observed peak becomes larger with an increase in the length of the side-chain. By examining Fig. 13 carefully, the appearance of more than two peaks is expected if the compensation between σ_b and σ_s is incomplete. Therefore, we have calculated the chemical shift (σ_{cal}) again as a function of K , where $\sigma_{cal} = \sigma_b + K\sigma_s$. It is noted that the observed data can be interpreted if the value of K is assumed to be smaller with an increase in the length of the side-chain of the polyolefins. In the chemical shift calculation, the value of K decreases gradually as 0.4 (PHEX), 0.3 (PHEP), and 0.2 (PO or PN) from PHEX to PN. However, it is difficult to assign the C1 peaks in detail from only these chemical shift data. In order to add the peak intensity data to the chemical shift values, we have calculated the relative peak intensities in the hexad level using the three parameters of the bicatalytic sites model. The assignments are included in Fig. 18. The tacticity chemical shifts of the C1 carbons of PB and PPE are also calculated by using the five-state RIS models proposed by Wittwer and Suter,³⁶ which assumes mutually independent side groups for these polymers. This model eliminates the need for the constant K . However, the agreement between the calculated and observed chemical shifts for this more complete RIS modelling was poor compared with the above results. Therefore, at this stage, it is still necessary to include a constant such as K .

4.4. Poly(3-methyl-1-butene)

The ¹³C INADEQUATE technique is useful to assign each peak of a concentrated polymer solution. However, it is difficult to apply this method to low-solubility natural abundant polymers because of the low sensitivities

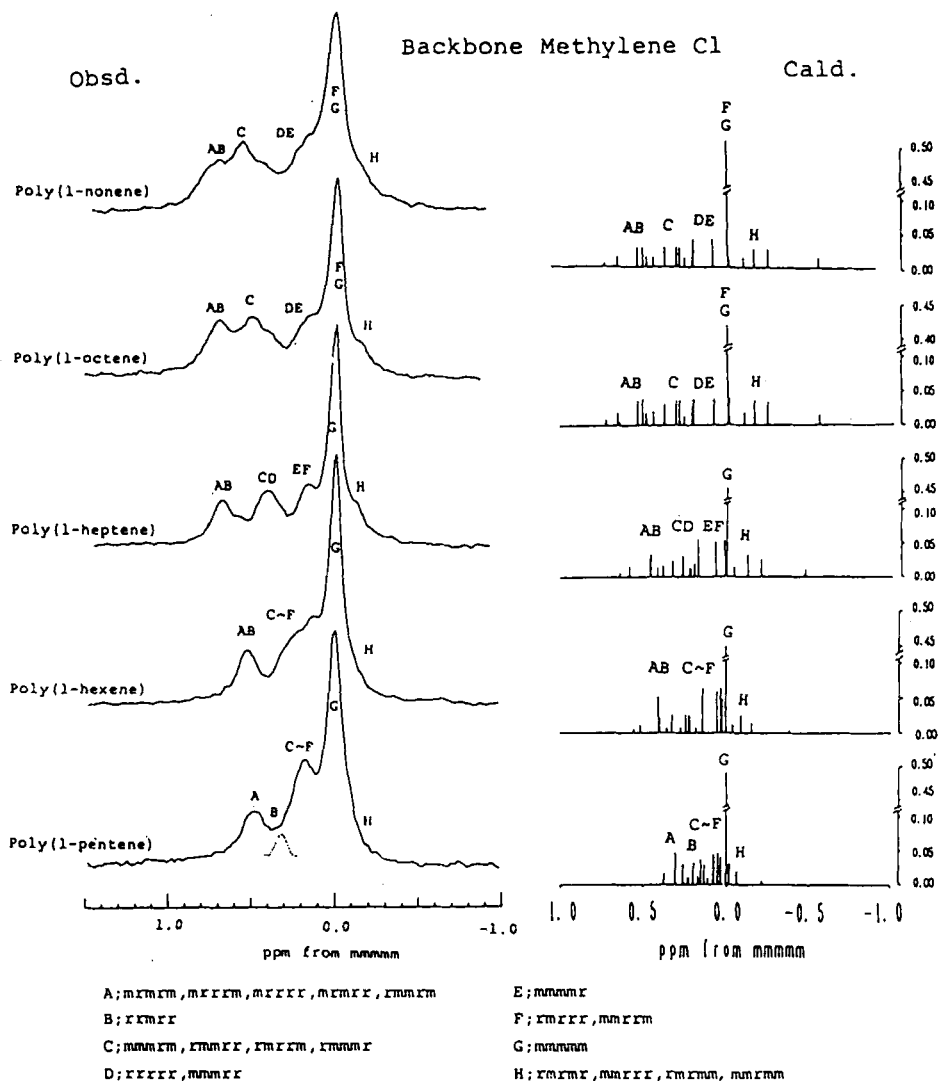


Fig. 18. Observed and calculated stick spectra of the C1 carbons of polyolefines on the basis of the calculated chemical shift and peak intensities. In the chemical shift calculation, the values of K used are 0.6 (PPE), 0.4 (PHEX), 0.3 (PHEP), and 0.2 (PO or PN). Relative pentad intensities are calculated with the parameters of the two-catalytic sites model determined from the C3 peak.

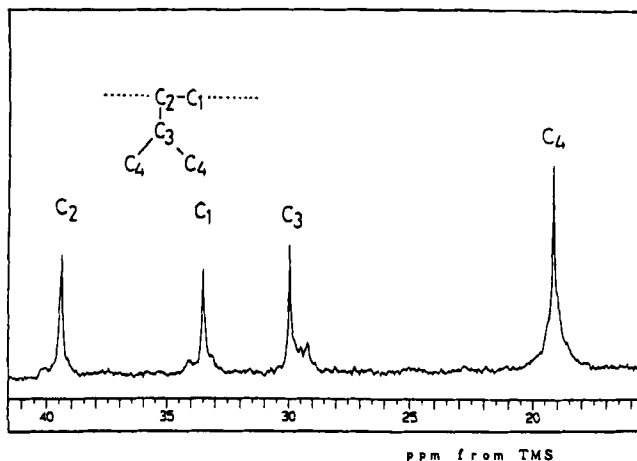


Fig. 19. ^{13}C NMR spectrum of poly(3-methyl-1-butene) at 140°C .

found such as for poly(3-methyl-1-butene), poly(3MB1) (solubility into *o*-dichlorobenzene is only 1% w/v at 140°C). The ^{13}C NMR chemical shift calculation is application to this branched polymer.⁷² Figure 19 shows ^{13}C NMR spectrum (67.8 MHz) of poly(3MB1) at 140°C . Four main peaks are assigned to each carbon on the basis of the Lindeman-Adams empirical rules. There are small peaks at the side of the individual main peaks: C1, C2 and C3. Peak broadening is also observed for the methyl carbon C4 of the side-chain, indicating the presence of racemic units in the chain although this sample is assumed to be predominantly isotactic. Several small peaks appear to low frequency of the main peak of the C3 carbon. This is a similar spectral pattern as for the C3 carbons attached directly to the methine carbons of the backbone chain of isotactic PP and PB.³⁴

The ^{13}C NMR chemical shifts of the C1 and C3 carbons are calculated by assuming the stereochemical configuration in hexad and heptad levels, respectively, using the calculation model for PP.²⁰ Because of the presence of two methyl groups in the side-chain of poly(3MB1), an additional strong repulsive interaction, τ^* (<1) will occur between the side-chain and backbone. This is taken into account especially when calculating the bond probability of poly(3MB1) where both adjacent backbone bonds are *trans*. By comparison of the observed and calculated shifts range of C1 and C3 peaks split by the tacticity, the value of τ^* was determined (0.4). The values of the γ -effect are taken to be -5.3 or -3.7 ppm which represent shielding increase relative to the *trans* arrangement dependent on the species of carbon atom included in the chemical shift calculation. However, the γ -effect of -7.7 ppm is adopted between the methyl carbons, which are locally in the same situation as the arrangement of the carbons in the head-to-head units of PP.⁶¹

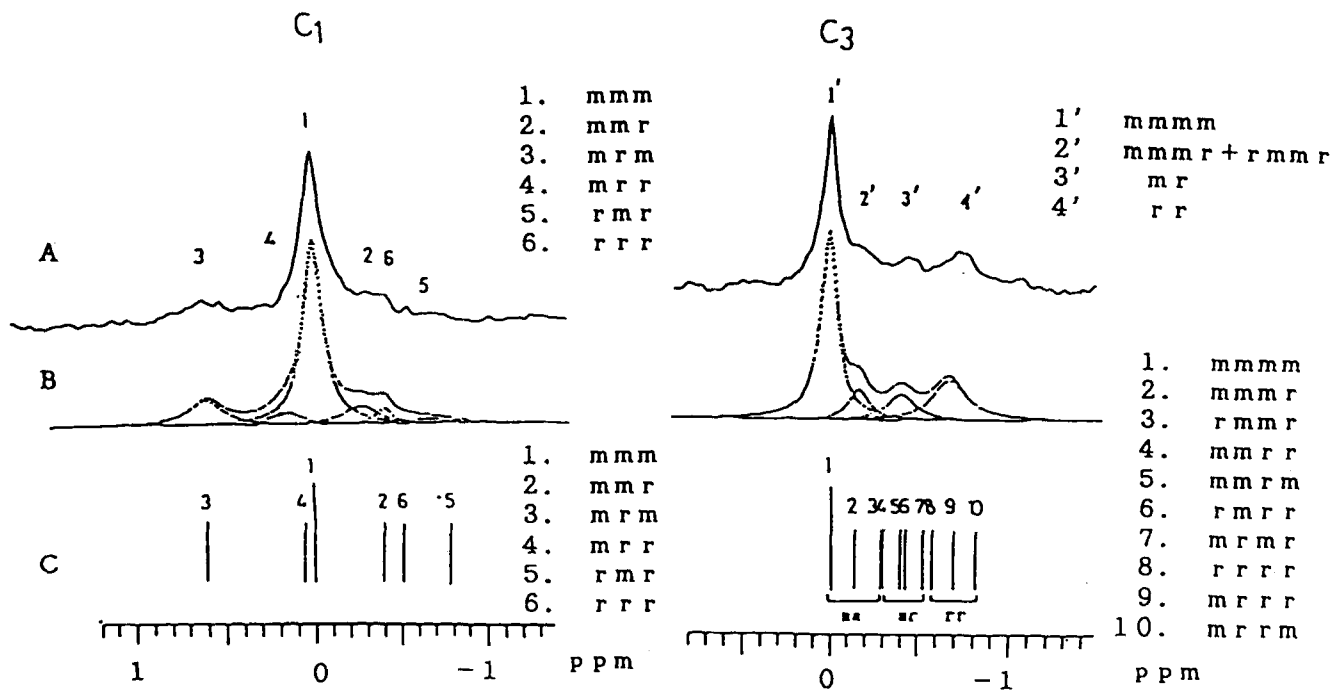


Fig. 20. ^{13}C NMR peaks of the C1 and C3 carbons of poly(3-methyl-1-butene). A, observed peaks; B, simulated peaks assuming Lorentzian lineshapes; C, stick spectra of the calculated chemical shifts relative to the chemical shift of the isotactic peak.

The calculated chemical shifts are shown as stick spectra and compared with the observed shifts in Fig. 20. Because of the low resolution of the observed peaks, the tetrad and pentad peaks are calculated again on the basis of the calculated hexad and heptad peaks (Table 16). Peaks 1–6 of the C1 carbon are assigned to *mmm*, *mmr*, *mrmm*, *mrr*, *rmr* and *rrr*, respectively. Thus, the peaks at the highest and lowest frequency are assigned to *mmr* and *rmr*, respectively, which is similar to the case of PP. A comparison of the calculated and observed chemical shifts was also performed for the C3 carbon of poly(3MB1) (Fig. 20). Peaks 1–4 are assigned to *mmmm*, *mmmr* + *rmmr*, *mr* and *rr* with increasing shielding. This order is essentially the same as that for PP and PB.³⁴ The relative peak intensities for C1 and C3 carbons are summarized in Table 16. The index of isotacticity of this sample is estimated to be 0.74 from the C1 peak and 0.72 from the C3 peak. These values are in agreement, indicating the validity of the assignment.

So far, detailed ¹³C NMR analysis for the tacticity has not been reported for C3 branched polyolefins. Zambelli *et al.* have reported ¹³C NMR spectrum of poly[(RS)3-methyl-1-pentene] in solution.⁷³ All peaks are broad except for the C5 terminal methyl peak of the side chain and further assignment has not been performed. Sacchi *et al.* have also observed the ¹³C NMR spectrum of poly[(RS)3,7-dimethyl-1-octene] in solution.⁷⁴ However, any assignment due to the tacticity has not been reported. The ¹³C NMR chemical shift calculation is also useful for the assignment of C3 branched polyolefins as well as polyolefins with linear side-chains.

Table 16. Observed and calculated ¹³C chemical shifts and the relative intensities of C1 and C3 carbons of poly(3MB1).

Carbon type	Sequence type	ν_{obs}^a (ppm)	$\Delta\nu_{\text{obs}}$ (ppm)	ν_{calc}^b (ppm)	Relative intensity
C ₁	1 <i>mmm</i>	33.45	0.00	0.00	0.59
	2 <i>mmr</i>	33.15	-0.30	-0.40	0.11
	3 <i>mrmm</i>	34.05	0.60	0.60	0.14
	4 <i>mrr</i>	33.55	0.10	0.05	0.07
	5 <i>rmr</i>	32.70	-0.75	-0.79	0.04
	6 <i>rrr</i>	33.05	-0.40	-0.52	0.05
C ₃	1 <i>mmmm</i>	29.89	0.00	0.00	0.55
	2 <i>mmmr</i>	29.75	-0.14	-0.14	} <i>mm</i> 0.11
	3 <i>rmmr</i>	29.75	-0.14	-0.29	
	4 <i>mmrr</i>			-0.31	
	5 <i>mmrm</i>	29.45	-0.44	-0.40	} <i>mr</i> 0.12
	6 <i>rmrr</i>			-0.43	
	7 <i>mrmm</i>			-0.53	
	8 <i>rrrr</i>			-0.58	} <i>rr</i> 0.22
	9 <i>mrrr</i>	29.15	-0.74	-0.70	
	10 <i>mrmm</i>			-0.82	

^aIn ppm from TMS.

^bChemical shifts are expressed in ppm relative to the chemical shift of the isotactic peak.

5. ETHYLENE-OLEFINE COPOLYMERS

5.1. E-P copolymers

5.1.1. Comonomer sequence

A COMONOMER SEQUENCE DEPENDENCE OF THE ^{13}C NMR CHEMICAL SHIFT DUE TO THE γ -EFFECT

By improvement in sensitivity and resolution of ^{13}C NMR spectra, one has been able to observe a number of split peaks arising from different pentad or hexad sequences in polyolefines. In the spectrum of stereoregular E-P copolymer, observed splittings of methylene carbon resonances should depend on up to hexad comonomer sequences. However, empirical rules^{10111,59} and sequential analysis⁷⁵ based on the spectrum of copolymers with different compositions cannot provide the hexad assignments. The pioneering empirical rules proposed by Grant and Paul¹⁰ and by Lindeman and Adams¹¹ do not reflect the effect of comonomer sequences longer than pentads. Cheng and Bennett's method,⁵⁹ which accounts for the substituent effect as well as for the tactic configurational sequences, does not provide full hexad assignments of E-P comonomer sequences. These studies have allowed us to determine sequence distribution in E-P copolymers as far as the triad level,^{57,76-78} because the previous assignments have ambiguities in the PPEP-, EPEP-, PPEE-, and EPEE-tetrads due to the contributions from sequences longer than tetrad.

It has been proved that the γ -effect on ^{13}C NMR chemical shifts is sensitive to the long-range stereosequences.^{4151,79} A sequential environment affects the probability of bond conformations producing a *gauche* arrangement between the carbon atom of interest and that in the γ position. The typical example is the difference of tactic-heptad chemical shifts between the isotactic and atactic polypropylene chains (see Section 4.1.1).⁵¹ It is plausible that the γ -effect is sensitive to the differences in comonomer sequences.

In order to confirm the applicability of the γ -effect method to the chemical shift prediction of comonomer sequences, ^{13}C NMR chemical shifts due to the γ -effect were calculated for the carbon atoms in 2,4,6-trimethyloctane; 2,4,8,10-tetramethylundecane; 3,5,7,9,11,13,15-heptamethylheptadecane and 2,6,8,10,12,14-hexamethylpentadecane.⁸⁰ As shown in Fig. 21, these compounds have different sequences due to the substitution of a monomer unit between ethylene and propylene. Mark's RIS model⁶⁸ was used for the calculation. The γ -effect of methine carbons on methyl carbons and methyl carbons on methine carbons is taken to be -5.3 ppm, and the γ -effect of methine, methylene, and methyl carbons on methylene carbons is taken to be -3.7 ppm. The calculation was performed

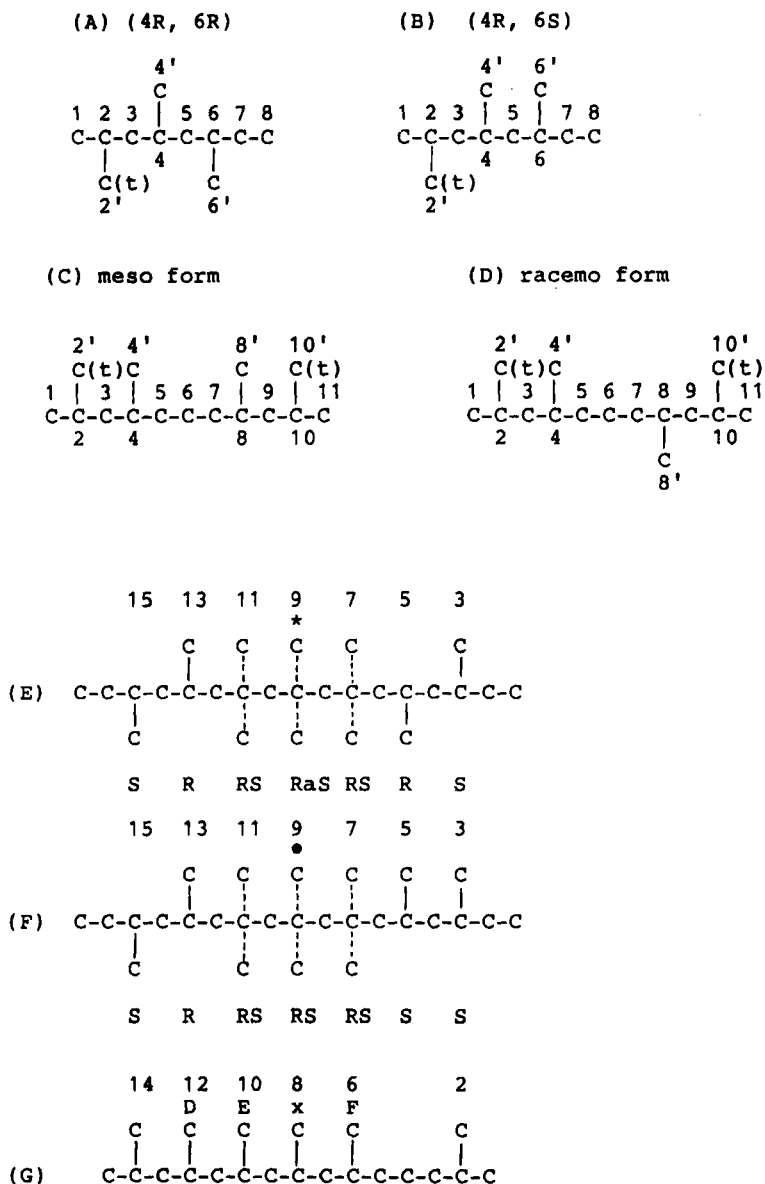


Fig. 21. Model compounds for polypropylene and ethylene-propylene copolymer. (A), (B) 2,4,6-trimethyloctane; (C), (D) 2,4,8,10-tetramethylundecane; (E), (F) 3,5,7,9,11,13,15-heptamethylheptadecane; (G) 2,6,8,10,12,14-hexamethylpentadecane; (t): *threo* relationship to delta methyl carbon.

at 120, 137, 140°C corresponding to the experimental conditions of the ^{13}C NMR measurements.

The carbons of interest are numbered, 1, 2, 2', and 3 in the compounds (A), (B), (C), and (D), and are marked by asterisks in the compounds (E), (F), and (G). These carbons are taken to be included in the same monomer unit surrounded by the different sequences. The influence of the monomer unit substitution on the chemical shifts is investigated by the calculated chemical shifts due to the γ -effect, and compared with the stereo sequence dependence. The calculated and observed chemical shifts^{12,64,81,82} are shown in Tables 17, 18, and 19. The calculated chemical shift difference for carbons 1 in the compounds (A) and (B) depends on the different configurations of the methine carbons 6. This value coincides with the observed one. The calculated chemical shift difference for carbons 1 in the compounds (C) and (D) depends on the indirect long-range influence⁷⁹ from the different configurations of methine carbons 8. The predicted peak positions of carbons 1 in the compounds (C) and (D) are in the intermediate region between those of (A) and (B). These chemical shift differences between the compounds (A, B) and the compounds (C, D) depend on the change of comonomer sequences, namely, on the existence or absence of the methyl

Table 17. Observed and calculated chemical shifts of carbons, 1, 2', 2 and 3, in the model compounds (A)–(D).

Carbon no.	Compound	Obsd ^a (ppm)	$\Delta\nu_{\text{obsd}}^b$ (ppm)	$\Delta\nu_{\text{calcd}}^b$ (ppm)
1	(A)	23.54	-0.20	-0.253
	(B)	23.74	0.0	0.0
	(C)	23.58	-0.16	-0.212
	(D)	23.58	-0.16	-0.222
2'	(A)	22.77	-0.12	-0.226
	(B)	22.89	0.0	0.0
	(C)	22.83	-0.06	-0.009
	(D)	22.83	-0.06	-0.002
2	(A)	26.01	-0.06	-0.052
	(B)	26.01	-0.06	-0.027
	(C)	26.07	0.0	0.001
	(D)	26.07	0.0	0.0
3	(A)	47.96	-0.60	-0.582
	(B)	48.56	0.0	0.0
	(C)	47.66	-0.90	-0.634
	(D)	47.62	-0.94	-0.602

^aObserved at 140°C in Refs 81,82. Chemical shifts are expressed from the resonance of tetramethylsilane.

^bChemical shifts are expressed relative to that of peak appearing at the highest frequency, which is set to be 0.00 ppm, and negative sign indicates a shielding increase.

Table 18. Observed chemical shifts and calculated γ -effects of the carbon 9 in the model compounds (E) and (F).

Model	Pentad	Obsd ^a (ppm)	Calcd γ -effect (ppm)
(E)	<i>mmmr</i>	21.55	-6.369
(E)	<i>mrmm</i>	20.85	-6.841
(E)	<i>rmrr</i>	20.85	-6.919
(E)	<i>rrrm</i>	20.17	-7.613
(F)	<i>mmmm</i>	21.78	-6.199
(F)	<i>rmmr</i>	21.33	-6.537
(F)	<i>mmrr</i>	21.01	-6.723
(F)	<i>mrmr</i>	20.71	-7.064
(F)	<i>rrrr</i>	20.31	-7.434
(F)	<i>mrrm</i>	20.04	-7.816

^aObserved at 140°C by Zambelli *et al.*¹². Chemical shifts are expressed from the resonance of tetramethylsilane.

Table 19. Observed chemical shifts and calculated γ -effects of the carbon marked by an asterisk in the model compound (G). Symbols, e and t means *erythro* and *threo* relationship to the carbon marked by an asterisk, respectively.

Model	Methyl carbon			Pentad	Obsd ^a (ppm)	Calcd γ effect (ppm)
	X	Y	Z			
(G)	e	e	e	<i>P[*]mP^mP^mPE</i>	21.61	-6.331
(G)	t	e	e	<i>P[*]P^mP^mPE</i>	21.42	-6.502
(G)	e	e	t	<i>P^mP^mP[*]PE</i>	21.01	-6.733
(G)	e	t	e	<i>P[*]P[*]P^mPE</i>	20.91	-6.883
(G)	t	e	t	<i>P[*]P^mP[*]PE</i>	20.85	-6.953
(G)	t	t	e	<i>P^mP[*]P^mPE</i>	20.78	-7.010
(G)	e	t	t	<i>P[*]P[*]P[*]PE</i>	20.33	-7.473
(G)	t	t	e	<i>P^mP[*]P[*]PE</i>	20.19	-7.655

^aObserved at 140°C by Zambelli and Gatti.⁶⁴ Chemical shifts are expressed from the resonance of tetramethylsilane.

substituent 6'. In the case of carbons 2 and 2', a similar description is possible to explain the trends of chemical shift values.

The shielding increases of carbons 3 in the compounds (C, D) due to the γ -effect are 0.63 and 0.60 ppm, respectively. The total shielding increases of 0.88 and 0.85 ppm are estimated by the addition of those from the γ -effect to those from the empirical four-bond effect¹¹ of 0.25 ppm. These values coincide well with those observed.^{81,82} The chemical shift difference of carbons 3 between compounds (A) and (B) arises from the stereosequence effect. The chemical shift differences of carbons 3 between compounds (C,

Table 20. Chemical shift differences due to the substitution of the propylene unit by ethylene unit.

No.	Pentad	Obsd ^a	Calcd ^a
(1)	P ^m P ^m P ^m P ^m P	0.0	0.0
	P ^m P ^m P ^m P ^r P	-0.23	-0.20
	P ^m P ^m P ^m PE	-0.17	-0.132
(2)	P ^r P ^m P ^m P ^r P	0.0	0.0
	P ^r P ^m P ^m PE	0.09	0.03
(3)	P ^r P ^r P ^m P ^m P	0.0	0.0
	P ^r P ^r P ^m PE	-0.10	-0.09
	P ^r P ^r P ^m P ^r P	-0.16	-0.17
(4)	P ^m P ^r P ^m P ^m P	0.0	0.0
	P ^m P ^r P ^m PE	-0.07	-0.17
	P ^m P ^r P ^m P ^r P	-0.14	-0.223
(5)	P ^r P ^r P ^r PE	0.0	0.0
	P ^r P ^r P ^r P ^r P	-0.02	-0.039
	P ^r P ^r P ^r P ^m P	-0.16	-0.140
(6)	P ^m P ^r P ^r PE	0.0	0.0
	P ^m P ^r P ^r P ^m P	-0.15	-0.161

^aChemical shifts are expressed relative to that of peak appearing at the highest frequency, which is set to be 0.00 ppm.

D), and compounds (A), and (B) arise whether the methyl carbon 6' is present or not (effect of comonomer sequence).

The observed and calculated chemical shifts of carbons marked by asterisks in compounds (E), (F), and (G) shown in Tables 18 and 19 indicate the stereosequence dependence of the ¹³C chemical shift. These results are summarized in Table 20 as the calculated shifts of tactic pentads and those of the corresponding PPPPE pentad sequences. The observed and calculated shifts are illustrated by stick spectra in Fig. 22. The calculated relative peak positions as well as the magnitude of the chemical shift differences are in good agreement with the observed results.^{12,64} For example, the chemical shifts of the resonances of P^mP^mP^mPE and P^mP^mP^mP^rP is predicted to be 0.13 and 0.20 ppm from that of the P^mP^mP^mP^mP pentad, respectively. These calculated results agree with the observed shielding increases of 0.17 and 0.23 ppm. Other examples also indicate the good agreement of the calculated shifts with the observed ones. Thus, it is confirmed that the ¹³C chemical shift calculation, via the γ-effect, provides a reasonable estimate of the chemical shift differences arising from different comonomer sequences.

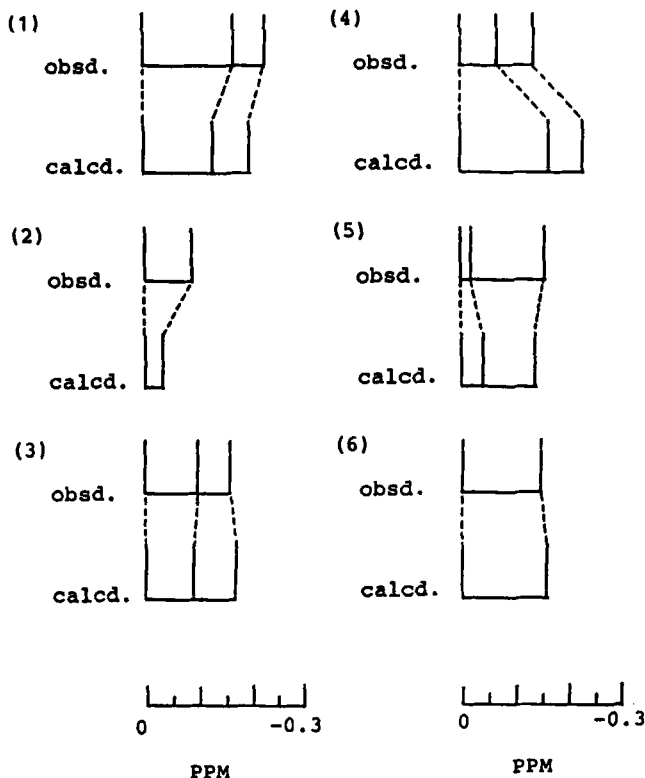


Fig. 22. Observed and calculated ^{13}C NMR chemical shifts of carbons of interest in the model compounds, (E), (F) and (G) (see Fig. 21) are illustrated by stick spectra corresponding to the summarized results in Table 20. Chemical shifts are expressed in ppm relative to that of the peak appearing at the lowest frequency which is set to be 0.00 ppm.

These comonomer sequence-dependent chemical shift differences are estimated to be comparable to those dependent on different stereosequences.

B HEXAD COMONOMER SEQUENCE ASSIGNMENTS

B(i) Calculation of the γ -EFFECT

The chemical shifts due to the γ -effect for the hexad methylene resonances in stereoregular E-P copolymer are calculated for two cases as follows.⁸³

case (I) P.....P(E-P hexad sequence) P.....P
15 meso dyads 15 meso dyads

case (II) E.....E(E-P hexad sequence) E.....E
15 ethylene units 15 ethylene units

Table 21. Calculated ^{13}C NMR chemical shifts due to the γ -effect for methylene carbons in ethylene-propylene copolymer.

Carbon type	No. No.	Sequence type	Chemical shift due to the γ -effect		
			Case (I) ppm	Case (II) ppm	Case (I)–Case (II) ppm
$S_{\alpha\alpha}$	1	PPPPPP	-3.582	-3.406	-0.176
	2	PPPPPE	-3.350	-3.254	-0.096
	3	EPPPPE	-3.114	-3.100	-0.014
	4	PPPPEP	-3.544	-3.441	-0.103
	5	PPPPEE	-3.536	-3.439	-0.097
	6	EPPPEP	-3.288	-3.273	-0.015
	7	EPPPEE	-3.280	-3.271	-0.009
	8	PEPPEP	-3.406	-3.390	-0.016
	9	PEPPEE	-3.395	-3.386	-0.009
	10	EPPPEE	-3.385	-3.382	-0.003
$S_{\alpha\gamma}$	11	PPPEPP	-3.125	-3.031	-0.094
	12	PPPEPE	-3.173	-3.069	-0.104
	13	EPPEPP	-2.843	-2.843	0.0
	14	EPPEPE	-2.889	-2.881	-0.008
	15	PEPEPP	-2.805	-2.805	0.0
	16	PEPEPE	-2.850	-2.842	-0.008
	17	EEPEPP	-2.789	-2.797	0.008
	18	EEPEPE	-2.834	-2.834	0.0
$S_{\alpha\delta}$	19	PPPEEP	-3.669	-3.565	-0.104
	20	PPPEEE	-3.681	-3.576	-0.105
	21	EPPEEP	-3.384	-3.376	-0.008
	22	EPPEEE	-3.396	-3.387	-0.009
	23	PEPEEP	-3.340	-3.331	-0.009
	24	PEPEEE	-3.351	-3.342	-0.009
	25	EEPEEP	-3.323	-3.323	0.0
	26	EEPEEE	-3.335	-3.334	-0.001
$S_{\beta\beta}$	27	PPEPP	-8.944	-8.885	-0.059
	28	PPEPE	-8.793	-8.760	-0.033
	29	EPEPE	-8.644	-8.636	-0.008
$S_{\beta\delta}$	30	PPEEP	-6.013	-5.979	-0.034
	31	PPEEE	-5.941	-5.911	-0.030
	32	EPEEP	-5.858	-5.855	-0.003
	33	EPEEE	-5.792	-5.786	-0.006
$S_{\gamma\gamma}$	34	PPEEPP	-1.903	-1.918	0.015
	35	PPEEPE	-1.939	-1.950	0.011
	36	EPEEPE	-1.979	-1.981	0.002
$S_{\gamma\delta}$	37	PPEEEP	-2.410	-2.419	0.009
	38	PPEEEE	-2.422	-2.429	0.007
	39	EPEEEP	-2.448	-2.450	0.002
	40	EPEEEE	-2.459	-2.460	0.001

Table 21—*contd.*

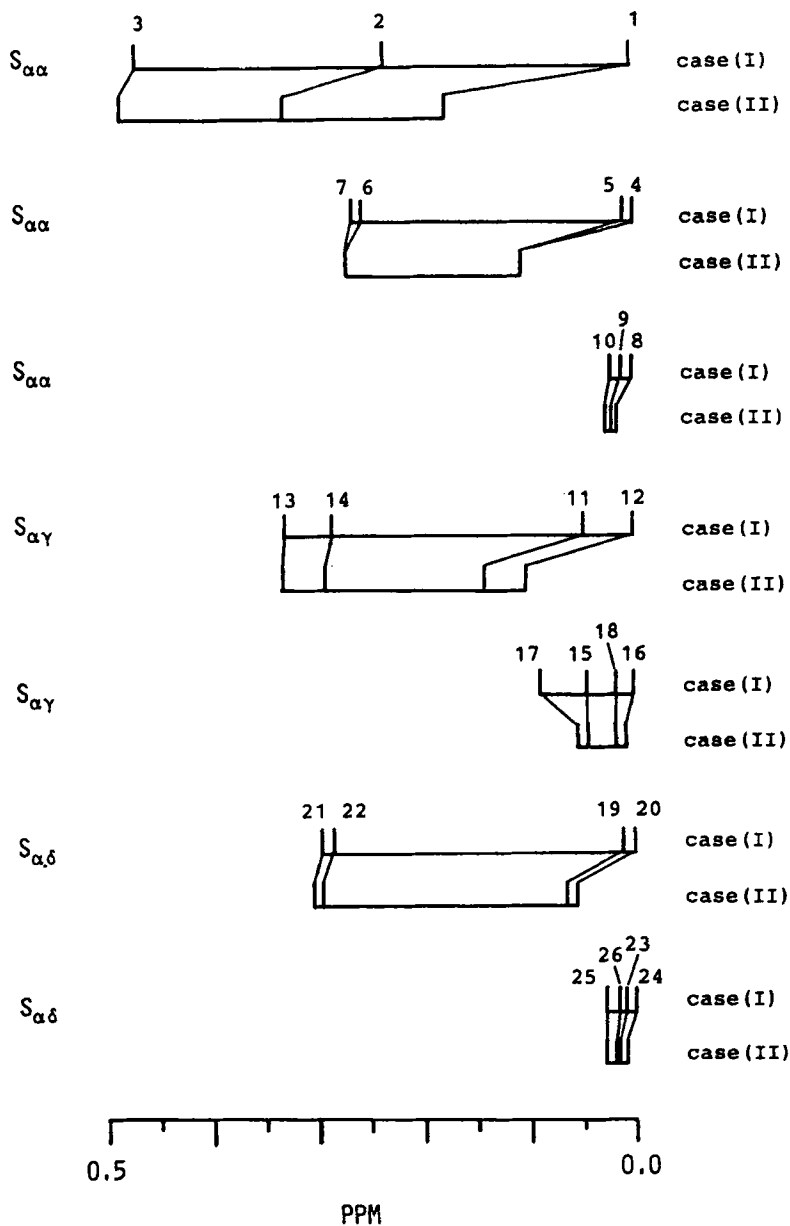
Carbon type	No. No.	Sequence type	Chemical shift due to the γ -effect		
			Case (I) ppm	Case (II) ppm	Case (I)–Case (II) ppm
$S_{\delta\delta}$	41	PEEEP	–3.087	–3.076	–0.011
	42	PEEEE	–3.014	–3.007	–0.007
	43	EEEEEE	–2.911	–2.938	0.007
	44	PEEEEE	–2.916	–2.918	0.002

where P and E denote monomeric units of propylene and ethylene, respectively. In cases (I) and (II), the comonomer sequences are sandwiched between two isotactic polypropylene sequences (15 meso dyads) and two polyethylene sequences (15 ethylene units), respectively. These surrounding sequences simulate propylene- and ethylene-rich chains. Thus, cases (I) and (II) correspond to the hexad sequences in the E–P copolymers of low and high ethylene contents, respectively.

In Table 21 are shown the calculated chemical shifts due to the γ -effect for the hexad and pentad methylene resonances of the stereoregular E–P copolymer. As shown by the stick spectra of calculated shifts shown in Fig. 23, the relative positions of pentad and hexad peaks for all types of methylene carbons are identical in both cases. This suggests that the order in which the peak appears does not depend on the surrounding sequences. Thus, the same assignments are given to methylene split peaks for both ethylene-rich and propylene-rich copolymers. On the basis of these calculated shifts, ^{13}C chemical shift assignments of the methylene carbons in the stereoregular E–P copolymer (PE-2) with an ethylene content of 7.0 mol% are provided⁸³ (sample PE-2 was prepared with $\delta\text{-TiCl}_3/\text{Et}_2\text{AlCl}$ catalytic system). The process of the hexad assignments of the $S_{\alpha\gamma}$ and $S_{\alpha\delta}$ carbons is introduced in the following subsection.

B(ii) Hexad assignments of $S_{\alpha\gamma}$ and $S_{\alpha\delta}$ carbons

In Fig. 24 are shown the $S_{\beta\beta}$ and $S_{\alpha\gamma}$ carbon resonance regions in the ^{13}C NMR spectrum of the E–P copolymer (PE-1) with an ethylene content of 0.8 mol%. The catalytic system used for the preparation of this sample is the same as for PE-2. It is confirmed from the spectrum that all ethylene units in sample PE-1 are isolated in the polypropylene chain (the fraction of PPP in the triad sequence distribution is 0.976). Both regions show single peaks with a sharp line shape. Referring to the observed spectrum of the model compound for the isolated ethylene unit in the E–P copolymer⁸⁴ and the chemical shift calculation for the methylene carbons in the isolated ethylene



(a)

Fig. 23. Comonomer sequence-dependent chemical shift differences in the respective methylene carbons of ethylene-propylene copolymer. Case (I), comonomer sequences of interest are isolated in the isotactic polypropylene sequences; case (II), comonomer sequences of interest are isolated in the polyethylene sequences.

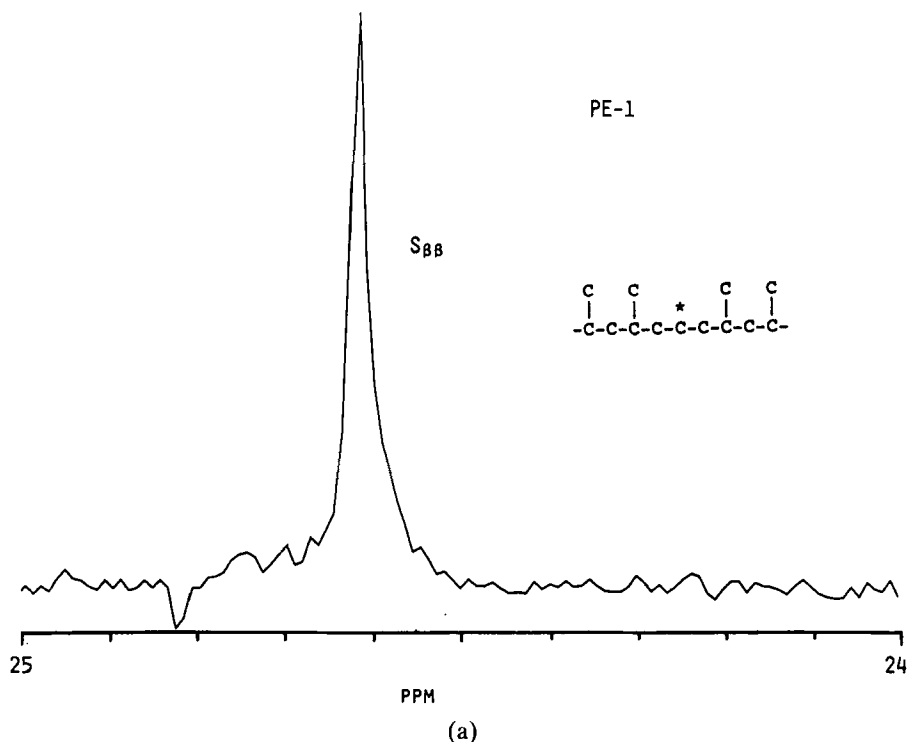
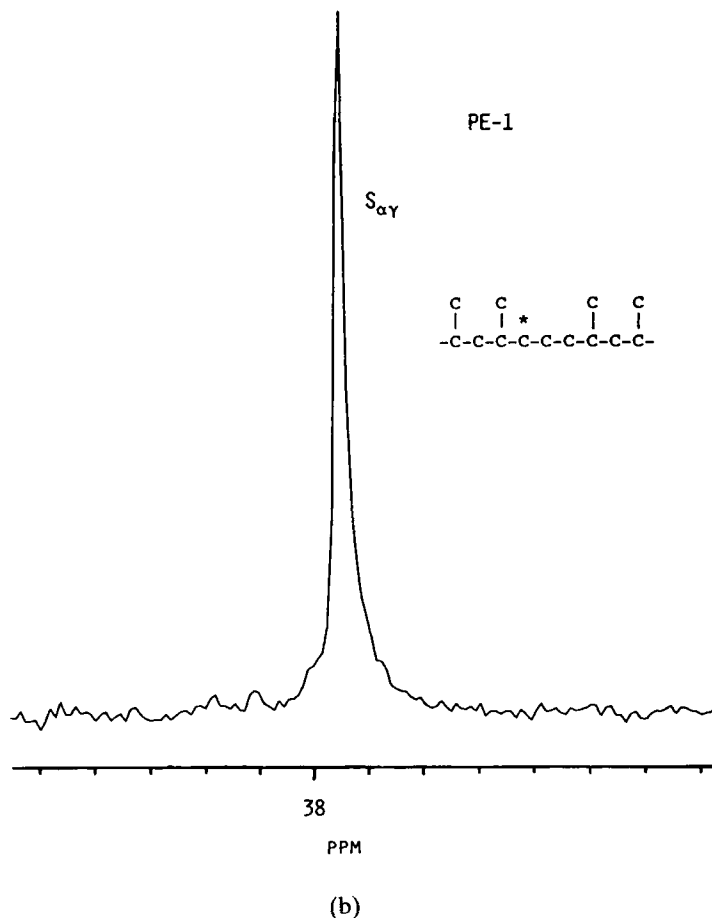


Fig. 24. ^{13}C NMR spectrum of the (a) $S_{\beta\beta}$ and (b) $S_{\alpha\gamma}$ resonance regions of ethylene-propylene copolymer with an ethylene content of 0.8 mol%.

Thus, it is safely assumed that in PE-2 the comonomer sequences of interest are isolated in the isotactic polypropylene sequences. This assumption corresponds to the calculation in case (I). Further, it is reasonable that the most shielded peak in each resonance region in the spectrum of PE-2 is attributable to the resonance of the most propylene-rich sequence.

In Fig. 25 are shown the $S_{\alpha\gamma}$ and $S_{\alpha\delta}$ regions in the spectrum of PE-2. In Tables 22 and 23 are shown the predicted chemical shift differences ($\Delta\nu_s$), which are calculated from the contributions of the γ -effect ($\Delta\nu_\gamma$) and of the four-bond effect ($\Delta\nu_e$) in the Lindeman-Adams empirical rule.¹¹ These calculated chemical shifts and the assignments proposed by Ray *et al.*⁷⁵ are shown by the stick spectra in Fig. 25. Since more than four peaks are observed in the resonance regions of the $S_{\alpha\gamma}$ and $S_{\alpha\delta}$ carbons, hexad assignments should be given for the split peaks. The chemical shifts of the EPPEPP and EPPEPE hexads are predicted from the γ -effect calculation to



be at high frequency of the shifts of the EPEP-centred hexads. The predicted chemical shifts of the EPPEEP and EPPEEE hexads are situated to high frequency of those of the EPEE-centred hexads. Thus, the peaks of the EPEP-centred hexads and EPEE centred hexads are sandwiched by the peaks of PPEP-centred hexads and PPEE-centred hexads, respectively. In Fig. 26 are shown the observed chemical shifts of the $S_{\alpha\gamma}$ carbons and those calculated by the γ -effect method and Cheng's empirical rule.²⁶ Cheng's empirical rule predicts three peaks in this region. The γ -effect method predicts eight hexad peaks which well reproduces the observed splittings.⁸⁶ Pentad and hexad assignments of the other methylene peaks are similarly provided from the calculated chemical shifts due to the γ -effect.⁸³

PE-2

Assignments in this study

11. PPPEPP	19. PPPEEP
12. PPPEPE	20. PPPEEE
13. EPPEPP	21. EPPEEP
14. EPPEPE	22. EPPEEE
15. PEPEPP	23. PEPEEP
16. PEPEPE	24. PEPEEE
17. EEPEPP	25. EEPEEP
18. EEPEPE	26. EEPEEE

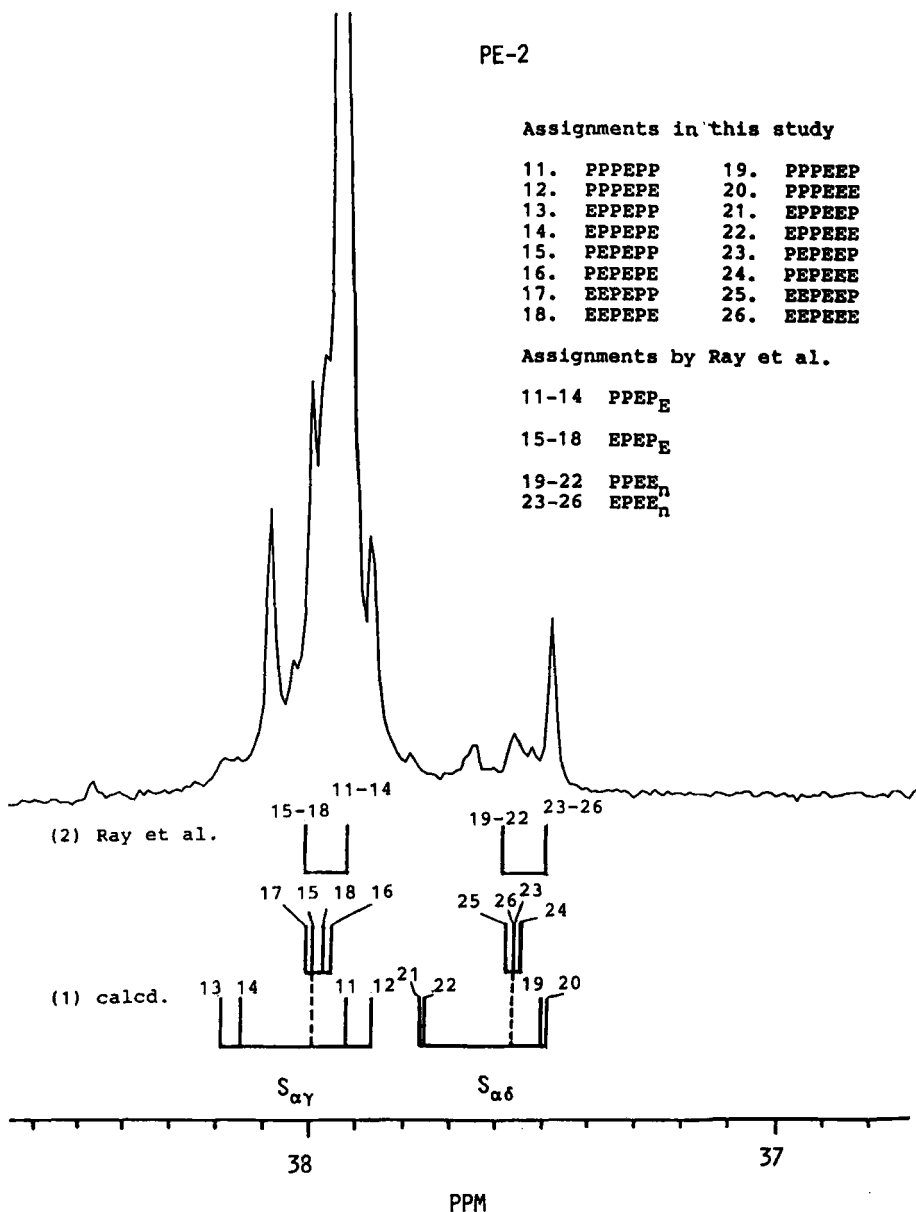
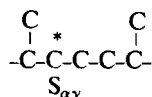
Assignments by Ray *et al.*11-14 PPEP_E15-18 EPEP_E19-22 PPEE_n23-26 EPEE_n

Fig. 25. ^{13}C NMR spectrum of $S_{\alpha\gamma}$ and $S_{\alpha\delta}$ resonance regions of PE-2. The assignments(2) by Ray *et al.*⁷⁵ and the calculated chemical shifts(1) are shown as stick spectra at the bottom of the figure.

Table 22. Observed chemical shifts (ν) and the observed and the calculated chemical shift differences ($\Delta\nu$) of $S_{\alpha\gamma}$ carbons.


No.	Sequence type	$\Delta\nu_e^{a,b}$ (ppm)	$\Delta\nu_\gamma^{b,c}$ (ppm)	$\Delta\nu_s^{b,d}$ (ppm)	ν (ppm)	$\Delta\nu_{\text{obsd}}^b$ (ppm)
11	(P)PPPEPP(P)	0.0	0.0	0.0	37.941	0.0
12	(P)PPPEPE(P)	0.0	-0.048	-0.048	37.887	-0.054
13	(P)EPPEPP(P)	0.0	0.284	0.284	38.094	0.153
14	(P)EPPEPE(P)	0.0	0.234	0.234	38.049	0.108
15	(P)PEPEPP(P)	-0.25	0.320	0.070	38.004	0.063
16	(P)PEPEPE(P)	-0.25	0.275	0.025	37.977	0.036
17	(P)EEPEPP(P)	-0.25	0.336	0.086	38.004	0.063
18	(P)EEPEPE(P)	-0.25	0.291	0.041	37.977	0.036

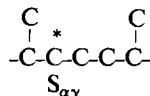
^aCalculated by the Lindeman-Adams empirical rule¹¹.

^bChemical shift differences are expressed relative to the peak of PPPEPP resonance, which is set to be 0.00 ppm.

^cCalculated by the chemical shift calculation via the γ -effect.

^dSum of the chemical shift differences $\Delta\nu_\gamma$ and $\Delta\nu_e$.

$$(\Delta\nu_s = \Delta\nu_\gamma + \Delta\nu_e).$$

Table 23. Observed chemical shifts (ν) and the observed and calculated chemical shift differences ($\Delta\nu$) of $S_{\alpha\delta}$ carbons.


No.	Sequence type	$\Delta\nu_e^{a,b}$ (ppm)	$\Delta\nu_\gamma^{b,c}$ (ppm)	$\Delta\nu_s^{b,d}$ (ppm)	ν (ppm)	$\Delta\nu_{\text{obsd}}^b$ (ppm)
19	(P)PPPEEP(P)	0.0	0.0	0.0	37.501	0.0
20	(P)PPPEEE(P)	0.0	0.012	0.012	37.501	0.0
21	(P)EPPEEP(P)	0.0	0.285	0.285	37.672	0.171
22	(P)EPPEEE(P)	0.0	0.273	0.273	37.672	0.171
23	(P)PEPEEP(P)	-0.25	0.329	0.079	37.582	0.081
24	(P)PEPEEE(P)	-0.25	0.318	0.068	37.546	0.045
25	(P)EEPEEP(P)	-0.25	0.346	0.096	37.582	0.081
26	(P)EEPEEE(P)	-0.25	0.334	0.084	37.582	0.081

^aCalculated by Lindeman-Adams empirical rule¹¹.

^bChemical shifts are expressed relative to the peak of PPPEEP resonance, which is set to be 0.00 ppm.

^cCalculated by the chemical shift calculation via the γ -effect.

^dSum of the chemical shift differences $\Delta\nu_\gamma$ and $\Delta\nu_e$.

$$(\Delta\nu_s = \Delta\nu_\gamma + \Delta\nu_e).$$

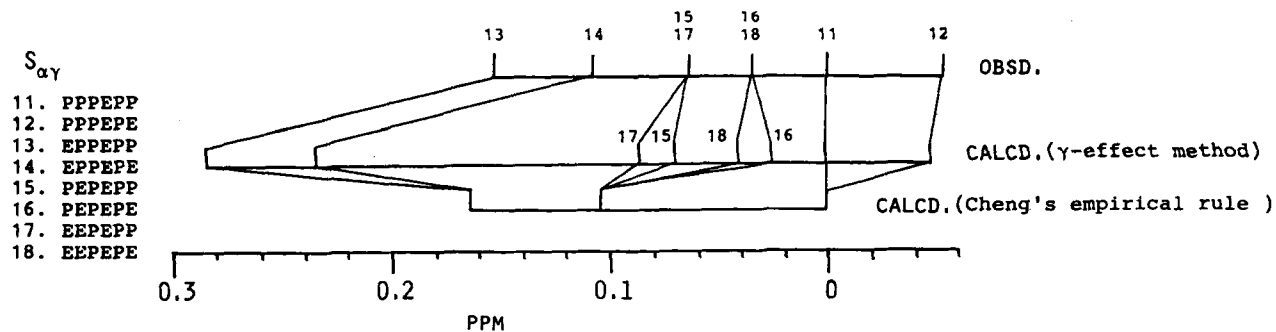


Fig. 26. The observed and calculated chemical shift differences of the $S_{\alpha\gamma}$ carbons among methylene-centred hexad comonomer sequences.

Table 24. Tetrad distribution for samples PE-2.

Tetrad	Obsd	Calcd (model M)	Calcd (model MM)
PPPP	0.771	0.756	0.762
PPPE	0.091	0.109	0.102
EPPE	0.006	0.004	0.005
PPEP	0.096	0.104	0.104
EPEP	0.011	0.008	0.010
PPEE	0.007	0.013	0.006
EPEE	0.003	0.001	0.003
PEEP	0.004	0.007	0.004
PEEE	0.002	0.001	0.003
EEEE	0.001	0.000	0.001
SS ^a /10 ⁻⁴		6.77	2.70

^aSum of the squares of the deviations between the observed and calculated sequence distributions.

B(iii) Polymerization mechanism (confirmation of hexad assignments by the prediction of peak intensities)

On the basis of these hexad assignments, the tetrad sequence distribution in PE-2 is determined by using the relationship:

$$[EEE] = [EEEE] + 0.5[PEEE] \quad (17)$$

where $[EEE] = 0.5[S_{88}] + 0.25[S_{\gamma\delta}]$ and $[PEEE] = [S_{\gamma\gamma}]$, as shown in Table 24. Since the ratios $[EPPE]/[PEEE]$ and $[EPEP]/[PPEE]$ are not equal to unity but 1.50 and 1.57, respectively, and the ratios $[PPEE]/[EPPE]$ and $[EPEP]/[PEEP]$ are 1.17 and 2.75, respectively, far from 2.0, neither one- nor multisite Bernoullian models can provide satisfactory fittings for the tetrad distribution.⁸⁷⁻⁹⁰ Thus, one-site (model M) and two-site (model MM) Markovian models (see Section 2.3.) were investigated as the copolymerization statistics. As shown in Table 24, the fitting for the tetrad distribution by model M produces large deviations in the calculated fractions of EPEP, PPEE, EPEE and PEEP tetrads. Model MM provides excellent fittings to the tetrad sequences. The optimum values of the parameters of model MM are as follows:

$$fp = 0.979 \text{ (fp : the fraction of a polymer produced at site 1)} \quad (18)$$

$$\text{site 1 : } p_{22} = 0.939, p_{11} = 0.041 \text{ (1 : ethylene, 2 : propylene)} \quad (19)$$

$$\text{site 2 : } p_{22} = 0.418, p_{11} = 0.454 \text{ (1 : ethylene, 2 : propylene)} \quad (20)$$

Table 25. Observed and calculated fractions of hexad sequences in $S_{\alpha\gamma}$ and $S_{\alpha\delta}$ carbons.

Carbon type	Sequence type	Obsd	Calcd (M)	Calcd (MM)
$S_{\alpha\gamma}$	PPPEPP	0.077	0.090	0.090
	PPPEPE	0.006	0.006	0.007
	EPPEPP	0.010	0.006	0.007
	EPPEPE	0.003	0.000	0.001
$S_{\alpha\gamma}$	PEPEPP+EEPEPP	0.011	0.007	0.008
	PEPEPE+EEPEPE	0.008	0.000	0.003
$S_{\alpha\delta}$	PPPEEP+PPPEEE	0.006	0.011	0.005
	EPPEEP+EPPEEE	0.002	0.001	0.001
$S_{\alpha\delta}$	PEPEEP+EEPEEP+EEPEEE	0.002	0.001	0.003
	PEPEEE	0.001	0.000	0.001

The validity of these hexad assignments is confirmed by the comparisons between the experimentally determined fractions of hexad sequences in the $S_{\alpha\gamma}$ and $S_{\alpha\delta}$ resonances and those calculated by model MM shown in Table 25. (The observed fractions of hexad sequences were determined by the curve resolution method as shown in Fig. 27.) The fractions predicted by model MM correspond well to the observed fractions except for the fraction of PEPEPE + EEPEPE, indicating that the proposed hexad assignments are reasonable.⁸³

C 2D INADEQUATE SPECTRUM (PENTAD ASSIGNMENTS OF METHINE CARBONS)

In Fig. 28 are shown the expanded doublet peaks of the methyl and methine carbons of the 2D INADEQUATE spectrum (Fig. 4) of the stereoregular ethylene-propylene copolymer. By tracing the revealed connectivities (i.e. presented by solid lines in the 2D spectrum) between the methyl and methine carbons, the pentad assignments of methine resonances (shown in Table 27) are provided with respect to the methyl pentad assignments shown in Table 26. The pentad assignments of the methyl carbons are given by comparison between the observed and calculated chemical shifts. The γ -effect calculations for the methyl carbons were performed in a similar manner as for the methylene carbons. In the resonance regions of the $T_{\beta\delta}$ and $T_{\delta\delta}$ carbons, the pentad assignments are established from the high-resolution 2D spectrum, in which broad peaks with shoulders in the 1D spectrum are observed separately.³⁰ The analytical method based on the 2D INADEQUATE NMR spectrum and chemical shift calculations is very powerful for the assignment of the ^{13}C NMR spectra of olefine copolymers.

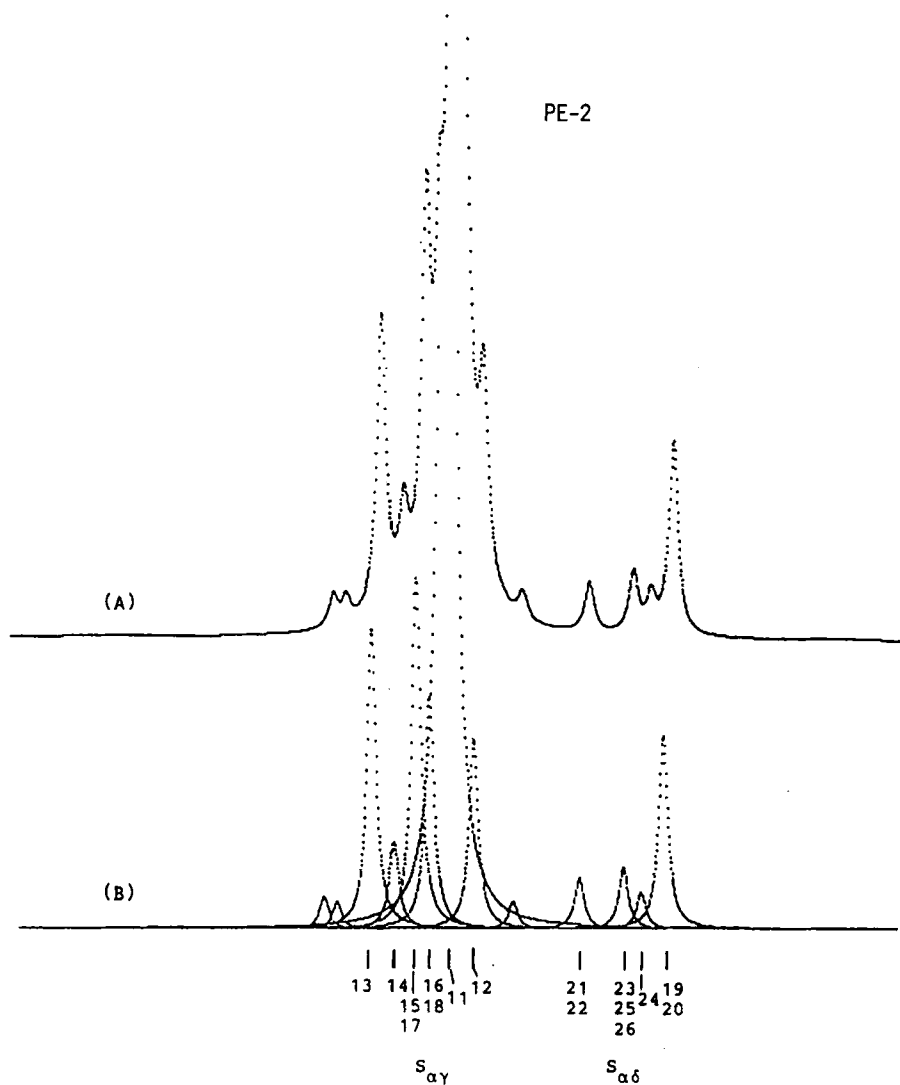


Fig. 27. Curve fitting results for the $S_{\alpha\gamma}$ and $S_{\alpha\delta}$ resonances. (A) Reproduced spectrum. (B) Results of curve resolution.

5.1.2. Stereoirregularity

The influence of the tacticity of the propylene unit on the ^{13}C NMR chemical shifts of the methylene carbons in the ethylene unit of E-P copolymer with a low ethylene content has been investigated by the calculated chemical shifts due to the γ -effect.⁸⁵ From the ^{13}C NMR spectra of the model compounds for the isolated ethylene unit in the polypropylene

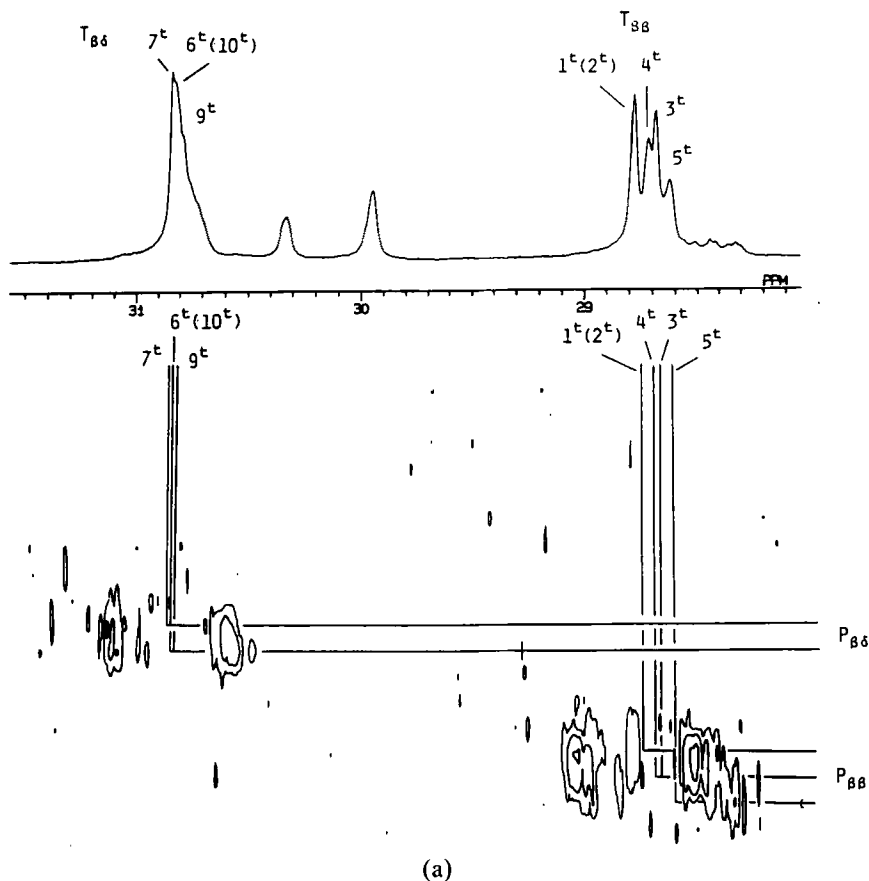


Fig. 28. Expanded doublet peaks of (a) and $T_{\beta\beta}$ and $T_{\beta\delta}$ carbons, (b) the $T_{\delta\delta}$ carbons, and (c) the $P_{\beta\beta}$, $P_{\beta\delta}$ and $P_{\delta\delta}$ carbons in the 2D INADEQUATE spectrum of the stereoregular ethylene-propylene copolymer.

sequences, Zambelli *et al.*⁴⁶ have indicated that this influence causes the splitting of such methylene peaks. However, these previous works cannot provide satisfactory assignments of the ^{13}C NMR spectrum of the stereoirregular ethylene-propylene copolymer in which all of the ethylene units are not isolated, because complicated peak splittings arising both from the different comonomer sequences and from the different tacticity sequences are observed. It has been difficult to evaluate the tacticity of the stereoirregular E-P copolymer.

It has been confirmed that the γ -effect is sensitive not only to the tactic sequences but also to the comonomer sequences.⁸⁰ In order to provide the spectral assignments and evaluate the tacticity, the chemical shift due to the γ -effect of the $S_{\alpha\gamma}$ and $S_{\alpha\delta}$ carbons in the stereoisomers of the respective

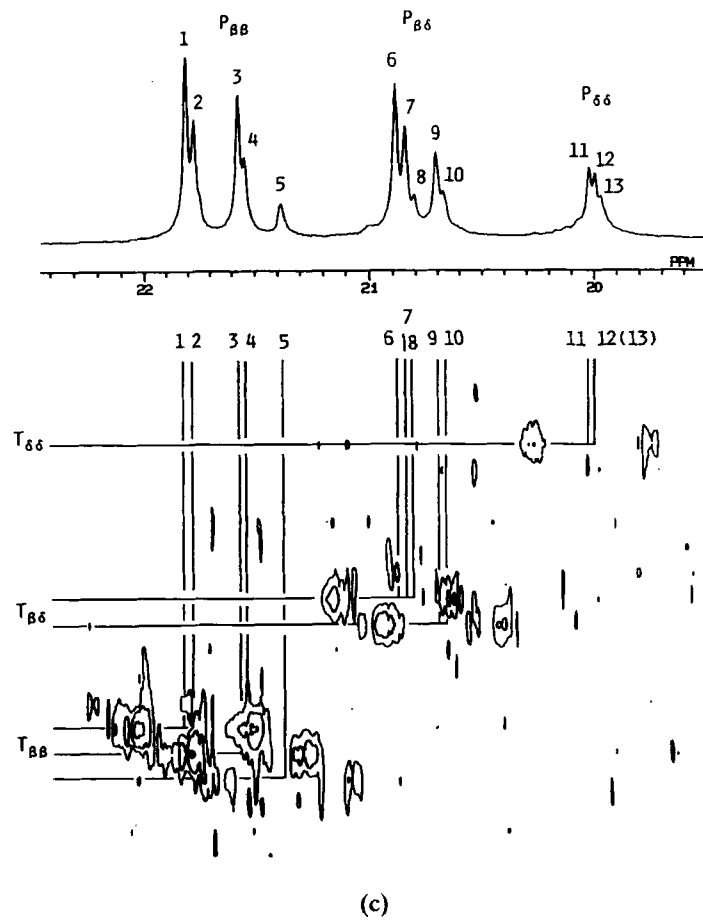
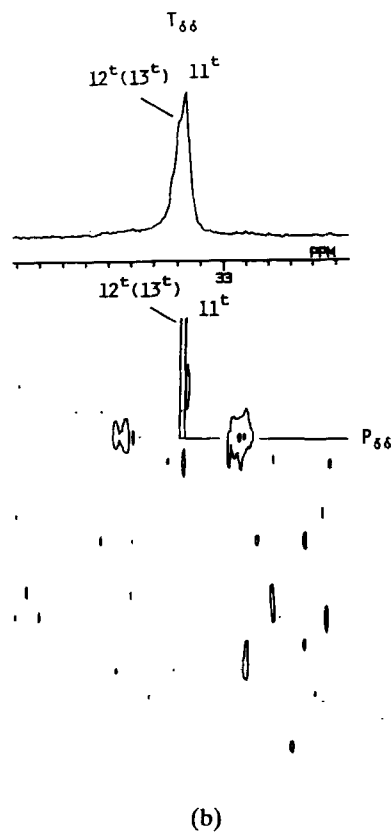


Table 26. Pentad assignments and chemical shift differences of methyl carbon resonances.

Carbon type	Peak no.	Assignment	Chemical shift differences ^a (ppm)	
			Calcd	Obsd
$P_{\beta\beta}$	1	PPPPP	0.0	0.0
	2	PPPPP-centred heptad	—	-0.04
	3	PPPPE	-0.254	-0.24
	4	PPPPE-centred heptad	—	-0.27
$P_{\beta\delta}$	5	EPPPE	-0.413	-0.38
	6	PPPEP	0.0	0.0
	7 ^b	PPPEP-centred heptad (or PPPEE)	—	-0.04
	8 ^b	PPPEE (or PPPEP-centred heptad)	-0.014	-0.08
	9	EPPEP	-0.252	-0.18
$P_{\delta\delta}$	10	EPPEE	-0.269	-0.21
	11	PEPEP	0.0	0.0
	12	PEPEE	-0.027	-0.02
	13	EEPEE	-0.044	-0.05

^aExpressed relative to the chemical shifts of the methyl carbons in PPPPP, PPPEP, and PEPEP sequences, respectively, which are set to be 0.00 ppm.

^bThe assignments of these peaks are not confirmed owing to the very small chemical shift differences between them.

Table 27. Pentad assignments of methine carbon resonances.

Carbon type	Peak no.	Assignment (pentad sequence)
$T_{\beta\beta}$	1 ^t (2 ^t)	PPPPP and PPPPP-centred heptad
	3 ^t	PPPPE
	4 ^t	PPPPE-centred heptad
	5 ^t	EPPPE
$T_{\beta\delta}$	6 ^t (10 ^t)	PPPEP and EPPEE
	7 ^t	PPPEP-centred heptad or PPPEE
	9 ^t	EPPEP
$T_{\delta\delta}$	11 ^t	PEPEP
	12 ^t (13 ^t)	PEPEE and EEPEE

hexad comonomer sequences were calculated.⁸⁶ In Fig. 29 are shown the model compounds used for the calculation of the chemical shifts of the hexad comonomer sequences. The calculation was performed for the carbon atoms marked by asterisks in all possible types of stereoisomers of these compounds.

In Fig. 30 are shown the $S_{\alpha\gamma}$ and $S_{\alpha\delta}$ resonance regions in the spectrum of the boiling heptane soluble fraction of the stereoregular E-P copolymer (PES7). In Tables 28 and 29 are shown the calculated and observed chemical shift differences among the stereosequence-dependent hexads, where the designations P^mP or P^rP and PE^mP or PE^rP mean that the configurations determined by the steric relationships between the successive propylene (P) units and those between the propylene units across the ethylene (E) unit are *meso* (*m*) or *racemo* (*r*), respectively. Referring to the spectral analysis of the E-P copolymers by Cheng,⁹¹ stereosequence-dependent split peaks are observed in the region from 38.3 to 39.1 ppm. Further, the chemical shifts of the $S_{\alpha\gamma}$ peaks (No. 11, 12, . . . , 18) and the $S_{\alpha\delta}$ peaks (No. 19, 20, . . . , 26) agree with those of the stereoregular (isotactic) hexad peaks in Fig. 25. Thus, peaks (No. 11, 12, . . . , 26) are assigned to stereoregular hexad comonomer sequences. The calculated chemical shift differences arising from different stereosequences are shown as stick spectra referring to the peaks of $P^mP^mPE^mP^mP$ (No. 11), $P^mP^mPE^mPE$ (No. 12), $EP^mPE^mP^mP$ (No. 13), EP^mPE^mPE (No. 14), $P^mP^mPEE^mP$ (No. 20), P^mP^mPEEE (No. 19), EP^mPEE^mP (No. 21), and EP^mPEEE (No. 22). The chemical shift differences of the EPEP- and EPEE-centred hexads dependent on stereosequences are negligibly small as shown in Tables 28 and 29. By comparing the observed and calculated chemical shift differences, peaks 28 and 32–34 are assigned to different stereoisomers of PPEP-centred hexads and peaks 27 and 29–31 to those of PPEE-centred hexads. These assignments agree with those proposed by Cheng⁹¹ with regard to the carbon types. The broad line widths of peaks 29–34 suggest the overlap of a number of stereosequence dependent resonances as predicted by the calculated chemical shift differences. On the basis of the resultant assignments in Tables 28 and 29, dyad tacticities of successive propylene units in PPEP and PPEE are determined as follows:

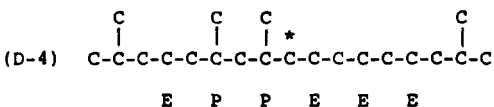
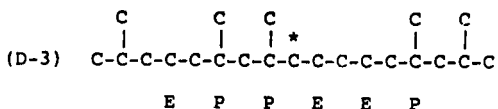
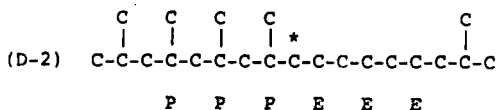
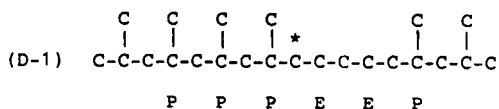
$$[P^mP^mPEP] = 0.858 \quad [P^rPEP] = 0.142 \quad (21)$$

$$[P^mP^mPEE] = 0.774 \quad [P^rPEE] = 0.226 \quad (22)$$

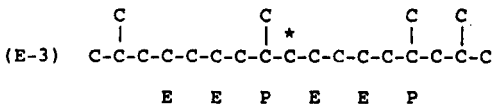
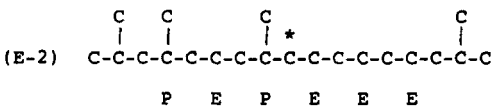
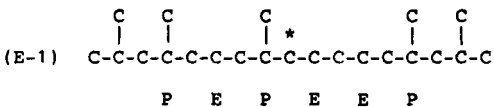
5.2. B-P copolymers

^{13}C NMR chemical shift differences among comonomer sequences longer than pentad in a stereoregular 1-butene-propylene copolymer with a low

Model compounds for PPEE-centered hexads of $S_{\alpha\delta}$ carbons



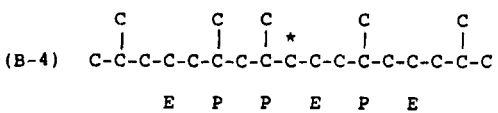
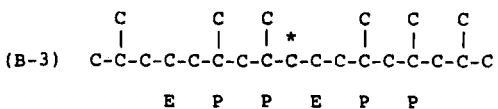
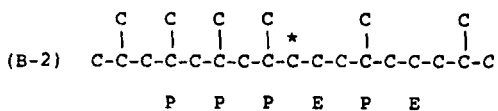
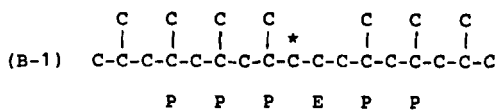
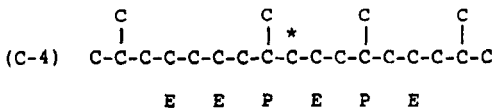
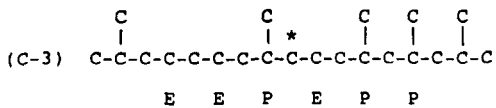
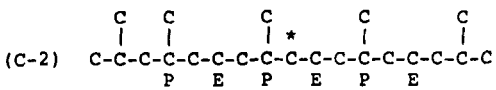
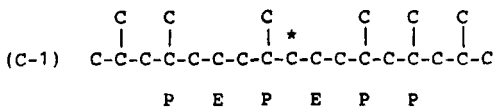
Model compounds for EPEE-centered hexads of $S_{\alpha\delta}$ carbons



(a)

Fig. 29. Model compounds used for the calculation of chemical shifts of the hexad comonomer sequences of (a) the $S_{\alpha\delta}$ and (b) the $S_{\alpha\gamma}$ carbons.

Model compounds for PPEP-centered hexads of $S_{\alpha\gamma}$ carbons

Model compounds of EPEP-centered hexads of $S_{\alpha\gamma}$ carbons

(b)

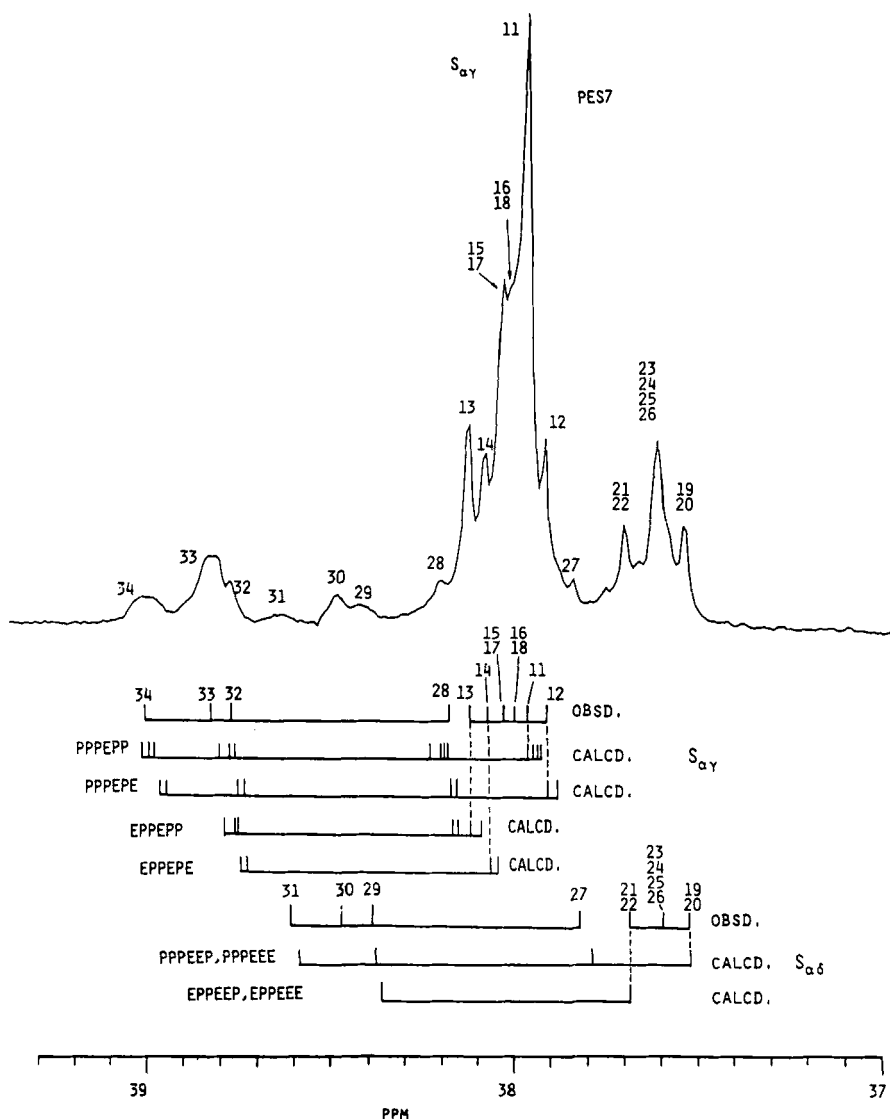


Fig. 30. ^{13}C NMR spectrum of the $S_{\alpha\gamma}$ and $S_{\alpha\delta}$ regions of boiling heptane soluble fraction of stereoregular ethylene-propylene copolymer. The observed and calculated chemical shifts are shown as stick spectra at the bottom of the figure.

Table 28. Calculated and observed chemical shift differences of S_{αγ} carbons among the stereosequence dependent hexads.

Hexad	Calcd ^a	Obsd ^a	Peak no.
P ^m P ^m PE ^r P ^r P	-0.052	0.0	11
P ^m P ^m PE ^r P ^m P	-0.040	0.0	11
P ^m P ^m PE ^m P ^r P	-0.030	0.0	11
P ^m P ^m PE ^m P ^m P	0.0	0.0	11
P ^r P ^m PE ^r P ^r P	0.216	0.224	28
P ^r P ^m PE ^r P ^m P	0.228	0.224	28
P ^r P ^m PE ^m P ^r P	0.236	0.224	28
P ^r P ^m PE ^m P ^m P	0.265	0.224	28
P ^r P ^r PE ^r P ^r P	0.793	0.799	32
P ^r P ^r PE ^r P ^m P	0.807	0.799	32
P ^r P ^r PE ^m P ^r P	0.808	0.799	32
P ^r P ^r PE ^m P ^m P	0.835	0.854	33
P ^m P ^r PE ^r P ^r P	1.009	1.034	34
P ^m P ^r PE ^m P ^r P	1.022	1.034	34
P ^m P ^r PE ^r P ^m P	1.025	1.034	34
P ^m P ^r PE ^m P ^m P	1.047	1.034	34
P ^m P ^m PE ^r PE	-0.027	0.0	12
P ^m P ^m PE ^m PE	0.0	0.0	12
P ^r P ^m PE ^r PE	0.242	0.278	28
P ^r P ^m PE ^m PE	0.266	0.278	28
P ^r P ^r PE ^r PE	0.819	0.853	32
P ^r P ^r PE ^m PE	0.837	0.853	32
P ^m P ^r PE ^r PE	1.035	1.088	34
P ^m P ^r PE ^m PE	1.050	1.088	34
EP ^m PE ^m P ^r P	-0.028	0.0	13
EP ^m PE ^m P ^m P	0.0	0.0	13
EP ^m PE ^r P ^m P	0.037	0.071	28
EP ^m PE ^r P ^r P	0.049	0.071	28
EP ^r PE ^r P ^r P	0.630	0.646	32
EP ^r PE ^r P ^m P	0.644	0.646	32
EP ^r PE ^m P ^r P	0.644	0.646	32
EP ^r PE ^m P ^m P	0.670	0.701	33
EP ^m PE ^r PE	-0.025	0.0	14
EP ^m PE ^m PE	0.0	0.0	14
EP ^r PE ^r PE	0.655	0.691	32
EP ^r PE ^m PE	0.673	0.691	32
PE ^m PE ^r P ^r P	-0.041	0.0	15
PE ^m PE ^m P ^r P	-0.026	0.0	15
PE ^m PE ^r P ^m P	-0.026	0.0	15
PE ^r PE ^r P ^r P	-0.007	0.0	15
PE ^m PE ^m P ^m P	0.0	0.0	15
PE ^r PE ^r P ^m P	0.007	0.0	15
PE ^r PE ^m P ^r P	0.007	0.0	15
PE ^r PE ^m P ^m P	0.033	0.0	15

^aExpressed relative to the chemical shifts of S_{αγ} carbons in P^mP^mPE^mP^mP, P^mP^mPE^mPE, EP^mPE^mP^mP, EP^mPE^mPE, and PE^mPE^mP^mP sequences, respectively, which are set to be 0.00 ppm.

Table 29. Calculated and observed chemical shift differences of $S_{\alpha\delta}$ carbons among the stereosequence dependent hexads.

Hexad	Calcd ^a	Obsd ^a	Peak no.
P ^m P ^m P ^{ee} P	-0.002	0.0	20
P ^m P ^m P ^{ee} ^m P	0.0	0.0	20
P ^r P ^m P ^{ee} P	0.265	0.298	27
P ^r P ^m P ^{ee} ^m P	0.267	0.298	27
P ^r P ^r P ^{ee} P	0.841	0.936	30
P ^r P ^r P ^{ee} ^m P	0.842	0.936	30
P ^m P ^r P ^{ee} P	1.056	1.086	31
P ^m P ^r P ^{ee} ^m P	1.057	1.086	31
P ^m P ^m P ^{eee}	0.0	0.0	19
P ^r P ^m P ^{eee}	0.267	0.298	27
P ^r P ^r P ^{eee}	0.842	0.936	30
P ^m P ^r P ^{eee}	1.057	1.086	31
EP ^m P ^{ee} P	-0.002	0.0	21
EP ^m P ^{ee} ^m P	0.0	0.0	21
EP ^r P ^{ee} P	0.675	0.710	29
EP ^r P ^{ee} ^m P	0.676	0.710	29
EP ^m P ^{eee}	0.0	0.0	22
EP ^r P ^{eee}	0.676	0.710	29
PE ^m P ^{ee} P	-0.002	0.0	23
PE ^m P ^{ee} ^m P	0.0	0.0	23
PE ^r P ^{ee} P	0.032	0.0	23
PE ^r P ^{ee} ^m P	0.033	0.0	23

^aExpressed relative to the chemical shifts of $S_{\alpha\delta}$ carbons in P^mP^mP^{ee}^mP, P^mP^mP^{eee}, EP^mP^{ee}^mP, EP^mP^{eee}, and PE^mP^{ee}^mP sequences, respectively, which are set to be 0.00 ppm.

1-butene content have been calculated using the γ -effect method.^{31,92} Since the bond conformational probability of the main chain should be influenced by the side chain conformation, Mark's⁶⁸ RIS model for an ethylene-propylene copolymer was modified for the application of a 1-butene-propylene copolymer considering the rotational isomeric states of bond j (Fig. 31) in the side-chain. Modified matrices for the interdyad bond pair (about $i-1$ and i) meeting at CH-CH₃ and CH-CH₂-CH₃ groups are $U'_{p(d)}$ and $U'_{b(d)}$, respectively.

$$U'_{p(d)} = \begin{bmatrix} \eta & 1 & \tau \\ \eta & 1 & \tau\omega \\ \eta & \omega & \tau \end{bmatrix}$$

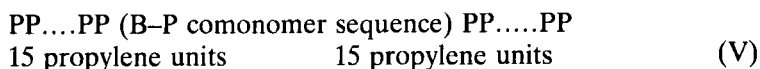
$$U'_{b(d)} = \begin{bmatrix} \eta \times a & b & \tau \times c \\ \eta \times c & d & \tau\omega \times e \\ \eta \times b & \omega \times f & \tau \times d \end{bmatrix}$$

$$\beta_{kl} = \begin{bmatrix} a & b & c \\ c & d & e \\ b & f & d \end{bmatrix}$$

where $a = \tau + 2\omega$, $b = \tau + \omega + 1$, $c = \tau\omega + \omega + 1$, $d = \tau\omega + 2$, $e = \tau\omega^2 + 2$, $f = \tau + 2$

$$[U'_{b(d)}]_{kl} = [U'_{b(d)}]_{kl} \times \beta_{kl}$$

The matrix $U'_{b(d)}$ for a 1-butene unit is obtained by multiplying every element in $U'_{p(d)}$ with the appropriate β_{kl} .^{36,93} Elements in β_{kl} denote statistical weights corresponding to three conformations (t , g , and \bar{g}) of the side-chain, determined by combination of the rotational isomeric states of the bonds $i-1$ and i in the main-chain. The Matrices $U'_{p(d)}$ and $U'_{b(d)}$ correspond to the *dextro*(d) configuration of propylene and 1-butene units. Matrices for the *levo* configuration can be obtained in a similar manner. Since the calculation is performed for the stereoregular copolymer, only $U'_{p(d)}$ and $U'_{b(d)}$ are used for the matrix multiplication.¹⁸ The model sequence of a stereoregular 1-butene-propylene copolymer of a low 1-butene content is:



where P and B denote propylene and 1-butene, respectively. The value of the γ -effect of the methine carbons on the propylene methyl carbons and on the side-chain methylene carbons is -5.3 ppm. The value of the 1-butene methyl carbons and the methine carbons on the backbone methylene carbons and the backbone methylene carbons on the 1-butene methyl carbons is -3.7 ppm. The value of the statistical weight, η , is taken to be 1.0, and the values of the four-bond pentad interference (ω) and three-bond *gauche* interactions (τ) are characterized with $E\omega = 6300 \text{ J mol}^{-1}$ and $E\tau = 2100 \text{ J mol}^{-1}$, respectively. The temperature assumed in the calculation is 120°C , corresponding to the experimental condition of the NMR measurement. The calculated results are summarized in Table 30.

In Fig. 32 is shown the propylene methyl carbon region in the ¹³C NMR

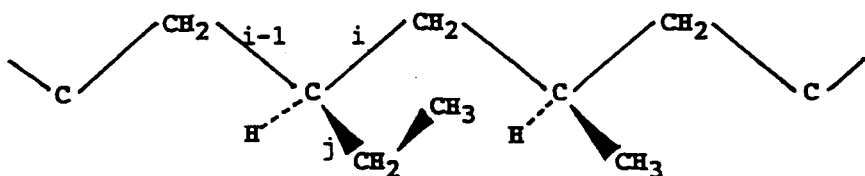


Fig. 31. Planar zigzag conformation of a 1-butene-propylene copolymer.

Table 30. Calculated ^{13}C NMR chemical shift differences in the resonance regions of methyl and methylene carbons of 1-butene-propylene copolymer.

Carbon ^a	Comonomer Sequences ^a	Chemical shift differences (ppm) ^b
$\begin{array}{c} \text{C} \quad \star \quad \text{C} \\ \quad \quad \\ -\text{C}-\text{C}-\text{C}-\text{C}-\text{C}- \\ \quad \quad \\ \text{P} \quad \quad \text{P} \end{array}$	BBPPBB	0.000
	BBPPBP	-0.048
	PBPPBP	-0.096
	BBPPPB	-0.185
	BBPPPP	-0.222
	PBPPPB	-0.233
	PBPPPP	-0.273
	BPPPPB	-0.370
	BPPPPP	-0.410
	PPPPPP	-0.451
$\begin{array}{c} \text{C} \\ \\ \text{C} \quad \star \quad \text{C} \\ \quad \quad \\ -\text{C}-\text{C}-\text{C}-\text{C}-\text{C}- \\ \quad \quad \\ \text{B} \quad \quad \text{P} \end{array}$	BBPB	0.000
	PBPB	-0.187
	BBPP	-0.183
	PBPP	-0.270
$\begin{array}{c} \text{C} \quad \quad \text{C} \\ \quad \quad \\ \text{C} \quad \star \quad \text{C} \\ \quad \quad \\ -\text{C}-\text{C}-\text{C}-\text{C}-\text{C}- \\ \quad \quad \\ \text{B} \quad \quad \text{B} \end{array}$	BBBB	0.000
	BBBBP	-0.096
	PBBP	-0.203
$\begin{array}{c} \text{C} \\ \\ \text{C} \quad \star \\ \\ -\text{C}-\text{C}-\text{C}- \\ \\ \text{B} \end{array}$	PPBPP	0.000
	BPBPP	-0.032
	BPBPB	-0.064
	PBBPP	-0.133
	BBBPP	-0.170
	PBBPB	-0.170
	BBBPPB	-0.201
	PBBBBP	-0.265
	BBBBBP	-0.313
	BBBBBB	-0.350
$\begin{array}{c} \star \\ \\ \text{C} \\ \\ -\text{C}-\text{C}-\text{C}- \\ \\ \text{P} \end{array}$	PPPPP	0.000
	BPPPP	-0.032
	BPPPB	-0.074
	PBPPP	-0.154
	PBPPB	-0.191
	BBPPP	-0.196
	BBPPB	-0.239
	PBPBP	-0.318
	BBPBP	-0.360
	BBPB	-0.403
$\begin{array}{c} \star \\ \\ \text{C} \\ \\ -\text{C}-\text{C}-\text{C}- \\ \\ \text{B} \end{array}$	PBP	0.000
	BBP	-0.026
	BBB	-0.052

^aC, P, and B denote carbon atom, propylene unit, and 1-butene unit, respectively.

^bChemical shift differences are expressed by ppm relative to those of the peaks appearing at the highest frequency, set to be 0.000 ppm.

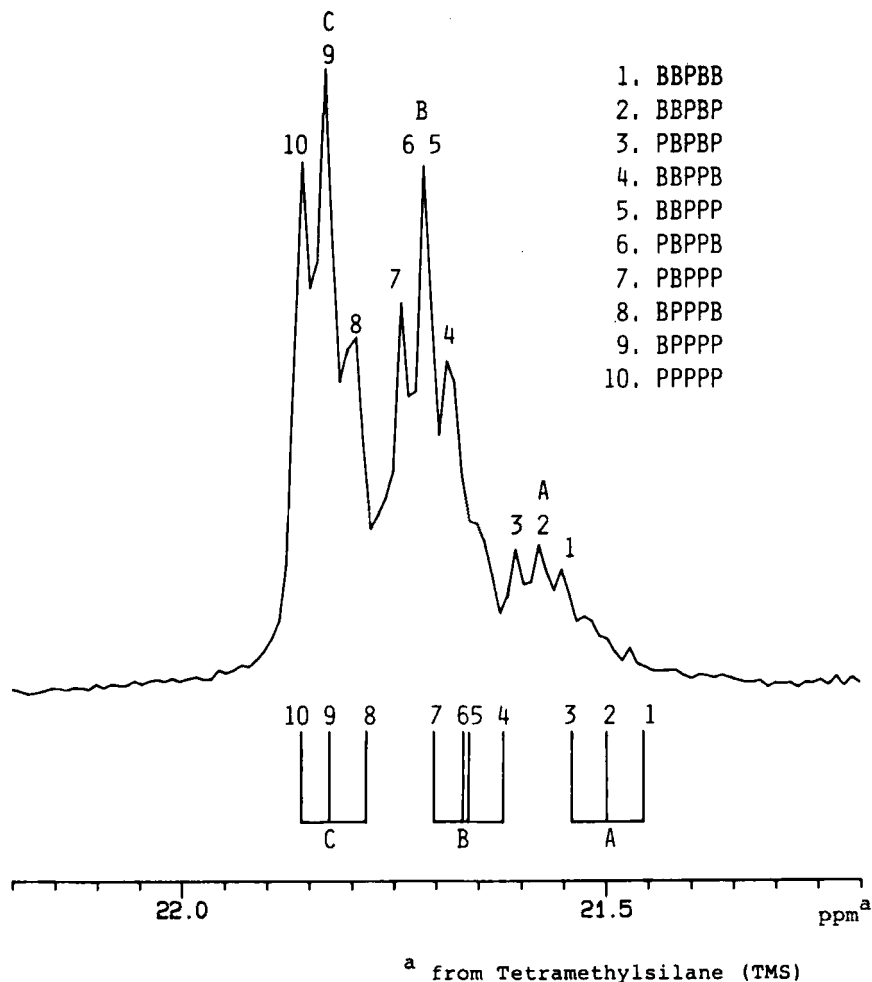


Fig. 32. Propylene methyl carbon region in the ^{13}C NMR spectrum of a 1-butene-propylene copolymer. The calculated chemical shifts are shown as stick spectra at the bottom of the figure.

spectrum of a 1-butene-propylene copolymer with the calculated chemical shifts of pentad comonomer sequences shown as stick spectra. The calculated spectra predict that resonances of BPB-, BPP-, and PPP-centred pentads appear as the respective groups A-C of the split peaks. In Fig. 33 are shown the connectivities among methyl, methine and methylene carbons in propylene units revealed on the 2D INADEQUATE spectrum. By tracing these connectivities, peaks A-C are assigned to the BPB, BPP, and PPP triads, respectively. Thus, the assignments of peak groups A-C based

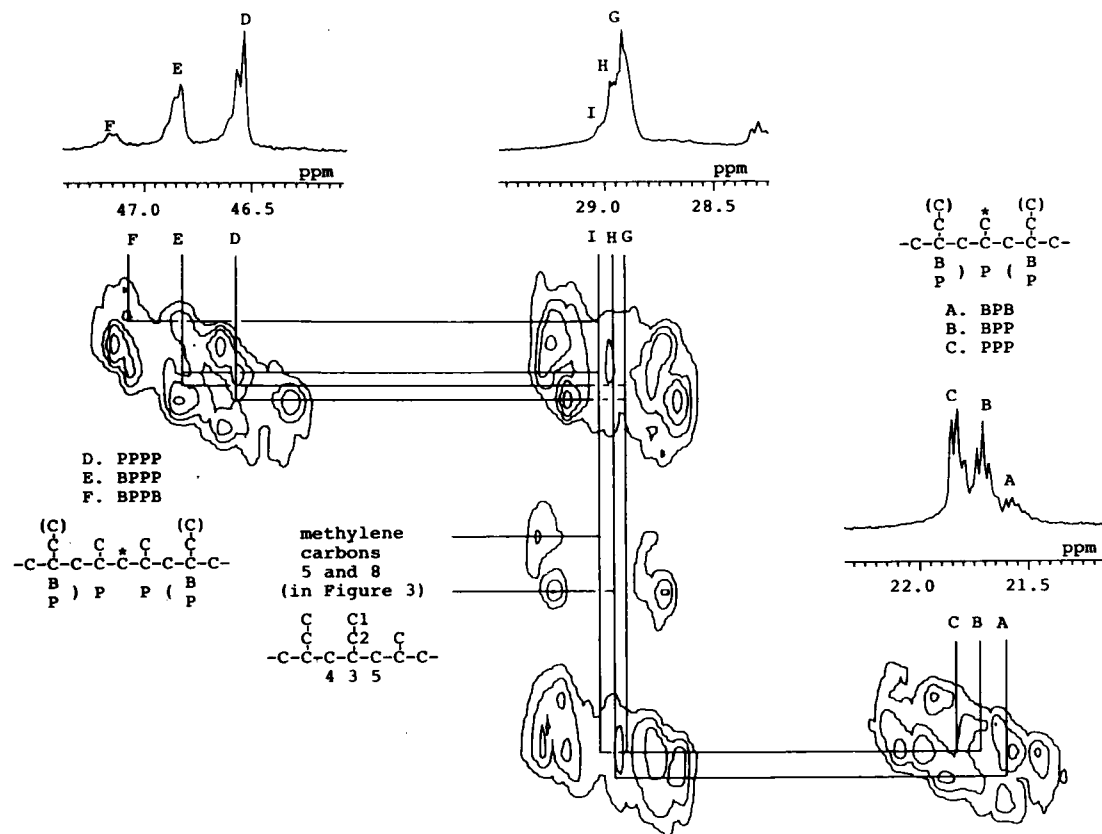


Fig. 33. Propylene methyl, methine, and methylene resonance regions in 2D INADEQUATE spectrum of a stereoregular 1-butene-propylene copolymer. Connectivities among methyl, methine, and methylene carbons in a 1-butene-propylene copolymer represented by solid lines A-H, B-I-E, B-I-F, C-G-D, and C-G-E.

on the chemical shift due to the γ -effect are consistent with those confirmed by the 2D INADEQUATE spectrum, indicating that the γ -effect method is reliable for the chemical shift predictions.³¹ The assignments of the central methylene carbons in PP-centred hexads and side-chain methyl carbons of the 1-butene unit in B-centred pentads are provided similarly.³¹ Pentad and hexad assignments based on the γ -effect method agree well with Cheng's assignments⁹⁴ by a reaction probability model. Further, the calculated chemical shifts³¹ of $\alpha\alpha$ -CH₂ carbons in BP- and BB-centred tetrads are also consistent with Cheng's assignments.⁹⁴ This removes the ambiguities found in previous tetrad assignments.⁹⁵⁻⁹⁷

6. CONCLUSION

^{13}C NMR spectroscopy is the most powerful method for studying aspects of the primary structure of polyolefines and olefine copolymers such as stereochemical configuration (tacticity), regioirregularity, chain-end structure and the sequences of the copolymers. In this chapter, we describe mainly two approaches for the assignment of the ^{13}C NMR spectra of these polymers, one is ^{13}C NMR chemical shift calculations on the basis of the γ -effect on the ^{13}C chemical shift, using the RIS model, and the other is the 2D INADEQUATE method. The calculation of ^{13}C chemical shifts on the basis of the γ -effects and the RIS model have also been successfully applied to the ^{13}C NMR tacticity assignments of other polymers such as poly(vinyl chloride)¹⁰⁰ and polystyrene.¹⁰¹ These calculations clarify the origin of the peak splitting due to the tacticity of the polymer in solution and provide methods to examine the tacticity dependent- and time-averaged local conformations calculated with the RIS model. The solid-state ^{13}C NMR spectra of polyolefines are also well interpreted in terms of the γ -effect. On the other hand, another method, 2D INADEQUATE, is especially useful for the sequence analysis of polyolefines and, hereafter, this will be used for the tacticity assignments in addition to the chemical shift calculations.

ACKNOWLEDGEMENTS

The authors thank Professor G. A. Webb of the University of Surrey for his encouragement and helpful comments on this chapter.

REFERENCES

1. F. A. Bovey, *High Resolution NMR of Macromolecules*, Academic Press, New York, 1972.

2. I. Ando and T. Asakura, in *Annual Reports on NMR Spectroscopy*, ed. G. A. Webb, 1980, **10A**, 81.
3. F. C. Stehling, *J. Polymer Sci. (a)*, 1964, **2**, 1815.
4. F. Heatley and A. Zambelli, *Macromolecules*, 1969, **2**, 618.
5. F. C. Stehling and J. R. Knox, *Macromolecules*, 1975, **8**, 595.
6. J. C. Randall, *Polymer Sequence Determination—Carbon-13 NMR Method*, Academic Press, New York, 1977.
7. F. A. Bovey and L. W. Jelinski, *Chain Structure and Conformation of Macromolecules*, Academic Press, New York, 1982.
8. F. A. Bovey, *Nuclear Magnetic Resonance Spectroscopy*, 2nd edn, Academic Press, New York, 1988.
9. I. Ando, T. Yamanobe and T. Asakura, *Progress in NMR Spectroscopy*, 1990, **22**, 349.
10. D. M. Grant and E. G. Paul, *J. Amer. Chem. Soc.*, 1964, **86**, 2984.
11. L. P. Lindeman and J. Q. Adams, *Anal. Chem.*, 1971, **43**, 1245.
12. A. Zambelli, P. Locatelli, G. Bajo and F. A. Bovey, *Macromolecules*, 1975, **8**, 687.
13. A. Zambelli, D. E. Dorman, A. I. R. Brewster and F. A. Bovey, *Macromolecules*, 1973, **6**, 925.
14. J. B. Stothers, *Carbon-13 NMR Spectroscopy*, Academic Press, New York, 1972.
15. K. Seidman and G. E. Maciel, *J. Am. Chem. Soc.*, 1977, **99**, 659.
16. M. Barfield and S. H. Y. Yamamura, *J. Am. Chem. Soc.*, 1990, **112**, 4747.
17. T. M. Birshstein and O. B. Ptitsyn, *Conformations of Macromolecules*, Interscience, New York, 1966.
18. P. J. Flory, *Statistical Mechanics of Chain Molecules*, Interscience, New York, 1969.
19. R. H. Boyd and S. M. Breitling, *Macromolecules*, 1972, **5**, 279.
20. U. W. Suter and P. J. Flory, *Macromolecules*, 1975, **8**, 765.
21. F. C. Schilling and A. E. Tonelli, *Macromolecules*, 1980, **13**, 270.
22. A. Zambelli, P. Locatelli, A. Provasoli and D. R. Ferro, *Macromolecules*, 1980, **13**, 270.
23. M. Mauzac, J. P. Vairon and P. Sigwalt, *Polymer*, 1977, **18**, 1193.
24. T. Asakura, K. Omaki, S.-N. Zhu and R. Chûjô, *Polymer J.*, 1984, **16**, 717.
25. T. Asakura, M. Demura, K. Yamamoto and R. Chûjô, *Polymer*, 1987, **28**, 1037.
26. H. N. Cheng and M. A. Bennett, *Makromol. Chem.*, 1987, **188**, 2665.
27. A. Bax, R. Freeman and T. Frenkiel, *J. Am. Chem. Soc.*, 1981, **103**, 2102.
28. T. Asakura, K. Hirano, M. Demura and K. Kato, *Makromol. Chem., Rapid Commun.*, 1991, **12**, 215.
29. K. Hikichi, T. Hirai, M. Ikura, K. Higuchi, K. Eguchi and M. Ohuchi, *Polym. J.*, 1987, **19**, 1317.
30. T. Hayashi, Y. Inoue, R. Chûjô and T. Asakura, *Polym. J.*, 1988, **20**, 895.
31. A. Aoki, T. Hayashi and T. Asakura, *Macromolecules*, 1992, **25**, 155.
32. T. Asakura, N. Nakayama, M. Demura and A. Asano, *Macromolecules*, 1992, **25**, 4876.
33. Y. Inoue, Y. Itabashi and R. Chûjô, *Polymer*, 1984, **25**, 1640.
34. S. N. Zhu, X. Z. Yang and R. Chûjô, *Polym. J.*, 1983, **15**, 859.
35. A. Abe, R. I. Jernigan and P. J. Flory, *J. Am. Chem. Soc.*, 1966, **88**, 631.
36. H. Wittwer and U. W. Suter, *Macromolecules*, 1985, **18**, 403.
37. J. E. Mark, *J. Chem. Phys.*, 1972, **57**, 2541.
38. T. Asakura, I. Ando and A. Nishioka, *Makromol. Chem.*, 1976, **177**, 1493.
39. P. J. Flory and Y. Fujiwara, *Macromolecules*, 1969, **2**, 315.
40. T. Asakura, I. Ando and A. Nishioka, *Makromol. Chem.*, 1976, **177**, 523.
41. S.-N. Zhu, T. Asakura and R. Chûjô, *Polym. J.*, 1984, **16**, 895.
42. H. N. Cheng, *Polym. Bull.*, 1985, **14**, 347.
43. H. L. Fisch, C. L. Mallows and F. A. Bovey, *J. Chem. Phys.*, 1966, **45**, 1565.
44. Y. Inoue, A. Nishioka and R. Chûjô, *Makromol. Chem.*, 1973, **168**, 163.
45. J. C. Randall, *J. Polym. Sci.*, 1976, **14**, 2083.

46. A. Zambelli, P. Locatelli, A. Provasoli and D. R. Fero, *Macromolecules*, 1980, **13**, 267.
47. R. Chûjô, *Kagaku*, 1980, **36**, 78.
48. J. Furukawa, *J. Polym. Sci., Polym. Lett. Ed.*, 1965, **3**, 23.
49. T. Hayashi, Y. Inoue and R. Chûjô, *Macromolecules*, 1988, **21**, 3129.
50. H. N. Cheng and M. Kakugo, *Macromolecules*, 1991, **24**, 1724.
51. T. Hayashi, Y. Inoue, R. Chûjô and T. Asakura, *Polymer*, 1988, **29**, 138.
52. T. Hayashi, Y. Inoue, R. Chûjô and T. Asakura, *Macromolecules*, 1988, **21**, 2675.
53. D. P. Burum and R. R. Ernst, *J. Magn. Reson.*, 1980, **39**, 163.
54. D. M. Doddrell and D. T. Pegg, *J. Am. Chem. Soc.*, 1980, **102**, 6388.
55. A. Bax, R. Freeman and S. P. Kempell, *J. Am. Chem. Soc.*, 1980, **102**, 4849.
56. R. Freeman and T. Frenkiel, *J. Am. Chem. Soc.*, 1982, **104**, 5545.
57. J. C. Randall, *Macromolecules*, 1978, **11**, 33.
58. L. Braunsweiler, G. Bodenhausen and R. R. Ernst, *Mol. Phys.*, 1983, **48**, 535.
59. H. N. Cheng and M. A. Bennett, *Makromol. Chem.*, 1987, **188**, 135.
60. A. E. Tonelli, *Macromolecules*, 1978, **11**, 565.
61. T. Asakura, Y. Nishiyama and Y. Doi, *Macromolecules*, 1987, **20**, 616.
62. T. Asakura, I. Ando, A. Nishioka, Y. Doi and T. Keii, *Makromol. Chem.*, 1977, **178**, 791.
63. C. J. Carman and C. D. Wilkes, *Rubber Chem. Technol.*, 1971, **44**, 781.
64. A. Zambelli and G. Gatti, *Macromolecules*, 1978, **11**, 485.
65. A. Grassi, A. Zambelli, L. Resconi, E. Albizzati and R. Mazzocchi, *Macromolecules*, 1988, **21**, 617.
66. T. Hayashi, Y. Inoue, R. Chûjô and T. Asakura, *Macromolecules*, 1988, **21**, 2675.
67. A. Zambelli, P. Locatelli and G. Bajo, *Macromolecules*, 1979, **12**, 154.
68. J. E. Mark, *J. Chem. Phys.*, 1972, **57**, 2541.
69. P. Pino and R. Mullaupt, *Angew. Chem., Int. Ed. Engl.*, 1980, **19**, 875.
70. T. Asakura and N. Nakayama, *Polymer*, 1992, **33**, 650.
71. T. Asakura, M. Demura and Y. Nishiyama, *Macromolecules*, 1991, **24**, 2334.
72. T. Asakura and N. Nakayama, *Polym. Commun.*, 1991, **32**, 213.
73. A. Zambelli, P. Ammendola, M. C. Sacchi, P. Locatelli and G. Zannoni, *Macromolecules*, 1983, **16**, 341.
74. M. C. Sacchi, I. Tritto, P. Locatelli and D. R. Ferro, *Makromol. Chem., Rapid Commun.*, 1984, **5**, 731.
75. G. J. Ray, P. E. Johnson and J. R. Knox, *Macromolecules*, 1977, **10**, 773.
76. C. J. Carman, R. A. Harrington and C. E. Wilkes, *Macromolecules*, 1977, **10**, 536.
77. J. R. Paxon and J. C. Randall, *Anal. Chem.*, 1978, **50**, 1777.
78. M. Kakugo, Y. Naito, K. Mizunuma and T. Miyatake, *Macromolecules*, 1982, **15**, 1150.
79. A. E. Tonelli, *Macromolecules*, 1979, **12**, 255.
80. T. Hayashi, Y. Inoue, R. Chûjô and T. Asakura, *Polym. J.*, 1988, **20**, 107.
81. A. Zambelli, P. Locatelli and G. Bajo, *Macromolecules*, 1979, **12**, 154.
82. A. Zambelli, M. C. Sacchi and P. Locatelli, *Macromolecules*, 1979, **12**, 783.
83. T. Hayashi, Y. Inoue, R. Chûjô and T. Asakura, *Polymer*, 1988, **29**, 1848.
84. A. Zambelli, G. Bajo and E. Rigamonti, *Makromol. Chem.*, 1978, **179**, 1249.
85. A. E. Tonelli, *Macromolecules*, 1978, **11**, 634.
86. T. Hayashi, Y. Inoue, R. Chûjô and T. Asakura, *Polymer*, 1988, **29**, 2208.
87. J. F. Ross, *J. Macromol. Sci. Chem.*, 1984, **A21(4)**, 453.
88. J. F. Ross, International Symposium of Transition Metal Catalyzed Polymerization, Akron, USA, June 16, 1986, paper 60.
89. J. F. Ross, *J. Macromol. Sci. Chem.*, 1987, **A24(2)**, 211.
90. C. Cozewith, *Macromolecules*, 1987, **20**, 1237.
91. H. N. Cheng, *Macromolecules*, 1984, **17**, 1950.
92. A. Aoki, *Polym. Commun.*, 1990, **31**, 130.

93. A. Abe, *J. Am. Chem. Soc.*, 1968, **90**, 2205.
94. H. N. Cheng, *J. Polym. Sci., Polym. Phys. Ed.*, 1983, **21**, 573.
95. A. Bunn and M. E. A. Cudby, *Polymer*, 1976, **17**, 548.
96. J. C. Randall, *Macromolecules*, 1978, **11**, 592.
97. T. Usami, Y. Kosugi and T. Takeuchi, *J. Polym. Sci., Polym. Phys. Ed.*, 1979, **17**, 1413.
98. Y. Doi, *Macromolecules*, 1979, **12**, 248.
99. W. V. Smith, *J. Polym. Sci., Polym. Phys. Ed.*, 1980, **18**, 1573.
100. A. E. Tonelli, F. C. Schilling, W. H. Starnes, Jr, L. Shepherd and I. M. Plitz, *Macromolecules*, 1979, **12**, 78.
101. A. E. Tonelli, *Macromolecules*, 1983, **16**, 604.

Index

- α -helix, 146, 148
- Acids, phenol resin stability and, 201–2
- Additivity, 22, 54–8
- Allophanate, 226
- AMBER force field, 62
- Anionic polymerization, 302
- Anisotropic environments, protein structure and, 128
- Anisotropy
 - chemical shift, 176–7
 - orientational 137–9
- Atactic polypropylene, 341–4
- Atomic bonds, *see* Bond aspects
- Atoms in molecules, and shielding calculations, 95–7
- Azo-bis(isobutyronitrile), 229, 304, 308–9, 316
- Azo-bis(methyl isobutyrate) (AIBMe), 309–10, 312
- Bacillus brevis*, 130
- Bacteriorhodopsin, 128–9
 - dynamics of, 144–5
 - structural constraints, 145–6
- Bader's theory, 95–7
- Bases, and phenolic resin stability, 201–2
- Becke exchange potentials, 116
- Benzoyl peroxide (BPO), 303–5, 318
- Bernoullian model, 335, 359
- Biot–Savart law, 76, 79–80
- Bisphenol A dicyanate, 269
- Bisphenol A polycarbonate, 272–3
- Biuret-rich MDI-based resins, 227–39
- Bond angle deformation, 7–12
- Bond extension, 7–12
 - angle deformation, 7–12
 - remote, 17–19
- Bond length, diatomic molecules, 5–6
- Born–Oppenheimer approximation, 76
- Buckingham equation, 25
- Butanediol-2,2,3,3-d₄, 242–4
- 1-Butene-propylene copolymers, 391–401
- Calmodulin, 61–2
- ¹³C CP-MAS NMR spectroscopy
 - 4'-cyanophenyl-4-*n*-pentoxybenzoate, 267
 - epoxy resins, 258–61
 - epoxy resin curing, 274
 - glass bead/PA-6 composites, 274
 - Hytrel copolymer and, 263
 - isocyanate-rich/biuret-rich MDI-based resins, 227–39
 - naphthalene-based thermotropic polyesters, 269
 - nylons, 245–9
 - olefin/polyolefin copolymers, 325–404
 - PET, 266–7
 - poly(α -methyl- α -*n*-ethyl- β -propiolactone), 267
 - polyamide-6, 273
 - poly(β -hydroxyalkanoate), 267
 - poly(butylene terephthalate), 261–6
 - poly(*N,N*-dimethylacrylamide), 272
 - polypivalolactone polymorphs, 267
 - poly(*p*-oxybenzoate), 267
 - poly(*p,p*-biphenylene terephthalate), 267
 - polyurethanes, 241–3
 - urea-formaldehyde resins, 205–18
 - see also* ¹⁵N CP-MAS NMR spectroscopy
- ¹³C magnetization generation, 174–5
- Chain end structures, polymers, 303–7
- CHAPSO, 143
- Charge-field perturbation method, 52
- Chemical modification, and tensor sensitivity, 139–40
- Chemical shift anisotropy, 176–7
- Chemical shift calculation
 - Cheng method, 329–30
 - conformational analysis, 331–5
 - γ -shielding, 333–5
 - Lindeman–Adams method, 328–9
 - RIS model, 331–3
- Cheng method, 329–30
- Coat proteins, *see* Viral coat proteins
- Complete active space self-consistent field (CASSCF) method, 113–15

- Complex systems, and NMR chemical shift, 51–63
 additivity, 54–8
 dynamic averaging, 58–60
 electron field effects, 58–60
 scaling, 54–8
 shielding, short-/long-range effects, 51–3
 shift prediction, 60–4
- Composite materials resins, 273–4
- Conformational analysis, chemical shift calculations, 331–5
 RIS and, 331–3
 γ -shielding effect, 333–5
- Co-ordinate polymerization, 302
- Copolymer monomer sequences, in polymers, 293–6
- Copolymerization, monomer reactivity in, 312–16
 non-NMR methods and, 315–16
- Correlation, and shielding *ab initio* calculations, 106–117
 density functional theory, 115–17
 GIAO MP2, 107–109
 multi-configuration IGLO, 112–15
 SOLO and, 109–12
- Coulomb gauge, 79, 82
- Coupled density functional theory, 115–17
- Coupled Hartree–Fock method, 4, 96
see also Hartree–Fock theory
- Cross-polymerization, 172–6
- Cryoelectron microscopy, 134
- Crystallization, 128, 142–4
- Cured furfuryl alcohol resins, 182–5
- Cured phenolic resins, 186–200
 thermal decomposition, 197–200
- Cyanate resins, 269–71
- 4'-Cyanophenyl-4-*n*-pentoxybenzoate, 267
- Cyclophilin, 133
- Cyclosporin A, 133
- Density functional theory, 115–17
- Derivative Hartree–Fock theory, 52
see also Hartree–Fock theory
- Detergent micelles, 134
- Deuterium-enriched monomers, 299
- Deuterium NMR, 179, 256–7
 nylon, 256–7
- Diacylphosphatidylcholine, 161
- Diamagnetic anisotropy liquid crystalline preparations, 143
- Diamagnetic field, 81
- Diaminodiphenylsulfone, 258–9
- Diatomic molecular bond lengths, 5–6
- Dihedral angle, 12–17
- Dilute spins, high-resolution solid-state NMR, 172–8
 crosspolarization, high power ^1H decoupling, 172–6
 dynamic nuclear polarization, 176
 magic angle spinning (MAS), 176–8
 CP-MAS linewidth, 178
 ^{14}N - ^{13}C polar interaction, 177–8
 rotors, 176
- Dimyristoyl phosphatidylcholine, 138
- Dipolar-dephasing $^{13}\text{C}/^{15}\text{N}$ CP-MAS NMR 189–97
- Dipolar-dephasing CP-MAS NMR spectroscopy, 174–6
- Direct polarization, 174
- Dispersion, 25–7
- Distance, and intermolecular shielding surfaces, 19–21
- Ditchfield's GIAO method, 83, 96, 98, 101
- DNA, 130
- Dodecylphosphocholine, 130
- Dynamic averaging, shielding surfaces, 29–50, 58–60
 intermolecular shifts, 39–50
 isotope effects, 34–9
 temperature and, 31–4
- Dynamic nuclear polymerization, 176
- Dynamics, and protein function, 124–5
- Electric field effects, 25–7, 58–60
- Electric field, and NMR chemical shift, 25–7
- Electron microscopy, 134
- Empirical chemical shift calculations
see Chemical shift calculation
- ENZYMIZ program, 60
- Epoxy resin curing, 274
- Epoxy resins, 258–61
- Escherichia coli*, 144
- Ethylene-olefin copolymers, 370–91
 comonomer sequence, 370–87
 stereoirregularity, 387–91
- Ethylene-propylene copolymers, 370–91
 comonomer sequence, 370–87
 ^{13}C NMR chemical shift, γ -effect, 370–5

- hexad comonomer sequence
 - assignments, 375–87
 - stereoirregularity, 387–91
- Filamentous virus coat proteins, 130
- Flap angles, 103–6
- Florenyl methoxycarbonyl chemistry, 144
- Flygare's method, 33
- Fock Hamiltonians, 107
 - see also* Hamiltonians
- Formaldehyde, 201–3
 - phenol resins, 185–203
 - urea resins, 203–24
- Formalin, and phenolic resin stability, 201–2
- Fourier transform NMR, 172
- Free induction decay, 173, 239–40
- Furfuryl alcohol resins, 180–5
- γ -aminopropyltriethylsilane, 273
- γ -effect, and ethylene-propylene copolymer, 370–5
 - calculation, 375–7
- γ -gauche effect, 12
- γ -shielding effect, 333–5
- Gap energy, 104–6
- Gas/liquid to gas/solution shifts, 47–50
- Gas-phase chemical shifts, 40–2
- Gauche-trans conformational jumps, polyurethanes, 242–3
- Gauche transformation, 12
- Gauge-including Atomic Orbitals (GIAO) 5, 12, 22, 39, 51, 83, 84, 95, 96, 102, 107
 - Ditchfield's, 84, 98, 101
 - MP2, 107–9
- Glassbead/PA-6 composites, 274
- Global shape, NMR trace, and shielding surfaces, 27–9
- Glucagon, 134
- Goldman-Shen experiment, 240–1
- Gramicidin, 124, 127–8, 130–2, 139, 141, 148
 - dynamics, 157–8
 - and structure-function, 158–60
 - and lipid interactions, 160–1
 - lipid phase effects, 161
 - solvent history dependence, 160–1
 - structural constraints, 148–52
 - conformational analysis, 150–2
 - structural refinement, 152–7
 - structure-function dynamics, 158–60
- tryptophan in, 160
- Grand Canonical Monte-Carlo (GCMC) scheme, 44, 46, 47, 62
- GRASP program, 159
- Hahn spin echo experiments, 299
- Halobacterium halobium*, 129
- Hamiltonians, 76–9, 171
- Hartmann-Hahn condition, 172–3
- Hartree-Fock theory, 72–5, 81–5, 95, 100–3, 106–9, 112–13, 115–17
- Herzfeld-Berger spinning sideband method, 263
- Heteronuclear chemical shift correlation spectroscopy, 272
- Hexad assignments, prediction of peak intensities, 385–7
- Hexad assignments, $S_{\alpha\gamma}/S_{\alpha\delta}$, 377–85
- Hexad comonomer sequence assignments, ethylene-propylene copolymer, 375–7
- High-power ^1H decoupling, 172–7
- High resolution electron microscopy, 134
- High resolution solid-state NMR, organic resins, 172–9
 - deuterium NMR, 179
 - dilute spins, 172–8
 - ^1H NMR, 178
- High resolution structural biology, 125–6
- HIV-protease, 127, 144
- ^2H NMR, *see* Deuterium NMR
- Hohenberg-Kohn theorem, 115
- Homopolymer tacticity, 288–93
- HPLC, and gramicidin-lipid interactions, 160–1
- Hydrobenzoic acid, 269
- Hydrogen bonding, 22–4, 126
- Hydrogen-selected pulse sequence, 299
- Hydrolysis, of urea-formaldehyde resins, 222–4
- Hydroquinone, 269
- 4-Hydroxybenzoic acid, 269
- 2-Hydroxy-6-naphthoic acid, 269
- Hytrel, 262–4
- IGAIM, *see* Keith-Bader IGAIM approach
- INADEQUATE, 327, 338–9
 - spectrum (pentad assignments, methine carbons), 386

- Incredible Natural Abundance Double Quantum Transfer Experiment
see INADEQUATE
- Individual Gauge for Localized Orbitals (IGLO), 4, 12, 51, 83–4, 96–7, 107, 111–15
multi-configuration, 112–15
- INEPT, 338
- Initiators, and polymer end-group detection, 303–12
breakdown, radical–radical reaction, 307–8
kinetics of, 308–12
vs. non-NMR methods, 310–12
mechanisms, 303–7
- Insensitive Nuclei Enhanced by Polarization Transfer, *see* INEPT
- Intermolecular shielding surfaces, 19–24
- Intramolecular shielding surfaces, 5–19
- Isocyanate resins, 225–45
phase separation, in polyurethane, 239–45
- Isocyanurate-rich MDI-based resins, 227–39
- Isophthalic acid, 269
- Isotactic polypropylene, 341–4
- Isotope effects, 34–9
- Isotope shifts, 35–9
one-bond, 37
three-bond, 38–9
two-bond, 38–9
- Isotopic labelling, 144
- Karplus relationship, 293
- Keith–Bader IGAIM approach, 95–7
- Kohn–Shams theory, 115
- Labelled initiator synthesis, 318
- Labelled monomers, 296–7
- Labelling, NMR, synthetic polymers, 283–323
- Lewis acids, 225
- Light-harvesting complex, 134
- Lindeman–Adams method, 328–9, 345, 360
- Linewidth, CP-MAS spectra, dilute spins, 178
- Lipid bilayers, 129–32
see also Gramicidin
- Lipid phase, and gramicidin, 161
- Lipids, and gramicidin, interactions, 160–1
- Local Reaction Field model, 60
- Localized Orbital Local Origin Method (LORG), 4, 6, 21, 51, 84, 96–7, 107, 110–12
second order (SOLO), *see* Second Order LORG
- Locally dense basis sets, 90–4
- Long-range shielding effects, 51–3
- Magic angle spinning (MAS), 176–8
 ^{14}N – ^{13}C dipolar interactions, 177–8
rotors, for large volumes, 176
and urea-formaldehyde resins, 205–22
 ^{13}C CP, 205–18
 ^{15}N CP, 218–22
- Magnetically oriented model membranes, 143
- Markovian model, 335, 359–60
- MDI *see* Methylene bis(phenyl isocyanate)
- Membrane lipid bilayers, 129–32
- Mercury method, 315
- Methine carbons, pentad assignments, 386–7
- 4,4-Methylene bis(phenyl isocyanate), 227–39
- Methyl methacrylate (MMA), 289–90
- Møller–Plesset perturbation theory (MPT), 107–8
- Monomers, labelled, 296–7
- Monte-Carlo simulation, 342
- Multiconfiguration IGLO, 107, 112–15
- Multidimensional NMR, synthetic polymers, 283–323
- Naphthalene-based thermotropic polyesters, 269
- ^{14}N – ^{13}C dipolar interactions, MAS, 177–8
- ^{15}N CP-MAS NMR spectroscopy
isocyanate-rich/biuret-rich MDI-based resins, 227–39
nylons, 249–56
urea-formaldehyde resins, 218–22
- N-formyl-L-amino acid amide, 10, 13, 15, 61
- Nitroxide trapping technique, 315–16
- NMR chemical shielding, *see under* Shielding

- NMR chemical shift, 1–69
 complex systems' applications, 51–63
 additivity, 54–60
 prediction and, 60–3
 scaling, 51–3
 short-range/long-range, and
 shielding, 51–9
 dynamic averages, 29–50
 intermolecular shifts, 39–50
 isotope effects, 34–9
 temperature and, 31–4
 shielding surfaces, 4–29
 electric field effects, 25–7
 global shape for traces on, 27–9
 intermolecular, 19–24
 intramolecular, 5–19
 NMR observation, 338–9
 INADEQUATE, 327, 338–9
 INEPT, 338
 NMR spectroscopy, solid-state, 135–44
see also under Proteins
 NMR spectroscopy, solution, 132–4
N,N-dimethylolurea, 209, 210, 216, 218
 Nonaethylnonadecane, 354–5, 357
 Nonamethylnonadecane, 354, 356–7
 Novolak resins, 185–6, 190–3
 Nylons, 245–61
 solid-state NMR spectroscopy of
 ^{13}C , 245–9
 ^2H , 256–7
 ^{15}N , 249–56
- Olefin copolymers, ^{13}C NMR
 assignments, 325–404
- One-bond isotope shifts, 37
- Onsager's reaction field, 88–90
- Orbital shielding analysis, 100–6
- Organic resins, 169–285
 composite material resins, 273–4
 cyanate resins, 269–71
 epoxy resins, 258–69
 furfuryl alcohol resins, 180–5
 isocyanate resins, 225–45
 nylons, 245–57
 phenol-formaldehyde resins, 185–203
 polyester resins, 261–9
 polymer blend resins, 272–3
 solid-state NMR of, 171–9
 deuterium, 179
 high resolution, 173–8
 urea-formaldehyde, 203–24
- Orientation anisotropy, 137–9
- Orientation methods, 142–4
 CHAPSO, 143
 DMPC, 143
 shear, 143–4
- Peak simulation, 336
- Peptides, 123–67
- Perdrew correlation potentials, 116
- Pf1 virus, 130
- Phenol-formaldehyde resins, 185–203
 curing of, 186–97
 stability of, 201–3
 thermal decomposition, 197–201
- PhoE porin, 134
- 7-Phosphanorobornenes, 100–6
- Phosphatidylcholine, 161
- Phospholipase A, 134
- Pino model, 359
- Polyamide-6, 273–4
- Poly(*p,p*-biphenylene terephthalate),
 267
- Poly(1-butene), 327, 354–63
 regioirregularity, 360–3
 stereoirregularity, 354–60
- Poly(1-butene) copolymers, 391–401
- Poly(butylene terephthalate), 261–2
- Poly(*N,N*-dimethylacrylamide), 272
- Polyester resins, 261–9
- Poly(ethylene terephthalate), 266–7,
 272–3
- Poly(1-heptene), 363–5
- Poly(1-hexene), 363–5
- Poly(β -hydroxyalkanoate), 267
- Polymer-blend resins, 272–3
- Polymer chain microstructure, 288–96
 copolymer monomer sequence,
 293–6
 homopolymer tacticity, 288–93
- Polymer end-groups, 297–317
 and non-NMR methods, 310–12
 chain-end structure, 303–7
 initiation efficiency, 308–12
 initiation mechanisms, 303–7
 monomer reactivity, in
 copolymerization, 312–16
 and non-NMR methods, 315–16
 polymer properties, 316
 radical–radical reactions, 307
- Polymer stereochemistry, 288–293
 terminology in, 289
- Polymerization, mechanisms of, 335–6
- Polymers, properties of, 316

- Polymers, synthetic, 283–323
 Poly(3-methyl-1-butene), 365–9
 Poly(α -methyl- α -*n*-ethyl- β -propiolactone), 267
 Poly(methyl methacrylate) (PMMA), 289–93
 Poly(1-nonene), 363–5
 Poly(1-octene), 363–5
 Polyolefins, 339–69
 PHEP, 363–5
 PHEX, 363–5
 PN, 363–5
 PO, 363–5
 poly(1-butene), 354–63
 polypropylene, 339–54
 PPE, 363–5
 Polyolefins, ^{13}C NMR assignments, 325–404
 Poly(*p*-oxybenzoate), 267
 Poly(1-pentene), 363–5
 Polypeptides, *see* Peptides
 Polypivalolactone polymorphs, 267
 Polypropylene, 339–54
 chain end, 352–4
 regioirregularity, 345–52
 stereoirregularity, 339–44
 Polyurethane phase separation, 239–45
 Polyurethanes, 226
 Post-Hartree-Fock, *see* Hartree-Fock theory
 Protein-lipid bilayer, 127–8
 Protein-solvent interactions, 126–8
 Proteins, 123–67

 Radical polymerizations, 301
 Radical-radical reactions, 307–8
 Relative reactivity, of monomers, copolymerization, 312–16
 non-NMR methods, 315–16
 Remote bond extension, 17–19
 Resins, *see* Organic resins
 Rotational isomeric state (RIS) model, 331–3
 γ -shielding effect, 333–5

 Scaling, intermolecular shielding, 21–2, 54–8
 Schiff's base, 129
 SCRF, *see* Self-consistent reaction field
 SDS, 147
 Second Order LORG (SOLO) 4, 21, 54, 107, 109–12

 Self-consistent field approaches, shielding calculations, 82–106
 atoms in molecules approach, 95–7
 large system, 84–8
 locally dense basis sets, 90–4
 orbital shielding analysis, 100–7
 reaction field, 88–90
 theoretical, 82–4
 water cluster, 98–100
 Self-consistent reaction field, 88–90
 Shear, 143–4
 Shielding *ab initio* calculations, 71–122
 correlation effects, 106–17
 density functional theory, 115–17
 GIAO MP2, 107–9
 multiconfiguration IGLO, 112–15
 SOLO, 109–12
 problems in, 72–5
 self-consistent field approaches, 102–6
 atoms in molecules approach, 95–7
 large system, 84–8
 locally dense basis sets, 90–4
 orbital shielding analysis, 100–7
 reaction field, 88–90
 theoretical, 82–4
 water cluster, 98–100
 theory, 75–81
 Shielding surfaces, 4–29
 electric field effects, 25–7
 global shape for traces on, 27–9
 intermolecular, 19–24
 intramolecular, 5–19
 Shielding tensors, 137–42
 averaging of, 140–2
 characterization of, 137–9
 orientation anisotropy, 137–9
 sensitivity of, 139–40
 Short-range shielding effects, 51–3
 Sodium dodecyl sulphate, 147
 Solid-state NMR spectroscopy, 135–44
 interactions, 135–7
 isotopic labelling, 144
 tensors, 137–42
 averaging, 140–2
 characterization, 137–9
 orientation anisotropy, 137–9
 sensitivity, 139–40
 Solid-state NMR spectroscopy, organic resins, 171–285
 of cyanate resins, 269–71
 of epoxy resins, 258–61

- of furfuryl alcohol resins, 180–5
- of isocyanate-derived resins, 225–45
- of nylons, 245–57
 - ^{13}C , 245–9
 - ^2H , 256–7
 - ^{15}N , 249–56
- of phenol-formaldehyde resins, 185–203
- of polyester resins, 261–9
- of resins in composite materials, 273–4
- of resins in polymer blends, 272–3
- urea-formaldehyde resins, 203–24
 - see also* High resolution solid-state NMR, organic resins
- Solution NMR, 132–4
- Solvents, protein interactions with, 126–8
- Sorbate-sorbate interaction, 42–4
- Spectral subtraction, 297
- Spin trapping, 315–16
- Staphylococcal nuclease, 61–2
- Starch, 272
- Structural biology, 123–8
 - anisotropic environments, 128
 - dynamic characterization, 124–5
 - high resolution, 125–6
 - protein-solvent interactions, 126–8
- Suter-Flory RIS model, 341
- Synthetic membranes, 123–67
 - viral coat proteins, 146–7
- Synthetic polymers, 287–323
 - and shielding, in a molecule, 30–5
 - solid state ^2H NMR, nylons, 256–7
- Tetraglycidyl(diaminodiphenyl)-methane, 258–9
- Tetrahydrofuran, *see* THF
- TFE, and protein-solvent interactions, 127
- THF, 131
- Three-dimensional crystallization, 134
- 2,4-Toluenediyl diisocyanate, 242–4
- Torsion angles, 142
- Trans* conformation, 12
- Two-dimensional crystallization, 134
- Two-dimensional INADEQUATE, *see* INADEQUATE
- Two-dimensional NMR, 291, 299
- Urea-formaldehyde resins, 203–24
 - ^{13}C CP-MAS NMR of, 205–18
 - ^{15}N CP-MAS NMR of, 218–22
 - stability, and hydrolysis, 222–4
- Variable contact time, 174
- Vibration correction, 33–4
- Viral coat proteins, 130, 146–8
 - membranes, 146–7
- Water cluster calculation, 98–100
- Water, and protein-solvent interactions, 126–7
- Xenon, 42–7
- X-ray crystallography, 132
- Zeolites, xenon in, 42–7
- Ziegler-Natta catalytic systems, 335
- Z-surfaces, 63
- Temperature, 73, 137–8
 - and curved phenolic resins, 197–200
 - gramicidin dynamics and, 157–8
 - polyurethane and, 244–5
 - Rising Elution Fractionation, 336

This Page Intentionally Left Blank